Study of viscous and viscoelastic flows with reference to laminar stirred vessels

Hall, James Joseph

Study of viscous and viscoelastic flows with reference to laminar stirred vessels

James J Hall

A thesis submitted for the degree of

Doctor of Philosophy

to the Faculty of Engineering

University of London

Department of Mechanical Engineering

King's College London

September 2005

To Mum and Dad

Abstract

This thesis describes a numerical and experimental investigation into the flow behaviour of Newtonian and viscoelastic fluids to improve understanding of their flow behaviour in relation to laminar mixing operations in stirred vessels.

First, through rheometric experimentation the flow behaviour of viscoelastic polyisobutylene solutions is characterised under simple shear deformation. These data provide essential understanding of the fluids' properties and quantification of the fluid parameters needed for the formulation of related constitutive models. These models are then optimised to obtain accurate predictions for the linear and non-linear properties of the fluids.

Subsequently, simulations of the flow of viscoelastic fluids were made for a range of fluid properties and flow geometries. However, simulations were possible only over idealised blade/baffle geometries, due to numerical limitations and the very substantial computational cost involved. These simulations provide an insight into the flow behaviour of these fluids, and in particular, help to differentiate between viscous and elastic forces such as, creeping flow and elastic recoil, and between non-linear effects such as, changes in shear and elongational viscosity, and normal stress differences, which are predominant in dynamic mixing processes.

In the third part of the work, extensive experimental studies of laminar mixing in stirred tanks were performed. Ensemble averaged, time-resolved and phase-resolved (ensemble-averages over 1^0 of impeller shaft revolution) measurements of the velocity variations were obtained by laser-Doppler anemometry in a mixing vessel of 80.5 mm diameter, stirred by a Rushton impeller. The ensemble-average measurements show a change in the angle of discharge from the impeller blade as the flows become increasingly more laminar. Additionally, inward pumping is prevalent at low Reynolds numbers (Re), in the vicinity of the impeller blades. Comparison of phase-resolved measurements for viscoelastic and Newtonian fluids shows significant differences in the impeller pumping behaviour due to the viscoelasticity of the former. Non-Newtonian fluids show evidence of a chaotic

motion in the vicinity of the blade, as revealed by the energy spectra obtained from the time-resolved measurements.

The implications of the experimental and simulation results for laminar non-Newtonian fluid mixing and for the further development of modelling approaches are discussed.

Acknowledgements

The results described in this thesis could only have been achieved by the co-operation and assistance of a number of people during the course of the research and the preparation of the thesis. First of all I would like to thank Professor M. Yianneskis who enthusiastically supported my work and provided constant supervision, encouragement, guidance and valuable advice and criticism. Among many other things, he gave me confidence and a belief in myself which allowed me to enjoy and savour special moments of the PhD. Without him, this research could not have been done.

I am very grateful to Dr Andrea Ducci, not only for his assistance and expert knowledge of LDA generously given, but for his lively demeanor and 'Italian' humour which made the long hours in the lab very enjoyable. Also, to Dr M. Micheletti for her help with, and introduction to, the experimental setup, and to Dr L Jupp and Dr Xue-Feng Yuan for their advice on the numerical work and relevant discussions.

My thanks go to Julian Greenberg for his assistance with all types of technical problems, at all times, and to all my work colleagues for numerous stimulating discussions; in particular I would like to acknowledge, Bilge Alban, Sandro Baldi, Christina Giannopapa, Hung Mak, Michail Stavropoulos and Paul Ward.

I should also like to thank King's College London and the Engineering and Physical Sciences Research Council for funding this research.

I would like to acknowledge all my closest friends, in particular my sister Katherine, for their continued moral support and all the exciting, fun times we spent together outside of my 'Viscoelastic World'.

Finally, enormous thanks must go to my Mum and Dad, to whom I am eternally grateful for their empathy, understanding and encouragement, and unyielding support and generosity, from beginning to end.

Contents

List of Figures

List of Tables

Nomenclature

ROMAN CHARACTERS

Symbols		Units
a	Viscoelastic slip parameter	-
a_{Tp}	Time-Temperature superposition shift factor	-
A	Non-linear viscoelastic term	-
b	Diameter of the focused laser beams	m
b_0	Diameter of the beam leaving the laser probe	m
b_x	Length of the measurement volume	m
b_y	Diameter of the measurement volume	m
B_t	Thickness of the baffles	m
B_w	Width of baffles	m
C	Minimum clearance distance between the bottom of the mixing vessel and the blades of the impeller	m
D	Diameter of the Rushton impeller and the height of the blade/baffle in the CFD geometry	m
$\mathbf{D}$	Strain rate tensor	s^{-1}
De	Deborah number	-
E	Beam expansion factor	-
$E(f)$	Energy spectrum (power spectral density) function calculated from resampled data	m^2s^{-1}
E_r	Percentage error	%
f	Frequency	Hz
f_D	Doppler frequency	Hz
f_{lens}	Focal length of the laser probe lens	m
f_s	Frequency shift	Hz
Fl	Flow number	-
Fl_c	Circulation flow number	-
G'	Elastic storage modulus	Pa
G''	Elastic loss modulus	Pa

Symbols		Units
G_k	Modulus of elasticity at each viscoelastic mode	Pa
h	Height of the small channel in the contraction flow geometry (CFD)	m
H	Height of the mixing vessel	m
H_1	Height of the blade/baffle geometry (CFD)	m
H_2	Height of the blade/baffle geometry, when the blade is coincident with the baffle (CFD)	m
I	Unit matrix	-
J	Inter-cylinder spacing distance	m
L_{circ}	Approximate length (in the x-direction) of the circulation region behind the blade (CFD)	-
$M_{i\phi}$	Number of samples at each impeller blade/baffle interval	-
M_i	Number of samples	-
M_k	Number of viscoelastic modes	-
n	Index of refraction	-
N	Impeller rotational speed	rev/s
N_1	First normal stress difference	Pa
N_2	Second normal stress difference	Pa
p	Pressure field (CFD)	Pa
P	Power drawn by the impeller	$Watts$
P_0	Power number	-
Q	Impeller pumping capacity	m^3s^{-1}
Q_c	Impeller circulation pumping capacity	m^3s^{-1}
r	Radial co-ordinate of the measurement volume	m
R	Cylinder radius (CFD)	m
Re	Reynolds number	-
t	Time	s
t_b	Impeller blade thickness	m
t_d	Impeller blade disk thickness	m
T	Diameter of the mixing vessel	m
T_p	Temperature	^0C

Symbols		Units
T_{p0}	Reference temperature	$25\ ^0C$
$< u >$	Mean velocity in the positive x direction (CFD)	ms^{-1}
u'_r	Radial r.m.s. velocity level	ms^{-1}
$u'_r(\phi)$	Radial r.m.s. velocity level at blade angle, ϕ	ms^{-1}
u'_z	Axial r.m.s. velocity level	ms^{-1}
$u'_z(\phi)$	Axial r.m.s. velocity level at blade angle, ϕ	ms^{-1}
U	Axial velocity (CFD), equal to v_x	ms^{-1}
U_θ	Instantaneous tangential velocity	ms^{-1}
U_r	Instantaneous radial velocity	ms^{-1}
U_z	Instantaneous axial velocity	ms^{-1}
$< U_r >$	Mean radial velocity	ms^{-1}
$< U_r(\phi) >$	Mean radial velocity at blade angle, ϕ	ms^{-1}
$< U_z >$	Mean axial velocity	ms^{-1}
$< U_z(\phi) >$	Mean axial velocity at blade angle, ϕ	ms^{-1}
v	Velocity field (CFD)	ms^{-1}
$v_{x,y,z}$	Component of velocity in the x, y or z direction (CFD)	ms^{-1}
V_{tip}	Impeller tip speed	ms^{-1}
W_{circ}	Approximate width (in the y-direction) of the circulation region behind the blade (CFD)	-
x, y, z	Traversing directions of the laser probe and co-ordinate axes of the CFD geometries	-
z	Axial co-ordinate of the measurement volume	m
z_1	Bottom right corner of the impeller blade	-
z_2	Top right corner of the impeller blade	-
z_a	The point of zero velocity below the impeller blade	-
z_b	The point of zero velocity above the impeller blade	-
Z_c	Function of confidence level (see equations 2.11 and 2.12)	-

GREEK CHARACTERS

Symbols		Units
α	Non-linear viscoelastic material parameter (Giesekus model)	-
$\bar{\lambda}$	Zero-shear averaged time constant	s
$\beta_{1,2,3}$	Positions in the blade/baffle geometry (CFD)	-
Δt	Time step size	s
δx	Cell size in the direction of the velocity	m
$\vec{\nabla}\cdot$	Divergence operator	m^{-1}
$\dot{\gamma}$	Shear strain rate	s^{-1}
$\dot{\gamma}_a$	Apparent shear strain rate	s^{-1}
$\dot{\varepsilon}$	Elongation strain rate	s^{-1}
ϵ	Non-linear viscoelastic material parameter (PTT model)	-
ϵ_d	Rate of dissipation of kinetic energy of turbulence	m^2s^{-3}
η	Dynamic shear viscosity	$Pa.s$
η'	$\frac{G''}{\omega}$	$Pa.s$
η''	$\frac{G'}{\omega}$	$Pa.s$
η^*	Complex viscosity	$Pa.s$
η^+	Dynamic transient shear viscosity	$Pa.s$
η_0	Dynamic zero-shear viscosity	$Pa.s$
η_N	Dynamic Newtonian shear viscosity	$Pa.s$
η_e	Dynamic elongation viscosity	$Pa.s$
η_k	Dynamic viscoelastic shear viscosity, at each viscoelastic mode, k, where, $\eta_k = \frac{G_k}{\lambda_k}$	$Pa.s$
$\frac{\delta}{\delta t}$	Viscoelastic convective time derivative	s^{-1}
$\vec{\nabla}$	Gradient operator	m^{-1}
k	Laser beam intersection angle	0
Λ	Wavelength	m
Λ^*	Fringe spacing in the measurement volume	m
Λ_{blue}	Wavelength of blue light	m
Λ_{green}	Wavelength of green light	m
λ_k	Relaxation time of each viscoelastic mode	s

Symbols		Units
λ_{long}	Longest mode of relaxation	s
ν	Kinematic shear viscosity	m^2s^{-1}
ν_0	Kinematic zero-shear viscosity	m^2s^{-1}
ω	Frequency of oscillation (rheometer plates)	Hz
ϕ	Blade angle	^{0}
ρ	Fluid density	kgm^{-3}
σ	Total Cauchy stress tensor	Pa
σ_b	r.m.s. value due to broadening contribution	ms^{-1}
σ_d	Total measured r.m.s. value	ms^{-1}
$\sigma_{g,f,t,i}$	r.m.s. broadening contributions due to velocity gradient, small scale fluctuations within the measurement volume, finite transit time and finite instrument bandwidth, respectively	ms^{-1}
σ_{mv}	Standard deviation of Gaussian intensity distribution of the measurement volume	ms^{-1}
σ_v	r.m.s. due to flow turbulence	ms^{-1}
τ_0	Scaling stress value, see equation 4.5	Pa
$\tau_{Ek(1)}$	Upper convective, viscoelastic 'extra stress' time derivative	$Pa.s^{-1}$
τ_{Ek}	Viscoelastic 'extra stress' at each mode, k	Pa
$\tau_{Ek}^{(1)}$	Lower convective, viscoelastic 'extra stress' time derivative	$Pa.s^{-1}$
τ_E	Total viscoelastic 'extra stress' contribution	Pa
τ_N	Total Newtonian stress contribution	Pa
θ	Tangential co-ordinate of the measurement volume	^{0}

ABBREVIATIONS

BSA	Burst spectrum analyser
CFD	Computational fluid dynamics
Co	Courant number
FDM	Finite difference method
FEM	Finite element method
FFT	Fast-Fourier transform
FIB	Flow induced birefringence
FVM	Finite volume method
HDPE	High density polyethylene
JSN	Johnson-Segalman viscoelastic constitutive model
LDA	Laser-Doppler anemometry
LDPE	Low density polyethylene
p.d.f.	Probability density function
PBT	Pitched-blade turbine
PIB	Polyisobutylene
PIB100	Polyisobutylene, viscosity = 100 x water
PIB2000	Polyisobutylene, viscosity = 2000 x water
PISO	Algorithm: Pressure implicit with splitting of operators
PIV	Particle image velocimetry
PTT	Phan-Thien and Tanner viscoelastic constitutive model
r.m.s.	Root mean square
r.p.m.	Revolution per minute
Si100	Silicon oil, viscosity = 100 x water
Si1000	Silicon oil, viscosity = 1000 x water
TTS	Time-Temperature superposition
UCM	Upper convective Maxwell constitutive model

Chapter 1

Introduction

1.1 Background

Fluid mixing processes are encountered in the manufacture of a large range of products in industries such as, chemical, biochemical, pharmaceutical and food processing. Around 25 % of all process engineering operations involve the mixing of fluids in stirred vessels, which are generally used to homogenise immiscible liquids; blend polymers, pastes and solids; and disperse gases, etc. Often these processes are accompanied by highly complicated and intricate flow structures, even more so in the case of non-Newtonian fluids, which are commonly used to make products such as; detergents, plastics, drugs and a variety of food products. Because of this, the design of efficient mixing processes is a rather complex and multi-faceted task. The design is based on such macroscopic quantities as mixing time and power consumption, both of which are known to depend on flow patterns which themselves are influenced by the fluid rheology. Poorly designed mixing processes can cause substantial increases in waste production, formation of undesirable by-products and loss in processing time and capacity, all at the expense of valuable raw materials and desired products.

Mixing operations involve costs of around $ 1 billion per annum in the USA alone (Smith and Smit (1988)). Consequently, a substantial effort has been devoted to acquire an improved understanding of such processes for both single- and multi-phase flows (see, for example, Tatterson (1991)). Studies of Newtonian fluids under transitional to turbulent flow conditions have received much attention by, for example, Hockey and Nouri (1996), Lee (1995), Nienow (1997) and Yianneskis et al. (1987). However, laminar mixing may be necessary in some cases as high rates of stirring are impractical in many applications, such as, dispersing particles or releasing bubbles from viscous liquids, manufacturing ointments

and creams, and in biochemical applications in which the constituent parts to be mixed may be shear-sensitive (e.g. macromolecules and fibres). Process-specific design of mixing vessels is sometimes impractical as industrial needs often require that equipment as generic as possible be employed for as many applications as is practical; consequently many stirred tanks intended for high shear turbulent flow applications may also find use in high viscosity or shear-sensitive mixing. Some polymerization processes involve high viscosity liquids (100 $Pa.s$ or more), relatively small mixers (especially for lab-scale tests) and low stirring rates.

Laminar mixing of Newtonian fluids in stirred vessels has not been studied as extensively as turbulent mixing but involves interesting phenomena. Kuncewicz (1992) and Dong et al. (1994), among others, have shown that segregated regions can exist in a stirred vessel for Reynolds numbers below 500, that can act as a barrier to mixing, with an associated increase of mixing time and by-products in industrial applications.

The vast majority of the reported studies have been concerned with Newtonian fluids, although many, if not most, fluids in industrial practice are non-Newtonian in nature. The mixing of complex, non-Newtonian, fluids in stirred tanks presents nevertheless significant challenges over and above those associated with similar flows of Newtonian fluids. Although many complex fluids exhibit high viscosities and the related flows are laminar in most, if not all regions of a stirred tank, the wide range of shear rates encountered in a vessel are accompanied by large fluid property variations. The rheology of most complex fluids is such that at low shear rates their behaviour is essentially Newtonian, while at higher rates it becomes increasingly non-Newtonian. Consequently, in view of the range of shear rates encountered in a stirred vessel as well as in many other flows, it is instructive to study viscous Newtonian fluids of similar viscosities and under similar flow conditions to those of the non-Newtonian ones, so as to facilitate interpretation and comparison of those characteristics stemming from viscous and those from non-Newtonian effects.

The handling of highly viscous fluids presents interesting and complex problems for both the fundamental understanding of the flows as well as of their practical implications for mixing process design. Processing of such fluids is en-

countered in commercial applications such as polysaccharide fermentations, distribution of additives in pastes and paint and vaccine production, to mention but a few. However, the generation of regions of poor mixing and of inhomogeneous distribution of reactants in such systems, in addition to the rheological behaviour complexities present when such fluids exhibit non-Newtonian behaviour, makes scale-up of such processes a complex task and limits the number of engineering tools that may be employed to improve process design. Slow mixing regions are normally formed around the impellers at low agitation rates and the size, shape and location of such regions is non-intuitive (Szalai et al., 2004).

As most viscous liquids, both Newtonian and non-Newtonian, are materials of relatively high costs and may involve complex formulation technology, the considerations applicable to thin Newtonian liquid mixing are not always relevant. Whereas for turbulent mixing, extending the mixing time and/or increasing rotational speed can often provide more rapid mixing and homogeneity, and power per unit volume and the costs of the mixing equipment are important factors in the design of turbulent mixing processes, this is not the case with viscous mixing where raw material cost and product quality are paramount.

Nevertheless, relatively little scientific effort has been expended on the behaviour and mixing of non-Newtonian fluids in comparison to those of Newtonian ones. Power consumption in non-Newtonian viscous and creeping flow can be predicted through primarily empirical correlations based on experimental data, see, for example, Tatterson (1991), but the development of new processes requires new experimentation and/or computer simulations. However, as simulations of such fluids are still full of uncertainties and approximations, there is urgent need for appropriate and more sophisticated numerical models to eliminate the need for measurement data for every new fluid/mixing configuration encountered in practice. Although the steady flow characteristics of laminar processes greatly facilitate both numerical modelling and experimentation, the lack of turbulent eddies in laminar mixing of such fluids, as well as the low diffusion coefficients make such mixing an area-controlled process: the interfacial area that can be made available through stirring must be maximized so that diffusion is enhanced and mixing is more effectively accomplished. Along with the non-linear behaviour

of the non-Newtonian fluids, the difficulties involved in the theoretical treatment of such flows have resulted in most cases in the study not of the full mixing environment (e.g. vessel and impeller), but of highly simplified situations, that closely mimic industrial flow conditions such as the fundamentals of extensional flow mixing, striation generation in idealized situations and similar topics (see, for example, the information provided by two of the most frequently used handbooks by Tatterson (1991), chapter 5 of this thesis, or the most recent handbook by Paul et al. (2004).).

The simulation of mixing of such fluids necessitates not only the development of rheological and molecular dynamics modelling approaches but also their implementation in the complex geometries of the vessels. Taking into account that typical calculation times, for even simple flows of such fluids, are of the order of weeks, for the simple two-dimensional flow past a cylinder in creeping flow (Baaijens, 1994b), a rigorous simulation of a stirred vessel flow is beyond the capabilities of most present computing systems and would require use of large clusters of machines for prohibitively long times.

Consequently, the research methodology adopted in the present work is twofold. First, rigorous modelling approaches are developed for complex fluids in simple flow situations that can offer insights into the dynamics of the flows and their implications for parts of a stirred vessel, such as the flow over a simplified representation of an impeller blade or baffle. The methodologies developed need however to be assessed through comparisons with experimental data and flow cases for which such data is available. Flows past a cylinder, past arrays of cylinders and through an expansion and/or contraction have been well documented experimentally and numerically and offer a suitable testing ground for the development and validation of the modelling methodology. They have been therefore selected for the first stage of the modelling work presented in this thesis. Subsequently, the flows past a two-dimensional blade/baffle are modelled to enable useful insights to be obtained for the results to be acquired in stirred vessels. In view of the aforementioned computing time limitations, the latter can only be acquired at present through experimentation and thus the second part of the approach adopted involves measurements of the flow of complex fluids in stirred

tanks.

The mixing vessel and impeller geometry selected for study is the 'standard configuration', with a Rushton impeller of diameter $D/T = 0.33$ set at a clearance $C = T/3 = 0.33$, as there is a plethora of similar data for both laminar (Lamberto et al. (1999) and Nouri and Whitelaw (1990b)) and turbulent flows (Lee (1995) and Yianneskis et al. (1987)) of Newtonian fluids in such a geometry. In this way comparisons can be made and differences stemming from the non-Newtonian nature of the stirred fluid can be identified which can be utilised for both the optimisation and design of related mixing processes and the identification of flow features that could be studied through simulation in future work.

1.2 Description and modelling of non-Newtonian fluids

Non-Newtonian, or complex fluids, are ones that do not obey Newton's law for a viscous fluid. A pseudoplastic, or shear thinning fluid is one example where the shear rate dependent viscosity, $\eta(\dot{\gamma})$, decreases with increasing shear rate, examples are polyethylene, polyacrylamide in water and most polymer solutions and melts. Nouri and Whitelaw (1990b) revealed changing flow patterns in a mixing vessel for a shear thinning CMC (sodium-carboxmethyl cellulose) solution. Dilatant, or shear thickening fluids behave oppositely, having a shear rate dependent viscosity that increases with increasing shear rate, an example is a suspension of titanium dioxide in a sucrose solution (Metzner and Whitlock, 1958). Other examples are; (i) viscoplastic fluids, which are those where a critical shear stress (or yield stress) has to be attained for fluid movement to begin, examples are certain types of paints and pastes, and toothpaste, which is frequently called a 'Bingham' fluid; (ii) thixotropic fluids which are those that show a decrease in viscosity with time at a constant rate of shear, followed by a gradual recovery when the motion is stopped; (iii) rheopectic fluids which show the opposite behaviour and; (iv) viscoelastic fluids, which are the focus of this study and exhibit viscous and elastic properties, for instance, creeping and elastic recoil, which describes a near solid that goes on deforming under constant stress and a near liquid that recovers part

of its deformation after the imposing stress has been removed, respectively. In addition, non-Newtonian flows can exhibit changes in values for; (i) the first and second normal stress differences, $N_1(\dot{\gamma})$ and $N_2(\dot{\gamma})$, respectively, and; (ii) elongational viscosity, $\eta_e(\dot{\varepsilon})$, at high rates of deformation. These material parameters are all defined, along with others, in chapter 3. For a comprehensive discussion of these and other non-Newtonian fluid behaviour, see Bird et al. (1987).

This treatise primarily studies the flow behaviour of polymeric solutions, composed of polyisobutylene (PIB), a synthetic and impermeable rubber (used for common purposes such as the inner lining of tires and basketballs), dissolved in a solvent. Very small quantities of PIB are dissolved in a solvent such as tetradecane or decalin and the solution shows viscoelastic, shear thinning, normal stress difference effects and changes in elongational viscosity. The combination of these effects have shown flow phenomena such as 'die swell' and 'rod climbing' (Bird et al., 1987).

The equations governing the dynamics of viscoelastic fluids are formulated microscopically and/or macroscopically. The former refers to kinetic theories such as the Elastic Dumbbell model (Larson, 1999) and the latter to constitutive equations of continuum mechanics such as the Giesekus model (see next paragraph). Although numerical predictions can be obtained through microscopic simulations, this work is not within the scope of this treatise and therefore not described here. However, it is noteworthy to observe that almost all constitutive equations used today can be derived from kinetic theories. Macroscopic simulations involve the coupling of the constitutive equation for the polymer stress with the Navier-Stokes equations, which has been developed over many years for low molecular weight/Newtonian fluids and details of the coupling of these equations are given in chapter 2.

The search for appropriate constitutive equations for polymer solutions is a major research challenge for rheologists. Attempts to describe their complex flow behaviour have lead to the proposition of numerous and diverse constitutive equations. A detailed discussion of most of the models that have been proposed in the past can be found in, for example Bird et al. (1987) and Larson (1999) but for an overview of some of the available models, see table 1.1. It is also

noteworthy to observe that only partial differential models are covered in this study, as opposed to integral models, as they are easier to implement and proven to be less demanding, numerically (Bird et al., 1987). The Generalised Newtonian models (see table 1.1) are the most simple class of non-Newtonian models, they only describe the strain rate dependence of the viscosity, but neither normal stresses or any other non-Newtonian effects are included. However, linear viscoelastic, retarded motion expansion and quasi-linear models (see table 1.1) are designed to incorporate viscoelasticity and small changes in normal stress difference effects but it is only the most sophisticated non-linear viscoelastic models (e.g. JSN, Giesekus and PTT) that have proven to successfully predict and accurately capture, over a range of shear rates; (i) non-linear flow behaviour, such as those exhibited by, $\eta(\dot{\gamma})$, N_1 and $\eta_\varepsilon(\dot{\varepsilon})$, and; (ii) fluid flow behaviour in arbitrary geometries, such as the benchmark, flow past a cylinder case (Baaijens, 1994b).

The appropriate equations chosen for the present investigation of a polyisobutylene solution are based on the findings of many researchers, such as, Baaijens (1994b), Barakos and Mitsoulis (1995), Bird et al. (1987), Larson (1999), Phan-Thien and Dou (1999) and Quinzani et al. (1995), which concluded that the non-linear viscoelastic Giesekus and PTT models are the most suitable for polymer solutions. Chapter 2 provides a detailed description of these models and how they are implemented and solved numerically. Chapter 3 compares the performance of these models for each of the polyisobutylene solutions under simple deformation which are subsequently implemented for benchmark geometries in chapters 4 and 5.

1.3 Literature review

During the past few years there has been growing awareness of problems related to incomplete or inefficient mixing in the laminar flow regime and consequently an increasing number of publications have concentrated on low Reynolds number flows. Laminar mixing of even Newtonian fluids in stirred tanks presents significant differences from turbulent mixing, with chaotic flows being present (Lamberto et al., 1999) or flow direction changes (Bartels, 1988) that are not

fully understood. Lamberto et al. (1999) investigated the laminar flow structure in an unbaffled stirred vessel mixed by a Rushton impeller and reported that for low Reynolds numbers ($5 < Re < 100$), the position and size of circulation regions, above and below the impeller, that were segregated from the rest of the flow, were dependent on Re and their position relative to that of the impeller blades. These regions exchanged material with the bulk flow only through diffusion and consequently large concentration gradients that persisted for several hours of mixing. The circulation flow was also quantified and found to be 4 times the pumping capacity of the impeller. Szalai et al. (2004) analysed laminar mixing in a tank stirred with four Ekato Intermig impellers and showed the problems encountered achieving homogeneous mixing at low Re. The problem was attributed to severe fluid compartmentalisation creating a significant barrier to mixing in the axial direction; varying the agitation rate at periodic intervals was one proposed solution to this. Zalc et al. (2002) make an interesting and counter-intuitive observation that higher Re does not necessarily lead to more efficient mixing and found that optimal injection locations and mixing rates showed a non-trivial dependence on Re. Dyster et al. (1993) studied the radial discharge flows from a Rushton turbine impeller and for $Re \leq\sim 20$, showed that: $Fl \propto Re$ and $Po \propto Re^{-1}$, where Fl and Po are the Flow and Power numbers, respectively:

$$Fl = \frac{Q}{ND^3} \tag{1.1}$$

and:

$$P_0 = \frac{P}{\rho N^3 D^5} \tag{1.2}$$

where; N is the impeller rotational speed in rev/s; D the impeller diameter in m; ρ the density of the fluid in kgm^{-3}; P the power drawn by the impeller in $Watts$, and; Q the impeller pumping capacity in m^3s^{-1}.

One significant difference that has been reported for laminar fluid mixing in stirred tanks in comparison to the turbulent flows is a change in flow pattern as Re is decreased. This was observed with axial (pitched-blade) turbines: Hockey et al. (1989) found through flow visualisation tests that the predominantly axial flow from a pitched-blade turbine (PBT) became mainly radial as Re was decreased and the angle at which the flow left the turbine varied with Re. In a related

investigation, Hockey and Nouri (1996) reported a sudden drop in power number at $Re = 1200$ in a 294 mm diameter vessel stirred by a PBT ($D = T/3$) and associated this drop with the transition from radial (at lower Re) to axial (at higher Re) flow pattern mentioned earlier. Interestingly, Distlehoff et al. (1995) experimenting with a geometrically similar vessel and impeller but 50 % smaller ($T = 147$ mm) found the drop in power number to occur at $Re = 650$, i.e. half of the Re value of Hockey and Nouri (1996); the latter comment that the dependency of flow transition on Re for different impeller sizes was not surprising as both Reynolds numbers yield the same tip velocity, and velocity and pressure fields around the blades were similar, and that there is direct proportionality, therefore, of transition to impeller size. Hockey and Nouri (1996) stated rather confusingly that the transition was quantified by the velocity measurements of Nouri and Whitelaw (1990a), but that investigation was only concerned with Rushton impeller measurements and there is no evidence of any change in flow direction whatsoever in the paper; indeed all the data presented are for two vessel sizes and are very similar. No similar changes in flow pattern have been reported with the Rushton or other radial flow impellers.

Flow behaviour is complicated further when non-Newtonian fluids are mixed and with this in mind, some researchers have investigated the flow behaviour of such fluids in parallel with that of a Newtonian fluid to more easily observe highly non-Newtonian behaviour. For instance, Bartels (1988) reported mean radial velocities in the impeller stream of a Rushton turbine, for; (i) a Newtonian (a glycerine and water mixture) and; (ii) a non-Newtonian, viscoelastic solution (polyacrylamide); by comparison the latter showed flow reversal near the impeller. While Greene et al. (1982) studied the mixing of water (Newtonian) and aqueous polyacrylamide solution by an axial flow impeller (a 6-blade PBT) and observed an increase of the impeller discharge angle with increasing concentrations of polyacrylamide. Both viscoelastic behaviours were attributed to the viscoelastic and N_1 effects in the fluid. For such fluids, the first normal stress difference is reported to have the highest value near the impeller and the lowest near the wall (Ulbrecht and Carreau, 1985) and the elastic force which opposes the centrifugal one, if it is sufficiently high, will overcome the inertial

force resulting in a decreased pumping capacity and even an inward flow towards the impeller blades, and an outward flow above and below the blades, in the case of a Rushton turbine.

In the laminar mixing of both Newtonian and non-Newtonian fluids in stirred vessels there are changes of flow pattern with Reynolds number that are not well understood. Such changes are evident from quantities such as the flow number (Fl) that indicates the pumping capacity of an impeller. These changes indicate the developing behaviour of the flow at low Re. For example, Fl for Newtonian fluids was reported to be proportional to $Re^{0.2}$ for $12 < Re < 14000$ and to $Re^{0.5}$ for $1.5 < Re < 12$ by Dyster et al. (1993), while for shear-thinning fluids Koutsakos et al. (1990) found that Fl was proportional to Re for $10 < Re < 14$ and to $Re^{0.2}$ for $14 > Re > 800$. However, Venneker (1999) reported that the variation of Fl with Re measured with non-Newtonian fluids did not deviate from those found with Newtonian fluids and suggested that the differences found by Koutsakos et al. (1990) may stem from the fact that three of the five liquids used by them had essentially the same flow index and that their fluids were not only shear-thinning but also viscoelastic. Venneker (1999) suggested that with the viscoelastic fluids the first normal stress difference may cause an inward flow near the impeller, reducing partly the inertia-driven flow and consequently the Fl. This is supported by the power consumption characteristics reported by Koutsakos et al. (1990) and Nienow et al. (1983), which showed an increase in power number in comparison to Newtonian fluids and this was attributed to the viscoelasticity of the fluids. Venneker (1999) reported that the flow index affected the width of the impeller discharge profile, which widened with decreasing index.

Much effort has been expended on the study of non-Newtonian fluid mixing, since the early work of Metzner and Taylor (1960), that reported that fluid shear rates decreased more rapidly with increasing distance from the impeller blades in pseudoplastic fluids than in Newtonian ones and that motion in a pseudoplastic fluid system increased exponentially with impeller speed, in contrast to the linear increase observed in Newtonian mixing. However, the findings reported are not always in agreement. For example, for pseudoplastic fluids, Kamiwano et al. (1990) reported that for $Re = 100$ both the apparent viscosity at the impeller

tip as well as the power versus Reynolds number curve were different to those suggested by earlier works by Mistubishi and Hirai (1969) based on a modified Reynolds number model, which they attributed to the simplification of the velocity distribution employed in the earlier work. It is important to note that as the viscosity of non-Newtonian fluids varies with the shear rate and therefore with *Re*, flow differences observed may be due to non-Newtonian effects as well as changes of *Re*. It is therefore essential, in order to separate such effects, to compare non-Newtonian fluid mixing results with those obtained with Newtonian fluids of similar (but constant) viscosity, and such comparisons therefore should form part of this work. The amount of data obtained to date with viscoelastic fluids is small, but these have shown significant differences with Newtonian fluid flows and are worthy of further study, especially for low *Re* flows/high viscosity fluids (Venneker, 1999).

Another issue of importance in laminar mixing is the effect that flow instabilities have on the overall mixing behaviour in a stirred tank. Such macro-instabilities stem from either precessional motions around the impeller shaft that are present in most swirling flow configurations (Nikiforaki et al., 2003), or geometry-specific instabilities (Galletti et al., 2004a), that are superimposed onto the precessional ones. Galletti et al. (2004b) reported that precessional instabilities are present under laminar flow conditions as well, but occur at a higher frequency than turbulent flow instabilities. Such instabilities can be very important for laminar mixing as Lamberto et al. (1996) have shown that using time-dependent impeller speed variations can enhance mixing in stirred vessels by breaking up segregated regions and a similar effect may be achieved by flow instabilities.

An important implication of mixing non-Newtonian fluids in comparison to similar but Newtonian laminar flows is that the non-linear rheology of the fluid may trigger chaotic flow behaviour. Alvarez et al. (2002) have given indications of such behaviour from visualisations of the flow of non-Newtonian fluids in stirred tanks; they investigated the mechanisms of mixing and the creation of structures in laminar stirred vessels for Newtonian and non-Newtonian fluids and focused on the importance of chaotic mixing. Consequently, non-Newtonian mixing in stirred

tanks, is likely to take place in a non-intuitive manner that deserves extensive study.

In relation to this, there is increasing evidence that efficient convective mixing in stirred tanks operated in laminar flow conditions may only be possible in the presence of chaos (Harvey et al. (2000), Lamberto et al. (1996) and Lamberto (1997)). But only from experiments is it possible to view such behaviour for viscoelastic fluids, due to the complications encountered when attempting to simulate chaotic flow phenomena.

As the simulation of non-Newtonian mixing in complex geometry vessels is not feasible at present, as mentioned earlier, a number of researchers have attempted to couple numerical and experimental studies of fluid mixing of non-Newtonian fluids by concentrating primarily on simple geometries: Eccentric cylinder or journal bearing flow mixers (Leong and Ottino (1989), Leong and Ottino (1990), Anderson et al. (2000a), Anderson et al. (2000b) and Jana et al. (1994)) and lid-driven cavity mixers (Swanson and Ottino (1990), Niederkorn and Ottino (1993), Niederkorn and Ottino (1994), Kumar and Homsy (1996) and Fan et al. (2000)). This is due to their simplicity for use in simulations, the availability of analytical solutions for some fluid types and the relative ease of doing experimental validation experiments. The moving lid cavity mixer can be seen as a simplified two-dimensional representation of the flow channel in a single screw extruder, while the eccentric cylinder can be seen as a simplified stirrer in a tank. These geometries have been studied using the best available simulation techniques, i.e. FVM[1] (finite volume method), FEM[2] (finite element method) and FDM[3] (finite difference method), by the use of shear thinning inelastic fluids and constant viscosity quasi-linear elastic fluids (see table 1.1). The studies have shown shear thinning to have a generally detrimental effect on the mixing efficiency due to the increase in size and number of isolated islands in the flow and a reduction in the size of chaotic mixing zones in time-periodic flows.

Another example is of the work of Moore and Cossor (1995) who studied laminar flow velocity distributions of a yield stress fluid, in a stirred tank, for both a

[1]see Versteeg and Malalasekera (1995).

[2]see Stasa (1985).

[3]see Mitchell and Griffiths (1980).

Rushton and a pitched blade impeller. Firstly, using laser-Doppler anemometry (LDA) to obtain measurement data and secondly, by using two non-Newtonian models to obtain numerical predictions for; (i) a yield stress fluid (Bingham model) and; (ii) a Generalised non-Newtonian fluid (Power-law model). Due to the nature of the yield stress fluid, Moore and Cossor (1995) approximated the movement of the impeller by a rotating cylinder concentric to a stationary one (representing the outer wall of the vessel). The measured distribution of the predominantly tangential velocities on the centreline of each impeller was predicted by both models, and at certain impeller speeds the measurement data showed fluid velocity values falling to zero at a 'cavern boundary', which was predicted by the Bingham model. Present day, non-linear, viscoelastic models (such as those already introduced, see table 1.1) could not be expected to be used for these problems, to obtain predictions for viscoelastic fluids, such as those of this treatise, due to the models' inevitably high demands on computer resources and the likelyhood of numerical divergence at high flow rates (this is discussed in this chapter, and shown in chapters 4 and 5). Consequently, simpler flow approximations, such as those made in this thesis, are employed, to model, as accurately as possible, the mixing of the viscoelastic fluids.

Thakur et al. (2003) used torque measurement data to investigate the mixing of three Newtonian and two complex fluids (2 % xanthan solution and a polyacrylamide aqueous solution), using a flat-bladed impeller: power consumption and effective shear rate were quantified as functions of impeller geometry and pseudoplasticity in the laminar regime, and, by using the Power-law model for each fluid, they concluded that an estimation of the effective shear rate can be made independently of the fluid rheology. This research also confirmed that flat-bladed impellers could be valuable tools for dispersive mixing in highly shear-thinning fluids, as they maintained a high shear rate level (which, for the fluids of this treatise, can expect to cause havoc to the fluid), regardless of pseudoplasticity. The findings of this work appear rather surprising and do not seem to corroborate earlier works or be in accord with intuitive physical insight, as it might be reasonably expected that Power-law approaches should be affected by the fluid rheology. Such findings may partly be a result of the approximations enlisted in

simplified Power-law formulations and clearly a more rigorous treatment is called for.

However, a rigorous understanding of the effect of viscoelasticity remains elusive due to both the difficulties in using viscoelastic fluid models in simulations and the inability to clearly separate the effects caused by shear thinning and viscoelasticity in real fluids. For example, Niederkorn and Ottino (1993) found that the small variations in the velocity field caused by a mildly elastic Maxwell fluid model (see table 1.1) had a significant and negative impact on the mixing in eccentric cylinder flows that was confirmed in experiments with a matching Boger[4] fluid. In contrast, Kumar and Homsy (1996), found the viscoelasticity introduced by the Oldroyd-B fluid model increased the rate of chaotic mixing. Fan et al. (2000) duplicated the simulated condition of Niederkorn and Ottino (1993) using a more accurate simulation technique and found the Maxwell fluid to be nearly indistinguishable from the Newtonian case. They summarised the reason for the discrepancy between their results and the experiments of Niederkorn and Ottino (1993) was due to inaccuracies in the determination of the properties of the experimental fluid combined with the inability of the fluid models used in the simulation to take into account any shear thinning effects on the viscosity and normal stress differences found in the experimental fluid. Subsequently, researchers such as, Connelly and Kokini (2004) studied the effects of shear thinning and viscoelasticity, firstly with the use of the Oldroyd-B model and secondly with the more sophisticated Phan-Thien Tanner (PTT) model (for an arbitrary fluid) in a simplified, two-dimensional version of a commercial mixer, consisting of a paddle in a cylinder, and showed that the shear thinning and elastic effects caused changes in velocity profiles, which lead to changes in the mixing mechanism.

To the best knowledge of the author, only two papers can be found in the literature concerning the full three-dimensional flow simulation of viscoelastic fluids in a stirred vessel but neither with the use of non-linear viscoelastic models, only with simplified rheological models (Youcefi et al. (1997) and Anne-Archard and Boisson (1995)). In particular, simulations with the use of an Oldroyd-B model led to a rise of power consumption when the level of elasticity is increased (Anne-

[4]Fluids that are elastic but have a constant viscosity.

Archard and Boisson, 1995). Bertrand et al. (1999) carried out simulations and studied the effects of viscoelasticity of a second-order fluid on macroscopic quantities such as mixing time and power consumption and showed that a simple rheological model is capable of predicting a rise in power draw when the level of elasticity is increased. For three-dimensional simulations, over the range of flow rates shown, in most cases, good qualitative agreement is made with the experimental data. However, it is also true that differences, as large as approximately 30 % are shown by quantitative comparisons to the experimental data. These levels of inaccuracies are most probably the result of tackling three-dimensional problems with simplified rheological models.

The lack of numerical investigations of non-linear viscoelastic mixing flow, which has already been mentioned, can be explained: three-dimensional fluid flow simulations involving implicit non-linear viscoelastic equations, such as the PTT model, require large amounts of CPU time and can be intricate to perform due to the hyperbolic nature of the stress equation, which commonly shows numerical divergence at high deformation rates. For these reasons, many studies have dealt with two-dimensional benchmark flow geometries, such as, flow past a cylinder, flow past an array of cylinders and through contraction/expansion geometries to elucidate and hopefully resolve the problems encountered whilst trying to implement such models. Essentially, in a benchmark geometry the fluid is subjected to a combination of elongation and shear deformation, but to levels comparable to those encountered in more complex geometries such as a mixing vessel and therefore more effort can be focussed on the rheological characterisation of the fluid and the numerical methodologies employed to solve the equations.

Many experimental studies of non-Newtonian, viscoelastic fluids in benchmark geometries have been made with techniques such as laser-Doppler anemometry (LDA) and particle image velocimetry (PIV) for velocity measurement, and flow induced birefringence (FIB) for stress measurement, to validate an abundance of numerical predictions using a variety of constitutive models (some of which are outlined in table 1.1). The types of fluids studied also include other viscoelastic materials such as polymer melts, for example, low density polyethylene (LDPE) and high density polyethylene (HDPE): Hartt and Baird (1996) and Luo (1996)

obtained model predictions for the flow of a LDPE melt past a symmetrically confined cylinder and through a 5.75:1 abrupt circular contraction flow, respectively. In other cases, arbitrary fluids were studied, for example; Manica and De Bortoli (2004) simulated power-law fluids in two-dimensional 3:1 sudden expansion flows; Mitsoulis (2004) simulated a Bingham fluid past a two-dimensional symmetrically confined cylinder; Oliveira and Pinho (1999) and Sasmal (1995) obtained predictions for UCM and PTT model fluids through a two-dimensional 4:1 sudden contraction and; Wapperom and Renardy (2005) obtained predictions for UCM and Oldroyd-B model fluids past a two-dimensional symmetrically confined cylinder.

However, this literature review primarily concerns studies of polymeric solutions similar to those in this treatise, and benchmark geometries, namely, flow past a symmetrically confined cylinder, through a contraction and past an array of three symmetrically confined cylinder: Baaijens (1994b) reported FIB and LDA measurement data for 5 and 9 % PIB in tetradecane solution along with numerical predictions using the non-linear PTT and Giesekus models for flow past a symmetrically confined cylinder. To the best knowledge of the author this is the only measurement data available for similar fluids as those in this study and for this reason, the data are used to validate the respective numerical predictions obtained in chapter 4. A number of other studies used this measurement data, including Barakos and Mitsoulis (1995), Dou and Phan-Thien (1998) and Phan-Thien and Dou (1999) to validate predictions made using, among others, the Giesekus and PTT models. The work of the latter two studies was carried out using the finite volume method with an unstructured grid and the former using the finite element method with a structured grid. Barakos and Mitsoulis (1995) obtained stable and successfully validated numerical solutions for flow past a symmetrically confined cylinder, using K-BKZ[5] model predictions for velocity and stress values. Dou and Phan-Thien (1998) and Phan-Thien and Dou (1999) obtained stable and successfully validated numerical solutions by implementing parallel computer processing and alternative numerical techniques to solve the PTT and UCM models.

[5]An integral constitutive equation, for reference, see Bird et al. (1987).

Quinzani et al. (1995) carried out LDA and FIB measurements of the flow of 5 % PIB in tetradecane solution through a 4:1 planar contraction to study the effects of elongational deformation. The measurement data was used to calculate the elongational viscosity along the centreplane and these measurements were then compared to predictions of constitutive models, including the Oldroyd-B, Giesekus and PTT models, for elongational viscosity. Therefore, in this instance, predictions for the whole flow domain were not obtained. However, Mompean and Deville (1997) used the data of Quinzani et al. (1995) to successfully validate a finite volume simulation of an Oldroyd-B fluid through a two-dimensional 4:1 planar contraction and subsequently used the model to obtain predictions for a three-dimensional contraction.

Contrary to single cylinder and contraction flow studies, to the best knowledge of the author, neither LDA or FIB measurement data is available for flow of similar polymeric fluids past arrays of three cylinders. However, Talwar and Khomami (1995) obtained predictions using the Giesekus and PTT constitutive models, for a 2 % polyacrylamide solution flowing past a periodic square array of cylinders and validated these predictions with measurement data of Skartsis et al. (1992). Szady et al. (1995) also studied a periodic square array of cylinders but with the UCM fluid model. Additionally, a number of works have taken particular interest in Boger fluids: Arora et al. (2002) and Verhelst and Nieuwstadt (2004) obtained measurement data using the LDA and PIV techniques, respectively, and Smith et al. (2003) used the Oldroyd-B model to obtain predictions, each for the flow past a linear periodic array of cylinders. Smith et al. (2003) used the experimental data of Liu (1997) to validate the predictions, and Liu (1997) subsequently obtained Giesekus model predictions for arbitrary polymer solutions in the same geometry (Liu et al., 1998).

1.4 Summary

The above review has shown that much information has been obtained for the flows produced in a stirred vessel. In particular there is an abundance of measurement data for the flows produced by pitched blade, axial and radial impellers

for Newtonian fluids. However, the flow structure and behaviour of more viscous Newtonian fluids, in laminar flows is not as well established as that of transitional and turbulent flows. The characteristics of the laminar flows, especially near the impeller, are not well understood and a number of conflicting findings have been reported, for example the change in angle of flow discharge from the blade as Re decreases and the dependency that they have on each other. This has lead to conflicting reports for Fl and P_0 which affect the position and size of circulation zones and are of primary interest in laminar mixing: There is sufficient evidence showing that severe fluid compartmentalisation leads to large concentration gradients that can persist for several hours of mixing, causing many problems achieving homogenous mixing at low Re. Thus, a better understanding of laminar flows in the vicinity of the impeller is therefore required.

By comparison to the above, non-Newtonian flows in stirred vessels have received even less attention, due to the rheological complexities shown by mixing of such fluids. In particular, little is known for polymeric solutions similar to those in this study, especially in the vicinity of the impeller blade, where published work has shown differences in flow pattern and discharge angle of certain non-Newtonian fluids by comparison to Newtonian fluids, of similar viscosity, when others have shown similarities. Studies have also found difficulty differentiating between the causes of the non-Newtonian effects, such as viscoelasticity and normal stress differences and consequently sought computational solutions to assist the understanding of such behaviour. However, due to numerical limitations it has only been possible to approximate and simplify the flow behaviour; some have used simplified rheological models including Power-law and Oldroyd-B models in flow geometries that approximate that of a mixing vessel such as concentric and eccentric cylinders, and a number of researchers have used more sophisticated models (for example, PTT and Giesekus) in benchmark flows. As yet, results for non-linear, viscoelastic flows past blade/baffle obstructions have not been presented and these could provide a useful insight into the behaviour of these fluids.

1.5 Objectives of the present investigation

The preceding review of the published literature indicates that knowledge of laminar Newtonian flows in a mixing vessel is far from complete and especially for mixing with a radial (Rushton) impeller (which is the subject of this treatise), there is little information. The angle of flow discharge from the impeller blade and the flow patterns produced by the impeller have not been fully determined and deserve further investigation. Furthermore, less is known of viscoelastic flows, which exhibit rises in first normal stress differences and changes in shear and elongational viscosity, for which some published literature reports similar mixing flow behaviour and contrarily, some report a remarkably different behaviour, by comparison to that of a Newtonian fluid. It is not only these conflicting findings that cause concern, in addition, very little is known of the non-Newtonian effects causing the changes. It is with this in mind that researchers have sought a combination of experimental and theoretical work to help understand the behavioural characteristics of non-Newtonian fluids. However, these studies are in their infancy and deserve much more attention to elucidate the problems.

The preceding review shows that very few authors have attempted to combine non-linear viscoelasticity with mixing in a stirred vessel, both numerically and experimentally, without making approximations and it is in this study that an alternative methodology is adopted to help resolve the numerous problems encountered in the industrial mixing of such fluids.

1.6 Review of numerical techniques

As far as modelling of complex non-Newtonian flows is concerned, numerical simulations of viscoelastic polymeric fluids are of practical relevance to develop, optimise, and gain a better understanding of the mixing of these fluids in stirred vessels. However, as already mentioned, three-dimensional simulations of such fluids, in a stirred vessel is not possible at present, due to the complexity of; (i) the rheological behaviour which has to be captured with a representative constitutive equation; (ii) the adequate determination of the equations' parameters (this process is, at present, full of inaccuracies), and; (iii) the numerical problems

that are encountered with the constitutive equation, which requires sophisticated numerical techniques and extensive computational power. For these reasons, a series of idealised flow geometries was studied to help develop the modelling approaches and provide insights into viscoelastic fluid behaviour, rather than attempt to model the flow behaviour in the stirred vessel. The first step towards this goal is to study benchmark geometries, namely, flow past a symmetrically confined cylinder, past 3 symmetrically confined cylinders and through a contraction. Predictions for velocity and/or stress can be validated against the measurements of, for example, Baaijens (1994b) and Quinzani et al. (1995) which not only validates and rigorously tests the models under a combination of shear and elongational flow but improves the choice of model parameters used, as discussed later in this section. The final stage involves two-dimensional simulation of the flows past a blade/baffle with the aims being to (i) provide an insight into the flow behaviour around the blade/baffle; (ii) obtain predictions for velocity and stress (including normal stress differences) and how they are each influenced by the obstruction to the flow and; (iii) show the severity of the non-linear behaviour as the flow rates are increased.

However, before the above can be conducted, model parameters are determined using rheometric flows, i.e. simple shear or elongational flow. The rheology of the fluids is then characterised by material functions, which can be used to fit model parameters of the constitutive equations. Measurements in elongational flows are proven exceedingly difficult to implement, especially at low elongation rates ($\dot{\epsilon} \leq 5000$) and the data are often unreliable. Although a small amount of data has been published for polymer solutions and is used for comparison in this study, it is not as extensive as the simple shear measurement data available. Since benchmark flows involve mixed shear and elongational behaviour, evaluation of constitutive equations in complex flows can give more reliable model parameters and distinguish better between the adequacy of the different constitutive equations, than can (at least) the rheometric flows[6], nowadays it is recognised that rheometric flows do not contain enough information to capture all necessary fluid

[6]It is emphasised that agreement with material functions in simple shear and/or elongational flows must be retained.

parameters. The disadvantage of this strategy is that the comparison between computations and experiments will not only be influenced by the accuracy of the constitutive equation, but also by the accuracy of the numerical method for benchmark simulations. However, recent progress on numerical methods for non-Newtonian flows has shown reliable computations are possible. Nevertheless, it requires constant attention.

In viscoelastic flows the dimensionless Deborah number (De) characterises the importance of elasticity in the flow and is defined as the ratio of elastic to viscous forces:

$$De = \bar{\lambda}\dot{\gamma} \tag{1.3}$$

where, $\bar{\lambda}$ is the zero-shear averaged time constant and defined in equation 3.14. A typical range for practical flows of polymeric materials is approximately $1 < De < 100$ and for the mixing vessel measurements of chapter 6, a maximum of 107 is reached. In the past, numerical computations with the use of non-linear viscoelastic constitutive models failed to converge at De of the order of unity, but recently developed numerical techniques have shifted this limit to higher values of approximately 2. However, more recent studies, including those of this treatise, exceed this.

The ideal numerical simulation for practical purposes must be accurate, fast, stable, robust and capable of dealing with three-dimensional, time-dependent and non-isothermal flow conditions at high De. For the reasons already discussed in this introduction, such simulations can not be made presently. However, with the use of a Computational Fluid Dynamics (CFD) package (OpenCFD, 2004), relatively fast, stable, robust and accurate predictions are obtained for planar, isothermal flows in benchmark geometries at De exceeding those obtained by other workers, for similar fluids (full details of the CFD implementation is given in chapters 2 and 4. For reference, other studies of steady, non-isothermal flows have been made by Baaijens (1994a) and Baloch et al. (1992) and time-dependent computations in two dimensions by Baaijens (1993) and Olsson (1994) (this is not within the scope of the present study). Three-dimensional non-linear viscoelastic computations are presently hindered by the enormous computational power that is required.

Therefore, the above survey has indicated that new and/or more detailed knowledge and clarification is required in the following areas:

1. Rheometric characterisation of the PIB solutions.

2. Optimisation of the non-linear, viscoelastic constitutive equations; firstly in simple rheometric flows and secondly in more complex geometries where predictions can also be validated against available measurement data.

3. Determination of; (i) the most suitable models for respective PIB solutions and; (ii) the range of De for which accurate flow simulations can be made.

4. Simulation of Newtonian and PIB solutions past a blade/baffle and quantification of the distribution of strain rates, shear stresses, velocities and, where applicable, normal stress differences, in the vicinity of the blade/baffle.

5. Determination of the velocity values from measurement data, obtained in a mixing vessel stirred by a Rushton turbine impeller for Newtonian and PIB solutions.

6. Quantification of the changes in flow discharge from the impeller blade and flow patterns in the vicinity of the blade, and the dependency on Re and/or N from the measurement data.

7. Visualisation of non-linear effects both numerically and experimentally.

1.7 Review of experimental techniques

For the experimental part of the work reported in this thesis, Laser-Doppler Anemometry (LDA) was the measurement technique selected. LDA is a non-obtrusive and accurate technique that does not require calibration and at present a most convenient technique for the measurement of velocity characteristics in stirred tanks (Ducci (2004) and Micheletti (2004)). LDA is well suited for the measurement of the complex flow encountered around impellers and has been extensively used since its first application in a stirred tank by Reed et al. (1977). Ensemble-averaged, time- and phase-resolved measurements can be made with

LDA and therefore the periodic structure around impeller blades can be determined. Particle image velocimetry (PIV) is also well suited for such flows, but in view of the numerous changes of the working fluid envisaged in this work, recalibration would be frequently required to ensure high accuracy of measurement; for this reason it was decided not to employ PIV. Thus, the LDA technique is selected for the present work. The principles of the technique and its application to mixing vessel flows are discussed in detail in chapter 2.

1.8 Outline of thesis

The remainder of this thesis is divided into six chapters. In the following chapter the design of the mixing vessel and impeller along with the modelling and experimental methodologies employed, are described. The modelling of rheometric behaviour of the PIB solutions is the subject of chapter 3, where, three differential, constitutive models are used to model the non-linear response of the fluid. Subsequently, the models have been applied to simulate two-dimensional flows past a symmetrically confined cylinder, for which experimental data on the velocities, shear stress distribution and normal stress difference have been reported (Baaijens, 1994b) and the capabilities of the models are assessed in chapter 4. The flows past three symmetrically confined cylinders, through a contraction geometry and past a confined blade/baffle are then studied numerically in chapter 5 to extract useful insights into the behaviour of the fluids in flow regions with shear rates and flow features that show similarities with parts of stirred vessel flows. The experiments performed in a stirred vessel, to determine the velocity field with laser-Doppler anemometry, are then presented and discussed in chapter 6. The thesis closes with an outline of the major findings of the work and recommendations are made for future research.

Fluid Model	Example	Typical Flows Described
Generalised Newtonian fluid	Power-Law Model Bingham Model Carreau-Yasuda Model Cross Model	Steady shear flows (viscous effects only)
Linear viscoelastic fluid	Maxwell Model Jeffreys Model Generalised Maxwell Model	Small displacement gradients
Retarded motion expansion	2nd-Order Fluid 3rd-Order Fluid	Velocity gradients and time derivatives are small
Quasi-linear viscoelastic fluid	Oldroyd B or convected Jeffreys model Upper Convective Maxwell model(UCM)	A transitional stage at which fully admissible constitutive equations are developed
Non-linear viscoelastic fluid	Giesekus model Phan-Thien and Tanner model (PTT) Johnson-Segalman model (JSN)	Arbitrary

Table 1.1: Polymeric constitutive equations and their uses.

Chapter 2

Experimental setup and numerical implementation

2.1 Introduction

The aim of this chapter is to provide a full description of the experimental set-up used in this research, including the measurement technique, along with details of the methods of data analysis, possible errors and uncertainties associated with these measurements, and the equations used to model the viscoelastic fluids in the numerical work of this thesis.

Firstly, the layout of the mixing vessel stirred by a Rushton turbine, with which all the experiments were conducted, is outlined. A full description of LDA, which was the only measurement technique employed in this research, follows, where, the principles of LDA, the apparatus used, the optical configuration and the signal processing procedures are explained. Since LDA inherently yields discrete random velocity data, additional sections of this chapter are devoted to the analysis of the velocity data in order to statistically characterise the mean and fluctuating velocity fields. Finally, the possible sources of error in these measurements and an assessment of the uncertainty of the results are discussed. The chapter ends with a full description of the governing equations of fluid flow and the constitutive models for viscoelasticity that are implemented in this research to simulate the flow of these fluids.

2.2 Mixing vessel configuration

Figures 2.1 and 2.2 show the geometry of the mixing vessel and impeller, respectively, which are used in this investigation. The cylindrical mixing vessel has an

internal diameter, $T = 80.5\ mm$ and height (H), equal to the tank diameter, with four equally spaced vertical baffles of width, $B_w = T/10$, and thickness $B_t = 1$ mm fitted at right angles along the internal surface of the vessel. A six-bladed Rushton turbine of diameter, $D = T/3$, with a blade width and thickness of $0.24D$ and 1 mm, respectively, was used. In all experiments the impeller was set at a clearance from the vessel bottom, C, equal to $T/3$, and the fluid height in the vessel was equal to T. The dimensions of the mixing vessel and the impeller are identical to that used in the research of Micheletti (2004) and shown in table 2.1.

The vessel was installed on a square aluminium base plate (which houses a water bath to keep the experimental fluids at a constant temperature ($22^0C \pm 0.5^0C$)) on which the vessel was placed, in a shallow, cylindrical trough, approximately 5 mm deep so that the vessel could be easily rotated to enable measurements to be performed at different vertical planes, and; four square glass walls (6 mm thick) that incased the vessel. Both the vessel and the test section walls were made of Barium Flint glass (n, index of refraction = 1.59) and the gap between these was filled with the experimental fluid to minimise the refraction effects at the cylindrical surface of the vessel. The test section includes a detachable aluminium lid with two small holes which facilitate removal of the residual air trapped in the vessel after the lid is in place, and subsequently sealed to ensure air was not entrained into the fluid from the free surface whilst measurement data were being obtained. The lid was supported by four stilts and held firmly in place by screws between these two. Additionally, the lid supported the bi-directional variable speed DC motor to rotate the impeller: The impeller shaft was coupled to a shaft sleeving mounted on the detachable lid with its axis concentric with the vessel axis. The sleeving was supported by a bearing at either end and used to provide concentric rotation of the impeller shaft in addition to ease of alignment. The clearance between the impeller and the bottom of the vessel was set by sliding the impeller shaft up or down, and the shaft was locked to the sleeving by a grub screw. The sleeving was also coupled to an optical shaft encoder, which provided a marker pulse. For obtaining phase-resolved data (ensemble-averaged over 1^0 of impeller revolution, see section 2.4.3) the midpoint of the impeller blade was aligned with the marker pulse. By using the time of arrival of each velocity da-

tum, in relation to the occurrence of the pulse, the blade angle (from 0^0 to 59^0) could be determined.

The working fluids for the experimental part of this treatise are fully described in Chapter 6, but introduced in this section: Five fluids were studied; (i) Water; (ii) two Silicon oils (abbreviated, Si100 and Si1000), and; (iii) two polyisobutylene solutions (abbreviated, PIB100 and PIB2000). Experiments using these fluids were carried out over a range of Re ($0 < Re < 5000$) where the highest values were for measurements obtained with water.

To begin acquiring measurement data, a cylindrical coordinate system was set-up, with the radial, axial and azimuthal coordinates indicated in the following text by r, z and θ, respectively. Its origin was positioned at the centre of the vessel bottom, in a plane located half-way between two baffles. The instantaneous radial and axial components of velocity are denoted by, U_r and U_z, respectively, and enclosed with brackets to represent their mean values; $< U_r >$, and; $< U_z >$. The terms, u'_r and u'_z correspond to the r.m.s. levels of the velocity components. Instantaneous tangental velocity measurement data (U_θ) were not obtained in this study. For the phase-resolved measurement data, the values of $< U_r >$, $< U_z >$, u'_r and u'_z are functions of the phase, ϕ, of the impeller blade, where, $\phi = 0^0$ is the vertical plane through the middle of the blade. The impeller rotates in the clockwise direction, as viewed from above the vessel. Measurements of the velocity components (i.e. radial and axial) were performed in the same plane (i.e. $\theta = 0^0$, located half-way between two baffles).

2.3 Laser Doppler Anemometry

2.3.1 Introduction

Laser Doppler Anemometer (LDA), is a widely accepted tool for fluid dynamic investigations in gases and liquids and is used to measure velocities of flows or more specifically of small particles in flows. The technique has been used for more than three decades and is based on the measurement of laser light scattered by particles that pass through a series of interference fringes (a pattern of light and dark surfaces). The technology has numerous advantages over other techniques.

Its non-intrusive principle means that there is no need for physical contact with the flow, so no disturbances occur. Its directional sensitivity makes it very suitable for applications with reversing flow, which is a behavioural characteristic of fluid mixing and furthermore a relatively high spatial and temporal resolution can be obtained, it is very accurate and requires no calibration. These characteristics make LDA a valuable measuring technique with many applications. Details of the principles and practice of the LDA technique can be found in, for example, Drain (1980), Durrani and Greated (1977) and Durst et al. (1976). This section proceeds to describe; (i) the main principles of dual beam LDA; (ii) the LDA apparatus used in this research, including a description of the seeding particles used; (iii) the optical configuration and the signal collection technique employed, and finally; (iv) the methods for signal processing and data acquisition.

2.3.2 Principles of LDA

When two laser beams of equal intensity are focused to intersect with each other a pattern of light and dark interference fringes form, see figure 2.3. The orientation of these fringes is parallel to the bisector of the angle, κ, at which the two beams cross. The distance between these light and dark fringes, Λ^*, is termed the fringe spacing and is related to the angle, k and the wavelength of the laser light, Λ, by the equation:

$$\lambda^* = \frac{\Lambda}{2sin(\kappa/2)} \tag{2.1}$$

The interference fringes form an ellipsoidal shape, termed the measurement volume (or 'control volume') and is placed at the point where the velocity of the fluid is to be measured. Seeding particles (see section 2.3.3) are suspended in the fluid and as these particles, which are assumed to be moving at the same speed as the flow, pass the light fringes of the the control volume, light is scattered. The frequency of the variation of intensity of the scattered light results in the generation of 'Doppler bursts'. A typical Doppler signal, see figure 2.4, produced when a particle crosses the measurement volume in a direction perpendicular to the fringes, shows the sinusoidal intensity variation superimposed on the laser beams' Gaussian intensity distribution (which is termed the 'pedestal' part of

the signal, see figure 2.5). This Doppler signal is focused onto a photo-detector which in turn produces an output current proportional to the signal intensity. By using a suitable signal processor, velocity measurements can be obtained from the output current. The velocity U of a particle is related to the Doppler frequency, f_D (Drain, 1980) by:

$$f_D = \frac{2Usin(\kappa/2)}{\Lambda} \tag{2.2}$$

However, the Doppler signal does not provide information on the direction of the particle velocity, so particles moving with the same velocity but in opposite directions will produce the same Doppler signal. In order to resolve this directional ambiguity the interference fringes within the measurement volume are made to move in a direction perpendicular to the optical axis, by causing the two incoming laser beams to have slightly different optical frequencies, this is a technique known as frequency shifting. Particles moving in the opposite direction to the movement of the fringes will appear to be moving faster and the light detector will sense a higher frequency. By taking into account the applied frequency shift, f_s, velocity measurements can be obtained from the following expression:

$$U = (f_D \pm f_s)\frac{\Lambda}{2sin(\kappa/2)} \tag{2.3}$$

2.3.3 LDA apparatus and seeding particles

The velocity measurements were carried out with the use of a four-channel Dantec Ltd. LDA system. A 2-dimensional probe was used to measure two velocity components at 129 points, over the plane, $\theta = 0^0$, in the vessel (the points at which measurements were taken are shown and described in Chapter 6). To move the control volume, the probe was mounted on a light-weight, metallic traverse that could be moved in three orthogonal directions: x, y and z, each to an accuracy of 0.05 mm. An Argon Ion laser beam of wavelength, 457.514 nm, air cooled and providing a maximum output power of 500 mW, was used for all the experiments. A transmitter box was positioned in front of the laser and aligned with the incoming beam in order to maximise the amount of light collected and separate the green (514.5 nm) and blue (488 nm) wavelengths that

were used to obtain the 2-dimensional measurements of this thesis. Both the transmitter box and laser were positioned on a metallic, optical bench for proper alignment. Inside the transmitter box a Bragg cell splits the laser beam into two equal intensity beams, one of which is shifted by 40 MHz. Each beam is then separated into two wavelengths ($\Lambda_{green} = 514.54\ nm$ and $\Lambda_{blue} = 488\ nm$) and sent via fibre optics to the probe, which is designed to work in back-scatter mode: The probe transmitting the laser beams also receives the scattered light in an integrated single unit, and focused to form two measurement volumes, one perpendicular to the other. The light scattered by the seeding particles as they pass through is collected by the probe and sent to the photomultiplier, which in turn amplifies the signal ready for processing. Figure 2.6 shows a sketch of the LDA arrangement used for the 1-D experiments.

The working fluids, in the mixing vessel, were seeded with 1 μm, neutrally buoyant Titanium Dioxide, TiO_2, tracer particles. These particles were most suited to the laminar mixing experiments in this research, as they were small enough to follow the flow accurately at low Re, and large enough to scatter a sufficient amount of light to be detected by the photo-detector unit. Larger, 10 μm particles, which are most commonly used for turbulent mixing experiments, were initially used but were too heavy for the laminar flows of this research, and consequently would sink rapidly to the bottom of the vessel at low Re. When seeding the fluid, it was important that the concentration of the particles were kept sufficiently low to avoid obscuring the laser beams, and sufficiently high, to obtain large enough data rates. To achieve this, the seeding particles were mixed with a small amount of the fluid being used to form a suspension. This suspension was introduced to the working fluid gradually, so that an adequate number of Doppler bursts were observed on the oscilloscope.

2.3.4 Optical configuration and signal collection

The measurement volume dimensions can be varied with the use of a beam expander by using three interchangeable sets of lenses (with focal lengths of 240, 310 and 500 mm). Increasing the beam spacing and the use of smaller focal lengths results in a smaller measurement volume, which is typically used for steep ve-

locity gradients. The dimensions of the ellipsoidal measurement volume can be calculated from the following equations:

$$b_x = n\frac{b}{sin(\kappa/2)} \tag{2.4}$$

where b_x is the length of the measurement volume and b is the diameter of the focused laser beams, see figure 2.3. It should be noted that the elongation, in the direction of b_x, of the measurement volume due of the refractive index of the working fluid, n, is taken into account.

The diameter of the measurement volume, b_y, is given by:

$$b_y = \frac{b}{cos(\kappa/2)} \tag{2.5}$$

The diameter of the focused laser beams, b, is defined at $1/e^2$ of the maximum beam intensity, for beams with a Gaussian intensity distribution and is related to the focal length of the lens employed, f, the beam expansion factor, $E = 1.98$, and the diameter of the beam leaving the laser, $b_0 = 2.2\ mm$, through the expression:

$$b = \frac{4 f_{lens} \Lambda}{\pi E b_0} \tag{2.6}$$

The optimum dimensions for the measurement volumes were determined according to the required spatial resolution of the measurements, the velocity components measured and the measurement locations. For the range of Re studied in this investigation, one 2-dimensional probe fitted with a beam expander and a lens of 310 mm was used.

In order to ensure that the beams intersected each other, a pinhole of diameter, 0.5 mm, was placed in front of the beams at a distance equal to the focal length of the lens. The beams were then maneuvered to pass through this hole and in doing so confirmed their intersection.

For all experiments, the two velocity components were measured with the beams entering from the side of the vessel, with their optical axes normal to the wall of the test section. The beams were refracted as they entered the vessel due to the different refractive indices of air, glass and fluid, and consequently the intersection angle of the beams, κ, changed. Though the dimensions of the measurement volume changed due to a change in κ, the frequency to velocity

conversion factor (and the fringe spacing, Λ^*) did not change, due to the fact that when light enters a denser medium, its velocity decreases resulting in a shorter wavelength. By taking into account the refractive indices of these mediums, (which, for each working fluid, are shown in table 6.1) the position of the measurement volume could be determined.

2.3.5 Signal processing and data acquisition

The photo-multiplier amplifies the signal which is fed to and processed by a Burst Spectrum Analyser (BSA) to determine the dominant frequency, f_D, in the spectrum of the burst corresponding to the velocity of the particle that crossed the measurement volume. The measured velocity is validated when the frequency, f_D is at least four times higher than the second highest local peak in the spectrum of the burst. The Doppler bursts were monitored on an oscilloscope, where it was also possible to monitor the signal-to-noise ratio. In order to minimise the noise introduced to the signal by extraneous light sources, all the experiments were conducted with minimal background lighting and all reflective surfaces, in proximity of the vessel, were covered. Additionally, before each experiment, the alignment of the LDA apparatus was checked to ensure that the beams always operate at maximum light intensity. The BSAs (one for each component of velocity) were interfaced with a personal computer (Pentium III, 1000 MHz and 512 MB of RAM) to identify and analyse the Doppler bursts. The system operated in 'single measurement per burst' mode which is appropriate when there is only one particle in the measurement volume at any time, a condition that was monitored continuously and satisfied in the present study. This technique is contrary to 'continuous sampling' which has been known to yield higher levels of noise (Benedict and Gould, 1998).

In order to optimise the rate of collection of data, various setting, on each BSA, were finely tuned, and when doing so, the measured Doppler frequencies were monitored on the oscilloscope. Where necessary, the following settings could be adjusted: (i) The setting of the centre frequency, so that all measured Doppler frequencies were contained within the set bandwidth; (ii) The gain on the input signals, and; (iii) The optimum record length (number of samples used by the

BSA to digitise a Doppler burst). The record length was set to maximise the data rate while maintaining a high validation rate (number of validated bursts divided by total number of bursts detected, in %).

As already mention, the BSA operated in 'single measurement per burst' mode, i.e. only one measurement was performed per detected burst, and the measured frequencies were either 'time' stamped or 'angle' stamped. When time stamping, the arrival times of the measured data were clocked by the internal clock of the BSA. When the preset number of data had been obtained, the measured data together with their arrival times were acquired by the PC. The frequency data was then transformed to velocity data by the software. For angle stamping, measurements were synchronised with the shaft encoder (as already mentioned in section 2.2) pulses. Measured data was stamped with the pulse and then acquired by the PC.

At the onset of the experiments, an investigation into the number of samples required to achieve statistically independent results was carried out. For the higher Re flows, typically, $Re \geq 450$, it was found that at least 500 samples were required for each 1^0 blade angle (ϕ). Therefore, for each measurement, over 60000 velocity data were collected between the two impeller blades (i.e. 60^0 blade angle) so as to ascertain that there were a minimum of 500 data per blade angle. However, to achieve a sample number of this magnitude at lower Re, prolonged experimentation times were needed as the data rate decreased. Even though concerted efforts were made to optimise the concentration of tracer particles in the vessel, it was impossible to achieve this data rate at the lowest Re, especially at the extremities of the vessel where, in most cases, the flow was almost stagnant. However, the lower Re flows were laminar, and in theoretical terms, the variance of velocity is very small and therefore, only 50 samples were required for each 1^0 blade angle. For the ensemble-average measurements, typically, 10^3 to 10^4 samples were acquired over the whole range of Re studied.

Finally, all the measurement data with their corresponding time and angle stamps were saved on a disk file for off-line processing, which was done with purpose-written data processing routines in Matlab^{TM}. See the following section for a full description.

2.4 Data analysis

Laser-Doppler anemometry inherently yields individual velocity datum as particles pass randomly through the measurement volume. The preceding section has focused on how to obtain and process the Doppler signal in order to determine the local flow velocity from individual realisations. The discussion that follows is concerned with the analysis of the individual random data that is necessary in order to obtain the statistical properties of the fluctuating velocity.

2.4.1 Ensemble-averaged measurements

The simplest method of analysis is to calculate the statistics of the velocity data over a large number, M_i, of individual realisations. Each component of the mean velocity, $< U >$, and variance, $< U^2 >$, may be calculated respectively, from:

$$< U >= \frac{1}{M_i} \sum_{i=1}^{M_i} U_i \tag{2.7}$$

$$< U^2 >= \frac{1}{M_i} \sum_{i=1}^{M_i} (U_i - < U >)^2 \tag{2.8}$$

A measure of the amplitude of the velocity fluctuations can be obtained by the root mean square (r.m.s.) velocity:

$$u' = \sqrt{< U^2 >} \tag{2.9}$$

The shape of the probability density function (p.d.f.) of the velocity fluctuations can be characterised in more detail by higher order statistics, e.g. skewness and kurtosis. Definitions of these quantities and more information can be found in Tennekes and Lumley (1972).

2.4.2 Time-resolved measurements

Time-resolved measurements are required to estimate the velocity spectrum in order to characterise the velocity fluctuations in more detail. Most common algorithms for the estimation of the spectrum require that the data is evenly spaced in time. However, this is not possible as LDA data are randomly distributed in

time. Many signal reconstruction algorithms have been proposed in the literature. However, no method appears to be unconditionally superior to the others (Broersen et al. 2000) and therefore, the approach adopted in the present study was to use the 'nearest neighbour' interpolation technique to produce data evenly distributed in time followed by the usual data processing algorithms for the evaluation of the spectra. The nearest neighbour interpolation takes the value nearest to the original realisation for each new re-sampled value and has been found to work efficiently (Broersen et al. 2000). Amplitude spectra were obtained by applying Fast-Fourier Transforms (FFT) to the time-resolved data using the commercial software, MatLab^{TM}. The amplitude spectra show the distribution of the magnitude of the velocity fluctuations in the frequency domain. Energy spectra (see chapter 6.4.7) of the velocity data were also computed using built-in functions in MatLab^{TM}.

2.4.3 Phase-resolved measurements

The velocity data also contain periodic fluctuations due to the rotation of the impeller (velocity values as a function of the phase of the impeller blade) and it is therefore necessary to account for this effect when establishing the velocity and r.m.s. profiles. Each component of the phase-resolved mean velocity, $< U(\phi) >$ can be defined as:

$$< U(\phi) >= \frac{1}{M_{i\phi}} \sum_{i=1}^{M_{i\phi}} U_i(\phi) \tag{2.10}$$

where ϕ refers to a particular phase interval in the impeller cycle and $M_{i\phi}$ is the number of samples within each interval. The phase information in the present experiments was available from the output of the shaft encoder and therefore the above statistics could be readily calculated.

2.5 Measurement errors and uncertainty

In this section a brief analysis of the errors involved in the LDA measurements is made and where appropriate the uncertainties in the measurements are quantified.

2.5.1 Systematic errors inherent in LDA measurements

From equation 2.3, it follows that the systematic error inherent in LDA velocity measurements is largely affected by the accuracy with which the intersection angle between the laser beams and the frequency shift are known, and the accuracy of the measurement of Doppler frequency since the wavelength of the laser light is precisely known.

Inaccurate beam alignment and imperfections of the optical components results in a beam intersection angle, which might be different from that calculated in theory using geometrical principles and the optical characteristics of the various components. Therefore, it is always beneficial to measure the beam-crossing angle experimentally. This was achieved by projecting the laser beams onto a screen positioned at some distance from the point of intersection. The angle could then be determined by measuring the distance between the crossing point and the screen and the separation of the light spots on the screen. These distances were measured with an estimated accuracy of 1.3 % and 2.2 %, respectively.

2.5.2 Bias effects

When ensemble-averaged measurements are made with a constant seeding density in a turbulent to transitional flow, the measured probability density function (p.d.f.) is biased towards higher velocities (McLaughlin and Tiederman, 1973). This is due to the fact that more fast moving than slow moving particles are observed crossing the measurement volume over the measuring period. Many researchers, such as Hoesel and Rodi (1977), Drain (1980) and Durao et al. (1980) have tried to introduce correction methods but the reliability of such methods is often questionable. Although a suitable method to eradicate this type of error has not been devised as yet the work of the present study is primarily concerned with laminar flows. Consequently, the velocity bias errors are expected to be low, if not, negligible, and thus bias correction methods are not expected to improve the accuracy of the results.

2.5.3 Statistical errors

The number of samples for measurements of the ensemble-averaged mean and r.m.s. velocities can also result in an experimental error. Especially for laminar flows where the velocity of fluid flow at the extremities of the vessel are very small. Therefore, tests with different numbers of samples were made in various locations in the mixing vessel.

Statistical error may be estimated from the equations suggested by Yanta (1973) for mean velocity:

$$M_i = \left(\frac{Z_c}{E_r^2}\right)\left(\frac{r.m.s.}{mean}\right)^2 \tag{2.11}$$

and for the r.m.s. velocity:

$$M_i = \left(\frac{Z_c}{E^2}\right) \tag{2.12}$$

where, E is the percentage error and Z_c is the function of confidence level which is equal to 1.645, 1.96 and 2.58 for 90, 95 and 99 percent confidence levels, respectively. Assuming a turbulence level of 50 %, according to equations 2.11 and 2.12, a minimum sample size of 500 data points allows the mean velocity to be estimated with a maximum error of 3 % and a confidence level of 95 %. For the same confidence level, this sample size enables the r.m.s. value to be determined with a maximum error of 6.3 %.

The majority of flows in this research are laminar and therefore their turbulence levels are lower. However, although reduced levels of turbulence equates to smaller sample sizes (in accordance to equation 2.11), smaller sample sizes will boast error margins associated with the r.m.s. values (in accordance to equation 2.12). For this reason, regions of the vessel, where a sample size of approximately 500 could not be obtained (most commonly at its extremities), without excessively large experimentation times, were not studied and more attention was given to areas of the mixing vessel where they could be, i.e. near the impeller blade. The former most commonly occurred with the high viscosity Newtonian and non-Newtonian fluids.

2.5.4 Random errors in LDA measurements

In practice the random error can be determined by a number of repeated measurements. The repeatability of the LDA measurements is shown in chapter 6 where ensemble-average mean and r.m.s. velocities, obtained for water over a range of Re were compared to identical experiments obtained by Micheletti (2004). Additionally, all other velocity and r.m.s. measurements, for the other fluids were each carried out more than once and in all cases the overall difference was not more then 3 % for both the velocity and r.m.s. values.

2.5.5 Positioning errors

The error in positioning the measurement volume in the flow field depends on the accuracy of the transverse mechanism and the accuracy with which the measurement volume can be positioned at reference points with respect to all three orthogonal directions, x, y and z. The accuracy of the compound transverse table was 0.05 mm in all three directions. The accuracy with which the measurement volume can be positioned at reference points, taking into account the refractive index of the fluids, is of the order of 50 % of the size of the measurement volume in the associated direction: The corresponding positional errors were therefore 0.1 mm in each direction.

For the phase-resolved measurements, to align the marker pulse with the midpoint of the impeller blade, a laser beam positioned in the $y = 0 + D/2$ mm plane, which contained the $\theta = 0^0$ plane, was shone at the midsection of the impeller disk, $C = T/3$. The impeller shaft was rotated slowly until the midpoint of a chosen blade coincided with the laser beam, which was indicated by a signal burst on the oscilloscope. The shaft sleeving was then rotated to align the marker pulse with the position of the blade. The estimated uncertainty in aligning the marker pulse with the impeller blade was 0.2^0.

2.5.6 Non-turbulent broadening of the Doppler frequency

Non-turbulent broadening effects cause the variance of the measured Doppler frequency to be greater than that of the velocity, or, in other words, the probability

density function (p.d.f.) of the measured Doppler frequency is more spread than that of the velocity (hence the term broadening). Such broadening effects originate from a number of causes; gradients in mean velocity (σ_g); small velocity fluctuations within a measurement volume of finite dimensions (σ_f); the finite time taken by particles to cross the measurement volume (σ_t), and; the finite instrument bandwidth (σ_i). Broadening due to Brownian motion and laser line width have been shown by Durst et al. (1976) to have negligible effect. Therefore, the total mean square contribution of the broadening errors $(\sigma_b)^2$, is given by:

$$\sigma_b^2 = \sigma_g^2 + \sigma_f^2 + \sigma_t^2 + \sigma_i^2 \tag{2.13}$$

and the measured mean square of fluctuation σ_d^2 is the sum of the actual flow σ_v^2 and the broadening contributions σ_b^2:

$$\sigma_d^2 = \sigma_v^2 + \sigma_b^2 \tag{2.14}$$

When measurements are made across a velocity gradient, particles crossing different parts of the measurement volume will have different velocities. This may result in both broadening and skewing of the Doppler frequency spectrum, causing errors in both the mean and r.m.s. velocities. The magnitude of the error is a function of the particular velocity component distribution and the dimension of the measurement volume parallel to the gradient. The errors can be estimated by the following equations:

$$< U >_m = < U >_a + \left(\frac{\sigma_{mv}^2}{2}\right)\left(\frac{\partial^2 < U >}{\partial r^2}\right)_a \tag{2.15}$$

and

$$\left(\frac{u'}{< U >}\right)_m = \left|\left(\frac{\sigma_{mv}^2}{< U >}\right)_a \left(\frac{\partial < U >}{\partial r}\right)_a\right| \tag{2.16}$$

where $< U >_m$ is the measured mean velocity, $\left(\frac{u'}{<U>}\right)_m$ is the measured turbulent intensity, $< U >_a$ is the true velocity corresponding to a point measurement, and σ_{mv}^2 is the standard deviation of the measurement volume dimension along its long axis.

Equations 2.15 and 2.16 indicate that if the velocity gradient is nearly linear along the measurement volume, the error in the mean velocities will be small,

whereas if the mean velocity gradient is steep and non-linear, it will cause a large error in turbulent intensity, particularly if the mean velocity is small or there is a reversed flow.

The majority of experiments in this research concentrate on the transitional to laminar flow regimes i.e. $Re < 100$, and consequently the velocity gradients are less steep and therefore related errors may be expected to be small. Additionally, for all experiments, a small measurement volume was formed by expanding the laser beam diameter, as mentioned earlier; broadening effects due to velocity gradients were therefore minimised.

Broadening due to small scale velocity fluctuations within the measurement volume, σ_f, has been approximated by George and Lumley (1973):

$$\sigma_f^2 = \frac{2}{15}\sigma_{mv}^3 \left(\frac{\epsilon_d}{\nu}\right) \left(\frac{4\pi \sin\kappa}{\Lambda}\right)^2 \tag{2.17}$$

where σ_{mv} is the standard deviation of the measurement volume near the Kolmogorov microscale, ϵ_d is the turbulent energy dissipation rate, ν is the kinematic viscosity and the other symbols have their usual meanings (defined in section 2.3.2). This requires prior knowledge of the rate of turbulent energy dissipation, ϵ_d, and the Kolmogorov microscale, which have not been studied in this research. However, Melling (1975) estimated this error to be of the same order as the velocity gradient broadening.

Finite transit time broadening, σ_t, and instrument bandwidth broadening, σ_i, are important in spectrum analysis but not in frequency counting systems (Lee, 1995). The former is used in the research carried out in this thesis and the errors associated with this cannot be directly determined without an extensive knowledge of all the parts of the BSA instrument. However, Lee (1995) reported comparative error estimates by comparing measurements obtained with the burst spectrum analyser with those obtained with a frequency counter and the two values were similar (within 2 %) in all cases.

2.6 Numerical implementation

In this research, CFD is used to simulate the viscoelastic fluids in creeping flow conditions and it can employ a number of different numerical techniques, such as, finite difference, finite element, finite volume or any of the spectral methods available (for reference, see Versteeg and Malalasekera (1995)) to provide the numerical solutions to the governing conservation equations and the suitable viscoelastic constitutive equations. In this treatise the finite volume technique is used as it is particularly effective in 2 and 3 dimensional geometries where the finite volumes may have various shapes to accommodate complex geometries, and it is known to be computationally less demanding than the other methods (Anderson, 1995). In chapter 4 of this thesis, a full description of the finite volume technique is given, along with details of the discretisation schemes, algorithms and mesh designs used in this research.

The following sections introduce and fully describe the partial differential; (i) governing equations of fluid flow, which are formulated in Eulerian coordinates (Hulsen et al., 2000), and; (ii) viscoelastic constitutive equations. The method by which these equations are coupled and how variations of the constitutive models are formulated, are also shown and discussed.

2.6.1 Isothermal flow of incompressible, viscoelastic fluids

Isothermal flows of incompressible fluids are described by the equations for conservation of mass and momentum (neglecting gravity and body forces). Firstly, equation 2.18, shows the mass conservation (continuity) equation:

$$\vec{\nabla} \cdot v = 0 \tag{2.18}$$

where the divergence of the velocity field (v) is equal to zero, which is the necessary case for incompressible fluid flows.

Secondly, equation 2.19 shows the momentum balance equation:

$$\rho(\frac{\partial v}{\partial t} + v.\vec{\nabla}v) = \vec{\nabla} \cdot \sigma(t) - \vec{\nabla}p \tag{2.19}$$

where; the inertia term (left hand side of the equation) equals the diffusive term

(first term on the right hand side) minus the pressure gradient (second term on the right hand side) and; ρ is the density of the fluid, p is the pressure, t represents time and $\sigma(t)$ is the Cauchy stress tensor (equal to the inverse of the Finger tensor[1]).

To account for the viscoelastic effects it is convenient to decompose the Cauchy stress tensor into its Newtonian and viscoelastic components:

$$\sigma(t) = \tau_N + \sum_{k=1}^{M_k} \tau_{Ek}(t), \tag{2.20}$$

where, k is the mode number (discussed in more detail in section 3.4.2) incremented from 1 to M_k (the number of viscoelastic modes), τ_N is the purely viscous Newtonian stress term that represents the Newtonian solvent in the solution and τ_{Ek}(t) is the viscoelastic 'extra stress' term at each mode, of which, the sum equates to the total viscoelastic stress contribution, τ_E. The Newtonian stress term, τ_N, is defined as:

$$\tau_N = 2\eta_{\mathrm{N}}\mathbf{D}, \tag{2.21}$$

where, η_{N} represents the Newtonian dynamic viscosity and $\mathbf{D}$ is the strain rate tensor defined as:

$$\mathbf{D} = \frac{1}{2}(\vec{\nabla}v + \vec{\nabla}v^{\mathrm{T}}) \tag{2.22}$$

The Newtonian and total viscoelastic stress are substituted into the momentum balance equation, as follows:

$$\rho(\frac{\partial v}{\partial t} + v.\vec{\nabla}v) = \vec{\nabla} \cdot (\eta_{\mathrm{N}}(\vec{\nabla}v + \vec{\nabla}v^{\mathrm{T}}) + \tau_E(t)) - \vec{\nabla}p, \tag{2.23}$$

Only at the first time step (all the CFD cases of this treatise are transient before reaching steady state) is the viscoelastic contribution to the *momentum* balance equation equal to zero and the velocity and pressure fields solely calculated for the Newtonian solvent. The velocity and pressure fields are substituted into the viscoelastic constitutive equation at each mode, to solve for τ_{Ek} and the sum,

[1]The Finger tensor provides information about a material element that is rotated only and not stretched (Larson, 1999).

τ_E, is then substituted back into the momentum equation to solve for new velocity and pressure fields at subsequent time steps, until steady state and the minimum simulation time is reached. A full description of this cycle is given in chapter 4. The following section provides a detailed description of the viscoelastic constitutive equations.

2.6.2 The viscoelastic model

The search for an appropriate viscoelastic constitutive equation is a major research challenge. Not only are the equations expected to predict non-linear flow behaviour such as shear and elongation rate dependent viscosities, normal stress differences and elastic responses, but will ideally do so at relatively high flow rates in complex geometries. An overview of the available non-Newtonian and viscoelastic models is given in chapter 1 and detailed discussions can be found in, for example, Bird et al. (1987) and Larson (1999).

This section begins with a generic viscoelastic constitutive model (equation 2.24) that can be used, by varying terms in the equation, to represent the Giesekus, PTT and JSN non-linear constitutive models, which were introduced in the previous chapter:

$$A(\tau_{Ek}, \lambda_k)\frac{\tau_{Ek}}{\lambda_k} + \frac{\delta\tau_{Ek}}{\delta t} = G_k(\nabla v + \nabla v^T) \tag{2.24}$$

where, A is the non-linear term which controls the extent to which the viscosities and normal stress differences change at the higher deformation rates, and λ_k and G_k are the relaxation time and modulus of elasticity, respectively, at each viscoelastic mode. The total convective time derivative of the viscoelastic stress term, $\frac{\delta\tau_{Ek}}{\delta t}$, is represented as:

$$\frac{\delta\tau_{Ek}}{\delta t} = a{\tau_{Ek}}^{(1)} + (1-a)\tau_{Ek(1)} \tag{2.25}$$

where, 'a' is known as the slip parameter, which can take any value in the range, $0 \leq a \leq 1$. At $a = 0$, equation 2.25 takes its upper convective form, where the viscoelastic fluid element exhibits a non-affine response to an imposed deformation. At $a = 1$, equation 2.25 takes its lower convective form where the opposite effect is shown. More information about implementing simulations with different

values of 'a' is given in chapter 4. The lower convective term, $\tau_{Ek}{}^{(1)}$, is defined as:

$$\tau_{Ek}{}^{(1)} = \frac{d\tau_{Ek}}{dt} + \tau_{Ek}.\nabla v^T + \nabla v.\tau_{Ek} \tag{2.26}$$

and the upper convective term is defined as:

$$\tau_{Ek(1)} = \frac{d\tau_{Ek}}{dt} - \tau_{Ek}.\nabla v - \nabla v^T.\tau_{Ek} \tag{2.27}$$

where:

$$\frac{d\tau_{Ek}}{dt} = \frac{\partial \tau_{Ek}}{\partial t} + v.\nabla \tau_{Ek} \tag{2.28}$$

By changing; (a) the non-linear term, $A(\tau_{Ek}, \lambda_k)$; (b) the size of the slip parameter, 'a', and/or; (c) the size of material parameters, ϵ and α (see below), variants of equation 2.24 can be obtained. Examples are shown in table 2.2 and the following text describes this in more detail. When:

$$A(\tau_{Ek}, \lambda_k) = I \tag{2.29}$$

where I is a unit matix, equation 2.24 becomes the 'Oldroyd B' model at $a = 0$ and the Johnson-Segalman (JSN) model in the range, $0 < a < 1$. When:

$$A(\tau_{Ek}, \lambda_k) = exp[\frac{\epsilon \lambda_k}{\eta_k} tr(\tau_{Ek})]I \tag{2.30}$$

and $0 \leq a \leq 1$, equation 2.24 becomes the Phan-Thien and Tanner (PTT -a) model. When:

$$A(\tau_{Ek}, \lambda_k) = [1 + \frac{\epsilon \lambda_k}{\eta_k} tr(\tau_{Ek})]I \tag{2.31}$$

and $0 \leq a \leq 1$, equation 2.24 becomes the Phan-Thien and Tanner (PTT -b) model. There are two forms of the PTT model, both of which are studied in this treatise. When:

$$A(\tau_{Ek}, \lambda_k) = I + \frac{\alpha \lambda_k}{\eta_k} \tau_{Ek} \tag{2.32}$$

and $a = 0$, equation 2.24 becomes the Giesekus model.

Both of the PTT models and the Giesekus models have the extra material parameters, ϵ and α, respectively. These parameters take values that depend on the fluids that are being modelled but for those of this study the values are most effective in the range: $0 \leq \epsilon, \alpha \leq 1$. The upper convective Maxwell (UCM) model is obtained when ϵ and 'a' (in the PTT models), and α (in the Giesekus model) are zero.

The PTT and Giesekus constitutive models are non-linear viscoelastic models that are commonly used for the simulation of polymeric solutions, melts and/or dispersions. For reasons already discussed in chapter 1 these models are the only two that are used in this study. A more detailed study of these constitutive models is given in the following chapters.

2.7 Concluding remarks

An overview of the experimental configuration, the measurement technique, methods of data analysis, measurement errors and uncertainties and details of the numerical implementation, is provided in this chapter. The stirred mixing vessel facility and the LDA measurement technique was described at the beginning of the chapter before a full description of the LDA measurement technique was given. The analysis procedures of the velocity data were briefly described before the possible sources of error in the LDA measurements were discussed, where, an estimate of the associated uncertainty introduced in the results was given wherever possible. Finally, the governing equations and constitutive models used for the CFD calculations of this thesis are shown and described in full.

Vessel	
Diameter, T [mm]	80.5
Height, H [mm]	80.5
Wall thickness [mm]	1
Baffle width [mm]	8.05
Baffle thickness [mm]	1
Impeller	
Diameter, D [mm]	27
Blade thickness, t_b [mm]	1
Disk thickness, t_d [mm]	1

Table 2.1: Dimensions of the mixing vessel and the impeller

Constitutive equation	A(τ_{Ek}, λ_k)	a
PTT -a	$\exp[\frac{\epsilon\lambda_k}{\eta_k}\mathrm{tr}(\tau_{Ek})]I$	$0 \leq a \leq 1$
PTT -b	$[1 + \frac{\epsilon\lambda_k}{\eta_k}\mathrm{tr}(\tau_{Ek})]I$	$0 \leq a \leq 1$
Giesekus	$I + \frac{\alpha\lambda_k}{\eta_k}\tau_{Ek}$	0

Table 2.2: Mean velocity $< u >$, apparent shear rate $\dot{\gamma}_a$, time step size (Δt) and simulation time in terms of the number of λ_{long}'s (longest relaxation times), for the 2.5 % PIB solution, completed until divergence from a solution prevailed. All runs are transient and results were taken from a steady state condition.

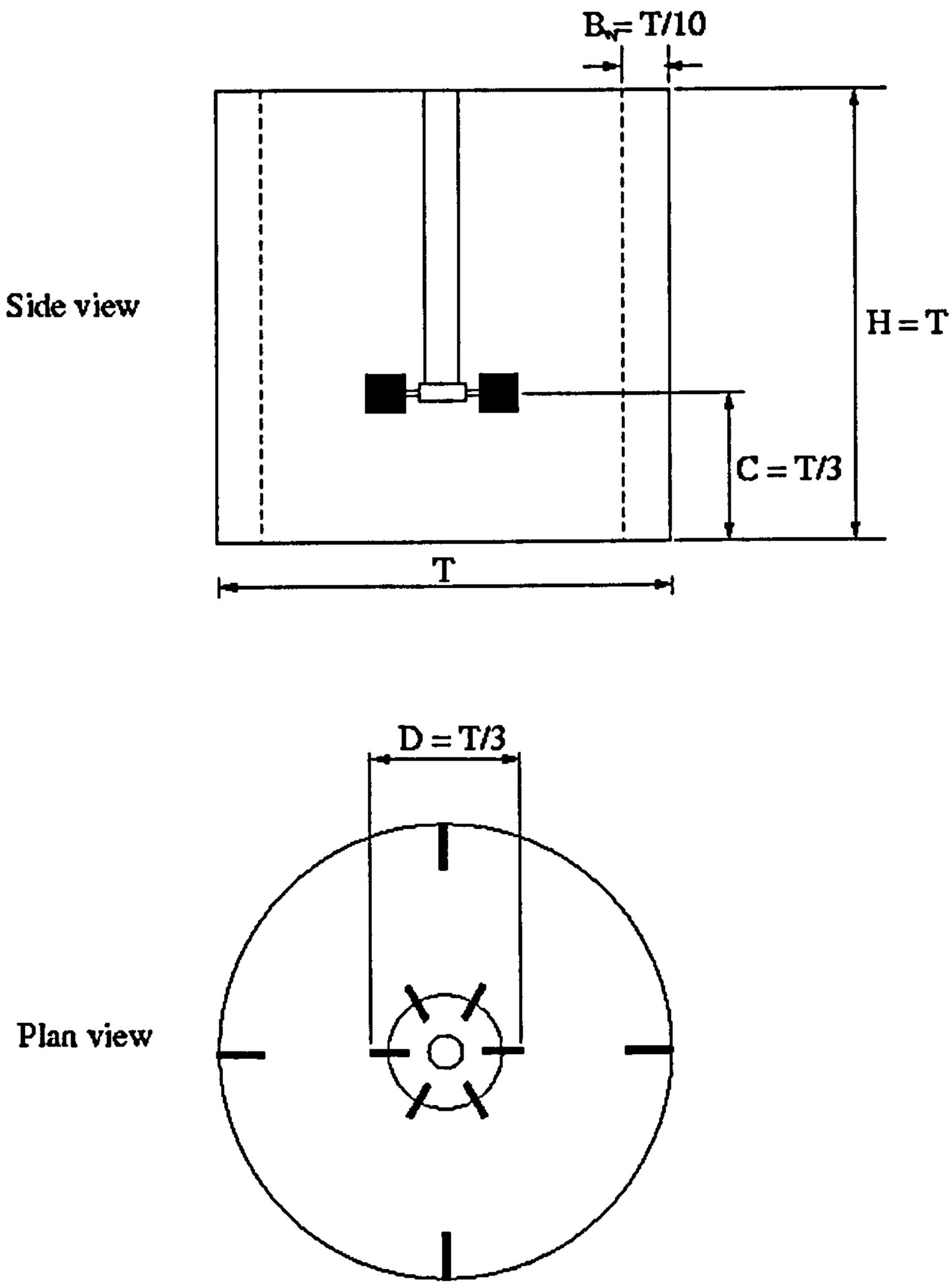

Figure 2.1: The geometry of the mixing vessel.

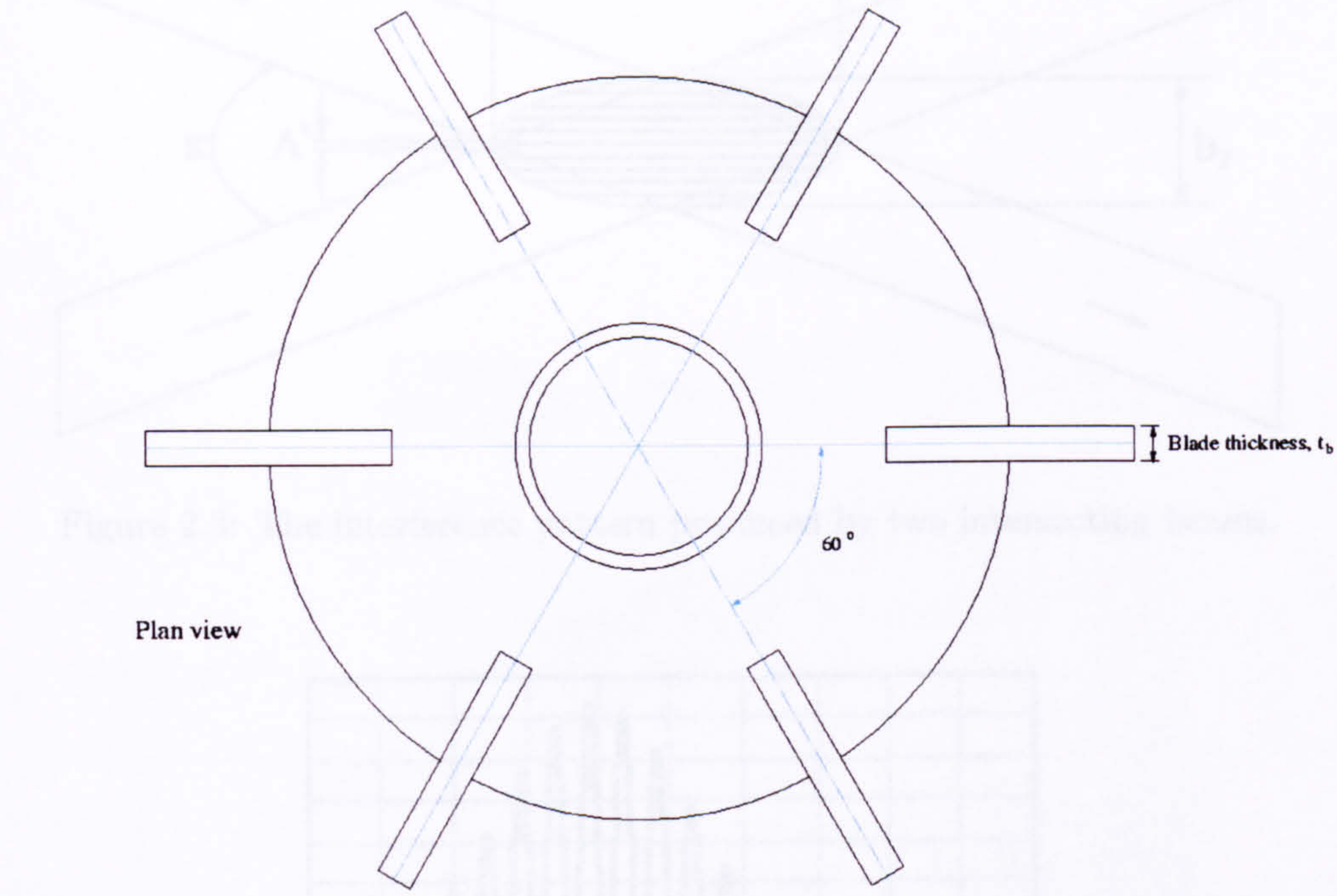

Figure 2.2: The geometry of the Rushton impeller blade.

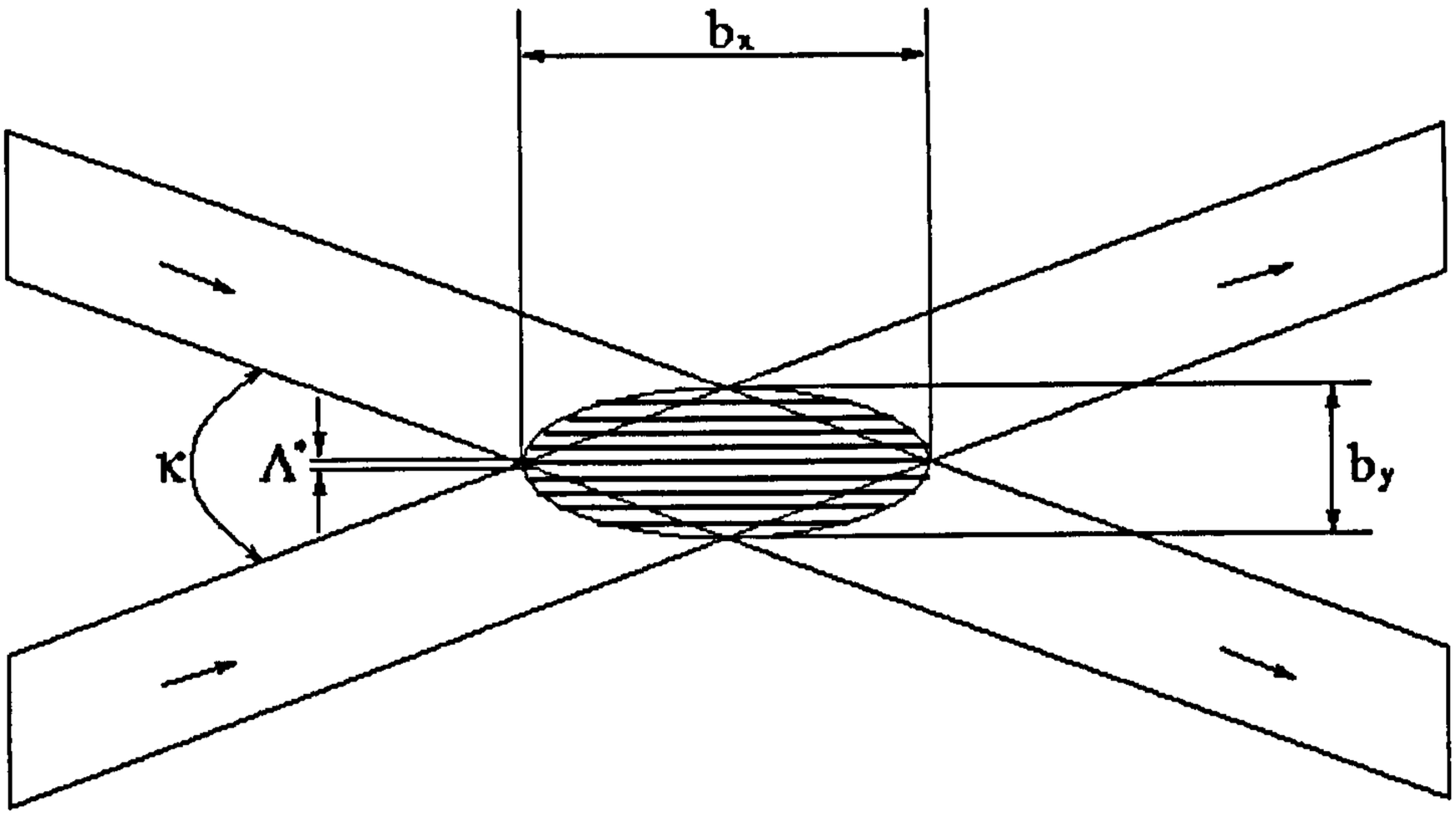

Figure 2.3: The interference pattern produced by two intersecting beams.

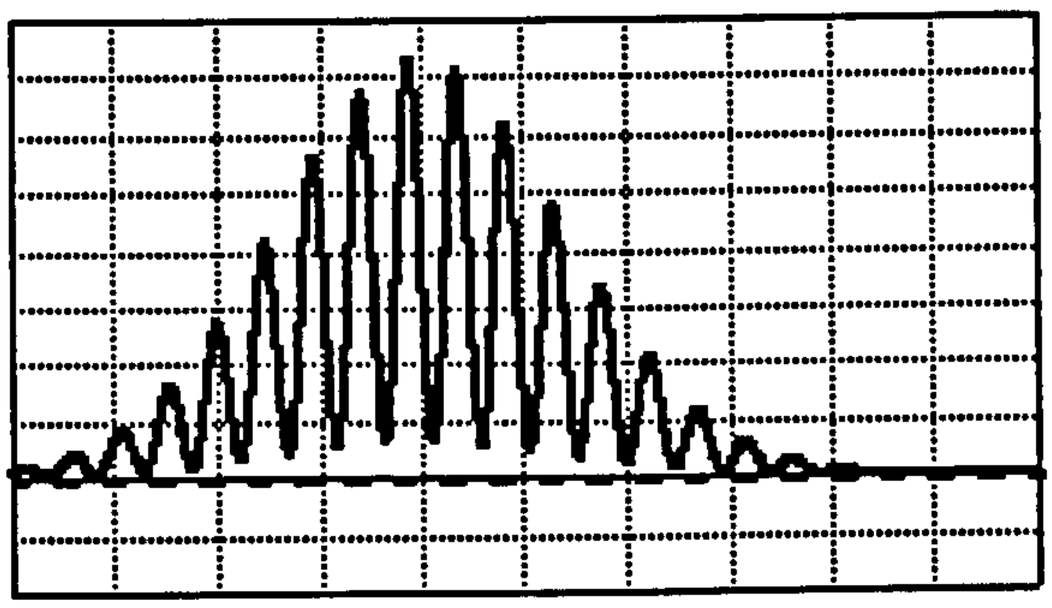

Figure 2.4: A Doppler burst produced by a particle crossing the measurement volume.

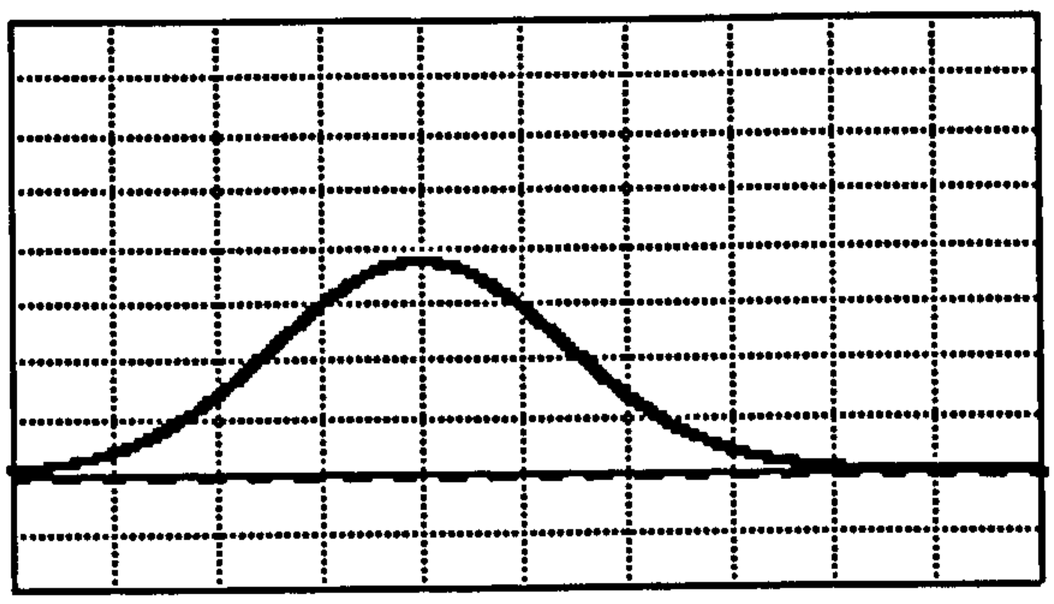

Figure 2.5: The laser beams' Gaussian profile.

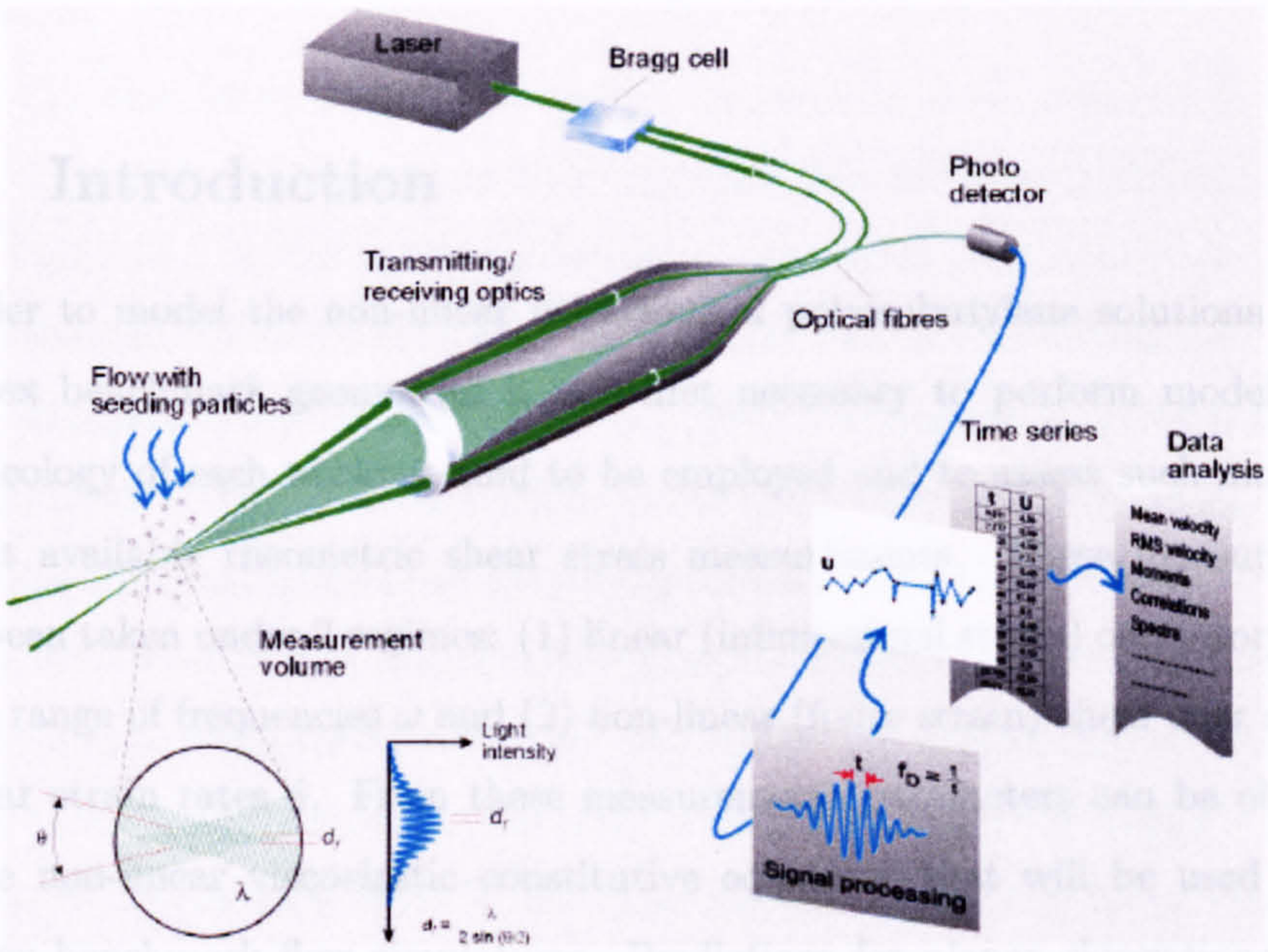

Figure 2.6: A sketch of a single channel LDA working in back-scatter mode (from www.dantecdynamics.com).

Chapter 3

Rheological characterisation of 2.5 % and 6 % PIB solutions in simple shear and elongation.

3.1 Introduction

In order to model the non-linear behaviour of polyisobutylene solutions within complex benchmark geometries it was first necessary to perform modelling of the rheology of each working fluid to be employed and to assess such modelling against available rheometric shear stress measurements. These measurements have been taken under 2 regimes: (1) linear (infinitesimal strain) oscillatory shear over a range of frequencies ω and (2) non-linear (finite strain) shear over a range of shear strain rates $\dot{\gamma}$. From these measurements parameters can be obtained for the non-linear viscoelastic constitutive equations that will be used in the complex benchmark flow simulations. Predictions for planar elongational flows will also be presented, although they have not been validated due to the lack of measurement data available: Physical and mechanical difficulties are frequently encountered when acquiring this data (Baaijens, 1994b), especially at relatively low shear rates, typically at $\dot{\epsilon} < 1000\ s^{-1}$, and for relatively low viscosity fluids, i.e. polymer solutions (Cambridge, 2002). It is only at higher strain rates, and for higher viscosity fluids that the elongational measurement apparatus, such as the four-roll mill, will produce accurate results.

Measurement data for two shear thinning polyisobutylene (PIB) solutions are introduced and presented in this chapter. These two liquids will be referred to as 2.5 % PIB and 6 % PIB respectively in the sequel and will be used as the only two model fluids hereafter. Each solution consists of a percentage (by weight) of

PIB dissolved in a tetradecane solution ($C14$), where $C14$ is a linear hydrocarbon ($C_{14}H_{30}$) in an isomeric mixture of 95 % purity.

Each fluid was prepared and stress measurements along with the respective Maxwell material parameters (see section 3.4.2) were obtained by Lee (2003). All modelling hereafter predicts material functions for each fluid of Lee (2003) although, in this study, the measurement data of are presented and compared to the measurement data for the same two fluids obtained by Cambridge (2002). The 2.5 % and 6 % PIB solutions were chosen primarily for their shear thinning and normal stress difference properties but also for ease of acquisition and relatively low toxicity.

To the best knowledge of the author, rheometric measurements or predictions, along with those for complex geometries have not been published for the 2.5 % PIB and 6 % PIB solutions, however predictions and measurements have been published for fluids exhibiting very similar material functions, see, for example, Baaijens (1994b), Baaijens et al. (1994), Baaijens et al. (1995), Barakos and Mitsoulis (1995), Dou and Phan-Thien (1998) and Quinzani et al. (1995). Consequently, comparisons can only be made with these similar fluids.

The remainder of this chapter is divided into 4 sections: Section 3.2 discusses the viscoelastic constitutive equations and section 3.3 defines the material functions for each working fluid. At the start of sections 3.4 and 3.5 master curves at a reference temperature of 25 ^{0}C for linear oscillatory and non-linear shear rate measurements, obtained by Cambridge (2002) and Lee (2003), are presented and compared. The comparison between these measurement data successfully shows the validation of the Cox-Merz rule, for each fluid. Subsequently, each section then proceeds to; (a) use the linear oscillatory measurements to determine the Maxwell material parameters for each fluid; (b) determine the non-linearity parameters of each viscoelastic constitutive model to make predictions under non-linear shear flow; (c) show how each model can successfully predict the fluids' response to a time-dependent non-linear shear, and finally; (d) obtain predictions for each fluid under elongational deformation.

3.2 Constitutive equations

The types of constitutive models used in this study have been introduced in chapter 2. Two non-linear viscoelastic constitutive equations have been used to fit the rheological data provided in this chapter. These equations are of the differential type: (1) the Phan-Thien Tanner model (Thien and Tanner, 1977), which has two versions, the first with an exponential form for A(τ_{Ek}, λ_k) and the second with a linear form for A(τ_{Ek}, λ_k), referred to as the PTT -a and PTT -b models, respectively, and; (2) the Giesekus model (Giesekus, 1982). These models are described in section 2.6.2. The PTT models and the Giesekus model have been implemented for polymer solutions and melts, not only in simple shear flow but in elongational and complex flows, see for example, Baaijens (1994b), Barakos and Mitsoulis (1995), Hartt and Baird (1996), Phan-Thien and Dou (1999) and Quinzani et al. (1995). These models predict the essential material functions which are necessary to characterise the viscoelastic fluids: these are, bounded extensional viscosity, shear-thinning viscosity and non-zero normal stress difference values. These models can also use a spectrum of relaxation times (see section 3.4.2), which help to more accurately obtain these predictions.

The two versions of the PTT model differ most strongly in their prediction of the elongational viscosity (η_ϵ). For the PTT -a model, the elongational viscosity goes through a maximum with increasing elongational strain rate ($\dot{\epsilon}$), for the PTT -b model the elongational viscosity is a monotone increasing function of $\dot{\epsilon}$ which approaches a constant value at $\dot{\epsilon} \rightarrow \infty$. This is described in more detail in section 3.4.5. The first behaviour is assumed to be more valid for polymer melts (Bird et al., 1987) and consequently much work has been carried out for polymer melts using the PTT -a model, see, for example, Baaijens et al. (1997), Hartt and Baird (1996) and Verbeeten et al. (2002). The second type of behaviour (PTT -b) is more valid for polymer solutions (Larson, 1988), especially at moderately low elongation strain rates, i.e. $\dot{\epsilon} = 10$. However, at higher elongation strain rates an elongational thinning is observed by Quinzani et al. (1995) for a similar concentrated polymer solution (5 % Polyisobutylene solution in tetradecane (C14)), which is, contrarily, more valid for the PTT -a model. Quinzani et al. (1995) studied six differential constitutive viscoelastic equations and found

that the stresses in shear, elongation and complex flows, for similar concentrated polymer solutions, were best described with the PTT -a model. In this study, comparisons are made between both PTT models and the Giesekus model, to make a full assessment of this, see sections 3.4.3 and 3.5.3.

All three constitutive equations are simulated as multimode models as it has been found in literature that multimode versions not only improve fits of rheometric shear and elongation flow but in complex flows as well (Baaijens, 1994b).

3.3 Definition of material functions

Experiments for 2.5 % and 6 % PIB have been performed for both linear oscillatory and non-linear steady shear flow and predictions have also been made for both. Measurement data for planar elongational flow have not been presented herein but predictions have been made and analysed under this regime.

All these flows are homogeneous, thus the matrix representation of the strain rate tensor **D** for simple shear is given by equation 3.1:

$$\mathbf{D} = \frac{1}{2}\begin{bmatrix} 0 & \dot{\gamma} & 0 \\ \dot{\gamma} & 0 & 0 \\ 0 & 0 & 0 \end{bmatrix} \tag{3.1}$$

where, $\dot{\gamma}$ is the shear strain rate. For planar elongation:

$$\mathbf{D} = \frac{1}{2}\begin{bmatrix} -\dot{\varepsilon} & 0 & 0 \\ 0 & 0 & 0 \\ 0 & 0 & \dot{\varepsilon} \end{bmatrix} \tag{3.2}$$

where, $\dot{\varepsilon}$ is the elongational strain rate. The definitions of the material functions then are:

Steady shear dynamic viscosity, η:

$$\eta = \frac{\sigma_{xy}}{\dot{\gamma}} \tag{3.3}$$

where σ_{xy} is the total steady shear stress.

First normal stress difference, N_1:

$$N_1 = \sigma_{xx} - \sigma_{yy} \tag{3.4}$$

where, σ_{xx} denotes the change in σ_x with respect to a change in the x direction and likewise for σ_{yy} and σ_{zz} but in the y and z directions, respectively.

Second normal stress difference, N_2:

$$N_2 = \sigma_{yy} - \sigma_{zz} \tag{3.5}$$

The second normal stress difference will not be used in the following chapters as it will not be relevant to the 2-dimensional simulations of this thesis.

Complex viscosity, η^*, as a function of the frequency of oscillation of the rheometer plates, ω:

$$|\eta^*(\omega)| = \sqrt{\eta'^2 + \eta''^2} = \eta(\dot{\gamma}) \tag{3.6}$$

where, η' and η'' are defined in equations 3.9 and 3.10. Finally, the planar elongational viscosity, η_ε:

$$\eta_\varepsilon = \frac{(\sigma_{zz} - \sigma_{xx})}{\dot{\varepsilon}} \tag{3.7}$$

The following text focuses on the realisation of these material parameters, both experimentally and numerically, for both viscoelastic fluids.

3.4 2.5 % Polyisobutylene Solution

3.4.1 Validation of the Cox-Merz rule

As mentioned earlier, linear oscillatory shear and non-linear steady shear flow measurements were taken by Cambridge (2002) and Lee (2003). The measurements for the 2.5 % PIB solution are described and discussed in this section, as they provide essential information for the development of the rheological models presented in this chapter. In order to model the non-linear flow behaviour, which is the essence of this investigation, the empirical Cox-Merz rule has to be firstly validated. A successful validation of this rule means that the shear viscosity, as a function of shear rate, $\eta(\dot{\gamma})$ (for non-linear experimentation) is almost identical

to the complex viscosity as a function of frequency, $\eta^*(\omega)$ (for linear experimentation), which is shown in equation 3.6. The Maxwell material parameters, i.e. η_k and λ_k, can only be calculated through linear rheometric experimentation but are needed for non-linear modelling. Validation of the Cox-Merz rule allows this to be possible. Most polymer melts and solutions obey the Cox-Merz rule (Larson, 1999).

For the oscillatory shear flow data obtained by Cambridge (2002) and Lee (2003) the 2.5 % PIB solution was deformed at an infinitesimal 20 % strain and at frequencies ω ranging from 0.1 to 150 s^{-1}. For the non-linear steady shear flow data obtained by Cambridge (2002) and Lee (2003), the fluid was deformed at shear strain rates $\dot{\gamma}$ ranging from 0.1 to 1000 s^{-1} and from 0.1 to 600 s^{-1}, respectively. All these measurements were taken at 5, 10, 15, 20, 25, 30, 35, 40, 45 and 50 ^{0}C. This range of temperatures did not affect the functional dependence of shear viscosity η on $\dot{\gamma}$ and ω; it merely altered the zero-shear[1] rate viscosity η_0 and the shear strain rate or frequency at which the transition from the plateau viscosity to the non-linear behaviour occurred (see figure 3.1). These data, obtained by Cambridge (2002) and Lee (2003), at these temperatures, were superposed onto a single 'master curve', at a reference temperature of 25 ^{0}C by means of the time-temperature superposition (TTS) technique (Bird et al., 1987). The shift factors a_{Tp} needed for TTS were determined from the plateau values of zero-shear rate viscosity η_0 by the relationship:

$$a_{Tp} = \eta_0(Tp)/\eta_0(Tp_0) \tag{3.8}$$

where Tp_0 represents the reference temperature of 25 ^0C and Tp represents the temperature of each measurement set. Four master curves at a reference temperature of 25 ^0C are shown in figure 3.1: Linear oscillatory and non-linear steady shear flow curves by Cambridge (2002) and by Lee (2003) are shown.

All four curves shown in figure 3.1 validate the Cox-Merz rule. This empirical relationship, shown in equation 3.6, predicts well the magnitude of complex viscosity $\eta^*(\omega)$ (obtained only from oscillatory shear data) as being equal to the

[1]The zero-shear rate viscosity η_0 is the plateau viscosity at infinitesimal shear strain rates, $\dot{\gamma}$ and frequencies, ω.

steady shear viscosity $\eta(\dot{\gamma})$ at corresponding values of frequency and shear strain rate, respectively, where:

$$\eta' = G''/\omega \tag{3.9}$$

and

$$\eta'' = G'/\omega \tag{3.10}$$

The definitions of G' and G'' are given in the following section. All four curves show a plateau region where $\eta(\dot{\gamma})$ and $\eta^*(\omega)$ are approximately equal to 1 $Pa.s$, at frequencies and shear strain rates over the range, $\omega, \dot{\gamma} \leq 1\ s^{-1}$. At shear strain rate values greater than this, i.e. $1 \leq \dot{\gamma} \leq 1000\ s^{-1}$, the steady shear curves begin to exhibit a non-linear characteristic, whereby the fluid begins to thin thus lowering the values of $\eta(\dot{\gamma})$. This phenomenom is known as shear thinning. In accordance to the Cox-Merz rule, the linear oscillatory measurements also exhibit this shear thinning phenomenon as $\eta^*(\omega)$ also decreases over the same range of frequencies ω. Both sets of linear oscillatory measurements obtained by Cambridge (2002) and Lee (2003) over the whole range of frequencies show excellent quantitative agreement with the sets of non-linear steady shear measurements obtained by Cambridge (2002) and Lee (2003).

3.4.2 Determination of the Maxwell material parameters

The Maxwell material parameters for the 2.5 % PIB solution were obtained by Lee (2003) using the respective rheometric linear oscillatory shear stress measurements over the range, $0.1 \leq \omega \leq 600\ s^{-1}$. An explanation of how these parameters are obtained is given below.

In order to begin modelling the response of this solution under finite deformation, the linear oscillatory shear data was used to obtain a range of shear viscosity (η_k) values over a spectrum of relaxation times[2] (λ_k) (The spectrum of relaxation times was chosen arbitrarily to best fit the linear oscillatory data). This was done by minimizing the difference between the measured (G'_j and G''_j) and the

[2]The relaxation time of a fluid is roughly the longest time required for the elastic structures in the fluid to relax, see Bird et al. (1987).

predicted ($G'(\omega_j)$ and $G''(\omega_j)$) material functions, for a total number (M_j) of frequencies ω_j, where G' and G'' are the storage and loss modulus, respectively (Bird et al., 1987). Equation 3.11 shows the quantity to be minimised.

$$\sum_{j=1}^{M_j}([\frac{G'(\omega_j)}{G'_j} - 1]^2 + [\frac{G''(\omega_j)}{G''_j} - 1]^2) \tag{3.11}$$

The predicted material functions ($G'(\omega_j)$ and $G''(\omega_j)$) were calculated by successive substitution of viscosity values into equations 3.12 and 3.13.

$$G'(\omega_j) = \sum_{k=1}^{M_k} \frac{\eta_k \lambda_k \omega_j^2}{1 + (\lambda_k \omega_j)^2} \tag{3.12}$$

$$G''(\omega_j) = \sum_{k=1}^{M_k} \frac{\eta_k \omega_j}{1 + (\lambda_k \omega_j)^2} \tag{3.13}$$

where k represents the number of the mode, M_k is the number of modes and j represents the frequency value.

Using 'superposition' of linear viscoelastic Maxwell models (Bird et al., 1987), each partial stress τ_{Ek} is calculated from the relaxation time λ_k and the viscosity η_k at mode 'k' and then summed to calculate the total viscoelastic stress, τ_E. Increasing the number of modes used results in a more accurate description of the measured data but also in an increase in the computational time needed. Using recommendations from the published literature by Baaijens (1994b), Baaijens et al. (1994), Baaijens et al. (1995), Barakos and Mitsoulis (1995), Dou and Phan-Thien (1998) and Quinzani et al. (1995) and the experimental data of Lee (2003), it was concluded that the optimum number of modes needed would be 5. The first mode describes the Newtonian viscosity of the solvent, where the Newtonian solvent stress τ_N contribution to the total stress tensor σ(t) is shown in equation 2.22 and typically the 4 subsequent modes describe the viscoelastic modes of stress.

The Maxwell material parameters, λ_k and η_k, at the 5 modes, must be obtained to begin making steps towards predicting the non-linear behaviour of the fluids under steady shear and elongational deformation at rates, ranging from 0.1 to 600 s^{-1}. These Maxwell material parameters are shown in table 3.1. Subsequently, by substituting values for λ_k and η_k back into equations 3.12 and 3.13,

predictions of the parameters $\eta'(\omega)$ and $\eta''(\omega)$ (defined by equations 3.9 and 3.10) were made and compared to the measured data. Such comparisons are shown in figures 3.2(a) and 3.2(b) for η' and η'' respectively. The predictions for $\eta'(\omega)$ over the range $0.1 \leq \omega \leq 100\ s^{-1}$ for which data is available and the respective predictions for $\eta''(\omega)$ over the range $1 \leq \omega \leq 100\ s^{-1}$ for which data is also available match the measured data extremely well. Predictions were also made for both figures outside of these ranges to; (a) show the corresponding variations at higher values of ω and; (b) highlight the plateau region of $\eta'(\omega) \approx 1.08\ Pa.s$ at lower frequencies, over the range $0.01 \leq \omega \leq 0.1\ s^{-1}$ (in figure 3.2(a)).

From the 5 modes of relaxation times, λ_k, shown in table 3.1, the zero-shear averaged time constant $\bar{\lambda}$ can be defined by equation 3.14:

$$\bar{\lambda} = \frac{\sum_k \eta_k \lambda_k}{\sum_k \eta_k} \tag{3.14}$$

For the present 2.5 % PIB solution; $\bar{\lambda} = 0.669\ s$.

3.4.3 Determination of PTT and Giesekus non-linearity parameters

Three non-linear models have been implemented, namely the Giesekus and the Phan-Thien and Tanner (PTT -a and PTT -b) models. However, in order to begin modelling the non-linear material functions, $\eta(\dot{\gamma})$, $\eta^+(\mathrm{t})$ (where η^+ is the transient viscosity, see equation 3.16), $\eta_\varepsilon(\dot{\varepsilon})$ and $N_1(\dot{\gamma})$, of a respective fluid under deformation the non-linearity parameters, 'a' , 'ϵ' and 'α' (introduced in chapter 2) in the non-linear viscoelastic constitutive equations, shown in table 3.1, had to be determined. This was done by minimising, 'q' in equation 3.15, for steady shear flows over a range of shear rates.

$$q = \sum_l [(\frac{N_{1,l} - N_{1,l}^{exp}}{N_{1,l}^{exp}})^2 + (\frac{\eta_l - \eta_l^{exp}}{\eta_l^{exp}})^2] \tag{3.15}$$

where l denotes the shear rate value and the superscript 'exp' denotes the measured (experimental) values of Lee (2003). At $a = 0$, ϵ and α were incremented from 0 to 1 for both of the PTT models and the Giesekus model, respectively. Optimum values for ϵ and α were selected at a minimum value of q, accurate

to 2 decimal places. For $0 < a \leq 1$ non-physical oscillations in the transient shear stress, for the PTT -a and PTT -b models, were observed, and also in the research of Baaijens (1994b). This improved the predictions of $\eta(\dot{\gamma})$ and $N_1(\dot{\gamma})$ but in order to gain convergence the time step had to be decreased further. At $a = 0$ the solutions for $\eta(\dot{\gamma})$ and $N_1(\dot{\gamma})$ are within the error of the experimental data and the described computations in the subsequent chapters proved to be impossible using both the PTT -a and PTT -b models with $a \neq 0$. Therefore, the value for 'a' was set to zero for the 2.5 % PIB solution.

The 5 mode PTT -a model produced a smaller residual for q indicating predictions of greater accuracy than those obtained with the PTT -b and Giesekus models, for $N_1(\dot{\gamma})$ and $\eta(\dot{\gamma})$, over the range of shear rates, $0.1 \leq \dot{\gamma} \leq 600\ s^{-1}$.

Non-linear predictions for $\eta(\dot{\gamma})$ were made using all three models and are compared in figure 3.3(a) to the measured data for $\eta(\dot{\gamma})$ of Baaijens (1994b), Cambridge (2002) and Lee (2003). All models show the same trend over the plateau region $0.1 \leq \dot{\gamma} \leq 1\ s^{-1}$, where $\eta \approx 1.08\ Pa.s$. The small degree of thinning predicted in this region is negligible when making comparisons to all the measurement data, as there are clearly experimental errors involved, as shown, for example, by the differences between the data of Cambridge (2002) and Lee (2003) for essentially identical fluids. The shear thinning indicated by the simulations for $\dot{\gamma} \leq 1\ s^{-1}$ is of a similar order to the scatter of the measurement data.

In the region $1 \leq \dot{\gamma} \leq 600\ s^{-1}$ all three models show shear thinning as $\eta(\dot{\gamma})$ decreases with increasing values of $\dot{\gamma}$. However the PTT -a model predictions are better than the PTT -b and Giesekus predictions as the fluid begins to shear thin more severely at approximately $\dot{\gamma} = 2\ s^{-1}$. The Giesekus and PTT -b models predict a much lower and higher viscosity, respectively, in the range, $2 \leq \dot{\gamma} \leq 600\ s^{-1}$. The measured data of Cambridge (2002) and Lee (2003) are in good agreement with each other and the data of Baaijens (1994b) for a similar fluid show a good qualitative comparison but clearly the fluid of Baaijens (1994b) behaves differently at higher shear strain rates.

Figure 3.3(b) shows predictions with the non-linear PTT -a, PTT -b and Giesekus models for $N_1(\dot{\gamma})$ against measured data of Baaijens (1994b), Cambridge (2002) and Lee (2003). All measurement data show almost exactly the same

quantitative trend over the range $2 \leq \dot{\gamma} \leq 600\ s^{-1}$ and the PTT -a and Giesekus models exhibit almost exactly the same quantitative trend over the range, $0.1 \leq \dot{\gamma} \leq 600\ s^{-1}$. In comparison, the PTT -b model makes better predictions for $N_1(\dot{\gamma})$ over the range, $50 < \dot{\gamma} \leq 600\ s^{-1}$. It is also noteworthy to observe small differences in the measurement data at the lower shear rates, which is attributed to the fact that accurate normal stress measurements are hard to obtain at low shear strain rates, i.e. $0 < \dot{\gamma} \leq 8\ s^{-1}$, so measurement data of Lee (2003) and Cambridge (2002) may not be as accurate over this range. However, differences of the same magnitude are also shown in the range, $100 \leq \dot{\gamma} \leq 600\ s^{-1}$, between the measurement data and predictions with the PTT -a and Giesekus models. This cannot be attributed to experimental uncertainty but instead to the influence of the non-linear parameters, ϵ and α in the PTT and Giesekus models, respectively. As discussed in section 3.4.5, these non-linear parameters control the elongation viscosity and thus affect the $N_1(\dot{\gamma})$ values. The larger the values of ϵ and α, the smaller the rate of increase of the $N_1(\dot{\gamma})$ values by comparison to the measurement data in the range, $\dot{\gamma} \geq 100\ s^{-1}$. Although the PTT -b model shows more accurate values in this range, it is still not as accurate as the PTT -a model over the whole range of shear strain rates, $0.1 \leq \dot{\gamma} \leq 600\ s^{-1}$, for η and $N_1(\dot{\gamma})$.

3.4.4 Transient shear flow

Figures 3.4(a), 3.4(b) and 3.5 show predicted values of η^+ for the PTT -a, PTT -b and Giesekus models, respectively, against the measured values of η^+ by Lee (2003) over the time interval from time, $t = 0$ to $t = 20\lambda_{long}$, where λ_{long} is the longest mode of relaxation[3], which is 3.77 s for this fluid[4]. The transient shear viscosity, η^+ is defined as:

$$\eta^+ = \frac{\sigma_{xy}}{\dot{\gamma}} \tag{3.16}$$

Shear strain rates of $\dot{\gamma} = 0.1$, 20, 100 and 600 s^{-1} were imposed from time $t = 0\ s$ to obtain the four corresponding curves shown in figures 3.4(a), 3.4(b) and

[3]The longest time taken for a polymer chain to relax (Bird et al., 1987)

[4]Unfortunately, accurate transient measurements of normal stress were not possible, due to strong oscillation in the normal force that depended on the rotation frequency of the plate.

3.5. However, there is a difference between the experiments and the calculations that is noteworthy and explains the differences between simulated and measured data during the initial period. Experimentally it takes the rheometer plate a finite time to reach the desired shear strain rates. Consequently, all simulation graphs show the predictions for transient viscosity starting at higher values. This also causes characteristics such as the stress overshoot to occur earlier in time. Predictions for the stress overshoot are illustrated in figures 3.4(a), 3.4(b) and 3.5 occurring at an approximate time of $t = 0.1$, 0.02 and 0.004 s for shear strain rates, $\dot{\gamma} = 20$, 100 and 600 s^{-1} respectively, for all models. The measured value at the overshoot, at shear strain rates of 20, 100 and 600 s^{-1} and the absence of an overshoot at $\dot{\gamma} = 0.1\ s^{-1}$ is predicted very well with the PTT -a and Giesekus models. The PTT -b model predicts all these quantities very well except the overshoot value at $\dot{\gamma} = 600\ s^{-1}$ which shows a much larger difference by comparison to the measurement data, than the other two models. The PTT -a model predicts more accurate values of η^+ at the overshoot and in the steady state region, $0.1 \leq t \leq 100\ s$ at all four shear strain rates. The PTT -a model also exhibits a better qualitative prediction for the overshoot when making a comparison to the measurement data for the 2.5 % PIB solution.

The difference in the initial time interval between experiment and calculation is attributed to the rheometer plate inertia; although it could be accounted for by means of a ramp from time $t = 0$ to $t \approx 0.04\ s$ it was not necessary as the two most important characteristics of the shear flow (the stress overshoot and final steady state values of η^+) were clearly reproduced by all models in figures 3.4(a), 3.4(b) and 3.5. However, if singularities in the stresses at time $t = 0$ s were encountered in these simulations, then a ramp would have been necessary in order to avoid this. However, they were not encountered and a ramp was therefore not needed.

3.4.5 Model predictions for planar elongational deformation

Figure 3.6 shows predictions for the steady state elongation viscosity η_ε as a function of the planar elongational strain rate, $\dot{\varepsilon}$, using all three models, for the 2.5 % PIB solution. All three models exhibit a plateau region at $\eta_\varepsilon = 4.36\ Pa.s$

over the range, $0.001 \leq \dot{\epsilon} \leq 0.1\ s^{-1}$. The PTT -a and Giesekus models both show elongational thinning at $\dot{\epsilon} \geq 0.1\ s^{-1}$ as η_ϵ begins to decrease. The PTT -a model exhibits stronger elongational thinning than the Giesekus model due to the non-linearity parameters in both models controlling the extent to which the fluid thins. The smaller the values of ϵ and α in the PTT and Giesekus models, respectively, the stronger the elongational thickening. The PTT -b model shows elongational thickening in the range $0.1 \leq \dot{\epsilon} \leq 600\ s^{-1}$ as does the PTT -b model used for a similar 5 % PIB solution of Baaijens (1994b). The behaviour of the PTT -b model is due to the characteristics of the linear form for A(τ_E, λ). However, as discussed in section 3.2 the PTT -a model should describe an elongational viscosity that passes through a maximum before thinning. This is not shown in figure 3.6 due to the fact that the non-linear parameter, 'a' had to remain at zero due to oscillations in the stress (this is described in more detail in section 3.4.3). By moving, 'a' away from zero a maximum is obtained, as shown by Quinzani et al. (1995), who published experimental elongation viscosity data for a similar 5 % PIB solution measured in a fluid analyzer RFX (Rheometrics, Inc.) based on opposing jet flow.

In the limit, as 'ϵ' and 'α' tend to zero, all models turn into the upper convective Maxwell model (UCM), (Bird et al., 1987) which has infinite extensional stresses above a certain elongational rate.

For the 2.5 % PIB solution, the empirical Newtonian relationship; $\eta_\epsilon = 3\eta$ does not hold in the plateau region $0.001 \leq \dot{\epsilon} \leq 0.1\ s^{-1}$. Contrarily, in this region, elongational viscosities of $\eta_\epsilon = 4.36\ Pa.s$ are predicted and consequently, for this solution the approximation; $\eta_\epsilon \approx 4\eta$ is satisfied in agreement with the finding of Quinzani et al. (1995) for a similar PIB solution.

3.5 6 % PIB Solution

3.5.1 Validation of the Cox-Merz rule

The 6 % PIB solution was treated in exactly the same way as the 2.5 % PIB solution, but has a different PIB concentration of and therefore shows different rheometric results. Linear oscillatory shear and non-linear steady shear flow

measurements were taken by Cambridge (2002) and Lee (2003) and are described and discussed for this solution, in the following sections.

For oscillatory shear flow, obtained by Cambridge (2002) and Lee (2003) the 6 % PIB solution was deformed at a 10 % strain and at frequencies ω ranging from 0.01 to 110 s^{-1}. For steady shear flow obtained by Cambridge (2002) and Lee (2003) the solution was deformed at shear strain rates $\dot{\gamma}$ ranging from 0.0005 to 1000 s^{-1} and from 0.01 to 600 s^{-1}, respectively. These measurements were taken at 5, 10, 15, 20, 25, 30, 35, 40, 45 and 50 ^0C. This range of temperatures did not affect the functional dependence of viscosity η on $\dot{\gamma}$ and ω; it merely altered the zero-shear rate viscosity η_0 and the shear strain rate at which the transition from constant viscosity to the non-linear behaviour occurred. The data, obtained by Cambridge (2002) and Lee (2003), at these temperatures, were again superposed onto a single 'master curve' at a reference temperature of 25 ^{0}C by means of the time-temperature superposition (TTS) technique (Bird et al., 1987).

Four master curves at a reference temperature of 25 ^{0}C for non-linear steady shear viscosity and oscillatory shear obtained by Cambridge (2002) and Lee (2003) are shown and compared in figure 3.7. All four curves show excellent agreement over the whole range of frequencies ω and shear strain rates $\dot{\gamma}$, successfully validating the empirical Cox-Merz rule. For an explanation of the Cox-Merz rule, see section 3.4.1. All four curves show a plateau region of $\eta(\dot{\gamma})$, $\eta^*(\omega) \approx 17$ $Pa.s$ at a frequency and shear strain rate over the range, $\dot{\gamma},\omega \leq 0.1$ s^{-1}. At frequency and shear strain rate values greater that this i.e. for $0.1 \leq \dot{\gamma},\omega \leq 1000$ s^{-1}, the steady shear curves begin to move into the non-linear region whereby the fluid begins to shear thin, thus lowering the values of $\eta(\dot{\gamma})$. In accordance to the Cox-Merz rule, the linear oscillatory measurements also exhibit this shear thinning phenomenon over the same range of frequencies ω. Both sets of linear oscillatory measurements obtained by Cambridge (2002) and Lee (2003), over the whole range of frequencies show excellent quantitative agreement with the sets of non-linear steady shear measurements also obtained by Cambridge (2002) and Lee (2003).

3.5.2 Determination of the Maxwell material parameters

The Maxwell material parameters for the 6 % PIB solution were obtained by Lee (2003) using the respective rheometric shear stress measurements over the range $0.1 \leq \dot{\gamma} \leq 600\ s^{-1}$. In order to model the response of the 6 % PIB solution under deformation, the linear oscillatory shear data is used to obtain Maxwell material parameters, λ_k and η_k, for this fluid. Section 3.4.2 described in detail the method employed to obtain the linear Maxwell material parameters of a respective fluid and for the 6 % PIB solution, these parameters are presented in table 3.2.

Using 'superposition' of linear viscoelastic Maxwell models (Bird et al., 1987), each partial stress τ_{Ek} is calculated from the relaxation time λ_k and the viscosity η_k at mode 'k' and summed to calculate the total viscoelastic stress, τ_E. As with the 2.5 % PIB solution, it was found that increasing the number of modes used results in a more accurate description of the measured data but also in an increase in the computational time needed. Using recommendations from published literature by Baaijens (1994b) and the experimental data of Lee (2003), it was concluded that the optimum number of modes needed would be 5. Again, the first mode is used to describe the Newtonian solvent stress (see equation 2.22) and the subsequent modes are used to describe the viscoelastic modes of viscosity.

As explained in section 3.4.2, values for λ_k and η_k from table 3.2 are substituted back in to equations 3.12 and 3.13 to obtain predictions for $\eta'(\omega)$ and $\eta''(\omega)$. Figures 3.8(a) and 3.8(b) show the comparison between measured values of η' and η" to the linear oscillatory Maxwell predictions for $\eta'(\omega)$ and $\eta''(\omega)$. Measured data was available for both graphs over a range of frequencies, $0.1 \leq \omega \leq 100\ s^{-1}$ and predictions within this range match the data extremely well. Predictions were also made outside of this measured data range of frequencies, $0.1 \leq \omega \leq 100\ s^{-1}$ to; (a) show the corresponding variations at lower and higher values of ω and to; (b) highlight the plateau region of $\eta' \approx 17\ Pa.s$ at $0.01 \leq \omega \leq 0.1\ s^{-1}$ in figure 3.8(a).

From the 5 modes of relaxation times λ_k shown in table 3.2, the zero-shear viscosity averaged time constant $\bar{\lambda}$ can be defined, see equation 3.14. For the 6 % PIB solution; $\bar{\lambda} = 1.26\ s$.

3.5.3 Determination of PTT and Giesekus non-linearity parameters

In section 3.4.3 equation 3.15 showed how 'q' is reduced to a minimum as the non-linearity parameters, 'ϵ' and 'α' for both PTT models and the Giesekus model, respectively, are incremented from 0 to 1. By reducing q to a minimum for all models, with $a = 0$, optimum values for 'ϵ' and 'α' are found. For $0 < a \leq 1$ in the PTT models, non-physical oscillations in the transient shear stress occur at a period just after the stress overshoot. These oscillations in stress do improve the steady state PTT predictions for $\eta(\dot{\gamma})$ and $N_1(\dot{\gamma})$ but require smaller time steps to obtain solution convergence. The solution for $\eta(\dot{\gamma})$ and $N_1(\dot{\gamma})$ at $a = 0$ for the range of shear rates is within the experimental error of the data and computation in subsequent chapters proved to be impossible using the PTT models with $a \neq 0$.

For the 6 % PIB solution the 5 mode Giesekus model produced a smaller residual for q, thus making better predictions than the PTT -a and PTT -b models for $N_1(\dot{\gamma})$ and $\eta(\dot{\gamma})$ over the range of shear rates $0.02 \leq \dot{\gamma} \leq 600\ s^{-1}$. This was also shown previously for a fluid very similar to the 6 % PIB solution by Baaijens (1994b).

Non-linear predictions for $\eta(\dot{\gamma})$ were made using all models and are compared in figure 3.9(a) to the measured data for $\eta(\dot{\gamma})$ of Baaijens (1994b), Cambridge (2002) and Lee (2003). All models show the same trend over the range $0.1 \leq \dot{\gamma} \leq 0.7\ s^{-1}$, where $\eta(\dot{\gamma}) \approx 17.4\ Pa.s$. The small degree of shear thinning predicted in this region is negligible when making comparisons to all measurement data, as there are clearly experimental errors involved, as shown, for example, by the differences between the data from Cambridge (2002) and Lee (2003) for essentially identical fluids. The shear thinning indicated by the simulations for $\dot{\gamma} \leq 1\ s^{-1}$ is of a similar order to the scatter of the measurement data. In the region $1 \leq \dot{\gamma} \leq 600\ s^{-1}$ all models show shear thinning as $\eta(\dot{\gamma})$ decreases with increasing values of $\dot{\gamma}$. However, the Giesekus model predictions are better than those of the PTT -a and PTT -b models. As the fluid begins to shear thin more severely at approximately $\dot{\gamma} = 10\ s^{-1}$ the PTT models predict a higher viscosity at shear rates $10 \leq \dot{\gamma} \leq 600\ s^{-1}$. The measured data of Cambridge (2002) and Lee (2003) are in good agreement with each other and the data of Baaijens (1994b) for a

similar fluid show a good qualitative comparison but clearly the fluid of Baaijens (1994b) again behaves differently at higher shear rates.

Figure 3.9(b) shows predictions with both of the non-linear PTT and Giesekus models for $N_1(\dot{\gamma})$ against measurement data of Baaijens (1994b), Cambridge (2002) and Lee (2003). All models exhibit almost exactly the same qualitative trends and predict measurement data extremely well over the range of shear rates $0.1 \leq \dot{\gamma} \leq 3\ s^{-1}$. Over the range of shear rates $3 \leq \dot{\gamma} \leq 600\ s^{-1}$ the PTT -b model predicts slightly higher values of $N_1(\dot{\gamma})$ when compared to the PTT -a and Giesekus models and makes marginally more accurate predictions in the shear rate region $100 < \dot{\gamma} \leq 600\ s^{-1}$. However, the Giesekus model makes excellent predictions over the whole range of shear rates $0.1 \leq \dot{\gamma} \leq 600\ s^{-1}$. The Giesekus model does predict moderately lower values of $N_1(\dot{\gamma})$ compared to measurement data by Cambridge (2002) and Lee (2003) over the range $200 \leq \dot{\gamma} \leq 600\ s^{-1}$, however there are clearly experimental errors involved, as shown, for example, by the difference between Cambridge (2002) and Lee (2003) and the measurement date by Baaijens (1994b) for essentially an identical fluid. The reduction in $N_1(\dot{\gamma})$ by the Giesekus model over the range $200 \leq \dot{\gamma} \leq 600\ s^{-1}$ is of a similar order to the difference in this measurement data and can be considered negligible. The PTT -a model predicts the lowest values of $N_1(\dot{\gamma})$ in the range $60 \leq \dot{\gamma} \leq 600\ s^{-1}$ (despite very accurate predictions being made at lower shear rates) due to the influence of the non-linear parameter, ϵ. As discussed in section 3.4.3, the larger the values of ϵ, the smaller the gradient of change in values for $N_1(\dot{\gamma})$ in the range $\dot{\gamma} \geq 60\ s^{-1}$.

3.5.4 Transient shear flow

Figures 3.10(a), 3.10(b) and 3.11 show the predicted and measured transient shear viscosity values η^+ (defined in equation 3.16) for the PTT -a, PTT -b and Giesekus models, respectively over the time interval $t = 0$ to $t = 20\lambda_{long}$ where $\lambda_{long} = 5.56\ s$ for this fluid[5]. Shear strain rates of, $\dot{\gamma} = 0.03$, 20, 200 and 600 s^{-1} were imposed at time, $t = 0\ s$ to obtain the four corresponding curves shown

[5]Unfortunately, accurate transient measurements of normal stress were not possible, due to strong oscillation in the normal force that depended on the rotation frequency of the plate.

in figures 3.10(a), 3.10(b) and 3.11. As with the 2.5 % PIB solution, there is a difference between the simulated and measured data during the initial period. This is attributed to the rheometer plate inertia and is explained in detail in section 3.4.4.

Predictions for the stress overshoot are illustrated in both figures 3.10(a), 3.10(b) and 3.11 occurring approximately at times, $t = 0.1$, 0.01 and 0.004 s at shear strain rates of, $\dot{\gamma} = 20$, 100 and 600 s^{-1}, respectively for all models. At all these shear strain rates the quantitative value at the overshoot is predicted very well with the PTT -a and Giesekus models but not as well with the PTT -b model, especially at shear stain rates of $\dot{\gamma} = 200$ and 600 s^{-1}. The absence of an overshoot is well predicted at shear rates of 0.03 s^{-1} by all three models. However, over the whole range of shear rates, the Giesekus model does produce much better predictions than either of the PTT models, for the stress overshoot and for values of η^+ over the steady state region $0.1 \leq t \leq 100$ s. The Giesekus model also exhibits a smoother and less sudden overshoot which provides a better qualitative prediction when making a comparison to the measurement data for the 6 % PIB solution.

3.5.5 Model predictions for planar elongational deformation

To the best knowledge of the author, elongation deformation measurements for the 6 % PIB solution or a similar solution are not available. Therefore, figure 3.12 shows only predictions for the steady state elongation viscosity η_ε as a function of the planar elongation rate $\dot{\varepsilon}$. All three models exhibit a plateau region of, $\eta_\varepsilon = 72.29\ Pa.s$ over the range $0.001 \leq \dot{\epsilon} \leq 0.1\ s^{-1}$ and all show elongational shear thinning at $\dot{\epsilon} \geq 0.1\ s^{-1}$ as $\eta_\varepsilon(\dot{\epsilon})$ begins to decrease. Figure 3.12 is qualitatively very similar to figure 3.6 as the PTT -a model again exhibits much stronger shear thinning than the Giesekus model over the range $0.1 \leq \dot{\epsilon} \leq 600\ s^{-1}$. However, the PTT -b model in figure 3.12 shows elongational thinning as opposed to the typical monotone elongation thickening characteristic of the PTT -b model (see section 3.2). However, fitting the PTT -b model with; $a \neq 0$, surmounts this (possibly) unrealistic feature but leads to oscillations in the stress (as mentioned

earlier). An explanation as to how the non-linear parameters, α and ϵ, in both models control the extent to which the fluid thins was given in section 3.4.5.

For the 6 % PIB solution, the empirical Newtonian relationship; $\eta_\epsilon = 3\eta$, does not hold over the plateau region $0.001 \leq \dot{\varepsilon} \leq 0.1\ s^{-1}$. Contrarily, in this region, elongational viscosities of; $\eta_\epsilon = 72.29\ Pa.s$ are predicted and consequently, for this solution, the approximation; $\eta_\epsilon \approx 4\eta$, is satisfied and in agreement with the finding of Quinzani et al. (1995) for a less concentrated 2.5 % PIB solution.

3.6 Discussion and conclusions

In this chapter, two polyisobutylene (referred to as 2.5 % and 6 % PIB) solutions rheometrically characterised by Cambridge (2002) and Lee (2003) under linear oscillatory (infinitesimal strain) and steady (finite strain) shear were considered. Master curves for the material functions; $\eta(\dot{\gamma})$,$\eta^*(\omega)$, $\eta^+(t)$ and $N_1(\dot{\gamma})$ were obtained using time-temperature superposition (TTS) at a reference temperature of 25 ^{0}C. The Cox-Merz rule has been validated proving that $|\eta(\dot{\gamma})| = \eta^*(\omega)$ for both fluids. The size of the material functions; $\eta(\dot{\gamma})$,$\eta^*(\omega)$, $\eta^+(t)$ and $N_1(\dot{\gamma})$ for the 6 % PIB solution are roughly one order of magnitude greater than for the 2.5 % PIB solution.

To model the non-linear response of these fluids under steady (finite strain) shear, Maxwell material parameters were obtained by Lee (2003) from the linear oscillatory data.

Three differential, 5 mode, constitutive viscoelastic models were used, namely the Giesekus and Phan-Thien and Tanner (PTT-a and PTT -b) models. The non-linearity parameters 'α' and 'ϵ' within these models were tuned to fit as accurately as possible the master curves for $\eta(\dot{\gamma})$ and $N_1(\dot{\gamma})$ under a non-linear regime, namely over the range $0.001 \leq \dot{\gamma} \leq 600\ s^{-1}$. The residual error '$q$' (see equation 3.15) had to be reduced to a minimum, as 'α' and 'ϵ' were incremented over the range 0 to 1. The best models to use for the 2.5 % and 6 % PIB solutions were found to be the 5 mode PTT -a and Giesekus models respectively. They each produced a lower value of 'q' for their respective fluids. Table 3.3 shows which model made the best predictions for each material function.

For both 2.5 % and 6 % PIB solutions, simulations using all three constitutive models have been quantitatively compared to measurement data by Lee (2003) and measurement data by Cambridge (2002) for identical fluids and to data by Baaijens (1994b) for similar fluids. Good agreement was found for all material functions when these comparisons were made.

The fitted models are used to profile the evolution of transient stress for both fluids. Each model predicts the stress overshoot where applicable and good predictions are made for the steady state value of transient viscosity η^+, although, some models made better predictions than others.

Although a limited amount of data was available, the models yielded physically reasonable predictions for planar elongational flows. Weak, moderate and strong thinning was shown for the Giesekus, PTT -b and PTT -a models respectively, for both fluids, except where the PTT -b model showed a characteristic monotone thickening for the 2.5 % PIB solution. This degree of thinning and/or thickening is due to the relatively large values of 'ϵ' and 'α' respectively.

In the following chapter each viscoelastic constitutive model is used to make predictions for and comparisons to LDA measurements of the 2.5 % and 6 % PIB solutions around a symmetrically confined cylinder.

M_k	Maxwell parameters		PTT -a		PTT -b		Giesekus	η_N [Pa.s]
	η_k [Pa.s]	λ_k [s]	a	ϵ	a	ϵ	α	
1			0.0	0.42	0.0	0.39	0.78	0.0998
2	0.306	0.0163						
3	0.391	0.100						
4	0.135	0.6151						
5	0.160	3.77						

Table 3.1: Parameters employed for 5 mode non-linear viscoelastic constitutive Giesekus, PTT -a and PTT -b models for the 2.5 % PIB solution at a reference temperature of 25 ^0C. The zero-shear viscosity averaged time constant; $\bar{\lambda} = 0.669$ s; η_N denotes the Newtonian solvent viscosity and; M_k is the number of modes.

M_k	Maxwell parameters		PTT -a		PTT -b		Giesekus	η_N [Pa.s]
	η_k [Pa.s]	λ_k [s]	a	ϵ	a	ϵ	α	
1			0.0	0.55	0.0	0.75	0.65	0.299
2	1.61	0.0154						
3	5.78	0.110						
4	7.44	0.781						
5	2.94	5.56						

Table 3.2: Parameters employed for 5 mode non-linear viscoelastic constitutive Giesekus, PTT -a and PTT -b models for the 6 % PIB solution at a reference temperature of 25 ^0C. The zero-shear viscosity averaged time constant; $\lambda = 1.26$ s; η_N denotes the Newtonian solvent viscosity and; M_k is the number of modes.

Material functions	2.5% PIB	6% PIB
$\eta(\dot{\gamma})$ [Pa.s]	PTT -a (5 mode)	Giesekus (5 mode)
$\eta^*(\omega)$ [Pa.s]	PTT -a (5 mode)	Giesekus (5 mode)
$\eta^+(t)$ [Pa.s]	PTT -a (5 mode)	Giesekus (5 mode)
$N_1(\dot{\gamma})$ [Pa]	PTT -a (5 mode)	Giesekus (5 mode)

Table 3.3: Evaluation of the non-linear viscoelastic constitutive equations that have been fitted for the two polyisobutylene solutions, 2.5 % PIB and 6 % PIB. For each solution and for each material function the best fitting model is listed.

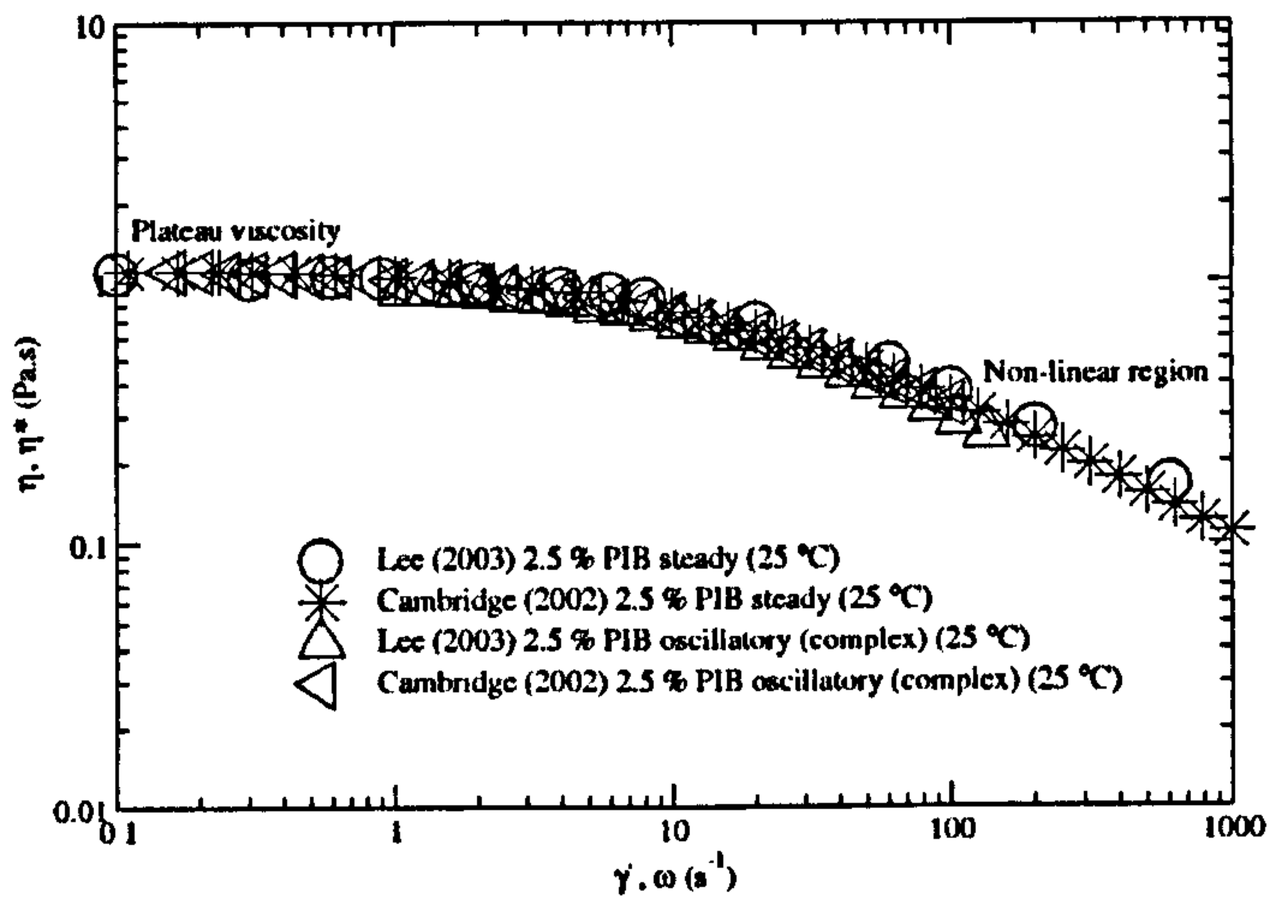

Figure 3.1: Comparison of two measured steady shear strain rate dependent viscosity, $\eta(\dot{\gamma})$ master curves with two measured complex viscosity, $\eta^*(\omega)$ master curves, at a reference temperature of 25 ^0C, to check the validity of the Cox-Merz rule for 2.5 % PIB.

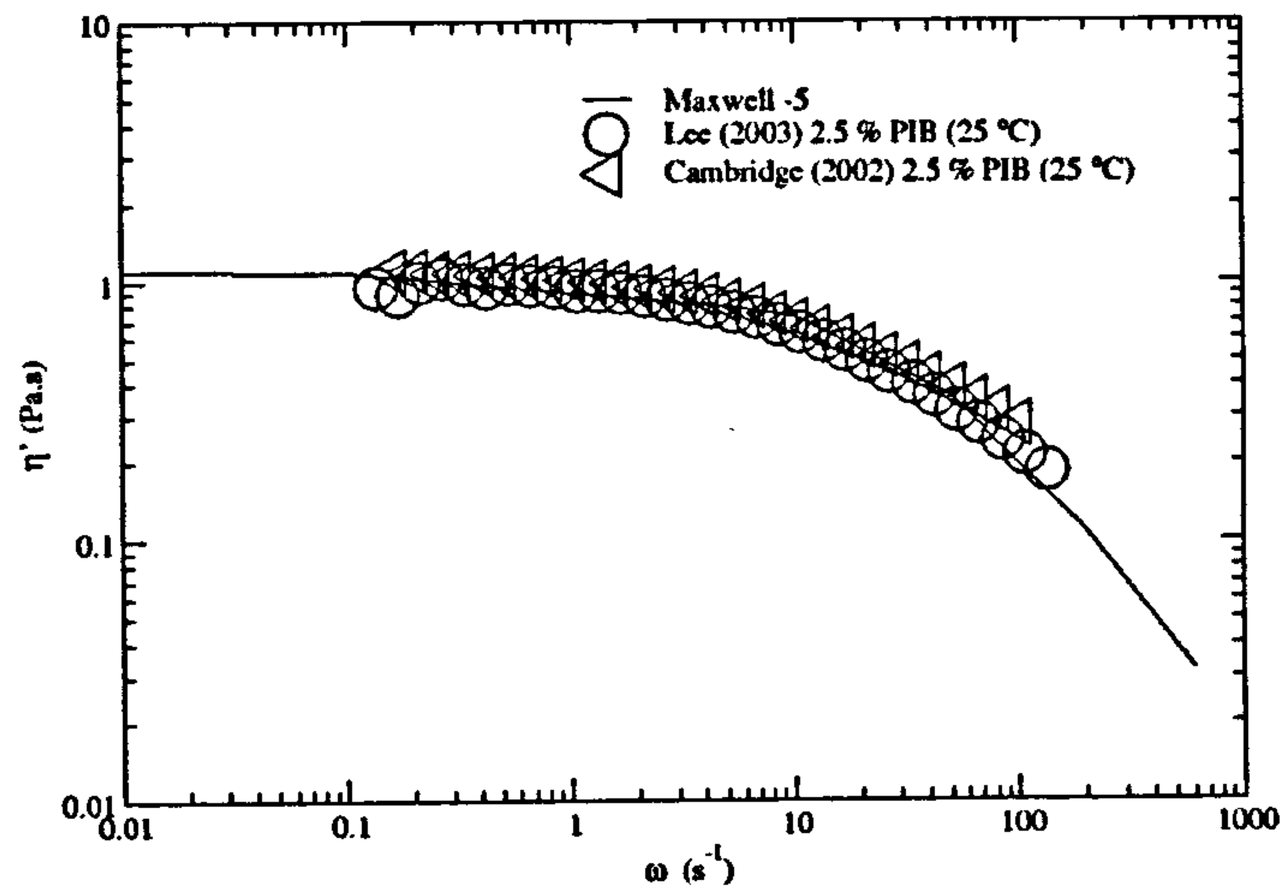

(a)

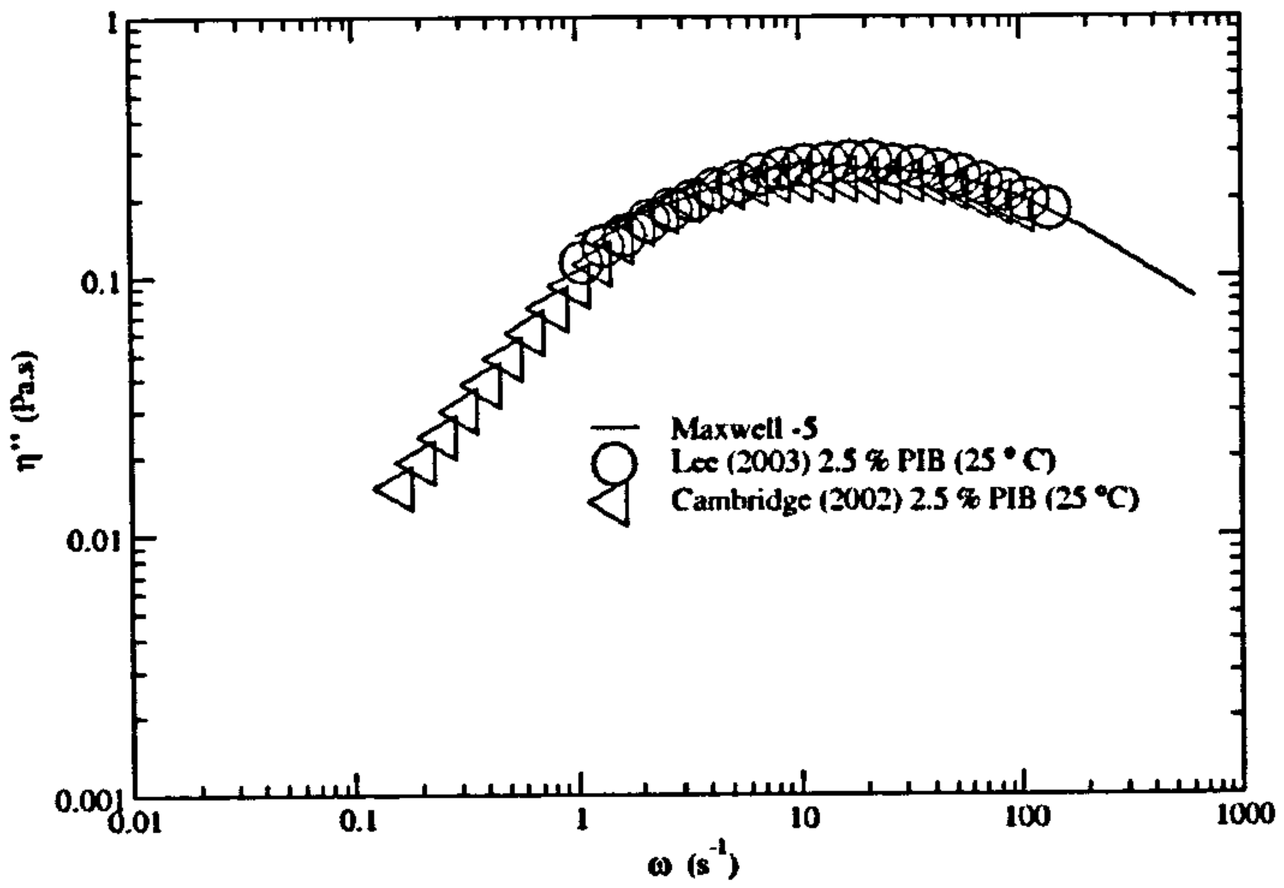

(b)

Figure 3.2: Comparison of measured values of; (a) $\eta'(\omega)$ and; (b) $\eta''(\omega)$, with their respective Maxwell model predictions under oscillatory shear flow, at a reference temperature of 25 ^0C, for 2.5 % PIB solution.

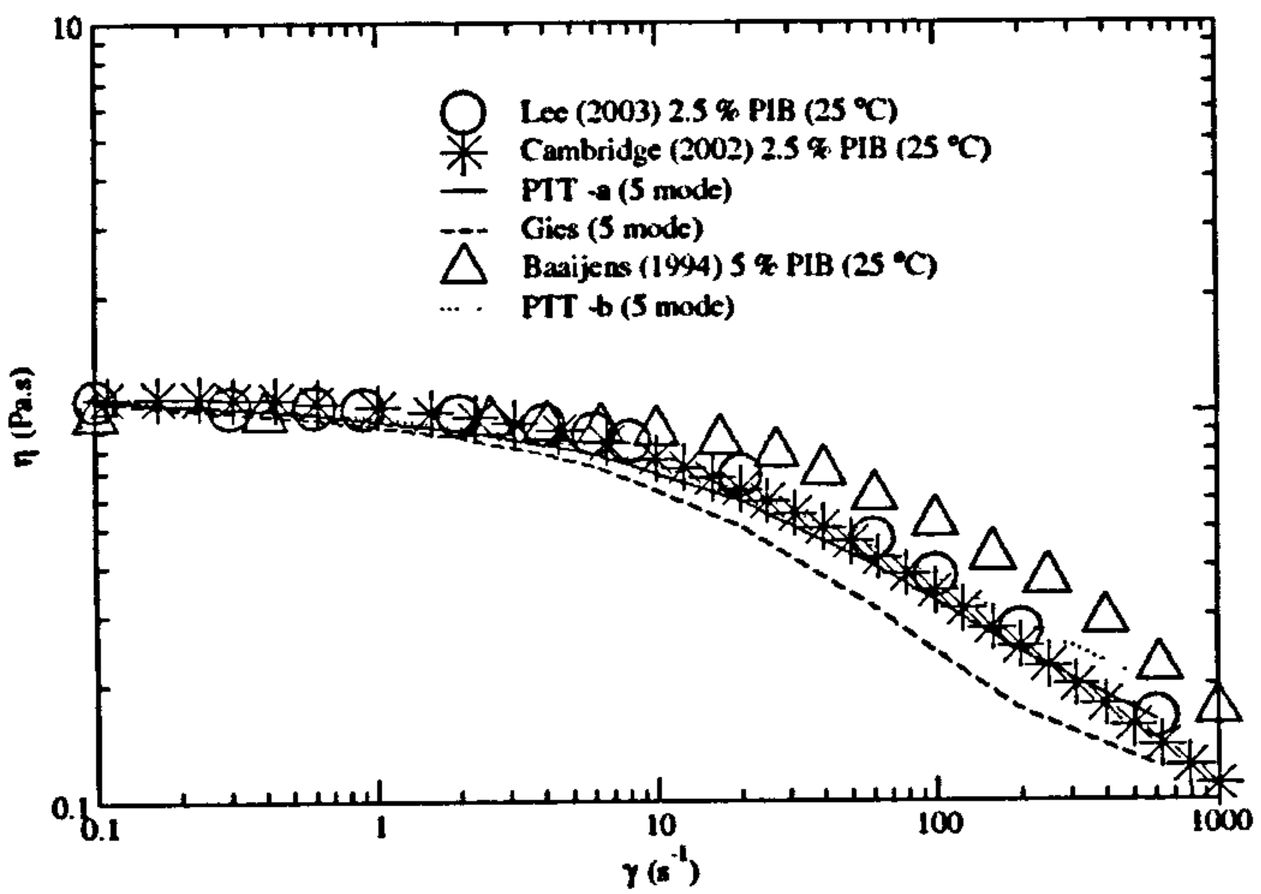

(a)

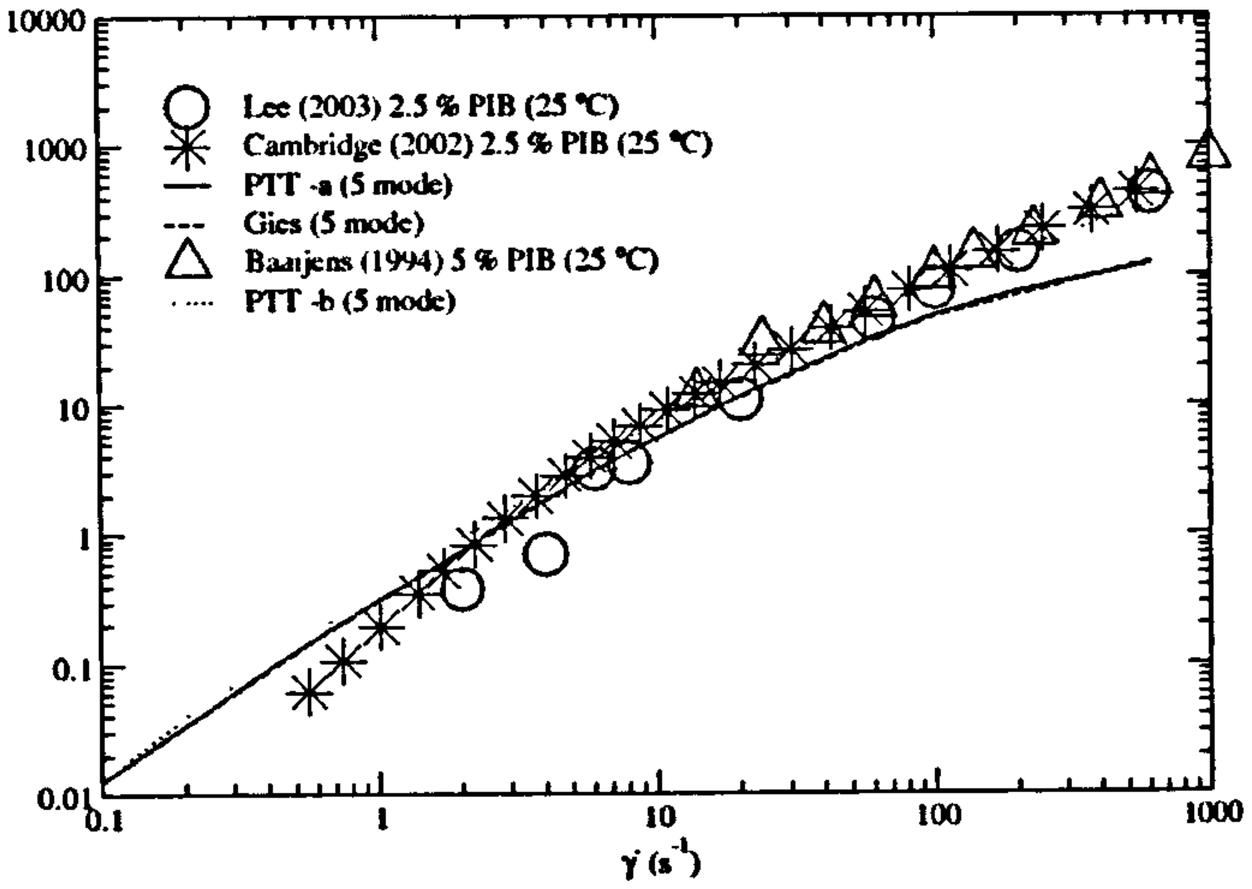

(b)

Figure 3.3: Comparison of measured values of non-linear steady state; (a) viscosity, $\eta(\dot{\gamma})$ and; (b) normal stress difference, $N_1(\dot{\gamma})$ with their respective non-linear model predictions, at a reference temperature of 25 ^0C, for 2.5 % PIB.

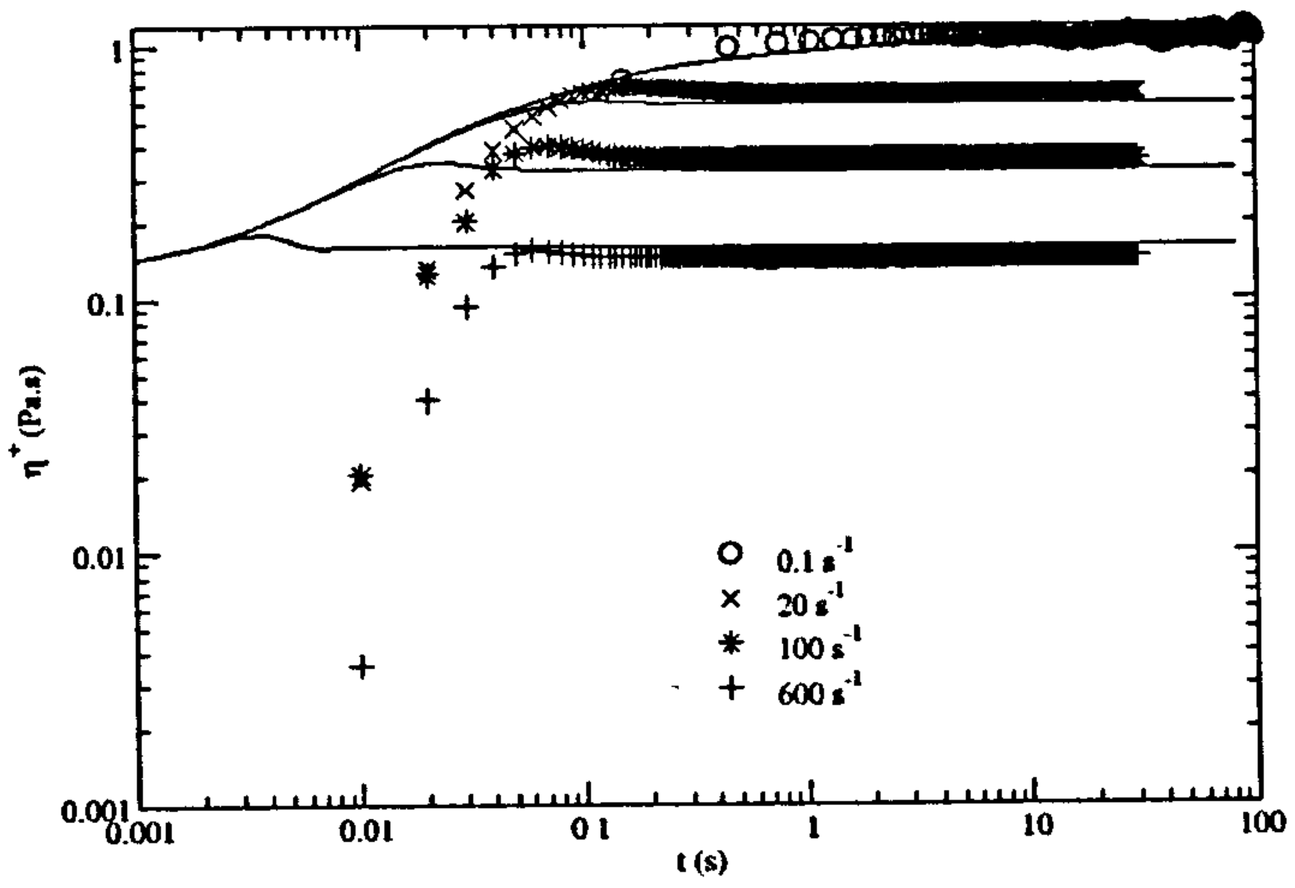

(a)

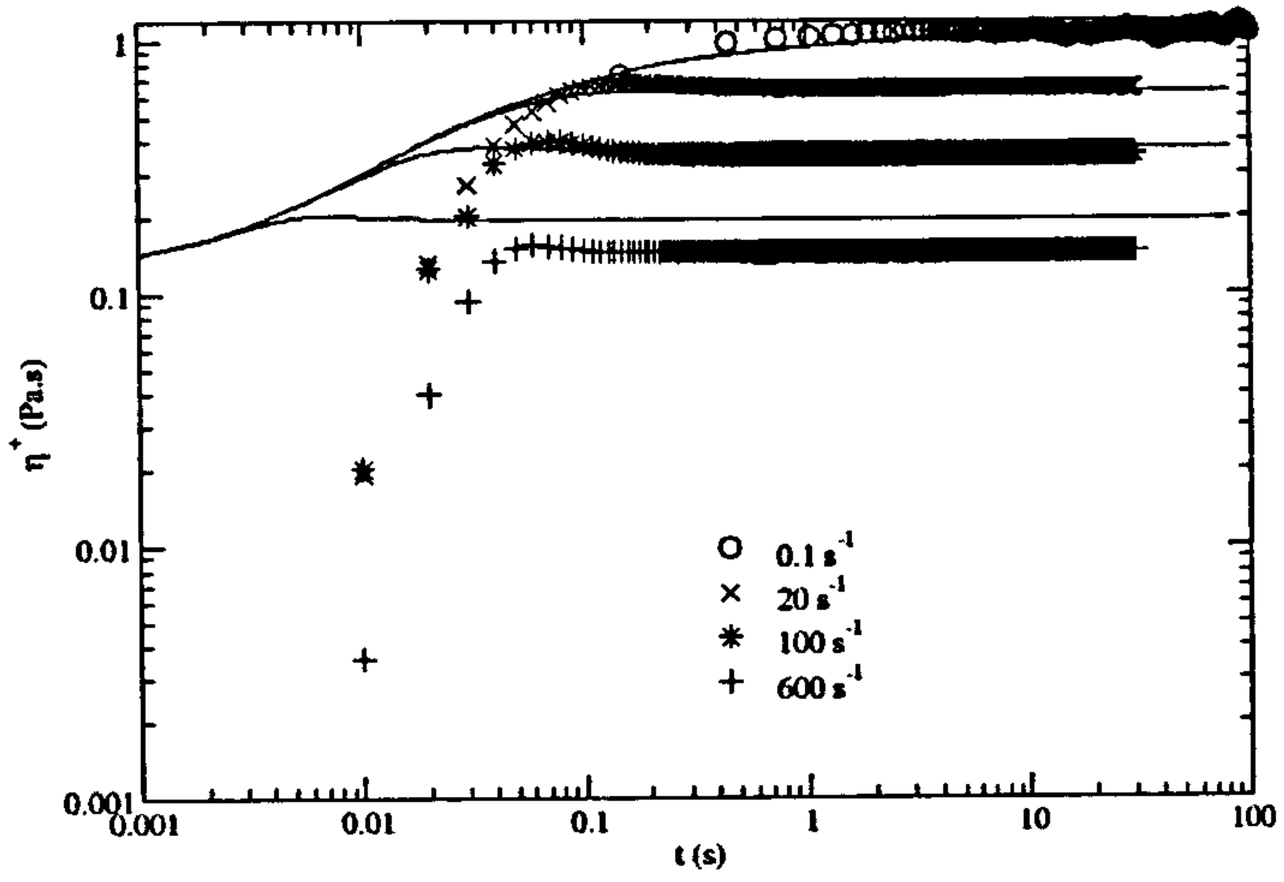

(b)

Figure 3.4: Comparison of measured values of transient viscosity, η^+ with; (a) PTT -a and; (b) PTT -b model predictions, both at a reference temperature of 25 ^0C, for 2.5 % PIB.

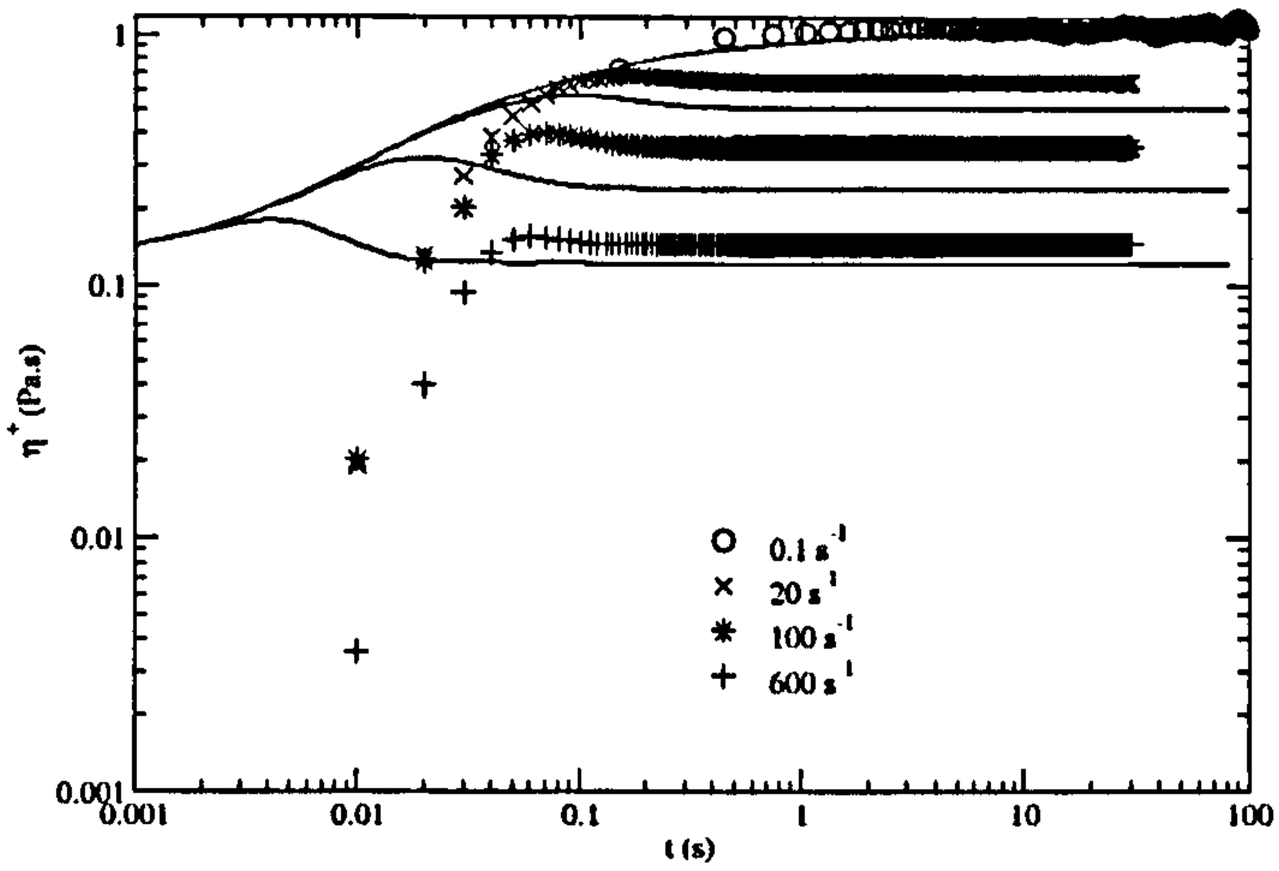

Figure 3.5: Comparison of measured values of transient viscosity, η^+ with Giesekus model predictions, at a reference temperature of 25 ^0C, for 2.5 % PIB.

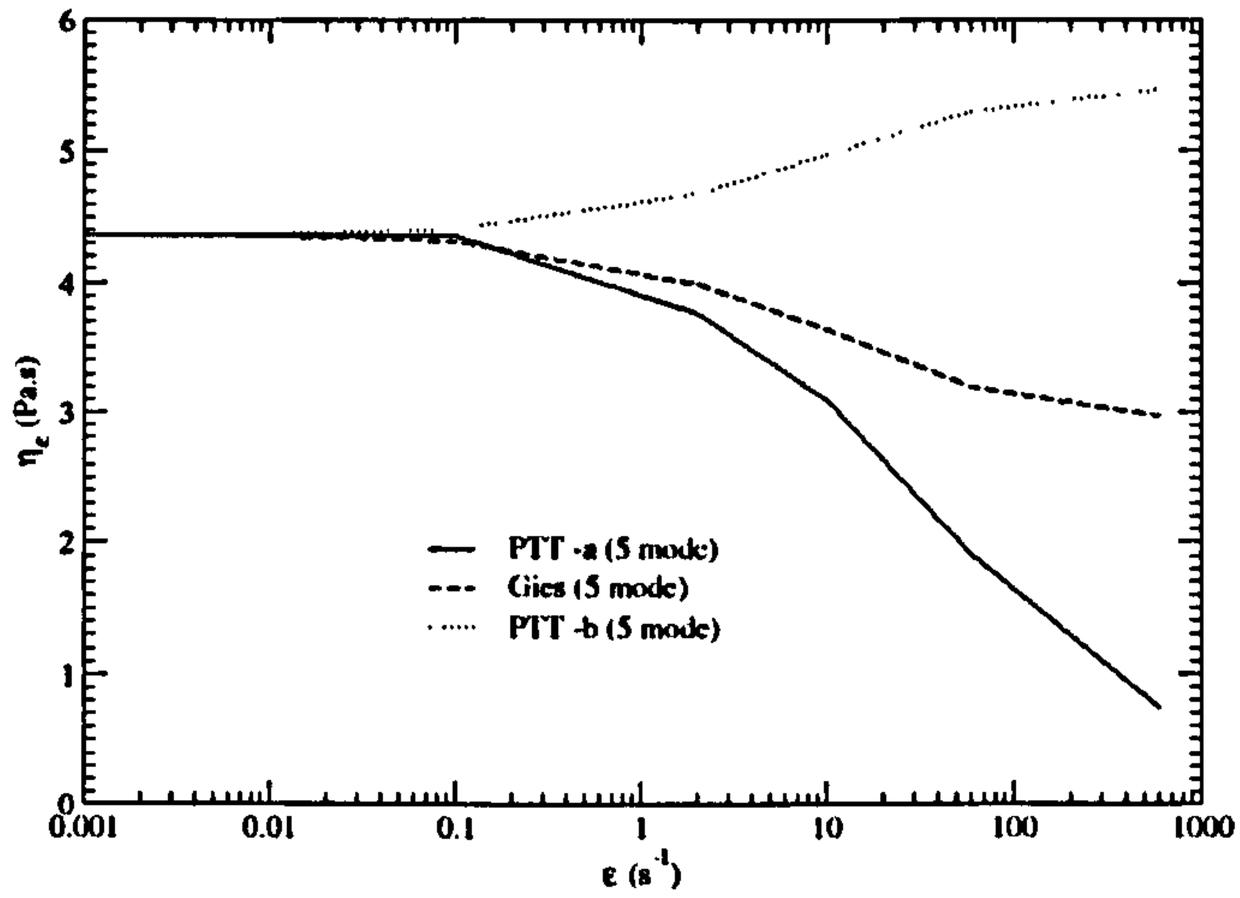

Figure 3.6: Comparison of PTT -a, PTT -b and Giesekus model predictions of planar elongational viscosity $\eta_\varepsilon(\dot{\varepsilon})$, at a reference temperature of 25 ^0C with material parameters fitted under linear shear flow for 2.5 % PIB.

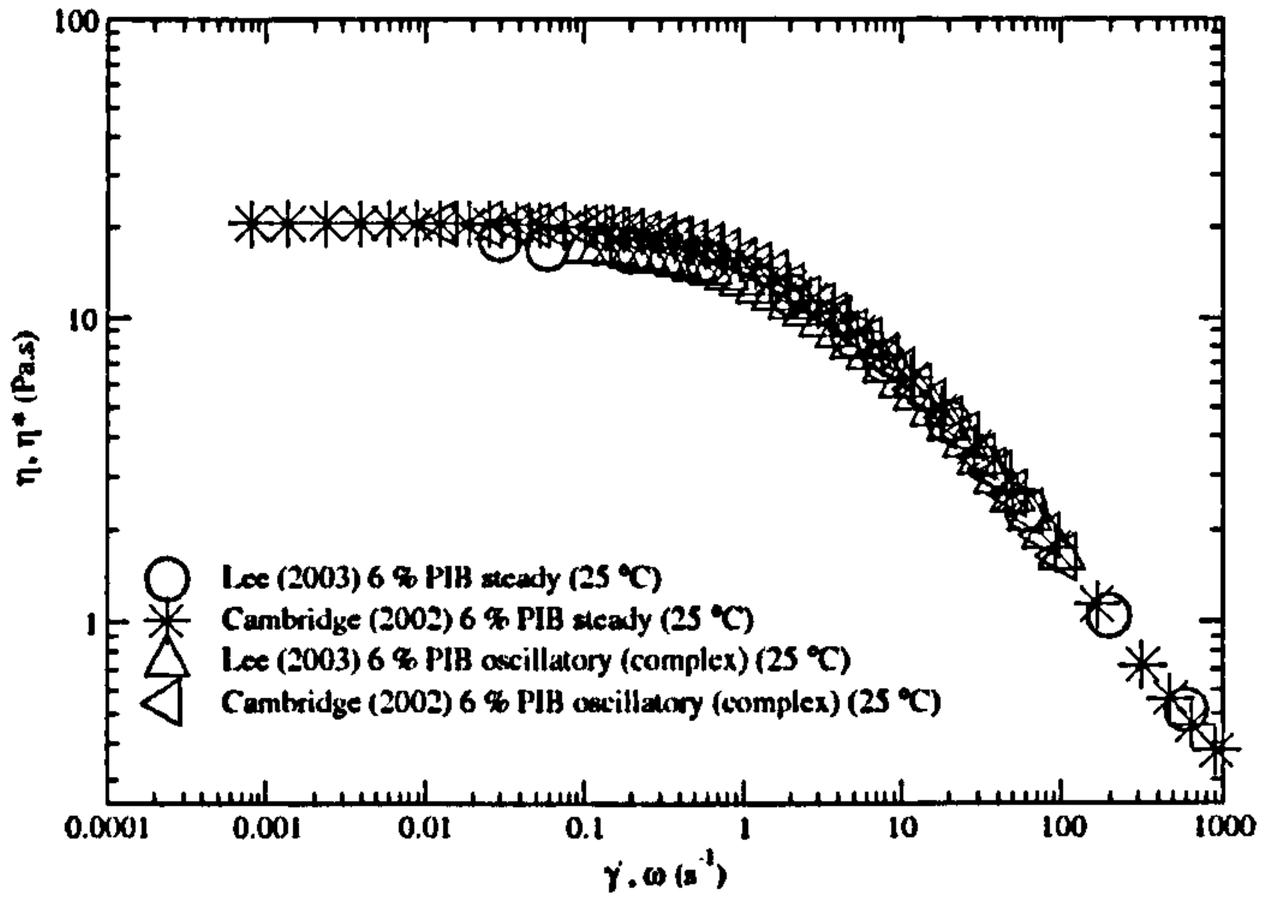

Figure 3.7: Comparison of two measured steady shear strain rate dependent viscosity, $\eta(\dot{\gamma})$ master curves with two measured complex viscosity, $\eta^*(\omega)$ master curves, at a reference temperature of 25 ^0C, to check the validity of the Cox-Merz rule for 6 % PIB

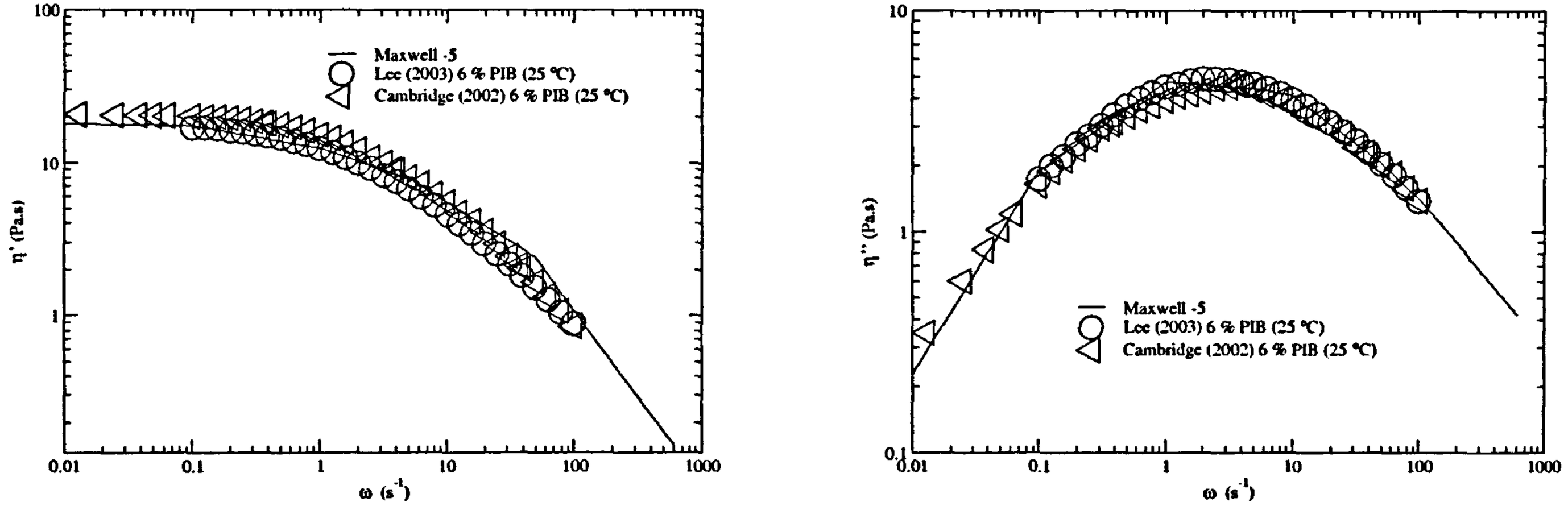

(a) (b)

Figure 3.8: Comparison of measured values of; (a) $\eta'(\omega)$ and; (b) $\eta''(\omega)$, with their respective Maxwell model predictions under oscillatory shear flow, at a reference temperature of 25 ^0C, for 6 % PIB.

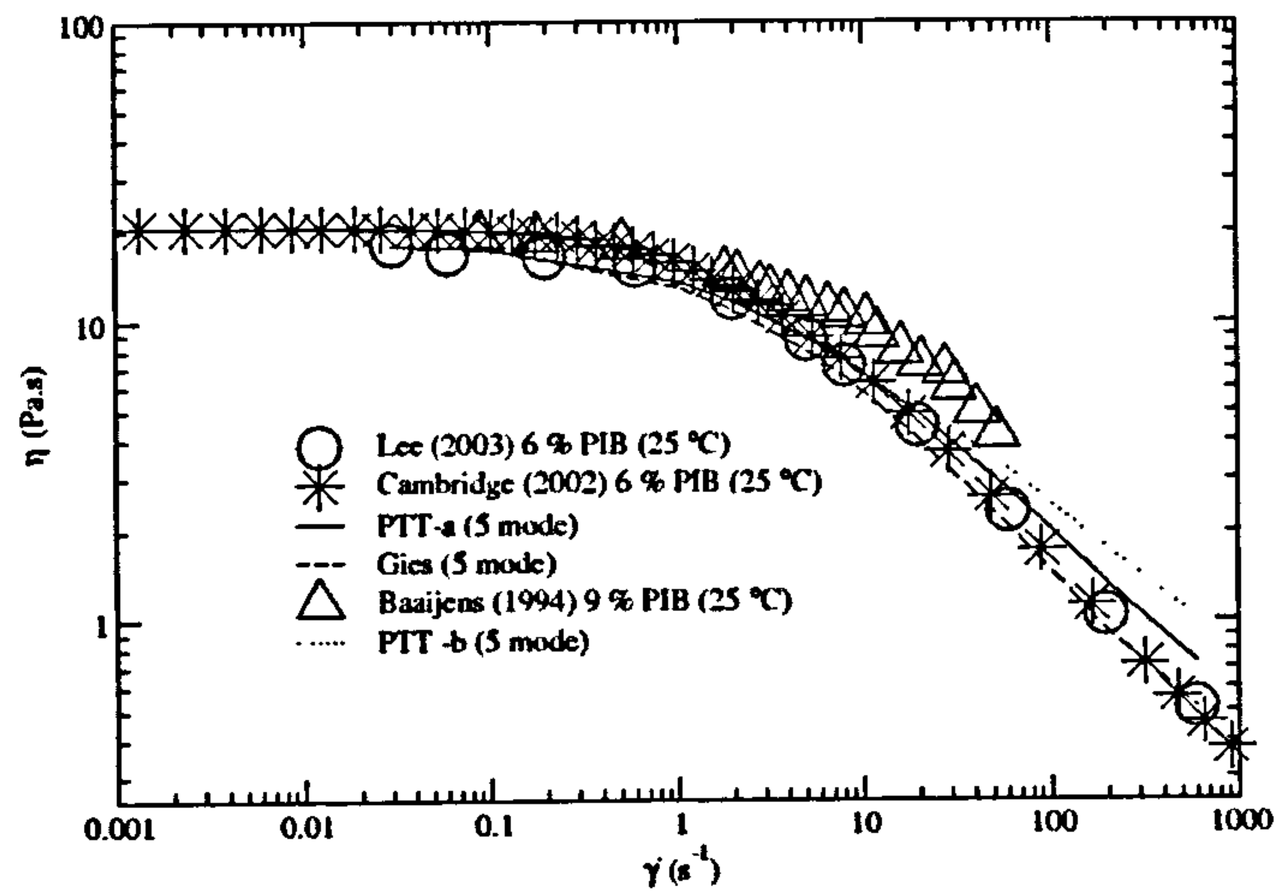

(a)

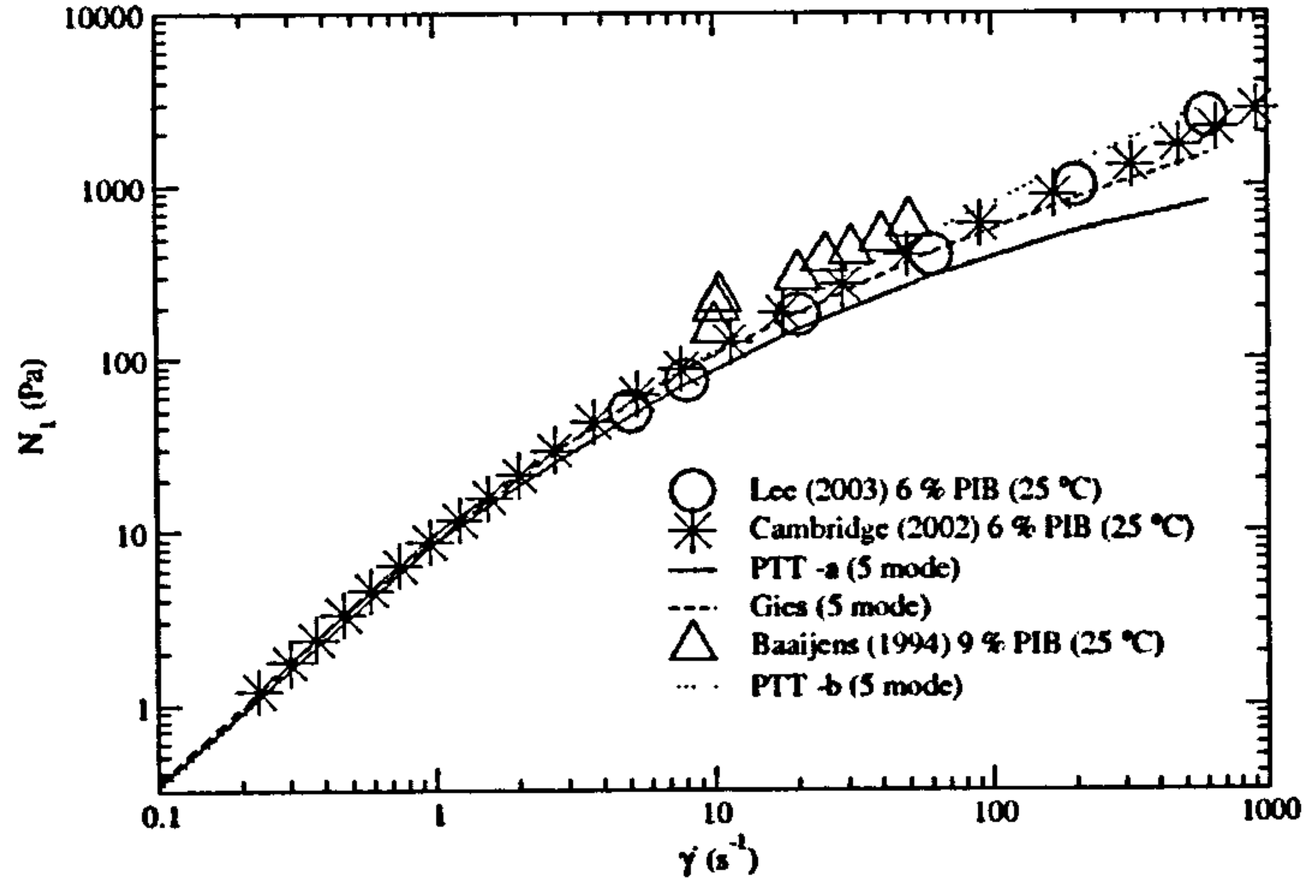

(b)

Figure 3.9: Comparison of measured values of non-linear steady state; (a) viscosity $\eta(\dot{\gamma})$, and; (b) normal stress difference $N_1(\dot{\gamma})$, with their respective non-linear model predictions, at a reference temperature of 25 ^0C, for 6 % PIB.

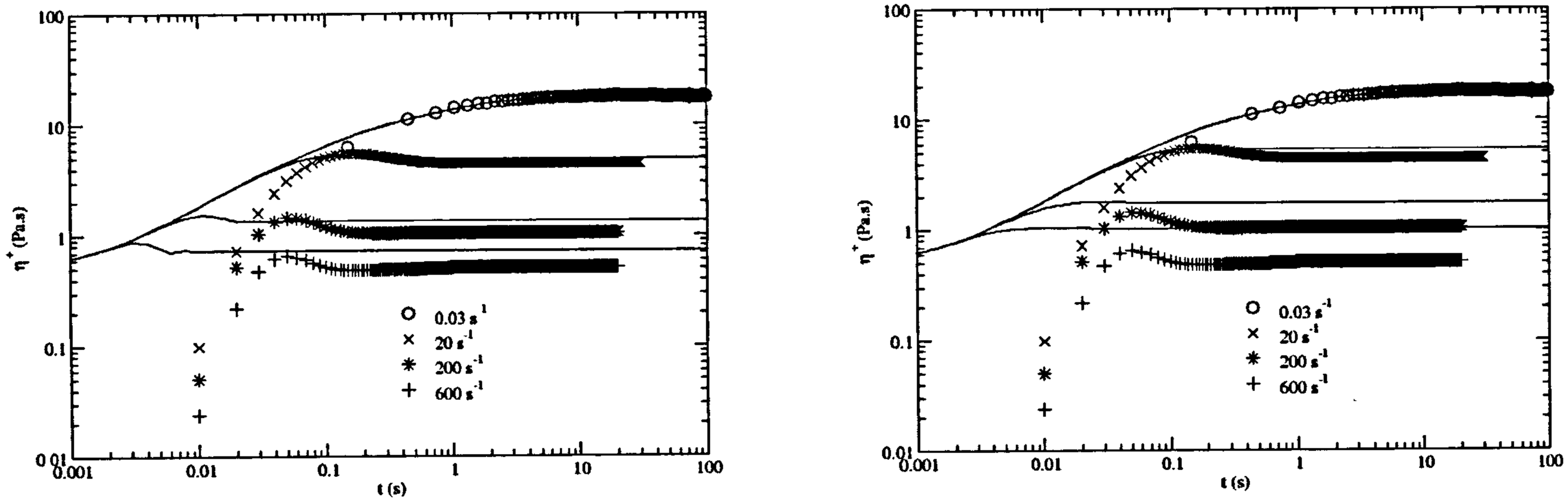

(a) (b)

Figure 3.10: Comparison of measured values of transient viscosity, η^+ with; (a) PTT -a and; (b) PTT -b model predictions, at a reference temperature of 25 ^0C, for 6 % PIB.

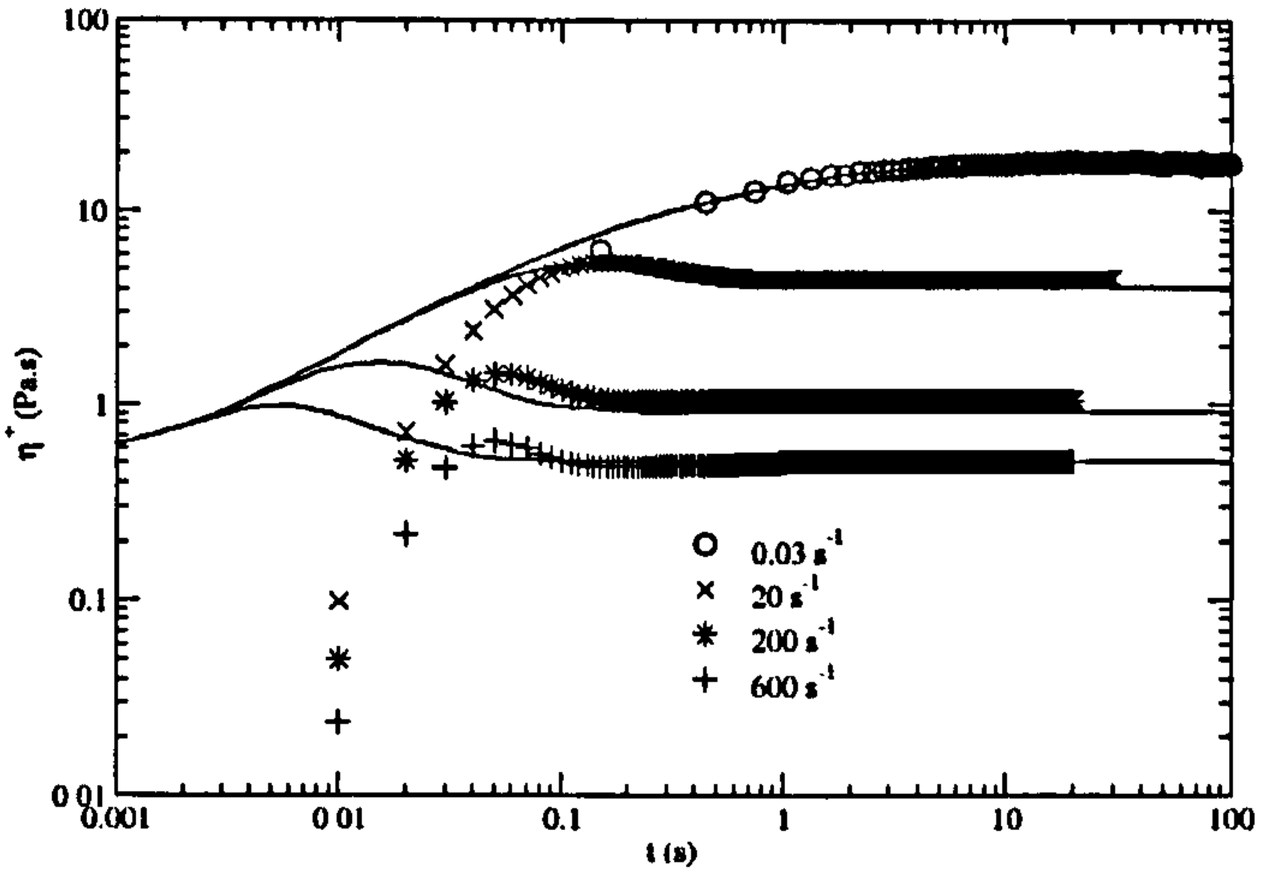

Figure 3.11: Comparison of measured values of transient viscosity, η^+ with Giesekus model predictions, at a reference temperature of 25 ^0C, for 6 % PIB.

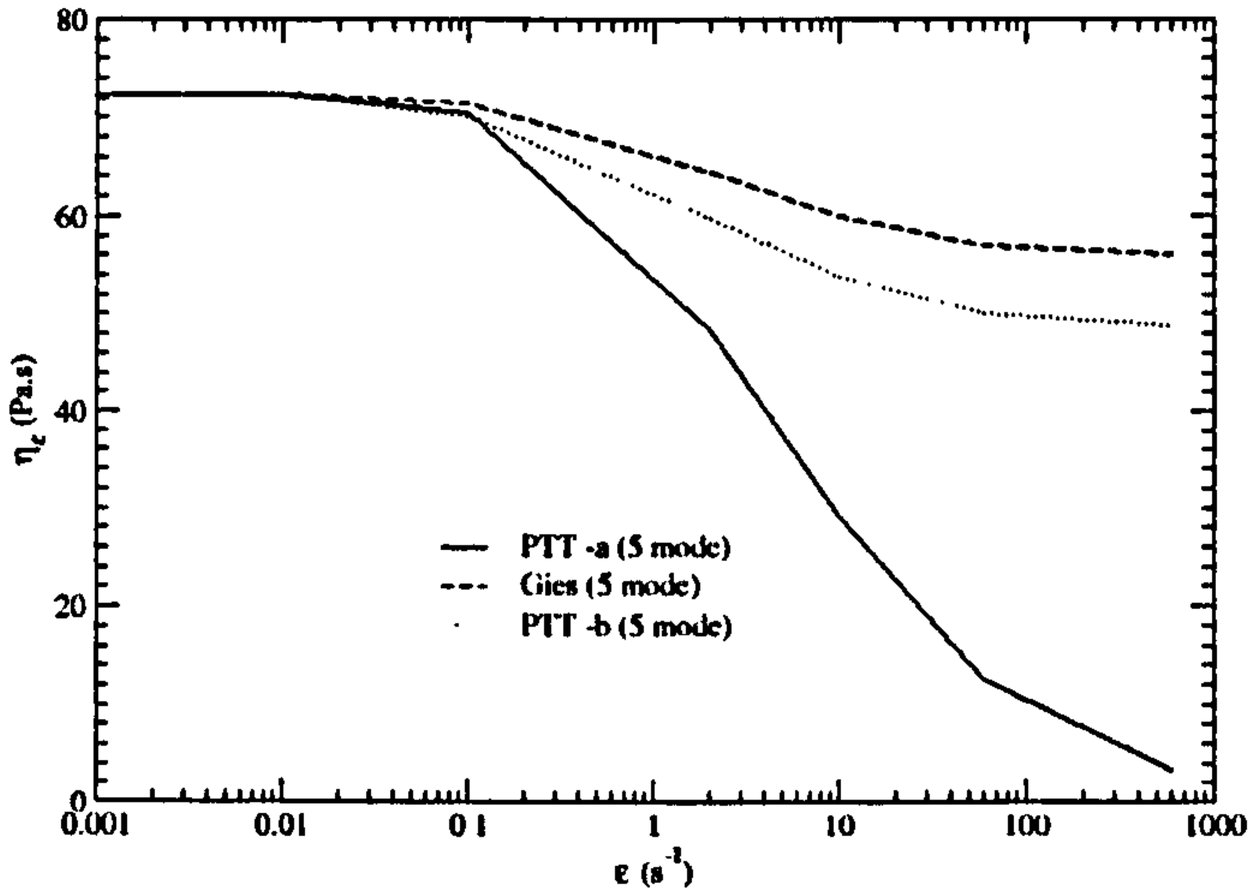

Figure 3.12: Comparison of PTT -a, PTT -b and Giesekus model predictions of planar elongational viscosity, $\eta_\epsilon(\dot{\epsilon})$, at a reference temperature of 25 ^0C with material parameters fitted in simple shear flow for 6 % PIB.

Chapter 4

Flow around a single cylinder

4.1 Introduction

Following the rheological characterisation of the two working fluids presented in the previous chapter, the first flow case selected for study is that around a single cylinder. This selection was made as this represents a geometrically simple configuration, for which published experimental data are available, so that understanding of the flow processes involved can be obtained and the modelling approach can be assessed, before dealing with other complex flows, for instance, flow through a contraction, and past cylinder arrays and idealised blade/baffle geometries.

The two-dimensional flow of the two polyisobutylene solutions past a symmetrically confined cylinder was investigated and the finite volume computations were compared with measurements of velocities and stresses using LDA and FIB experimental techniques respectively, by Baaijens (1994b) and Baaijens et al. (1995). The model fluids used are the 2.5 % PIB and 6 % PIB solutions, that have been rheologically characterised in chapter 3.

The Phan-Thien Tanner (PTT -a) and Giesekus constitutive equations have been used to describe the viscoelastic behaviour of the two model fluids as it was concluded in chapter 3 that they are the most suited to obtaining predictions for these fluids under shear and elongational deformation. Flows past a symmetrically confined cylinder will subject the fluids to deformations that are a combination of these. For the range of Deborah numbers (De) (see equation 4.2) presented in the sequel, the 5 mode PTT -a (from herein referred to as the PTT model) and 5 mode Giesekus models were used for the 2.5 % PIB and 6 % PIB solutions, respectively.

4.2 Flow of 2.5 % PIB solution past a symmetrically confined cylinder

4.2.1 Introduction

In this section the investigation of the flow of 2.5 % PIB past a symmetrically confined cylinder is described and discussed. A schematic of the geometry used herein is given in figure 4.1. This section then proceeds to: (a) Explain the numerical method used to solve for the velocity and pressure fields surrounding the confined cylinder, (b) Define the flow and boundary conditions imposed on the geometry, (c) Define the model parameters used for the 2.5 % PIB solution, (d) Compare and discuss the influence of; (i) a reduction in zero shear rate viscosity η_0 and; (ii) a non-optimised PTT model on the flow behaviour, (e) Present and discuss low De predictions and assess them against the measurement data of Baaijens (1994b) and Baaijens et al. (1995), (f) Present and discuss higher De predictions and assess them against the measurement data of Baaijens (1994b) and, (g) Present and discuss predictions at different De values.

4.2.2 Numerical method

All computational work carried out in this study solely involves the use of the finite volume method which is implemented with an open source CFD software package, OpenFOAM (OpenCFD, 2004). The system of partial differential equations solved by the finite volume method are described in chapter 2.

The Reynolds number, Re (see equation 4.4) of all flow solutions in this study is very low, i.e. 0.005 to 0.127, so the convective term could be neglected, as suggested by Baaijens et al. (1997) for a low density polyethylene melt. However, the full equation of conservation of momentum was used as work by Baaijens (1994b) showed that neglecting the convective term (Stokes flow approximation) influenced the solution of the velocity field by up to approximately 5 %.

The details of the solution procedure employed for all simulations carried out herein is described below but for a more comprehensive description see Versteeg and Malalasekera (1995) and/or Anderson et al. (2000a). The geometric domain

(figure 4.1) is discretised into a computational mesh consisting of a number of cells (finite control volumes), on which, the partial differential equations are subsequently discretised. The flow solution is then broken up into a set of time steps (Δt) to discretise the solution temporally. The solution to the flow problem (velocity, pressure, stress etc.) is defined at nodal points at the centre of each cell.

4.2.2.1 Equation discretisation

The volume integrals in the (a) diffusive term (first term on the right hand side of equation 2.19), (b) convective term (second term on the left hand side of equation 2.19), (c) gradient term (second term on the right hand side of equation 2.19), (d) divergence of viscoelastic stress term, $\nabla.\tau_E$ (see equation 2.23) and (e) first order time derivative term (first term on the left hand side of equation 2.19) are re-written as integrals over the entire bounding surface of each control volume by using Gauss' divergence theorem (Versteeg and Malalasekera, 1995). From the surface integrals of (a), (b), (c) and (d) a second-order accurate but unbounded central differencing technique is used to calculate cell centre values for the velocity and pressure fields, (Versteeg and Malalasekera, 1995) while for surface integrals of (e) a first order accurate in time, Euler implicit discretisation technique is used to calculate cell centre values (Versteeg and Malalasekera, 1995).

4.2.2.2 Temporal discretisation

Although the discretisation of temporal derivatives is described in above, the treatment of the spatial derivatives in a transient problem still has to be considered: All spatial derivatives are integrated with respect to time, from, t to $t + \Delta t$. The diffusive and convective terms are then discretised implicitly and the divergence and gradient terms are then discretised explicitly (Versteeg and Malalasekera, 1995).

4.2.2.3 Iterative solution procedure

In this study the PISO (Pressure Implicit with Splitting of Operators) algorithm has been used as the iterative procedure for solving equations 2.18 and 2.19 for

velocity and pressure. This algorithm is based on evaluating some initial solutions and then correcting them (Issa, 1986).

4.2.3 Flow and boundary conditions

In order to complete the description of the problem, the domain and boundary conditions have to be prescribed:

1. The fluid is driven past the cylinder from a zero flow rate condition at, $t = 0$ by a source term added to equation 2.19, at the centre of every control volume. These initial conditions are unique in comparison to that of other published literature where an initial Newtonian profile is used to initialise the flow, see, for example, Baaijens et al. (1995), Baaijens (1994b) and Barakos and Mitsoulis (1995). The source term is in the form of a rank 1 tensor parallel to the x axis and directed in the positive x direction (defined in figure 4.1). The source term acts as a pressure gradient across the flow domain, driving the fluid past the cylinder.

2. Two physical boundary conditions are prescribed to the flow domain for the respective incompressible fluid: (1) A non-slip impermeable wall, at $-8 \leq x/R \leq 21$, $y/R = 2$ and around the cylinder where the velocity is a fixed value and equal to that of the wall itself (i.e. zero velocity) and the pressure gradient is specified to be zero, since the flux through the wall is zero, (2) A plane of symmetry along the centreline at, $y/R = 0$ where the component of the gradient normal to the plane is zero. A plane of symmetry was used as the fluid properties are symmetric about the $y/R = 0$ axis (Baaijens, 1994b) and the computational time and memory space is subsequently halved.

3. An additional cyclic condition is specified at the entrance and exit boundaries, at $x/R = -8$ and $x/R = 21$, respectively, where fully developed flow conditions are calculated from the computations. This condition specifies that the entrance and exit boundaries are connected so that the flow profile is repeated and thus continuous.

4.2.3.1 Solution method for the viscoelastic models

The viscoelastic stress tensor τ_E in equation 2.24 is computed by using previous velocity and pressure fields computed in equation 2.19. The value for τ_E is then substituted back into the momentum balance equation (see equation 2.23), at a new time step and the new fields are calculated. The residual errors for the velocity v and pressure p fields are of the order 10^{-5} and 10^{-6}, respectively, which ensures good accuracy of results.

The viscoelastic computations are intrinsically unstable, which is a characteristic that is also shown in research by, for example, Baaijens (1994b) and Phan-Thien and Dou (1999)). Although all simulation results presented in this study reached steady state and ran for a period of time equal to, at least, $1\lambda_{long}$, at some point after this the simulations began to diverge after a period of time which depended on the rate of flow past the cylinder. For example, for the 2.5 % PIB solution, at low flow rates ($De = 0.225$) the computation ran indefinitely (the simulation was stopped after $20\lambda_{long}$), while for higher flow rates, for instance, $De = 2.90$ the initial simulation diverged at approximately $2\lambda_{long}$.

The size of the time step Δt is influenced by the likelihood of divergence for high flow rate problems and for this reason Δt was carefully selected for each case after extensive testing. The initial time step size is chosen so that it is not too large (to avoid hydrodynamic convergence problems, see the following section) and small enough to avoid early solution divergence due to intrinsic viscoelastic instabilities. The time step size (Δt) and the simulation time for those carried out herein, for the 2.5 % PIB solution is shown in table 4.1 for the entire range of De studied.

4.2.4 Simulation parameters

Having fixed the viscoelastic and geometric model parameters, the simulation parameters are those that remain to be calculated and modified to complete the problem. Parameters such as the Courant number (Co) must be continually monitored to ensure stable, robust and accurate solutions to the flow simulations: To ensure hydrodynamic stability, the maximum Co is kept below 1 ($Co \ll 1$), across the whole geometric domain. Co is defined as:

$$Co = \frac{\Delta t |v_{x,y,z}|}{\delta x} \tag{4.1}$$

where $|v_{x,y,z}|$ is the magnitude of the component of velocity in either the x, y or z direction, and δx is the cell size in the direction of the velocity. The maximum Co is calculated for each orthogonal direction. For further reference, see Anderson et al. (2000a).

Other simulation parameters, such as De, describe the ratio of elastic to viscous forces in the fluid, and is defined as:

$$De = \bar{\lambda}\dot{\gamma}_a, \tag{4.2}$$

where, $\dot{\gamma}_a$ is the apparent shear strain rate, defined as:

$$\dot{\gamma}_a = \frac{< u >}{R}, \tag{4.3}$$

where $< u >$ is the mean velocity in the positive, axial (x) direction (all planar flows of this chapter, and the following, are predominantly axial), calculated from the parabolic profile at $x/R = -5$ where the flow is fully developed (see figure 4.6 for an example of the fully developed profile) and R is the radius of the cylinder. The Re, which describes the ratio of inertial to viscous forces, is defined as:

$$Re = \frac{\rho R < u >}{\eta_0}, \tag{4.4}$$

where ρ is the density of the fluid.

In this chapter, and the following, the measurement data and predictions of velocity are only presented for those in the axial (x) direction. As mentioned above, all the flows are predominantly axial and therefore the primary interest is to validate the v_x values with the measurement data. In the sequel, v_x is denoted by U ($v_x = U$) and from here onwards all values of U are non-dimensionalised with the mean velocity $< u >$ and the stresses with τ_0, defined as:

$$\tau_0 = \frac{3\eta_0 < u >}{R} \tag{4.5}$$

where, τ_0 is the scaling stress and is defined identically to that used by Baaijens (1994b). This was done so that all the measurement data for the total stress

σ, including the first normal stress difference, N_1 that had been scaled by τ_0 in Baaijens (1994b) could be compared directly to predictions. The factor 3 in equation 4.5 is arbitrary and is included only to obtain a scaling that allowed all plots of velocity and stress to fit nicely in all figures presented hereafter (Baaijens, 1994b).

4.2.5 Mesh independence

Before a full study of the flow behaviour of both fluids can be carried out, it is first necessary to establish mesh independence for all the proceeding simulations.

Three finite volume meshes shown in figures 4.2, 4.3 and 4.4 have been used, containing 3948, 5720 and 11000 cells, respectively. The coarse mesh shown in figure 4.2 was used for initial calculations at low shear rates. However, poor hydrodynamic convergence behaviour at $De \geq 1$ indicated that a denser mesh should be used. A medium and a fine mesh shown in figures 4.3 and 4.4, respectively, were constructed for this reason.

Predictions for U, N_1 and σ_{xy} in the steady state have been compared for all 3 meshes at $De = 0.314$ along five cross sectional lines: $x/R = -5$, -2, -1.5, 1.5 and 2.0 (the center of the cylinder is at $x = 0$, $y = 0$ and the negative x - coordinates are upstream of this center, see figure 4.1). The profiles of U, N_1 and σ_{xy} are shown in figures, 4.6, 4.7, 4.8, 4.9, 4.10 and 4.11. The results presented in figures 4.6 to 4.11 show that all three meshes yield qualitatively identical results and quantitative differences, especially between the medium and fine mesh data for U, N_1 and σ_{xy} are around 1 to 2 % at most and near zero across most of the profiles shown. This percentage difference was small enough to be negligible and thus it was concluded that refinement in both the x and y directions did not influence the solution significantly at a low De. The convergence behaviour of the medium mesh, shown in figure 4.3, was tested over the range of De used in this study, for both the 2.5 % and 6 % PIB solutions (this work is not shown herein, for reason of brevity) and was considered to be adequate for all the calculations of this chapter. An expanded view of the medium mesh in the vicinity of the cylinder is shown in figure 4.5. The number of cells in the region, $-2 \leq x/R \leq 2$ and $0 \leq y/R \leq 2$ is the same as the number of cells used in the work by Barakos

and Mitsoulis (1995). It is noteworthy at this point to make reference to work by Barakos and Mitsoulis (1995), Dou and Phan-Thien (1998) and Phan-Thien and Dou (1999) where comprehensive mesh tests were also carried out over a range of *De*.

4.2.6 The reduction in De and zero-shear rate viscosity and the influence of a non-optimised model

Before proceeding with a detailed presentation of the simulation results for the single cylinder flow case over a range of *De*, it is instructive to establish whether the predicted flow field is affected by small changes in *De* and/or *Re*, as the measurement data available are often obtained at slightly different *De* or *Re* values. Consequently, it has to be ascertained as to whether any differences between predictions and measurement data can be attributed to a small change in the values of such parameters.

Figure 4.12, as an example, shows that a small change (or reduction, in this case) in Deborah number (from $De = 0.314$ to 0.225) does not influence at all the predictions for U, N_1 and σ_{xy} (larger changes in *De* will be studied in subsequent sections).

Other parametric studies have also been carried out: (i) The influence of a small change in ϵ in the PTT model for the 2.5 % PIB solution and, (ii) A reduction in the dynamic zero shear rate viscosity η_0 for the 2.5 % PIB solution to match the zero shear rate viscosity η_0 of the 5 % PIB solution of Baaijens (1994b), for which the value of η_0 was reduced from 1.09 to 0.977. Both of these studies were carried out to assess the influence that small changes in ϵ and η_0 have on the flow of 2.5 % PIB around a symmetrically confined cylinder. The former of these two studies is similar to that carried out by Baaijens et al. (1997) and involves altering the value of ϵ so that the PTT model becomes non-optimised and thus the value for q (see equation 3.15) is not minimised either. However, there is still good qualitative agreement between the predicted and measured values for N_1 and η, with a new value for ϵ. The sensitivity of the non-linear parameter ϵ in the PTT model is shown by comparing optimised and non - optimised predictions for U, N_1 and σ_{xy} along 5 cross sectional lines, at $x/R = -5$, -2, -1.5, 1.5 and

2.0, at $De = 0.225$. These comparisons are shown in figures 4.13, 4.14, 4.15, 4.16, 4.17 and 4.18. There are negligible, if any, differences when comparing U for the optimised PTT model against U for the non-optimised model in figures 4.13, 4.14 and 4.15. In comparison there are more noticeable differences when comparing N_1 and σ_{xy} for the optimised PTT model against that of the non-optimised model in figures 4.16, 4.17 and 4.18. However, even these differences are approximately 2 % and are considered to be insignificant for the purposes of the discussion in this chapter.

The latter of these two studies involves reducing the value of the zero-shear rate viscosity η_0, of the optimised model, from $\eta_0 = 1.09$ to 0.98 (which matches that of the 5 % PIB solution of Baaijens (1994b)). The influence of this reduction can be shown by comparing U, N_1 and σ_{xy} along the 5 cross sectional lines, $x/R = -5$, -2, -1.5, 1.5 and 2.0 at $De = 0.225$ for the optimised model predictions, at $\eta_0 = 1.09$ and $\eta_0 = 0.98$, for the 2.5 % PIB solution (see figures 4.13, 4.14, 4.15, 4.16, 4.17 and 4.18). Again, there are negligible differences when comparing U in figures 4.13, 4.14 and 4.15, but small differences when comparing N_1 and σ_{xy} in figures 4.16, 4.17 and 4.18. These differences are again approximately of the order of 2 % and are considered insignificant for the following discussion of the data.

4.2.7 Comparison of computations with experimental data at De = 0.248

Before discussing the predictions for a range of De, it is first necessary to, where possible, validate the predictions for the 2.5 % PIB solution. The selection of the flow conditions to be compared was made in accordance with the availability of relevant measurement data. To begin with, a low De of 0.225 was used to emulate as closely as possible the behaviour of a Newtonian fluid. Predictions for U and N_1 were compared with the associated measurement data of Baaijens (1994b) for a 5 % PIB solution at $De = 0.248$, which are shown in figures 4.19, 4.20, 4.21, 4.23, 4.24, 4.22 and 4.25, and discussed in the following sections. As mentioned in section 4.2.7.5, measurement data is not available for the σ_{xy} measurements at $De = 0.248$, so predictions for this could not be validated. The De for the

predictions and the measurements are not identical but as shown in section 4.2.6, this should not affect the accuracy of the validation.

When making such comparisons, the error bounds of the measurement data must also be taken into account (Baaijens (1994b) did not cite the error margins in U, N_1 and σ_{xy}). In addition, some of the measurement data of Baaijens (1994b), especially those for N_1 obtained using FIB, show considerable scatter (up to around 100 %) in some flow cases and therefore all comparisons with such data must be made with care.

4.2.7.1 Axial velocities along various cross sections

Figures 4.19 and 4.21 show excellent quantitative agreement between the measurement data and predicted values for the axial velocities U made using the 5 mode PTT model along the cross sectional lines $x/R = -5$ and 1.5, respectively. Slightly larger differences of approximately 8 % are found between measurement data and predictions along the cross sectional line $x/R = -2$, shown in figure 4.20 and caused by a small under-prediction in U in the region $-2 \leq y/R \leq -1.5$ and $1.5 \leq y/R \leq 2$ and a slightly larger over prediction in U in the region $-0.25 \leq y/R \leq 0.25$. Overall, along the three cross sections, excellent agreement is found between the measurement data and the predicted velocity values. Although these predictions are within the error bounds of the measurements, the differences are easily attributed to; (1) the resolution of the LDA system; (2) the error incurred whilst extrapolating measurement data from Baaijens (1994b) and; (3) background noise levels (up to 3 %, as reported by Baaijens et al. (1995)).

To emphasise the presence of experimental error it is particularly noteworthy to consider the FIB measurement data for N_1 obtained by Baaijens (1994b), shown in figures 4.23 and 4.24, at $De = 0.248$. This data not only shows considerable scatter, up to 50 % in figure 4.24, for example, but also strong asymmetry in figure 4.23, of the order of 100 %. This asymmetry is not present at a higher De, namely at $De = 2.32$ (see section 4.2.8) so it is very likely that it is not a feature of imperfect/asymmetric flow development, but rather of errors in the FIB technique. A more recent publication by Baaijens et al. (1995) showed results for the same fluid without this asymmetry and scatter. Subsequently, these

new results are used for comparison herein. The results for N_1 are discussed in section 4.2.7.3.

4.2.7.2 Axial velocities along the centreline

Figure 4.22 compares predictions and measurement data for axial velocities along the centreline ($y/R = 0$), upstream and downstream of the cylinder. Excellent quantitative agreement is found between the predictions and the measured data of Baaijens (1994b), with small differences of 3 % that can be easily attributed to any of the three reasons mentioned in section 4.2.7.1.

4.2.7.3 First normal stress differences along various cross sections

As reported by Baaijens (1994b), the measurement data for N_1, at the lowest De ($De = 0.248$), at cross sections; $x/R = -1.5$ and $x/R = 1.5$ were not accurate, since the birefringence of the fluid was of the same magnitude as the (small) spatial variation in the background signal, see figures 4.23 and 4.24. However, one year later, Baaijens et al. (1995) published a new set of measurement data to replace that of Baaijens (1994b). This new set of data showed greater accuracy and an absence of asymmetry. An explanation as to how these results were improved was not given by Baaijens et al. (1995) but one can only assume that the above problem experienced by Baaijens (1994b) was eradicated. Predictions for N_1, at $De = 0.225$ were thus compared to measurement data of Baaijens et al. (1995), for N_1, at $De = 0.248$. Measurement data for N_1, at $De = 0.248$, by Baaijens (1994b) are included for reference.

Figure 4.23 compares predictions for N_1 at $De = 0.225$ to measurement data for N_1, at $De = 0.248$, at the cross section $x/R = -1.5$. The predictions show excellent qualitative agreement with measurement data across the range $-2 \leq y/R \leq 2$. However, in comparison to the measurement data of Baaijens et al. (1995) the predictions show an approximate under-prediction of 40 % and an error margin of approximately 15 % at the walls of the duct (at $y/R = -2, 2$) and over the range, $-1.5 \leq y/R \leq 1.5$, respectively. These margins of error are also shown in the work of Baaijens et al. (1995) and are well within the bounds of experimental error when considering the approximate 100 % difference between

predictions and measurement data of Baaijens (1994b).

Figure 4.24 compares predictions for N_1, at $De = 0.225$ to measurement data for N_1, at $De = 0.248$, at the cross section $x/R = 1.5$. When making a comparison to measurement data of Baaijens et al. (1995), the predictions, at $x/R = 1.5$ are more accurate than those upstream of the cylinder, at $x/R = -1.5$, with an under-prediction of approximately 30 % and an overall error margin of approximately 10 %, at the walls of the duct and in the range $-2 \leq y/R \leq 2$, respectively. This is again, well within the bounds of experimental error when comparisons are made to the measurement data of Baaijens (1994b), which show an error margin of 100 %.

The possible sources of the margins of error between the predictions and measurement data for the first normal stress difference values N_1 are discussed in section 4.2.7.5.

4.2.7.4 First normal stress differences along the centreline

Figure 4.25 compares predictions for N_1, at $De = 0.225$ with measurements for N_1 at $De = 0.248$ along the centreline $y/R = 0$. Apart from a small underestimation of the maximum value of N_1 downstream of the cylinder at $x/R = 1.5$, the predictions show excellent quantitative agreement with both sets of measurement data by Baaijens et al. (1995) and Baaijens (1994b). A small overall error margin of approximately 8 % is shown, when comparing the predictions to the measurement data of Baaijens et al. (1995) and slightly larger error margin when compared to the measurement data of Baaijens (1994b). Again, the possible sources of these errors are discussed in section 4.2.7.5.

4.2.7.5 Shear stresses along various cross sections

Measurement data is not available for a similar solution, at an identical or similar De (i.e. at $De = 0.248$) and for this reason only predictions are shown here. Figure 4.18 shows the simulation profile for σ_{xy}, using the optimised 5 mode PTT model, which shows the same qualitative trend as that predicted by Baaijens (1994b) and Baaijens et al. (1995) along the same cross section. Despite the lack of measurement data at $De = 0.248$, measurement data for σ_{xy}, at $De = 2.32$, for

the 5 % PIB solution of Baaijens (1994b) was available and therefore comparisons have been made in section 4.2.8.5.

In conclusion, the comparison of predictions for velocity and normal stress difference with the measurement data of Baaijens (1994b) and Baaijens et al. (1995) showed excellent quantitative agreement upstream and downstream of the cylinder, for low De ($De = 0.225$) flows. Although direct comparisons could not be made for shear stress σ_{xy} due to the lack of measurement data, all predictions for velocity and stresses are indicative of the typical flow characteristics of this fluid and provide confidence in those reported here.

Simulation predictions for the velocity, U (see figures 4.19, 4.20, 4.21 and 4.22) and the first normal stress difference N_1, along the centerline, (see figure 4.25) show excellent quantitative agreement well within the error bounds of the measurement data. However, higher percentage differences are evident in the comparison of the predictions with measurement data for N_1 in figures 4.23 and 4.24. This higher percentage difference is also shown in work by, Baaijens et al. (1994), Baaijens (1994b) and Barakos and Mitsoulis (1995), and the cause can be attributed to; (1) the resolution of the FIB system; (2) the error incurred whilst extrapolating measurement data from Baaijens et al. (1994) and; (3) the low birefringence of the fluid, which compares with the noise signals of the instruments used for the measurements at low De (Baaijens, 1994b). As already discussed, this problem was eradicated by Baaijens et al. (1994) (see section 4.2.7.3) but adds doubt to the accuracy of the measurement data being used.

It is also possible that the model fails to fully capture the flow kinematics in the regions where high normal stress difference values are encountered, such as in the wake of the cylinder, in the region $-0.5 \leq y/R \leq 0.5$, or at the extremities of the domain for instance, at the wall ($y/R = -2, 2$) where shear stain rates are higher and thus causing stronger shear thinning, or along the centreline where N_1 ($y/R = 0$) values are evidently large. This non-linear behaviour is harder to model, as already shown from simpler rheometric results in the previous chapter, especially at higher flow rates (and therefore higher De). The effects that an increase in shear strain rate has on these areas of high non-linear activity is discussed in section 4.2.8.

Additional profiles for U, at $x/R = -1.5$ and $x/R = 2$ and shear stress σ_{xy} at $x/R = -1.5$ are shown in figure 4.26, together with the data at all the other cross-sections already discussed. The flow properties are well reproduced across the whole flow field. The main features of the predicted low De flow around a cylinder are described below before moving on to compare higher De predictions with measurement data.

The inlet flow profile for $U/ < u >$, at $x/R = -5$ is parabolic in shape. Along the centreline (at $y/R = 0$) the flow then begins to decelerate from a maximum of 1.56 at $x/R = -5$ to 1.05 at $x/R = -2$ and then to 0.51 at $x/R = -1.5$. Within the regions; $-2 \leq \mathrm{y/R} \leq -1$ and $1 \leq \mathrm{y/R} \leq 2$, the flow begins to accelerate as it moves past the cylinder, reaching maximums for $U/ < u >$ of 1.06, 1.30 and 1.56 at $x/R = -5$, $x/R = -2$ and $x/R = -1.5$, respectively. Downstream of the cylinder the flow starts to recover and by $x/R = 5$ it has regained its parabolic shape. The predictions at other cross-sections (not shown for brevity) indicated that the maximum peak in the profile resulting from the acceleration of the flow past the cylinder is not evident after the cross-section; $x/R = 2$.

Two profiles of N_1, at the cross sections $x/R = -1.5$ and 1.5 are shown, as measurement data was only available at these cross sections. Upstream and downstream of the cylinder the values of N_1 are at their highest close to the walls of the duct where $|N_1| \approx 1$, and for the centreline plots, $|N_1| \approx 2$ is the highest value reached downstream of the cylinder.

For the same reason, only two profiles of shear stress σ_{xy} are shown in figure 4.26. The profiles upstream and downstream of the cylinder are very similar. The shear stress is at a maximum at the wall of the duct where $|\sigma_{xy}| \approx 1$, and smaller peaks in shear stress are evident in the region; $y/R = -1$ and 1 where $|\sigma_{xy}| \approx 0.5$.

4.2.8 Comparison of computations with experimental data at De = 2.315

The lower De flows studied in the previous section are compared to those of a higher De, namely at $De = 2.315$, in this section. The flow behaviour of U, N_1 and σ_{xy} were qualitatively similar to those of the lower De flows with some small

quantitative differences, see below.

In the work by Baaijens (1994b), for the 5 % PIB solution, the highest De reached experimentally for a symmetrically confined cylinder flow was 2.315. In figures 4.27 to 4.33, measurement data, at this De, for U, N_1 and σ_{xy} are compared to that of Baaijens (1994b) for the lower De flows ($De = 0.248$), and to predictions for the 2.5 % PIB solution, of this study, at $De = 0.225$ and $De = 2.90$ (except in the case where measurement data is not available for σ_{xy} at $De = 0.248$). There is a small difference in De between the predicted values and the respective measurement data but this can be deemed insignificant, as mentioned in section 4.2.6. Predictions for U, N_1 and σ_{xy} at $De \geq 2.315$ are subsequently presented in section 4.2.9 but, to the best knowledge of the author, the highest De reported experimentally, in all the literature remains at 2.315.

4.2.8.1 Axial velocities along various cross sections

Figure 4.27 shows measurement data at $De = 0.248$ and $De = 2.315$, for the 5 % PIB solution of Baaijens (1994b) and predictions at $De = 0.225$ and $De = 2.315$, for U values, along the cross section at $x/R = -5$. When comparing the two sets of measurement data within the regions $-2 \leq y/R \leq -1$ and $1 \leq y/R \leq 2$ there is a small increase in U, as the De is increased. Comparably, there is a reduction in U in the region $-0.75 \leq y/R \leq 0.75$, also as the De is increased. Overall, in the region $-2 \leq y/R \leq 2$, there is a small difference of approximately 8 % between both sets of measurement data. The predictions at $De = 0.225$ and $De = 2.90$ show a similar trend as the De is increased. There is an overall difference of approximately 8 % between the two sets of predictions and a reduction in velocity is shown in the region, $-0.75 \leq y/R \leq 0.75$. There is however the absence of a small increase in velocity in the regions, $-2 \leq y/R \leq -1$ and $1 \leq y/R \leq 2$ where a small increase was shown by the measurements.

Figure 4.28 shows measurement data at $De = 0.248$ and $De = 2.315$, for the 5 % PIB solution of Baaijens (1994b) and predictions at $De = 0.225$ and $De = 2.315$, for U values, along the cross section, $x/R = -2$. When comparing the two sets of measurement data, a reduction in U values of approximately 5 % is shown, in the regions $-2 \leq y/R \leq -0.75$ and $0.75 \leq y/R \leq 2$, as the De is

increased. There appears to be no change in U anywhere outside of this region. The predictions for U at $De = 0.225$ and $De = 2.90$ show exactly the same trend, also with an approximate 5 % reduction in U, in the regions $-2 \leq y/R \leq -0.75$ and $0.75 \leq y/R \leq 2$.

Figure 4.29 shows measurement data at $De = 0.248$ and $De = 2.315$, for the 5 % PIB solution of Baaijens (1994b) and predictions at $De = 0.225$ and $De = 2.315$, for the U values, along the cross section at $x/R = 1.5$. A comparison of the two sets of measurement data show a reduction in U of approximately 5 % in the regions $-1.25 \leq y/R \leq -0.8$ and $0.8 \leq y/R \leq 1.25$ and a moderate increase in U, in the region, $-2 \leq y/R \leq -1.6$ and $1.6 \leq y/R \leq 2$, as the De is increased. The predictions for U at $De = 0.225$ and $De = 2.90$ show identical percentage differences in U, over the same regions, although, the PTT model seems to fail to capture the small increase in U that is shown experimentally in the region, $-0.2 \leq y/R \leq 0.2$, as the De is increased.

4.2.8.2 Axial velocities along the centreline

Figure 4.30 shows measurement data at $De = 0.248$ and $De = 2.315$ and predictions at $De = 0.225$ and $De = 2.90$, for U values, along the centreline ($y/R = 0$) upstream and downstream of the cylinder. When comparing the two sets of measurement data, they both show the same trend over the region $-5 \leq x/R \leq -1$ and $1 \leq x/R \leq 5$. There is a relatively large reduction in U values, of approximately 5 %, in the region $-5 \leq x/R \leq -3$ and $3 \leq x/R \leq 5$, and a smaller reduction in the region $-3 \leq x/R \leq -1$ and $1 \leq x/R \leq 3$, as De is increased. The two sets of predictions show exactly the same trend along with an identical reduction in U in the same regions. The only difference is the presence of a predicted overshoot in U, observed downstream of the cylinder in the region $2.5 \leq x/R \leq 4$, at $De = 2.90$. This overshoot is also predicted by Baaijens (1994b), for a similar fluid, at a similar De.

4.2.8.3 First normal stress differences along various cross sections

Figure 4.31 shows measurement data at $De = 0.248$ and $De = 2.315$ and predictions at $De = 0.225$ and $De = 2.90$, for values of N_1 along the cross section

$x/R = -1.5$. The largest differences between the two sets of measurement data are shown over the region $-0.5 \leq y/R \leq 0.5$, where there is approximately a 20 % decrease, and at the wall where there is approximately a 30 % increase, as the De increases. When comparing the two sets of predictions they both show the same trend as that of the measurement data but with slightly larger percentage differences, especially in the region, $-1.5 \leq y/R \leq -1$ and $1 \leq y/R \leq 1.5$. More interestingly, the predicted values at $De = 2.90$ show better accuracy than the lower De predictions when compared to their respective measurement data sets.

Figure 4.32 shows measurement data at $De = 0.248$ and $De = 2.315$ and predictions at $De = 0.225$ and $De = 2.90$, for values of N_1 along the cross section, $x/R = 1.5$. The largest differences between the two sets of measurement data are shown over the region $-2 \leq y/R \leq -1$ and $1 \leq y/R \leq 2$ where there is approximately a 40 % increase, and over the region $-0.75 \leq y/R \leq -0.25$ and $0.25 \leq y/R \leq 0.75$, where there is approximately a 50 % decrease, as the De increases. When comparing the two sets of predictions they both show the same trend but with slightly smaller percentage differences between them. However, the predictions at $De = 2.90$ fail to capture the large values for N_1 that are shown by the measurement data at $De = 0.248$ and 2.315 in the region, $-0.25 \leq y/R \leq -0.25$. This could be attributed to the error within the model as the increasing shear strain rates and stresses across the geometry become more difficult to predict at a higher De.

4.2.8.4 First normal stress differences along the centreline

Figure 4.33 shows measurement data at $De = 0.248$ and $De = 2.315$ and predictions at $De = 0.225$ and $De = 2.90$ for N_1 values along the centreline ($y/R = 0$), upstream and downstream of the cylinder. The largest difference between the two sets of measurement data is shown downstream of the cylinder, where there is an approximate reduction of 25 % in the peak value for N_1, as the De is increased. In contrast, a much smaller difference is shown upstream of the cylinder. Over the whole region $-5 \leq y/R \leq 5$ an approximate error margin of 15 % is shown. The two sets of predictions show the same qualitative trend as the measurement data both upstream and downstream of the cylinder also with an approximate

error margin of 15 %.

4.2.8.5 Shear stresses along cross sections

As mentioned in section 4.2.7.5, measurement data is not available for the shear stress values (σ_{xy}) along any cross section at $De = 0.248$. However, measurement data is available by Baaijens (1994b) for the shear stress, at $De = 2.315$. Figure 4.34 shows measurement data at $De = 2.315$ and predictions at $De = 0.225$ and $De = 2.90$, for σ_{xy} along the cross section $x/R = 1.5$. The largest difference between the two sets of predictions are shown at the walls of the duct where there is a decrease in $|\sigma_{xy}|$ of approximately 25 %, and in the region $-1 \leq y/R \leq -0.5$ and $0.5 \leq y/R \leq 1$, where there is also a decrease in $|\sigma_{xy}|$ of approximately 15 %, as the De increases. It noteworthy at this point to highlight an error margin of approximately 20 % when comparing the predictions to the measurement data at $De = 2.9$ and 2.315, respectively. This is comparable to the margin of error described in section 4.2.7.3 for the same fluid, at the lower De.

In conclusion, the work presented in section 4.2.8 clearly shows how an increase in De affects the flow behaviour of the fluid. Figures 4.27 to 4.33 show predictions using the 5 -mode PTT model, at $De = 0.225$ and $De = 2.90$ along with measurement data of Baaijens (1994b), at $De = 0.248$ and $De = 2.315$, for the axial velocity U, first normal stress difference N_1 and shear stress σ_{xy}, upstream and downstream of the cylinder. The degree to which the measurement data changed, and the percentage difference incurred, as the De increased is almost identical to that shown by the predictions. Apart from some small discrepancies, which are discussed below, it can be concluded that the predictions made for the higher De flows (at $De = 2.90$) are within the error margins discussed in section 4.2.7, thus the predictions make good quantitative agreement and are indicative of the flow behaviour at a higher De.

As discussed in chapter 3 the 2.5 % PIB solution shows; (1) a thinning effect when subjected to increased shear and elongation strain rates ($\dot{\gamma}$ and $\dot{\epsilon}$, respectively) and; (2) an increase in normal stress difference when subjected to an increased shear strain rate. These effects are also shown in this chapter whereby the fluid is influenced by a combination of shear and elongational deformation,

especially in the vicinity of the cylinder.

The fluid is found to thin most predominately in an area adjacent to the walls of the duct where relatively high levels of shear exist. As mentioned in section 4.2.8.1 measurement data in figure 4.27 showed a small increase in U, in the region $-2 \leq y/R \leq -1$ and $1 \leq y/R \leq 2$, as the De increased. However, in this instance, this phenomena is not captured by the predictions and could be attributed to the model's failure in doing so. The thinning effect is more clearly shown in figure 4.34 where a reduction in shear stress is clearly shown by measurement data and predictions in the area adjacent to the wall, as the De is increased. Infact, section 4.2.8.5 describes a reduction in $|\sigma_{xy}|$ along the whole cross section $-2 \leq y/R \leq 2$. Elongational thinning, possibly existing between the cylinder and the walls of the duct, could have contributed to this.

An increase in N_1 values is shown clearly in figure 4.31 and more significantly in figure 4.32 where relatively high levels of shear adjacent to the walls of the duct cause an increase in N_1. In figure 4.32 the predictions fail to capture the increase in N_1 along the centreline at $y/R = 0$ which could again be attributed to the model's failure in doing so. Arguably the effect of the change in N_1 along the whole cross section in figures 4.31 and 4.32 could cause the reduction in velocity values in figures 4.27, 4.28 and 4.29. It is impossible to speculate as to the effect of elongational rate on N_1 for such complex flow problems as a simple rheometric characterisation for this was not carried out.

4.2.9 Comparison of computations at different De

Sections 4.2.7 and 4.2.8 show predictions for U, N_1 and σ_{xy} at $De = 0.225$ and $De = 2.90$, using the 5 -mode PTT viscoelastic model, for the 2.5 % PIB solution. These predictions were also validated against measurement data of Baaijens (1994b) and Baaijens et al. (1995) in the range, $0.248 \leq De \geq 2.315$. To the best knowledge of the author, this is the largest range of De available, for measurement data, for a cylinder flow problem.

This section proceeds to show predictions for U, N_1 and σ_{xy}, for the 2.5 % PIB solution at intermediary stages between $De = 0.225$ and $De = 2.90$ and beyond, namely in the range, $De \leq 5.75$. Table 4.1 shows the range of Re and

De simulated for 2.5 % PIB. The simulations at $De = 3.601$ and $De = 5.746$ for which, to the best knowledge of the author, measurement data is not available for comparison are an extension to this line of work. In sections 4.2.9.1 to 4.2.9.5 the predictions for the lowest De flows (namely at $De = 0.225$) were employed as a benchmark for comparison purposes. In addition, the behaviour of the 2.5 % PIB solution at $De = 0.225$ is closest to that of a Newtonian fluid and comparisons with high De flows can help elucidate non-Newtonian behaviour characteristics.

4.2.9.1 Axial velocities along various cross sections

Figure 4.35 compares predictions for U at $De = 0.225$, 1.008, 1.857 and 2.90 along the cross section $x/R = -5$ and figure 4.43 compares values of U at $De = 0.225$, 3.601 and $De = 5.746$ along the same cross section. Both graphs show the same trend, that trend being a small reduction in the U values as the De is increased. Figures 4.36 and 4.44 at the cross section $x/R = -2$ and figures 4.37 and 4.45 at the cross section $x/R = 1.5$, over the same range of De numbers show this same trend, whereby there is a reduction in U as De is increased.

4.2.9.2 Axial velocities along the centreline

The reduction in axial velocity U as De is increased is also shown in figures 4.38 and 4.46 along the centreline at $y/R = 0$ upstream and downstream of the cylinder. With $De \geq 2.90$ (see figure 4.46) in the region $2.5 \leq x/R \leq 5$ there is also evidence of a larger overshoot in U in the wake of the cylinder at $De = 3.601$.

4.2.9.3 First normal stress differences along various cross sections

Figure 4.31 compares predictions for N_1 at $De = 0.225$, 1.008, 1.857 and 2.90 along the cross section $x/R = -1.5$ and figure 4.47 compares predictions for N_1 at $De = 0.225$, 3.601 and $De = 5.746$, at the cross section $x/R = -1.5$. Larger differences are noticed when comparing flow predictions at $De \geq 1$ to flow predictions at $De = 0.225$. However, there is only a marginal change in flow predictions for N_1 when solely comparing the predictions at $De \geq 1$.

Figure 4.40 compares predictions for N_1 at $De = 0.225$, 1.008, 1.857 and 2.90 along the cross section $x/R = 1.5$ and figure 4.48 compares predictions for N_1

at $De = 0.225$, 3.601 and $De = 5.746$, at the cross section $x/R = 1.5$. Again, larger differences are noticed when comparing flow predictions at $De \geq 1$ to flow predictions at $De = 0.225$. However, there is only a marginal change in flow predictions for N_1 when solely comparing the predictions at $De \geq 1$.

4.2.9.4 First normal stress differences along the centreline

The same trend, as mentioned above, is also shown in figures 4.41 and 4.49 when comparing values for N_1 along the centreline at $y/R = 0$ upstream and downstream of the cylinder for $De = 0.225$, 1.008, 1.857, 2.90, 3.601 and $De = 5.746$.

4.2.9.5 Shear stresses along various cross sections

The shear stress along the cross section $x/R = 1.5$ has been compared at $De = 0.225$, 1.008, 1.857, 2.90, 3.601 and 5.746 in figures 4.42 and 4.50. Large differences are again noticeable when comparing higher De simulations to those at $De = 0.225$, and less change is noticeable when comparing simulations for $De \geq 1$.

Sections 4.2.9.1 to 4.2.9.5 conclude that; (1) there is a much larger change in U, N_1 and σ_{xy} when comparing predictions in the range, $0.225 \leq De \leq 2.90$ to those in the range, $2.90 \leq De \leq 5.75$. This is because the former of these compares an approximate Newtonian fluid (at $De = 0.225$) to one whose elastic forces are much more dominant (at $De = 2.90$), thus more dramatically changing the behaviour of the flow over this range and consequently showing larger differences by comparison, and; (2) the general trend shown by each of the predicted values, as the De is increased from $De = 0.225$ to 5.75, is identical to that shown in section 4.2.8 by the measurement data of Baaijens et al. (1995) and Baaijens (1994b) over the range of $0.248 \leq De \leq 2.315$.

4.3 Flow of 6 % PIB solution past a symmetrically confined cylinder

4.3.1 Introduction

In this section a second fluid has been studied, namely the 6 % PIB solution, past a symmetrically confined cylinder. This model fluid has a viscosity and elasticity closer to that of a polymer melt. The same PIB and tetradecane as in the previous section of this chapter are used, but now with a higher percentage of PIB. A schematic of the geometry used is defined in figure 4.1 and identical to that used for the 2.5 % PIB solution. The computational method used and the flow and boundary conditions implemented are also identical to those used for 2.5 % PIB and described in sections 4.2.2 and 4.2.3. The model parameters for the 6 % PIB solution have been calculated in section 3.5 and are used with the 5 mode Giesekus model to obtain the predictions.

After a mesh test was carried out, it was found that the finite volume mesh containing 5720 cells, identical to that used for the 2.5 % PIB solution (see figure 4.3), also provided mesh independent results for the 6 % PIB solution . This test is not shown here for reason of brevity. However, a parametric study was not carried out for 6 % PIB due to the very small effect that changes in the non-linear model parameters and zero-shear rate viscosity appeared to have on the computational flow predictions for 2.5 % PIB in section 4.2.6.

4.3.2 Comparison of computations with experimental data

To the best knowledge of the author the only measurement data available for either an identical or similar fluid to the 6 % PIB solution is the 9 % PIB solution studied by Baaijens (1994b) past a symmetrically confined cylinder. The two fluids show very similar rheometric characteristics, as shown in section 3.5. Measurement data is available at various cross sections and centrelines at $De = 5.61$ and is used for comparison with predictions made in this section. Due to the higher levels of viscosity and elasticity shown by the 6 % PIB solution, all the predictions demand more computational power in comparison to those of the 2.5

% PIB solution. For this reason, only two predictions are made: At $De = 5.61$ and $De = 6.53$, the former for comparison with the measurement data by Baaijens (1994b) and the latter for the study of the effects as the De is increased. Table 4.2 shows the time step size (Δt), simulation time and values for $< u >$, De and Re, along with additional parameters defined for these simulations.

4.3.2.1 Axial velocities along various cross sections

Figure 4.51 shows measurement data at $De = 5.61$ for the 9 % PIB solution of Baaijens (1994b) and predictions at $De = 5.61$ and $De = 6.53$ for U values along the cross section at $x/R = -2$. The predictions at $De = 5.61$, in comparison to the measurement data at an identical De show an increase in U of approximately 20 % in the region $-1 \leq y/R \leq 1$. Comparably, there is a reduction in U in the region $-2 \leq y/R \leq -1$ and $1 \leq y/R \leq 2$ of approximately 10 %. Overall, in the region $-2 \leq y/R \leq 2$, there is a difference of approximately 15 % between the predictions and the measurement data at $De = 5.61$. As the De is increased the predictions at $De = 6.53$ show a reduction in U, in the region, $-1 \leq y/R \leq 1$ and a small increase in the region $-2 \leq y/R \leq -1$ and $1 \leq y/R \leq 2$.

Figure 4.52 shows measurement data at $De = 5.61$ for the 9 % PIB solution of Baaijens (1994b) and predictions at $De = 5.61$ and $De = 6.53$ for U values, along the cross section at $x/R = 1.5$. The predictions at $De = 5.61$, in comparison to the measurement data at an identical De show an increase in U of approximately 15 % in the region $-1.25 \leq y/R \leq -0.5$ and $0.5 \leq y/R \leq 1.25$. Comparably, there is a reduction in U in the regions closer to the walls at $-2 \leq y/R \leq -1.25$ and $1.25 \leq y/R \leq 2$. Contrarily the predictions make excellent agreement in the wake of the cylinder in the region $-0.5 \leq y/R \leq 0.5$. Overall, there is a difference of approximately 10 %. As the De is increased the predictions at $De = 6.53$ show an identical trend as that described above for U along the cross section at $x/R = -2$.

4.3.2.2 Axial velocities along the axial lines

Figure 4.53 shows measurement data at $De = 5.61$ and predictions at $De = 5.61$ and $De = 6.53$, for U values, along the centreline at $y/R = 0$, upstream

and downstream of the cylinder. The predictions at $De = 5.61$ show excellent agreement when compared to the measurement data at an identical De. The largest difference is in the region $-4 \leq x/R \leq -2$ where the predictions are approximately 10 % larger. Overall, in the region $-6 \leq x/R \leq 8$, there is a difference of approximately 5 % between the predictions and the measurement data at $De = 5.61$. As the De is increased the predictions at $De = 6.53$ show a reduction in U in the region $-3.5 \leq y/R \leq -2$ and $2 \leq y/R \leq 2.5$ and an increase further away from the cylinder both upstream and downstream.

Figure 4.54 shows measurement data at $De = 5.61$ and predictions at $De = 5.61$ and $De = 6.53$, for U values, along the axial line at $y/R = 1.5$, upstream and downstream of the cylinder. The predictions at $De = 5.61$ show excellent agreement when compared to the measurement data at an identical De far away from the cylinder, both upstream and downstream. The only difference is that of approximately 15 % close to and upstream of the cylinder, in the region $-1.25 \leq x/R \leq -0.5$ where larger velocity values are predicted. Overall, in the region $-6 \leq x/R \leq 6$, there is a difference of approximately 10 % between the predictions and the measurement data at $De = 5.61$ and as the De is increased the predictions at $De = 6.53$ show an insignificant change.

4.3.2.3 First normal stress differences along various cross sections

Figure 4.55 shows measurement data at $De = 5.61$ and predictions at $De = 5.61$ and $De = 6.53$, for N_1 values along the cross section, upstream of the cylinder at $x/R = -1.5$. The predictions at $De = 5.61$, in comparison to the measurement data at an identical De show a relatively large increase in N_1 in the region $-0.5 \leq y/R \leq 0.5$ and decrease in the regions close to the wall at $-2 \leq y/R \leq -1.5$ and $1.5 \leq y/R \leq 2$, both of approximately 35 %. The predictions at $De = 6.53$ are very similar in comparison to the predictions at $De = 5.61$ except at the walls of the duct where a small increase in N_1 is shown.

Figure 4.56 shows measurement data at $De = 5.61$ and predictions at $De = 5.61$ and $De = 6.53$, for N_1 values along the cross section, downstream of the cylinder at $x/R = 1.5$. The predictions at $De = 5.61$, in comparison to the measurement data at an identical De show relatively good agreement except in

the region $-0.5 \leq y/R \leq 0.5$ where there is approximately a 40 % decrease. The predictions at $De = 6.53$ are almost identical to the predictions at $De = 5.61$.

4.3.2.4 First normal stress differences along axial lines

Figure 4.57 shows measurement data at $De = 5.61$ and predictions at $De = 5.61$ and $De = 6.53$ for N_1 values along the centreline at $y/R = 0$, upstream and downstream of the cylinder. The predictions at $De = 5.61$ show good agreement when compared to the measurement data at an identical De upstream and far away from the cylinder. However, these predictions underestimate the overshoot directly upstream of the cylinder and over the region $1 \leq x/R \leq 6$, downstream of the cylinder by approximately 30 %. The predictions at $De = 6.53$ are almost identical to the predictions at $De = 5.61$ except for a small increase in the overshoot directly upstream of the cylinder.

Figure 4.58 shows measurement data at $De = 5.61$ and predictions at $De = 5.61$ and $De = 6.53$ for N_1 values along the axial line at $y/R = 1.5$, upstream and downstream of the cylinder. The predictions at $De = 5.61$ show good qualitative agreement when compared to the measurement data at an identical De but underestimate the values of N_1 by approximately 75 % over the whole region $-6 \leq x/R \leq 6$. Larger differences of approximately 300 % are shown further downstream and upstream of the cylinder. The predictions at $De = 6.53$ are almost identical to the predictions at $De = 5.61$.

4.3.2.5 Shear stresses along various cross sections

Figure 4.59 shows measurement data at $De = 5.61$ and predictions at $De = 5.61$ and $De = 6.53$, for σ_{xy} values along the cross section at $x/R = -1.5$. The predictions at $De = 5.61$ show good qualitative agreement when compared to the measurement data at an identical De although an error margin of approximately 100 % is shown across the whole cross section. Larger differences of approximately 300 % are shown at the regions adjacent to the walls of the duct. The predictions at $De = 6.53$ show no change.

Figure 4.60 shows measurement data at $De = 5.61$ and predictions at $De = 5.61$ and $De = 6.53$, for σ_{xy} values along the cross section at $x/R = -1.5$. The

predictions at $De = 5.61$ again show good qualitative agreement when compared to the measurement data at an identical De with much smaller error margins of approximately 20 % along the whole cross section in comparison to the same predictions made upstream of the cylinder. The largest differences of approximately 25 % are shown at the walls of the duct and in the region $-0.75 \leq y/R \leq 0.75$ The predictions at $De = 6.53$ show no change.

4.3.2.6 Shear stresses along axial lines

Figure 4.58 shows measurement data at $De = 5.61$ and predictions at $De = 5.61$ and $De = 6.53$ for σ_{xy} values along the axial line at $y/R = 1.5$, upstream and downstream of the cylinder. The predictions at $De = 5.61$ show good qualitative agreement when compared to the measurement data at an identical De except for the prediction of a small overshoot directly downstream of the cylinder at $x/R = 1$ which is not shown by the measurement data. Over the whole region $-6 \leq x/R \leq 6$ there is a difference of approximately 25 % which is relatively small when considering the error margins incurred by the stress predictions in sections 4.3.2.4 and 4.3.2.5.

In conclusion, the work presented in this section compares predictions of U, N_1 and σ_{xy}, using the 5 mode Giesekus model for the 6 % PIB solution at $De = 5.61$, to measurement data of Baaijens (1994b), at similar De, at various cross sections and axial lines, upstream and downstream of the cylinder. Predictions were also made at $De = 6.53$ so the effects of an increase in De could also be investigated. The predictions made for the 6 % PIB solution show error margins that are larger than that of the 2.5 % PIB solution. The largest differences are shown for N_1 and σ_{xy} where approximate error margins well exceeded that of the 2.5 % PIB solution. The most accurate predictions were those of the velocity values along the centreline and axial line ($y/R = 1.5$) where error margins or approximately 10 % were shown. These margins of error could only tenuously be explained by the experimental error incurred whilst obtaining measurement data from Baaijens (1994b), see section 4.2.7.1. However, one should be careful that the interpretation of these discrepancies is not solely that the Giesekus model failed to characterise the fluid in such complex flows. The 9 % PIB solution of

Baaijens (1994b), from which measurement data was taken, underwent changes in rheological properties, for example a reduction in zero-shear rate viscosity η_0, as this highly viscoelastic fluid was subjected to high shear and elongational strain rates through the complex geometry, see Baaijens (1994b). This degradation has not been taken into account for the 6 % PIB solution, for which predictions were made, thus one can only speculate that the size of the margins of error incurred herein would have been reduced. It can however be said that the predictions show excellent qualitative agreement in all instances and are indicative of the flow behaviour for such a fluid.

To the best knowledge of the author, the predictions obtained for U, N_1 and σ_{xy} at a higher De (at $De = 6.53$) and the comparisons with the lower De predictions (at $De = 5.61$) have not been carried out in any other published literature. For this reason, trends cannot be compared, however all the predictions at a higher De are again indicative of the flow behaviour of a fluid such as the 6 % PIB solution.

4.4 Discussion and conclusions

The flow of well characterised polyisobutylene solutions has been studied for the steady planar flow past a symmetrically confined cylinder. Two model fluids were used: A 2.5 % PIB and 6 % PIB solution. Computations were performed using the finite volume method for two highly non-linear viscoelastic models, namely the PTT -a and Giesekus models on the 2.5 % and 6 % PIB solutions respectively. A mesh test was carried out for both fluids over the range of De studied as work by Phan-Thien and Dou (1999) showed that numerical convergence, especially at higher De depended on this. A crude mesh failed to capture the non-linear behaviour of the fluids in regions of high shear and continuum mechanics begins to break down at a length scale comparable to polymer size for very fine meshes (Phan-Thien and Dou, 1999). Other studies such as those in section 4.2.6 were also carried out to test the sensitivity of the viscoelastic models and their incorporated parameters. The predictions for both fluids were compared to LDA and FIB measurement data of Baaijens (1994b) and Baaijens et al. (1995) for similar

fluids over a range of De.

For the 2.5 % PIB solution the predictions for velocity at $De \leq 2.315$ showed excellent quantitative agreement with the LDA measurement data. The largest difference of approximately 8 % was shown upstream of the cylinder at $x/R = -2$ which is accounted for by the possible causes of error in section 4.2.7.1. Some larger differences are shown for the shear and normal stresses when comparisons are made to the FIB measurement data, which have also been accounted for but discrepancies such as those in figure 4.32 in the region $-0.25 \leq y/R \leq -0.25$ have posed a small doubt in the model's capability to fully capture the larger values of N_1, as the fluid begins to show elastic responses at higher flow rates. The predictions at $2.315 \leq De \leq 5.75$ follow the same trend as that of lower De measurement data for all values of U, N_1 and σ_{xy}. This provides confidence in the numerical accuracy of the predictions at a De exceeding that of all available measurement data for a similar or identical fluid.

For the 6 % PIB solution the predictions show larger errors for all predictions when compared to that of the 2.5 % PIB solution and factors contributing to these differences have been given in section 4.3.2.6. However, all the predictions show good qualitative agreement with LDA and FIB measurement data, especially the predictions for U along the cross sections and axial lines which show relatively good quantitative agreement with maximum differences of approximately 15 %.

Overall, it is concluded that: (1) Neither fluid showed any negative velocities or vortex regions at any point in the flow domain. The laminar behaviour was characterised by the 5 mode PTT -a and Giesekus models which made excellent quantitative and qualitative predictions (especially for the axial velocity, U) for the 2.5 % and 6 % PIB solutions, respectively, (2) The predictions obtained are unique in respect that; (i) to the best knowlege of the author no literature has published predictions for fluids identical to the ones studied herein; (ii) for the 2.5 % and 6 % PIB solutions or for any similar fluids, no published literature has reported a De as high as 5.75 and 6.53 respectively, using the finite volume method with a structured grid; (iii) the solution procedure is alternate, see section 4.2.3 and, finally (3) This chapter has rigorously exposed the limitations of these viscoelastic models in characterising the flow behaviour of such fluids at

high deformation rates, enabling a more realistic progression towards other complex geometries and finally towards their use in an industrial application such as mixing.

$< u >$ [m/s]	$\dot{\gamma}_a$ [s^{-1}]	τ_0 [Pa]	De [-]	Re [-]	Δt [s]	simT [s]
0.00151	0.336	1.10	0.225	0.00500	$1 * 10^{-3}$	$20\lambda_{long}$
0.00678	1.51	4.93	1.008	0.022	$1 * 10^{-5}$	$5\lambda_{long}$
0.0125	2.77	9.08	1.86	0.0410	$1 * 10^{-5}$	$3\lambda_{long}$
0.0195	4.33	14.2	2.90	0.064	$1 * 10^{-5}$	$2\lambda_{long}$
0.0242	5.38	17.6	3.60	0.0800	$1 * 10^{-5}$	$2\lambda_{long}$
0.0387	8.6	28.1	5.75	0.128	$1 * 10^{-5}$	$1\lambda_{long}$

Table 4.1: Mean velocity $< u >$, apparent shear rate $\dot{\gamma}_a$, scaling stress τ_0 dimensionless numbers, De and Re, time step, δt and simulation time, simT (in terms of the number of longest relaxation times (λ_{long})), for predictions with a symmetrically confined cylinder, for the 2.5 % PIB solution. For definitions of τ_0, De, Re, $< u >$ and $\dot{\gamma}_a$, see section 4.2.4.

$< u >$ [m/s]	$\dot{\gamma}_a$ [s^{-1}]	τ_0 [Pa]	De [-]	Re [-]	Δt [s]	simT [s]
0.0200	4.44	241	5.61	0.00483	$1 * 10^{-3}$	$1\lambda_{long}$
0.0233	5.18	280	6.53	0.00561	$1 * 10^{-5}$	$1\lambda_{long}$

Table 4.2: Mean velocity $< u >$, apparent shear rate $\dot{\gamma}_a$, scaling stress τ_0 and dimensionless numbers, De and Re, time step, δt and simulation time, simT (in terms of the number of longest relaxation times (λ_{long})), for predictions with a symmetrically confined cylinder, for the 6 % PIB solution. For definitions of τ_0, De, Re, $< u >$ and $\dot{\gamma}_a$, see section 4.2.4.

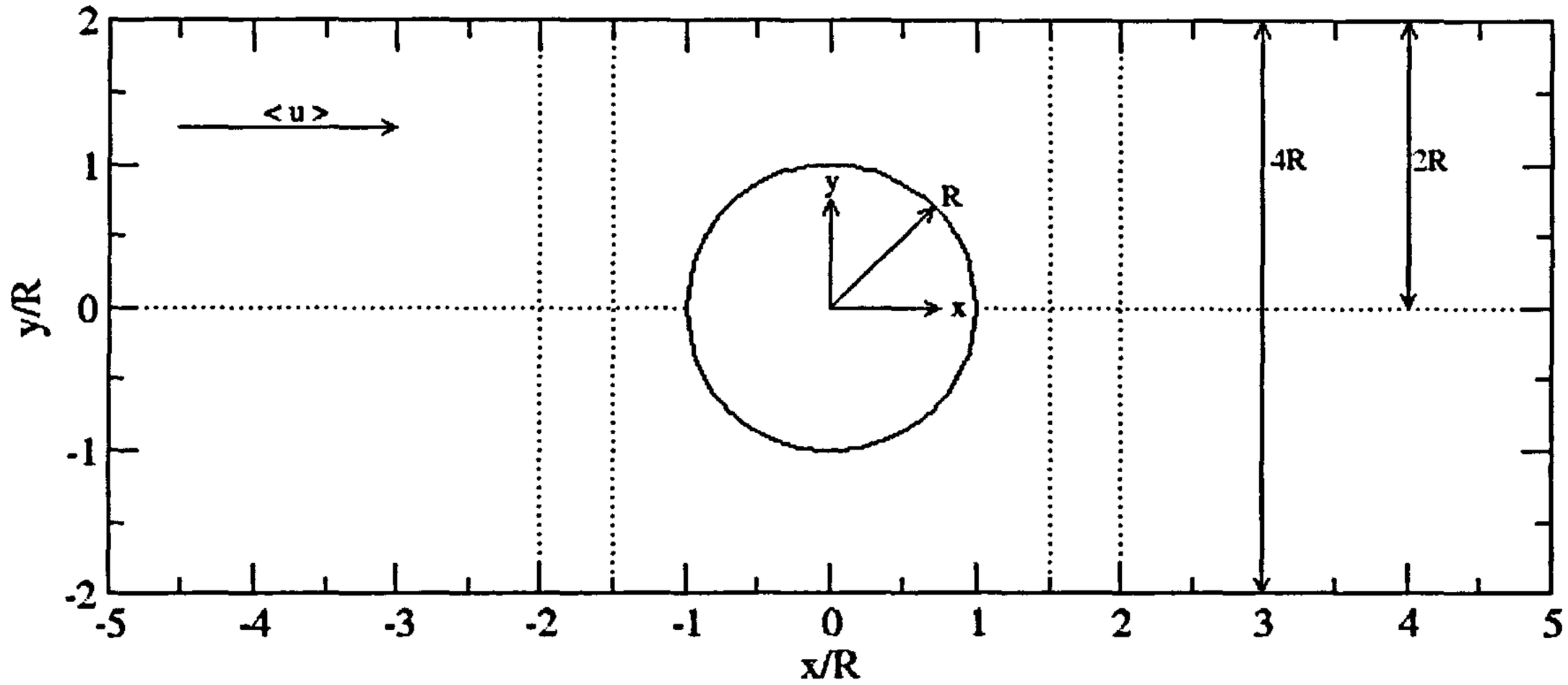

Figure 4.1: Schematic representation of the cross sectional view of the symmetrically confined cylinder geometry. Radius (R) of the cylinder is 0.0045 m, height of the channel is $4R$ and the total length in the x direction is 0.130 m. The center of the cylinder is at $x = 0$, $y = 0$ and the mean flow is in the positive x direction.

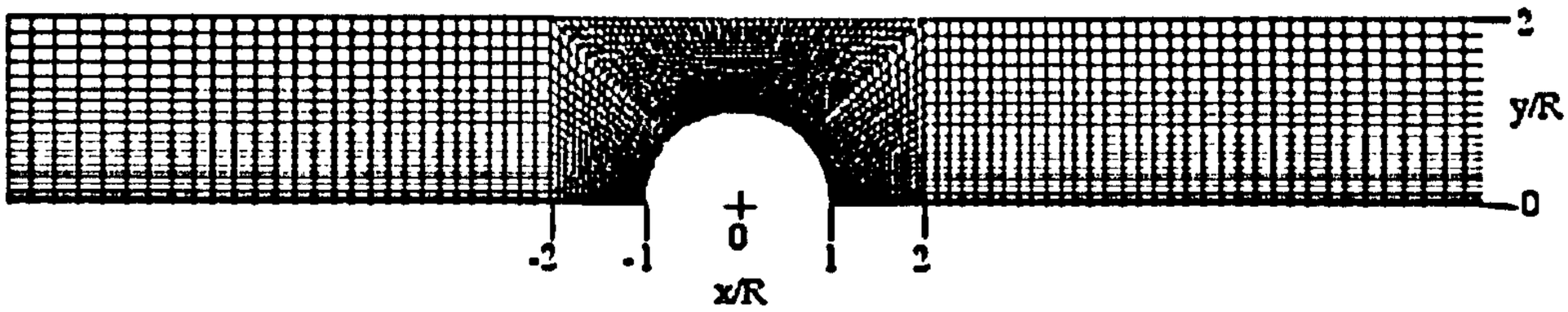

Figure 4.2: The coarse finite volume mesh geometry around a symmetrically confined cylinder, used for the mesh independence simulations, containing 3720 cells.

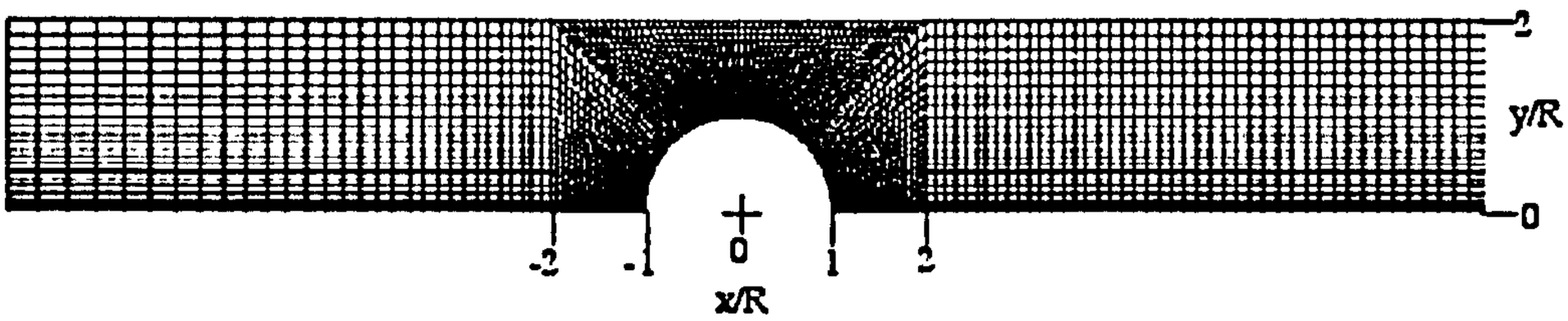

Figure 4.3: The medium finite volume mesh geometry around a symmetrically confined cylinder, used for most simulations in this chapter, containing 5720 cells.

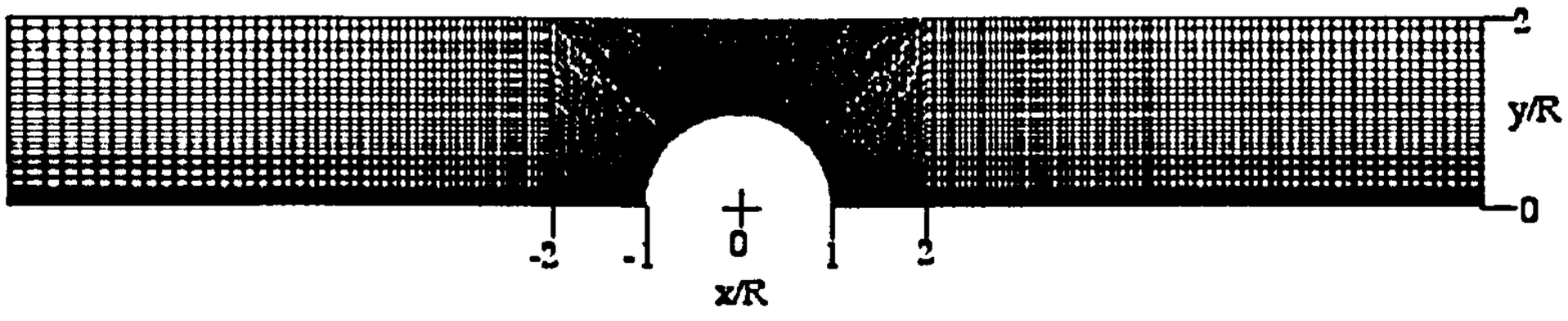

Figure 4.4: The fine finite volume mesh geometry around a symmetrically confined cylinder, used for the mesh independence simulations, containing 11000 cells.

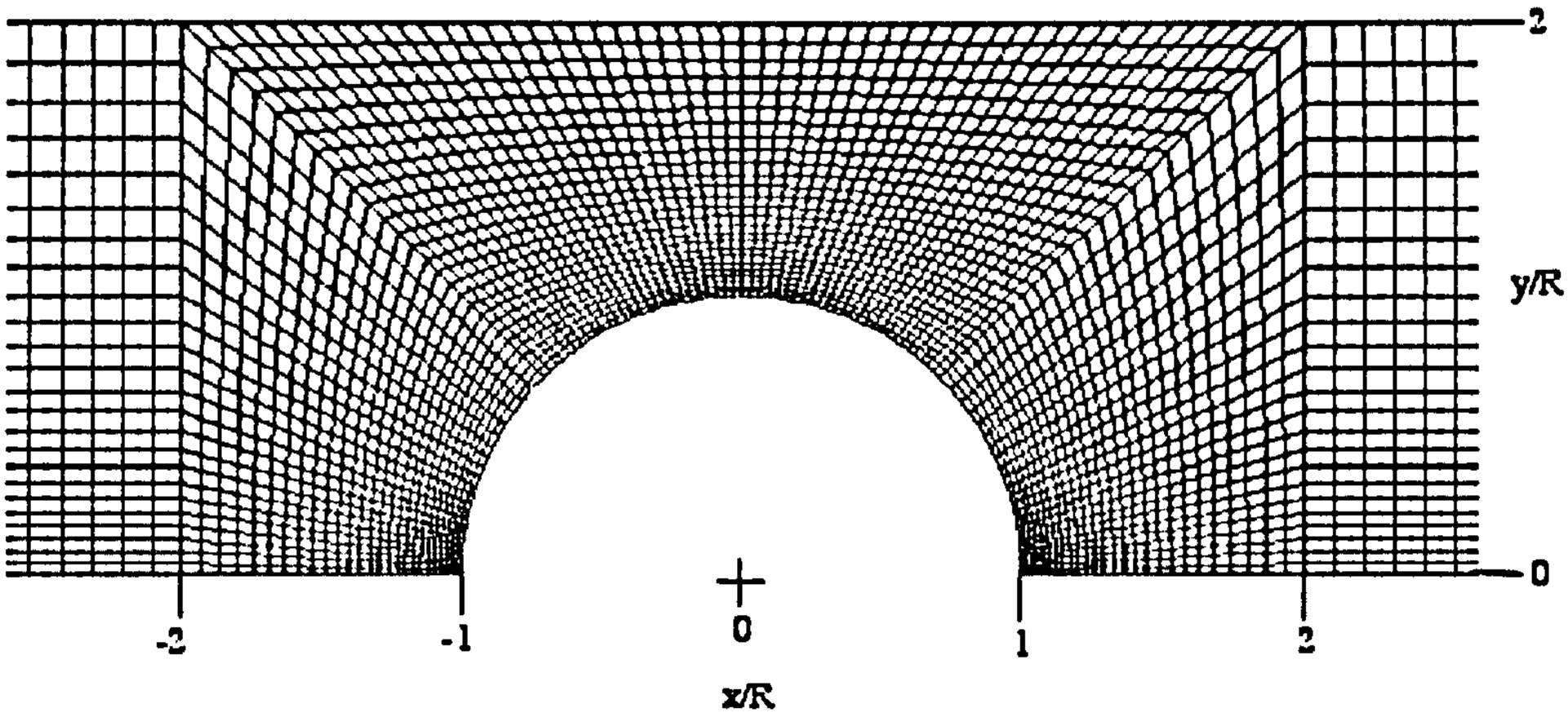

Figure 4.5: A closer view of the medium finite volume mesh geometry around a symmetrically confined cylinder, used for most of the simulations in this chapter.

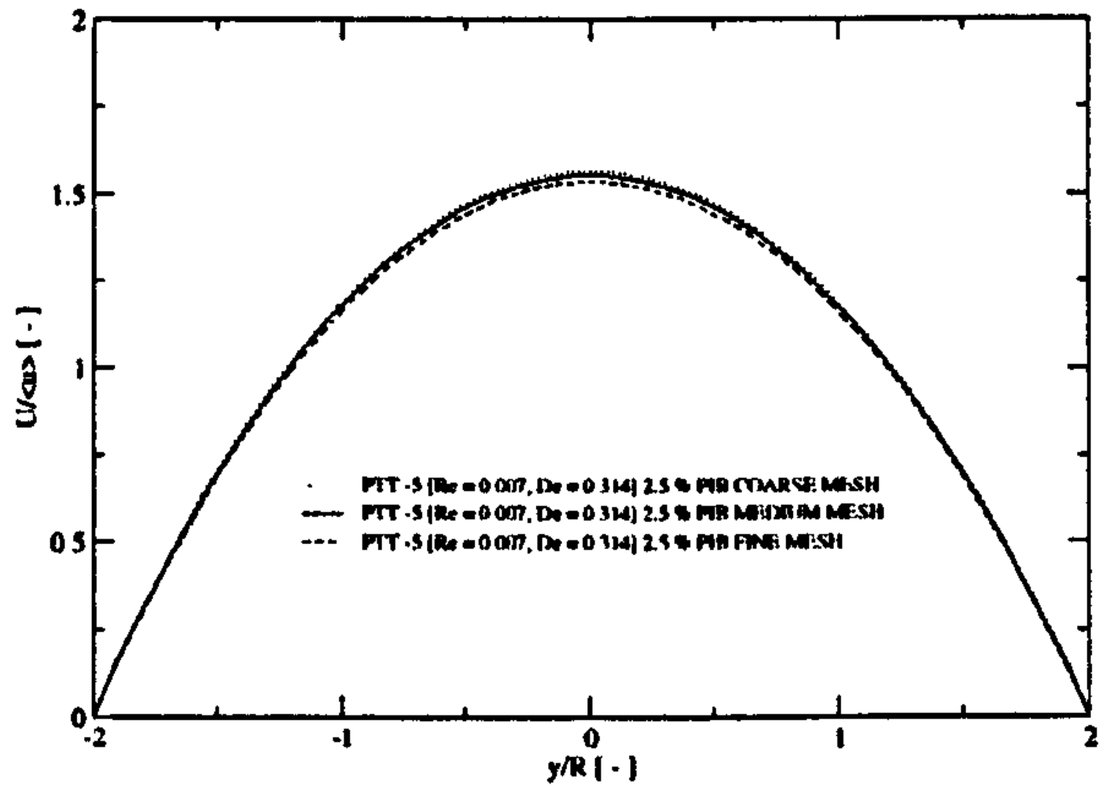

Figure 4.6: Comparison of predictions for the axial velocity (U) values in the fully developed region ($x/R = -5$) at $De = 0.314$, for three different mesh densities, for the 2.5 % PIB solution.

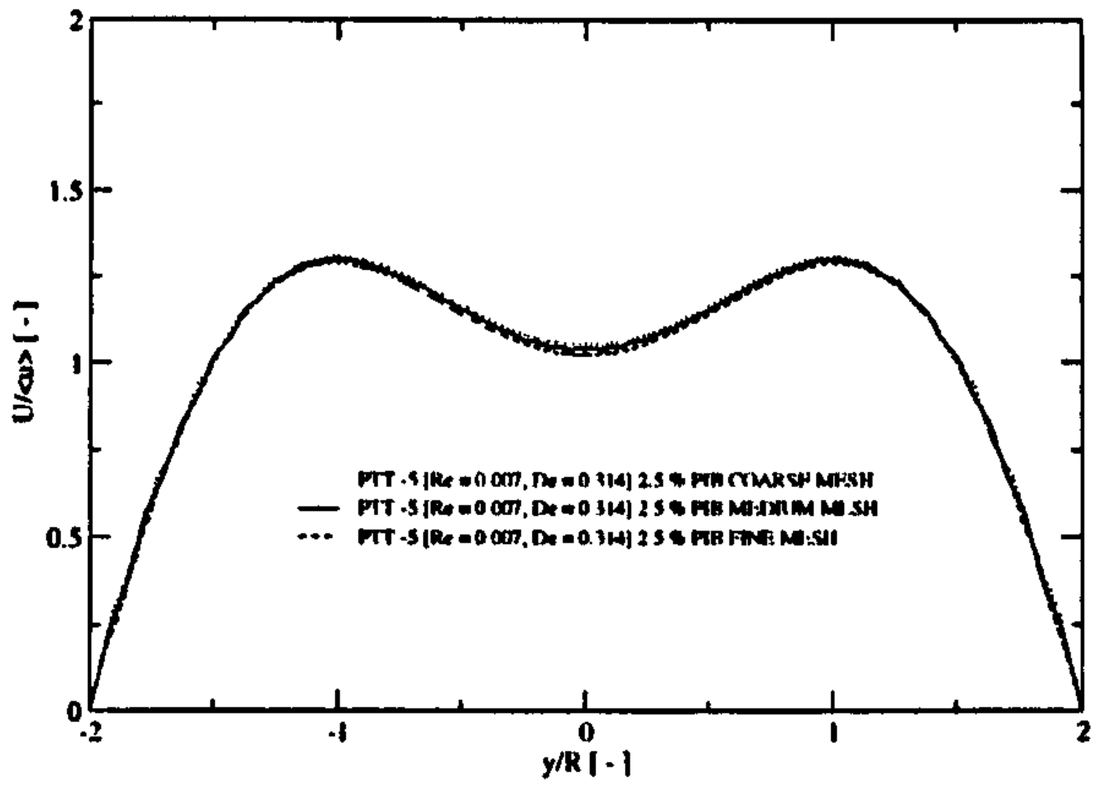

Figure 4.7: Comparison of predictions for the axial velocity (U) values upstream of the cylinder ($x/R = -2$) at $De = 0.314$, for three different mesh densities, for the 2.5 % PIB solution.

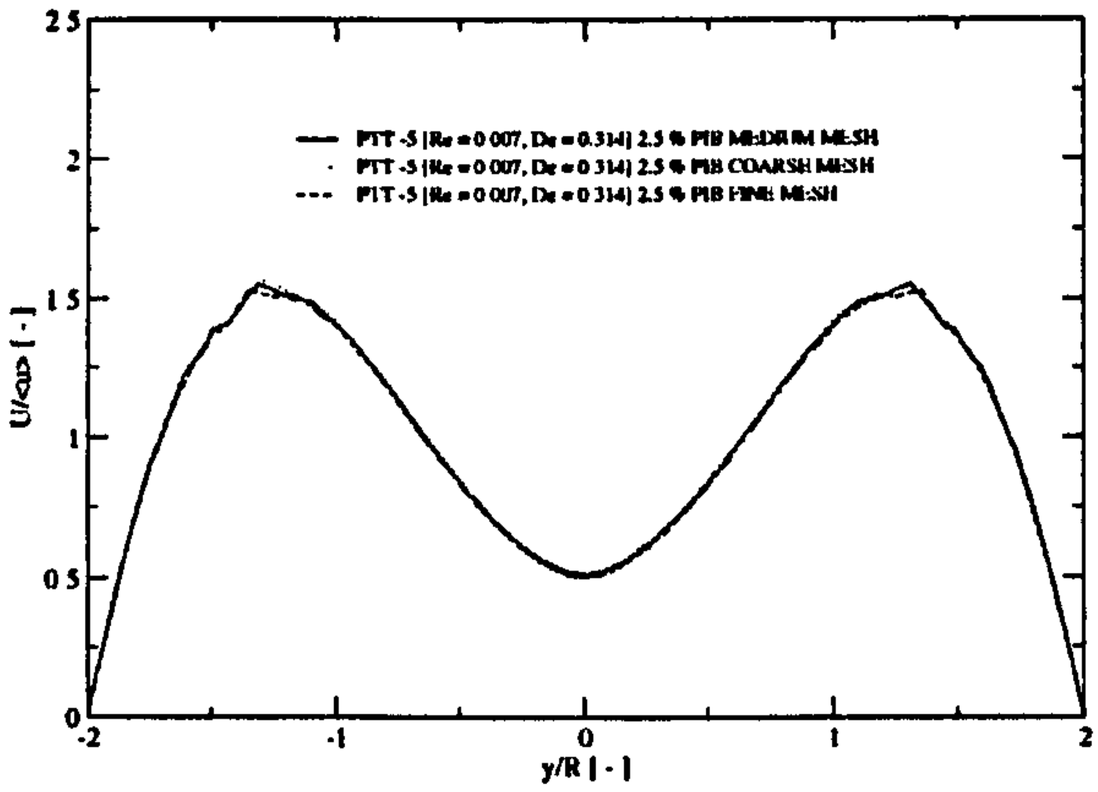

Figure 4.8: Comparison of predictions for the axial velocity (U) values downstream of the cylinder ($x/R = 1.5$) at $De = 0.314$, for three different mesh densities, for the 2.5 % PIB solution.

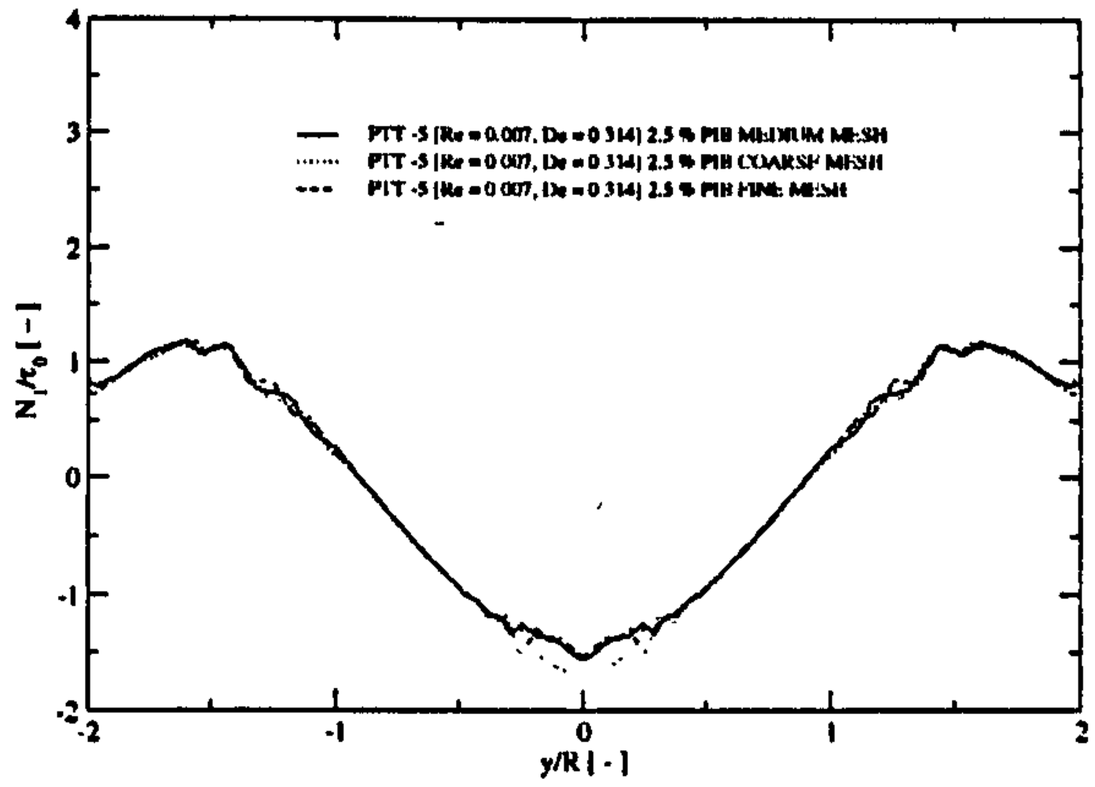

Figure 4.9: Comparison of predictions for the first normal stress difference (N_1) values upstream of the cylinder ($x/R = -1.5$) at $De = 0.314$, for three different mesh densities, for the 2.5 % PIB solution.

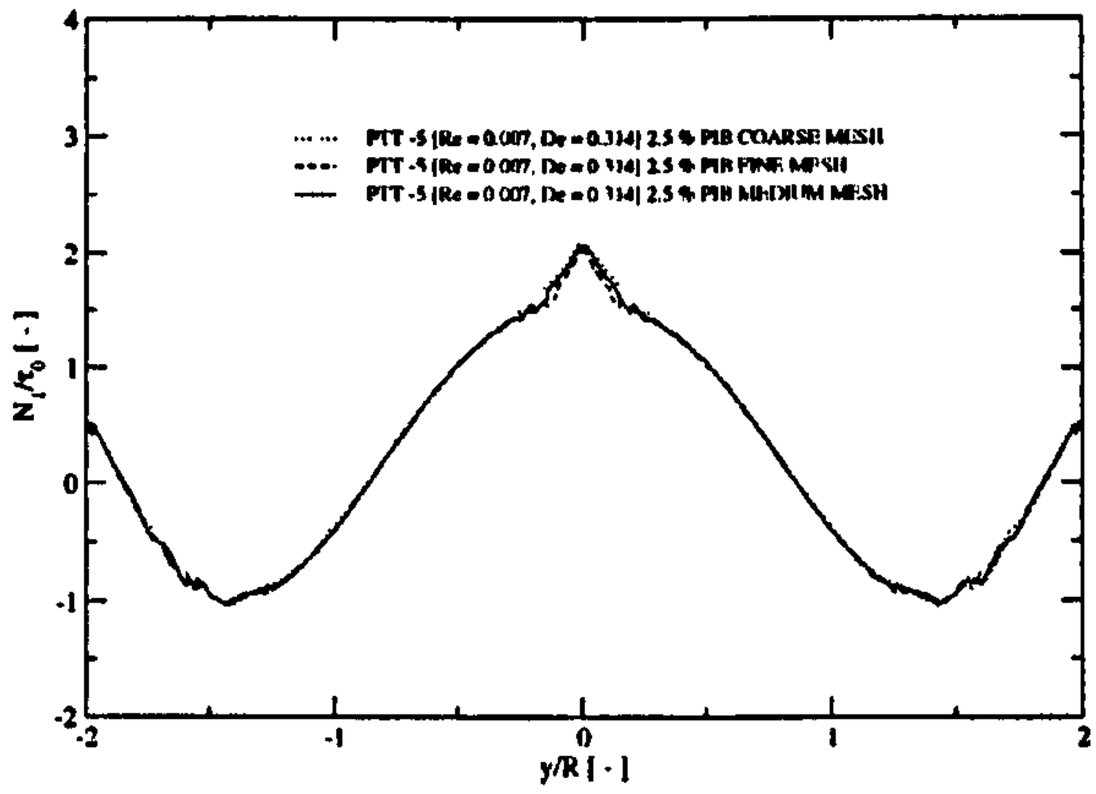

Figure 4.10: Comparison of predictions for the first normal stress difference (N_1) values downstream of the cylinder ($x/R = 1.5$) at $De = 0.314$, for three different mesh densities, for the 2.5 % PIB solution.

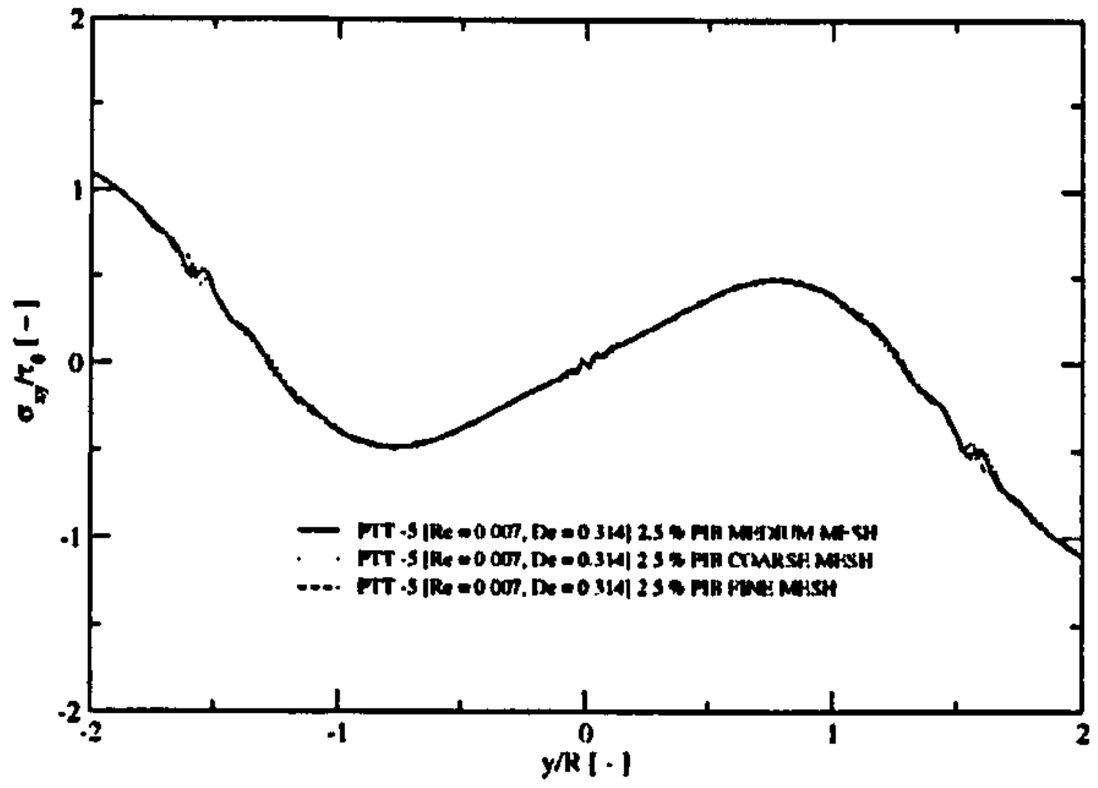

Figure 4.11: Comparison of predictions for the shear stress (σ_{xy}) values downstream of the cylinder ($x/R = 1.5$) at $De = 0.314$, for three different mesh densities, for the 2.5 % PIB solution.

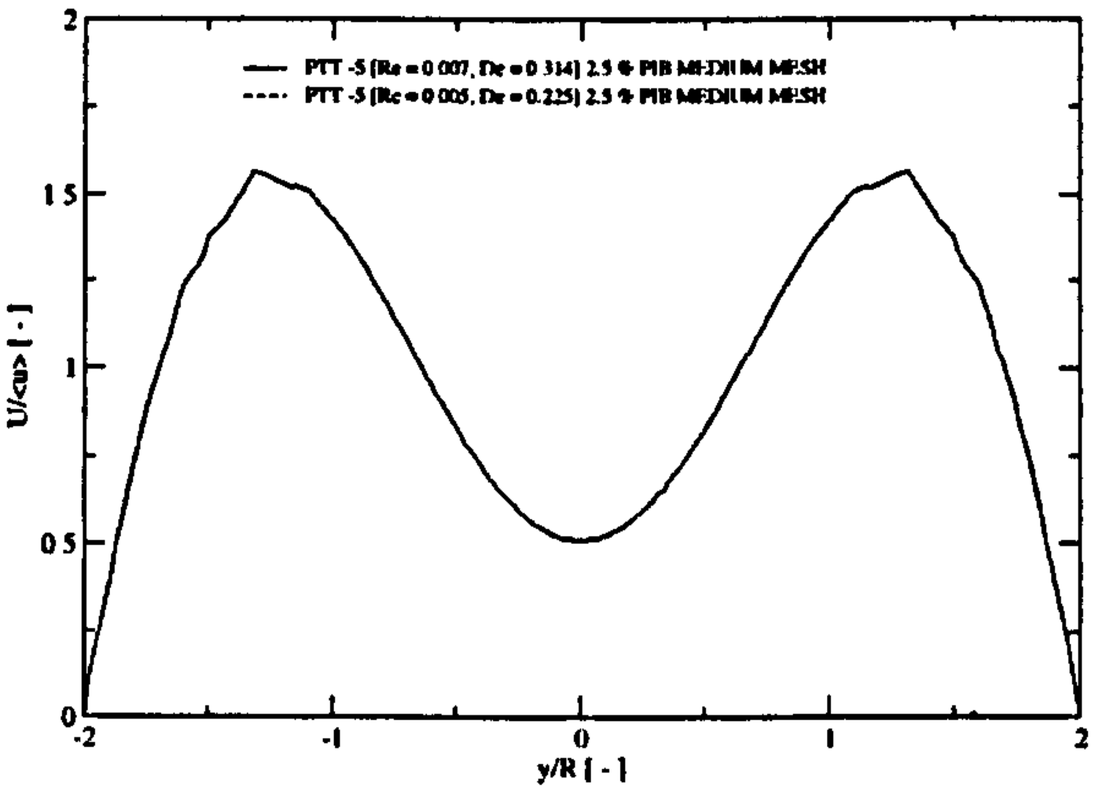

Figure 4.12: Comparison of predictions for the axial velocity (U) values upstream of the cylinder ($x/R = -1.5$) at $De = 0.314$ and 0.225, for the 2.5 % PIB solution.

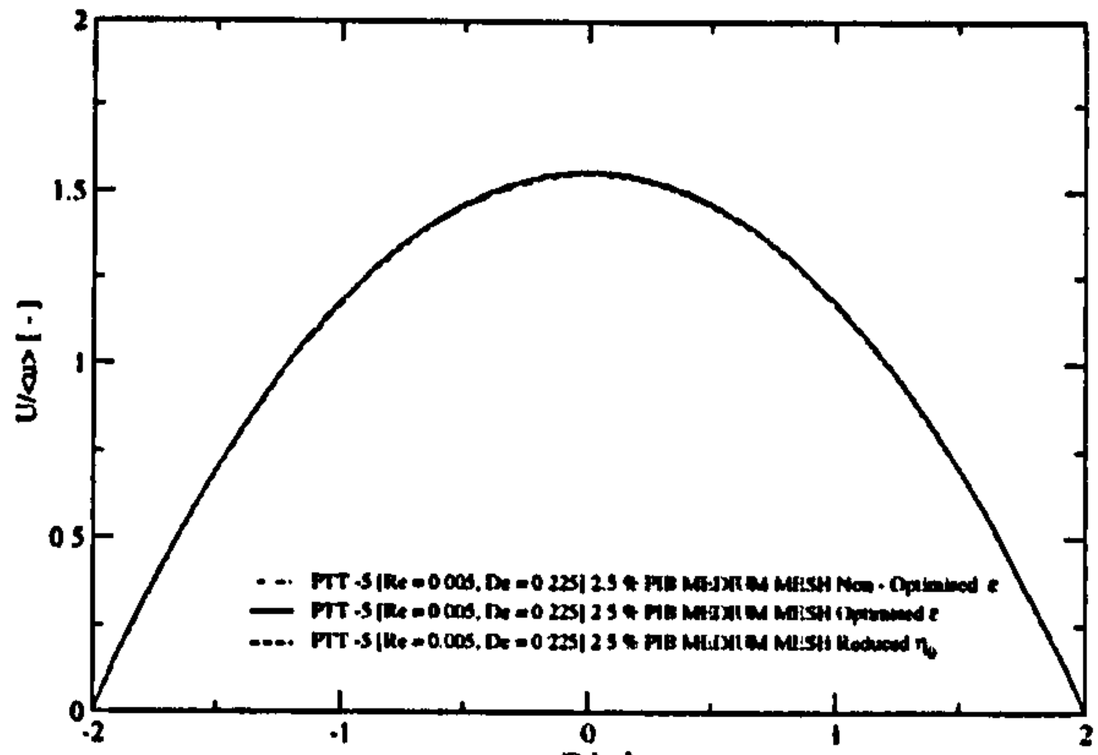

Figure 4.13: Comparison of predictions for the axial velocity (U) values in the fully developed region ($x/R = -5$) at $De = 0.225$, for a non-optimised and optimised model and for the reduced η_0 case, for the 2.5 % PIB solution.

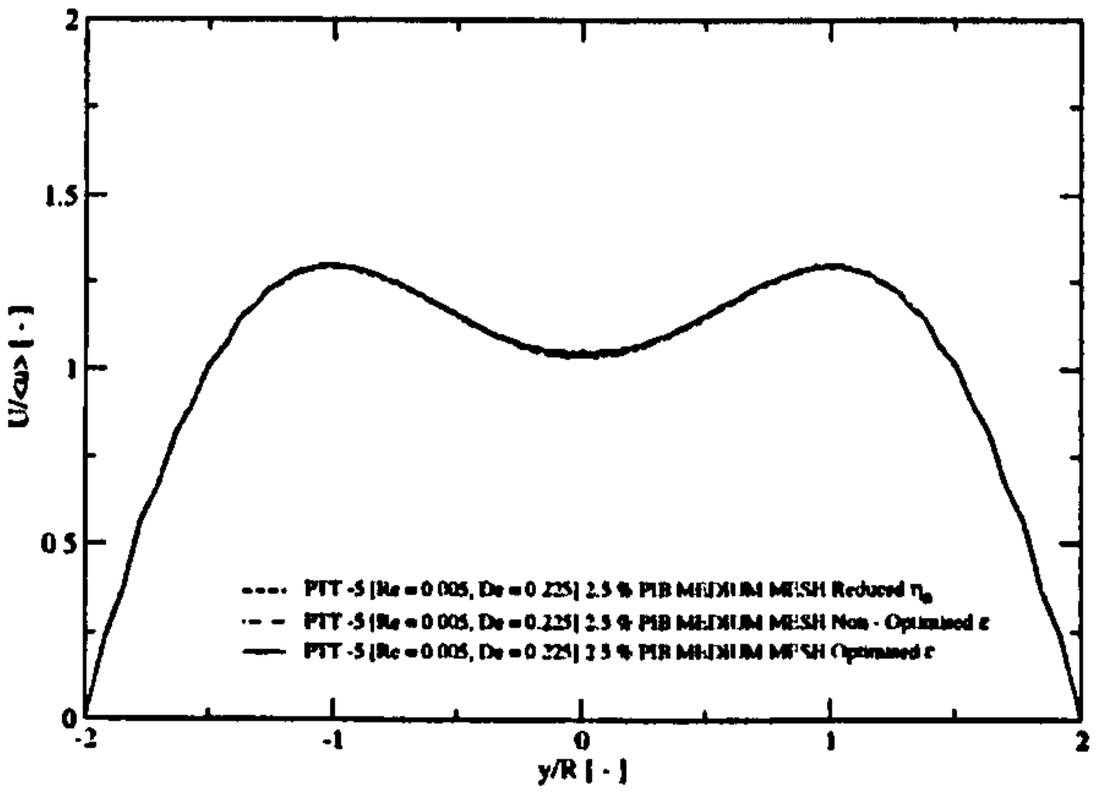

Figure 4.14: Comparison of predictions for the axial velocity (U) values upstream of the cylinder ($x/R = -2$) at $De = 0.225$, for a non-optimised and optimised model and for the reduced η_0 case, for the 2.5 % PIB solution.

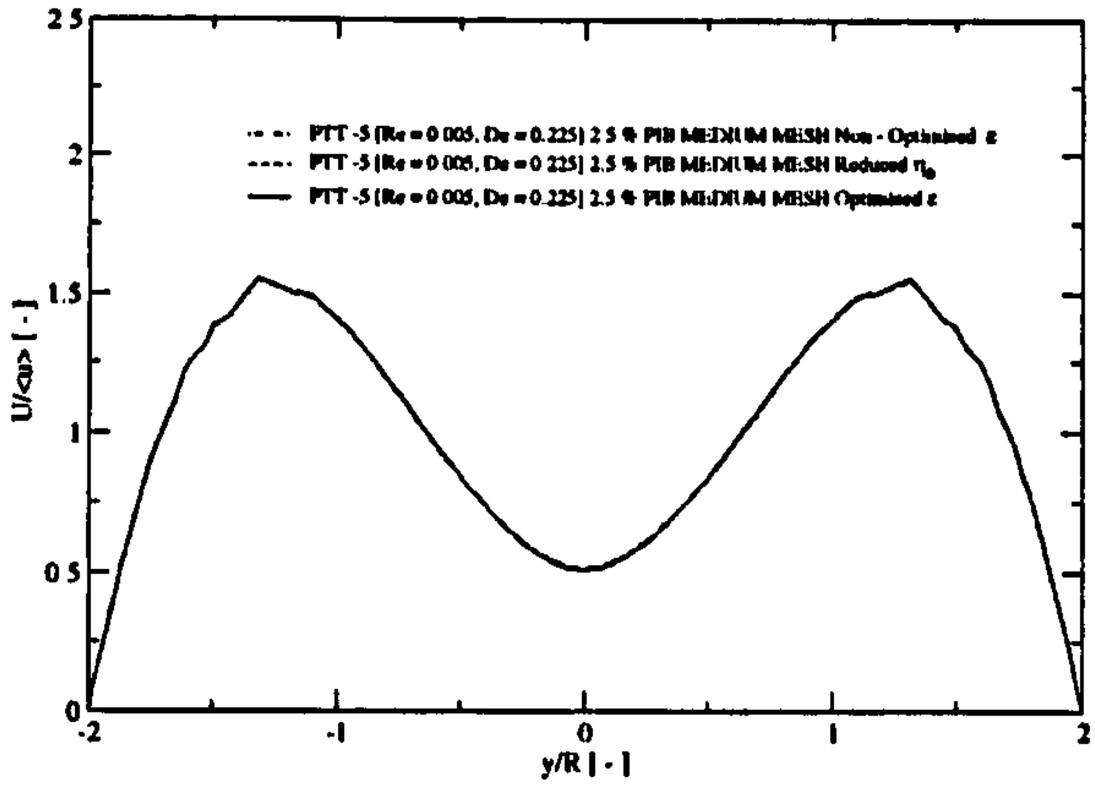

Figure 4.15: Comparison of predictions for the axial velocity (U) values downstream of the cylinder ($x/R = 1.5$) at $De = 0.225$, for a non-optimised and optimised model and for the reduced η_0 case, for the 2.5 % PIB solution.

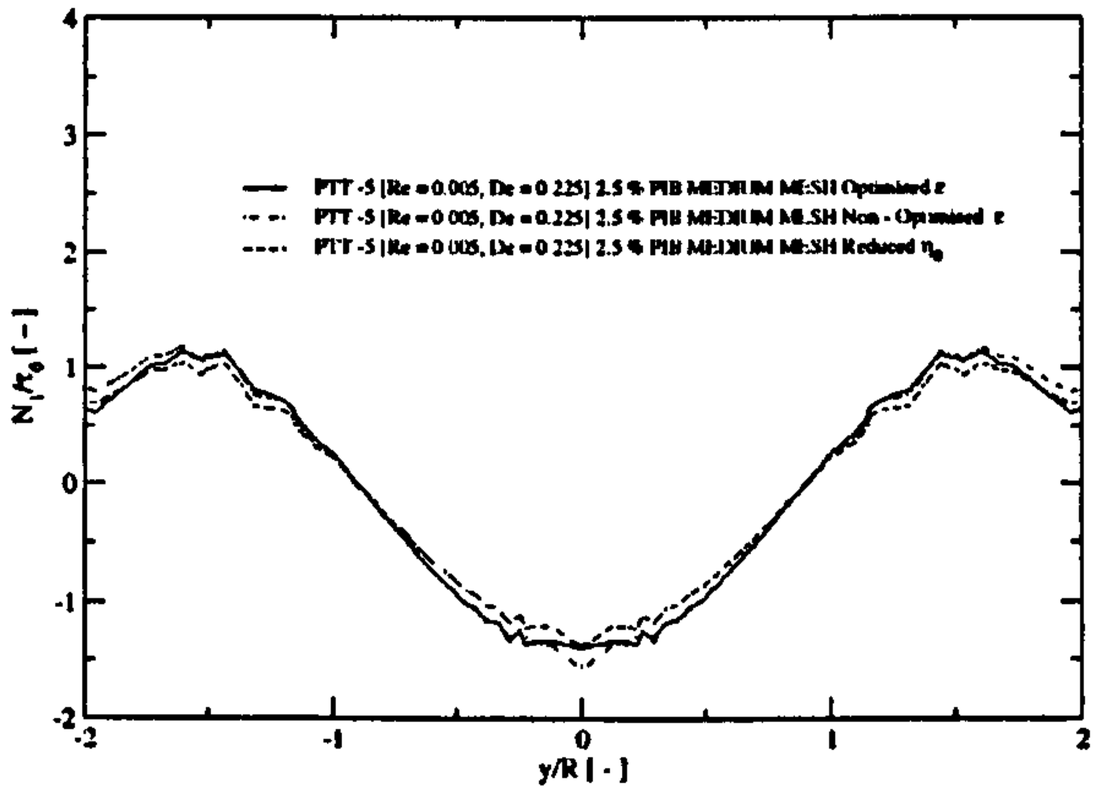

Figure 4.16: Comparison of predictions for the first normal stress difference (N_1) values upstream of the cylinder ($x/R = -1.5$) at $De = 0.225$, for a non-optimised and optimised model and for the reduced η_0 case, for the 2.5 % PIB solution.

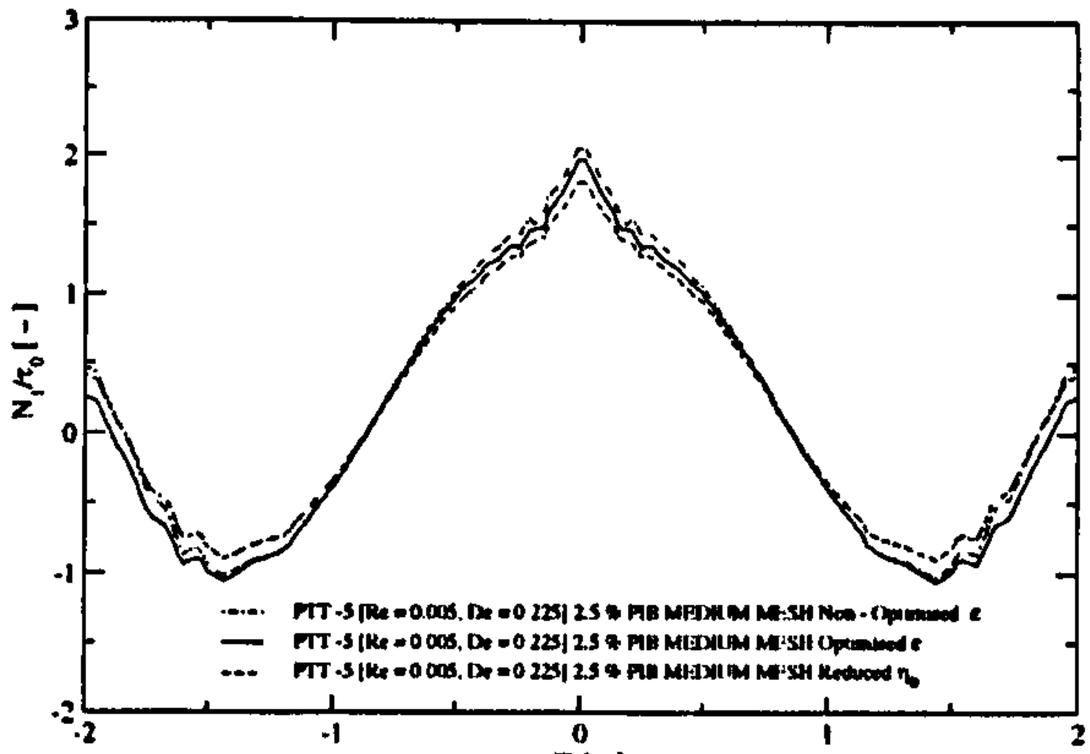

Figure 4.17: Comparison of predictions for the first normal stress difference (N_1) values downstream of the cylinder ($x/R = 1.5$) at $De = 0.225$, for a non-optimised and optimised model and for the reduced η_0 case, for the 2.5 % PIB solution.

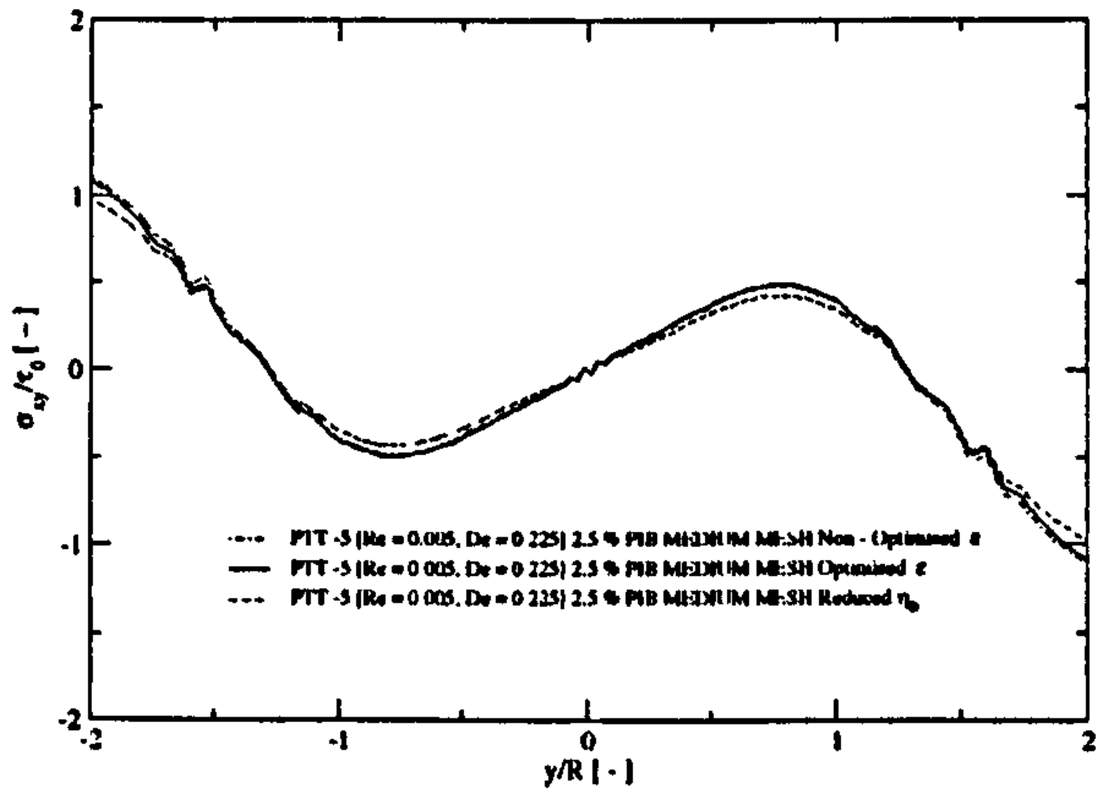

Figure 4.18: Comparison of predictions for the shear stress (σ_{xy}) values downstream of the cylinder ($x/R = 1.5$) at $De = 0.225$, for a non-optimised and optimised model and for the reduced η_0 case, for the 2.5 % PIB solution.

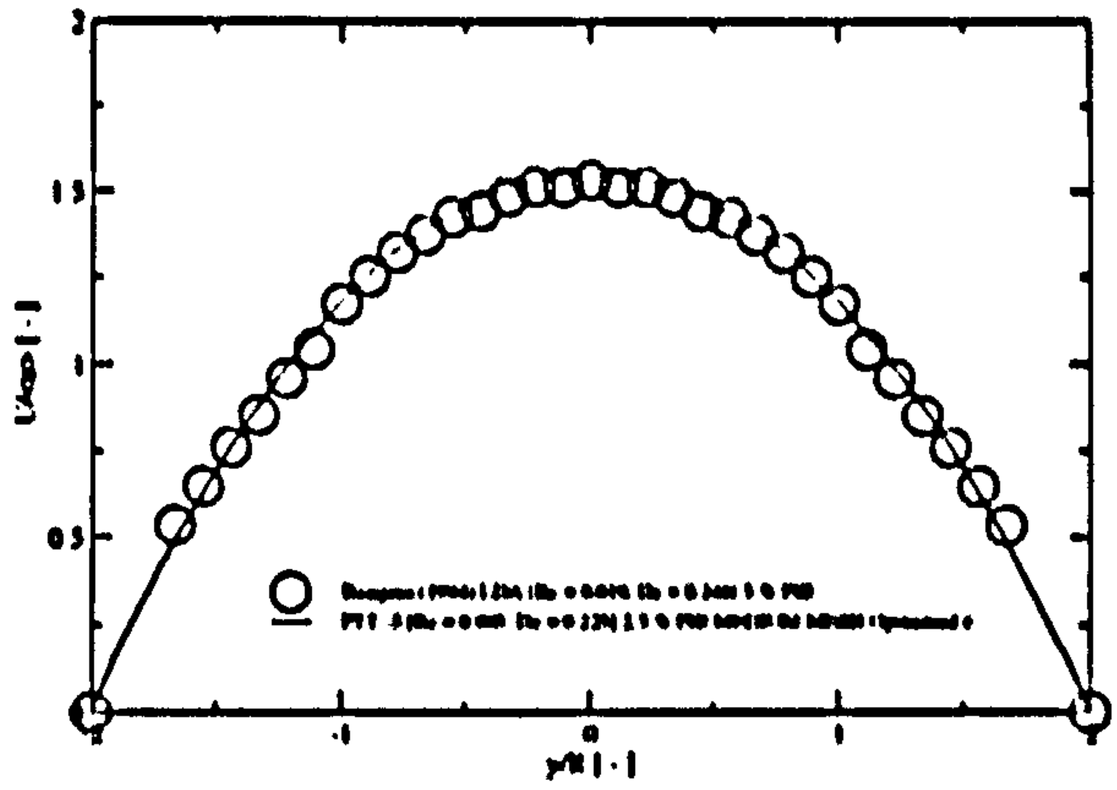

Figure 4.19: Comparison of predictions for the axial velocity (U) values upstream of the cylinder ($x/R = -5$) at $De = 0.225$, for the 2.5 % PIB solution with measurement data of Baaijens (1994b) for the axial velocity (U) values at $x/R = -5$, $De = 0.248$ and $Re = 0.019$, for the 5 % PIB solution.

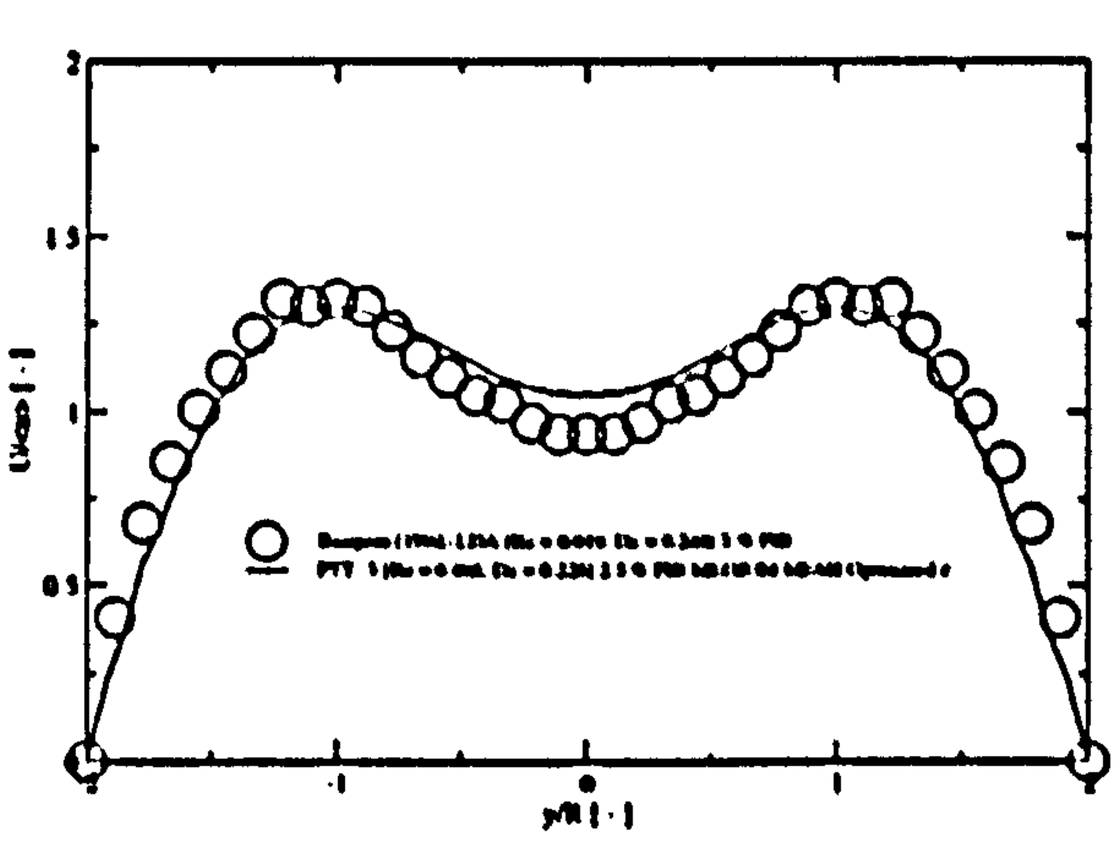

Figure 4.20: Comparison of predictions for the axial velocity (U) values upstream of the cylinder ($x/R = -2$) at $De = 0.225$, for the 2.5 % PIB solution with measurement data of Baaijens (1994b) for the axial velocity (U) values at $x/R = -2$ and $De = 0.248$, for the 5 % PIB solution.

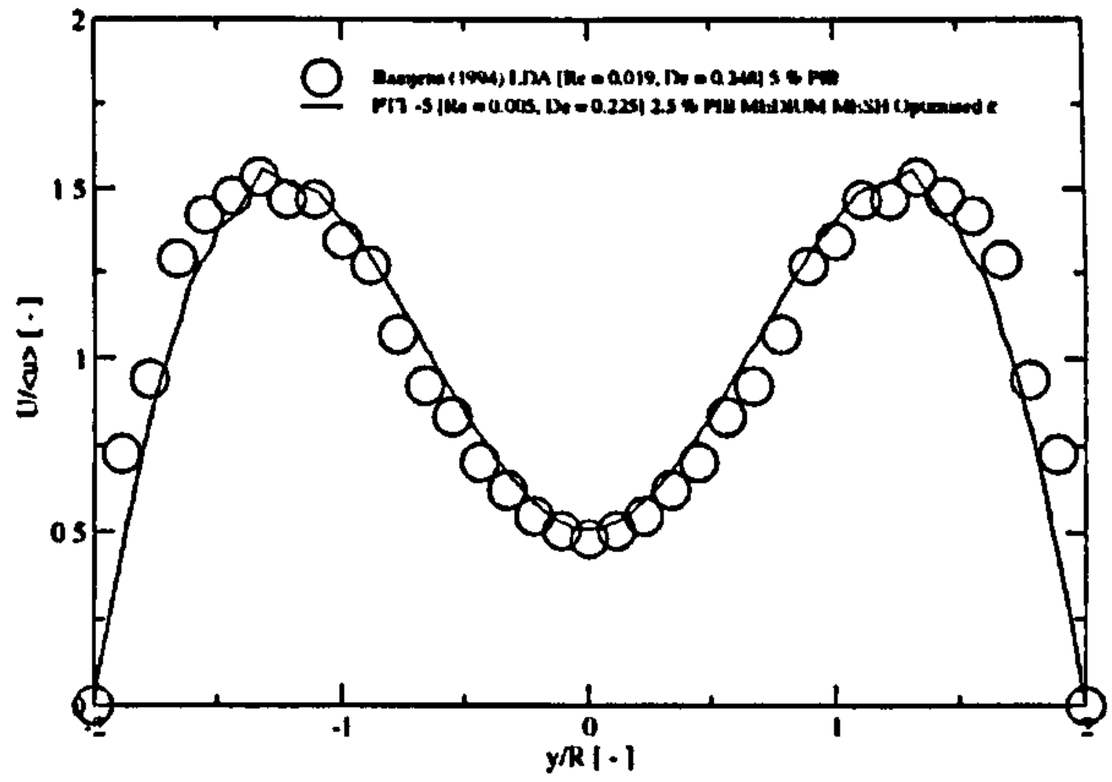

Figure 4.21: Comparison of predictions for the axial velocity (U) values downstream of the cylinder ($x/R = 1.5$) at $De = 0.225$, for the 2.5 % PIB solution with measurement data of Baaijens (1994b) for the axial velocity (U) values at $x/R = 1.5$ and $De = 0.248$, for the 5 % PIB solution.

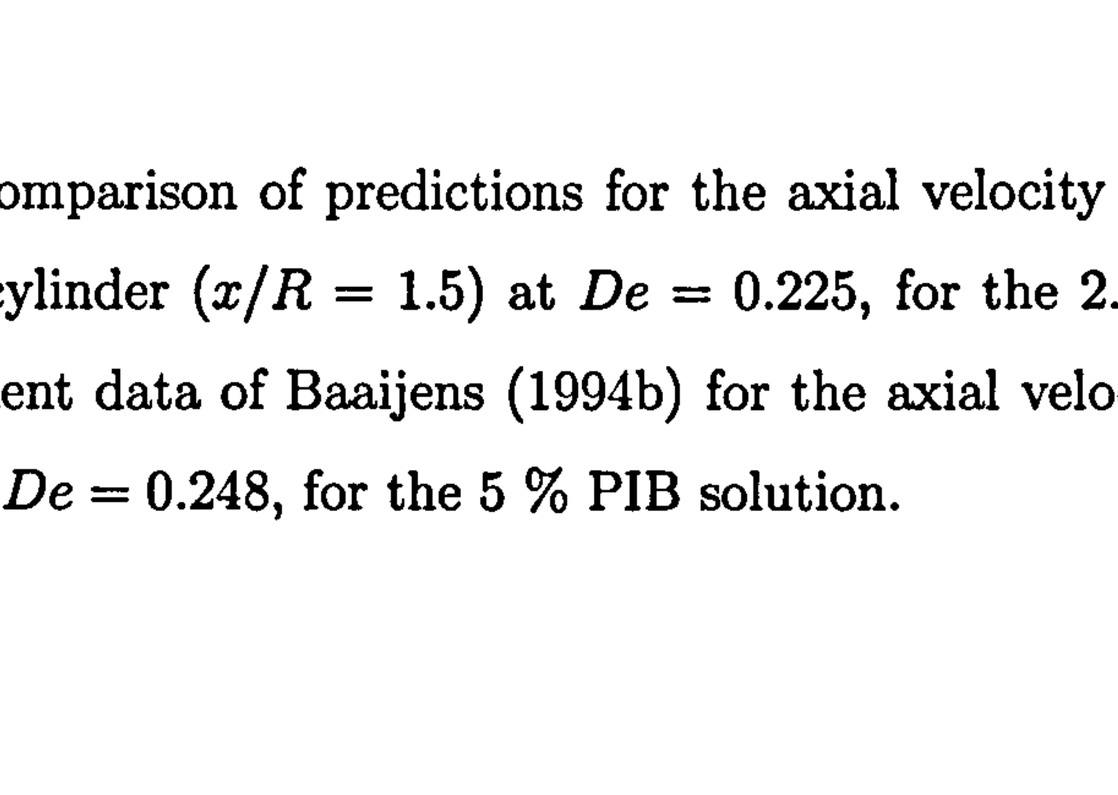

Figure 4.22: Comparison of predictions for the axial velocity (U) values upstream and downstream of the cylinder ($y/R = 0$) at $De = 0.225$, for the 2.5 % PIB solution with measurement data of Baaijens (1994b) for the axial velocity (U) values at $y/R = 0$ and $De = 0.248$, for the 5 % PIB solution.

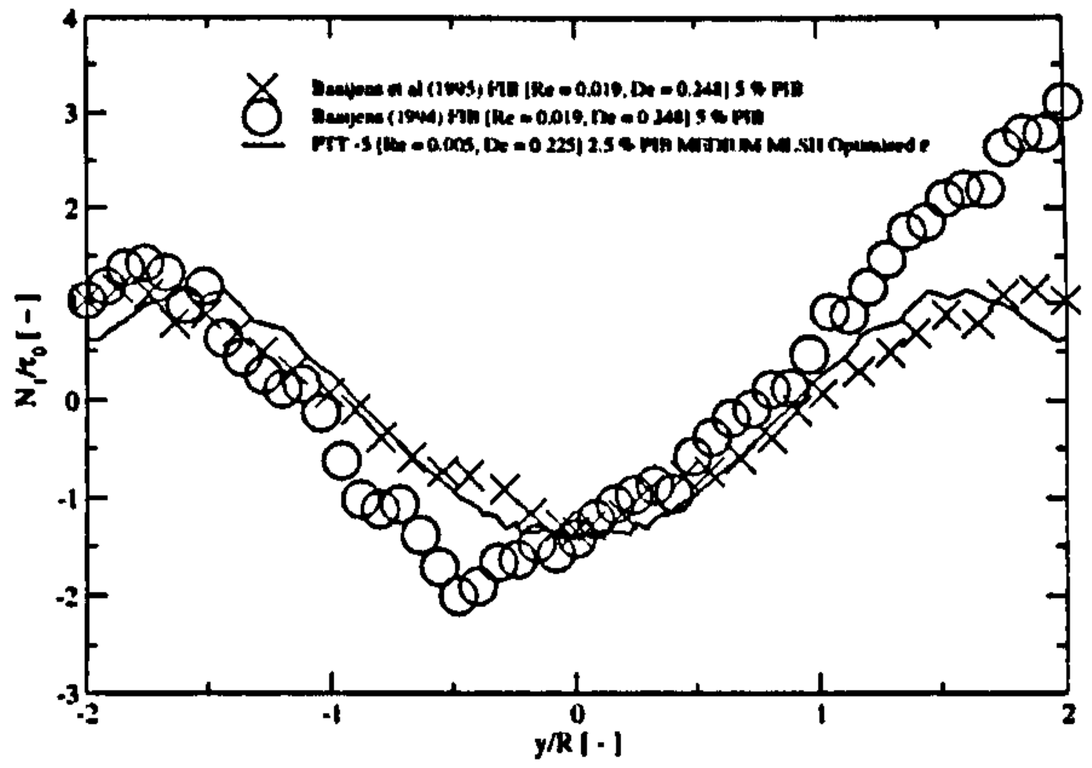

Figure 4.23: Comparison of predictions for the first normal stress difference (N_1) values upstream of the cylinder ($x/R = -1.5$) at $De = 0.225$, for the 2.5 % PIB solution with measurement data of Baaijens (1994b) for the first normal stress difference (N_1) values at $x/R = -1.5$ and $De = 0.248$ and 0.931, for the 5 % PIB solution.

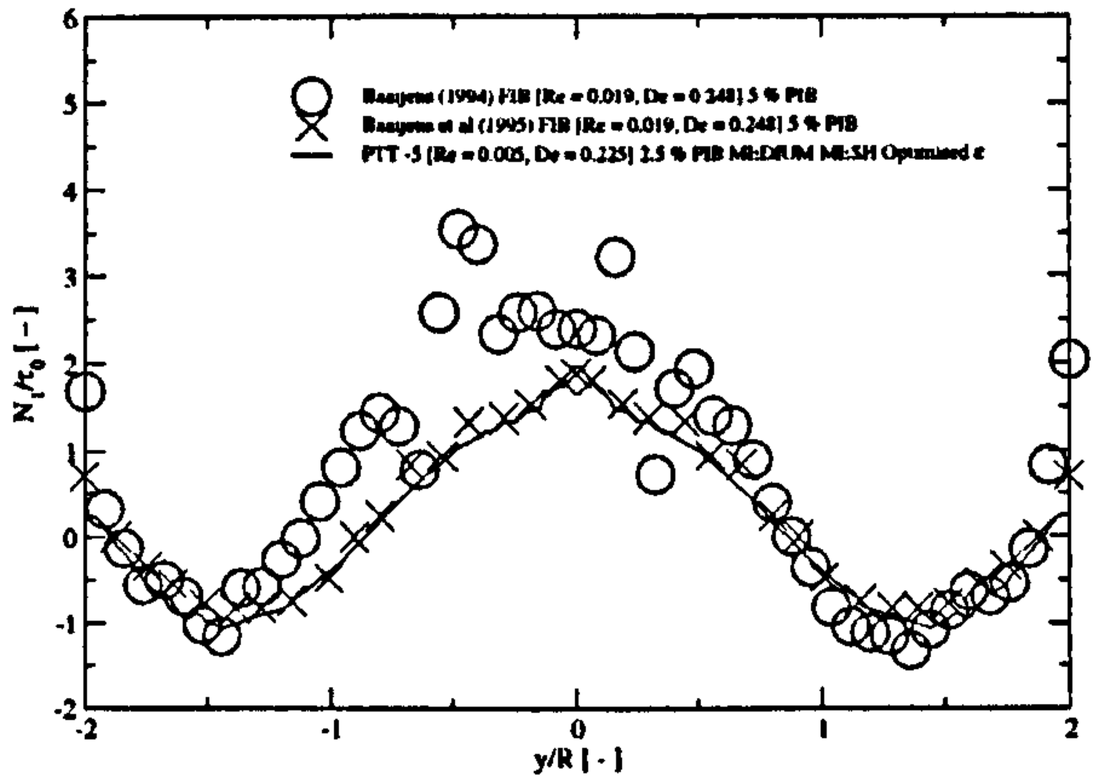

Figure 4.24: Comparison of predictions for the first normal stress difference (N_1) values downstream of the cylinder ($x/R = 1.5$) at $De = 0.225$, for the 2.5 % PIB solution with measurement data of Baaijens (1994b) for the first normal stress difference (N_1) values at $x/R = 1.5$ and $De = 0.248$ and 0.931, for the 5 % PIB solution.

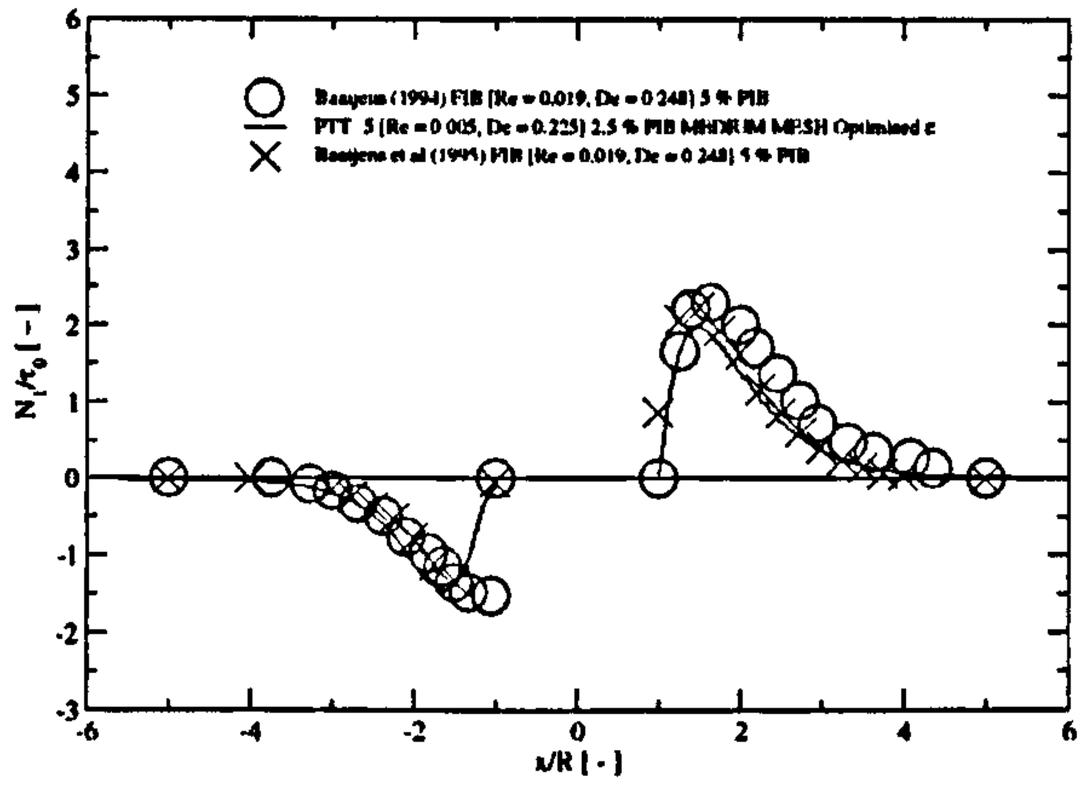

Figure 4.25: Comparison of predictions for the first normal stress difference (N_1) values upstream and downstream of the cylinder ($y/R = 0$) at $De = 0.225$, for the 2.5 % PIB solution with measurement data of Baaijens (1994b) for the first normal stress difference (N_1) values at $y/R = 0$ and $De = 0.248$, for the 5 % PIB solution.

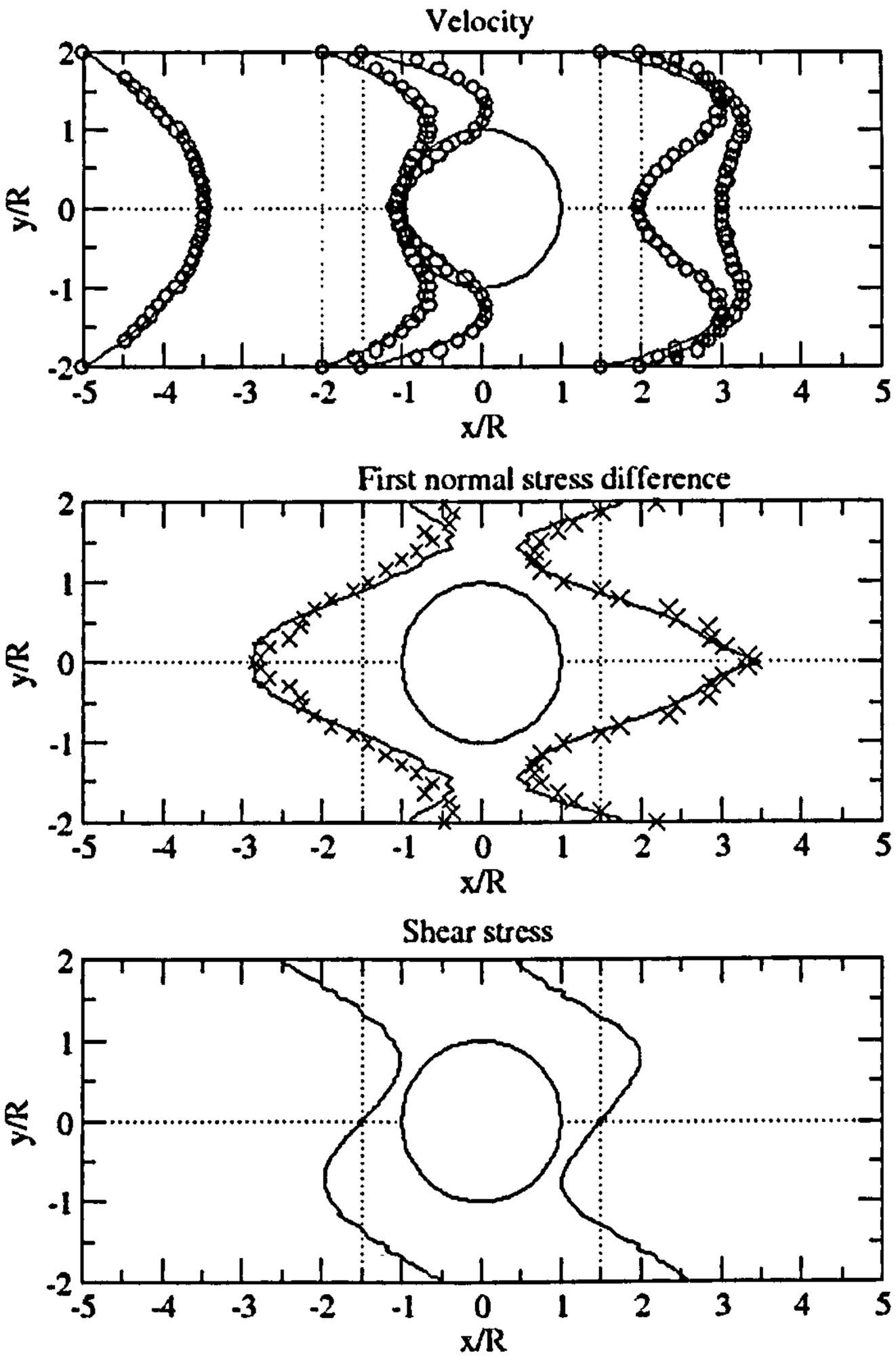

Figure 4.26: Comparison of predictions (-) using the 5 mode PTT model, for the 2.5 % PIB solution at $De = 0.225$ with measurement data of Baaijens (1994b), for the 5 % PIB solution at $De = 0.248$ (o) and 0.931 (x), past a cylinder confined symmetrically between two parallel plates: axial velocity (top), first normal stress difference (middle), shear stress (bottom). All velocities are non-dimensionalised with the mean velocity $< u >$ and the stresses with τ_0 (see section 4.2.4).

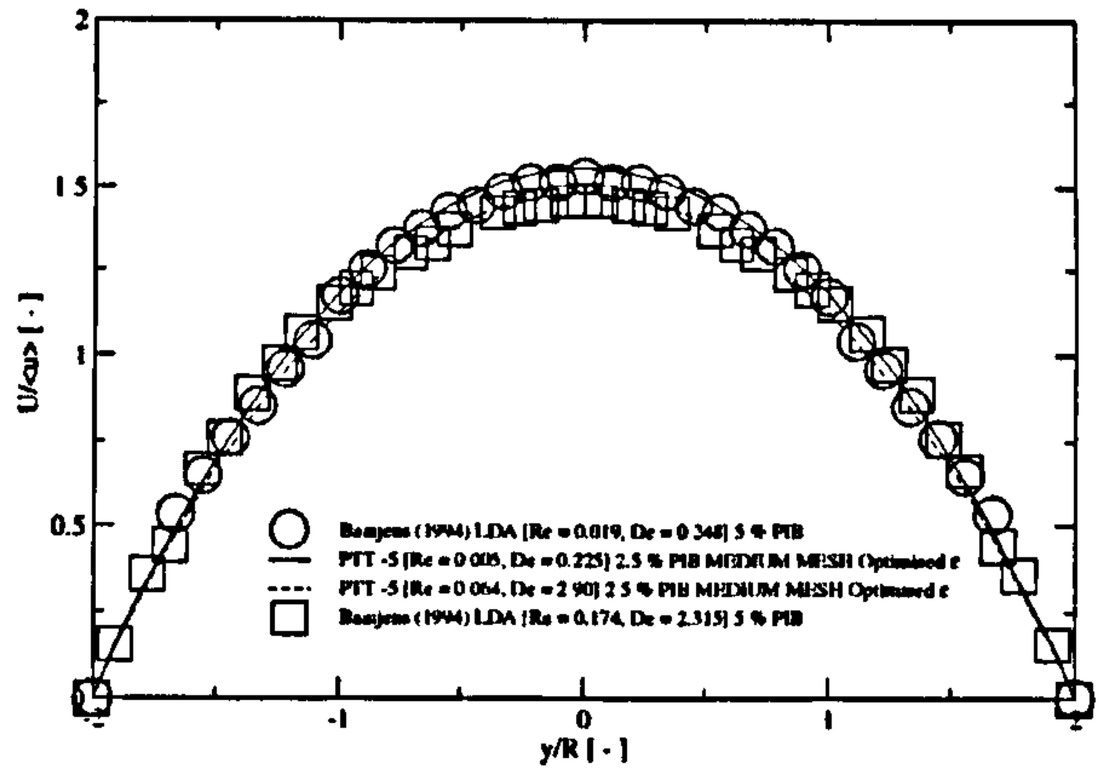

Figure 4.27: Comparison of predictions for the axial velocity (U) values in the fully developed region ($x/R = -5$) at $De = 0.225$ and 2.90, for the 2.5 % PIB solution with measurement data of Baaijens (1994b) for the axial velocity (U) values at $x/R = -5$ and $De = 0.248$ and 2.315, for the 5 % PIB solution.

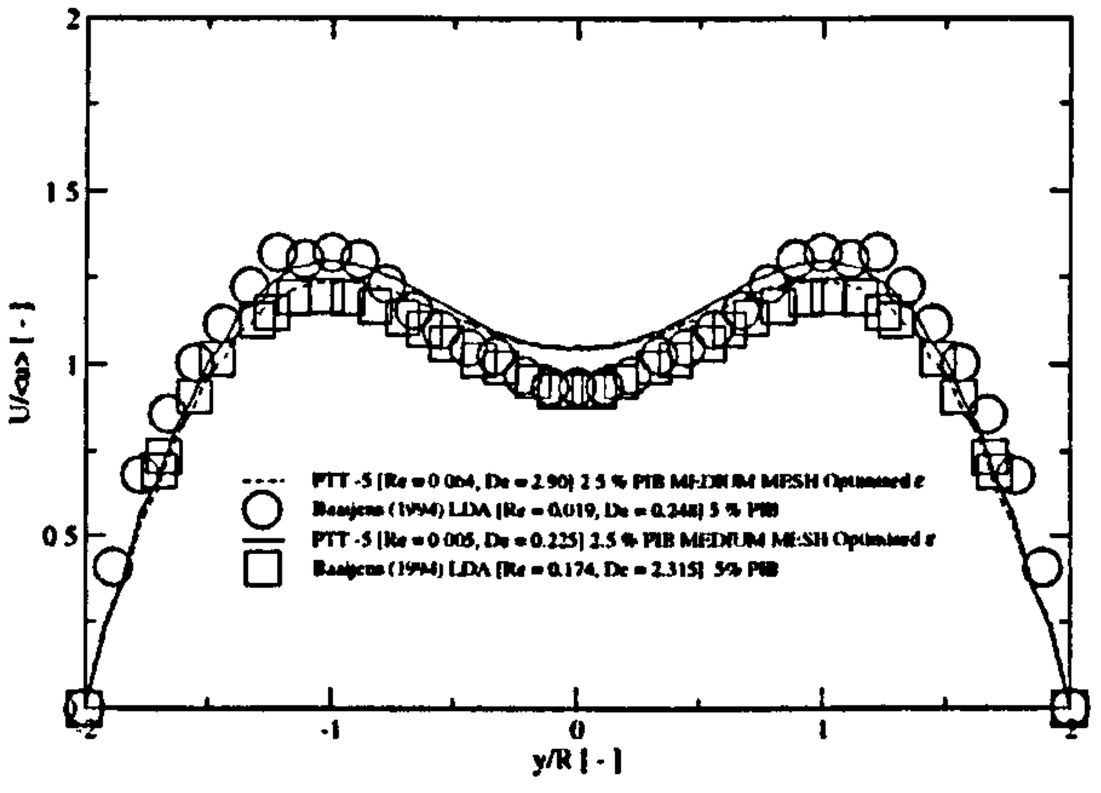

Figure 4.28: Comparison of predictions for the axial velocity (U) values upstream of the cylinder ($x/R = -2$) at $De = 0.225$ and 2.90, for the 2.5 % PIB solution with measurement data of Baaijens (1994b) for the axial velocity (U) values at $x/R = -2$ and $De = 0.248$ and 2.315, for the 5 % PIB solution.

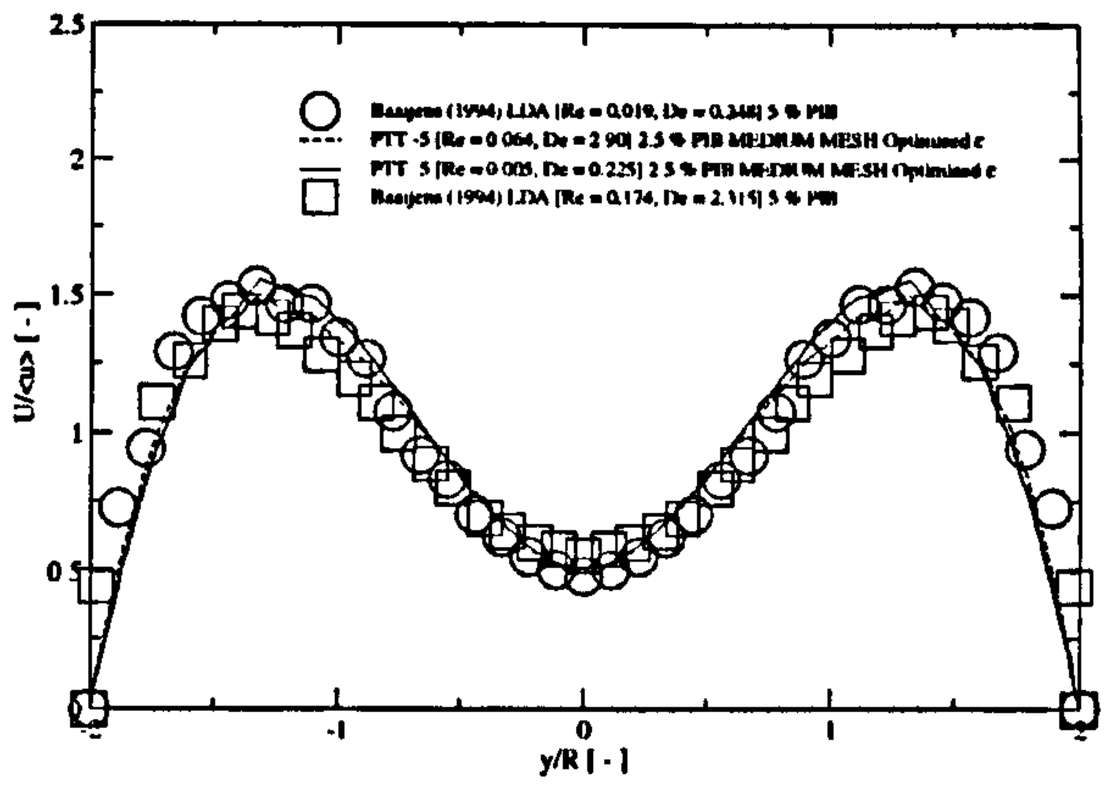

Figure 4.29: Comparison of predictions for the axial velocity (U) values downstream of the cylinder ($x/R = 1.5$) at $De = 0.225$ and 2.90, for the 2.5 % PIB solution with measurement data of Baaijens (1994b) for the axial velocity (U) values at $x/R = 1.5$ and $De = 0.248$ and 2.315, for the 5 % PIB solution.

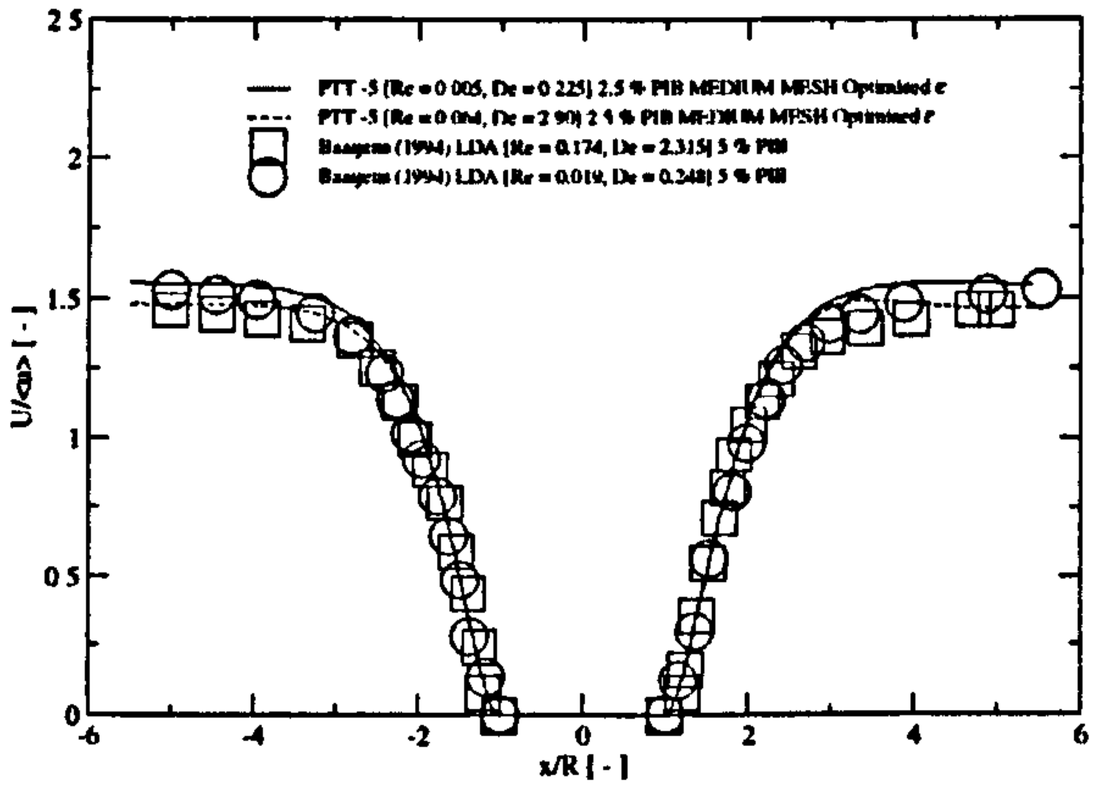

Figure 4.30: Comparison of predictions for the axial velocity (U) values upstream and downstream of the cylinder ($y/R = 0$) at $De = 0.225$ and 2.90, for the 2.5 % PIB solution with measurement data of Baaijens (1994b) for the axial velocity (U) values at $y/R = 0$ and $De = 0.248$ and 2.315, for the 5 % PIB solution.

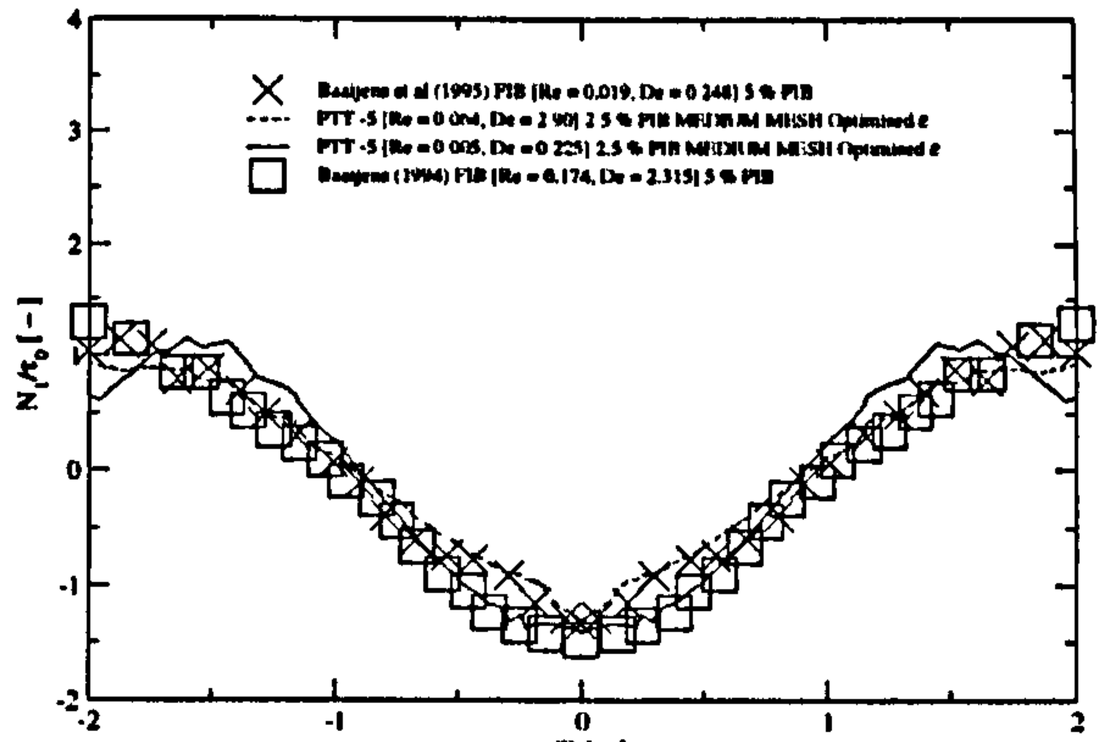

Figure 4.31: Comparison of predictions for the first normal stress difference (N_1) values upstream of the cylinder ($x/R = -1.5$) at $De = 0.225$ and 2.90, for the 2.5 % PIB solution with measurement data of Baaijens (1994b) for the first normal stress difference (N_1) values at $x/R = -1.5$ and $De = 0.248$, 0.931 and 2.315, for the 5 % PIB solution.

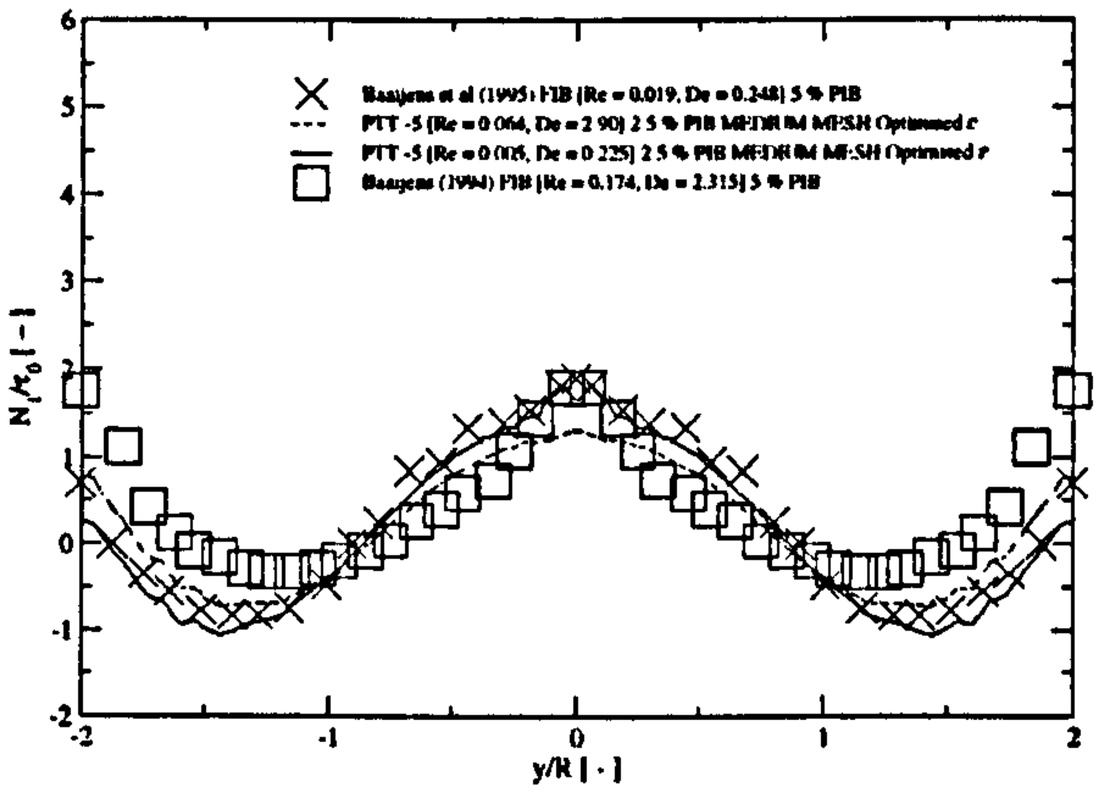

Figure 4.32: Comparison of predictions for the first normal stress difference (N_1) values downstream of the cylinder ($x/R = 1.5$) at $De = 0.225$ and 2.90, for the 2.5 % PIB solution with measurement data of Baaijens (1994b) for the first normal stress difference (N_1) values at $x/R = 1.5$ and $De = 0.248$, 0.931 and 2.315, for the 5 % PIB solution.

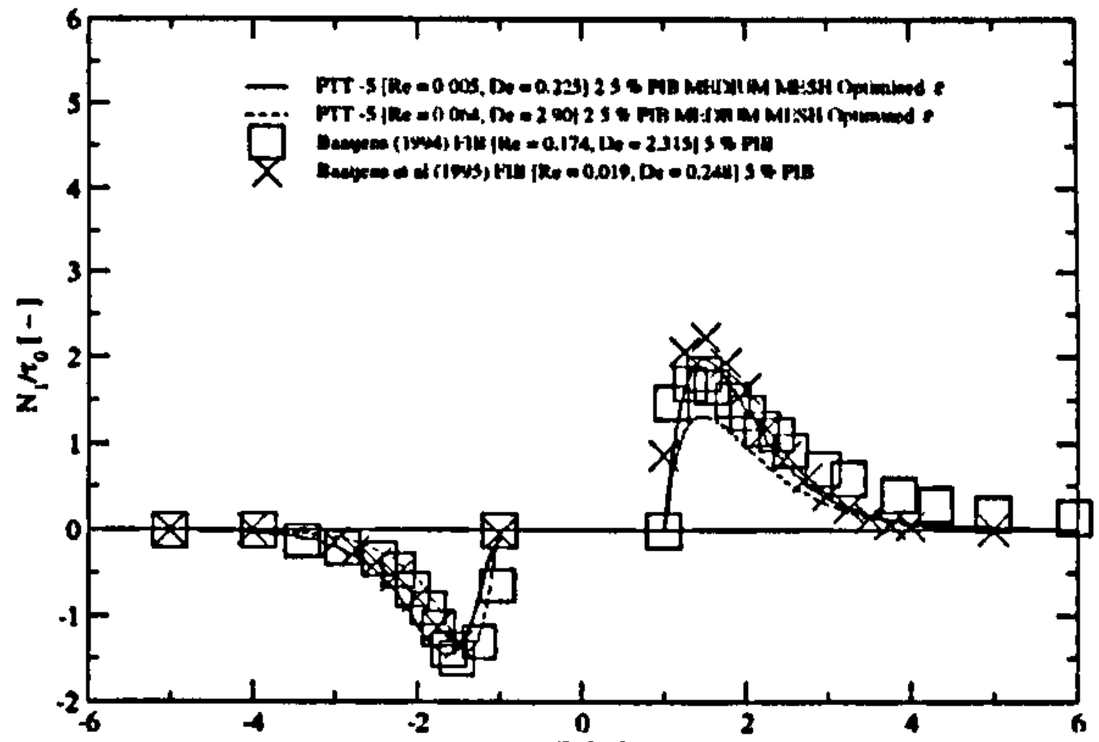

Figure 4.33: Comparison of predictions for the first normal stress difference (N_1) values upstream and downstream of the cylinder ($y/R = 0$) at $De = 0.225$ and 2.90, for the 2.5 % PIB solution with measurement data of Baaijens (1994b) for the first normal stress difference (N_1) values at $y/R = 0$ and $De = 0.248$ and 2.315, for the 5 % PIB solution.

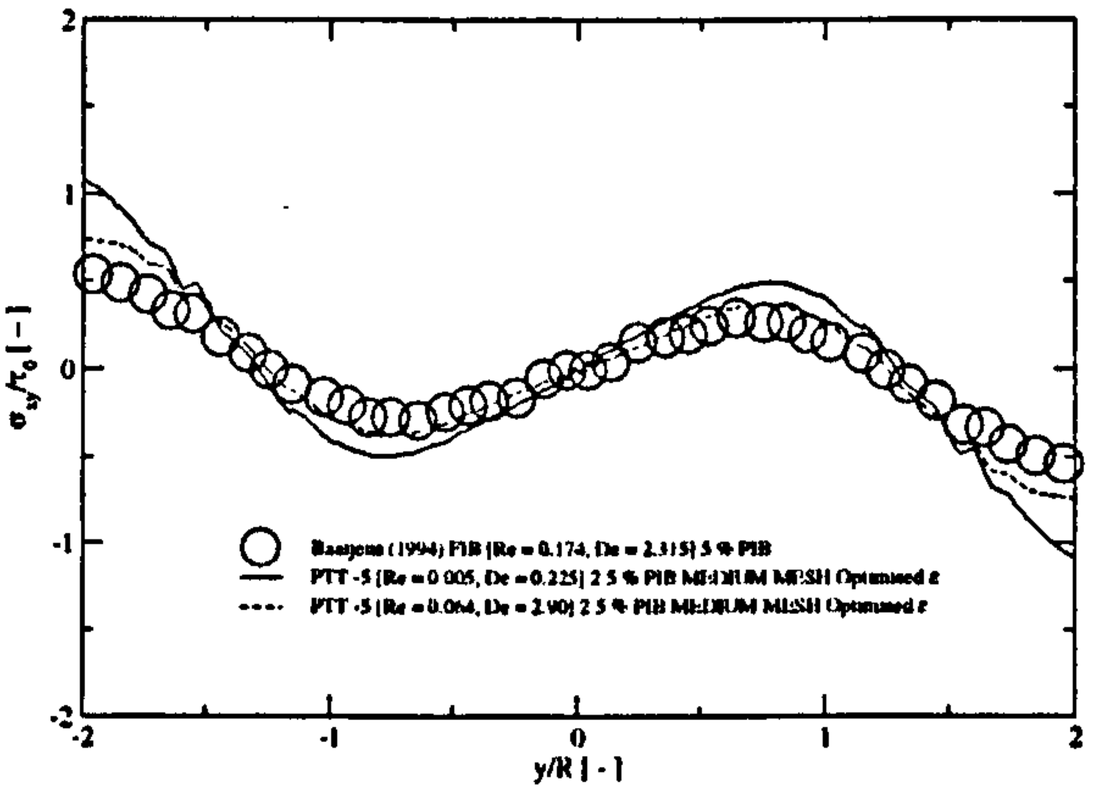

Figure 4.34: Comparison of predictions for the shear stress (σ_{xy}) values downstream of the cylinder ($x/R = 1.5$) at $De = 0.225$ and 2.90, for the 2.5 % PIB solution with measurement data of Baaijens (1994b) for the shear stress (σ_{xy}) values at $x/R = 1.5$ and $De = 2.315$, for the 5 % PIB solution.

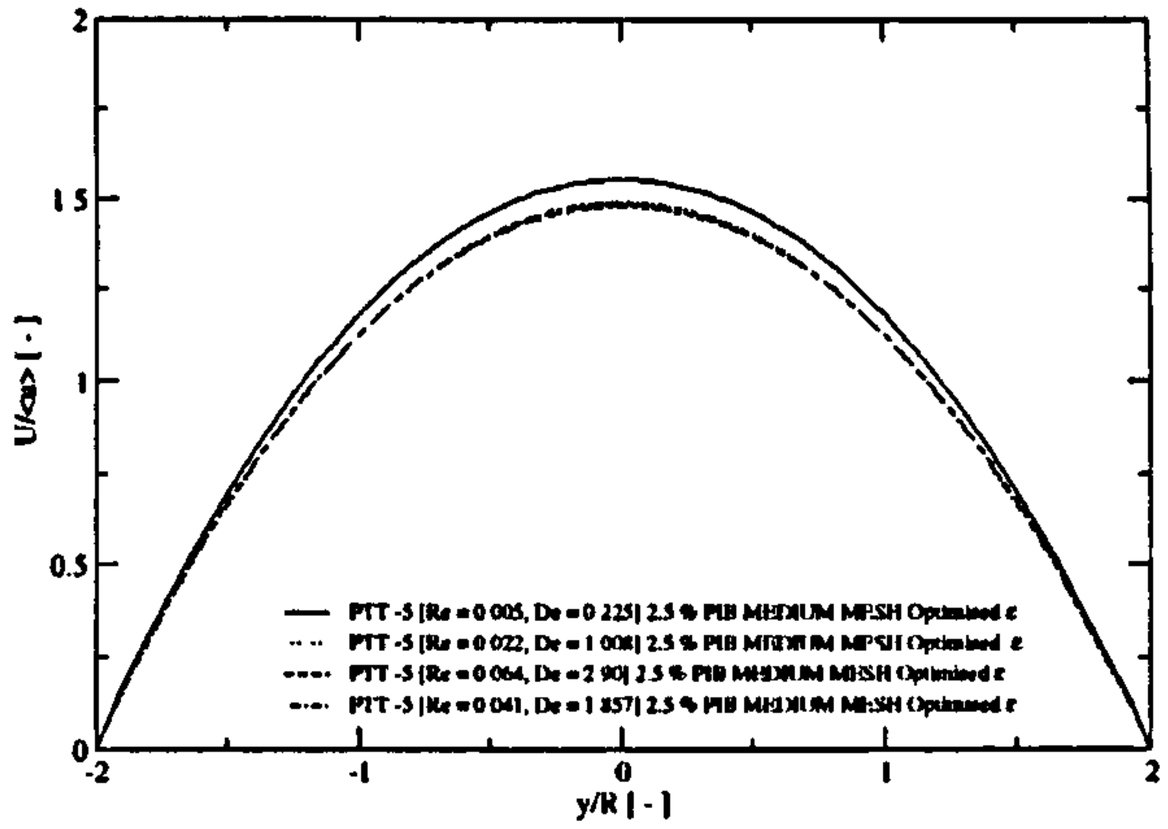

Figure 4.35: Comparison of predictions for the axial velocity (U) values in the fully developed region ($x/R = -5$) at $De = 0.225$, 1.008, 1.857 and 2.90, for the 2.5 % PIB solution.

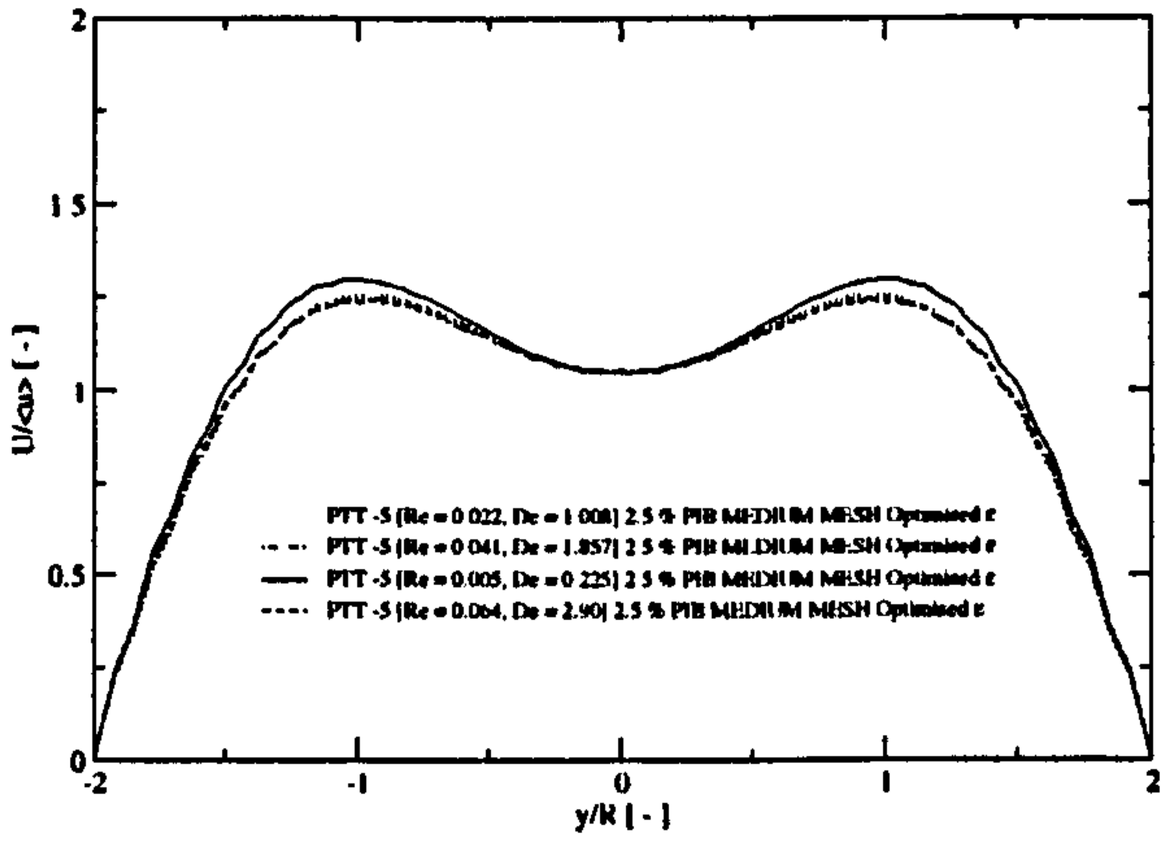

Figure 4.36: Comparison of predictions for the axial velocity (U) values upstream of the cylinder ($x/R = -2$) at $De = 0.225$, 1.008, 1.857 and 2.90, for the 2.5 % PIB solution.

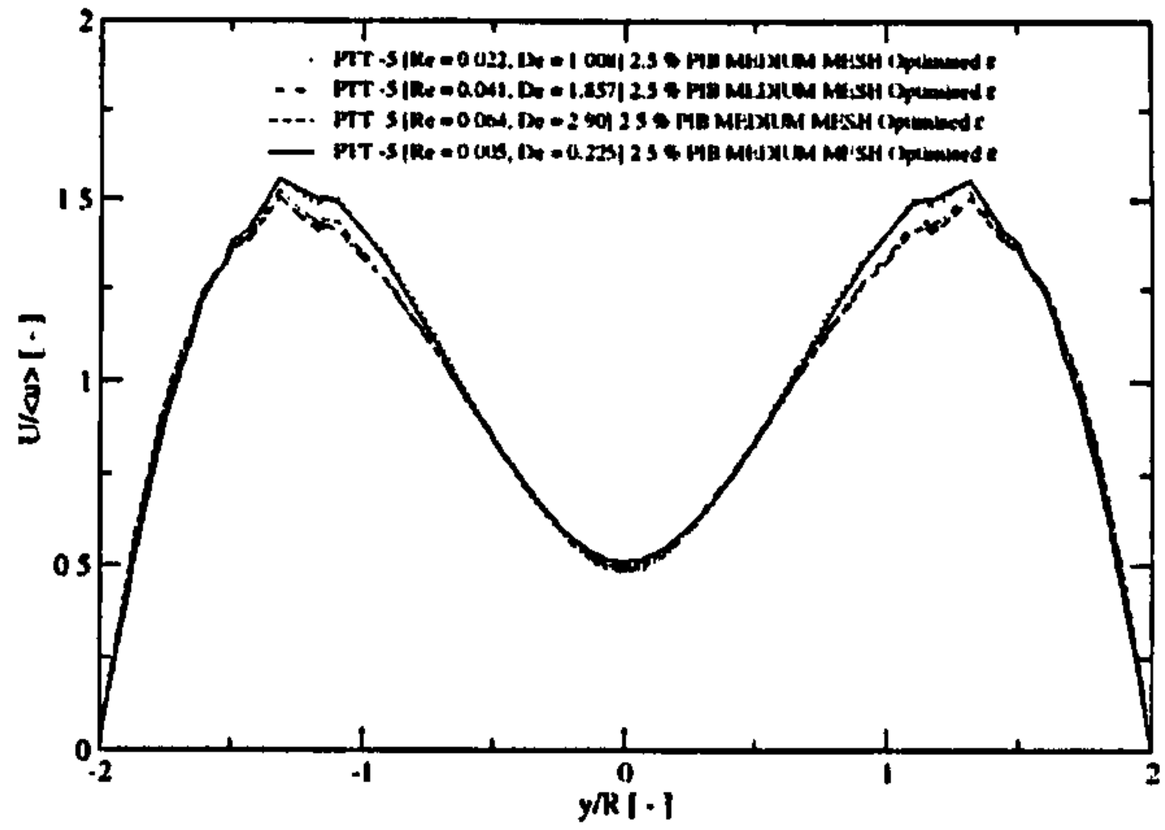

Figure 4.37: Comparison of predictions for the axial velocity (U) values downstream of the cylinder ($x/R = 1.5$) at $De = 0.225$, 1.008, 1.857 and 2.90, for the 2.5 % PIB solution.

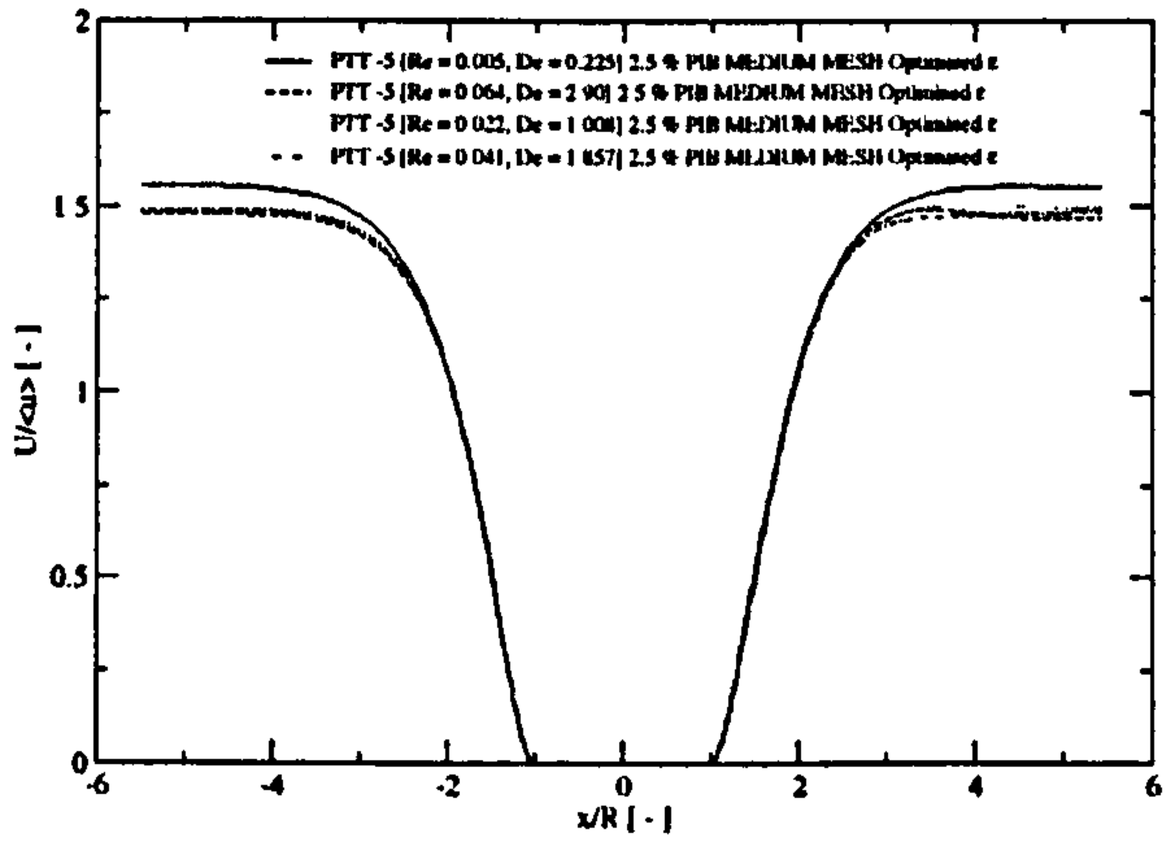

Figure 4.38: Comparison of predictions for the axial velocity (U) values upstream and downstream of the cylinder ($y/R = 0$) at $De = 0.225$, 1.008, 1.857 and 2.90, for the 2.5 % PIB solution.

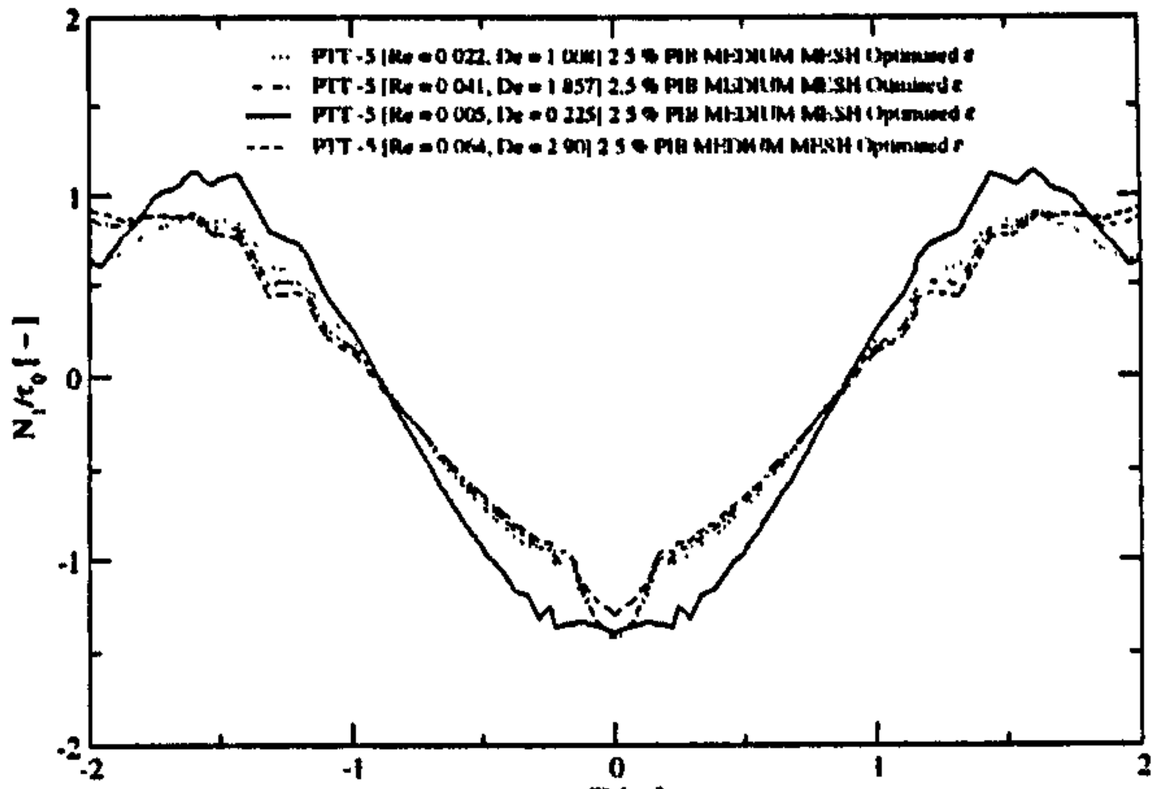

Figure 4.39: Comparison of predictions for the first normal stress difference (N_1) values upstream of the cylinder ($x/R = -1.5$) at $De = 0.225$, 1.008, 1.857 and 2.90, for the 2.5 % PIB solution.

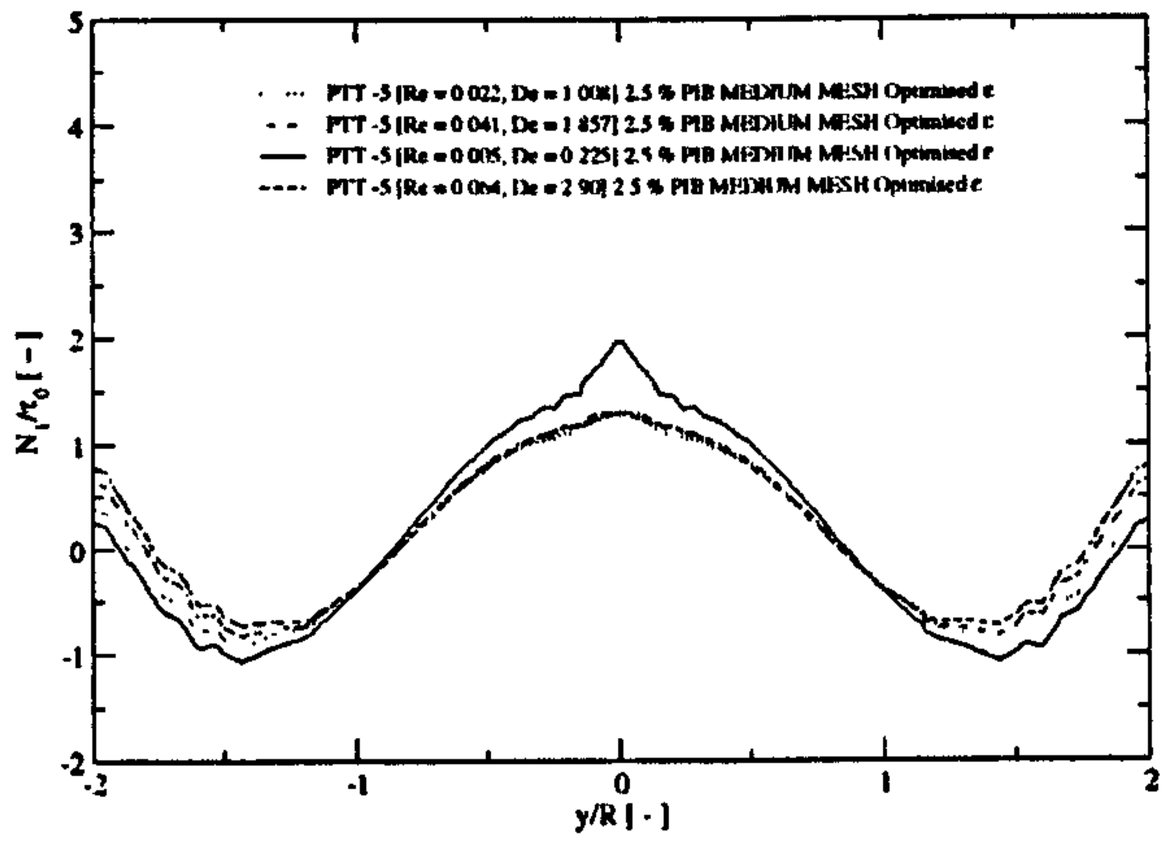

Figure 4.40: Comparison of predictions for the first normal stress difference (N_1) values downstream of the cylinder ($x/R = 1.5$) at $De = 0.225$, 1.008, 1.857 and 2.90, for the 2.5 % PIB solution.

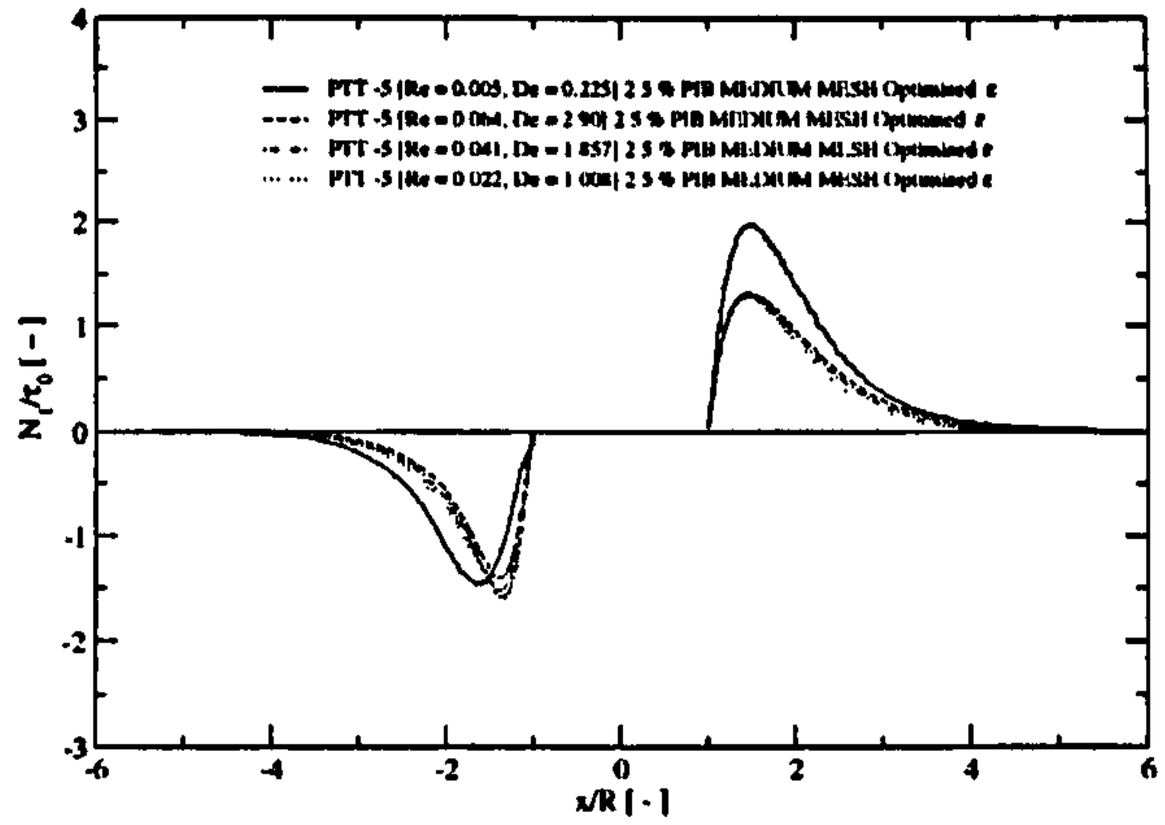

Figure 4.41: Comparison of predictions for the first normal stress difference (N_1) values upstream and downstream of the cylinder ($y/R = 0$) at $De = 0.225$, 1.008, 1.857 and 2.90, for the 2.5 % PIB solution.

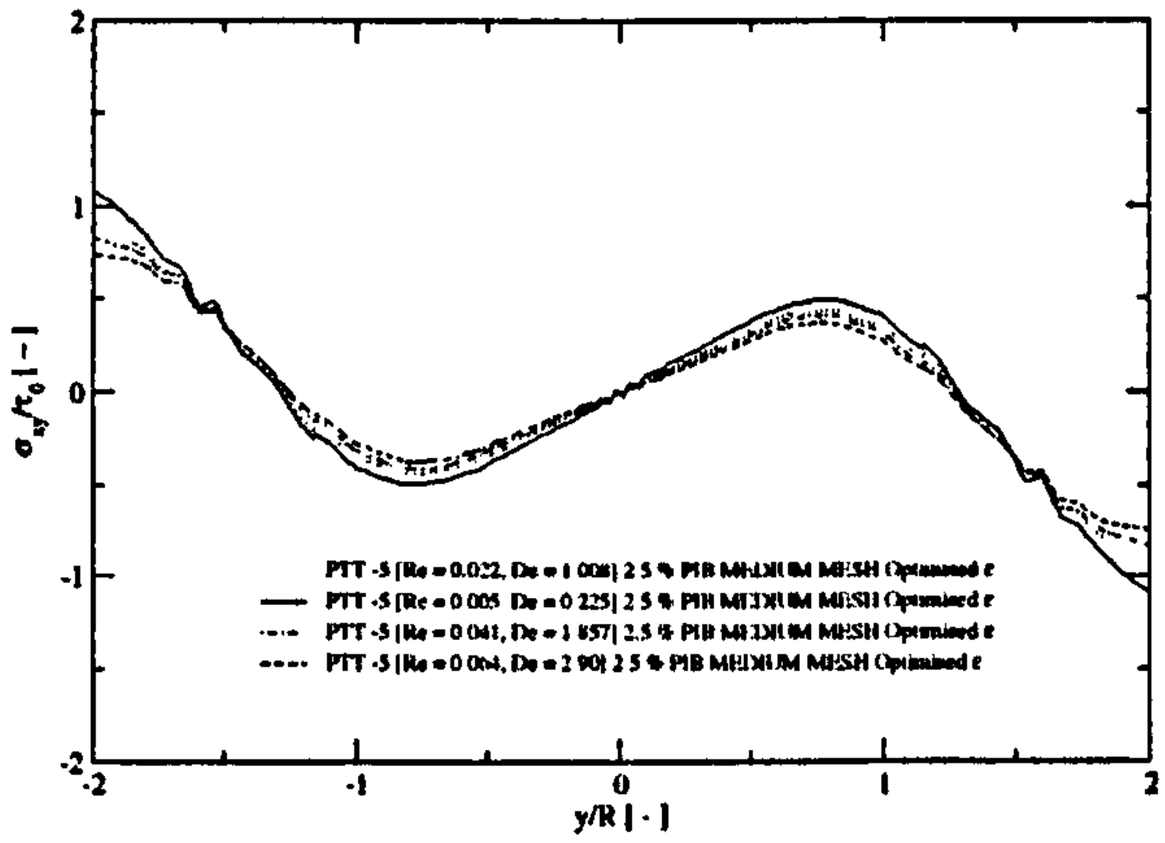

Figure 4.42: Comparison of predictions for the shear stress (σ_{xy}) values downstream of the cylinder ($x/R = 1.5$) at $De = 0.225$, 1.008, 1.857 and 2.90, for the 2.5 % PIB solution.

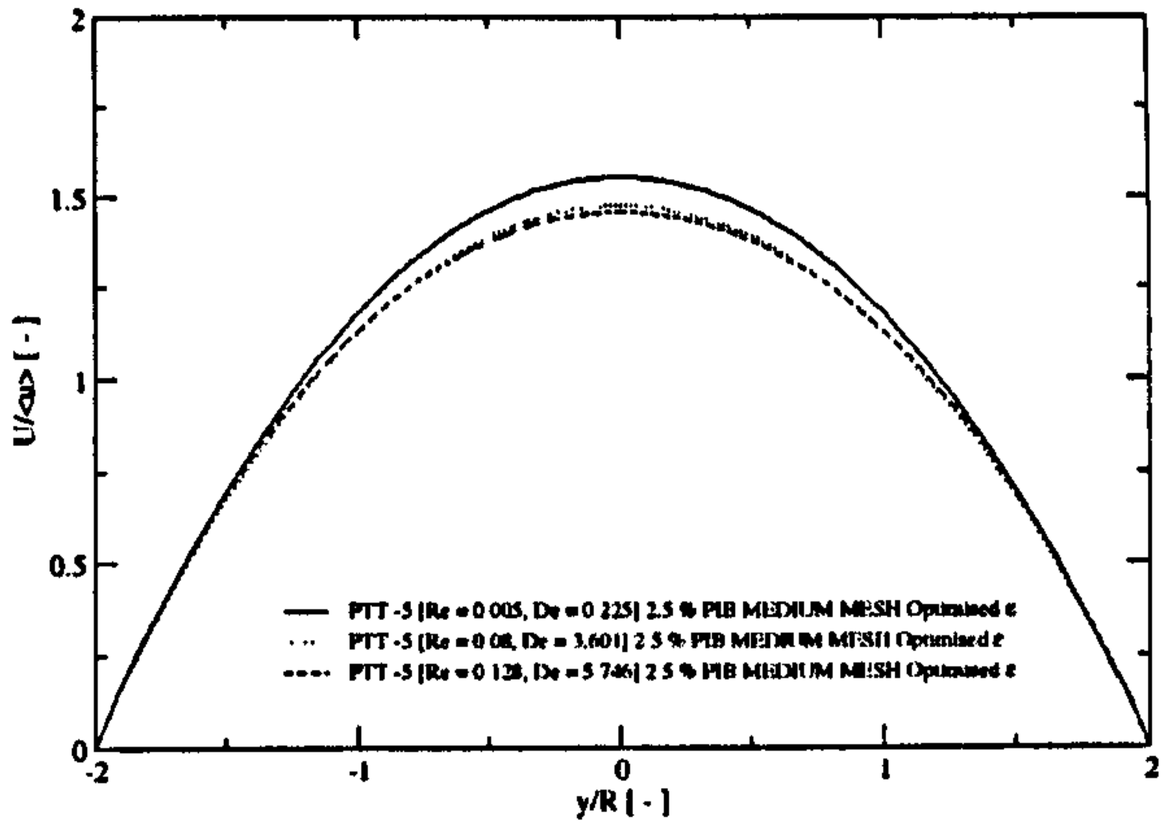

Figure 4.43: Comparison of predictions for the axial velocity (U) values in the fully developed region ($x/R = -5$) at $De = 0.225$, 3.601, and 5.746, for the 2.5 % PIB solution.

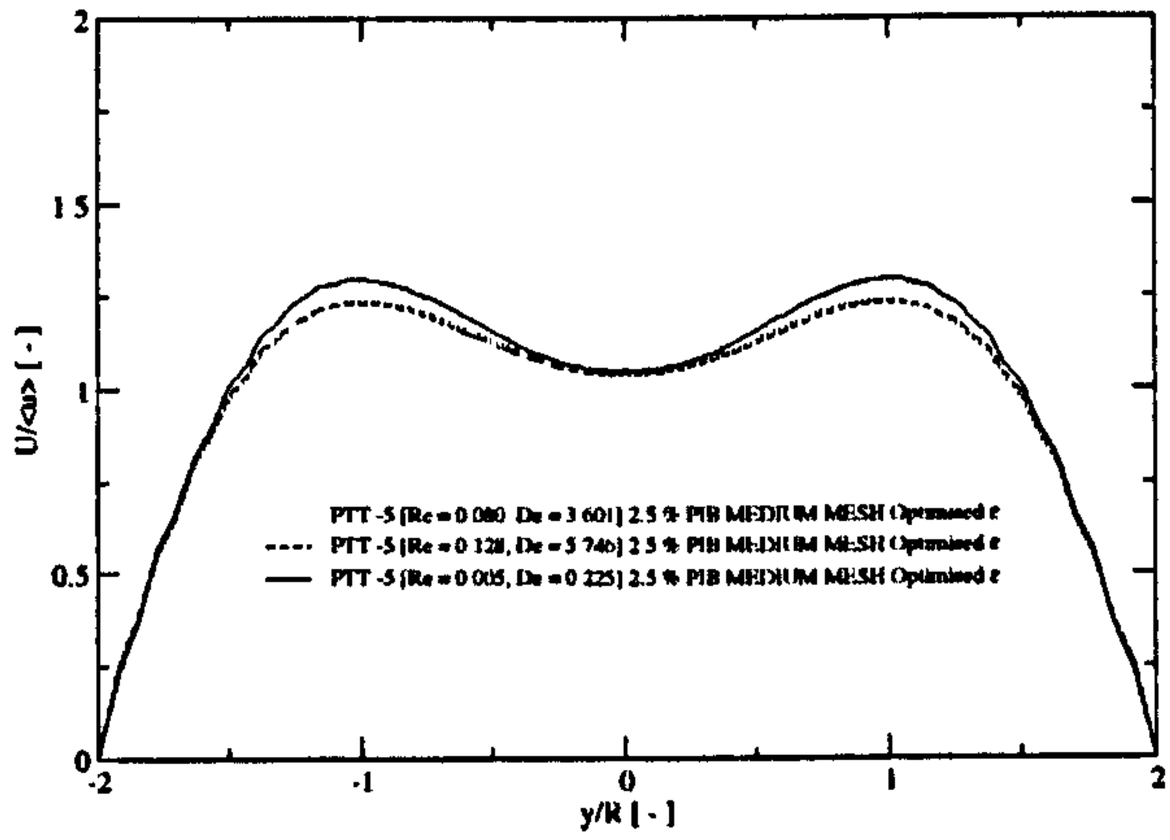

Figure 4.44: Comparison of predictions for the axial velocity (U) values upstream of the cylinder ($x/R = -2$) at $De = 0.225$, 3.601 and 5.746, for the 2.5 % PIB solution.

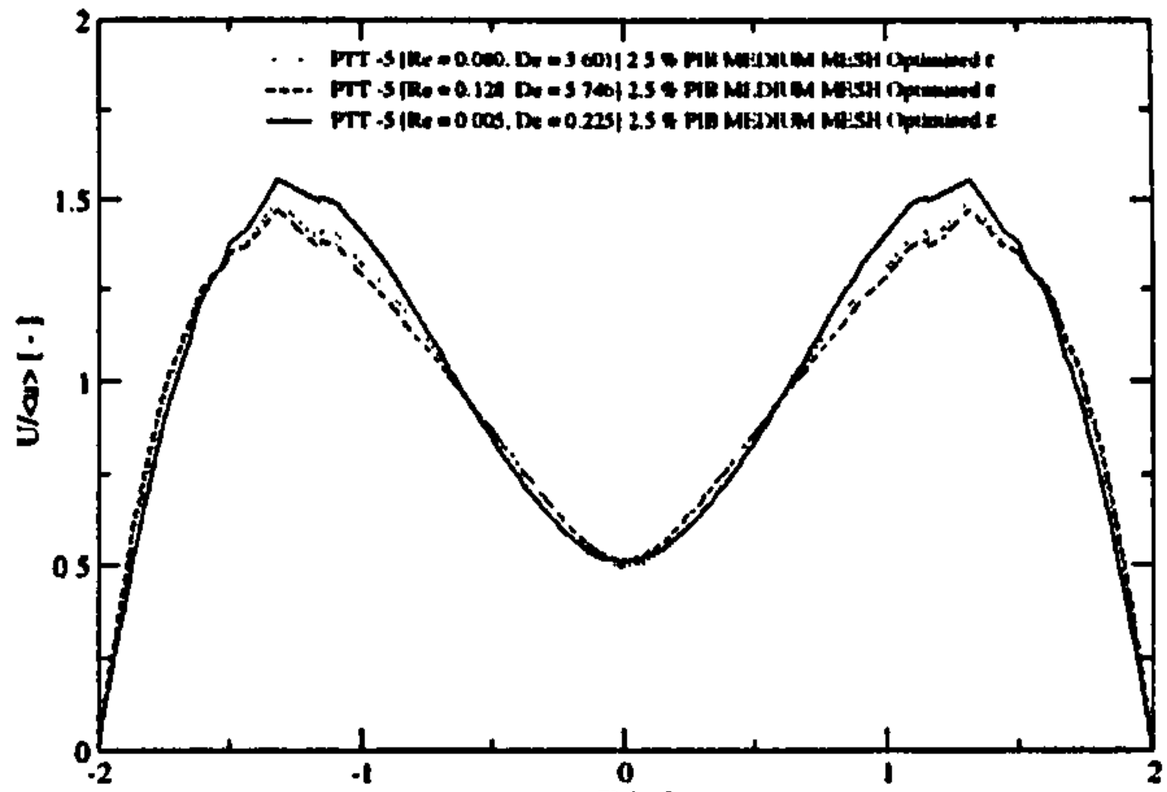

Figure 4.45: Comparison of predictions for the axial velocity (U) values downstream of the cylinder ($x/R = 1.5$) at $De = 0.225$, 3.601 and 5.746, for the 2.5 % PIB solution.

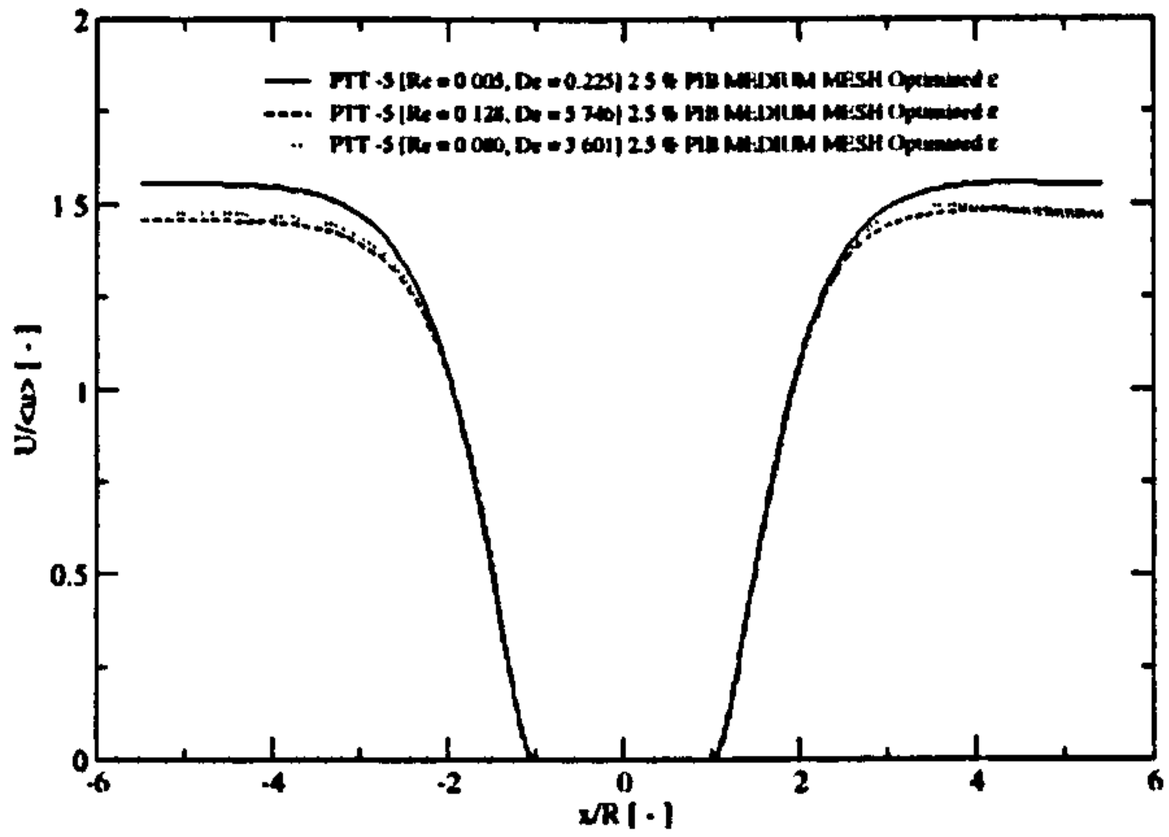

Figure 4.46: Comparison of predictions for the axial velocity (U) values upstream and downstream of the cylinder ($y/R = 0$) at $De = 0.225$, 3.601 and 5.746, for the 2.5 % PIB solution.

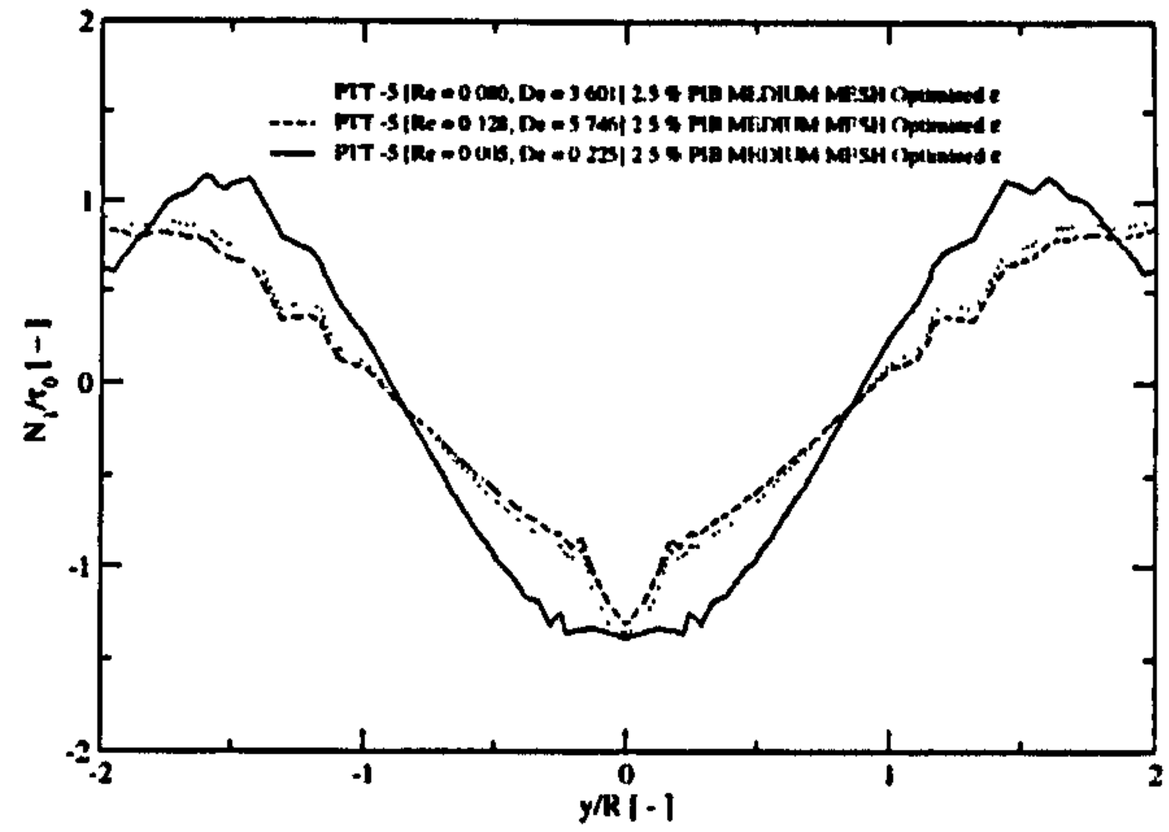

Figure 4.47: Comparison of predictions for the first normal stress difference (N_1) values upstream of the cylinder ($x/R = -1.5$) at $De = 0.225$, 3.601 and 5.746, for the 2.5 % PIB solution.

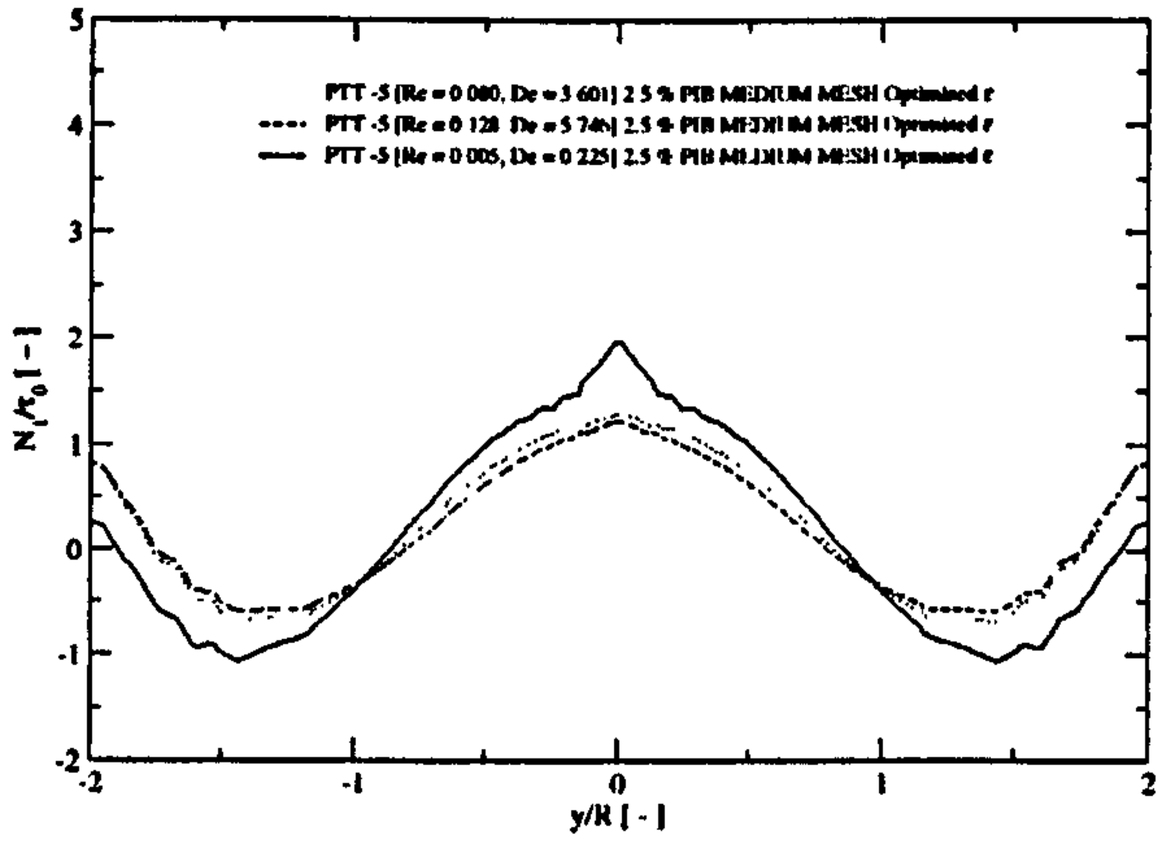

Figure 4.48: Comparison of predictions for the first normal stress difference (N_1) values downstream of the cylinder ($x/R = 1.5$) at $De = 0.225$, 3.601 and 5.746, for the 2.5 % PIB solution.

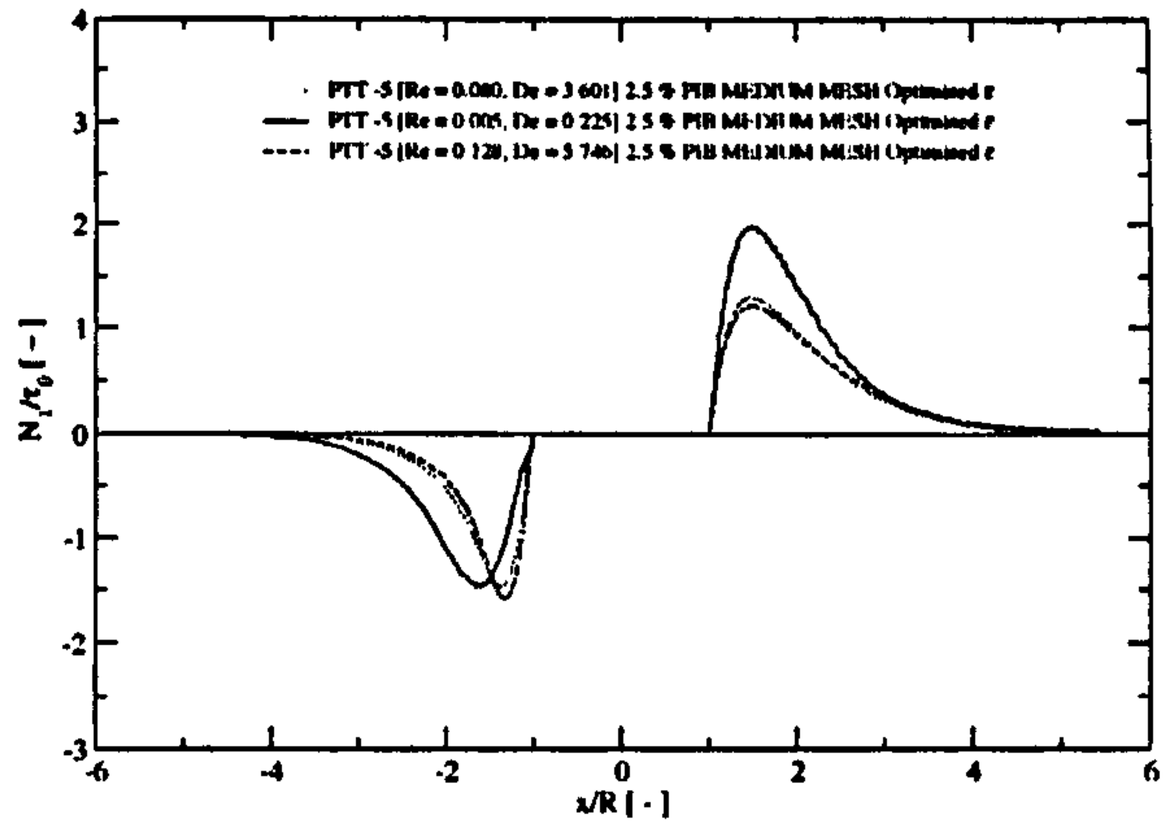

Figure 4.49: Comparison of predictions for the first normal stress difference (N_1) values upstream and downstream of the cylinder ($y/R = 0$) at $De = 0.225$, 3.601 and 5.746, for the 2.5 % PIB solution.

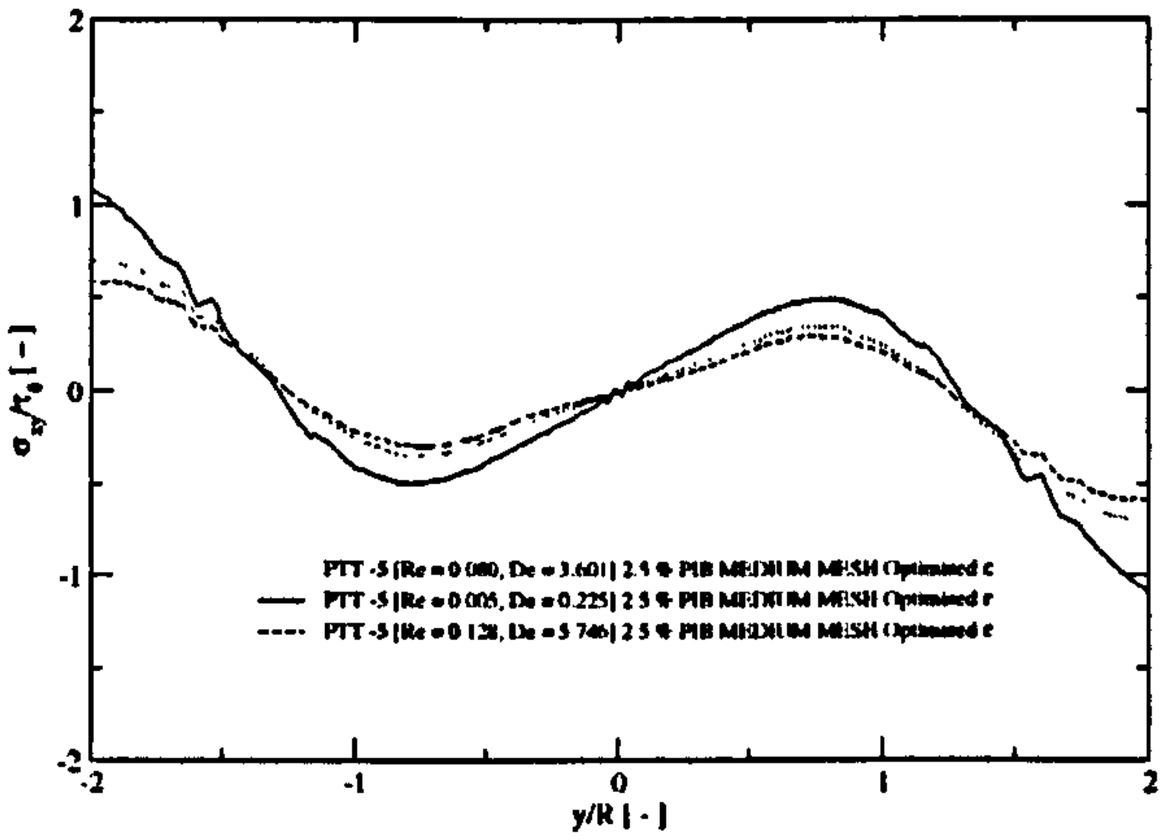

Figure 4.50: Comparison of predictions for the shear stress (σ_{xy}) values downstream of the cylinder ($x/R = 1.5$) at $De = 0.225$, 3.601 and 5.746, for the 2.5 % PIB solution.

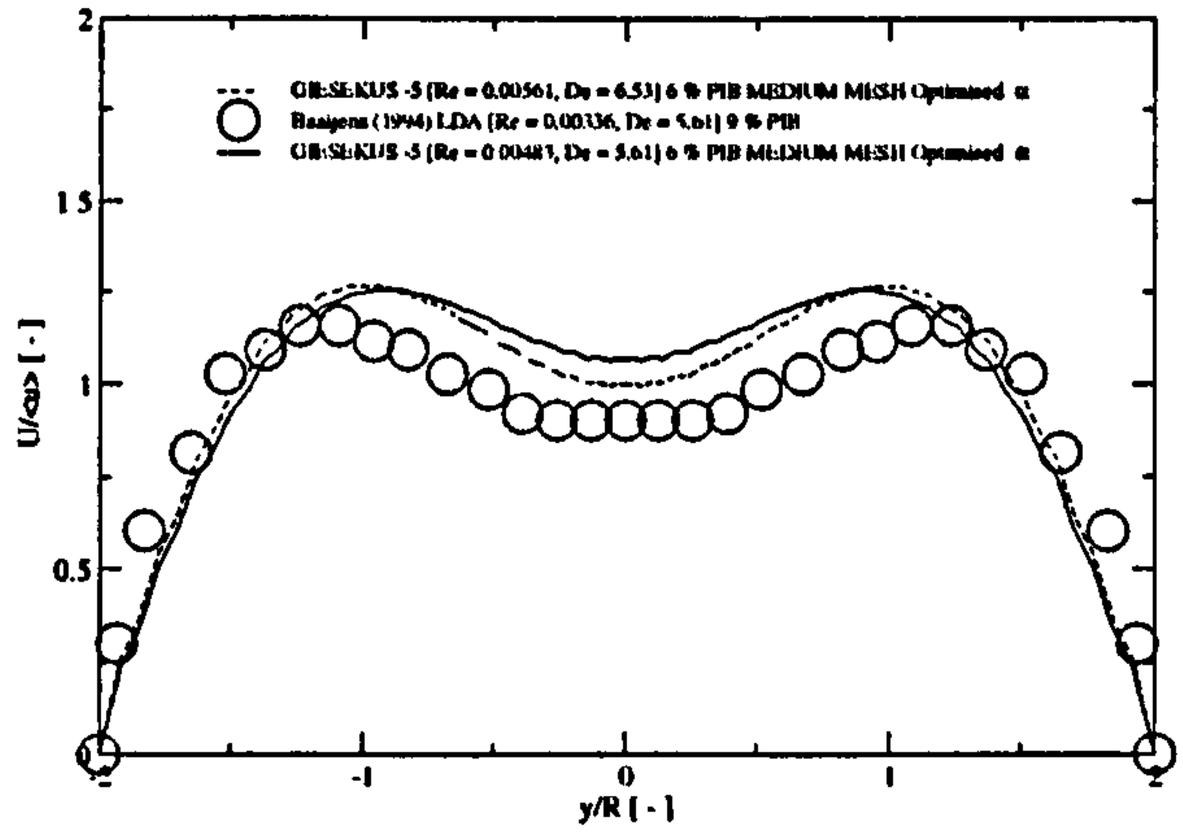

Figure 4.51: Comparison of predictions for the axial velocity (U) values upstream of the cylinder ($x/R = -2$) at $De = 5.61$ and 6.53, for the 6 % PIB solution with measurement data of Baaijens (1994b) for the axial velocity (U) values at $x/R = -2$ and $De = 5.61$, for the 9 % PIB solution.

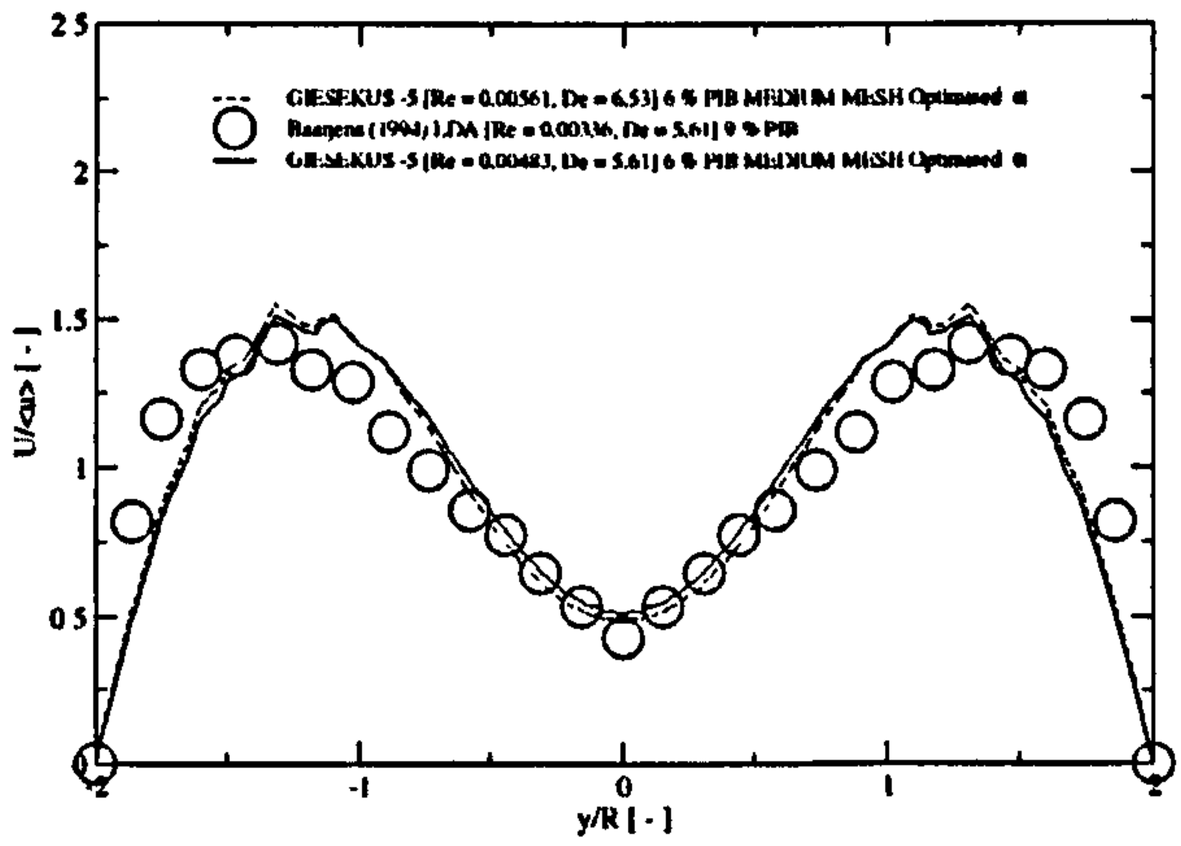

Figure 4.52: Comparison of predictions for the axial velocity (U) values downstream of the cylinder ($x/R = 1.5$) at $De = 5.61$ and 6.53, for the 6 % PIB solution with measurement data of Baaijens (1994b) for the axial velocity (U) values at $x/R = 1.5$ and $De = 5.61$, for the 9 % PIB solution.

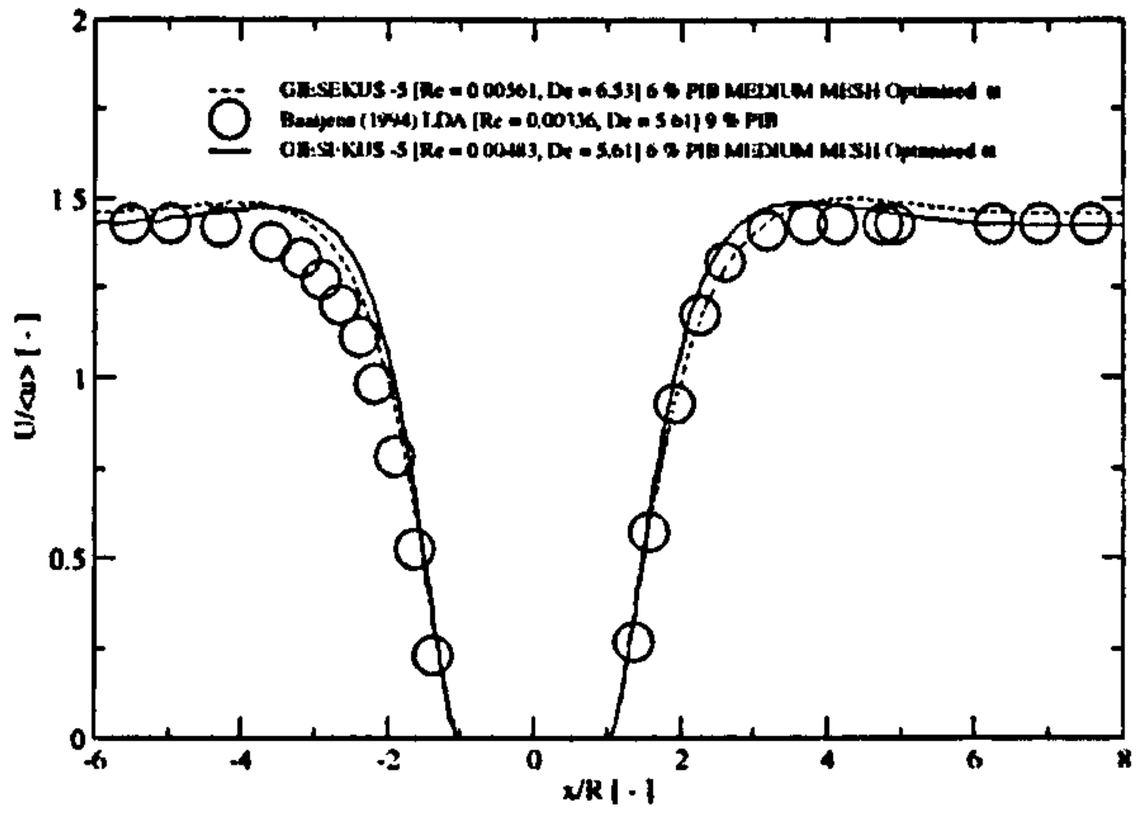

Figure 4.53: Comparison of predictions for the axial velocity (U) values upstream and downstream of the cylinder ($y/R = 0$) at $De = 5.61$ and 6.53, for the 6 % PIB solution with measurement data of Baaijens (1994b) for the axial velocity (U) values at $y/R = 0$ and $De = 5.61$, for the 9 % PIB solution.

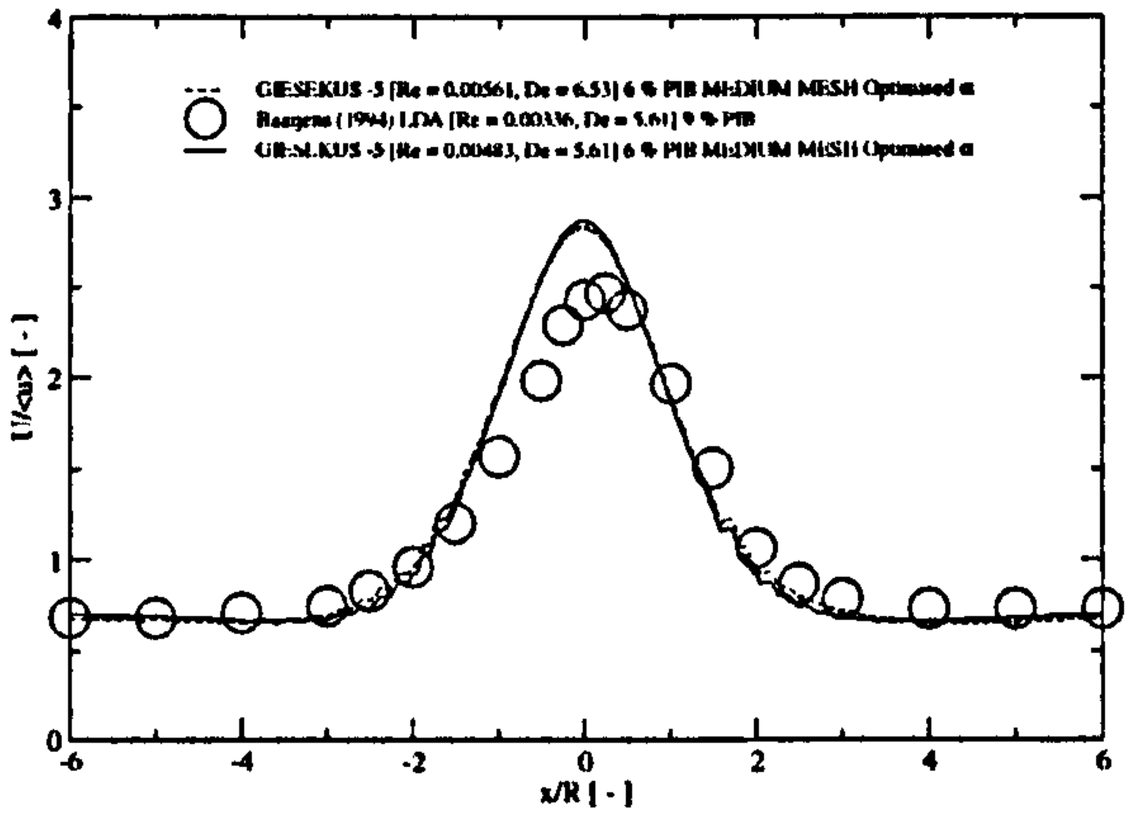

Figure 4.54: Comparison of predictions for the axial velocity (U) values upstream and downstream of the cylinder ($y/R = 1.5$) at $De = 5.61$ and 6.53, for the 6 % PIB solution with measurement data of Baaijens (1994b) for the axial velocity (U) values at $y/R = 1.5$ and $De = 5.61$, for the 9 % PIB solution.

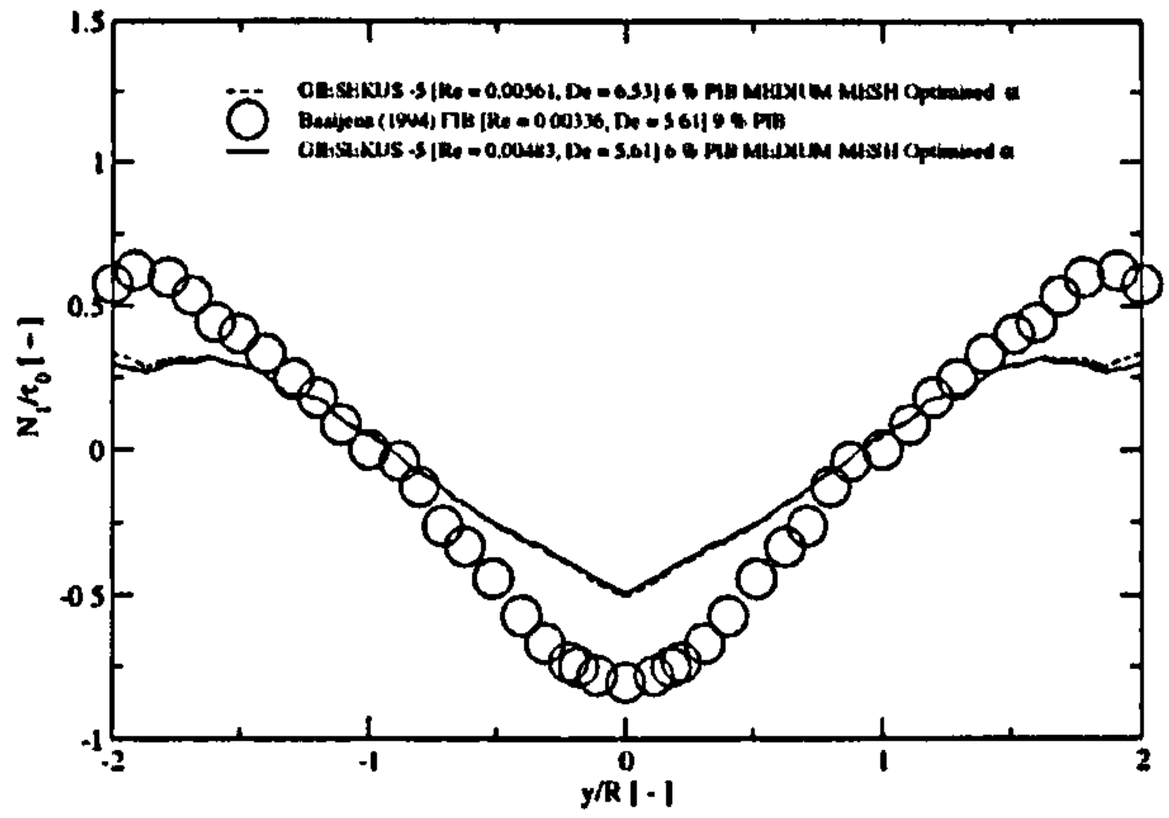

Figure 4.55: Comparison of predictions for the first normal stress difference (N_1) values upstream of the cylinder ($x/R = -1.5$) at $De = 5.61$ and 6.53, for the 6 % PIB solution with measurement data of Baaijens (1994b) for the first normal stress difference (N_1) values at $x/R = -1.5$ and $De = 5.61$, for the 9 % PIB solution.

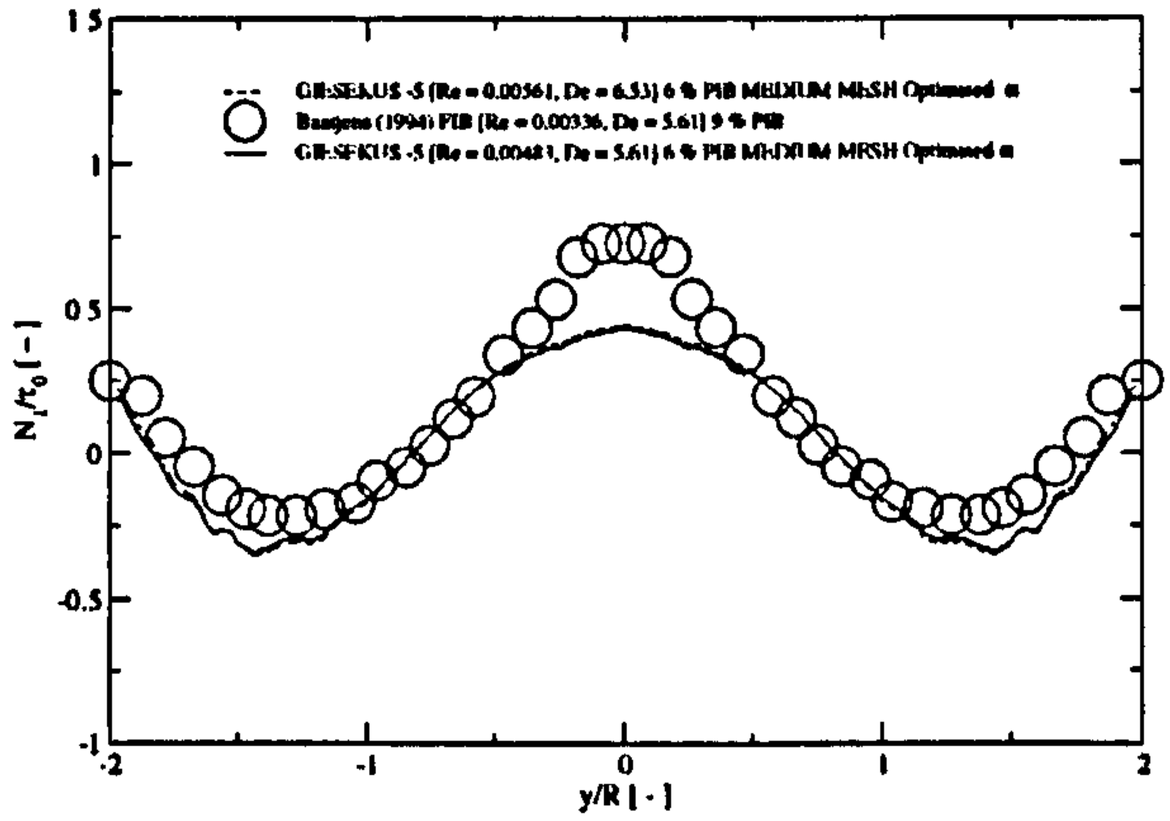

Figure 4.56: Comparison of predictions for the first normal stress difference (N_1) values downstream of the cylinder ($x/R = 1.5$) at $De = 5.61$ and 6.53, for the 6 % PIB solution with measurement data of Baaijens (1994b) for the first normal stress difference (N_1) values at $x/R = 1.5$ and $De = 5.61$, for the 9 % PIB solution.

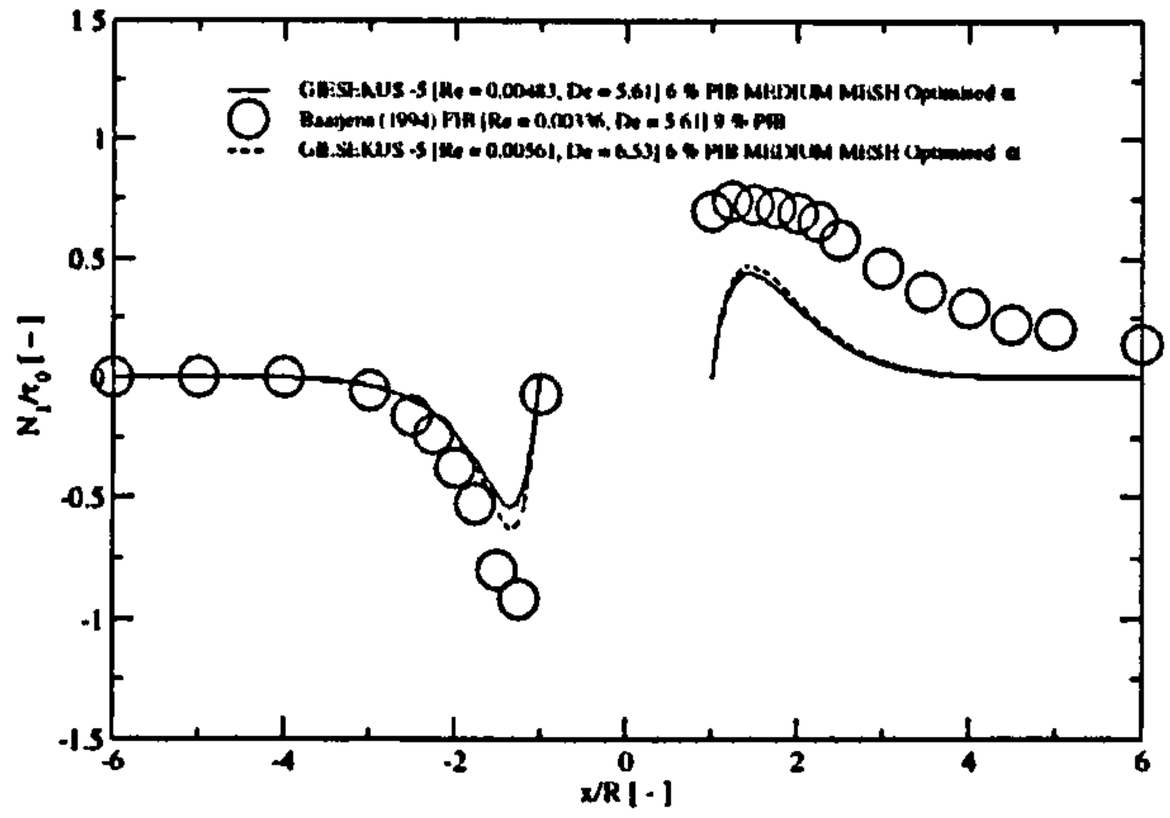

Figure 4.57: Comparison of predictions for the first normal stress difference (N_1) values upstream and downstream of the cylinder ($y/R = 0$) at $De = 5.61$ and 6.53, for the 6 % PIB solution with measurement data of Baaijens (1994b) for the first normal stress difference (N_1) values at $y/R = 0$ and $De = 5.61$, for the 9 % PIB solution.

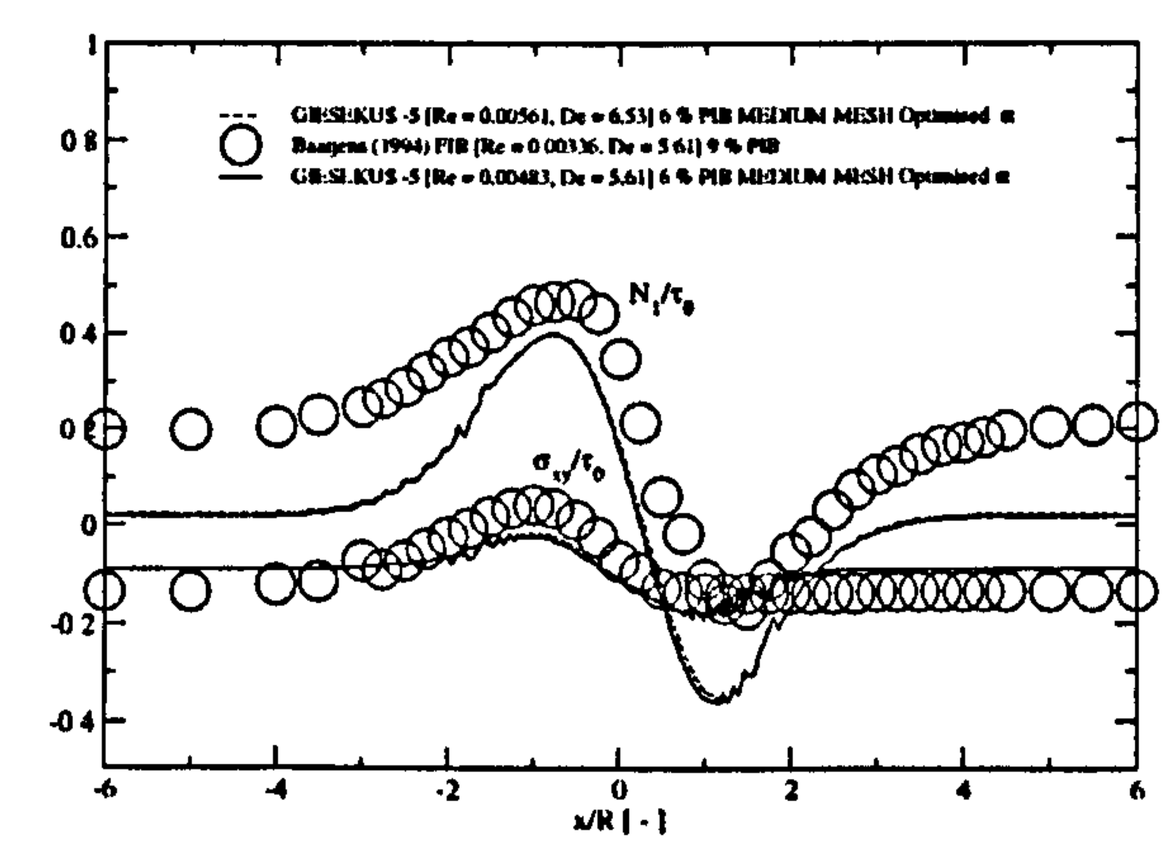

Figure 4.58: Comparison of predictions for the first normal stress difference (N_1) values and shear stress (σ_{xy}) values upstream and downstream of the cylinder ($y/R = 1.5$) at $De = 5.61$ and 6.53, for the 6 % PIB solution with measurement data of Baaijens (1994b) for the first normal stress difference (N_1) values and shear stress (σ_{xy}) values at $y/R = 1.5$ and $De = 5.61$, for the 9 % PIB solution.

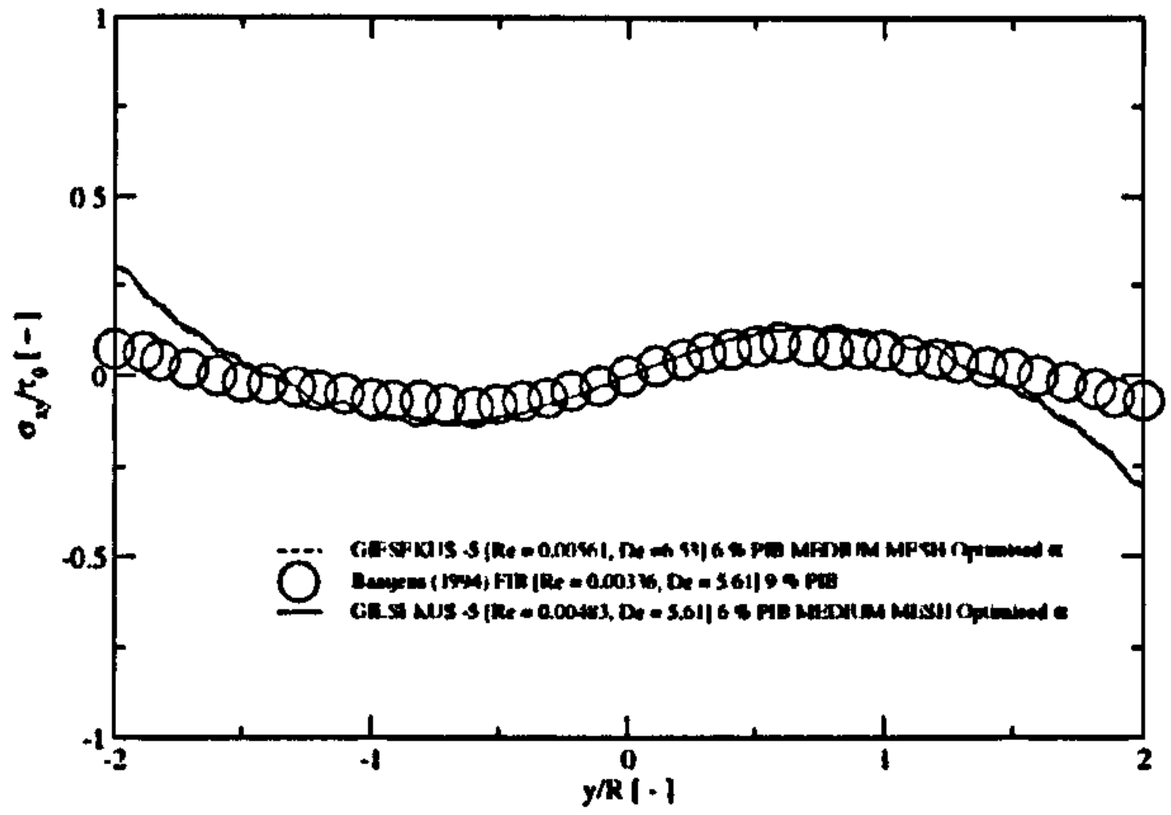

Figure 4.59: Comparison of predictions for the shear stress (σ_{xy}) values downstream of the cylinder ($x/R = -1.5$) at $De = 5.61$ and 6.53, for the 6 % PIB solution with measurement data of Baaijens (1994b) for the shear stress (σ_{xy}) values at $x/R = -1.5$ and $De = 5.61$, for the 9 % PIB solution.

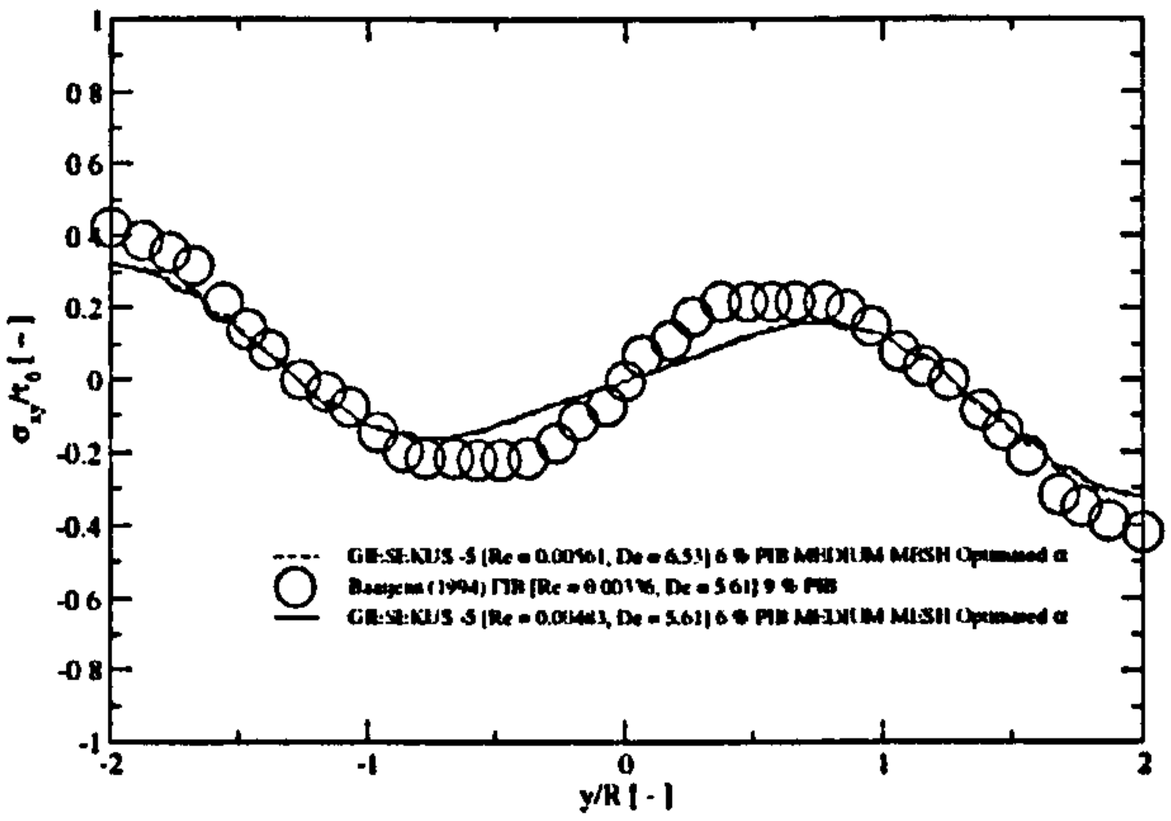

Figure 4.60: Comparison of predictions for the shear stress (σ_{xy}) values upstream of the cylinder ($x/R = 1.5$) at $De = 5.61$ and 6.53, for the 6 % PIB solution with measurement data of Baaijens (1994b) for the shear stress (σ_{xy}) values at $x/R = 1.5$ and $De = 5.61$, for the 9 % PIB solution.

Chapter 5

Flows over idealised blade and baffle geometries

5.1 Introduction

The aims of the work presented in this chapter are to model as accurately and as realistically as possible the characteristic deformation of the 2.5 % and 6 % PIB solutions, using non-linear, viscoelastic constitutive equations, in three different geometries, that have been selected to aid understanding of the laminar flow behaviour of these fluids in mixing vessels. The flow geometries selected are; (i) a planar array of symmetrically confined cylinders; (ii) a 4:1 sudden planar contraction and; (iii) a planar flow past a baffle. All geometries are introduced and described in the following text, together with the rationale for their selection.

A direct simulation of non-linear viscoelastic fluids in a stirred vessel is at present impossible due to the excessive computational demands of the problem, as was mentioned in Chapter 1. The geometry of a stirred vessel with rotating impeller blades far exceeds the complexity of the geometries that can be reasonably modelled at present and therefore, in order to facilitate understanding of laminar viscoelastic fluid flow past components (so-called 'internals') of a stirred vessel, the problem has been decomposed into more manageable parts: for example, the blades of the impeller and/or baffle are modelled individually with two different mesh geometries, of height, H_1 and H_2. The former, slightly larger, may be considered to represent a blade, relative to the wall of the vessel, while the latter, to represent the fluid flow through a smaller gap, which occurs in stirred vessel mixing when the blade is coincident with a baffle positioned on the wall of the vessel. There are however other effects that should be considered, before this study can be carried out, and these are: (1) The effect of a recurring obstruction

to the flow i.e. to emulate the passage of subsequent blades of a rotating impeller, or that of subsequent 'finger' baffles encountered in some viscous mixing geometries. (2) The effect of an obstruction such as a blade or baffle on the approaching flow. The first of these two effects is addressed in section 5.3 which analyses the flow past a planar, periodic array of symmetrically confined cylinders. The second is addressed in section 5.4, in which an axisymmetric, planar, 4:1 sudden contraction flow is analysed. Schematic representations of these geometries, are given in figures 5.1, 5.13 and 5.18.

It is not only useful to study these geometries to gain an insight into the viscoelastic effects but also because other authors have published predictions and in the case of the contraction flow, measurement data, where comparisons with the present predictions can be made.

For the array of cylinders, the reader is referred to Liu et al. (1998) who investigated the creeping flow behaviour of a Newtonian and an arbitrary viscoelastic polymer solution through simulations. For the latter, constitutive models such as the Giesekus one were employed. This work reported a critical inter-cylinder spacing for the viscoelastic fluid, at which flow separation is observed, different in size to that observed for the Newtonian fluid. Additionally, Verhelst and Nieuwstadt (2004) reported velocity measurements by a LDA study of a Newtonian glucose syrup and a Boger fluid in creeping flow; they reported that the velocity values for the viscoelastic fluid, at a critical inter-cylinder spacing, showed differences by comparison of the downstream and upstream values at each cylinder. This was explained by the presence of successive cylinders disturbing the wake produced by the cylinder upstream. This disturbance disappeared by increasing the inter-cylinder spacing above a critical value. By the studies of both these authors, it can be assumed that the 2.5 and 6 % PIB solutions, at a critical inter-cylinder spacing, may show different flow patterns downstream of each cylinder, but not if this distance is large enough. This is discussed later in this chapter.

For the contraction flow geometry, the reader is referred to Quinzani et al. (1995) who studied a 5 % PIB solution, similar to the 2.5 % PIB solution of this treatise, in an identical geometry. Quinzani et al. (1995) obtained measurement data for velocity and stress by LDA and FIB techniques, respectively, to

investigate the change in elongational viscosity along the centerplane. This data is used for validating the predictions obtained in this chapter. In conjunction, Quinzani et al. (1995) also assessed the capabilities of a number of constitutive non-Newtonian models, where their material parameters had been fitted under rheometric shear experiments. The PTT model emerges as the most accurate, which gives more confidence to the predictions obtained for the 2.5 % PIB solution of this thesis. Additionally, Sasmal (1995) , Mompean and Deville (1997) and Oliveira and Pinho (1999) obtained predictions using constitutive models such as the Oldroyd B, UCM and PTT, for planar contraction flows, to investigate the salient corner vortex in the main channel: As the *De* increases, this vortex grows in size and intensity and an additional lip vortex forms at the re-entrant corner, which both merge into one at higher *De*. A region of circulation can possibly be expected, for flows past an impeller blade, as the geometric configuration for this is similar: The flow is obstructed by the vertical wall and momentarily contracted before relaxing further downstream.

For the planar, blade/baffle geometries, to the best knowledge of the author, predictions or measurements have not been obtained for such flows. This chapter proceeds to this endeavour, by showing predictions for both PIB solutions flowing past the two blade/baffle geometries.

In the same manner as Chapter 4, the 5-mode Phan-Thien Tanner (PTT - a) and Giesekus constitutive models have been used to describe the viscoelastic behaviour of the 2.5 % and 6 % PIB solutions, respectively, in all the geometries. From herein the PTT -a model will be referred to as the PTT model. In this chapter, the only predictions validated are those of the 2.5 % PIB solution in the contraction flow geometry, where only in this instance are LDA and FIB measurement data of Quinzani et al. (1995) available for a similar 5 % PIB solution.

5.2 Numerical method

The numerical methodology employed to solve for the velocity and pressure fields in the geometries mentioned above is identical to that of the single cylinder flows

of Chapter 4, and is fully described in section 4.2.2. Furthermore, section 4.2.3 of Chapter 4 describes the flow and boundary conditions for the single cylinder case, which are similar to those used in this chapter, but not identical. Therefore, only the differences are described comprehensively in the following text.

Schematic representations of the array of cylinders, contraction and blade/baffle geometries are shown in figures 5.1, 5.13 and 5.18, respectively. Each figure shows the exact dimensions of the flow domain considered. The direction of the flow is labelled in the top left corner of each figure. Each geometry is spatially discretised in finite volumes to form the mesh, the density of which, is decided as follows: (1) For the array of cylinders (see figure 5.2), an identical mesh to that of the single cylinder geometry of Chapter 4 is used, where an identical number of control volumes are placed in the vicinity of the cylinders and at the extremities of the flow domain. The successfully validated predictions of the previous chapter not only gives confidence to the simulations for this geometry but provides the range of De, within which successful predictions have already been obtained. (2) For the contraction flows (see figures 5.14 and 5.15), the choice of mesh density is influenced by the findings of three authors, Sasmal (1995), Mompean and Deville (1997) and Oliveira and Pinho (1999), by which successful predictions for other viscoelastic fluids are obtained, and measurement data is also available by Quinzani et al. (1995), for a similar fluid, where the mesh density is designed to minimise the difference between the predictions and the measurement data. (3) Finally, for the blade/baffle flows (see figures 5.19, 5.20 and 5.21), the mesh is similar to that of the contraction flow, where the geometry is rectilinear with the absence of any curved surfaces such as those present in cylinder flows. The mesh is refined in areas where sharp corners are present, namely at the blade/baffle tip, and where circulation zones are expected i.e. downstream of the blade.

In order to complete the description of the problem, the domain and boundary conditions have to be prescribed for each geometry: The fluid is driven past the array of cylinders, through the contraction and past the blade/baffle obstruction, from a zero flow rate condition at time = 0, by a source term added to the momentum equation (see section 4.2.3 for a full description). Two physical boundary conditions are prescribed to the flow domains: (1) A non-slip impermeable wall,

where the velocity is a fixed value and equal to that of the wall itself (i.e. zero velocity) and the pressure gradient is specified to be zero, since the flux through the wall is zero. (2) A plane of symmetry about which the fluid properties are symmetrically distributed and consequently computational time and memory space is halved. For the array of cylinders, the former exists at $y/R = 2$ and around the cylinders, and the latter at $y/R = 0$. For the contraction flow, the former exists at $x/h = 0$ (in the region, $0 \leq y/h \leq 3$), $y/h = 3$ (in the region $-12 \leq x/h \leq 0$) and $y/h = 0$ (in the region $0 \leq x/h \leq 8$) and the latter at $y/h = -1$, where, h denotes the height of the small channel. And, for the baffle/blade flow, the former exists at $y/D = 5.12$ and $y/D = 3.81$, depending on the distances, H_1 and H_2, respectively, and the latter, at $y/D = 0$, where D denotes the height of the blade/baffle. Additionally, for the array of cylinders and the impeller blade geometries, cyclic conditions are specified at the entrance and exit boundaries, located on the left and right side of each schematic diagram, respectively. This condition specifies that the entrance and exit boundaries are connected so that the flow profile is repeated and thus continuous. In both cases the flow has enough time to become fully developed before passing the array of cylinders or the blade. However, due to the difference in size of the entrance and exit boundaries for the contraction flow, cyclic boundaries cannot be prescribed, instead, inlet and outlet boundaries are used, respectively. In this case, the domain is designed to be long enough upstream of the contraction to allow the flow to become fully developed before reaching the beginning of the contracted channel, at $x/h = 0$, and again, downstream, to allow the flow to develop fully again.

The solution method for the viscoelastic models, for each of the complex geometries is identical to that of the single cylinder flow for which a full description is given in section 4.2.3.1. However, to summarise: All the simulations presented in this chapter reached steady state; however, at some point after this, in high flow rate cases, the simulations diverge from this solution, as already observed for the single cylinder case. This is because of the intrinsic instability of the non-linear, viscoelastic constitutive models (see Baaijens (1994b), Phan-Thien and Dou (1999) and Chapters 1 and 4 of this thesis). For all simulations; simT $\geq 1\lambda_{long}$, which is the minimum criterion required for all simulations (see chap-

ter 4), and; the size of the time step, Δt, is chosen to be not too large, to avoid hydrodynamic convergence problems, and small enough to avoid early solution divergence, due to intrinsic viscoelastic model instabilities.

For all simulations of this chapter, for both the 2.5 and 6 % PIB solutions, the; (a) steady state mean velocity, $< u >$; (b) steady state apparent shear rate, $\dot{\gamma}_a$; (c) steady state scaling stress, τ_0; (d) dimensionless numbers: De and Re; (e) time step size, Δt, and; (f) simulation time, simT, are all shown in tables 5.1 to 5.8. The mean velocity is calculated far enough upstream where the flow is fully developed and the definitions for apparent shear rate, scaling stress and dimensionless numbers are given in section 4.2.4. Each table is discussed below.

For the array of cylinders, tables 5.1 and 5.2 show simulations for the 2.5 % and 6 % PIB solutions, respectively. Each table shows simulations at $De < 1$, for approximating a Newtonian fluid, and at $De \geq 1$, where values are almost identical to those at which simulations have already been validated, in the single cylinder geometry of Chapter 4, namely at $De = 2.34$ and 5.72, respectively. For each simulation; $Re < 0.01$, which is creeping flow; simT $\geq 1\lambda_{long}$, and; Δt is a factor of 100 smaller for the higher De flows, which leads to greater simulation times at higher De.

For the contraction flows, tables 5.3 and 5.4 show simulations for the 2.5 % and 6 % PIB solutions, respectively. For the 2.5 % PIB solution, predictions were obtained at $De = 1.39$ and 4.48, where the lowest De is validated against the measurement data of Quinzani et al. (1995). For the 6 % PIB solution predictions were obtained at $De = 1.73$ and 4.27 where, due to the lack of available measurement data, neither case is validated. Additionally, the higher De flows, for both fluids, are obtained within the respective range of De studied in the previous chapter. For each simulation; simT $\geq 1\lambda_{long}$, and; $Re \leq 0.02$, which satisfies the minimum criteria, and shows creeping flow behaviour, respectively.

The simulation parameters for the blade flows are shown in tables 5.5 to 5.8 for the 2.5 and 6 % PIB solutions and are discussed in section 5.5.

5.3 Flow past an array of three symmetrically confined cylinders

5.3.1 Introduction

In this section the investigation of the flow of a 2.5 % and a 6 % PIB solution past an array of confined cylinders is described and discussed. The flow geometry has already been introduced and shown in figure 5.1. All cylinders are of equal size. The domain is symmetric along the line, $y/R = 0$ and therefore only half of the geometry is simulated. The cylinders have a radius, $R = 0.0045\ m$, the planar channel has a height, $4R$ and length, $x = 0.13\ m$, which is identical to that of the single cylinder case of Chapter 4. The position of each cylinder is such that the inter-cylinder spacing distance, $J = 0.016\ m$ (see figure 5.1) is approximately the same as the maximum arc length between adjacent impeller blades ($\sim 0.014\ m$) of the turbine impeller used experimentally (see Chapter 2 and 6).

For both fluids, the fluid flow behaviour upstream from cylinder 1, at $x/R = -5$ is fully developed and shows an undisturbed, parabolic profile with insignificant difference by comparison to that of the single cylinder flow of the previous chapter, at almost identical De, which is intuitive, as the pressure gradients are almost identical and the flow is fully developed.

This section investigates the changes in flow pattern in the vicinity of each cylinder, to study the effects that; (a) multiple cylinders have on the flow and; (b) are caused by increasing levels of viscoelasticity as De is increased. Predictions for, U, N_1 and σ_{xy} are shown, where U is the axial velocity, equal to v_x and non-dimensionalised with the mean velocity in the x direction; $< u >$. All the stresses are non-dimensionalised with τ_0.

5.3.2 2.5 % PIB solution

Predictions of, U, N_1 and σ_{xy}, over a range of De, were recorded at several cross-sections of the geometry.

Figures 5.3, 5.4 and 5.5 show predictions for U, N_1 and σ_{xy}, respectively. Each figure for; (a) $De = 0.204$ and; (b) $De = 2.34$, and both for the cross-

sections: $x/R = 1.5$, 7.05 and 12.61, each a distance of $x/R = 1.5$ downstream from the centre of cylinders 1, 2 and 3, respectively. For each figure, at both De, an insignificant difference is shown by comparison of the profiles at each cross-section, consequently showing that, in this vicinity, the flow pattern for each cylinder is identical. The fluid behaviour is described as follows: The U values, at both De, are zero at the walls of the domain and show a double peaked profile as they increase from zero to a maximum value a small distance from the wall and subsequently, approaching the centreline, they decrease. The N_1 values, at both De, are positive at the walls and become negative a small distance from them. Approaching the vicinity of the cylinder, these values pass back through zero again to their largest positive values at the centreline. However, at $De = 0.204$, these values show an apex shape at the centreline, opposed to a more rounded configuration for the higher De. This is observed in Chapter 4 for the single cylinder case at a similar De. The σ_{xy} values, at both De, are greatest in magnitude at the walls of the domain, they subsequently pass through zero a small distance from the walls, reach a peak, and then approach zero at the centreline.

An identical study was also carried out but instead, a distance $x/R = 1.5$, upstream of the cylinder, and the same result prevailed: Over the range of De studied, the flow pattern at each cross-section was identical. For this reason, the results are not shown here.

Additionally, studies were made at the following cross-sections: $x/R = -5$, and ± 2, see figure 5.1 for a schematic representation to locate these cross-sections. The profiles at the cross-sections, $x/R = -5$ and $x/R = \pm 2$ are not included in this study, because; the profiles at $x/R = -5$, where the flow is fully developed, is identical to that of a single cylinder case (see chapter 4) and; at a distance $x/R = \pm 2$ from each cylinder, although the fully developed profile is disturbed by the cylinders, it is not disturbed to the same extent as shown in regions closer to the cylinder, namely at $x/R = \pm 1.5$ (described above), which is of more interest to the reader. Furthermore, a presentation of the finding, at cross-sections a distance, $x/R = \pm 2$ from the centre of each cylinder would only reiterate what was found at the cross-sections, $x/R = \pm 1.5$, described and shown above.

The fluid flow at $x/R = \pm 1.5$ is dominated by the presence of the cylinder, which causes the fluid to flow away from the centreline in the direction of the channel wall. After the cylinder, at $x/R = 2$, the profile begins to return back to the parabolic shape but not before it is influenced by the second cylinder in, what appears to be, an identical way. This is repeated again for the third cylinder.

Due to this absence of change shown above, the cross-section $x/R = 1.5$, downstream from cylinder 1 is chosen for study in the following text, where the effect of increasing De is investigated.

Figures 5.6 and 5.7 compare predictions at $De = 0.204$ with those at $De = 2.34$. Figure 5.6 shows small decreases in values of U (approximately 5 %), in the region $-1.5 \leq y/R \leq -0.5$ and $0.5 \leq y/R \leq 1.5$, as De increases, indicating an increase in resistance to the flow as the elastic forces in the fluid become more dominant. Figure 5.6(b) shows; (i) increases in $|N_1|$, as De increases, at locations adjacent to the walls of the geometry (at $y/R = -2$ and 2) and; (ii) decreases in $|N_1|$ in the region $-1.75 \leq y/R \leq 1.75$. Finally, figure 5.7 shows a decrease in values of $|\sigma_{xy}|$, over the whole cross-section ($-2 \leq y/R \leq 2$) as De increases. For all these predicitons, the same trends have been shown in chapter 4, for the single cylinder flows: Their behaviour with respect to increasing De can again be explained by the combination of shear and/or elongational thickening/thinning in the flow domain.

5.3.3 6 % PIB solution

For the 6 % PIB solution, the same cross-sections are studied; $x/R = -5$, -2, -1.5, 1.5 and 2, and the same flow behaviour to that of the 2.5 % PIB solution, which is described in the previous section, is shown. Figures 5.8, 5.9 and 5.10 show predictions for U, N_1 and σ_{xy}, respectively, each at; (a) $De = 0.135$ and; (b) $De = 5.72$. Each figure shows predictions for: $x/R = 1.5$, 7.05 and 12.61, corresponding to a distance, $x/R = 1.5$ downstream from cylinders 1, 2 and 3, respectively. As in the previous section, for all predictions, insignificant differences were exhibited when results at the same De were compared. This is also the case for comparisons of the other cross-sections and for reason of brevity, are not shown here.

Figures 5.11 and 5.12 compare predictions at $De = 0.135$ with those at $De =$

5.72, and identical trends are shown to that described in the previous section, for the 2.5 % PIB solution, except the differences are approximately 2 to 3 times larger for the 6 % PIB solution. This can be attributed to; (i) stronger viscoelastic effects present in this solution, with higher concentrations of PIB, and; (ii) the higher *De* difference used for these flow predictions.

5.3.4 Summary

At the beginning of this chapter, it was reported that Verhelst and Nieuwstadt (2004) showed measurement data for a Boger fluid, in an identical geometry to that studied here, and reported flow instabilities caused by the presence of other cylinders, at a critical inter-cylinder spacing. However, it is also reported by Verhelst and Nieuwstadt (2004) that these instabilities only occur above a certain flow rate. The absence of flow instabilities in the preceding investigation for the 2.5 % and 6 % PIB solutions can therefore be explained by; (i) the inter-cylinder spacing being larger than the critical one and; (ii) the flow rate being smaller than that which is required to cause them. As the inter-blade and inter-baffle spacing of the mixing vessel geometry considered in chapter 6 is similar in size and/or greater to that of the inter-cylinder spacing, flow instabilities might not be present at similar flow rates.

In conclusion, for both fluids, over the range of *De* studied, the presence of additional cylinders do not appear to alter the flow behaviour or to induce instabilities in the vicinity of the cylinders. The flow patterns for U, N_1 and σ_{xy}, show this. They each show the same behaviour, at the same positions, in the vicinity of each cylinder. An increase in *De* shows changes in velocity, first normal stress differences and shear stress, similar to those already shown in chapter 4.

5.4 Flow through a planar contraction

5.4.1 Introduction

This section investigates the flow through an axisymmetric, planar, 4:1 sudden contraction (see figure 5.13). The geometry is designed so that the fluid passes

through the main channel, height, $4h$ and then through the contracted channel, height, $h = 0.00225$ m. The main channel, $12h$ long, allows the flow to become fully developed before reaching the sudden contraction. At the contraction, the fluid flow rate increases, to satisfy continuity, and is simultaneously subjected to a combination of strong elongational and shear stresses. The length of the contracted channel, $8h$, also allows the fluid to become fully developed.

In the following sections the flow behaviour of the 2.5 % and 6 % PIB solutions is considered, where only the former is validated against LDA and FIB measurement data (Quinzani et al., 1995) for a similar 5 % PIB solution, through an identical sudden contraction geometry. For the 6 % PIB solution, only predictions are shown as, to the best knowledge of the author, measurement data for similar or identical fluids is not available. For both fluids, predictions for U and N_1 are obtained, at a De within the range studied in the previous chapter, along the centreline of the geometry only. Other cross-sections were not studied as it is only along the centreline that Quinzani et al. (1995) provides measurement data, and furthermore it is here that high levels of elongational deformations are reported. The latter is of particular interest as it provides additional information on the elongational behaviour of these fluids that, for reasons given in chapter 3, could not otherwise be obtained by rheometric experimentation. It is due to the high level of elongational deformation that the shear stress values have less influence on the flow behaviour and for reason of brevity values of σ_{xy} are not shown in this section.

5.4.2 2.5 % PIB

Figures 5.16(a) and 5.16(b) show predictions of U and N_1, respectively, for the 2.5 % PIB solution. Predictions are obtained for $De = 1.39$ and 4.48 where the former is compared to measurement data of Quinzani et al. (1995), for a similar 5 % PIB solution, at an identical Deborah number, $De = 1.39$. All the results are obtained at $y/h = -1$, along the line of symmetry, where the flow is subjected to large elongational deformation.

For U, at $De = 1.39$ the predictions are in good agreement with the measurement data and show a difference of approximately 5 % by comparison. As the

De increases (to $De = 4.48$), in the contraction channel ($x/h \geq 0$), an increase in resistance to the flow is observed and subsequently the velocity values decrease. Although this effect is small, this could be attributed to an increase in viscosity, predominantly caused by strong elongational deformation, or equally by the changes in N_1 (see below) contributing to the small increase in resistance to the flow of the fluid. Contrarily, this is not shown upstream, in the main channel where predictions at both De are identical and within 1 % of the measurement data. Both predictions and measurement data show an identical trend: An exponential increase in velocity as the fluid approaches the contraction channel, followed by values that plateau on entry.

For N_1, in figure 5.16(b), the predictions obtained at $De = 1.39$ show an approximate difference of 15 % by comparison to the measurement data of Quinzani et al. (1995), which is slightly larger than the margin of error expected experimentally. However, the previous chapter showed similar margins of error by comparison to the measurement data of Baaijens (1994b), for the single cylinder case. An increase in De shows relatively small changes in N_1, by comparison: A decrease of approximately 10 % is shown in the main channel and an increase of approximately 8 % in the contraction channel. Both the measurement data and predictions for N_1 show a similar trend: An exponential increase in values leading up to the contraction channel, just before entry these values reach a peak, and as the fluid begins to move through the contraction channel, the values show a steep exponential decrease, becoming asymptotic at zero, at approximately $x/h = 2$.

For both the U and N_1 values, the flow in the main channel appears unperturbed to within a distance of approximately $4h$ from the contraction channel. The acceleration of the fluid through the contraction is rapid and leads to large deformation rates. However, from the N_1 values, it appears that the maximum stresses occur just before the flow enters the contraction. Subsequently, as the fluid passes through the contraction channel the stresses relax from this maximum but are not fully relaxed by the point the velocity field seems to reach its fully developed form in the channel. This can be explained: Increasing the De by increasing the flow rate results in a larger average velocity and a longer distance travelled by the fluid, per unit of the relaxation time.

5.4.3 6 % PIB

Measurement data is not available to validate the predictions obtained for the 6 % PIB solution and therefore only predictions are shown. Figures 5.17(a) and 5.17(b) show predictions for U and N_1, respectively, each at $De = 1.73$ and $De = 4.27$.

For U, the predictions obtained at both De exhibit almost identical trends: Values of U increase exponentially as the flow approaches the contraction and suddenly plateau at the entrance, which is identical to the aforementioned 2.5 % PIB solution. Differences are shown in the main channel, in the region $-6 \leq x/h \leq 0$, of the order of approximately 5 %, where the higher De flow shows larger velocities, but an insignificant difference is shown at the plateau region.

For N_1, the trends closely resemble those of the 2.5 % PIB solution: The first normal stress difference values increase exponentially leading up to the contraction channel, reaching a peak just before entry and as the fluid begins to move through the contraction channel the values show a steep exponential decrease, becoming asymptotic at zero, at approximately $x/h = 2$. However, contrary to what is shown for the 2.5 % PIB solution, large decreases in values for N_1 are observed in both channels, of the order of approximately 50 % as De increases (see below).

5.4.4 Summary

This section provides predictions for velocity and normal stress difference values along the centreline of a contraction geometry. The predictions for the 2.5 % PIB solution have been validated with measurement data of Quinzani et al. (1995) at $De = 1.39$, which not only gives confidence to the model's capability to provide accurate predictions for flows that are assumed to be predominantly elongational where elastic forces are greater than the viscous (i.e. $De > 1$), but again to the numerical methodologies used in this thesis.

The change in velocity that both fluids show as they reach the contraction channel is suspected to cause the polymer chains to stretch which appear to simultaneously cause a rise in N_1 values. However, in the contraction channel, although the velocities are higher, there is no gradient of change and therefore

the polymer chains begin to relax and subsequently the N_1 values decrease.

With an increase in De the 2.5 % PIB solution shows small changes that are fully described above. For 6 % PIB, a considerable decrease is shown which, at this point, is assumed to be caused by numerical inaccuracies caused by the model's inability to capture the N_1 values at the higher rates of deformation. Due to the possible occurrence of the aforementioned numerical inaccuracies, analyses of the 6 % PIB solution will proceed to be made with caution.

5.5 Flow past a blade/baffle

5.5.1 Introduction

In this section, numerical predictions are presented for the 2.5 and 6 % PIB solutions using the PTT and Giesekus constitutive models, respectively. Two separate geometries are considered; (1) with height H_1 and; (2) with height H_2 (see figure 5.18). Both geometries are 0.13 m long, identical to that of the cylinder geometries and long enough to allow the flow to become fully developed before reaching the blade. The dimensions of the blade are identical to that of the impeller used in the stirred vessel (described in chapter 2 and used in chapter 6). The flow domain is planar, therefore the change in flow dynamics with respect to a change in the depth of the mixing vessel is not included in this study, due to inherent complexities involved simulating such a problem (see Chapters 1 and 4 of this thesis). Direct comparisons can of course not be made with measurement data for the stirred vessel, as the flow patterns are fundamentally different i.e. the blade is not moving and the velocity values are near zero adjacent to the tip of the blade, where conversely, for a stirred vessel, the impeller is rotating and the values are greatest at this point. Essentially, the geometry attempts to capture the creeping flow behaviour of each fluid passing the blade and the viscoelastic effects caused by an obstruction such as this, to provide a useful insight into the mixing process of these fluids. To the best knowledge of the author, neither experimental or numerical work has been carried out for flow geometries such as these, and for this reason, comparisons cannot be made with measurements and/or predictions. However, the Giesekus and PTT constitutive models are

successfully validated over a range of De, in the other benchmark geometries, and can therefore be implemented with some level of confidence in the following sections.

For the 2.5 % PIB solution, tables 5.5 and 5.6 show the simulation parameters, for a flow geometry with height, H_1 and H_2, respectively. The mean velocity, $< u >$ is calculated far enough upstream of the impeller blade, where the flow is fully developed and parameters, $\dot{\gamma}$, τ_0, De and Re are defined in section 4.2.4. For each geometry, predictions are obtained in the region $0.185 \leq De \leq 3.59$, which is within the range of De studied for the single cylinder flows. For the 6 % PIB solution, tables 5.7 and 5.8 show the simulation parameters for the flow geometry with height, H_1 and H_2, respectively. For simulations in the range, $De \leq 1.57$. Obtaining predictions at De greater than this was not possible with manageable values of Δt. For both fluids, the range, $0.0004 \leq Re \leq 0.167$ indicates creeping flow and the values of Δt are a factor of 10 times smaller for the higher De flows. Additionally the tables show that all simulations meet the minimum criteria: simT $\leq 1\lambda_{long}$.

The following study is divided into three sections: (1) Predictions for U, N_1 and σ_{xy} are shown and described for both PIB solutions along a cross-section adjacent to the tip of the impeller blade. (2) The distribution of the U, N_1 and σ_{xy} values in the vicinity of the blade/baffle are shown and studied by use of contour and vector plots. (3) An arbitrary Newtonian fluid is introduced and fully described in section 5.5.4, to study the flow behaviour in the surrounding area of the blade, at higher Re, which cannot be investigated for the viscoelastic flows due to the inevitable onset of numerical instabilities when doing so.

5.5.2 Profiles of U, N_1 and σ_{xy} adjacent to the tip of the blade/baffle

To begin understanding the effects of viscoelasticity in the vicinity of the blade, a cross-section extending in a direction perpendicular to the tip of the blade/baffle towards the vessel wall (β_1 to β_3) and with a smaller gap (β_1 to β_2) (see figure 5.18), is chosen for study. For the 2.5 and 6 % PIB solutions, predictions are obtained over the range of De shown in tables 5.5 to 5.8, but due to the relatively

small changes in, U, N_1 and σ_{xy} values, over the range studied, in most cases, only the minimum De and maximum De predictions are shown in the following figures.

Figures 5.22 and 5.23 show values for the axial velocity, U, for the 2.5 and 6 % PIB solutions, respectively. Both figures show the cross-sections; (a) β_1 to β_3 and; (b) β_1 to β_2. For both fluids, at both cross-sections, the velocity values increase from zero at the tip of the blade and vessel wall/baffle and reach a maximum in between these points. However, this profile is not symmetric along the line equidistance between the tip of the blade and the wall/baffle, as it is further upstream. Instead, the peak values are found nearer the blade. Hence, the rate of change of velocity is greater at the tip of the blade/baffle, than at the wall. This is explained by the fluid increasing velocity around the blade to satisfy the continuity of mass. For both fluids, at both cross-sections, an increase in De causes a reduction in magnitude, of less than 5 % which indicates small levels of resistance to the flow, possibly caused by thickening of the fluid. By comparison of both cross-sections, a smaller gap causes slightly larger values of U, at both De, which is intuitive, as the flow cross-section reduces in size and thus the flow rate increases.

Figures 5.24 and 5.25 show values of N_1, for 2.5 % and 6% PIB respectively, along the same cross-sections. In all cases, the greatest values of N_1 are adjacent to the tip of the blade and by moving a small distance in a direction away from the tip, the values rapidly decrease towards zero, to values approximately 95 % smaller. These smaller values are relatively larger in the areas close to the blade and wall/baffle, and smallest approximately half way in between. This can be explained: The acceleration of the fluid is most rapid, adjacent to the tip of the blade, and subjects the polymer chains to large extensional and shear stresses, which induce high levels of normal stress difference. Further from the tip of the blade, the acceleration is less rapid and smaller values of N_1 and σ_{xy} predominate. The fluid can be expected to relax downstream from the blade. By close examination these figures, for both fluids, at the tip of the blade, show larger values for N_1 at lower De. This is discussed in the following paragraph. Moving a small distance from the tip, an increase in De causes the opposite effect:

For the 2.5 % PIB solution (see figure 5.24), an increase in De causes an increase in N_1, of approximately 5 %, and for the 6 % PIB solution (see figure 5.25), a smaller increase of approximately 2 % is shown. For both fluids, N_1 reaches larger maximum values when a 'baffle' is present, which is explained by larger deformation rates, induced by the reduction in the flow cross-sectional area.

Figures 5.26 and 5.27 show values of σ_{xy}, for the 2.5 % and 6% PIB solutions, respectively, along the same cross-sections. At the tip of the blade the lowest De yields the largest values of σ_{xy}. Although this behaviour subsequently explains the larger values of N_1, in this location (see above), it is not intuitively understood. A possible reason is that, at lower De, the flow is, in relative terms, more laminar, and as the De increases, at higher flow rates, the velocity vectors are no longer parallel to the tip of the blade, and this causes the levels of σ_{xy} to decrease. Moving a small distance from the tip of the blade, the values of σ_{xy} rapidly decrease to zero, at all De. The values become negative, and their magnitudes increase, approaching the vessel wall/baffle. Decreases in magnitude, of the order of 5 %, with increasing De, are shown at this location.

5.5.3 Distribution of predicted values in the vicinity of the blade/baffle

This section investigates the distribution of values for U, N_1 and σ_{xy} over the whole flow domain, with particular interest in the changes in flow behaviour, and viscoelastic effects, in the vicinity of the blade. It is shown in the previous section that both fluids show identical qualitative trends and in some cases, similar quantitative trends, along the cross-sections adjacent to the tip of the blade. In this section, predictions of the U, N_1 and σ_{xy} values show a similar behaviour for both fluids, and for this reason, only predictions for the 2.5 % PIB solution are presented in the following discussion.

Vector plots for U, and contour plots for N_1 and σ_{xy}, are shown in this section. The plots show the magnitudes of these values and their effects on the flow behaviour in the area surrounding the blade.

Figure 5.28 shows velocity vectors, for the 2.5 % PIB solution, for the impeller blade geometries with; (a) height, H_1 and; (b) height, H_2, at $De = 2.62$ and 2.34,

respectively. Both plots show laminar flow with the absence of any significant region of circulation in front of, or behind the blade. The plots at a lower De are indistinguishable from these and for this reason are not shown here. The previous section shows increases in velocity with a smaller gap and the vector plots in figure 5.28(b) shows that the increase does not noticeably change the flow behaviour surrounding the blade.

Figure 5.29 shows values of N_1 for the flow geometry with; (a) height, H_1, at $De = 2.62$ and; (b) height, H_2, at $De = 2.34$. Upstream of the impeller blade, both figures show areas of small negative value in the region $1 \leq x/D \leq 8$ and $y/D < 1.5$, which increase in magnitude as the flow approaches the blade at approximately $x/D \geq 9$. Downstream of the impeller blade, these small negative values are shown in the region $10.2 \leq x/D \leq 18$ (covering a slightly smaller region, for the H_2 geometry) and $y/D \geq 1$. Both figures indicate maximum values of N_1, discussed in the previous section, located at the tip of the blade, and rises in N_1, in front of the blade, and in a region downstream from the blade. The latter stems from the tip of the blade and extends towards the vessel wall/baffle. Contour plots at a lower De show a similar distribution of N_1, with slightly smaller magnitudes, and for reason of brevity, are not shown here.

Figure 5.30 shows values of σ_{xy}, for the flow geometry with; (a) height, H_1, at $De = 2.62$, and; (b) height, H_2, at $De = 2.34$. The values are distributed almost symmetrically along the centreline of the blade, at $x/D = 10.1$. Bulb like distributions of shear stress, with approximate values of 0.7, form in the region $5 \leq x/D \leq 16$ (covering a slightly smaller region, for the H_2 geometry) which stems from larger values of σ_{xy}, at the tip of the blade. The highest positive values are adjacent to the tip of the blade and the highest negative values, in the region adjacent to the wall/baffle, where the velocity values are shown to decrease, approaching this boundary.

5.5.4 Vortex structure of a Newtonian fluid in the vicinity of the blade/baffle

Areas of circulation are ubiquitous in mixing, both for laminar and turbulent flow regimes. They occur predominantly above and below the impeller blades,

see, for example, Alvarez et al. (2002) and chapter 6 of this thesis, for a range of different fluids. However, areas of circulation have not been observed in the previous section for neither PIB solution, partially because the flow is creeping ($Re < 0.2$), assuming the shape of the geometry and causing minimal disturbance to the flow pattern, but also because of the absence of flow instabilities, caused by viscoelastic effects: Increased values of De, do not appear to affect the flow behaviour significantly, to induce this behaviour. With the use of non-linear, viscoelastic, Giesekus and PTT models, obtaining predictions at significantly greater Re/De is proven impractical, and such simulations, to the best knowledge of the author, have not been reported. Therefore, this section studies the flow behaviour of an arbitrary Newtonian fluid, with the same zero shear viscosity as that of the 2.5 % PIB solution, namely $\nu_0 = 0.00136\ m^2 s^{-1}$, where computational limitations inherent to the viscoelastic flows will not be present, even at higher Re. The numerical solution procedure is identical to that described in chapters 2 and 4, except the viscoelastic stress in not solved for and consequently decoupled from Navier-Stokes equations.

Table 5.9 shows the range of Re, for which predictions are obtained for the arbitrary Newtonian fluid in the impeller blade geometry, with height, H_1. Predictions for the geometry with height, H_2 are identical and for this reason are not included. The table includes simulation time step sizes and values for L_{circ} and W_{circ}, which are the non-dimensionalised approximate length (in the x-direction) and width (in the y-direction), respectively, of the circulation region behind the blade.

The two lowest Re flows show the absence of any significant circulation zones, but as the Re increases, the zones develop and increase in size. Figures 5.31 to 5.35 show streamline plots for simulations at Re = 0.562, 1.56, 2.43, 15.02 and 55.65, which illustrate this growth. Additionally, figure 5.36 shows plots of L_{circ} and B_{circ} values versus Re. The L_{circ} values increase most rapidly in the range, $0 \leq Re \leq 15$ and show a continual increase over the whole range of Re. Contrarily, the W_{circ} values increase rapidly to a plateau in the range, $15 \leq Re$.

5.5.5 Summary

This section analysis the flow behaviour of both working fluids in and around the blade/baffle geometry. Both fluids behave almost identically in that they both show qualitative and quantitative similarities. This suggests that, for the range of De studied, in particular for the 6 % PIB solution, numerical inaccuracies were not encountered due to the absence of anomalous trends. The reader is referred back to the previous section where the centreline plots for N_1 in the contraction geometry, for 6 % PIB, showed a large reduction in value as De increased and it was assumed that such behaviour was attributed to numerical inaccuracies.

Over the range of De, both fluids show a flow pattern that passes over the blade/baffle with; (a) an absence of vortices in front of and behind the blade/baffle; (b) maximum velocity gradients (increasing from zero) and maximum values of N_1 and σ_{xy} in the area adjacent to the tip, and; (c) areas in front and behind the blade, that stem from the tip, and areas adjacent to the wall of the geometry that show positive and negative changes in N_1 and σ_{xy} values. From these results it is also noteworthy to observe, in the region adjacent to the tip, a decrease in N_1 and σ_{xy} values as De increases but conversely, an increase in the region further away from this area. This has been explained in the previous section.

Section 5.5.4 shows the behaviour of a Newtonian fluid (with the same zero-shear viscosity as 2.5 % PIB) in the vicinity of the impeller blade/baffle in the range, $0 \leq Re < 56$. At approximately $Re = 1.5$ a region of recirculation develops behind the blade and as the Re increases, the length of this region increases. Additionally, the width of the recirculation zone reaches a maximum value equal to the height of the impeller blade/baffle, D, at approximately, $Re \geq 10$. This behaviour has not been shown by the viscoelastic fluids as simulations cannot be carried out in this range of Re due to the aforementioned numerical limitations prevalent in such flows.

5.6 Discussion and conclusions

As discussed in chapter 1, numerical instabilities are inherent to the simulation of viscoelastic fluids and these limit; (i) the size of De for which predictions can be achieved and; (ii) the complexity of the mesh geometry that can be used. These limitations have been discovered for two viscoelastic fluids where predictions, over a range of De, have been shown and validated in chapter 4. With this in mind, the aim of this chapter is to obtain predictions for viscoelastic fluids in idealised blade/baffle geometries which themselves exhibit at least one geometric feature of a 3-dimensional mixing vessel, stirred by a Rushton impeller, such as that introduced in chapter 2, and for which experimental data is obtained in the following chapter. The first idealised geometry is an array of cylinders, the second is a contraction flow and the third is a blade/baffle flow.

The array of cylinders represents a recurring geometry similar to that of a rotating impeller, so the inter-cylinder distance in the array is similar in size to the distance between the adjacent blades of the Rushton turbine. Additionally, the reader can have confidence in the results obtained here as the predictions for the single cylinder case, of the previous chapter, have already been successfully validated, over a similar range of De, against available measurement data. The presence of additional cylinders do not, in this study, appear to alter the flow behaviour or cause instability in the flow, as values obtained for U, N_1 and σ show an insignificant change by comparison at cross-sections upstream and downstream of each cylinder. However, Verhelst and Nieuwstadt (2004) showed the contrary: The onset of flow instability was reported for a Boger fluid in a similar geometry, at a critical inter-cylinder spacing where the cylinder were close enough, and at a certain flow rate that was high enough, to cause a chaotic motion in the flow pattern. It is suggested that the absence of flow instability and changes in flow pattern, in this study, be explained by; (i) the inter-cylinder spacing being larger than the critical one, and; (ii) the flow rate being smaller than that which is required to cause them, and not, therefore, by the models failure to do so. However, to the best knowledge of the author, the constitutive models used for this research have not predicted physical instabilities in the flow patterns of viscoelastic fluids in any such geometry, not least, chaotic motion and

one could postulate that it is the onset of such physical behaviour that could be causing numerical divergence at the highest strain rates. For a detailed discussion of chaotic behaviour the reader is referred to section 6.4.7 of the following chapter where such behaviour is realised for a polyisobutylene solution in a stirred mixing vessel.

The contraction flow geometry provides a totally different geometric configuration by comparison to the cylinder flows, i.e. the geometry exhibits an absence of curved surfaces and instead the flow is obstructed by a vertical wall, a sharp corner and abruptly contracted in a narrow channel. These flow features have not only been studied both numerical and experimentally by other researchers (where available measurement data is used for comparison here) but can be expected to be encountered in dynamic mixing; the fluid behaviour in a mixing vessel is complex (as the following chapter shows) but forms of fluid contraction, in the vicinity of the impeller and at the extremities of the vessel, can be expected. And, most certainly, the mixing vessel features walls and sharp corners (the blades and baffles) that obstruct the flow. Predictions for velocity and normal stress difference values were obtained for both fluids along the centreline of the geometry and those of the 2.5 % PIB solution, at $De = 1.39$, were validated against measurement data of Quinzani et al. (1995). Most predictions of the 6 % PIB solution showed qualitative similarities by comparison to 2.5 % PIB. However, a decrease of approximately 50 % in values for N_1, of 6 % PIB, are shown as De increases which isn't shown for the 2.5 % PIB solution. This difference is not necessarily incorrect but the anomalousness suggests that the models, although they have been successfully validated for the 2.5 % PIB solution has failed to fully capture the fluid behaviour at $De = 4.27$ and therefore reminds the reader that all the predictions should be obtained with caution. Despite this, the other predictions reveal interesting flow behaviour: At the entrance to the contraction channel steep changes in velocity values are accompanied, almost simultaneously, by a rise in N_1 values. This is suspected to be caused by the stretching of the polymer chains. Subsequently, on cessation of the fluid acceleration (namely, in either channel where a constant velocity is observed), the polymer chains relax and the N_1 values decrease to zero. Such behaviour is most likely to be observed

in the stirred vessel measurement data of the following chapter.

Finally, the blade/baffle geometry was used to model a single blade of a Rushton impeller. Predictions for both PIB fluids were obtained within the range of *De* studied for the other geometries and quantitative and qualitative similarities are shown by comparison of both fluids. Therefore, the predictions, although not validated, due to the lack of available of measurement data in this case, are presented here with confidence. A full description of the fluids' behaviour around the blade is given in the text, but in short, maximum values of N_1 and σ_{xy} are observed in a region adjacent to the tip of the blade where values of velocity increase most rapidly from zero. Maximum values for velocity are observed in a region approximately half way between the tip of the blade and the wall of the flow domain, in a direction perpendicular to the tip. At the highest *De* ($De = 2.34$) locally high, absolute, values of N_1 and σ_{xy} are observed in the vicinity of the blade, that stem from the tip. It is also interesting to observe the change in predictions of N_1 and σ_{xy} with an increase in *De*, in the region adjacent to the tip of the blade: Contrary to what is intuitive, these values decrease. This is explained by the change in flow direction which moves further away from being parallel to the tip and consequently reduces the amount of shear induced at this point, and the values decrease.

The Newtonian fluid, with a viscosity 1000 times that of water and equal to the zero-shear viscosity of the 2.5 % PIB solution showed a region of recirculation developing and growing in size behind the blade/baffle in the range, $0 \leq Re < 56$.

As already mentioned, in a dynamic mixing environment such as that of a stirred vessel, regions of recirculation are a common occurrence in the vicinity of the impeller blade, especially for high *Re* flows where these regions become large enough to occupy the majority of the space in the vessel. This is shown in the next chapter and by a number of authors referenced within.

$< u >$ [m/s]	$\dot{\gamma}_a$ [s^{-1}]	τ_0 [Pa]	De [-]	Re [-]	Δt [s]	simT [s]
0.00138	0.306	1.00	0.204	0.00454	$1 * 10^{-3}$	$20\lambda_{long}$
0.0157	3.49	11.4	2.34	0.0519	$1 * 10^{-5}$	$2\lambda_{long}$

Table 5.1: Mean velocity, $< u >$, apparent shear rate, $\dot{\gamma}_a$, scaling stress, τ_0, dimensionless numbers: De and Re, time step, Δt and simulation time, simT (in terms of the number of longest relaxation times (λ_{long})), for predictions of 3 symmetrically confined cylinders, for the 2.5 % PIB solution.

$< u >$ [m/s]	$\dot{\gamma}_a$ [s^{-1}]	τ_0 [Pa]	De [-]	Re [-]	Δt [s]	simT [s]
0.000479	0.107	5.78	0.135	0.000116	$1 * 10^{-4}$	$3\lambda_{long}$
0.0204	4.53	246	5.72	0.00492	$1 * 10^{-6}$	$1\lambda_{long}$

Table 5.2: Mean velocity, $< u >$, apparent shear rate, $\dot{\gamma}_a$, scaling stress, τ_0, dimensionless numbers: De and Re, time step, Δt and simulation time, simT (in terms of the number of longest relaxation times (λ_{long})), for predictions of 3 symmetrically confined cylinders, for the 6 % PIB solution.

$< u >$ [m/s]	$\dot{\gamma}_a$ [s^{-1}]	τ_0 [Pa]	De [-]	Re [-]	Δt [s]	simT [s]
0.00468	2.08	6.81	1.39	0.0154	$1 * 10^{-5}$	$7\lambda_{long}$
0.0150	6.70	21.9	4.48	0.0498	$1 * 10^{-5}$	$7\lambda_{long}$

Table 5.3: Mean velocity, $< u >$, apparent shear rate, $\dot{\gamma}_a$, scaling stress, τ_0, dimensionless numbers: De and Re, time step, Δt and simulation time, simT (in terms of the number of longest relaxation times (λ_{long})), for predictions of contractions flows, for the 2.5 % PIB solution.

$< u >$ [m/s]	$\dot{\gamma}_a$ [s^{-1}]	τ_0 [Pa]	De [-]	Re [-]	Δt [s]	simT [s]
0.00308	1.37	74.2	1.73	0.000743	$1 * 10^{-5}$	$3\lambda_{long}$
0.0076	3.38	183	4.27	0.00183	$1 * 10^{-6}$	$1\lambda_{long}$

Table 5.4: Mean velocity, $< u >$, apparent shear rate, $\dot{\gamma}_a$, scaling stress, τ_0, dimensionless numbers: De and Re, time step, Δt and simulation time, simT (in terms of the number of longest relaxation times (λ_{long})), for predictions of contractions flows, for the 6 % PIB solution.

$< u >$ [m/s]	$\dot{\gamma}_a$ [s^{-1}]	τ_0 [Pa]	De [-]	Re [-]	Δt [s]	simT [s]
0.00194	0.298	0.975	0.199	0.00924	$1 * 10^{-4}$	$20\lambda_{long}$
0.00827	1.27	4.16	0.851	0.0394	$1 * 10^{-4}$	$20\lambda_{long}$
0.0144	2.22	7.27	1.49	0.0689	$1 * 10^{-4}$	$10\lambda_{long}$
0.0255	3.923	12.836	2.624	0.122	$1 * 10^{-5}$	$9\lambda_{long}$
0.0349	5.365	17.555	3.589	0.166	$1 * 10^{-5}$	$6\lambda_{long}$

Table 5.5: Mean velocity, $< u >$, apparent shear rate, $\dot{\gamma}_a$, scaling stress, τ_0, dimensionless numbers: De and Re, time step, Δt and simulation time, simT (in terms of the number of longest relaxation times (λ_{long})), for predictions of blade flows, with $H_1 = 0.03325\ m$, for the 2.5 % PIB solution.

$< u >$ [m/s]	$\dot{\gamma}_a$ [s^{-1}]	τ_0 [Pa]	De [-]	Re [-]	Δt [s]	simT [s]
0.00180	0.276	0.904	0.185	0.00856	$1 * 10^{-4}$	$20\lambda_{long}$
0.00779	1.2	3.92	0.801	0.0371	$1 * 10^{-4}$	$20\lambda_{long}$
0.0177	2.72	8.89	1.82	0.0842	$1 * 10^{-5}$	$10\lambda_{long}$
0.0228	3.507	11.475	2.34	0.109	$1 * 10^{-5}$	$9\lambda_{long}$
0.0349	5.373	17.581	3.59	0.167	$1 * 10^{-5}$	$6\lambda_{long}$

Table 5.6: Mean velocity, $< u >$, apparent shear rate, $\dot{\gamma}_a$, scaling stress, τ_0, dimensionless numbers: De and Re, time step, Δt and simulation time, simT (in terms of the number of longest relaxation times (λ_{long})), for predictions of blade flows, with $H_2 = 0.02475\ m$, for the 2.5 % PIB solution.

$< u >$ [m/s]	$\dot{\gamma}_a$ [s^{-1}]	τ_0 [Pa]	De [-]	Re [-]	Δt [s]	simT [s]
0.00147	0.227	12.3	0.286	0.000514	$1 * 10^{-4}$	$20\lambda_{long}$
0.00744	1.15	62.1	1.45	0.00259	$1 * 10^{-5}$	$4\lambda_{long}$

Table 5.7: Mean velocity, $< u >$, apparent shear rate, $\dot{\gamma}_a$, scaling stress, τ_0, dimensionless numbers: De and Re, time step, Δt and simulation time, simT (in terms of the number of longest relaxation times (λ_{long})), for predictions of blade flows, with $H_1 = 0.03325\ m$, for the 6 % PIB solution.

$< u >$ [m/s]	$\dot{\gamma}_a$ [s^{-1}]	τ_0 [Pa]	De [-]	Re [-]	Δt [s]	simT [s]
0.00136	0.209	11.3	0.264	0.000474	$1 * 10^{-4}$	$20\lambda_{long}$
0.00809	1.24	67.5	1.57	0.00282	$1 * 10^{-5}$	$4\lambda_{long}$

Table 5.8: Mean velocity, $< u >$, apparent shear rate, $\dot{\gamma}_a$, scaling stress, τ_0, dimensionless numbers: De and Re, time step, Δt and simulation time, simT (in terms of the number of longest relaxation times (λ_{long})), for predictions of blade flows, with $H_2 = 0.02475\ m$, for the 6 % PIB solution.

Re [-]	Δt [s]	L_{circ} [-]	W_{circ} [-]
0.562	0.0001	-	-
1.086	0.0001	-	-
1.56	0.0001	0.8	0.5
2.43	0.0001	1.0	0.7
15.02	0.00001	4.2	1.0
36.2	0.00001	6.2	1.0
46.0	0.00001	7.4	1.0
50.76	0.00001	8.0	1.0
55.65	0.00001	8.4	1.0

Table 5.9: The Reynolds Number, Re, time step, Δt and size of the circulation region behind the blade, L_{circ}, for predictions of blade flows, with $H_1 = 0.03325\ m$, for an arbitrary Newtonian solution, with kinematic viscosity, $\nu = 0.00136\ m^2/s$.

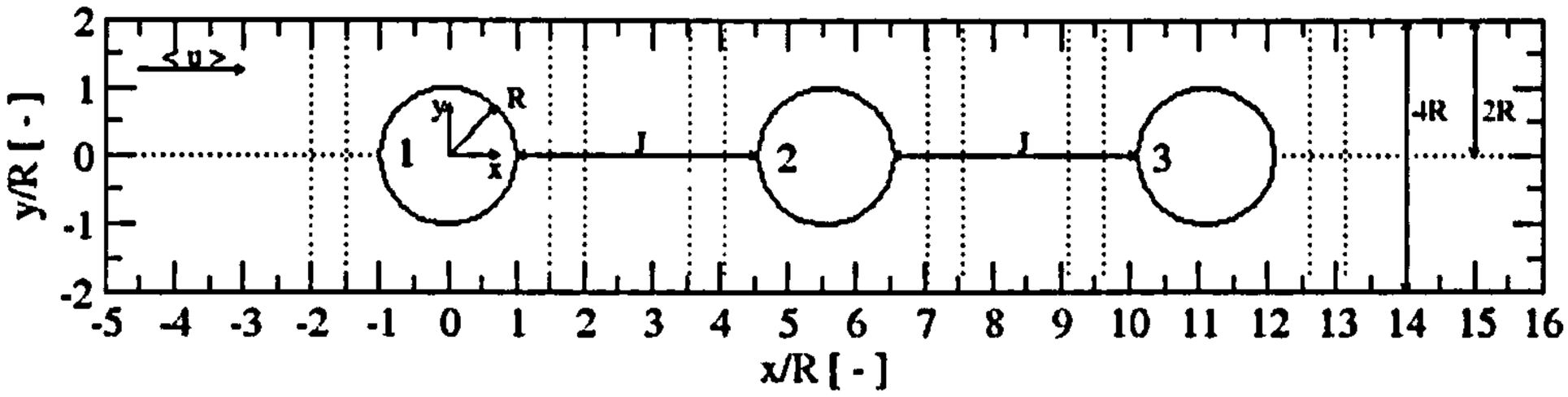

Figure 5.1: Schematic representation of the cross sectional view of the symmetrically confined 3 cylinder geometry. The radius (R) of each cylinder is 0.0045 m, the channel height is $4R$ and the total length in the x direction is 0.130 m. The center of cylinders 1, 2 and 3 are at; $x = 0$, $y = 0$; $x = 5.55$, $y = 0$ and; $x = 11.11$, $y = 0$, respectively. The mean flow is in the positive x direction and the contact distance between the cylinders is; $J = 0.016\ m$.

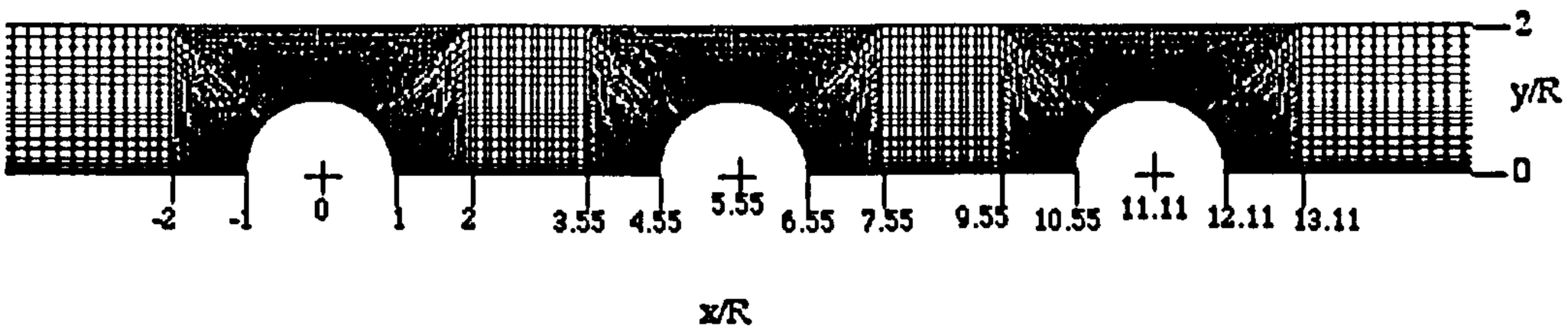

Figure 5.2: The finite volume mesh geometry surrounding 3 symmetrically confined cylinders, used for all 3 cylinder flow simulations in this chapter, containing 9840 cells.

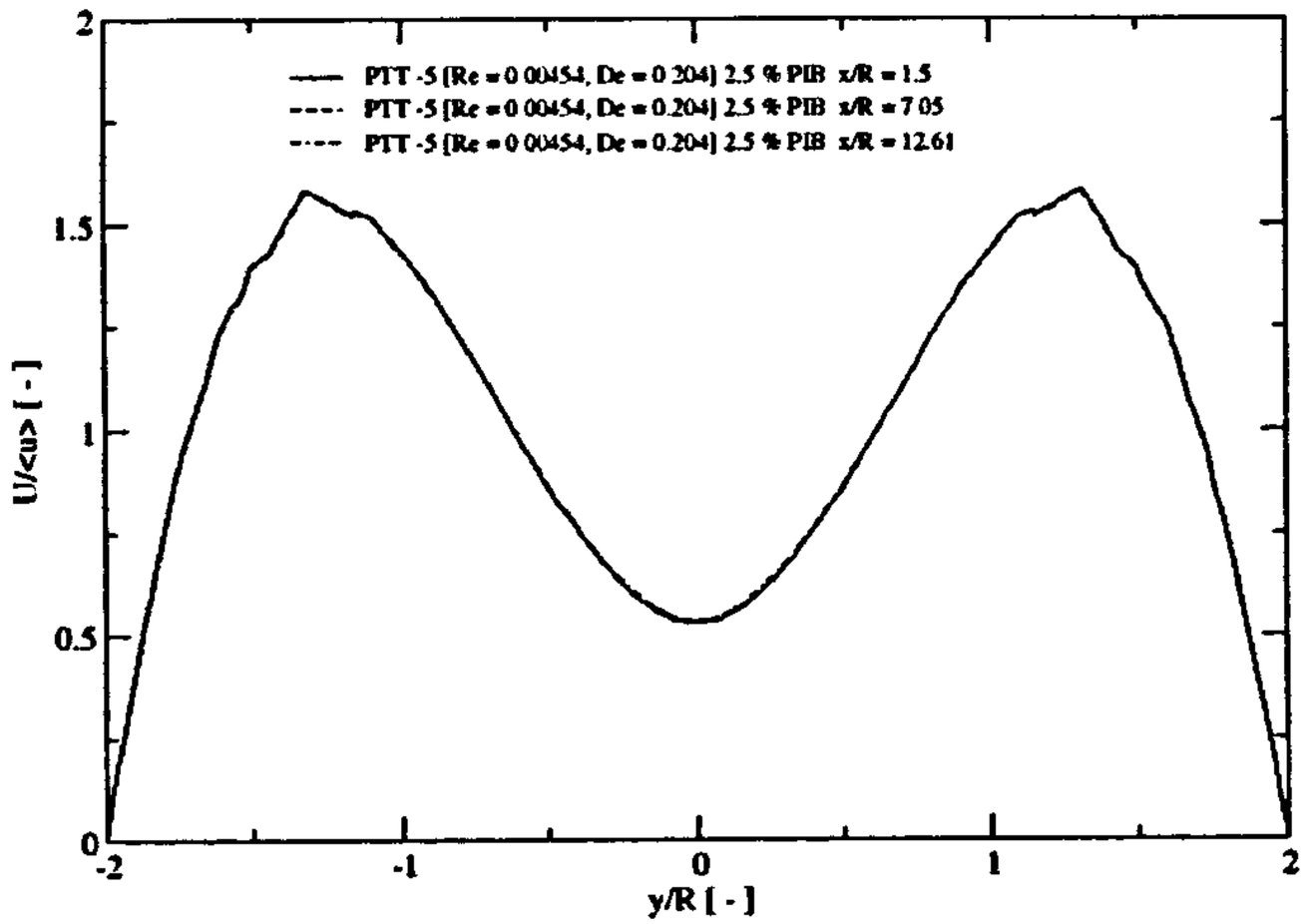

(a)

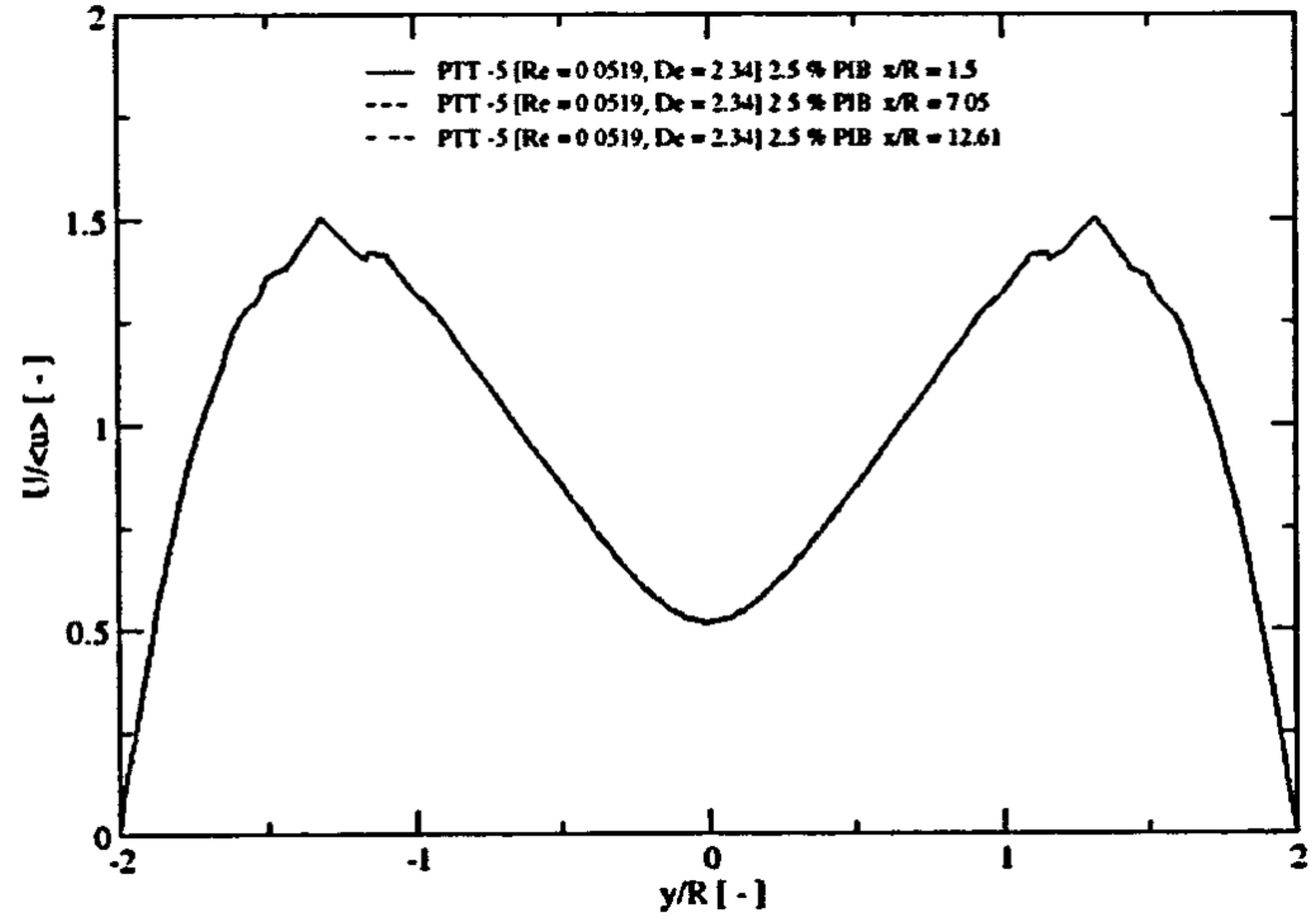

(b)

Figure 5.3: Comparison of predictions for the axial velocity (U) values downstream of each cylinder (at $x/R = 1.5$, 7.05 and 12.61) at; (a) $De = 0.204$ and; (b) $De = 2.34$, for the 2.5 % PIB solution.

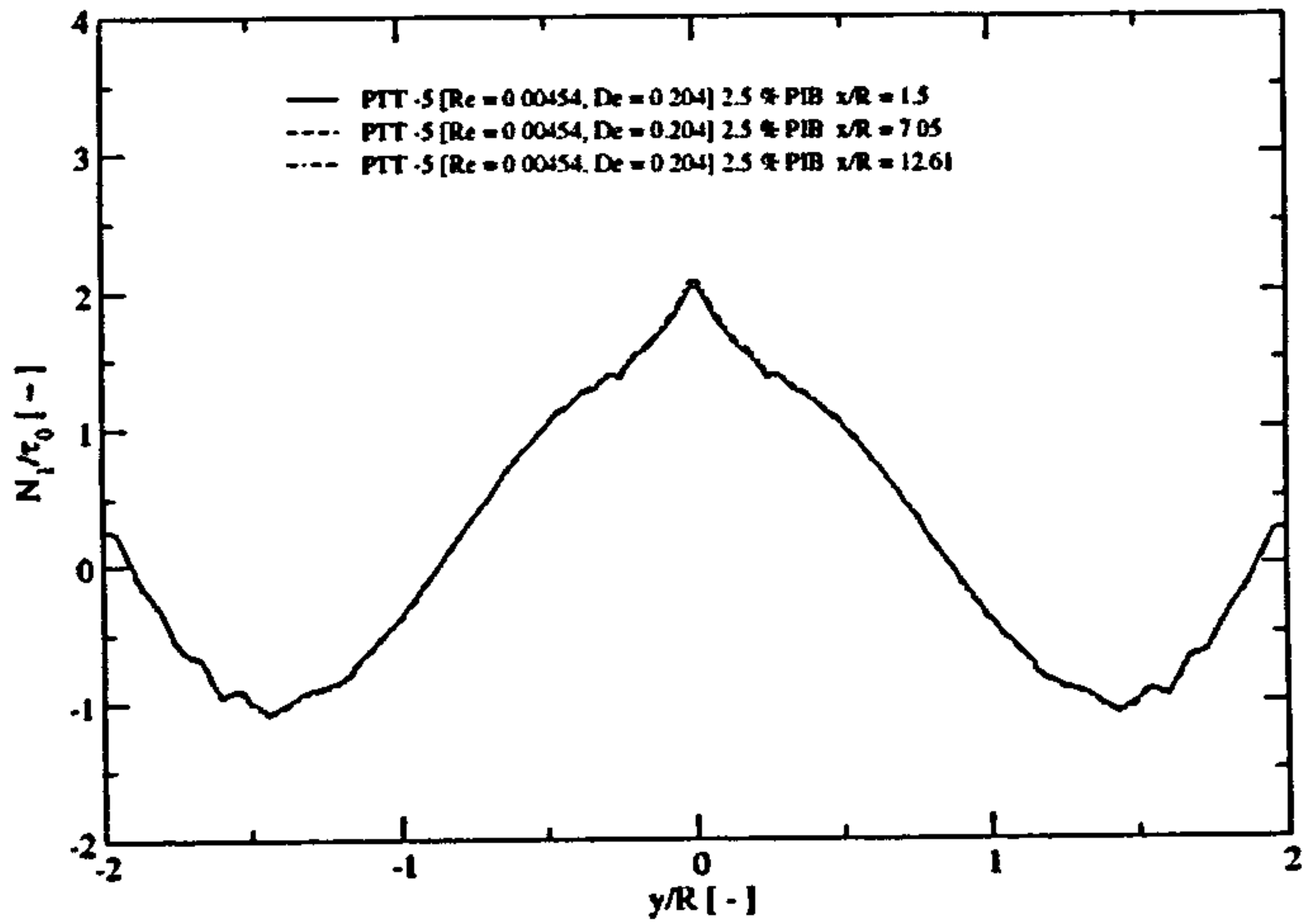

(a)

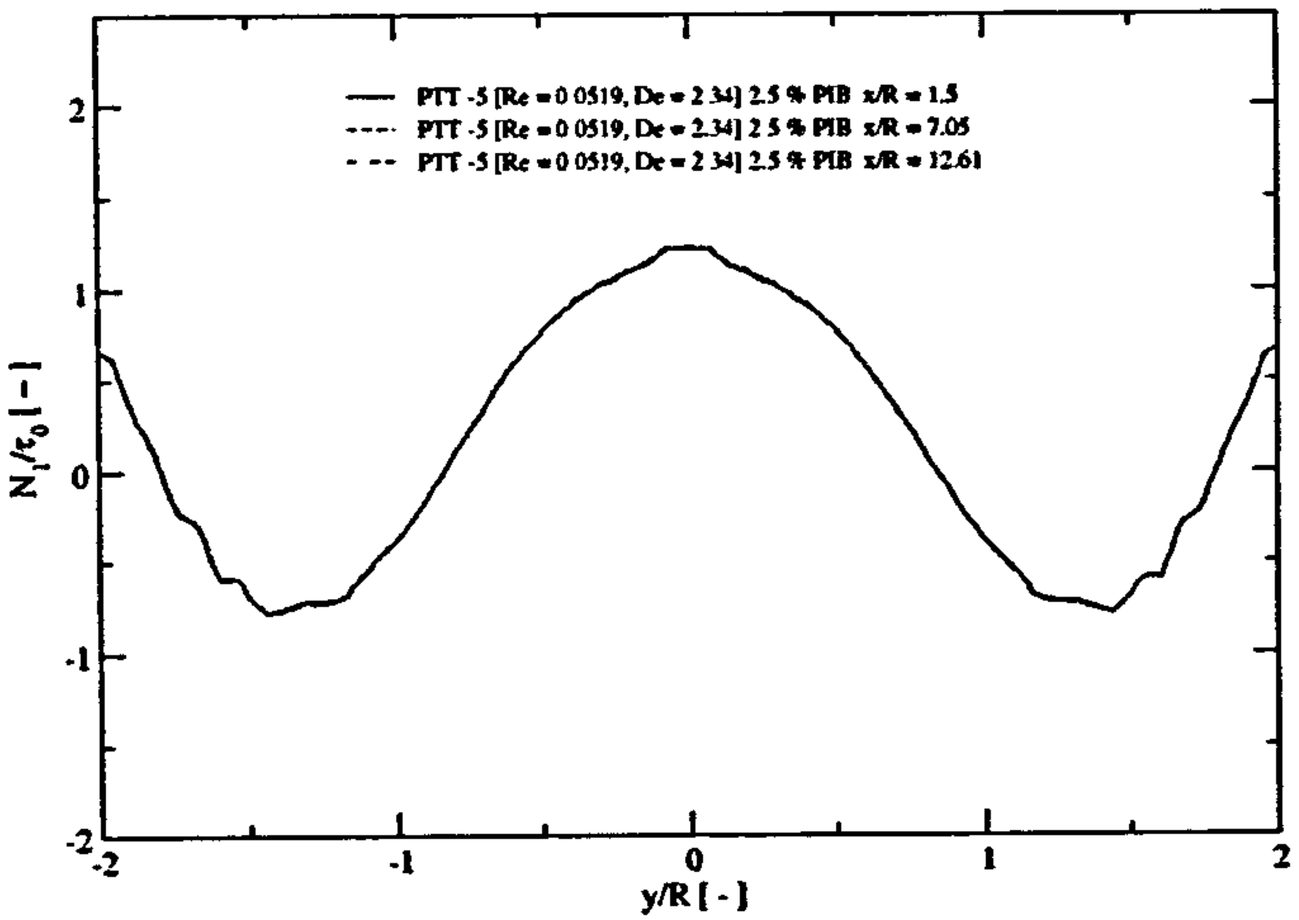

(b)

Figure 5.4: Comparison of predictions for the first normal stress difference (N_1) values downstream of each cylinder (at $x/R = 1.5$, 7.05 and 12.61) at; (a) $De = 0.204$ and; (b) $De = 2.34$, for the 2.5 % PIB solution.

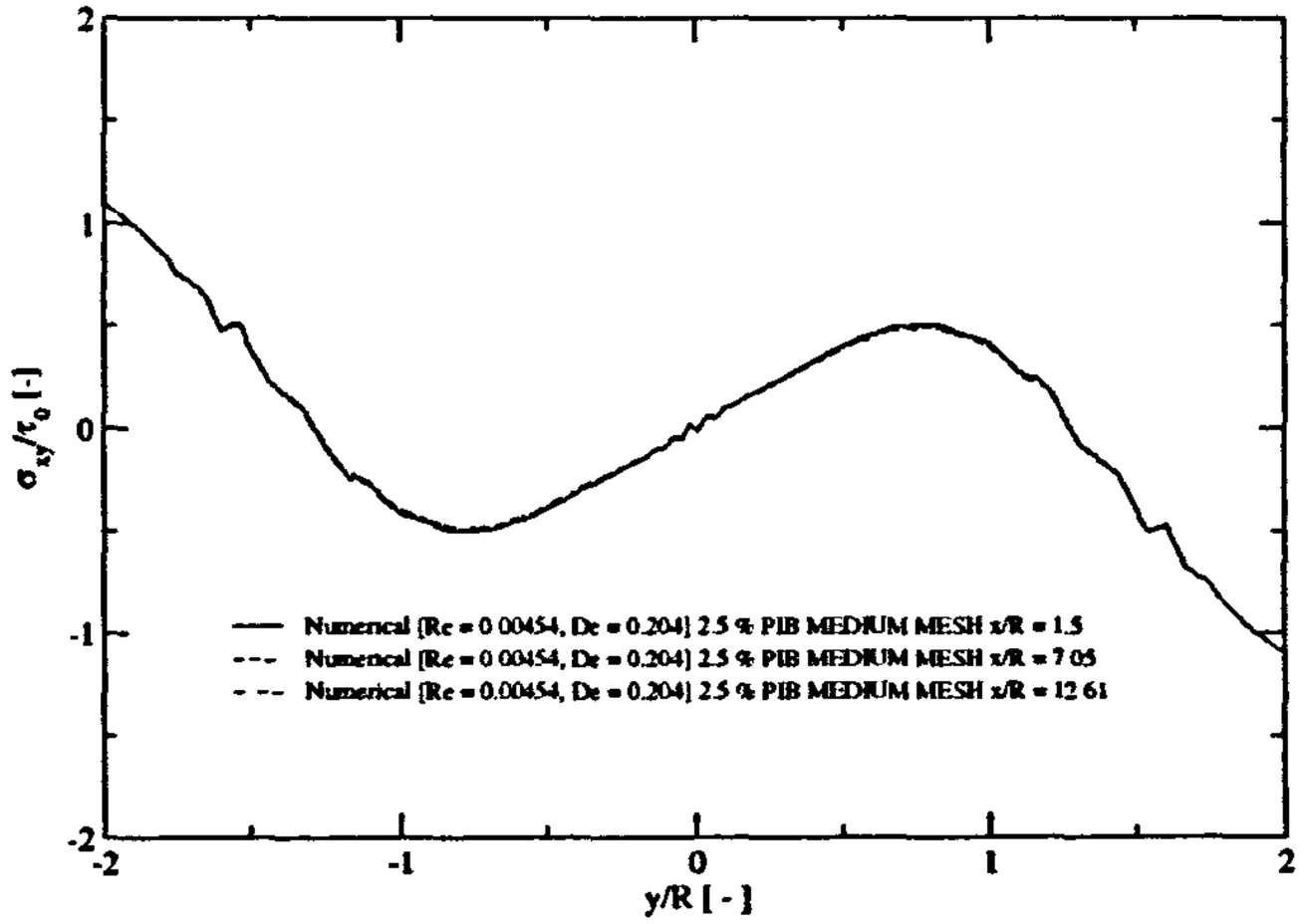

(a)

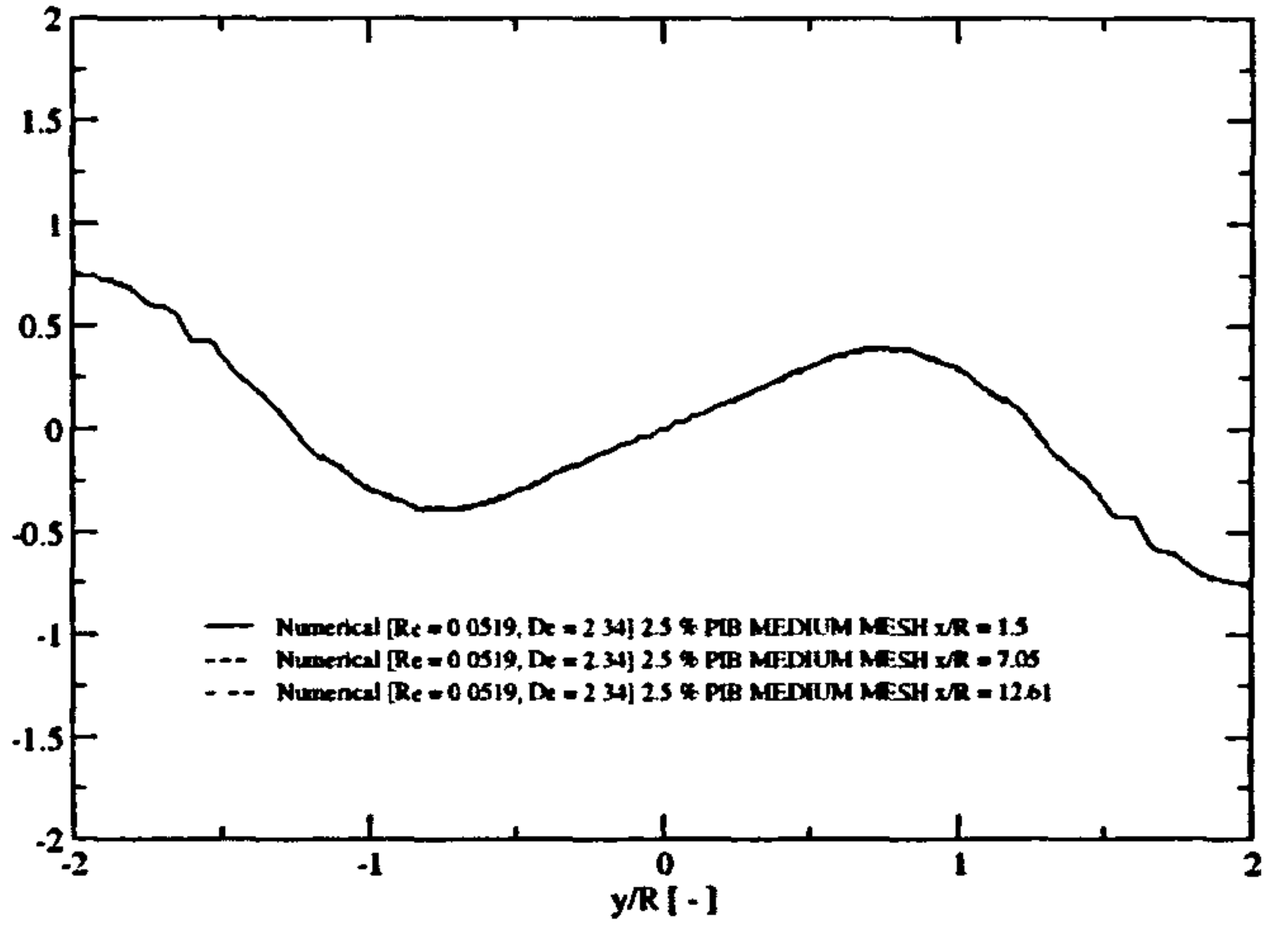

(b)

Figure 5.5: Comparison of predictions for the shear stress (σ_{xy}) values downstream of each cylinder (at $x/R = 1.5$, 7.05 and 12.61) at; (a) $De = 0.204$ and; (b) $De = 2.34$, for the 2.5 % PIB solution.

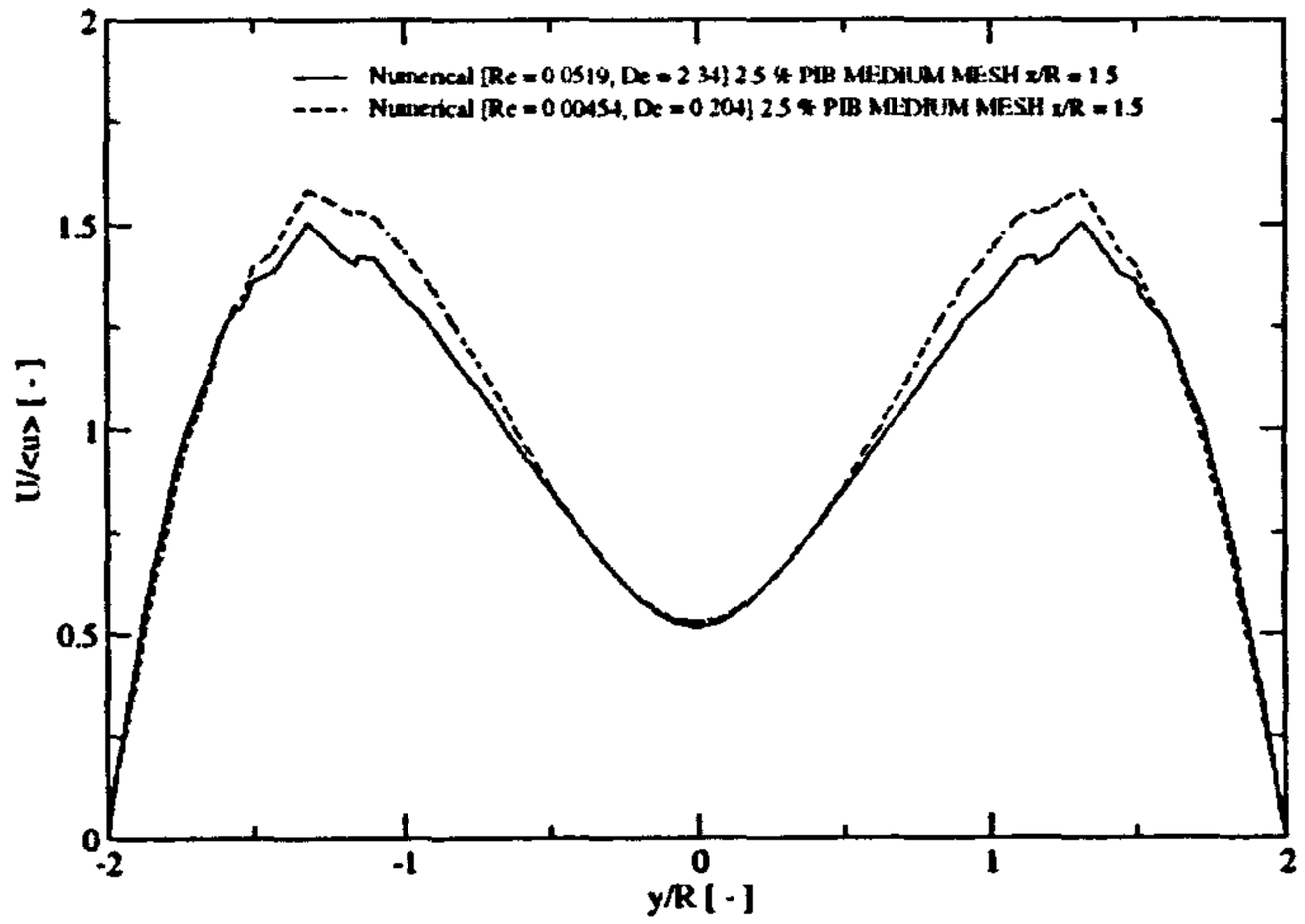

(a)

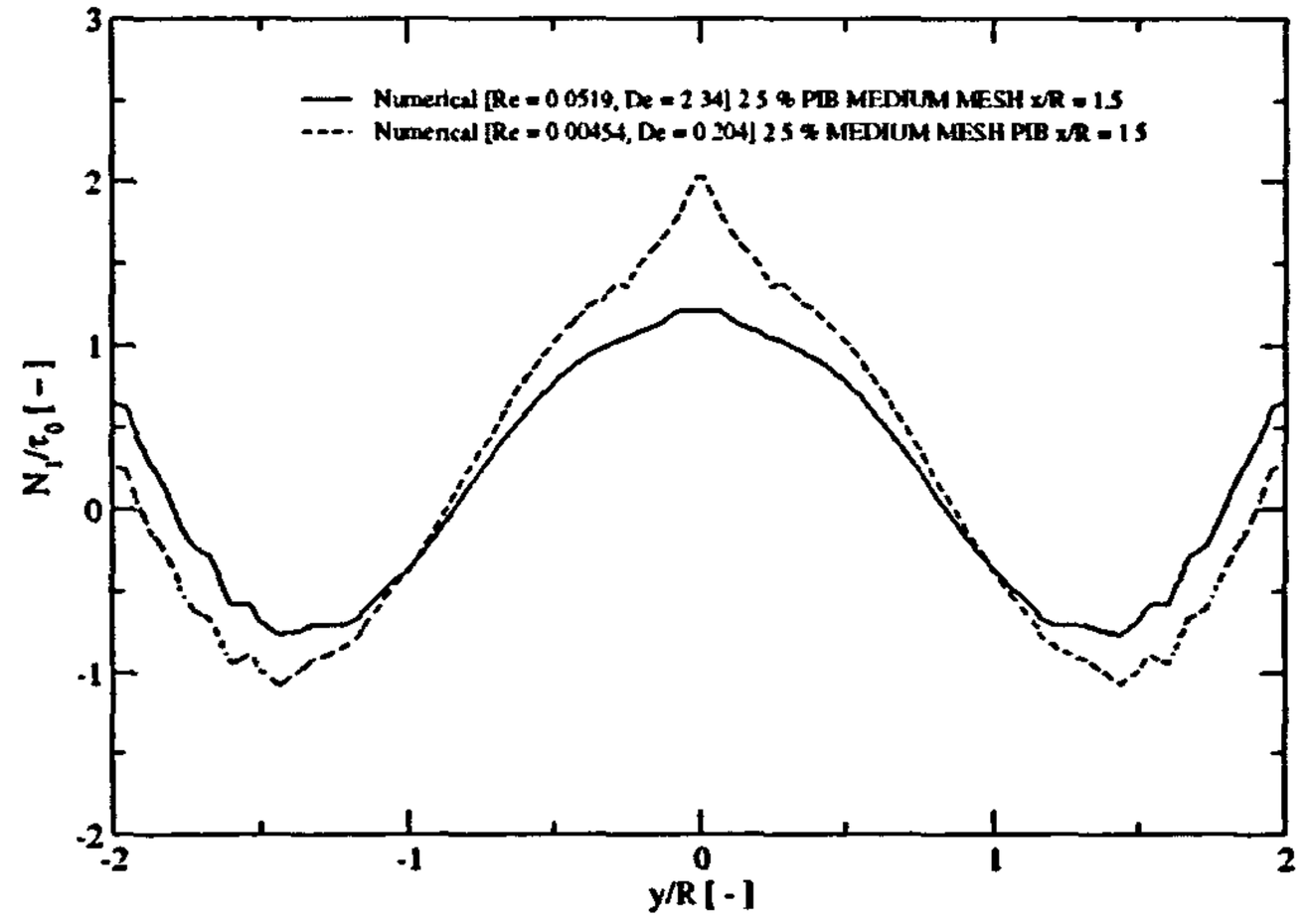

(b)

Figure 5.6: Comparison of predictions for the; (a) axial velocity (U) and; (b) first normal stress difference (N_1) values, downstream of the first cylinder ($x/R = 1.5$), at $De = 0.225$ and $De = 2.34$, for the 2.5 % PIB solution.

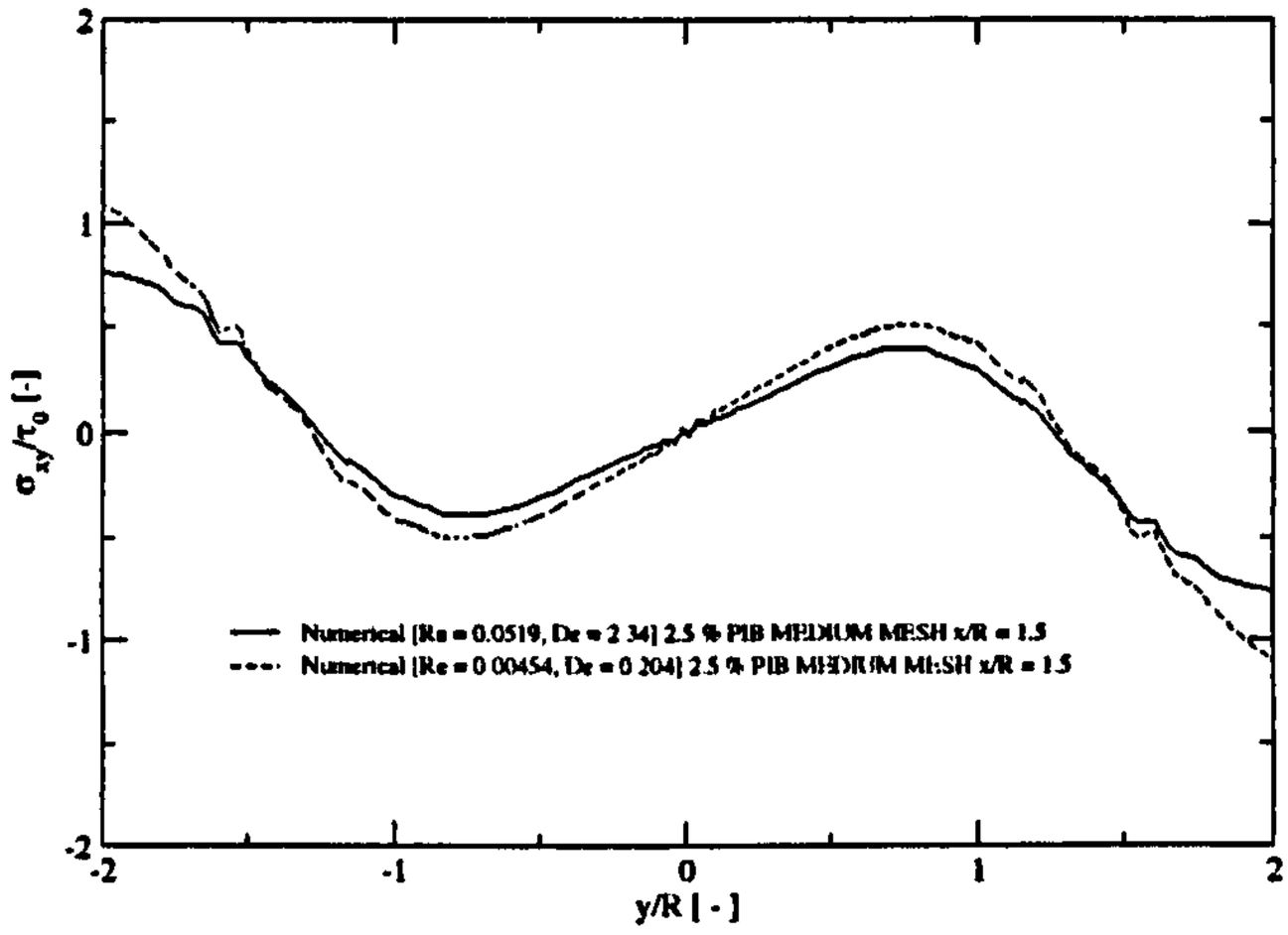

Figure 5.7: Comparison of predictions for the shear stress (σ_{xy}) values downstream of the first cylinder ($x/R = 1.5$), at $De = 0.225$ and $De = 2.34$, for the 2.5 % PIB solution.

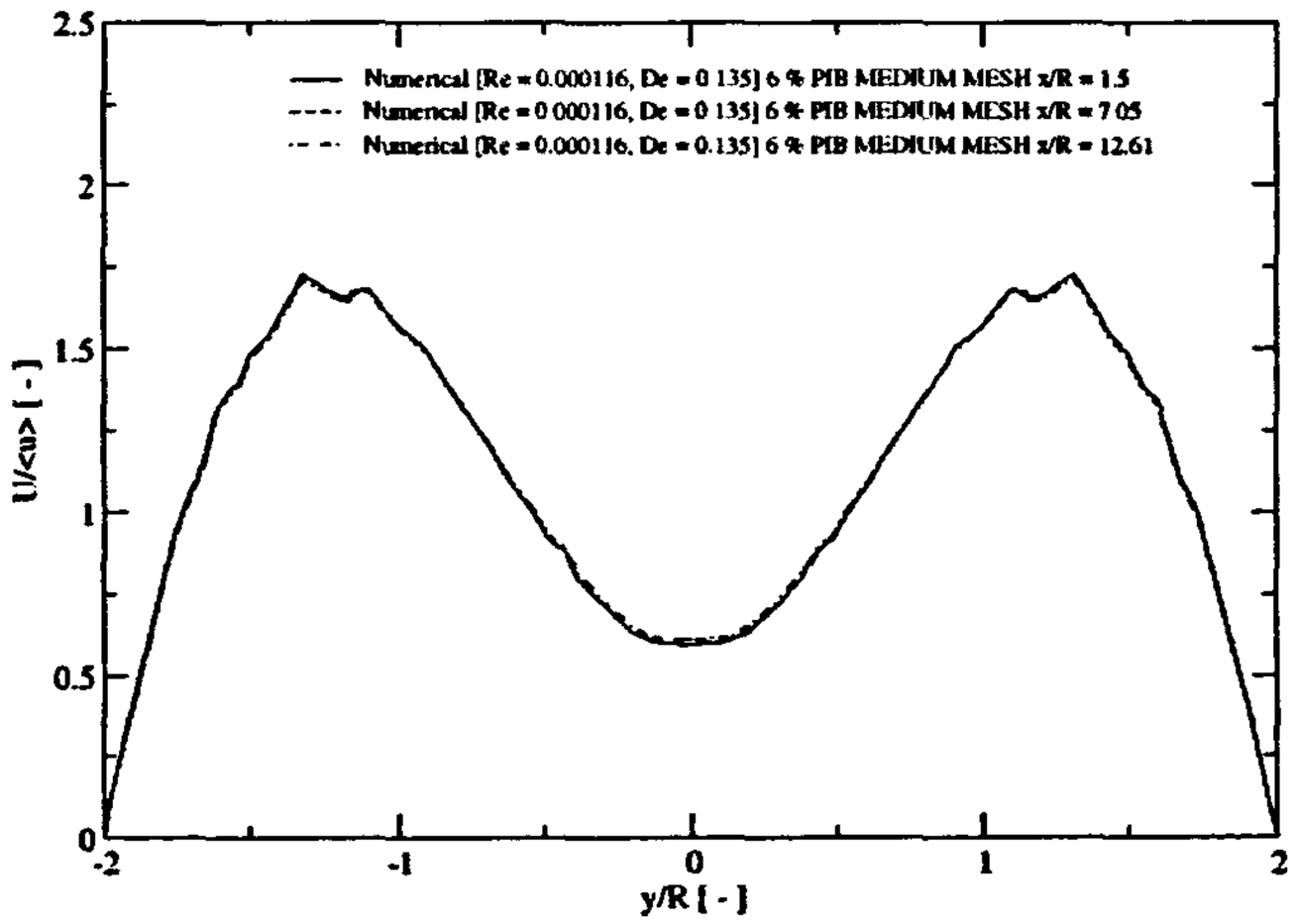

(a)

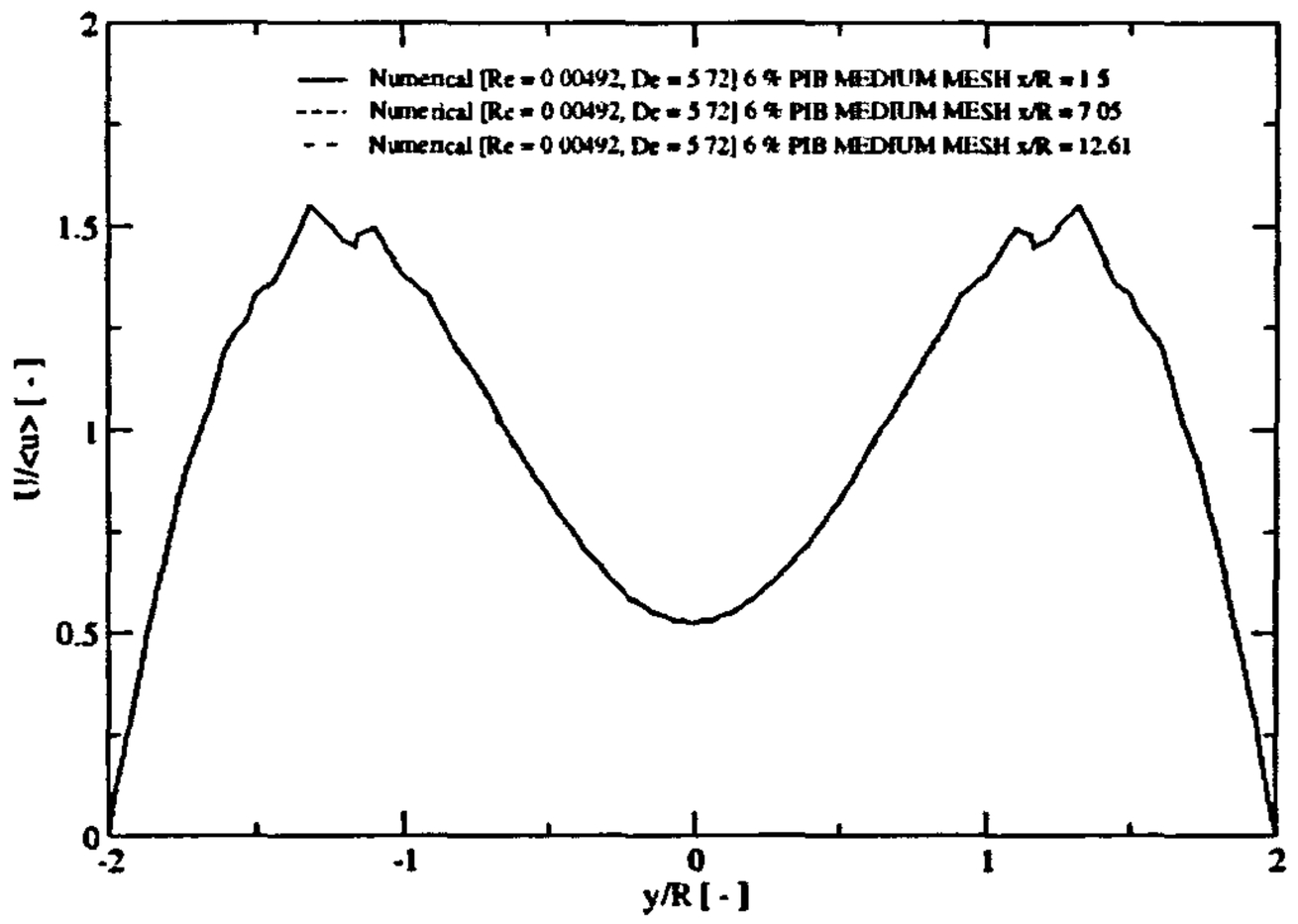

(b)

Figure 5.8: Comparison of predictions for the axial velocity (U) values downstream of each cylinder ($x/R = 1.5$, 7.05 and 12.61) at; (a) $De = 0.135$ and; (b) $De = 5.72$, for the 6 % PIB solution.

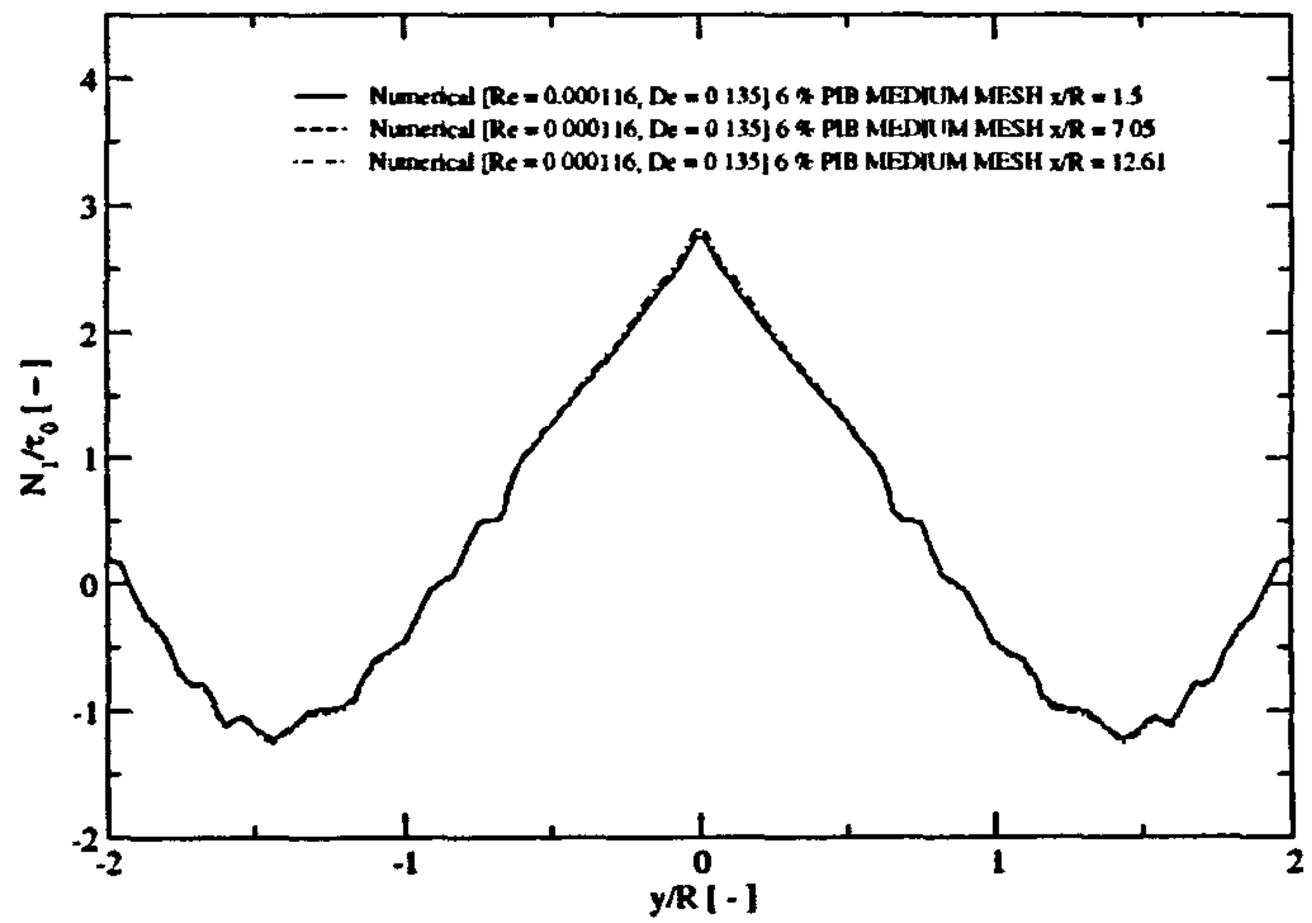

(a)

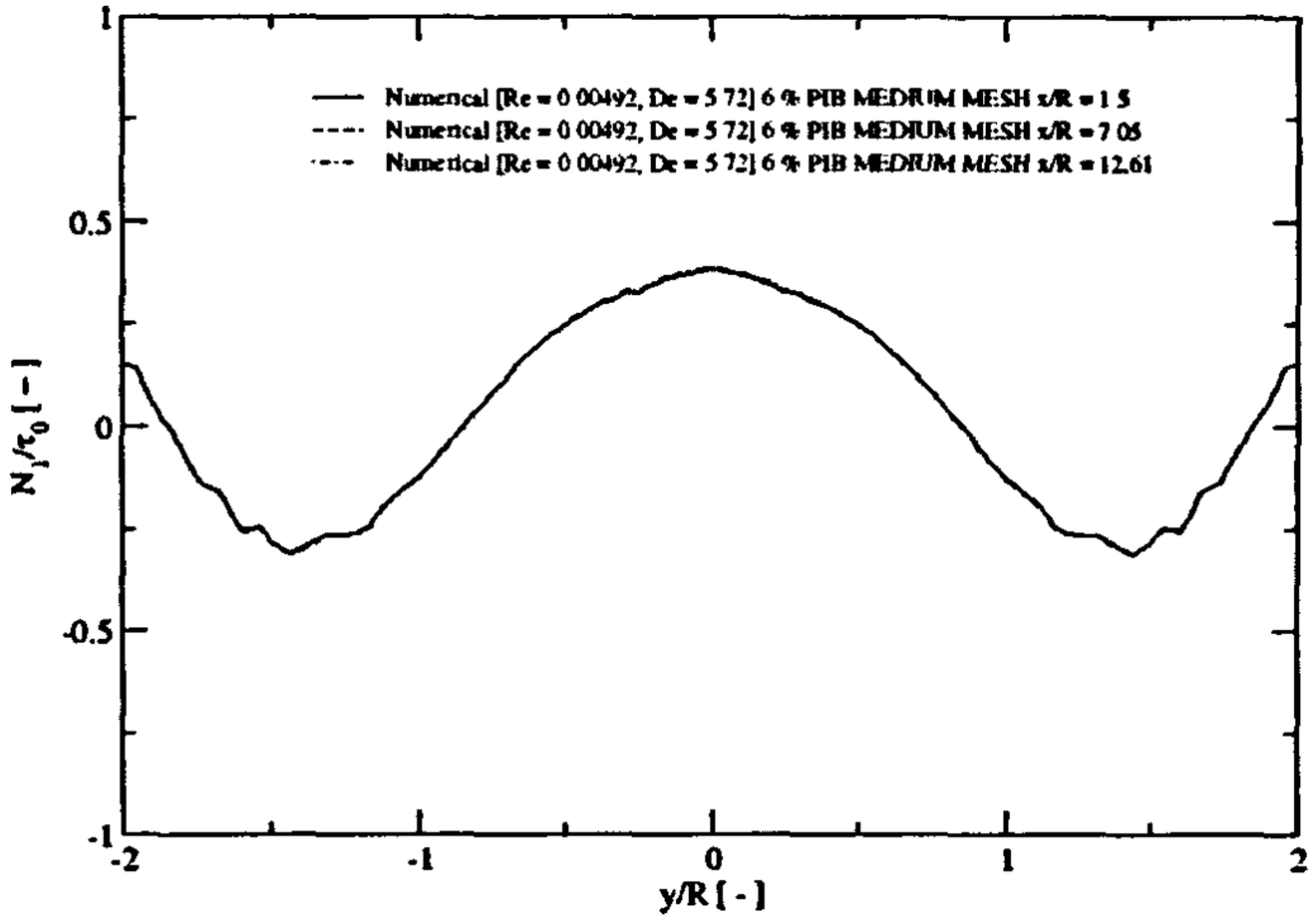

(b)

Figure 5.9: Comparison of predictions for the first normal stress difference (N_1) values downstream of each cylinder ($x/R = 1.5$, 7.05 and 12.61) at; (a) $De = 0.135$ and; (b) $De = 5.72$, for the 6 % PIB solution.

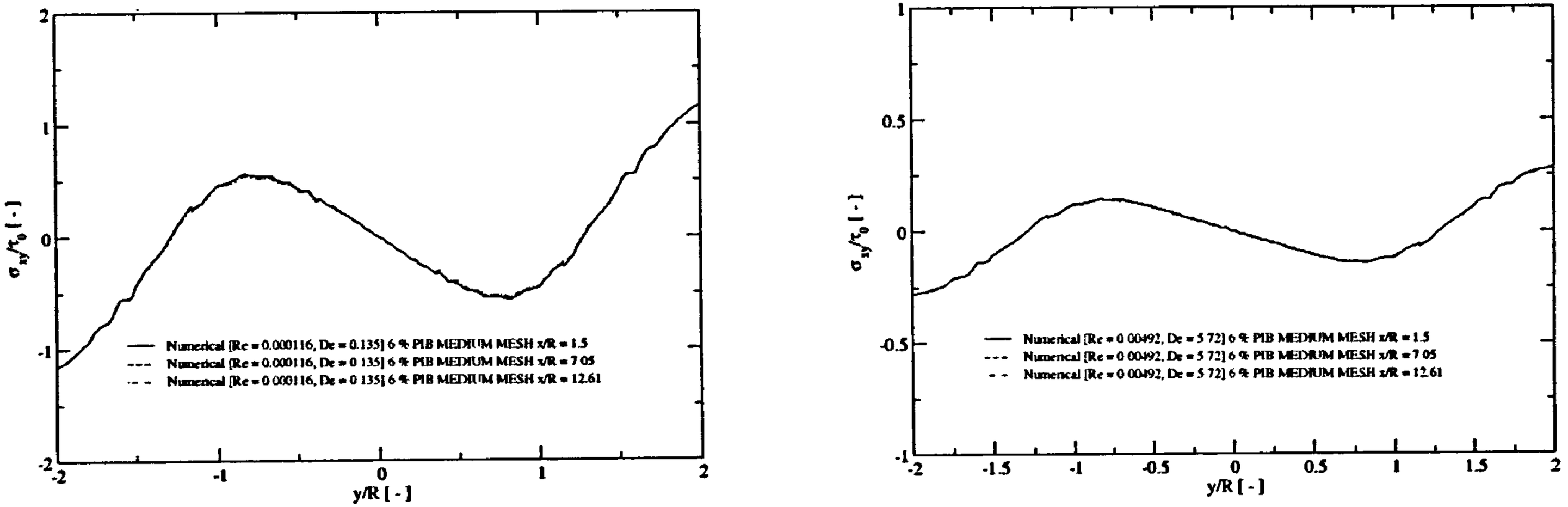

(a) (b)

Figure 5.10: Comparison of predictions for the shear stress (σ_{xy}) values downstream of each cylinder ($x/R = 1.5$, 7.05 and 12.61) at; (a) $De = 0.135$ and; (b) $De = 5.72$, for the 6 % PIB solution.

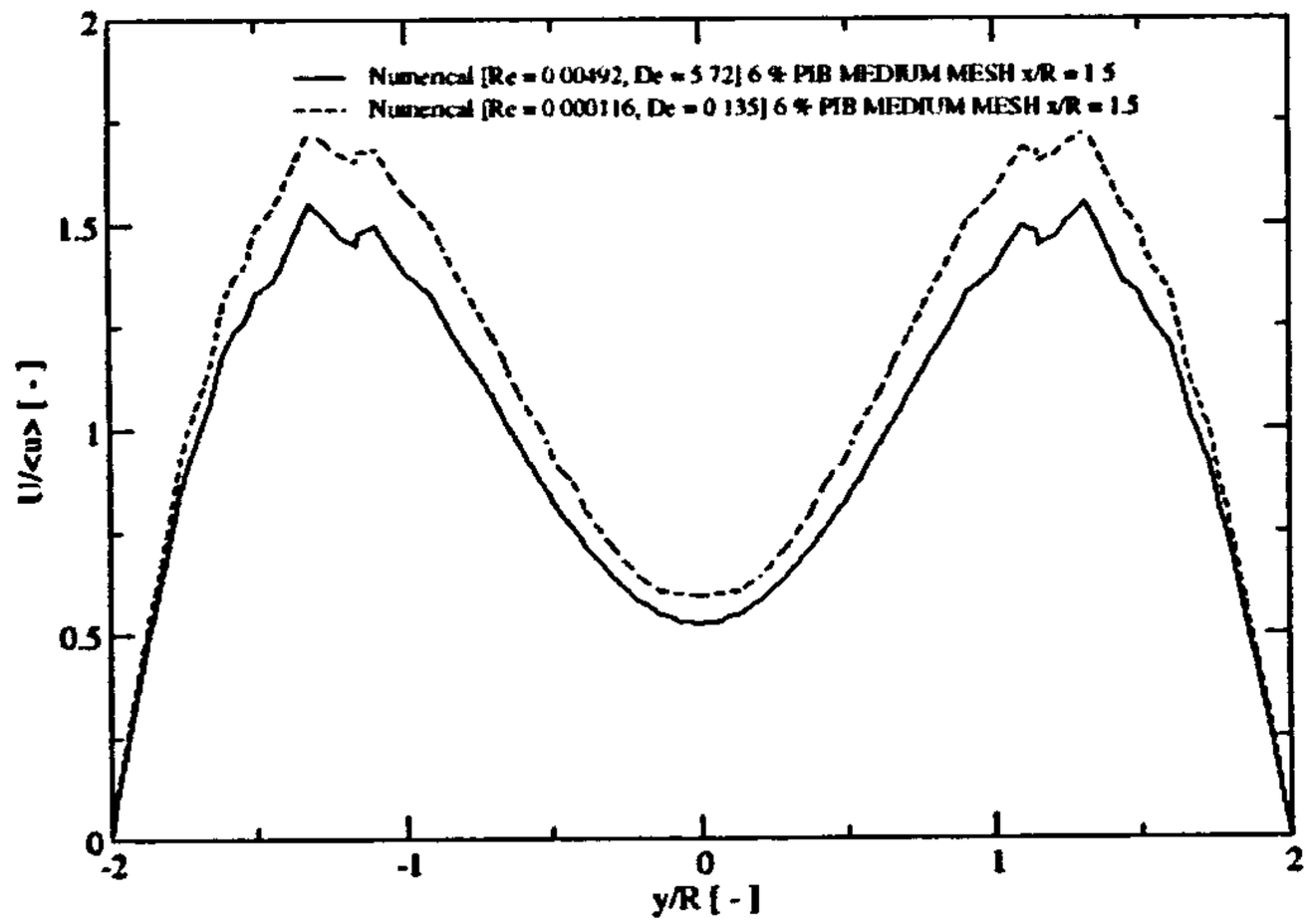

(a)

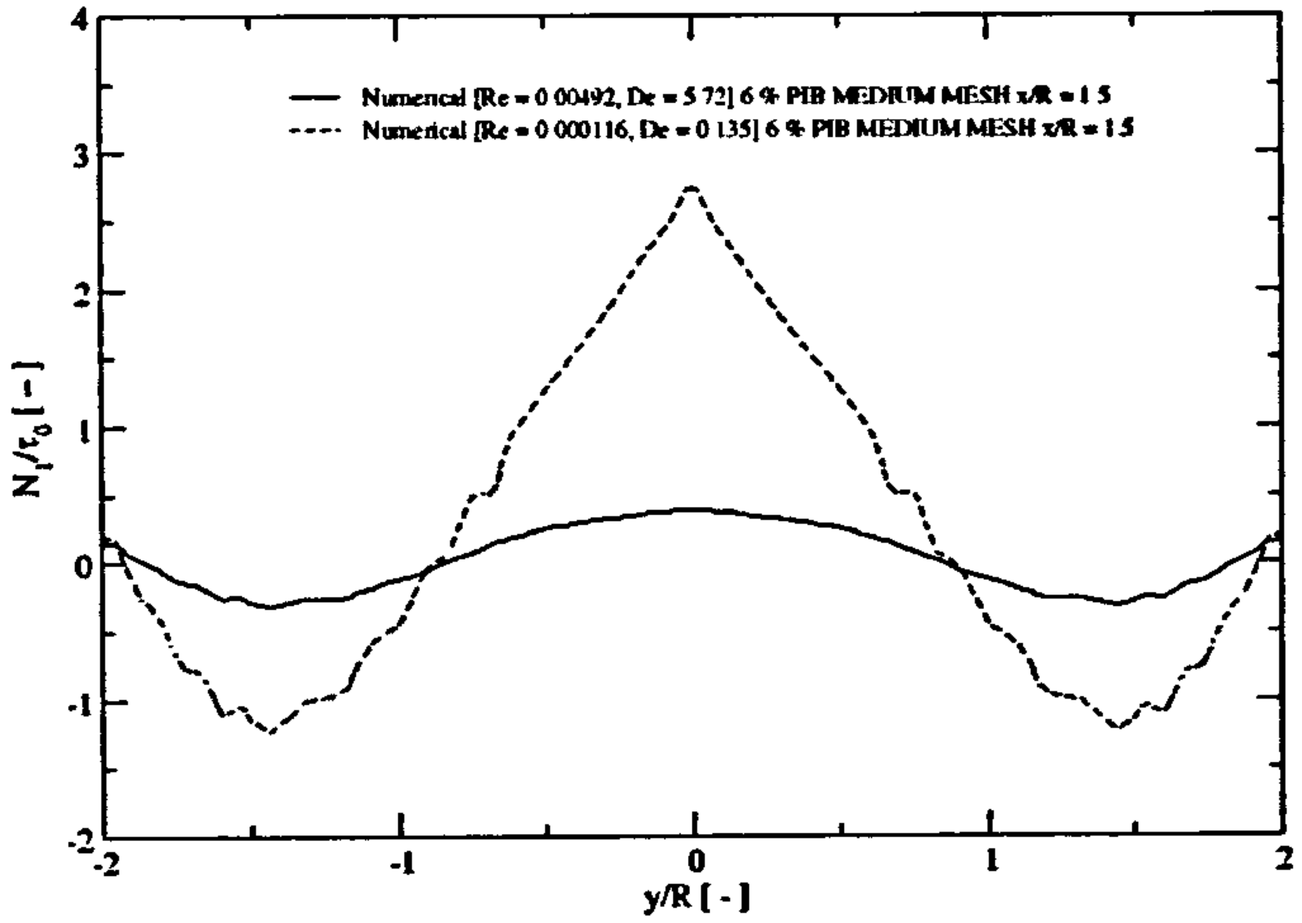

(b)

Figure 5.11: Comparison of predictions for the; (a) axial velocity (U) and; (b) first normal stress difference (N_1) values, downstream of the first cylinder ($x/R = 1.5$), at $De = 0.135$ and $De = 5.72$, for the 6 % PIB solution.

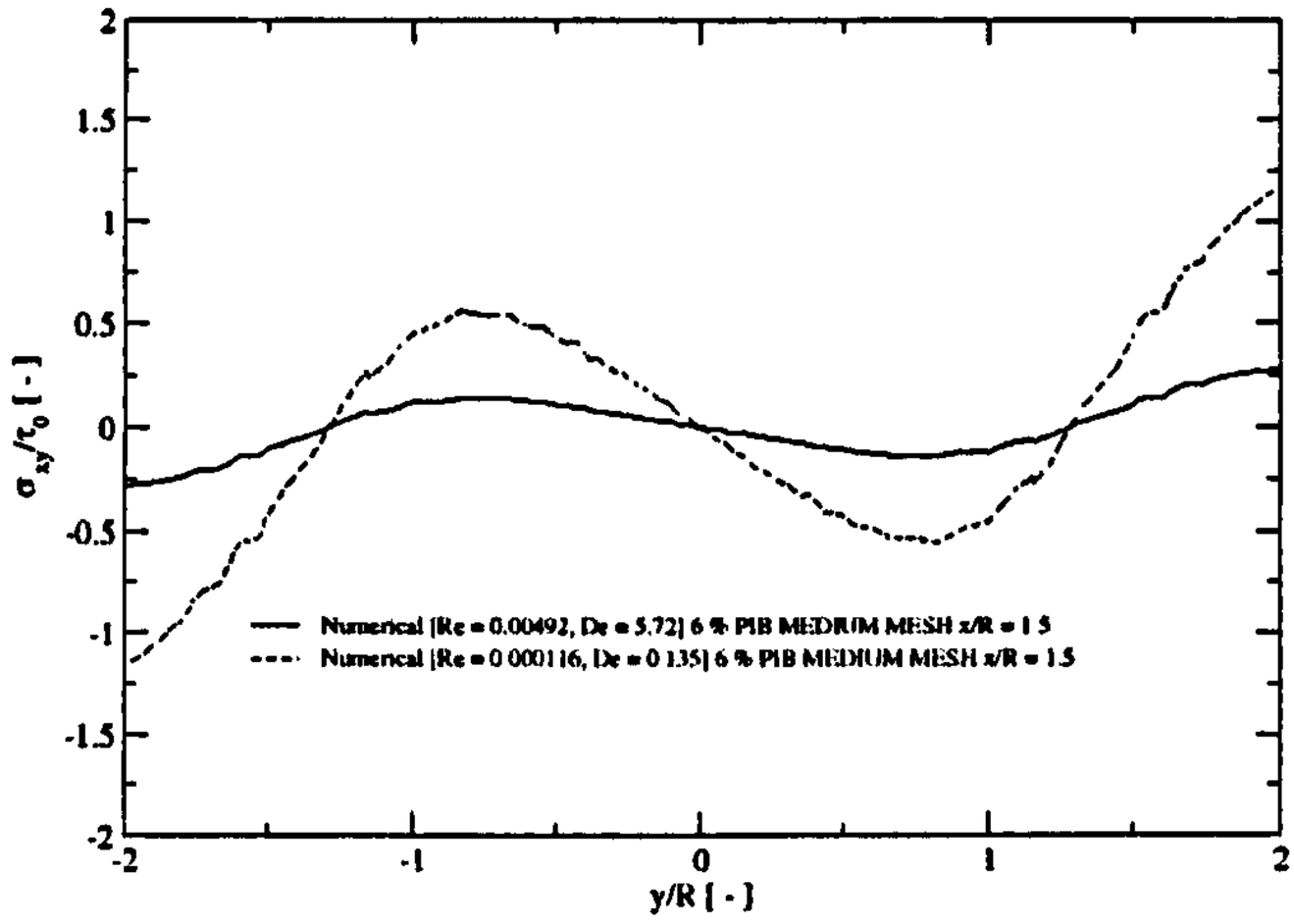

Figure 5.12: Comparison of predictions for the shear stress (σ_{xy}) values downstream of the first cylinder ($x/R = 1.5$), at $De = 0.135$ and $De = 5.72$, for the 6 % PIB solution.

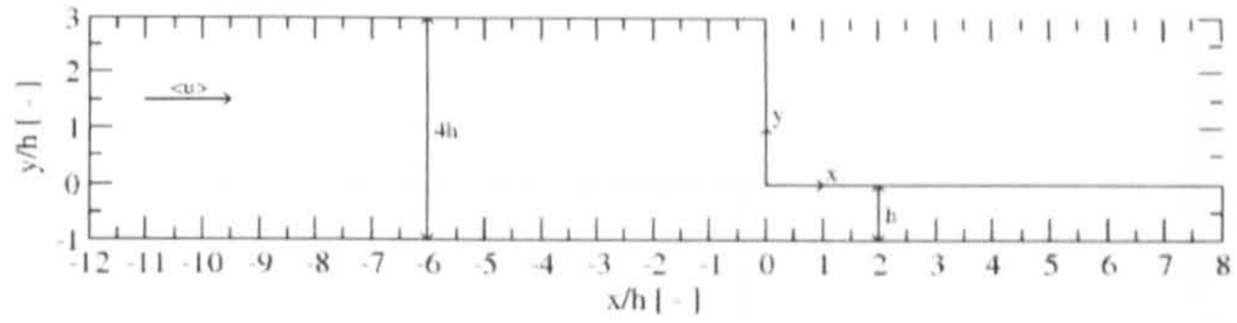

Figure 5.13: Schematic representation of the cross sectional view of the contraction flow geometry. Height (h) of the small channel is 0.00225 m, height of the large channel is $4h$ and the total length in the x direction in 0.045 m. The mean flow is in the positive x direction.

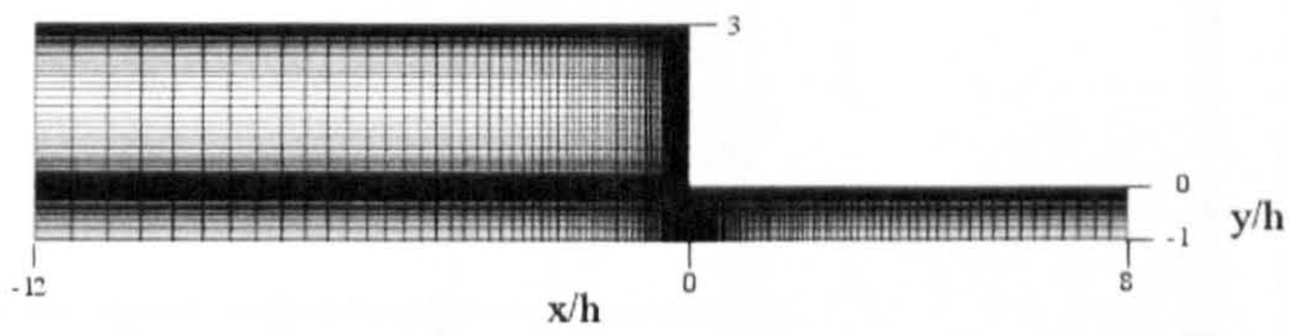

Figure 5.14: The finite volume mesh through the contraction flow geometry, used for all contraction flow simulations in this chapter, containing 9600 cells.

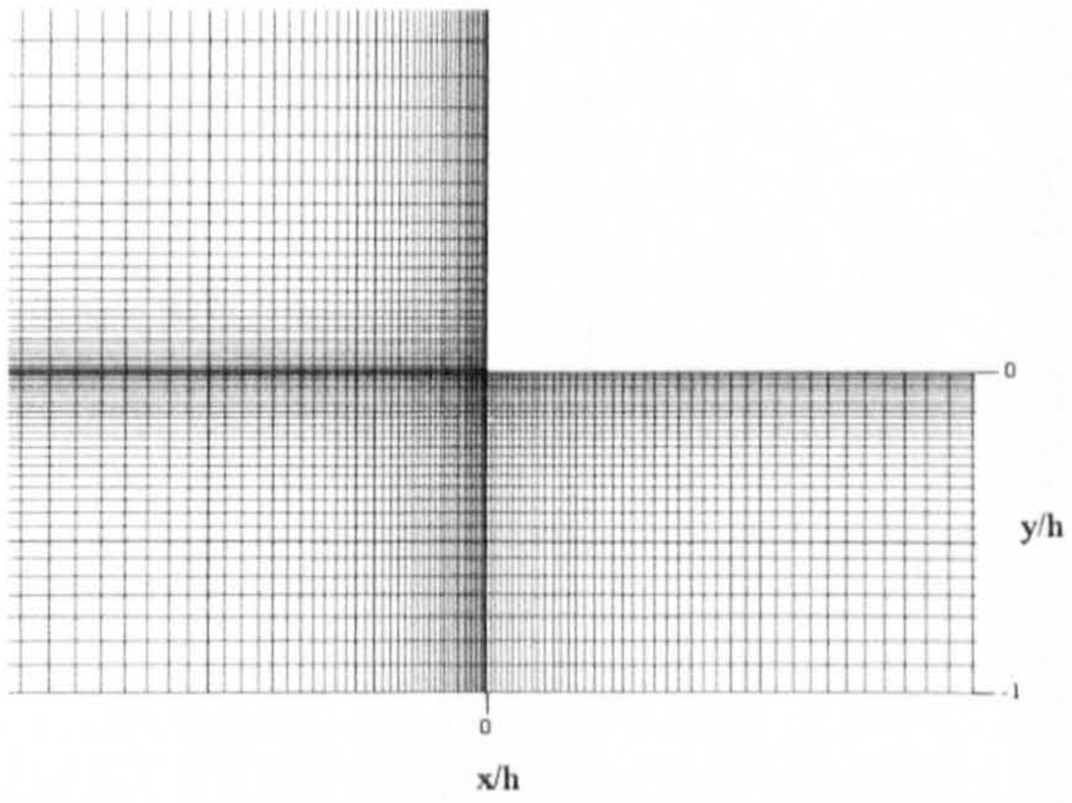

Figure 5.15: A closer view of the finite volume mesh through the contraction flow geometry.

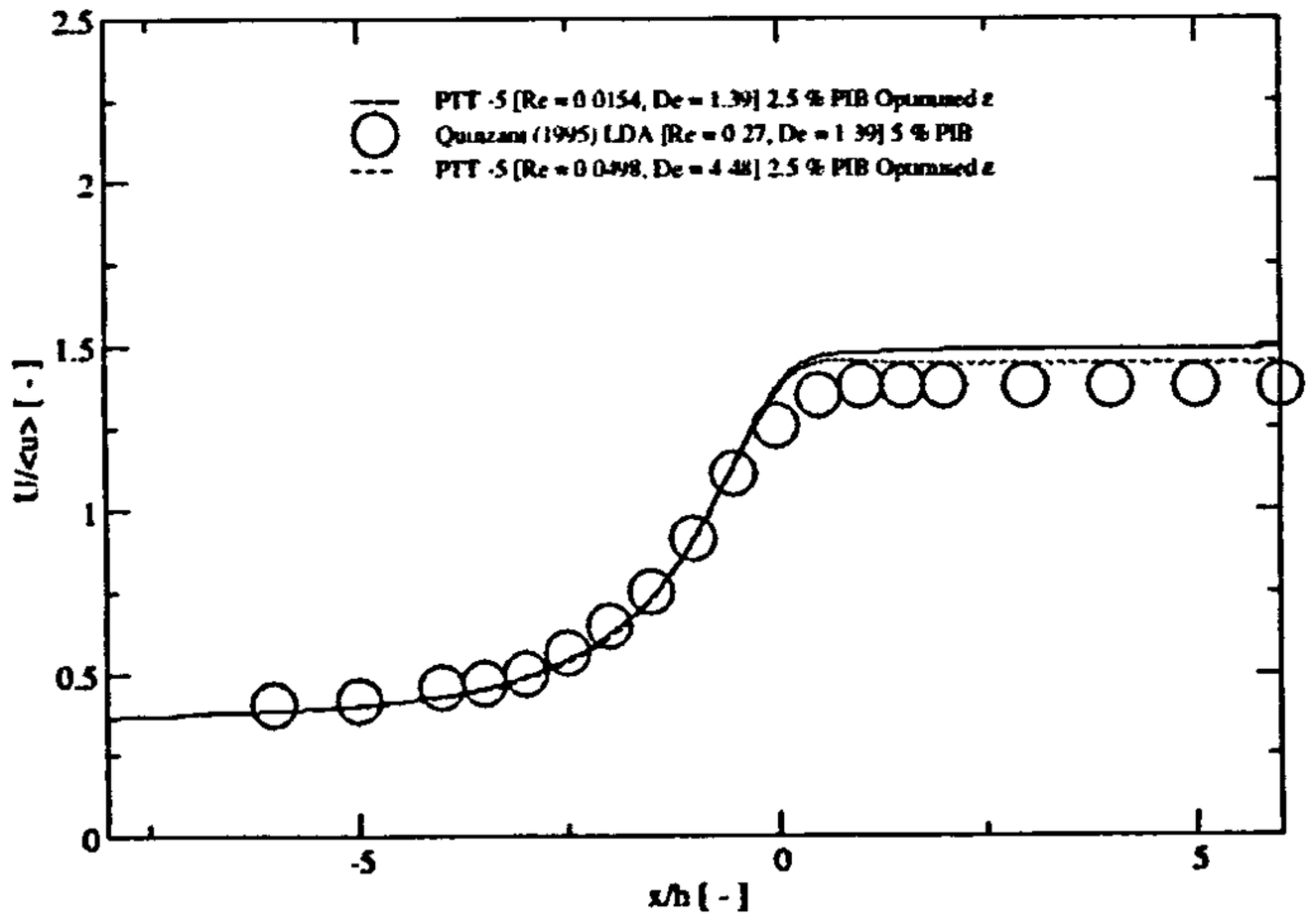

(a)

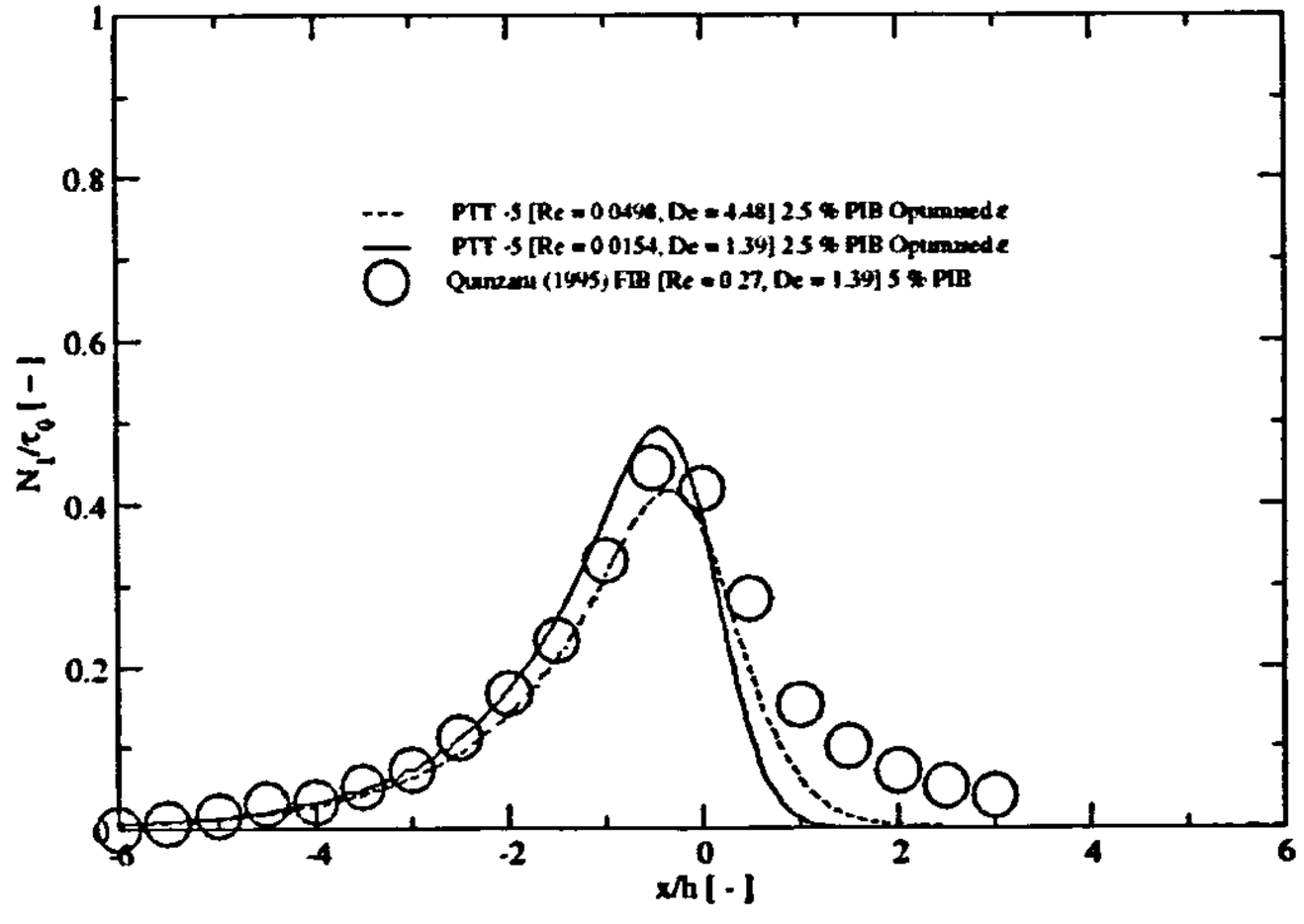

(b)

Figure 5.16: Comparison of predictions for the; (a) axial velocity (U) and; (b) first normal stress difference (N_1) values, upstream of, and through the contraction, at $y/h = -1$ and $De = 1.39$ and 4.48, for the 2.5 % PIB solution with measurement data of Quinzani et al. (1995) for the; (a) axial velocity (U) and; (b) first normal stress difference (N_1) values, respectively, at $y/h = -1$ and $De = 1.39$, for the 5 % PIB solution.

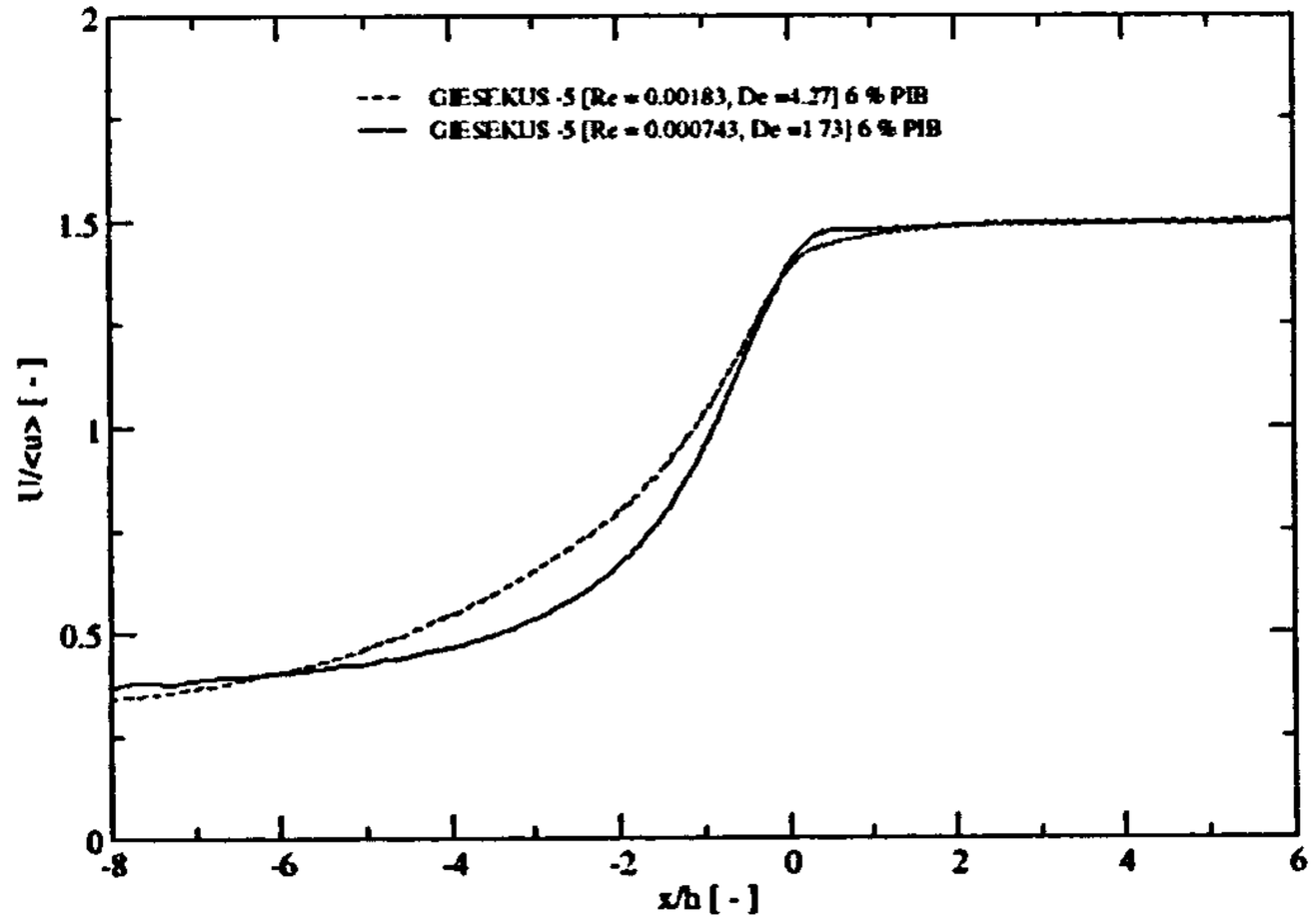

(a)

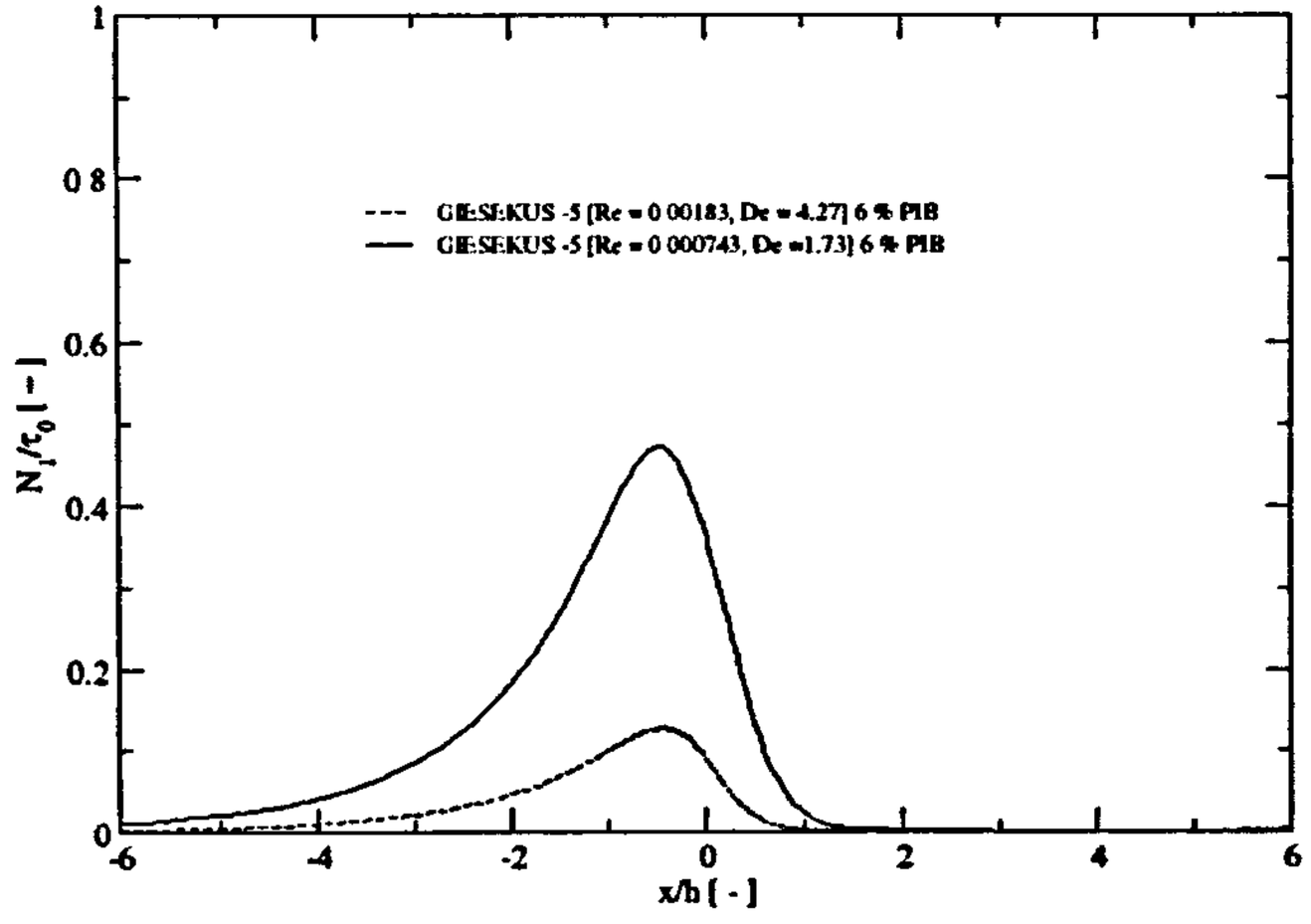

(b)

Figure 5.17: Comparison of predictions for the; (a) axial velocity (U) and; (b) first normal stress difference (N_1) values, upstream of, and through the contraction at $y/h = -1$, at $De = 1.73$ and 4.27, for the 6 % PIB solution.

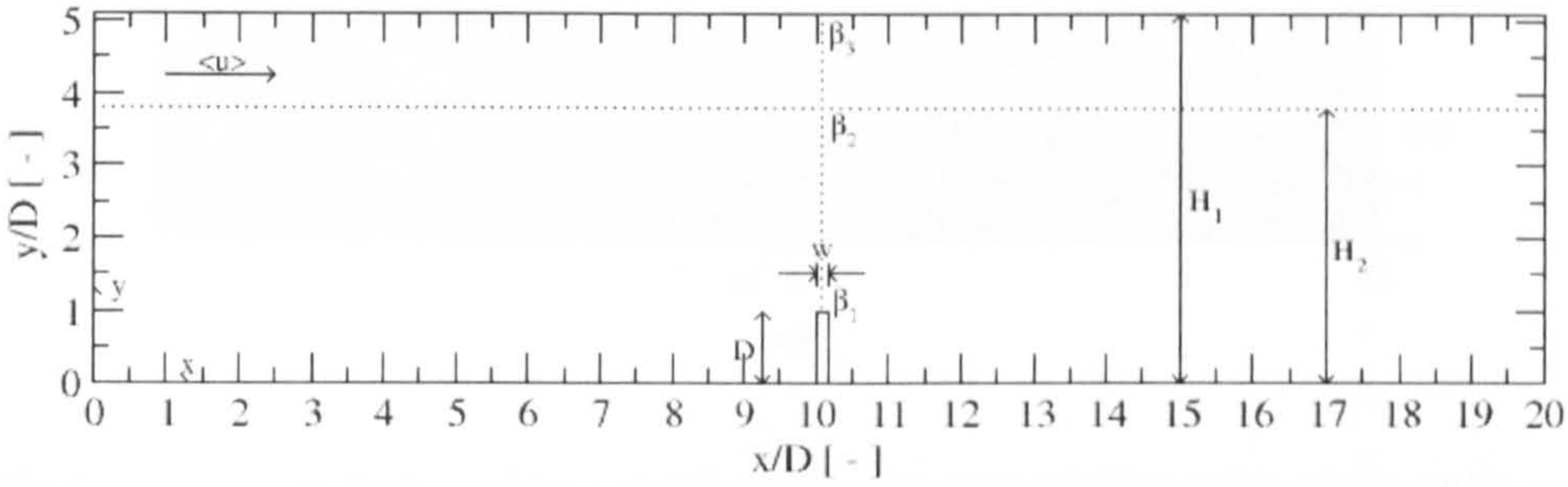

Figure 5.18: Schematic representation of the cross sectional view of the symmetrically confined impeller blade geometry. Blade height, $D = 0.0065\ m$ and width, $w = 0.0001\ m$. Maximum height, $H_1 = 0.03325\ m$, minimum height $H_2 = 0.02475\ m$ and total length, $x = 0.130\ m$. The mean flow is in the positive x direction.

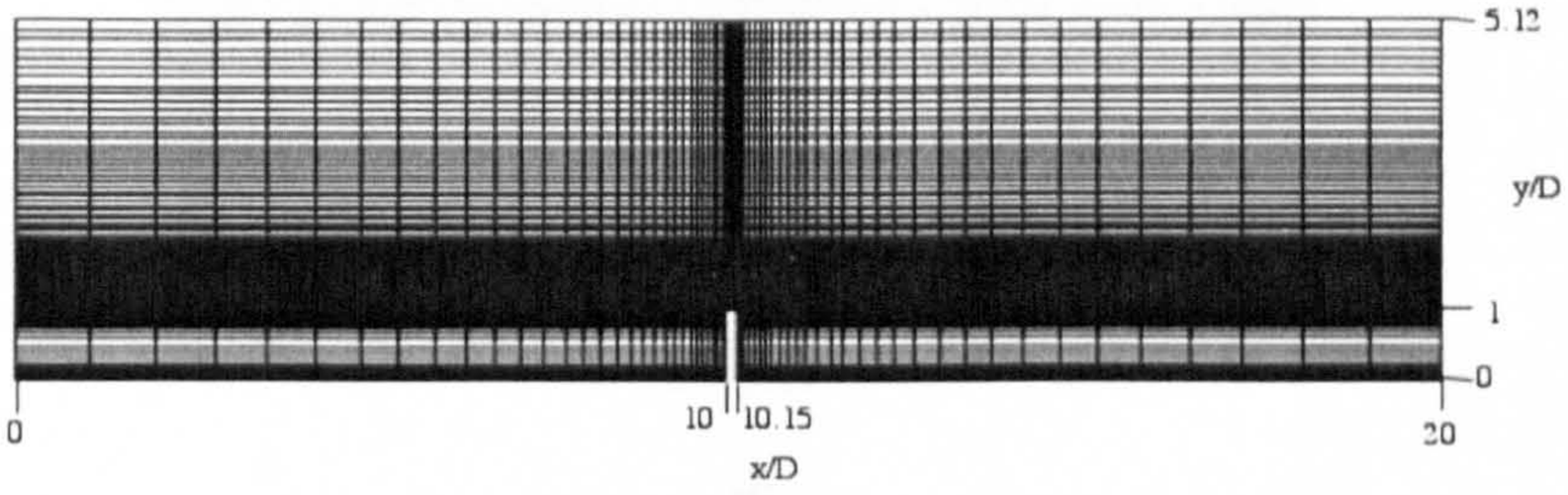

Figure 5.19: The finite volume mesh geometry surrounding a symmetrically confined impeller blade, with $H_1 = 0.03325\ m$, containing 5680 cells.

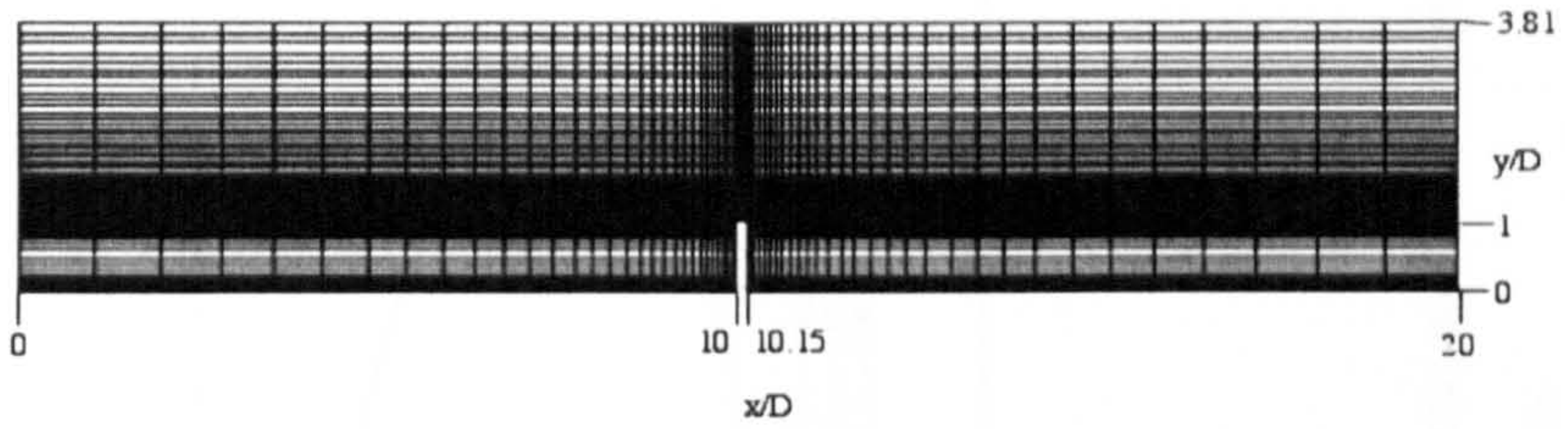

Figure 5.20: The finite volume mesh geometry surrounding a symmetrically confined impeller blade, with $H_2 = 0.02475\ m$, containing 4400 cells.

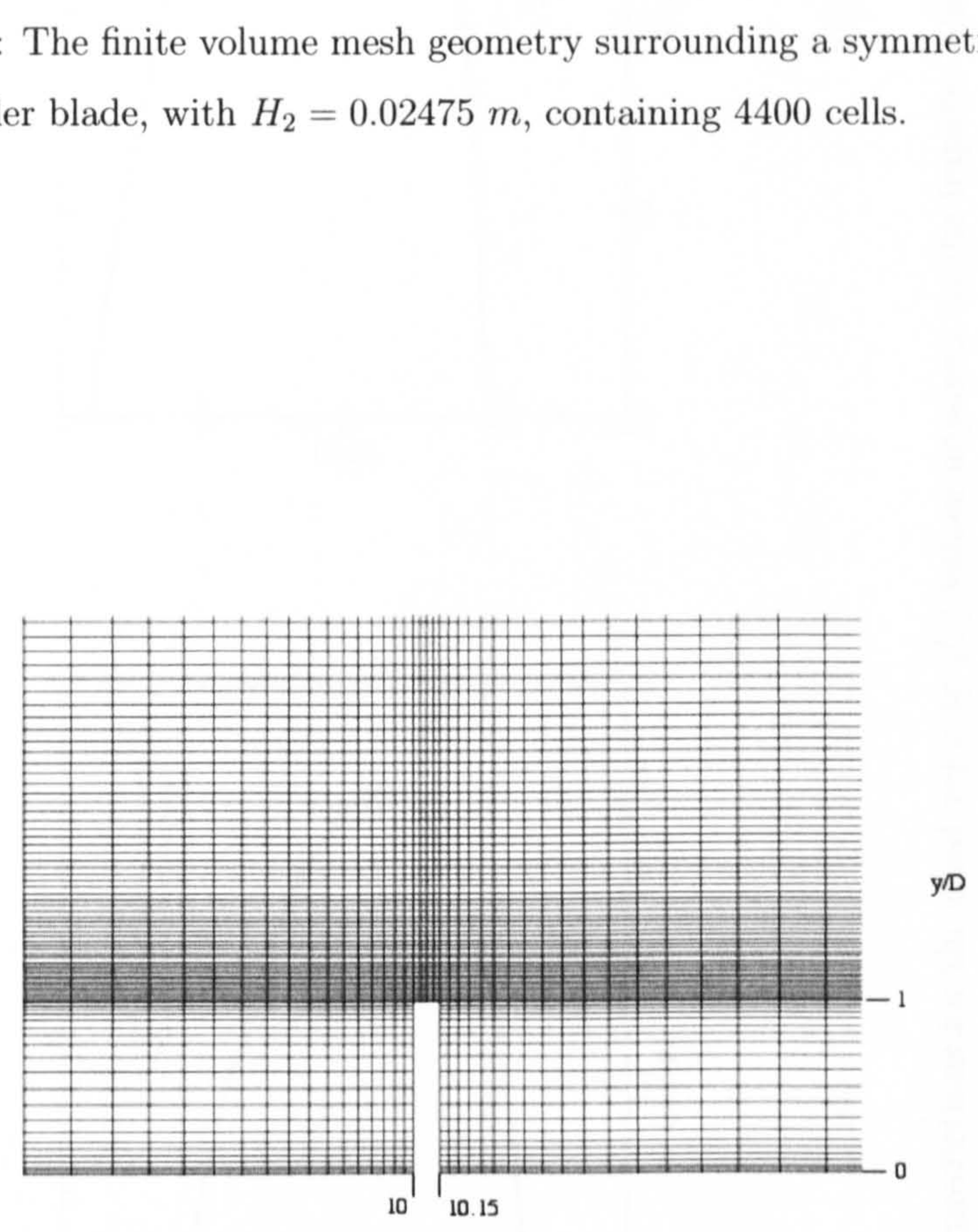

Figure 5.21: A closer view of the finite volume mesh geometry surrounding a symmetrically confined impeller blade.

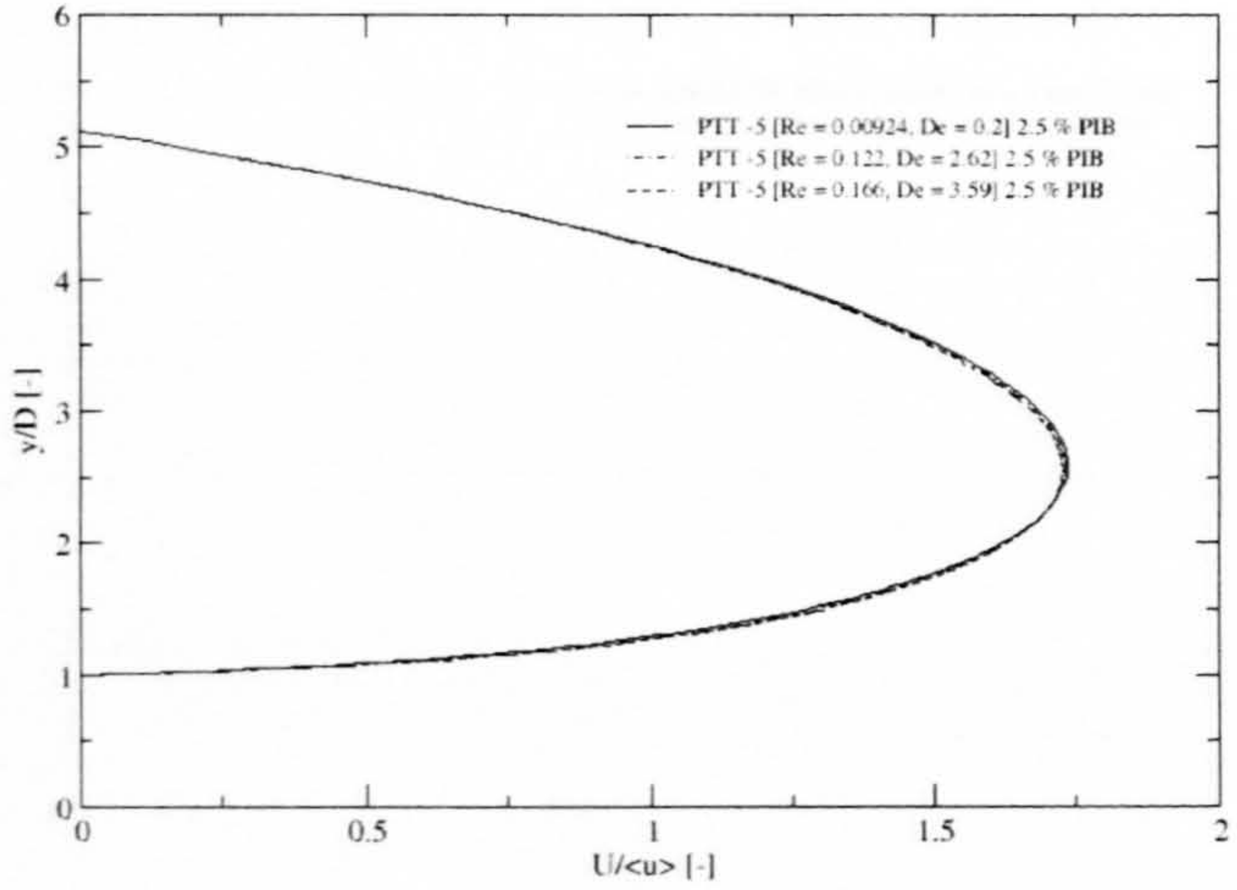

(a)

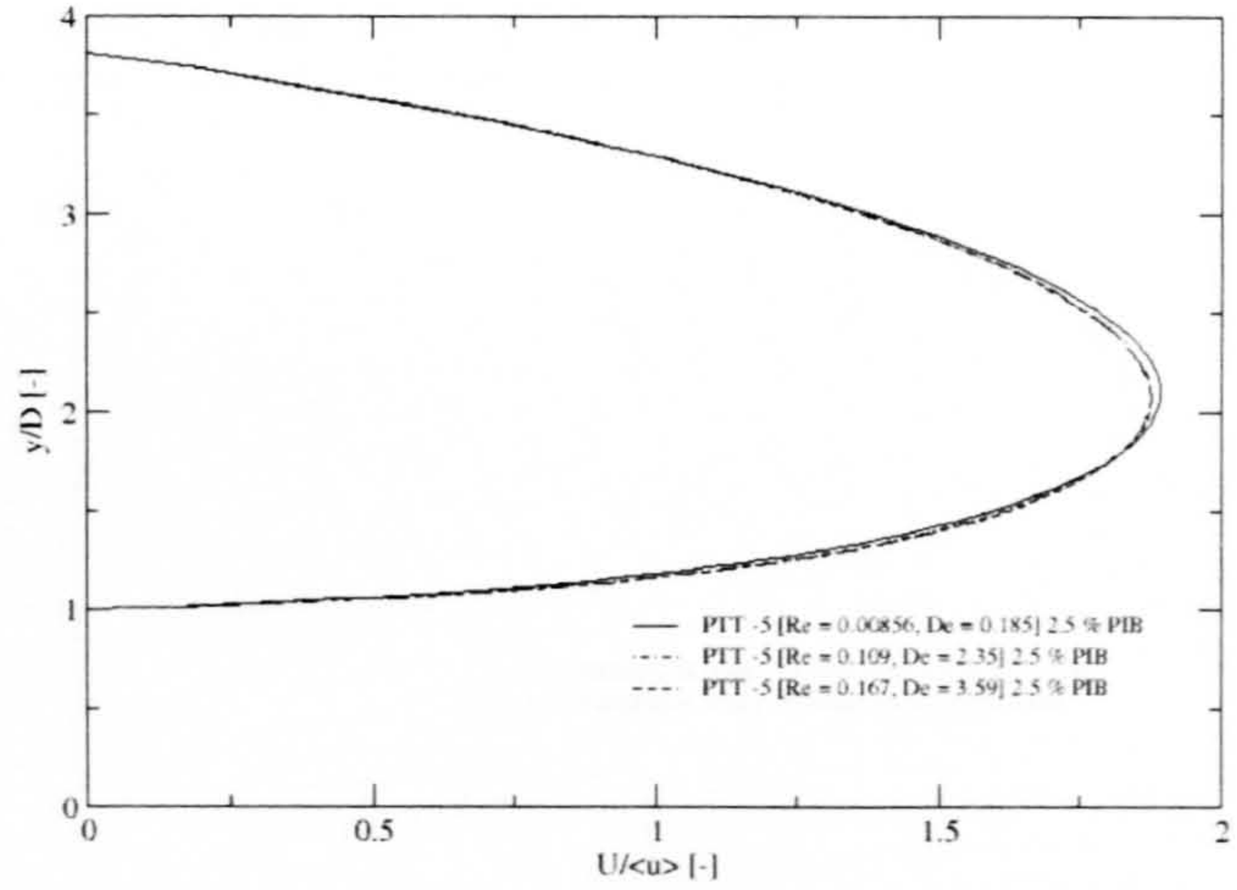

(b)

Figure 5.22: Comparison of predictions for the axial velocity (U) values adjacent to the impeller blade tip, along the cross-sections; (a) β_1 to β_3, for $De = 0.199$ to 3.59 and; (b) β_1 to β_2, for $De = 0.185$ to 3.59, both for the 2.5 % PIB solution.

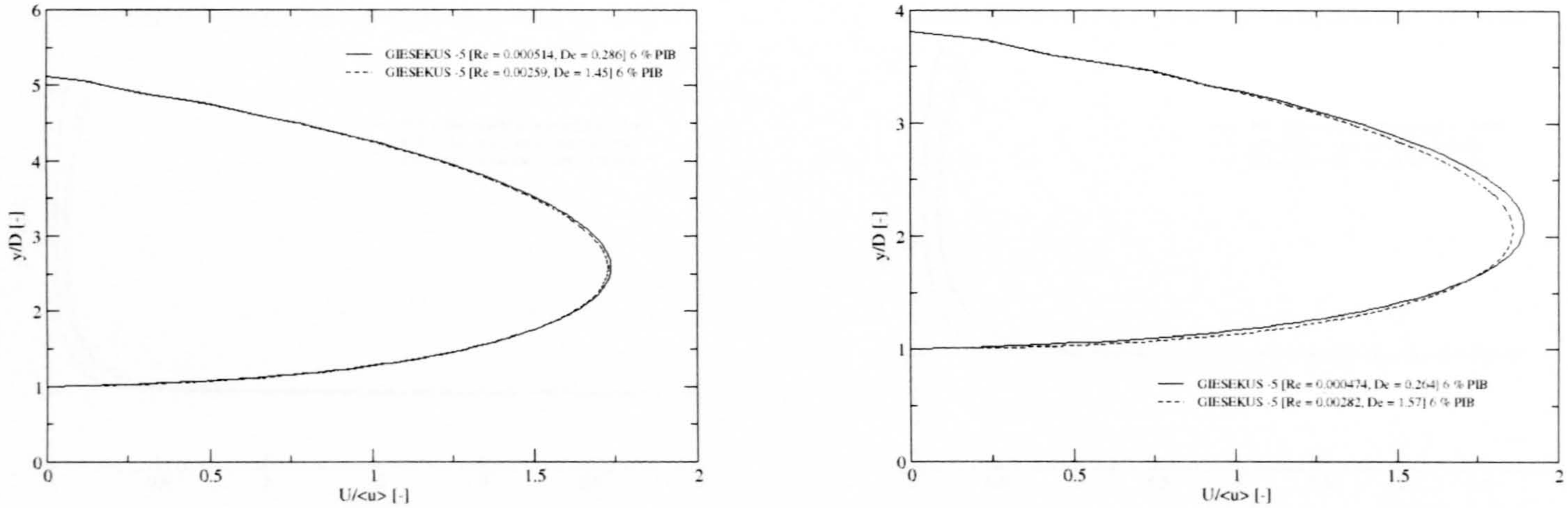

(a) (b)

Figure 5.23: Comparison of predictions for the axial velocity (U) values adjacent to the impeller blade tip, along the cross-sections; (a) β_1 to β_3, for $De = 0.286$ to 1.45 and; (b) β_1 to β_2, for $De = 0.264$ to 1.57, both for the 6 % PIB solution.

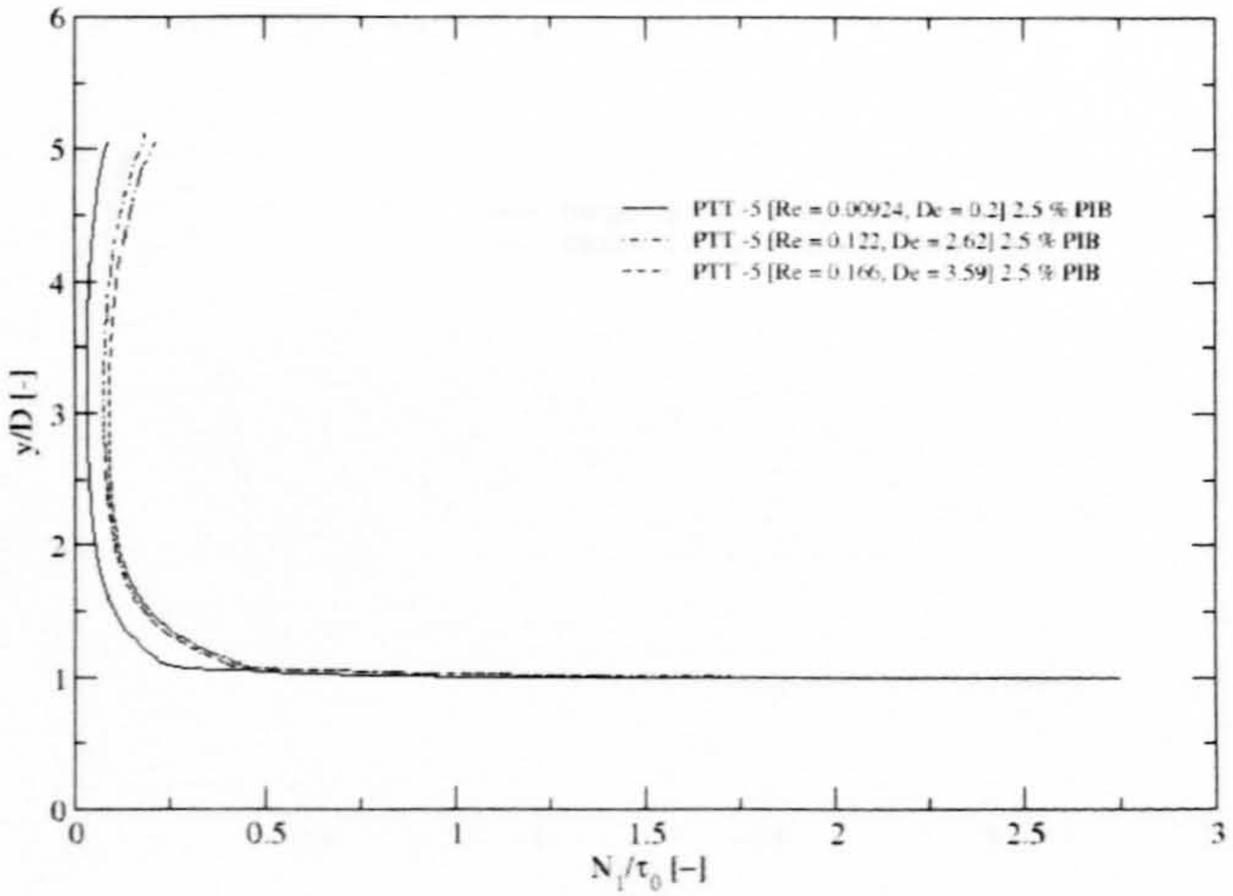

(a)

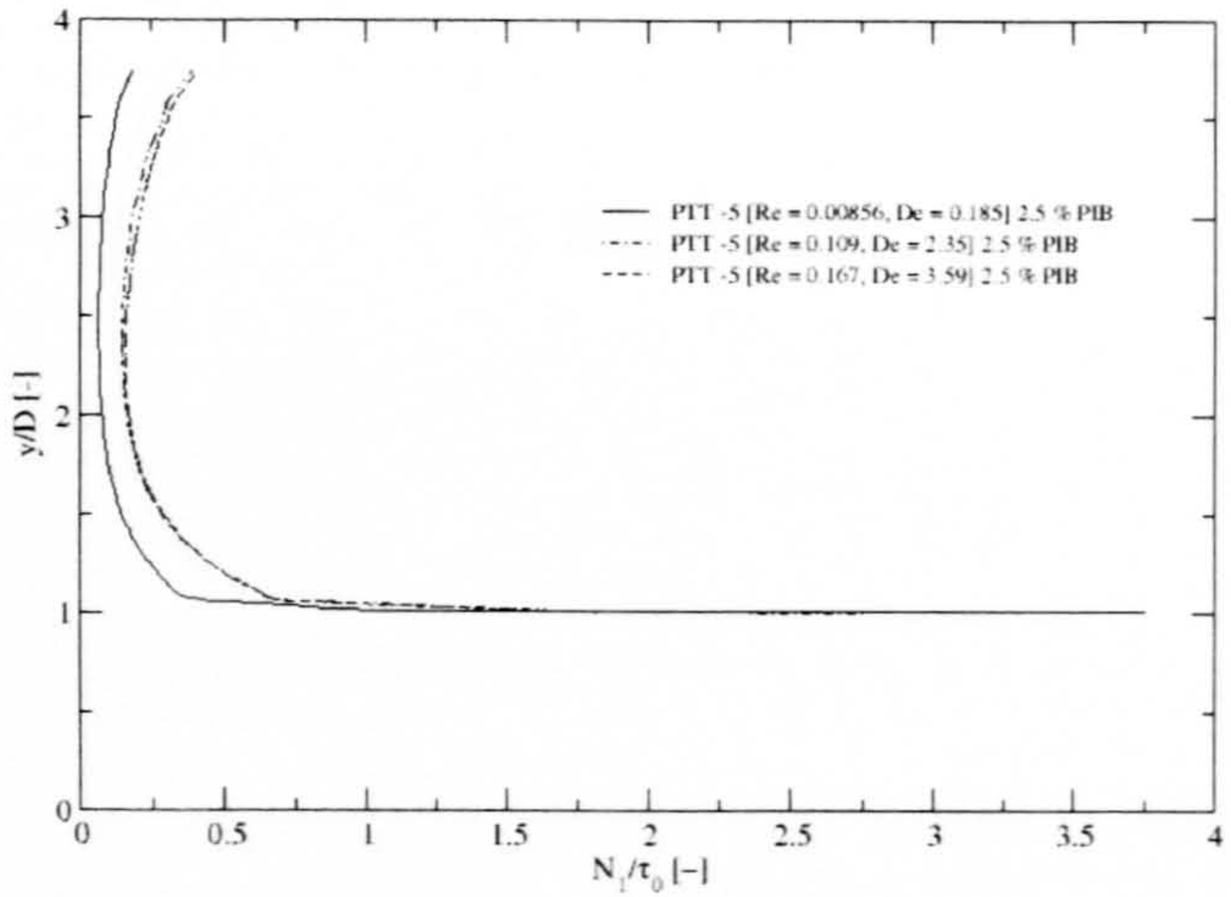

(b)

Figure 5.24: Comparison of predictions for the first normal stress difference (N_1) values adjacent to the impeller blade tip, along the cross-sections; (a) β_1 to β_3, for $De = 0.199$ to 3.59 and; (b) β_1 to β_2, for $De = 0.185$ to 3.59, both plots for the 2.5 % PIB solution.

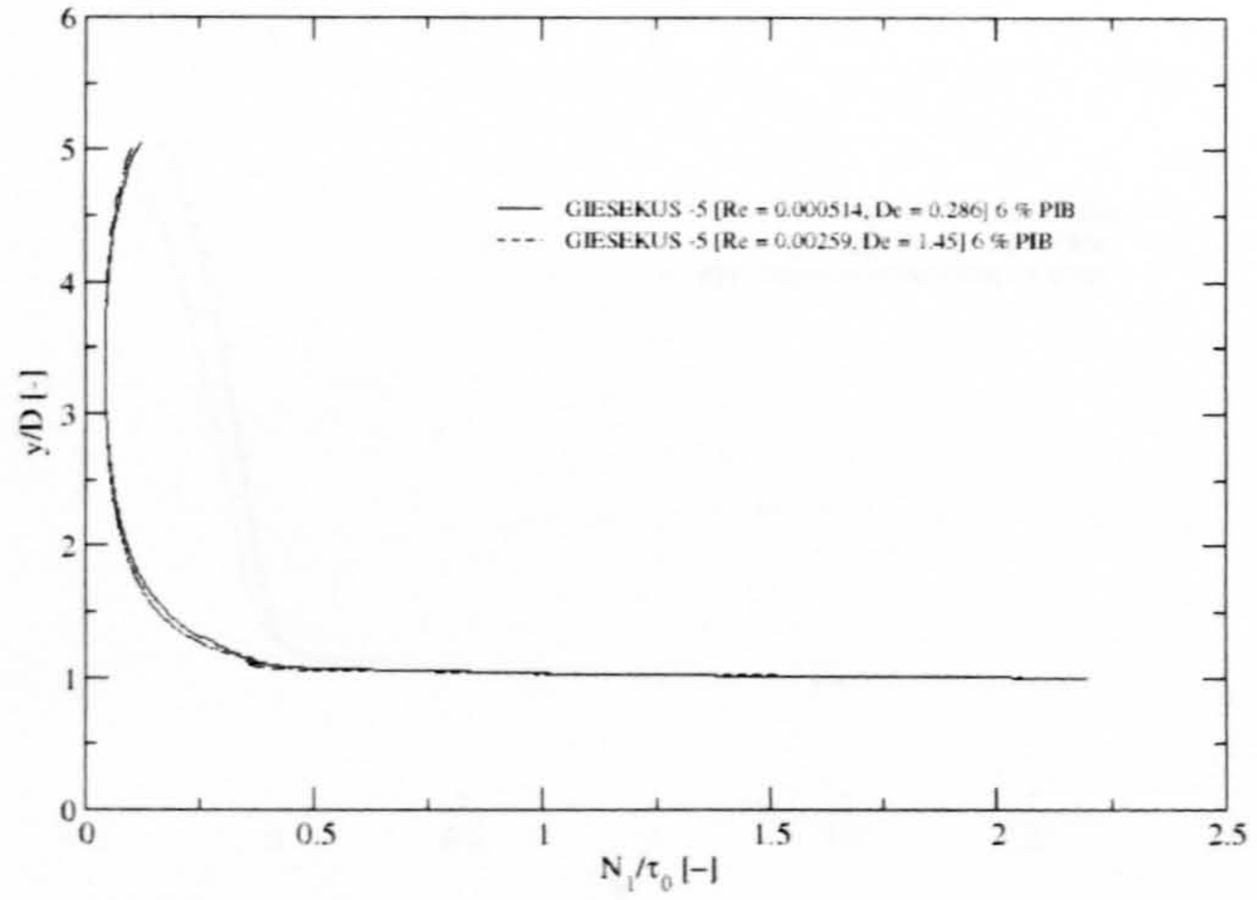

(a)

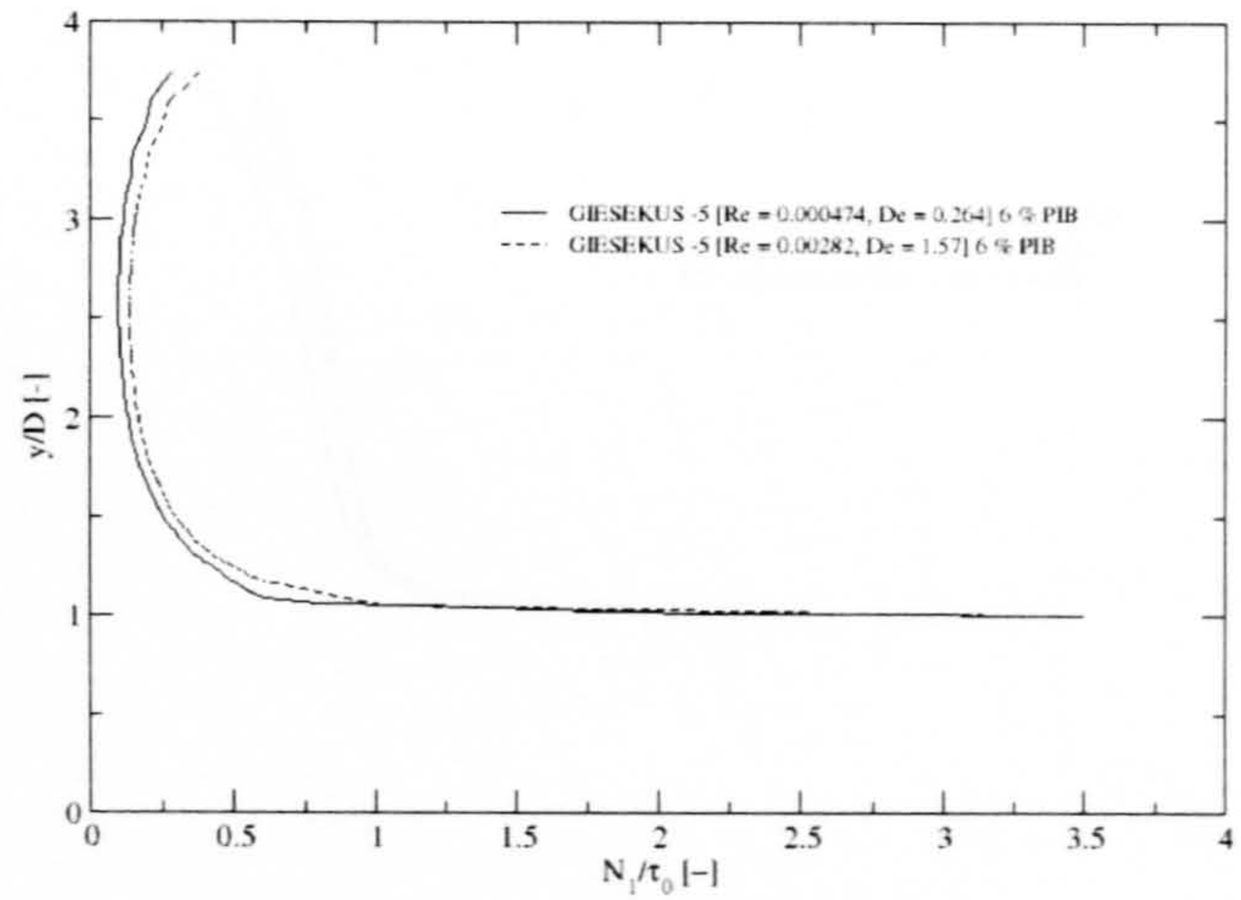

(b)

Figure 5.25: Comparison of predictions for the first normal stress difference (N_1) values adjacent to the impeller blade tip, along the cross-sections; (a) β_1 to β_3, for $De = 0.286$ to 1.45 and; (b) β_1 to β_2, for $De = 0.264$ to 1.57, both for the 6 % PIB solution.

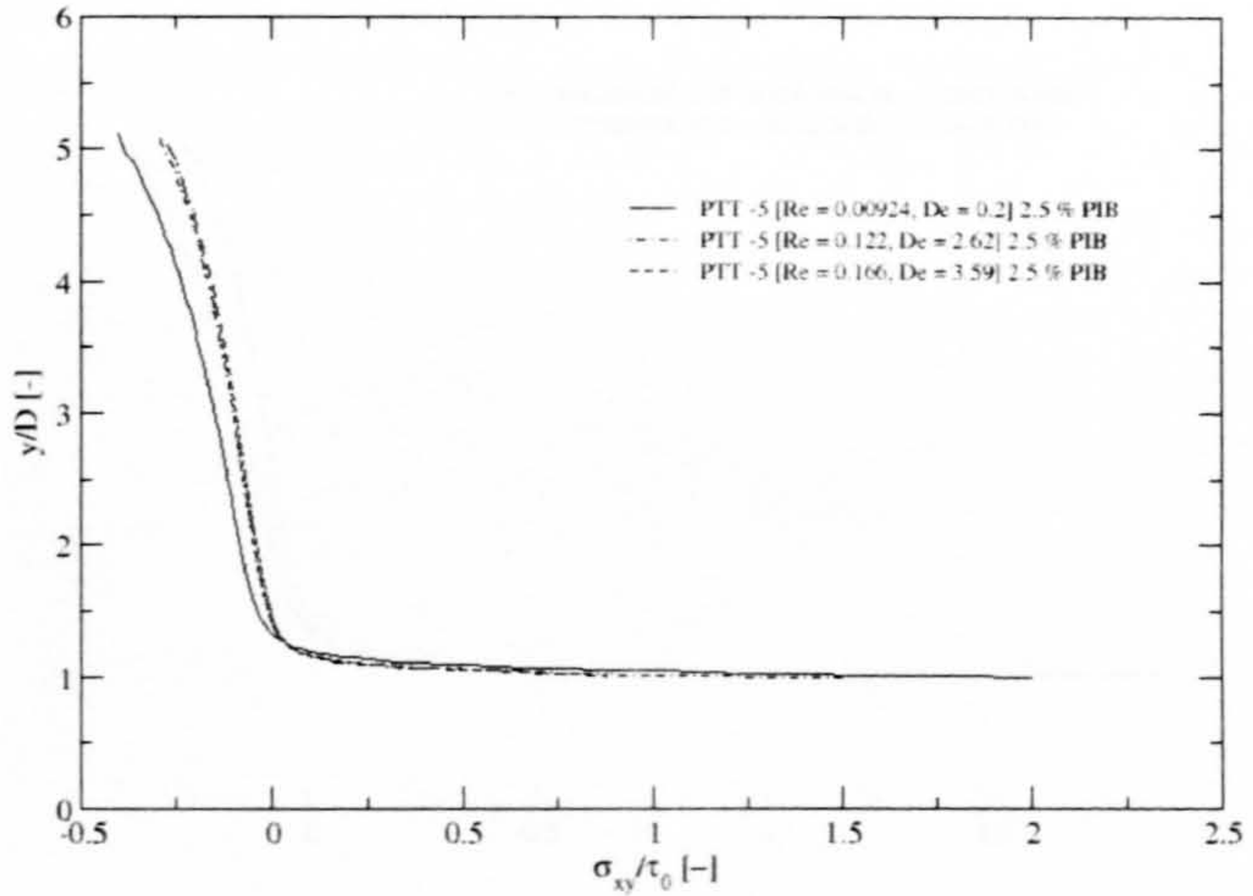

(a)

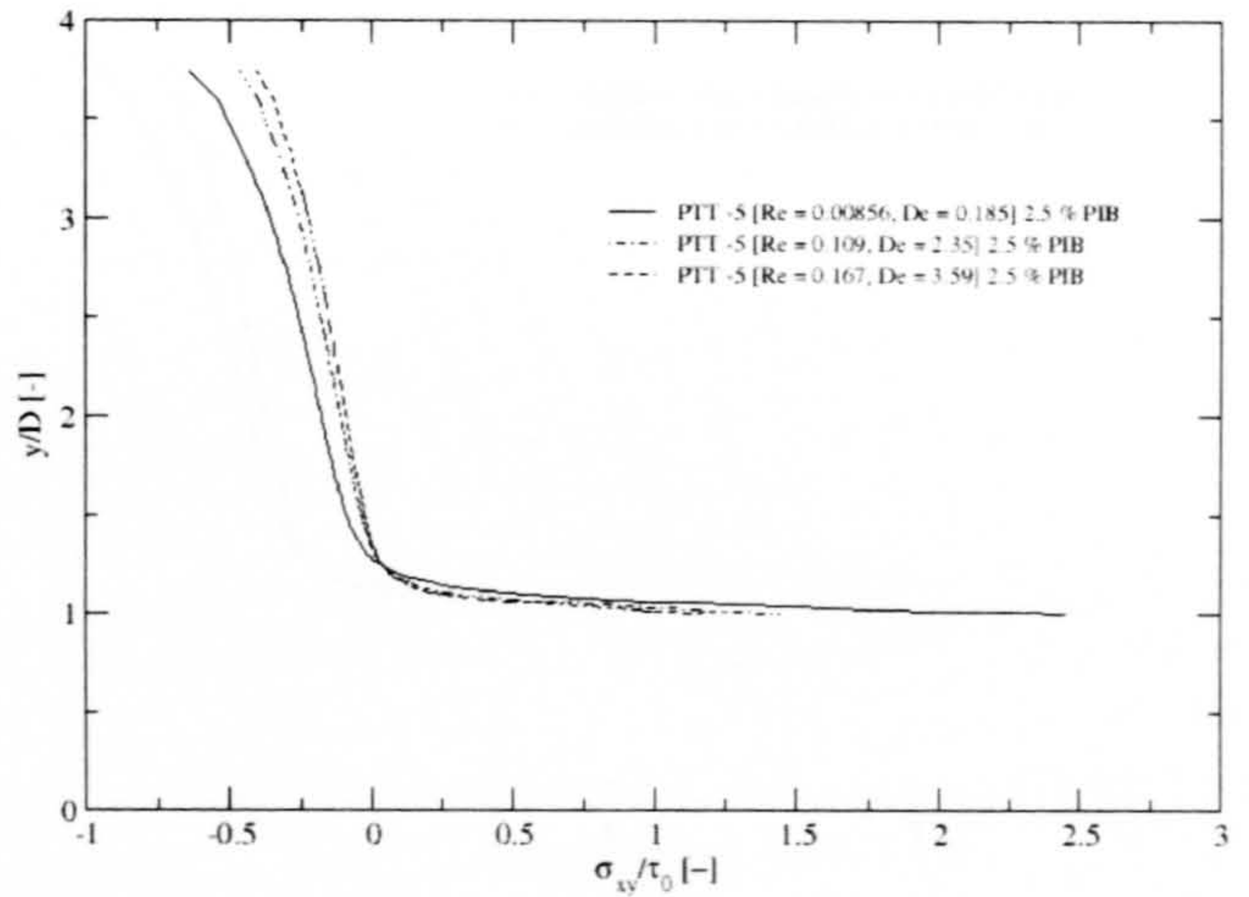

(b)

Figure 5.26: Comparison of predictions for the shear stress (σ_{xy}) values adjacent to the impeller blade tip, along the cross-sections; (a) β_1 to β_3, for $De = 0.199$ to 3.59 and; (b) β_1 to β_2, for $De = 0.185$ to 3.59, both for the 2.5 % PIB solution.

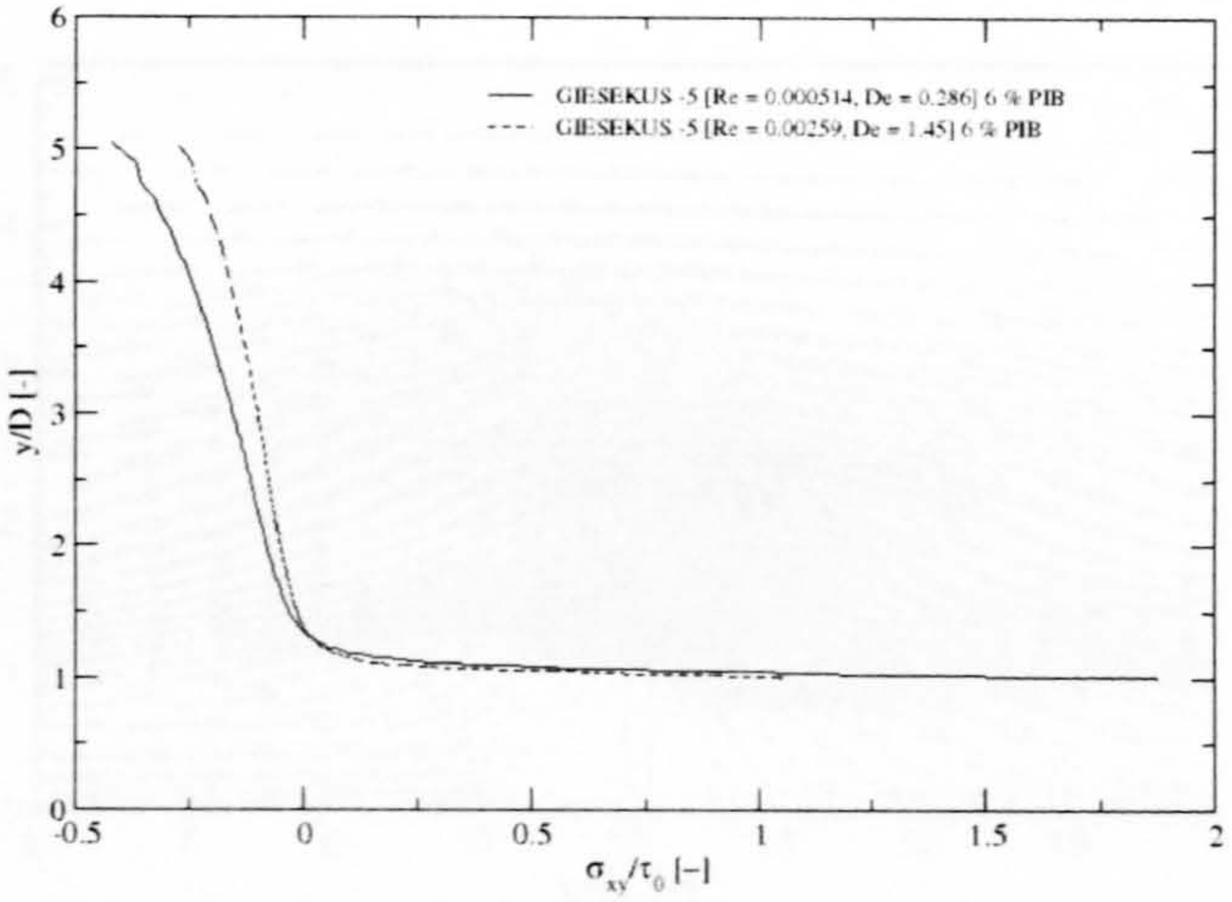

(a)

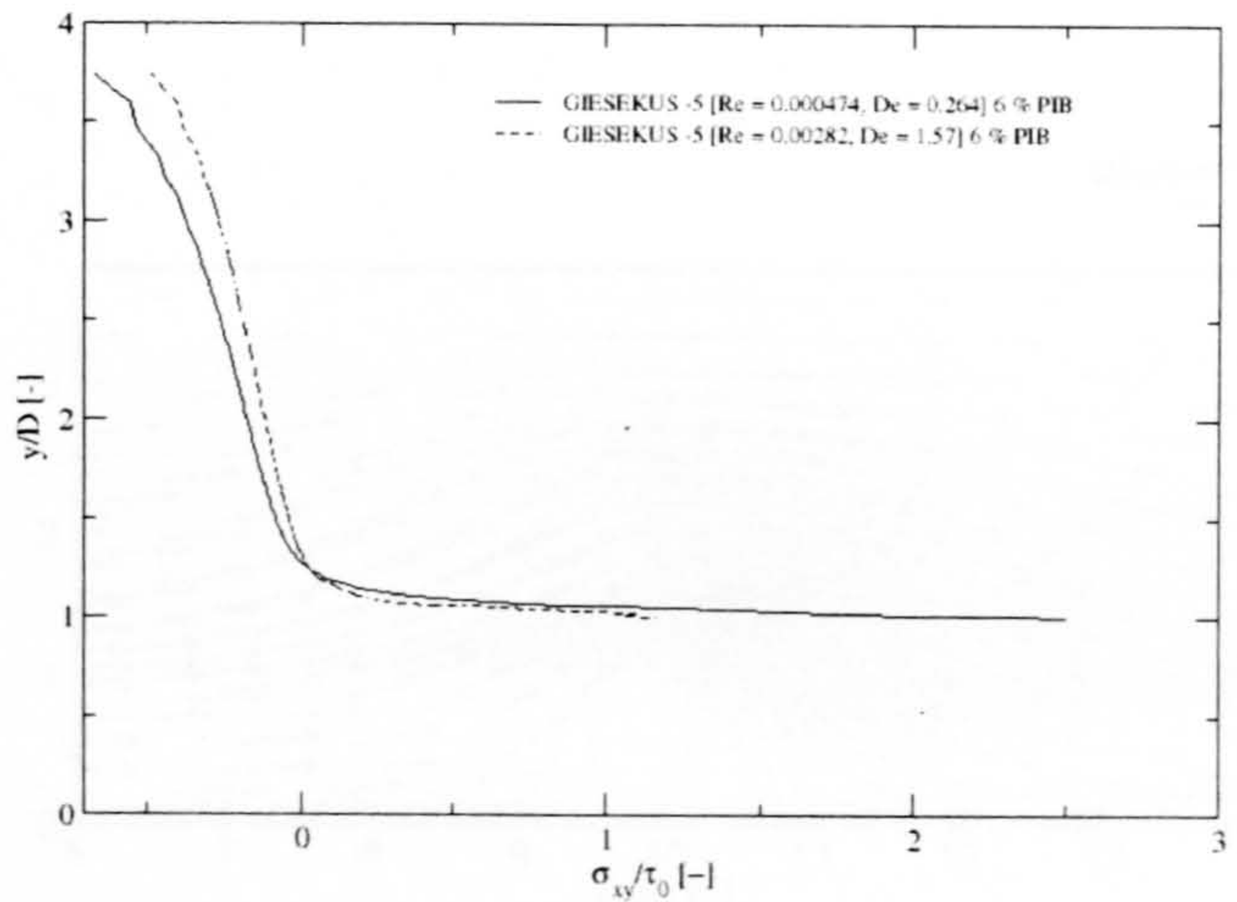

(b)

Figure 5.27: Comparison of predictions for the shear stress (σ_{xy}) values adjacent to the impeller blade tip, along the cross-sections; (a) β_1 to β_3, for $De = 0.286$ to 1.45 and; (b) β_1 to β_2, for $De = 0.264$ to 1.57, both for the 6 % PIB solution.

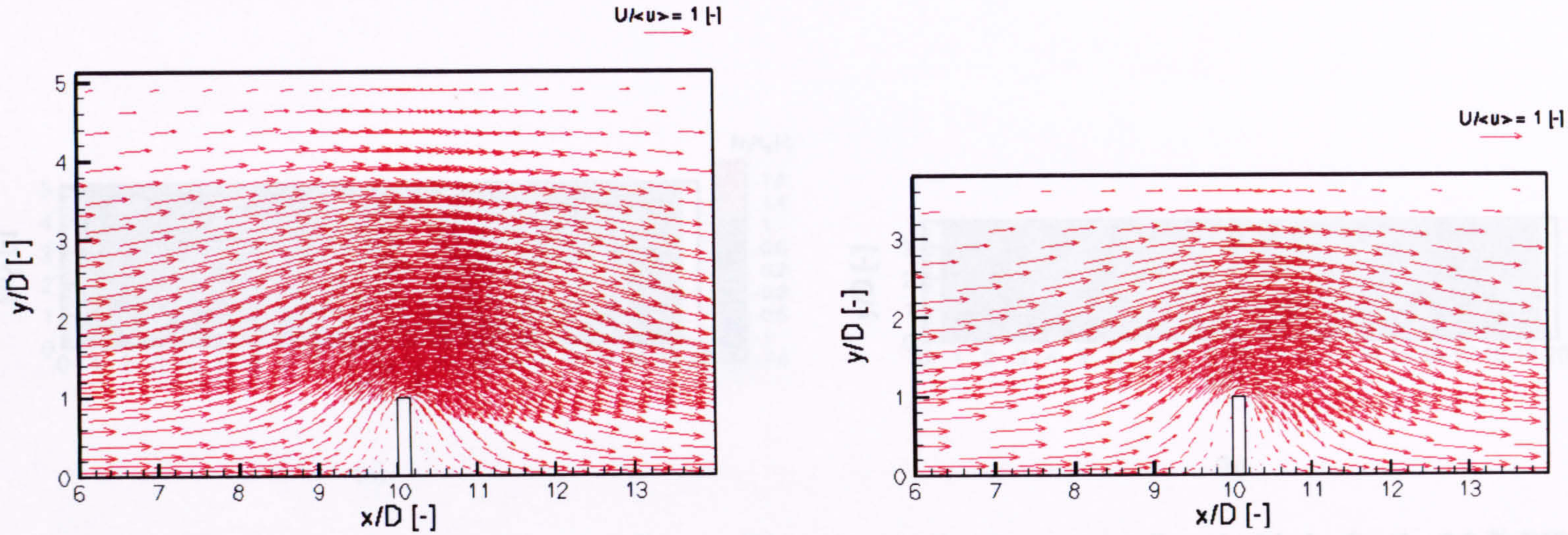

(a) (b)

Figure 5.28: Velocity vector plots in the area surrounding the blade, for the 2.5 % PIB solution; (a) with mesh height, H_1, at $De = 2.62$, and; (b) with mesh height, H_2, at $De = 2.34$.

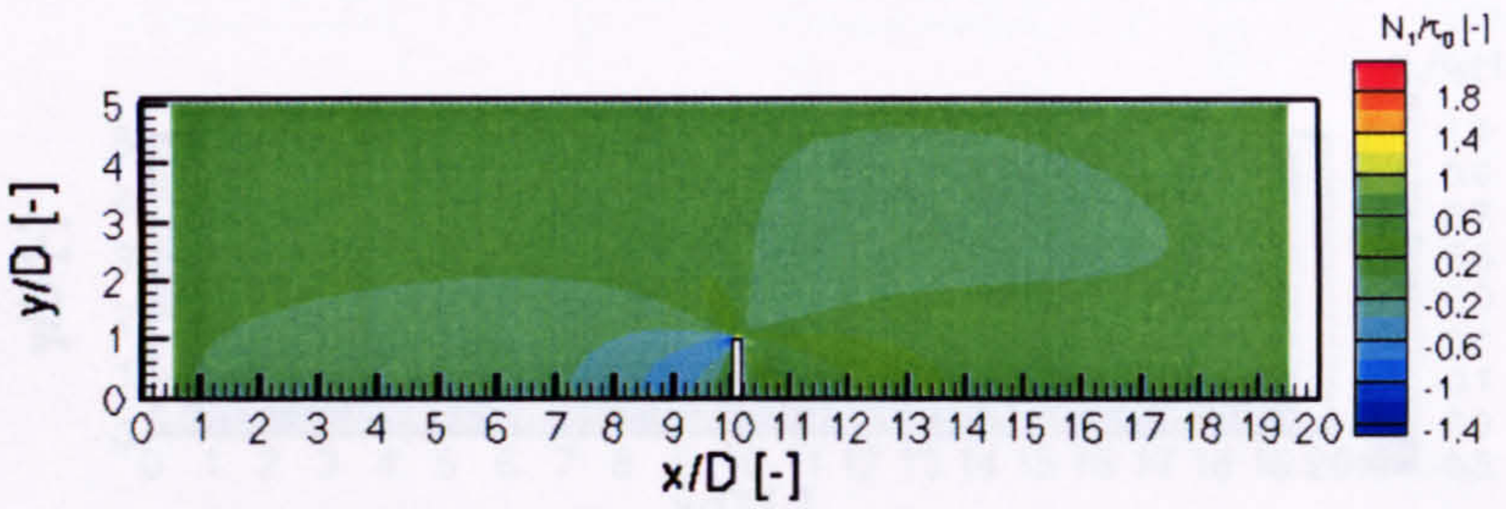

(a)

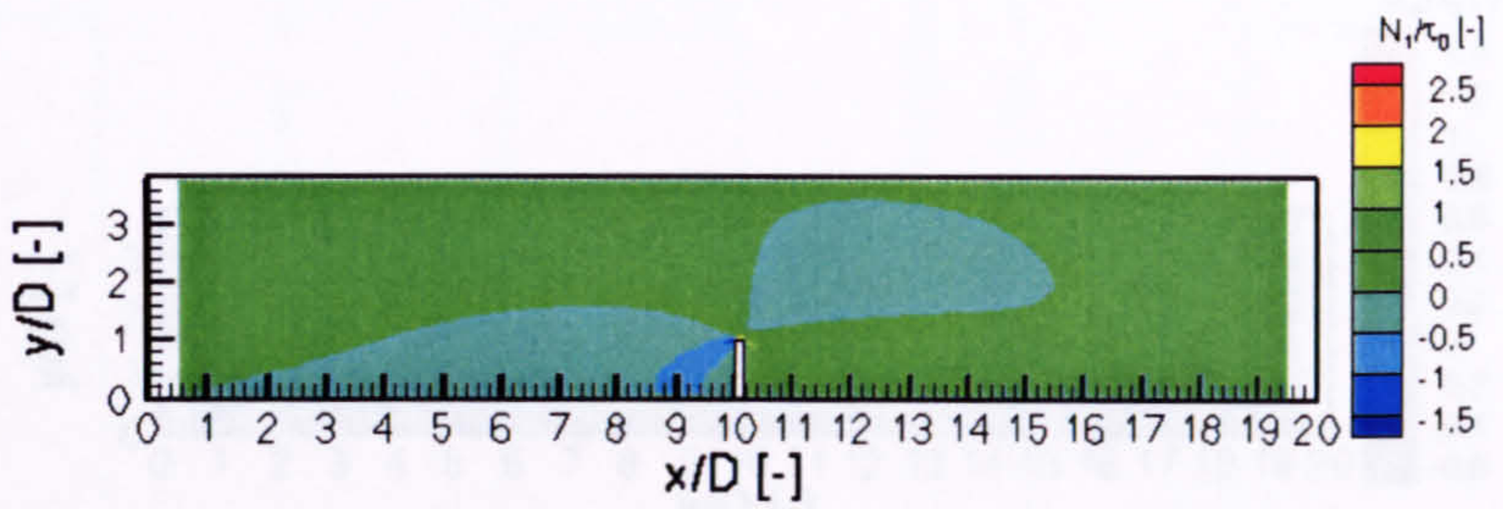

(b)

Figure 5.29: Contour plots of the first normal stress difference (N_1) values in the area surrounding the blade, for the 2.5 % PIB solution with; (a) mesh height, H_1, at $De = 2.62$, and; (b) mesh height, H_2, at $De = 2.34$.

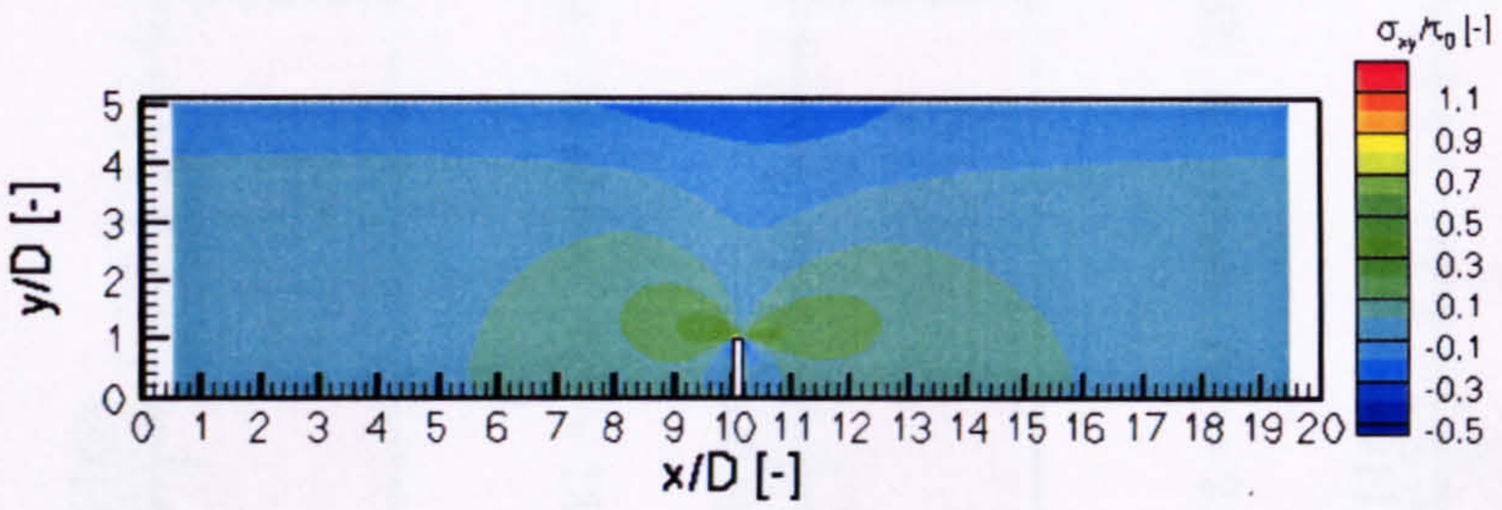

(a)

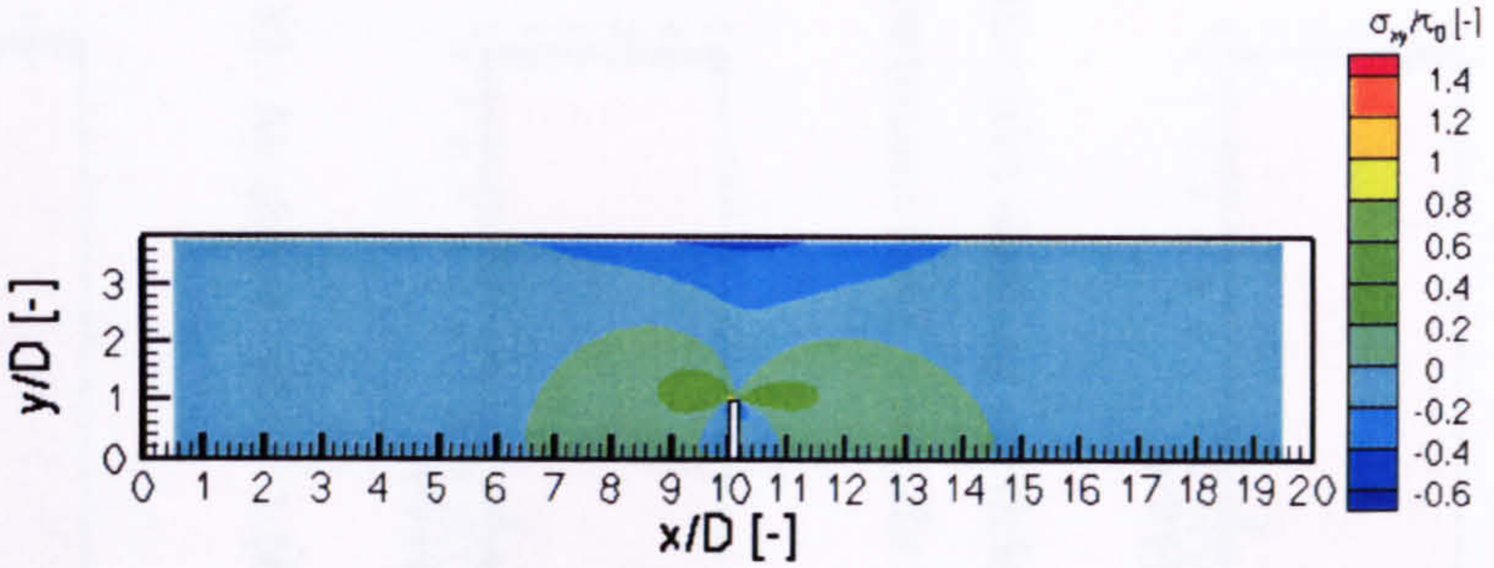

(b)

Figure 5.30: Contour plots of the shear stress (σ_{xy}) values in the area surrounding the blade, for the 2.5 % PIB solution with ; (a) mesh height, H_1, at $De = 2.62$, and; (b) mesh height, H_2, at $De = 2.34$.

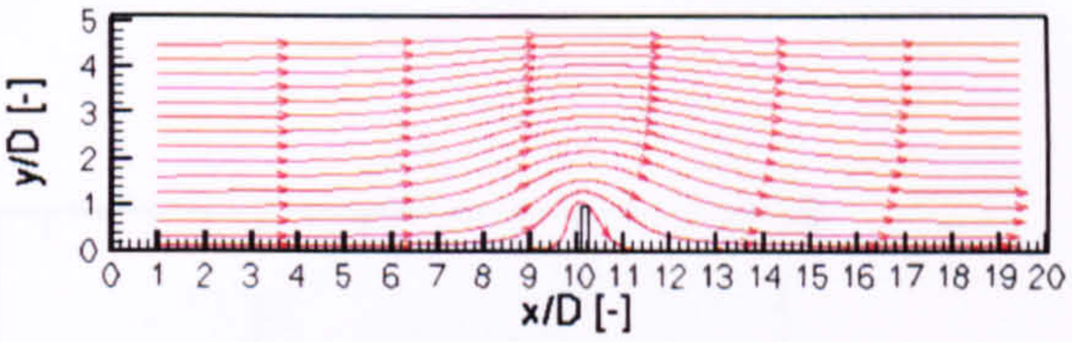

Figure 5.31: Streamline plot showing particle trajectories in the area surrounding the blade, for the Newtonian fluid, with $Re = 0.562$, and mesh height, H_1.

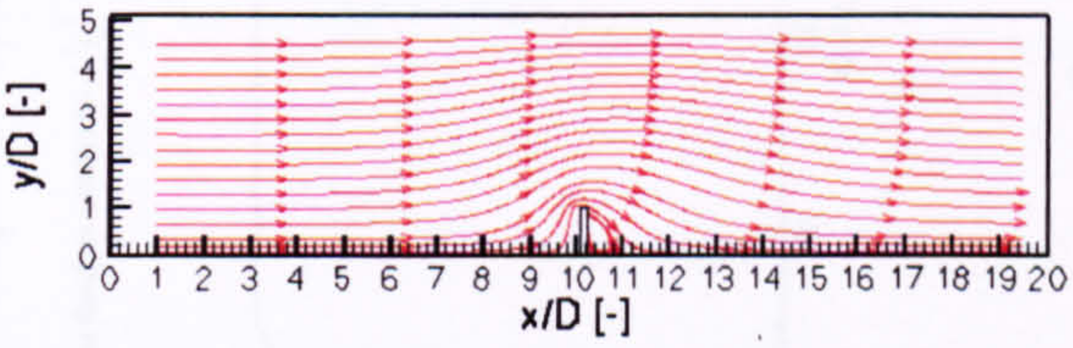

Figure 5.32: As above: $Re = 1.56$ and mesh height $= H_1$.

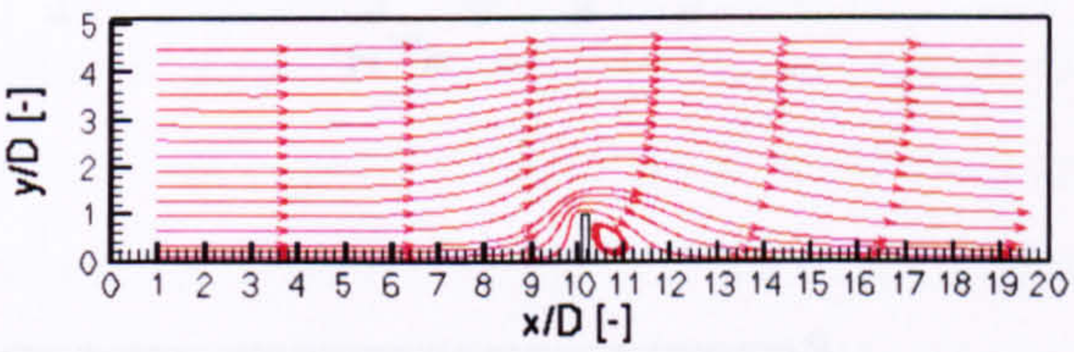

Figure 5.33: As above: $Re = 2.43$, mesh height $= H_1$.

Figure 5.34: As above: $Re = 15.02$, mesh height $= H_1$.

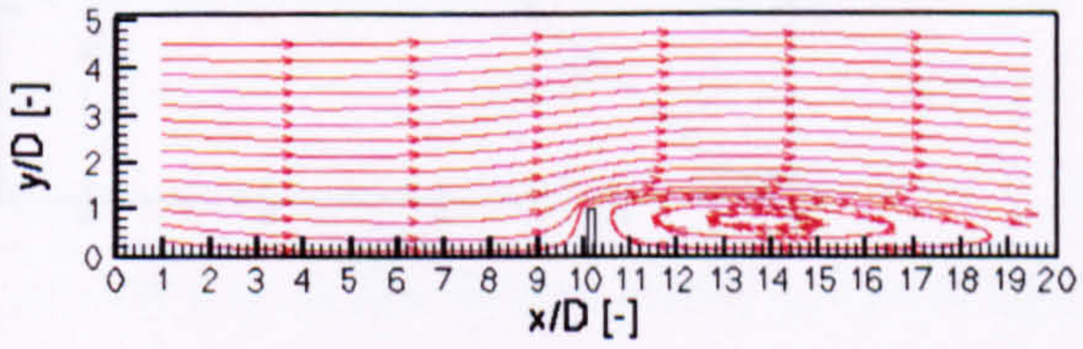

Figure 5.35: As above: $Re = 55.65$, mesh height $= H_1$.

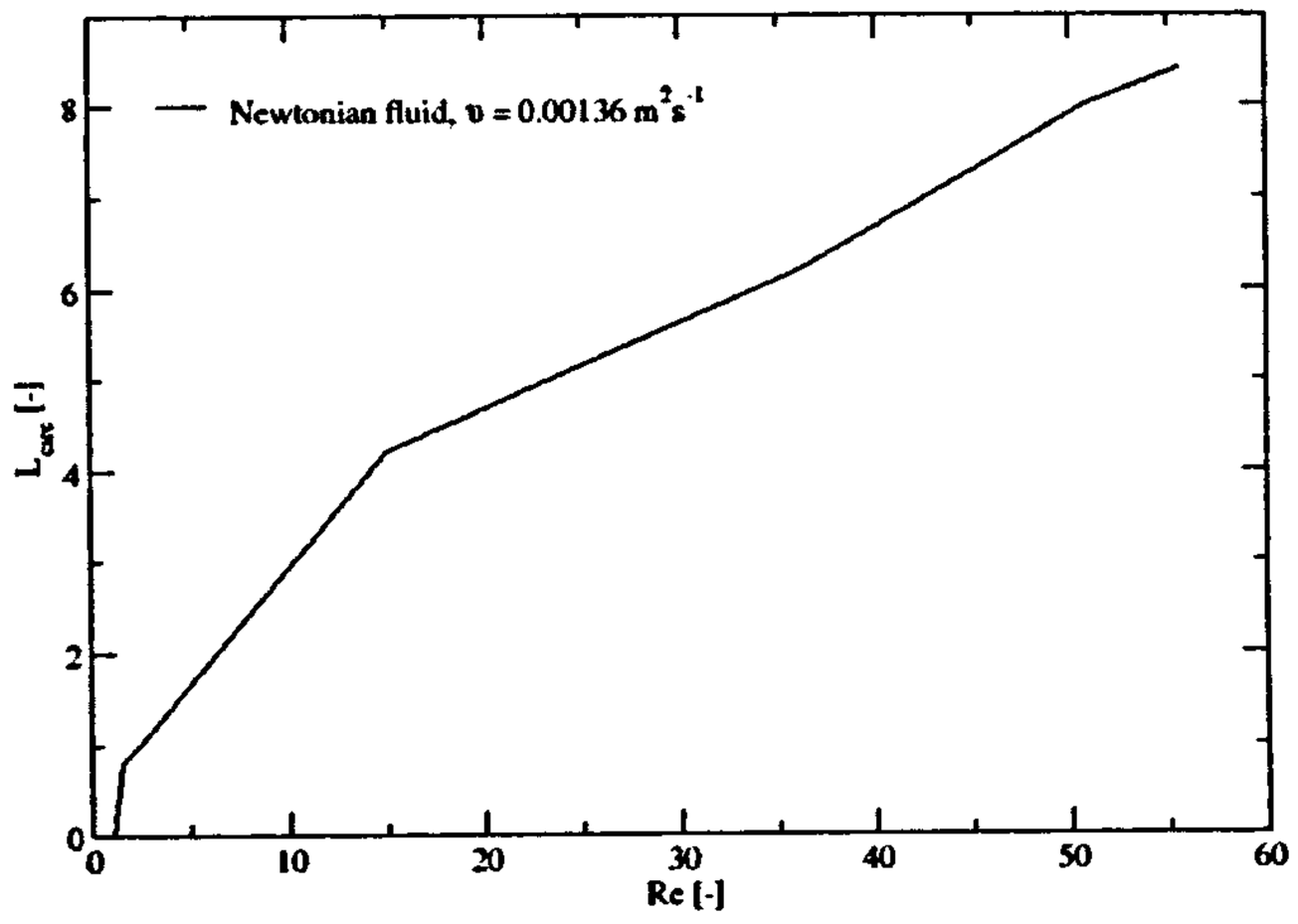

(a)

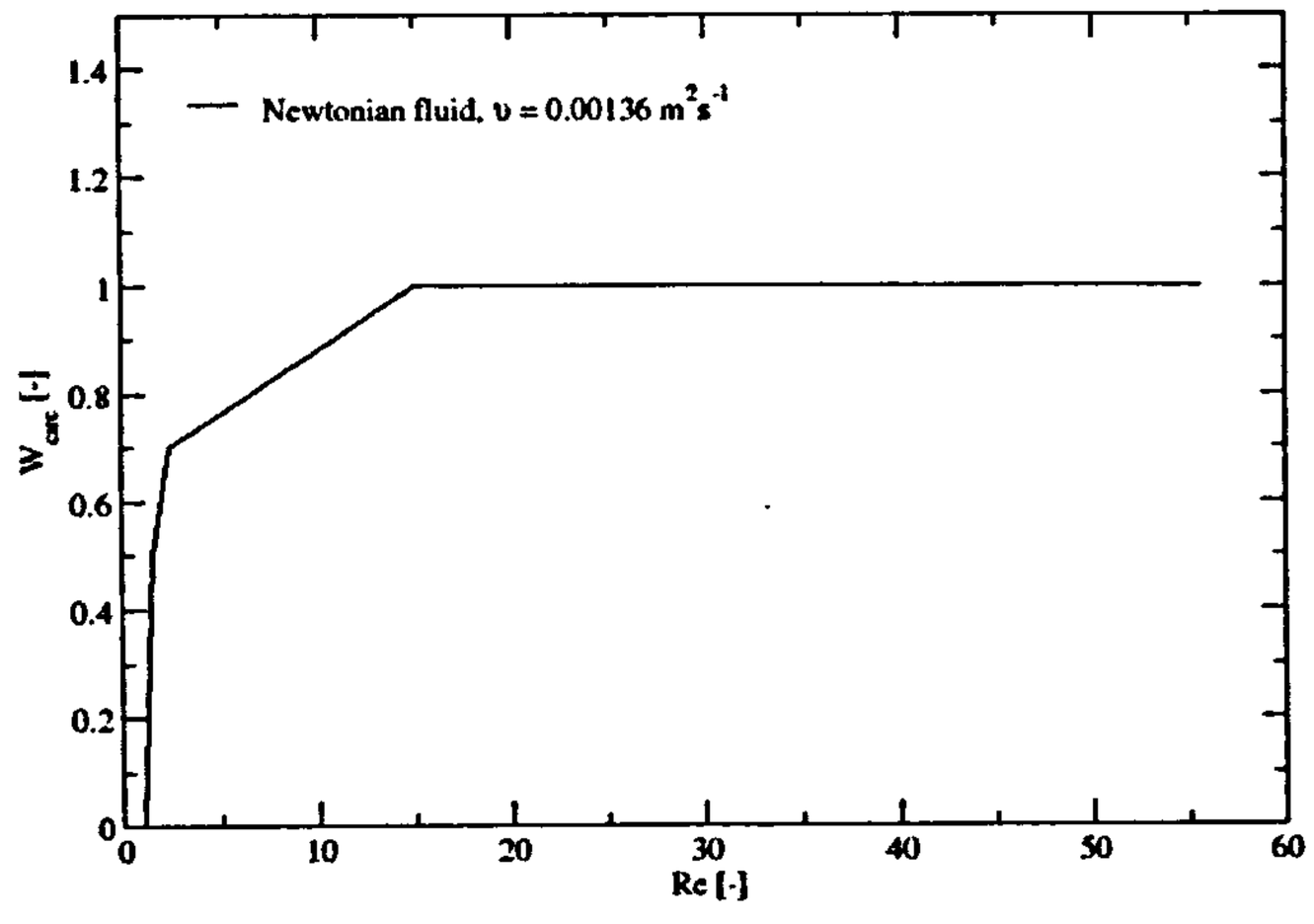

(b)

Figure 5.36: (a) L_{circ} and (b) W_{circ}, versus Re.

Chapter 6

Laminar flow mixing characteristics of viscous and viscoelastic fluids[1]

6.1 Introduction

In this chapter detailed LDA data on the velocity characteristics measured with water, Si100, Si1000, PIB100 and PIB2000 fluids (see table 6.1) are presented. These measurements are made in the impeller stream and bulk region of a vessel stirred by a single Rushton impeller. The mixing vessel used in this investigation and the LDA experimental techniques employed have been described in Chapter 2. The liquid column in the vessel was equal to the height of the mixing vessel, H, and the vessel diameter, T, where $H = T = 80.5\ mm$. The Rushton impeller employed has a diameter, $D = T/3 = 27\ mm$ and is positioned in the centre of the vessel with a clearance, $C = T/3\ mm$ from the base of the vessel. The impeller is rotated in the clockwise direction as viewed from above.

The origin of the co-ordinate system used is the centre of the base of the vessel. For ease of comparison between all working fluids at different Re, all distances are normalised with the vessel diameter, T, and all locations are described in terms of the normalised radial, r/T and normalised axial, z/T co-ordinates. All measurements are conducted in the $\theta = 0^0$ plane, located azimuthally halfway between two adjacent baffles (i.e. 45^0 away from each baffle).

At the start of the experiments ensemble-averaged LDA measurements ob-

[1]Some of the results presented in this chapter appear in Rice et al. (2005), 'Investigation of laminar flow in a stirred vessel at low Reynolds numbers', paper submitted to Chemical Engineering Science.

tained over 360^0 of impeller revolution were obtained for all working fluids. These measurements provide a useful insight into the behavioural characteristics, such as the position, size and shape of vortex structures in the vicinity of the impeller blade, and more interestingly help describe the dependence of such characteristics on Re and/or the rotational speed of the impeller blade, N. However, in order to have a more detailed understanding, phase-resolved LDA measurements were performed over 360^0 of impeller revolution where the data are arranged in 1^0 averages. Phase-resolved measurements can account for changes such as that of the shear rate and direction of fluid particles movement due to the passage of the impeller blades, which is of particular use when investigating the laminar mixing behaviour of the viscous Newtonian Silicon oils and viscoelastic, non-Newtonian polyisobutylene solutions. In addition, time-resolved velocity data (instantaneous velocity recordings) are used to obtain information about the frequency content of the velocity fluctuations.

The LDA measurements mentioned above are of the radial and axial velocity components (U_r and U_z respectively); and of the corresponding r.m.s. values[2] (u'_r and u'_z respectively) at 129 points in the $\theta = 0^0$ plane over the region $0 \leq r/T \leq 0.5$ and $0 \leq z/T \leq 1$. This region covers the whole of the $\theta = 0^0$ plane; the flow was confirmed to be symmetric about the centre of the impeller shaft at $r/T = 0$. The 129 points form a grid that becomes more refined in the vicinity of the blade where higher velocities are found and to reveal in more detail the structure, shape and size of the impeller-generated vortices. Conversely, the grid is more coarse at the extremities of the vessel where, in the case of laminar flows at low Re, much smaller velocities are found. The azimuthal location of these grid points, for the phase-resolved measurements is expressed in terms of the angle, ϕ, through which the impeller blade has passed. The angle, $\phi = 0^0$ is located at the centre of the leading blade and is calculated by the use of an optical shaft encoder which gives a marker pulse for every revolution of the impeller blade.

For the purpose of comparison with data of different fluids at varying Re, all

[2]As the flows studied were essentially laminar, ensemble-averaged r.m.s. data were obtained to indicate mainly the level of flow variation over 360^0 of rotation, while phase-resolved r.m.s. data can help indicate local flow variations due to transition to turbulence and/or non-linear/chaotic flow variations in non-Newtonian flow cases.

velocities have been normalised with the blade tip velocity, V_{tip} for each corresponding case:

$$V_{tip} = \frac{\pi N D}{60} \tag{6.1}$$

where, N is the impeller rotational speed, in this instance, in revolutions per minute. The normalised ensemble-averaged and phase-resolved mean[3] velocity values are denoted by $< U_r > /V_{tip}$ and $< U_z > /V_{tip}$, the normalised instantaneous velocity values are denoted by U_r/V_{tip} and U_z/V_{tip} and the normalised r.m.s. values are denoted by u'_r/V_{tip} and u'_z/V_{tip}, each for the radial and axial components, respectively.

Vector and contour plots are drawn, to facilitate the interpretation and presentation of all the LDA measurements. The first type of plot outlines half the mixing vessel in the $\theta = 0^0$ plane, which is symmetric about the axis $r/T = 0$, and incorporates half the impeller shaft and blade. The impeller blade is considered to be moving out of the plane of the paper towards the viewer. The second type of plot outlines the whole view from the top of the mixing vessel in the z/T plane and the impeller blade is considered to be moving clockwise. In the case of the vector and contour plots, a reference vector (V_{tip}) and contour scale is given, respectively.

6.2 Mixing flow characteristics of water

6.2.1 Introduction

Initially, the working fluid considered is water. This is selected for a number of reasons; (i) it is readily available, innocuous and non-corrosive; (ii) an abundance of data is readily available from a number of authors, Dyster et al. (1993), Greene et al. (1982), Hockey and Nouri (1996), Micheletti (2004) and Nouri and Whitelaw (1990b), to name a few, with which results can be compared over a wide range of Re, and; (iii) due to its relatively low viscosity, characteristic laminar flow behaviour at low Re can be studied and compared to that of flow at higher Re,

[3]The use of the term 'mean' velocity in this chapter is employed to indicate velocity averages over 360^0 (ensemble-averaged) or 1^0 (phase-resolved) of rotation.

up to and including those in the transitional to turbulent flow regimes. This is paramount if a more detailed understanding of the laminar flow behaviour of other more viscous Newtonian and viscoelastic fluids is obtained. By the use of ensemble-average velocity distributions, the aims of this section are to; (i) study the flow behaviour and how it changes at $Re = 4253$, $Re = 486$, $Re = 61$ and $Re = 49$; (ii) show how the mean radial and axial velocity components individually contribute to the change in flow pattern and; (iii) show the r.m.s. levels at each Re and how these levels change with Re.

6.2.2 Ensemble-averaged mean velocity measurements

The mean velocity vectors in the $\theta = 0^0$ plane at $Re = 4253$, 486, 61 and 49 are shown in figure 6.1. The highest Re is chosen so that a comparison can be made with the measurement data of other authors (see below) and thus provide a link with the data for the smaller Re. Each Re is rounded up to the nearest integer. At $Re = 4253$ and 486, in figures 6.1(a) and 6.1(b) the magnitude of the velocity vectors are greatest in the vicinity of the impeller blade, where the largest of these are adjacent and perpendicular to the impeller blade tip. As the flow moves further away, towards the side wall of the vessel, these radial velocities decrease in magnitude and the flow direction becomes predominantly axial. In both figures these large velocities generate regions of recirculation directly below and above the impeller blade. The vortex above the impeller blade occupies the regions, $0.33 \leq z/T \leq 0.78$ and $0.33 \leq z/T \leq 0.68$, for $Re = 4253$ and 486, respectively. The latter being notably smaller and caused by the reduction in Re. This is qualitatively in agreement with the findings of Micheletti (2004) for a reduction in Re in a turbulent flow field. It is also noteworthy to observe the presence of a secondary vortex structure of smaller velocities at the top of the mixing vessel, moving in an opposing, clockwise, direction in the region $0.68 < z/T$ and $0.78 < z/T$ for both figures, respectively which is also in agreement with Micheletti (2004).

In contrast to what is observed in figures 6.1(a) and 6.1(b), the flow behaviour observed for $Re = 61$ in figure 6.1(c) is remarkably different. The largest velocity vectors in the vicinity of the impeller blade are observed to form that of an 'S'

shaped flow pattern: Just above the top edge of the impeller blade, at $z/T = 0.4$ the velocity values are not predominantly radial in a direction away from the blade but in fact are moving towards it and downwards towards the base of the vessel, with the flow turning around at the centre of the blade, at $z/T = 0.33$, and then proceeding to move away from the blade and towards the base of the vessel (at approximately 45^0 to the horizontal). At $z/T = 0.2$ these vectors suddenly are directed inwards again and then upwards, back towards the impeller blade, creating a small area of recirculation beneath it. It is also shown that the fluid moves away from this 'S' shaped flow pattern at $z/T = 0.2$, at a position slightly further from the blade, and recirculates upwards near side wall of the vessel. The magnitudes of the velocity vectors here and at points at the extremities of the mixing vessel, become very small; this is due to the very low rotational speed of the impeller at $Re = 61$, and the inertial forces not therefore being large enough to cause flow patterns such as those observed in these regions at higher Re. Figure 6.1(d) shows an identical flow pattern at $Re = 49$, to that of $Re = 61$ with no velocity readings outside of this area. Only small differences are found between the flow patterns at $Re = 61$ and 49 so for discursive purposes the former will be used for comparison in this investigation.

It is now beneficial to analyse the normalised radial and axial velocity components and their individual effects on the flow patterns at each Re. The normalised radial velocity component, $< U_r > /V_{tip}$ in figures 6.2(a) and 6.2(b) at $Re = 4243$ and 486, respectively, share two similarities by comparison, those being; (i) large, positive values in the vicinity of the impeller blade, in the region $0.25 \leq z/T \leq 0.45$ and; (ii) small negative values at the centre of the primary vortex above the impeller blade. However, in contrast, figure 6.2(c) at $Re = 61$, shows relatively large negative and positive values adjacent to the top right and bottom right of the impeller blade tip, respectively and an additional region of negative values in the bottom left hand corner of the mixing vessel. These three regions show a directional change in radial velocity which is representative of the 'S' shaped flow pattern previously described. It is also important to observe the magnitude of $< U_r > /V_{tip}$ for each Re: For $Re = 4253$ the maximum value of $| < U_r > /V_{tip}|$ is adjacent to the midpoint of the impeller blade tip and is ap-

proximately $0.7V_{tip}$, which is in agreement with the work on turbulent mixing by Lee (1995) for a similar vessel configuration. As the flow becomes more laminar, at $Re = 486$ a maximum of $0.65V_{tip}$ is observed, which is a small reduction of almost 7 % by comparison. Conversely, figure 6.2(c) shows a maximum value of $0.16V_{tip}$, which is a reduction of approximately 75 % in comparison.

The normalised axial velocity components, $< U_z > /V_{tip}$ in figures 6.3(a) and 6.3(b) for $Re = 4253$ and $Re = 486$ share three similarities by comparison, those being; (i) large, positive values beneath the impeller blade; (ii) large, positive values adjacent to the side wall of the vessel in the region, $0.4 \leq z/T \leq 0.6$ and; (iii) large, negative values directly above the impeller blade. Similarities (i) and (ii) are representative of the vortex structure beneath the impeller blade as the flow moves upwards and towards it and the primary vortex structure above the blade as the flow moves up the vessel wall away from the impeller stream, respectively. Similarity (iii) is representative of the primary vortex structure as it recirculates back towards the impeller blade and down the shaft. Likewise, figure 6.3(c), for $Re = 61$ shows relatively large positive values of $< U_z > /V_{tip}$ adjacent to the wall of the vessel and beneath the impeller blade, but quite differently shows negative velocities contiguous to the tip of the impeller blade. The flow characteristics at this Re are again representative of the 'S' shaped flow pattern described previously as it; (i) recirculates beneath the impeller blade; (ii) detaches and recirculates upwards along the side vessel wall and; (iii) moves towards the centre of the impeller stream from above.

For discursive purposes it is helpful at this point to show profiles of the radial and axial velocity components at various radial positions in the mixing vessel (see figures 6.4 for the radial velocities and 6.5 and 6.6 for the axial) to more accurately quantify the results shown above and compare with those of other authors. For $< U_r > /V_{tip}$ the largest values are observed at the centreline of the impeller stream, at a radial position closest to the impeller (see figure 6.4(a) at $r/T = 0.22$), where maximum values of $0.7V_{tip}$ are reached. By moving a small distance away from the centreline of the impeller blade in a direction towards the top and bottom of the vessel, the values drop by approximately $0.6V_{tip}$. By moving further from the blade in the radial direction (see figure 6.4(b) at $r/T = 0.41$)

the maximum values decrease by approximately 50 %. In both figures small differences of the order of $0.05V_{tip}$ are observed between $Re = 4253$ and 486 but a further decrease in Re causes not only a large decrease in radial velocity but a change in flow pattern too. For instance, in figure 6.4(a), at $Re = 61$, $| < U_r > /V_{tip}|$ reaches a maximum just below and above the centreline of the impeller blade, which is different to that observed at higher Re. By moving further from the centreline of the impeller blade, both figures show these values tending to zero. The measurement data at $Re = 4253$ is also compared to that of Micheletti (2004) at $Re = 4250$. This comparison shows small differences of the order of 3 %, which is lower than the margin of experimental error present when making such measurements and thus an indicator of high fidelity, giving confidence to the accuracy of the present measurement data. For $< U_z > /V_{tip}$, the values at $Re = 4253$ and 486 at both $r/T = 0.15$ and 0.26 (see figures 6.5(a) and 6.5(b), respectively) are within 5 % of each other and it can be seen that the magnitude of the velocities above the blade are approximately equal to, and move in a direction opposed to, the ones beneath. As the Re is decreased to $Re = 61$ the profiles at these radial points change. A large decrease in $| < U_z > /V_{tip}|$ is observed where the value tends to zero at a distance far enough from the centreline of the impeller blade and in the case of $r/T = 0.26$, in figure 6.5(b) all values of $< U_z > /V_{tip}$ are negative, the largest of which are adjacent to the bottom of the blade. Conversely, further away from the blade, at $r/T = 0.41$ (in figure 6.6) the values are mostly positive and largest at the centre of the impeller blade. For higher Re the size of the axial velocities next to the wall at this point are clearly larger and cover a bigger region as they recirculate up the wall of the vessel. Additionally, a comparison is again made with the measurement data of Micheletti (2004) at $Re = 4250$ which shows insignificant differences of 3 % when compared to the measurement data at $Re = 4253$, this is within the bounds of experimental error and again gives confidence to the results obtained in this study.

The results already presented show that the flow behaviour at $Re = 61$ presents noticeable differences in magnitude, direction and flow pattern. The mixing flow pattern has changed by decreasing the Re from one similar to those

encountered in turbulent flow to the sigmoid pattern at low *Re*. Clearly, at the highest *Re* the flow may be turbulent and/or transitional in parts and it is worth considering in this respect the change in r.m.s. levels, which is investigated in the following section.

6.2.2.1 R.m.s. level distributions

The normalised r.m.s. levels, u'_r/V_{tip} and u'_z/V_{tip} in the $\theta = 0^0$ plane are shown in figures 6.7 and 6.8, respectively.

The highest levels of u'_r/V_{tip} are observed in the vicinity of the blade at approximately $0.3V_{tip}$ and $0.2V_{tip}$ for $Re = 4253$ and $Re = 486$, respectively. Likewise, the same is observed for u'_z/V_{tip}. These are expected to be present where steep mean velocity gradients are also present, namely in the vicinity of the impeller and those r.m.s. levels are shown to diminish with increasing radial and axial distance from the blade. Lee (1995) found r.m.s. levels of a similar magnitude for turbulent flow to those of the measurement data at $Re = 4253$, in this study. The local values of turbulence in figures 6.7(c) and 6.8(c) for $Re = 61$ are relatively high in the region close to the blade, but by comparison to that of the higher *Re* these values are very small, approximately $0.04V_{tip}$. This may be an indication of a change to a more laminar flow behaviour as the *Re* decreases. Small islands of locally high (but still rather small) r.m.s. values outside the vicinity of the impeller blade are also observed at $Re = 61$, in both the radial and axial directions, but these may be attributed to the very small velocity magnitudes in comparison to the experimental error in these regions.

As with the mean velocity values, profiles of the r.m.s. levels for u'_r/V_{tip} and u'_z/V_{tip}, at each *Re* are shown at radial positions in the vessel. Figures 6.9(a), 6.9(b), 6.10(a) and 6.10(b) re-emphasise how the levels of turbulence diminish to zero at $Re = 61$ and how the peaks in r.m.s. occur at the centreline of the impeller blade where the largest values are at radial positions closest to it. At $Re = 4253$ the r.m.s. levels are compared to the measurement data of Micheletti (2004) at $Re = 4250$ and a difference of the order of approximately 5 % is shown. This is again within the error bound of the measurements.

It is now clear from what is shown here that significant changes in the magni-

tude, direction and flow pattern of the mean velocity vectors occur with a decrease in Re in the range $61 \leq Re \leq 4253$. It has also been shown that the r.m.s. levels decrease. As the flow moves from a transitional regime at $Re = 4253$ and 486, to a more laminar one at $Re = 61$; the flow discharge from the tip of the blade changes and the recirculation zones move and change size. A different flow pattern forms, namely the 'S' shaped pattern and the r.m.s. levels diminish to zero. Due to the limitations of the impeller motor speed stability at very low N, the rotational speed could not be reduced further and studies at a Re lower than 61 and 49 for water could not therefore be made. However, these Re are induced by rotational impeller speeds of 5 and 4 rpm, respectively and are comparable to the speeds used by Bartels (1988) for laminar mixing. In order to make studies at lower Re, for the same vessel configuration, the viscosity of the fluid in the preceding sections is increased. The following section investigates the mean velocity values and r.m.s. levels of two viscous, Newtonian, Silicon oils. Phase-resolved measurements are also studied, for two reasons: First, to investigate flow behaviour at different angular position of the impeller blade; and second, to eliminate the mean velocity variation incorporated in 360^0 (ensemble-averaged) r.m.s. values, so that the true level of turbulence or the presence of chaotic motions can be discerned.

6.3 Mixing flow characteristics of viscous Newtonian Silicon oil solutions

6.3.1 Introduction

This section deals with the mixing flow behaviour of two Silicon oil solutions. They are referred to as Si100 and Si1000 and have a kinematic shear viscosity of 1 x 10^{-4} m^2s^{-1} and 1 x 10^{-3} m^2s^{-1}, respectively, see table 6.1. These fluids are similar to water such that they are innocuous, non-corrosive and readily available but the essential difference is that the viscosity is 100 and 1000 times greater, respectively, than that of water. Work by, for example Alvarez et al. (2002), Dyster et al. (1993), Hockey and Nouri (1996), Lamberto et al. (1999) Nouri and

Whitelaw (1990b) and Szalai et al. (2004) studied the mixing behaviour of similar high viscous Newtonian fluids such as, Glucose and Glycerol solutions and Maltose syrup but to the best knowledge of the author, work has not been published on laminar mixing of the Silicon oils presented herein. It is with this is mind that great care is taken in the analysis of the fluids' behavioural characteristics at a lower *Re*. The aims of this section are, inter alia; (i) to study, by ensemble-average measurement data the flow behaviour of both fluids in a laminar flow regime and show how the radial and axial, mean velocity and r.m.s. values are affected by the change in flow pattern; (ii) for Si1000, to show the position and size of the vortices at varying *Re*, and by phase-resolved measurement data, to investigate the change in mean velocity values due to the passage of the impeller blade.

6.3.2 Ensemble-averaged mean velocity distributions

The mean velocity distributions for both the Si100 and Si1000 solutions are presented for the $\theta = 0^0$ plane, in figures 6.11 and 6.16, respectively. The former at $Re = 50$, $Re = 1$ and $Re = 0.5$, and the latter at $Re = 28$, $Re = 10$ and $Re = 1$. The Si100 solution is used to make a preliminary study to gain an initial understanding of how such viscous fluids behave at a low *Re*. This is done by only taking ensemble-average LDA measurements in the vicinity of the impeller blade and the data used in a similar manner to that of water. The Si1000 solution is then used to make a more in depth study where the sample solution is optimally seeded for a high data acquisition rate and phase-resolved data are acquired and used for discursive purposes.

For Si100, at $Re = 50$ figure 6.11(a) shows predominantly radial velocities that discharge from the tip of the impeller blade and decrease in magnitude towards the wall of the vessel where they become mainly axial. This behaviour is different to that of water at an almost identical *Re* (see figures 6.1(c) and 6.1(d)) where the 'S' shaped flow pattern as previously described is not here shown. This result suggests that the flow behaviour of the higher viscosity, Si100 solution is not scaling with *Re*, however, this is not conclusive. It is intuitive to think that the flow behaviour will perhaps scale instead with the rotational speed of the

impeller blade, however this is neither true in this instance, as figure 6.11(c) shows: At $Re = 0.5$ the rotational speed of the impeller blade ($N = 4$) is almost identical to that of water at $Re = 61$ ($N = 5$) and the 'S' shaped flow pattern is still not observed. Instead, the mean velocity vectors (which are much smaller in magnitude) are all directed towards the bottom of the vessel. Although it is possible, of course, that an 'S' shaped flow pattern might be revealed in the two lowest Re cases if measurements were made over a larger region around the blade, but even if such motions are present, the resulting flow pattern would still be different to that at $Re = 49$ and 61 with water. They also show a distinct change by comparison to those at $Re = 50$ for the Si100 solution. Only small differences are shown between figures 6.11(b) and 6.11(c) for Si100 at $Re = 1$ and $Re = 0.5$, respectively, so for discursive purposes the former will be used for comparison in this investigation.

Figures 6.12 and 6.13 show a significant decrease in the radial and axial velocity values of approximately $0.35V_{tip}$ and $0.1V_{tip}$, respectively, accompanying the reduction in Re from 50 to 1 for Si100: For $Re = 50$, the radial and axial velocity components (see figures 6.12(a) and 6.13(a)) are $0.36V_{tip}$ and $0.1V_{tip}$, respectively, and for $Re = 1$ (see figures 6.12(b) and 6.13(b)) they are $0.015V_{tip}$ and $0.004V_{tip}$, respectively. These drops signify a further change in flow pattern as Re decreases. Also, the size of these radial velocities at $Re = 50$ are approximately 20 % smaller than that of water at a similar Re ($Re = 61$) and would imply, from what has already been observed for water, r.m.s. levels of near zero value. However, for Si100 a behaviour contrary to this is observed. Figures 6.14 and 6.15 show the radial and axial r.m.s. levels, respectively, at $Re = 50$ and $Re = 1$. The maximum radial r.m.s. levels are $0.09V_{tip}$ and $0.095V_{tip}$ at $Re = 50$ and $Re = 1$, respectively, and the maximum axial r.m.s. levels are $0.02V_{tip}$ and $0.126V_{tip}$, at $Re = 50$ and $Re = 1$, respectively. This indicates that radially there is a very small increase of 0.5 % and axially an increase of 10 % (neither of which is shown for that of water) with the decrease in Re. It has already been shown that the size of the velocity values are smaller for Si100 at the lowest Re and the part of the measured r.m.s. levels due to turbulence should be infinitesimal in this laminar flow regime. At this stage one can postulate that this increase in r.m.s. levels and

large decreases in radial and axial velocities with the decrease in Re for Si100 be attributed to the velocity vectors continually changing direction and magnitude in the vicinity of the impeller blade as it rotates. For instance, radial velocities being in a positive and then in a negative direction as the blade rotates. This behaviour is more likely for higher viscosity fluids like Si100 and Si1000 and would be an effect caused by the larger and more dominant (especially at lower speeds) viscous forces. However, in order to investigate this further the phase-resolved data is used and a more extensive discussion is made in section 6.3.3.

For Si1000, figures 6.16(a) and 6.16(b) show identical flow patterns for Re = 28 and 10, respectively. The flow patterns show the radial velocities discharge from the tip of the impeller blade, decrease in magnitude towards the wall of the vessel and become mainly axial before recirculating in two vortices, above and below the impeller blade. By comparison, figure 6.16(c) for $Re = 1$ shows a change in flow pattern identical to that in figure 6.11(b), for Si100 at $Re = 1$. This flow pattern being one where the mean velocity vectors discharge from the tip of the impeller blade at an angle towards the bottom of the mixing vessel. The results for $Re = 1$ (figure 6.16(c)) indicate that a pattern similar to the 'S' shaped one indicated by the water flow data at $Re = 49$ and 61 is indeed present, albeit occupying a larger region than for water, and it might be expected that a similar pattern would be present if the $Re = 0.5$ and 1 data for Si100 were obtained over a larger region. It must be stressed however, that although the overall 'S' shaped pattern is present, it is different to that observed in water, in both extent and velocity magnitude. The individual mean velocity components are not presented for Si1000 as the flow behaviour for this fluid is identical to those already observed for Si100 and water at a certain Re, however, the radial and axial r.m.s. values are shown in figures 6.17 and 6.18 as they also show an increase in the maximum radial and axial r.m.s. values with decreasing Re. However, as above, this will also be discussed with the phase-resolved data in section 6.3.3.

The mean velocities and r.m.s. values for the Si1000 solution have been presented over a range of Re and each have shown regions of recirculation above and below the impeller blade. The location of these recirculation regions exhibit different sizes and locations depending on the flow Re. The location and extent of

these regions is important for practical purposes as fluid trapped in such regions is likely to mix very slowly, if at all: They constitute 'segregation regions' where mixing is poor.

Consequently, an effort is first made to define the locations of these regions via the co-ordinates of their centres. Although they cannot be precisely identified without very detailed measurements, the locations near the middle of the vortices where both $< U_r > /V_{tip}$ and $< U_z > /V_{tip}$ are zero offer sufficient guidance and these locations are used to construct figure 6.19(a). It is found that the regions move outward in the radial direction and closer to the impeller in the axial direction as Re is increased. A similar observation can be made by reference to the data of Lamberto et al. (1999) for a Glycerine solution of similar viscosity to that of Si1000.

The extent that these regions cover is a little more difficult to define again without a very dense measurement grid, but the volume occupied by each of these regions can be estimated. Figure 6.19(b) shows the variation of the volume occupied by the regions above the blade. The area of the vortex is plotted as a percentage of the cross-sectional area of the mixing vessel against Re and is observed to increase with Re and considerably so at $Re > 10$.

6.3.3 Phase-resolved mean velocity measurements

It is now instructive to consider the phase-resolved radial and axial velocity variations at different phase angles to help illustrate the variation of flow pattern with ϕ. As mentioned in the introduction, all the phase-angle resolved LDA measurements are performed over 360^0 of impeller rotation where the data is arranged in 1^0 averages, but for simplicity all the plots presented in this chapter are made over 60^0 as the data is shown to repeat 6 times, once for each of the 6 blades. It must also be mentioned at this point that the phase-resolved data for all the working fluids of this chapter are on a CD in '.avi' movie file format and presented in Appendix B. Figures 6.20, 6.21 and 6.22 show the variations in the $\theta = 0^0$ plane, for $Re = 28$, $Re = 10$ and $Re = 1$, respectively at four angles of ϕ that are representative of the fluid behaviour.

Figure 6.20 shows the velocity vectors in four ϕ planes (8^0, 18^0, 33^0 and 48^0)

at $Re = 28$. It can be seen that at all ϕ angles, the flows discharged from the impeller blade tip towards the vessel wall. At each ϕ angle a vortex above and below the impeller blade is clearly observed, however plots showing the variation in the size and the locality of each vortex with a change in ϕ is not shown herein as this variation is very small.

By comparison, four noticeable differences are observed in figure 6.21 for the same four ϕ planes (8^0, 18^0, 33^0 and 48^0) at $Re = 10$. Those being; (i) the magnitude of the velocity vectors are smaller; (ii) the areas of the vortices above and below the impeller have decreased; (iii) the centres of the vortices are positioned closer to the impeller blade and; (iv) the flow has begun to show signs of inward pumping at the point adjacent to the centre of the impeller blade tip, at $\phi = 8^0$. It has already been said how the magnitude of the velocity vectors decrease with a drop in Re and this is reiterated in point (i) above. Differences, (ii) and (iii) we discussed previously, and shown in figures 6.19(a) and 6.19(b) for the ensemble-average velocities. Difference (iv) is discussed in the following paragraph in point (iii).

Figure 6.22 shows distinguishing differences at $Re = 1$ by comparison to both preceding figures, those being; (i) the magnitudes of the velocity vectors are even smaller; (ii) the prevalent vortices above and below the impeller of higher Re flows are no longer observed and; (iii) at $\phi = 8^0$ and $\phi = 18^0$ the flow clearly moves inward towards the impeller blade. This inward and outward pumping behaviour was mentioned in the previous section for Si100 at $Re = 1$ to suggest a likely reason why the r.m.s. levels in figure 6.15 increased with a decrease in Re. Now this observation has just been made for the Si1000 solution, it can be used to explain the increase in r.m.s. levels also observed for this fluid: Figures 6.17 and 6.18 show the radial and axial r.m.s. levels for the Si1000 solution, respectively. The radial r.m.s. levels having a value of approximately $0.09V_{tip}$, $0.08V_{tip}$ and $0.09V_{tip}$ for $Re = 28$, $Re = 10$ and $Re = 1$, respectively and $0.028V_{tip}$, $0.038V_{tip}$ and $0.046V_{tip}$ for $Re = 28$, $Re = 10$ and $Re = 1$, respectively, for the axial r.m.s. values. The axial r.m.s. values are small when compared to that of a turbulent flow for water (Lee, 1995), however, for $Re = 28$ the values are just over half the size of those at $Re = 1$. The inward pumping at $Re = 1$ is an effect of the

more dominating viscous forces of the Si1000 solution and causing the increase in r.m.s. levels; as the impeller blade rotates, the fluid moves around the tip, perpendicular to the $\theta = 0^0$ plane, instead of outwards towards the vessel wall, which only occurs at $\phi = 33^0$ and $\phi = 48^0$ where the inertia effects are more dominant.

The inward and outward pumping in the vicinity of the impeller blade is shown in more detail in figures 6.23, 6.24 and 6.25, for $Re = 1$, $Re = 10$ and $Re = 28$, respectively. They show the variations of $< U_r > /V_{tip}$ and $< U_z > /V_{tip}$ with ϕ over 60^0 (from the leading to the following blade), at $z/T = 0.373$ (which corresponds to the point closest to the top right edge of the impeller blade tip), at several radial distances from the blade: $r/T = 0.186$, 0.224, 0.261 and 0.411. Firstly, for $< U_r > /V_{tip}$, the magnitudes of velocity increase with an increase in Re and for each Re they are observed to decrease with increasing values of r/T: As the fluid moves away from the blade in the radial direction, the variation of the radial velocity profile with blade angle, under the influence of viscosity, becomes smoother. It can be seen that for the three Re examined, the maximum positive radial velocity occurs near the pressure side of the blade at approximately $\phi = 50^0$. However, only at $Re = 1$ (see figure 6.23) are negative velocities (velocity vectors pumping inwards, towards the blade) observed where for all values of r/T they occupy approximately half of the 60^0 between the leading and the following blade, namely in the region, $0^0 \leq \phi \leq 30^0$. This change in the direction of the velocities is known as reciprocating motion which in this case ($Re = 1$) causes a breakdown in the pumping, as the integration of the negative velocities is approximately equal to that of the positive which results in negligible net radial pumping. Secondly, for $< U_z > /V_{tip}$ interesting flow characteristics are also observed. As ϕ increases from 0^0 to 60^0, the motion of the impeller causes the fluid to flow either upwards away from or downwards towards the centre of the impeller stream. At $Re = 1$ both these flow directions are observed, where the axial velocity is negative before becoming positive. At $Re = 10$ (see figure 6.24(b)) this is again true but the positive axial velocities are not as large and occur in a smaller region, $45^0 \leq \phi \leq 60^0$. It can also be said that this is only true at $r/T = 0.186$ and 0.224 (the points closest to the blade),

the two points furthest away from the blade only show positive velocities (with little fluctuation) as the flow begins to recirculate up the vessel wall. At $Re = 28$ (see figure 6.25(b)) the fluid always flows downwards, towards the centre of the impeller blade, except at $r/T = 0.411$ (the point furthest from the blade) where it flows upwards.

In figures 6.26 and 6.27 an alternative display of the variation of $< U_r > /V_{tip}$ with ϕ over 360^0 is shown for $Re = 1$ and $Re = 28$, respectively. The normalised radial velocity components are measured at the point; $r/T = 0.186$ (the closest point of measurement to the impeller blade tip) and $z/T = 0.333$ (the centreline of the impeller blade) and viewed from the top of the vessel. Only the radial velocity components can be shown in this plane and in any case the axial components are very small by comparison. Essentially, both figures show the radial velocity components forming a daisy-petal like shape over 360^0. The shape is repeated six times, once for the passage of each blade. For $Re = 1$, it is observed that approximately half of the radial velocity values are negative, directed inward, towards the blade (see figure 6.26). For $Re = 28$ (see figure 6.27), all velocities are positive, much larger in magnitude and the flow pattern is different. Figure 6.28 shows a combination of the previous two plots with the addition of a profile at $Re = 10$ and a blue line which indicates the position; $r/T = 0.186$, $z/T = 0.333$. The Re increases in the direction of the arrow and it is clear by this increase there is also an increase in the magnitude of $< U_r > /V_{tip}$.

To conclude, a number of different points have been addressed here for the Silicon oil solutions; (i) from the ensemble-averaged data the flow behaviour is shown not to scale well with Re and/or N; (ii) there is evidence of a similar 'S' shaped flow pattern to that observed for water at similar Re and/or N but the extent of this pattern is greater for the viscous fluids and the change to this pattern occurs at different Re/N than for water; (iii) the location and size of the re-circulation regions have shown to move further from the impeller blade tip and increase, respectively with an increase in Re, which is analogous to that observed by Lamberto et al. (1999) for a Newtonian fluid at a similar Re and; (iv) the correlation of decreasing r.m.s. levels with decreasing Re observed in the previous section has not been shown in this one due to the changing in flow

discharge direction, both radially and axially, which was shown by phase-resolved data as the impeller passes through 60^0: Positive radial flow near the pressure side of the blade, which vanishes at the blade tip is then followed by localised reverse flow at the suction side of the impeller blade. It is this transition at low *Re*, which has hitherto remained unreported in the literature, which is the focus of the research presented in Rice et al. (2005). By decreasing the *Re* different flow patterns have been observed and different significance of inertial and viscous forces has been noted. However, it is in the following section that an introduction to two non-Newtonian viscoelastic fluids is made where further differences are identified.

6.4 Mixing flow characteristics of non-Newtonian viscoelastic fluids

6.4.1 Introduction

This section formally introduces and discusses the mixing flow behaviour of two non-Newtonian, viscoelastic solutions. They are referred to as PIB100 and PIB2000 and have a kinematic zero-shear viscosity (ν_0) of 1.25 x 10^{-4} m^2s^{-1} and 2.14 x 10^{-3} m^2s^{-1}, respectively, see table 6.1. The former has an almost identical viscosity to that of Si100 and the latter is approximately twice that of Si1000. Each PIB solution is made from polyisobutylene (PIB) (ACROS Organics, ca. $M_w \approx 8.4$ x 10^5, (C_4H_8)n) dissolved in a solvent, decahydronaphthalene (decalin) (Sigma -Aldrich, ca. $M_w \approx 138$, $C_{10}H_{18}$, an aromatic hydrocarbon, in an isomeric mixture of 98 % purity). The fluids were prepared by cutting the polyisobutylene into cubes of $\sim$ 0.5 cm^3, that were added in the appropriate amount to the decalin in 1 l bottles, while stirring with a magnetic stirrer at ambient temperature ($\sim$ 24 ^0C). After stirring for at least 10 days the bottles were rotated on a rolling machine for approximately one week to improve the homogeneity of the solution.

The composition of the PIB100 and PIB2000 is 2.5 % PIB/decalin and 6 % PIB/decalin, respectively. The percentage mass of PIB to solvent is exactly

the same as that used and studied in Chapters 3 to 5. However, it will also be observed from the rheometric graphs presented in section 6.4.2 that the zero-shear viscosity is lower. This is because the solvent used here is an aromatic hydrocarbon, as opposed to a linear one and the polymer chains cannot entangle themselves as easily with the aromatic ring structures and for this reason deform more easily under shear. Additionally the aromatic hydrocarbon is less expensive and easier to acquire. For more information on this, see Fieser (1962).

The aims of this section are to; (i) rheologically characterise the PIB100 and PIB2000 solutions in simple shear; (ii) characterise the flow of the solutions in the mixing vessel through ensemble-averaged mean velocity measurements over a range of Re; (iii) comprehensively study the flow discharge from the impeller for all working fluids at a location adjacent to the blade; (iv) characterise the flow and circulation flow numbers, (Fl and Fl_c, respectively); (v) investigate the change in mean radial discharge velocities and r.m.s. values with increasing values of r/T from the centre of the impeller blade; (vi) study the effects of De on the impeller discharge flow angle; (vii) determine the distribution of shear rates in the vessel at varying Re; (viii) with the use of phase-resolved data investigate the change in shear rate and mean velocity values with the passage of the impeller blade, and finally; (ix) investigate the presence of chaotic flow in mixing of the non-Newtonian fluids.

6.4.2 Rheological characterisation of PIB100 and PIB2000 in simple shear

The PIB100 and PIB2000 solutions have identical rheometric material properties to those already observed for the 2.5 % and 6 % PIB solutions presented in Chapter 3. These properties being strain rate dependent; (i) viscosity and; (ii) first normal stress difference. Chapter 3 provides a full description of the technique and apparatus used to obtain the rheometric results for all the polymeric solutions presented in this treatise. For the PIB100 and PIB2000 solutions the rheometric results obtained from steady shear measurements are presented in figures 6.29 and 6.30, respectively. As already mentioned in Chapter 3, elongation deformation measurements are not available as such experiments are deemed difficult to

carry out for (relatively) low viscosity fluids like the solutions in this study, but a numerical investigation along with the presentation of experimental results of other authors, for similar fluids are shown in Chapter 3. Therefore, each figure shows the non-linear steady state viscosity ($\eta(\dot{\gamma})$) and first normal stress difference ($N_1(\dot{\gamma})$) values as functions of shear strain rate ($\dot{\gamma}$). Both solutions show a decrease in viscosity (shear thinning) and a rise in first normal stress difference, with increasing shear strain rate. However, there are noticeable differences by comparison; (i) for PIB100, a lower zero-shear viscosity (η_0) is exhibited and higher shear strain rates are needed to induce the non-linear behaviour of shear thinning, and; (ii) for PIB100, lower values of N_1 are exhibited and again, higher shear strain rates are required to induce the first normal stress difference effects. From this, it is clear that the PIB2000 solution is not only more viscous but also shows stronger non-linear (viscoelastic) effects. At this stage it is important to note that the rheological changes caused by evaporation or degradation of the PIB and Si solutions were continually monitored prior to, during and after the mixing experiments using the parallel plate rheometer.

With the understanding that the PIB100 and PIB2000 fluids will exhibit non-linear behaviour under increased levels of shear stress, great care was taken in acquiring the mixing vessel measurement data for each fluid. With this in mind, the PIB100 solution is used in order to make an initial study at a Re ranging from 1 to 240. Using ensemble-average LDA measurement data, velocity plots (in the same manner as that of the Newtonian fluids in the preceding sections of this chapter) and shear strain rate distribution plots in the vicinity of the impeller blade are shown. These results provide an initial understanding of how the viscoelastic fluid behaves whilst being mixed. Then, a more in depth study is made for the PIB2000 solution where ensemble-average as well as phase-resolved data is used to study velocity, r.m.s. and shear strain rate distributions.

6.4.3 Ensemble-averaged mean velocity distributions

The mean velocity distributions for PIB100 are shown in figures 6.31 and 6.32 at $Re = 240$, $Re = 80$, $Re = 40$, $Re = 8$ and $Re = 1$ and likewise for PIB2000 in figure 6.33 at $Re = 13$, $Re = 7$ and $Re = 0.7$. The highest Re for each fluid is

the greatest that can be obtained, due to the limitations of the motor. The Re values are calculated by using the zero-shear viscosity value (as opposed to its apparent value, which is changing with shear strain rate) and chosen so that a comparison can be made with Si100 and Si1000. Where necessary, each plot is accompanied by the Deborah Number, De for that flow, which for this chapter, is calculated from the following equation:

$$De = \frac{\bar{\lambda} V_{tip}}{D}, \tag{6.2}$$

where the zero-shear averaged time constant, $\bar{\lambda}$ is defined in equation 3.14. For PIB100, $\bar{\lambda} = 0.0452$ and for PIB2000, $\bar{\lambda} = 0.891$.

For PIB100, at $Re \geq 1$, figures 6.31 and 6.32 show mixing flow characteristics already observed for water, Si100 and Si1000 at $Re \geq 486$, $Re = 50$ and $Re \geq 10$, respectively. Those being; (i) predominantly radial velocities (which increase with increasing Re) that discharge from the tip of the impeller blade and decrease in magnitude towards the wall of the vessel where, at a sufficiently high Re they become mainly axial and; (ii) primary vortices above and below the impeller blade that are observed to move further from the impeller blade tip in the radial direction and towards its centreline with increasing Re (see figure 6.19(a)). However, there is neither the onset of an 'S' shaped flow pattern in the region $Re \leq 240$ (as is observed for water) or flow discharge from the impeller blade tip towards the base of the mixing vessel (as is observed for Si100 and Si1000 at the lowest Re). This is discussed below.

For PIB2000, at $0.7 \leq Re \leq 13$, in figure 6.33 the LDA measurement data is only shown in a region closest to the impeller blade. Measurement data outside of this region is omitted due to the velocity values being very small in regions further from the impeller blade, especially at the mixing vessel walls, roof and base. This is a result of the high viscosity of the PIB2000 solution. For each Re the velocities discharge radially from the tip of the impeller blade and they are marginally larger at $Re = 13$ by comparison to those at $Re = 7$ and much larger in comparison to those at $Re = 0.7$. However, the velocities adjacent to the top and bottom sides of the impeller blade are as large, if not larger than the velocities discharging from the tip. A reason for this is given at the end of

section 6.4.4.

For PIB100 and PIB2000, the results described above show differences in the angle of flow discharge from the impeller blade tip by comparison to water, Si100 and Si1000. It has already been shown in all the ensemble-average plots for water, Si100 and Si1000 that at a low enough Re, namely $Re = 61$, $Re = 1$ and $Re = 1$, respectively, the velocity vectors discharge at an angle from the impeller blade tip directed towards the bottom of the mixing vessel. For PIB100 and PIB2000 at $Re = 1$ and $Re = 0.7$, respectively, this behaviour is not observed, instead the flow is shown to discharge radially.

This observation alone warrants a comprehensive study of the flow discharge for all the fluids, but before one can be conducted it must be said that researchers such as Bartels (1988) reported mean radial velocities in the impeller stream of a Rushton turbine, for both a Newtonian (a Glycerine and water mixture, properties not specified) and two non-Newtonian, Polyacrylamide liquids (0.07 % PAAm and 0.9 % PAAm, properties not specified). For the Newtonian fluid, the velocities were measured at a single point in the stream for 30 rpm $< N <$ 135 rpm. A linear variation of the velocity with N was indicated down to $N = 0$ rpm but the line becomes dashed for $N < 90$ rpm, indicating that the linear correlation is not actually supported by the data shown at the two lower speeds. However, the velocities dropped very sharply and were near zero for $N = 30$ rpm. For the 0.07 % PAAm fluid, a near-linear variation of velocity with N was obtained, but with the radial velocity reaching a near-zero value at $N = 30$ rpm and the data indicate negative (directed inwards) velocities for lower speeds. For the fluid with the most strongly non-Newtonian nature (0.9 % PAAm), negative radial velocities were measured for rotational speeds up to $N = 180$ rpm, and positive ones for higher N values. Unfortunately, data is not available to show the behaviour of the axial velocities of the non-Newtonian fluid, although additionally, Nouri and Whitelaw (1990b) studied the direction of the mean axial discharge velocities of a Newtonian Maltose syrup solution mixed by a pitched blade impeller at a point beneath the impeller blade and very close to the impeller shaft. Negative axial velocities were observed at a relatively low Re and show to suddenly become positive at a critical Re. The following study of the flow discharge incorporates

both Newtonian and non-Newtonian fluids and investigates the related change in both the radial and axial velocities.

6.4.4 Flow discharge investigation

In order to make a comprehensive study of the flow discharge behaviour, for all the working fluids, one point close to the impeller blade is chosen where changes in the radial and axial velocity with Re are deemed most prominent: $r/T = 0.224$, $z/T = 0.298$. This point is a small distance radially away from the bottom right edge of the impeller blade tip. The mean radial and axial velocities are investigated, along with the discharge angle ζ (defined in figure 6.34), which is calculated by simple trigonometry. Hockey and Nouri (1996) observed the change in discharge angle from a pitched blade turbine and suggested that impeller tip speed was the most suitable scaling parameter rather than Re; therefore, the twin approach of examination of both Re and N scaling is adopted in this work.

Figure 6.35(a) shows the normalised radial velocity at the measurement location versus Re for all working fluids. The behaviour of the Si100, Si1000, PIB100 and PIB2000 solutions is very similar over the whole range of Re. The radial velocities for the solutions are approximately zero (or have very small negative values) at $Re \leq 1$ but suddenly begin to increase quite rapidly at $Re \approx 2$. The values keep increasing until a maximum of approximately $0.2V_{tip}$, at $Re \approx 30$ is reached. Water behaves similarly by reaching a maximum value of approximately $0.175V_{tip}$ but at $Re \approx 60$. The mean radial velocity for all the fluids then proceeds to decrease, before showing a small increase at $Re \approx 300$. From this figure it is clear that the mean radial velocities for each fluid, except for water at $Re \lesssim 61$, scale with Re and that the radial velocities become infinitesimally small at $Re \leq 2$, to an extent where the difference between a flow that was inward or outwardly discharging would be within 2 % of each other and deemed negligible. The same results are shown in figure 6.35(b) where the mean radial velocity is plotted as a function of the rotational speed (N) of the impeller. The plot clearly shows how higher values for N are needed to generate the same maximum velocities as the viscosity of the working fluids increase. For instance, the maximum value of $< U_r > /V_{tip}$ for Si100 and Si1000 is at $N = 300$ rpm and $N = 2000$ rpm,

respectively. As already mentioned, data could not be obtained at higher values of N, for higher viscosity fluids (especially PIB2000) due to limitations of the impeller motor but values of N range from 1 to 2500 rpm which is considerably larger than that of Bartels (1988).

Figure 6.36(a) shows the normalised axial velocity versus Re for all the working fluids. For water, the change in radial velocity (described above) is more clearly understood by what is observed here for the axial velocities. In the region, $20 \leq Re \leq 60$, the mean axial velocities of water suddenly increase in the negative direction as Re increases. In the same region, the mean radial velocities increase from zero in the positive direction, thus the magnitude of both are increasing with Re. In the region, $60 \leq Re$ the axial velocities return to and pass through zero to become positive again. Thus, in this region there is less radial discharge and the radial velocities are shown to decrease (see above). This explanation is also coherent with what is observed in the ensemble-average velocity vector plots for water (see figure 6.1). However, for the Si100, Si1000, PIB100 and PIB2000 solutions, the mean axial velocities behave differently. In the region, $Re \geq 20$, the values of $< U_z > /V_{tip}$ increase from approximately zero (or a small negative region) to large positive values, where the values become coincident with that of water again, at a magnitude of approximately $0.08V_{tip}$, at $Re \approx 100$. But, at the same time this increase is accompanied by a decrease in radial velocity, as the water data also shows. These solutions do not show the same large negative axial velocities. An interesting observation is that as the Re begins to increase from 1 in the region, $1 \leq Re \leq 20$ it is only the radial velocities that show a change (an increase). At this point it is only the inertial forces in the radial direction that can overcome the viscous forces. In the region, $Re \leq 20$, the sign of the axial velocity values (and thus direction of axial discharge) becomes insignificant as they are all of very small size, approximately $0.02V_{tip}$. This attaches less importance to the axial discharge at low Re and also suggests that the direction is not being influenced by the viscoelastic forces in the PIB solutions over the whole range of Re.

It is clear that the values for both the Si and PIB solutions do not show a large increase in negative axial velocity as the water ones do, hence it may be

postulated that the axial velocities do not scale with Re for all the fluids over this range, thus this indicates that there is no direct scaling of flow pattern with Re. This is in contrast with the findings of Bartels (1988), Greene et al. (1982), Hockey and Nouri (1996) and Nouri and Whitelaw (1990b) who did not report such variation of the flow discharge behaviour for the Re ranges they studied ($0 < Re \leq 48000$). Figure 6.36(b) shows that the mean axial velocities do not scale with N either. It also shows how considerably larger values of N are needed to generate the larger axial velocities for the higher viscosity fluids. It is also clear that the maximum values of $< U_z > /V_{tip}$ are very small (of the order of $0.02V_{tip}$) for the highest viscosity, PIB2000 solution.

Figure 6.37(a) and 6.37(b) show the discharge angle, ζ as a function of Re and N, respectively. The discharge angle was difficult to measure accurately at low Re, namely at $Re < 5$ where the values of the radial and axial velocities are very small, especially for the most viscous Si and PIB fluids. Variations of ζ with Re in this range are therefore due to scatter of the experimental data. However, at $Re \geq 5$, figure 6.37(a) shows almost identical values for all the fluids, except for water, where large differences in the region, $10 \leq Re < 70$ are shown; the discharge angle for water has a considerably larger negative value ($\zeta \approx -50^0$) with the velocity vectors directed towards the bottom of the mixing vessel. The transition from a negative to a positive discharge angle for water occurs just outside of this region at $Re \approx 75$ and for the Si and PIB solutions, at $Re \approx 10$, which matches the behaviour observed for the radial and axial discharge velocities in the preceding figures. Figure 6.37(b) shows the values of ζ as a function of N. The largest discharge angles are generated for water, Si100 and PIB100 (the lowest viscosity fluids) where, $\zeta \approx 75^0$. However, this value for water is at, $N \approx 20$ but for the latter two, at $N \approx 1000$. It is also clear from this plot that the discharge angle for PIB2000 is negative at its highest Re/N; this is noteworthy and will be discussed later in this section.

Due to the noticeably different flow discharge behaviour of water flow by comparison to that of all the other fluids, the behaviour is shown not to scale with Re and subsequently with N. However, the behaviour of the Si and PIB solutions have shown a discharge behaviour that does scale with Re, despite the

fact that the PIB solutions might be expected to show viscoelastic behaviour, especially at large Re and perhaps influence a change in discharge magnitude and angle. However, as already mentioned, the study of the flow discharge from the impeller blade tip has only been made at one point adjacent to the blade, and for this reason care must be exerted in drawing conclusions. One can not assume from this, an absence of viscoelastic effects in the mixing of the PIB solutions. With this in mind, further studies are conducted.

It is common in mixing practice to calculate the flow numbers (Fl) and circulation flow numbers (Fl_c) from the ensemble-averaged LDA measurements of the mean radial velocities to assess the pumping capacity of the impeller at different operational conditions. Both numbers are calculated from the integration of the mean radial velocity profiles ($< U_r > /V_{tip}$) against z/T in the impeller stream. However, Fl concerns the flow profile adjacent to the tip of the impeller blade (or as close as possible), using the bottom and top right corners of the impeller blade tip (z_1 and z_2, respectively) as the axial limits of the integration, and is defined by:

$$Fl = \frac{Q}{ND^3} \tag{6.3}$$

where, Q is the impeller pumping capacity and defined as:

$$Q = 2\pi \int_{z_1}^{z_2} r.U_r.dr \tag{6.4}$$

where, r is the radial position of the mean radial velocities, which, in all calculations is, 0.015 m.

While the Fl_c number incorporates the fluid entrained into the impeller stream further away from the blade and the integration is carried out from the location of zero $< U_r > /V_{tip}$ below the blade to the corresponding location of zero $< U_r > /V_{tip}$ above the impeller blade tip (z_a and z_b, respectively). This number is defined by:

$$Fl_c = \frac{Q_c}{ND^3} \tag{6.5}$$

where, Q_c is the impeller circulation pumping capacity and defined as:

$$Q_c = 2\pi \int_{z_a}^{z_b} r.U_r.dr \tag{6.6}$$

Both Fl and Fl_c are plotted against Re in figures 6.38(a) and 6.38(b), respectively. The former for all working fluids and the latter for water, Si1000 and PIB100, as the required measurement data is only available for these fluids.

The variation of Fl values with Re shown in Figure 6.38(a), for all working fluids indicates that the pumping in the radial direction increases with Re. Additionally, the largest difference is shown by the comparison of water to the other fluids. For water, the value of Fl is considerably lower in the region, $60 \leq Re \leq 240$. This is possibly caused by the formation of the 'S' shaped flow pattern as Re decreases from a transitional value to one of a laminar flow, as one would expect the fluid pumping capacity determined from radial velocity measurements alone to decrease if it discharges at an angle to the blade, as opposed to radially. However, only small variations in Fl are shown by comparison of the Si and PIB solutions. Although direct comparisons cannot be made with the work of other authors for identical fluids and mixing vessel configuration, it is interesting to compare with the work of Yianneskis et al. (1987), where Fl values of 0.75 ± 0.15 are reported for water in turbulent flow. This value is comparable to a maximum of ~ 0.96 at $Re = 4253$ observed for water in figure 6.38(a) and gives confidence to the results obtained for the other fluids. Figure 6.38(b) shows the change in circulation flow number (Fl_c) with increasing Re and an interesting feature emerges: For water and Si1000 the values of Fl_c are shown to increase with increasing Re, but for PIB100, the values decrease with increasing Re in the region, $40 \leq Re \leq 80$, where at $Re = 80$; $Fl = Fl_c$, when for the other fluids the values of Fl_c are greater than Fl as the former includes the flow entrained into the impeller stream. A possible reason for this sudden decrease, in the absence of a change in the discharge flow direction for PIB100, is that the pumping capacity of the impeller in the region, $40 \leq Re \leq 80$ ($0.974 \leq De \leq 1.942$) is consumed by the onset of elastic forces in the fluid. As Re increases ($Re > 80$), so do the inertial forces and an increase in Fl_c is resumed. It must be noted though that as the data for water and Si1000 do not cover the entire Re range, the decrease in Fl_c observed for PIB100 may be present with these fluids as well.

The properties of the flow discharge stream of a Rushton turbine have often been assessed by consideration of the variation of the radial mean velocities and r.m.s. values along the impeller centreline. Dyster et al. (1993) have made such LDA measurements in viscous Newtonian fluids for laminar to turbulent flow regimes in the range, $5 < Re < 5 \text{ x } 10^4$ using fluids of different viscosities and/or at different impeller speeds. Dyster et al. (1993) reported the normalised mean radial velocities ($< U_r > /V_{tip}$) to drop with decreasing Re and this drop was substantial: $< U_r > /V_{tip}$ was almost an order of magnitude lower for $Re = 5$ compared with the turbulent flow variation reported by Van der Molen and Van Maanen (1978). In more detail: A substantial drop of around 50 % in $< U_r > /V_{tip}$ values compared to the turbulent flow ones was observed by Dyster et al. (1993) for $Re = 36$ with further decreases of around 30 % and 20 % accompanying a reduction of Re to 18 and 8, respectively. Dyster et al. (1993) also reports the normalised radial r.m.s. values (u'_r/V_{tip}) to drop with decreasing Re; two substantial drops in radial r.m.s. are observed, those being; (i) around 10 % in the region $501 \leq Re \leq 2500$ and; (ii) around 10 % again, in the region $42 \leq Re \leq 501$. It is also clear from all the results of Dyster et al. (1993) that the values for the radial mean velocity and r.m.s. values decrease with increasing values of r/T.

A study similar to that of Dyster et al. (1993) is carried out herein where values of $< U_r > /V_{tip}$ and u'_r/V_{tip} along the impeller centreline are compared at varying Re. It must be noted that use of the centreline profile is only appropriate when the direction of the discharge remains horizontal, i.e. in the radial direction, if the flow discharge direction changes, then clearly $< U_r > /V_{tip}$ will decrease, but this stems from directional changes not solely from the decrease in pumping capacity. For this reason, only selected Re profiles are plotted. Firstly, Newtonian profiles are presented: Figure 6.39(a) shows values of $< U_r > /V_{tip}$ dropping with a decrease in Re, by approximately 40 %, 50 % and 70 % at $Re = 50$, 28 and 10, respectively by comparison to the higher Re values at $Re = 486$ and $Re = 4253$, which themselves by comparison show very little difference (both having maximum values of $0.75V_{tip}$); figure 6.39(b) shows values of u'_r/V_{tip} dropping with a decrease in Re, by around 10 % from $Re = 4253$ (where the maximum

value is $0.3V_{tip}$) to 486 and by a further 10 % from $Re = 486$ to 50, 28 and 10. For both $< U_r > /V_{tip}$ and u'_r/V_{tip}, not only are the percentage decreases comparable to that of Dyster et al. (1993) but the values are too. Secondly, non-Newtonian fluid profiles are presented for PIB100 (insignificant differences were shown by comparison of these values to those of PIB2000, so are the only ones presented here): Figures 6.40(a) and 6.40(b) show values for $< U_r > /V_{tip}$ and u'_r/V_{tip} dropping with a decrease in Re, respectively, the former from values of $0.65V_{tip}$ to $0.025V_{tip}$ and the latter from $0.18V_{tip}$ to $0.1V_{tip}$, both in the range, $1 \leq Re \leq 240$. For the latter, only very small differences are shown in the region, $1 \leq Re \leq 80$. Both the Newtonian and non-Newtonian fluids show similar trends: A decrease in $< U_r > /V_{tip}$ and u'_r/V_{tip} with increasing r/T. The most interesting observation is that only small differences for $< U_r > /V_{tip}$ and u'_r/V_{tip} are shown by comparison of the Newtonian and non-Newtonian data at similar Re.

As already shown in equation 6.2, De quantifies the ratio of elastic to viscous forces in the PIB solutions and is a good indication as to whether non-Newtonian behaviour should be expected for that particular flow. As already shown experimentally and numerically in chapters 4 and 5, for $De \leq 1$ a behaviour similar to that of a Newtonian fluid is shown, and for $De > 1$ the elastic forces are more dominant than the viscous ones and induce non-linear behaviour. Figures 6.41(a) and 6.41(b) investigate the relationship between viscoelasticity and discharge angle by presenting values of ζ against De at a point adjacent to; (i) the bottom right corner and; (ii) the top right corner of the impeller blade tip, respectively. Some interesting features occur: For PIB2000 at the bottom right corner of the impeller blade tip (see figure 6.41(a)), in the region $20 < De < 200$ the discharge angle is negative and thus the flow is discharging towards the base of the vessel. At $De < 20$ the values are mostly negative but scattered, as it is difficult to take measurements at low De where the velocities are very small, so for this reason the analysis of these measurement data will be excluded. However, the PIB100 solution shows negative discharge angles at a lower De when they become positive at approximately $De = 0.3$ and increase positively here after, exhibiting fluid flowing towards the centreline of the impeller stream. At the top right corner of the impeller blade, exactly the same is true for both fluids at the higher De but

in the opposite direction where the flow discharge for PIB2000 is positive, thus flowing towards the top of the vessel and negative for PIB100 where the flow discharges towards the centreline of the impeller stream. Figure 6.41 clearly shows the direction of the fluid flow at the corners of the impeller tip, which is not obvious from the vector plots for these fluids. They also provide an indication of the range of De studied for these fluids and hence the influence the elastic forces may be having on such flow behaviour.

6.4.5 Shear strain rate distribution

Before a full discussion of non-Newtonian fluid effects can be made, an examination of the shear strain rates in the vessel is necessary: Both the average/maximum shear strain rate obtained in the $\theta = 0^0$ plane with different fluids/operating conditions, as well as the distribution of such shear strain rates. To this end, the shear strain rate distributions (obtained from the ensemble-average velocity measurements), across the measurement region around the impeller blade, were calculated from the LDA data, from which the average and maximum shear strain rates are determined. As over much of the vessel there was little flow generated by the impeller rotation, the shear strain rates (in most cases) were calculated only for a region surrounding the impeller blade. Radial and axial shear strain rates are calculated, $\partial U_r/\partial z$ and $\partial U_z/\partial r$, respectively over the whole range of Re but the latter is found to be considerably smaller, at most, five times, which would be expected from a radial impeller, such as the Rushton. Therefore, for reasons of brevity these are not presented in the following discussion but are included for completeness in Appendix C (see figures C.1 and C.2). Figures 6.42 and 6.43 show values of $\partial U_r/\partial z$ for PIB100 at $Re = 40$ and 240, and PIB2000 at $Re = 13$. Where possible comparisons are made with a Newtonian fluid of similar Re. In all cases, apart from one, the maximum values of $\partial U_r/\partial z$ are shown in the region adjacent to the impeller blade tip. For this one case, in figure 6.43(b)), the PIB2000 solution shows maximum shear strain rate values of 160 s^{-1} at the top and bottom sides of the impeller. Shear strain rates as high as 160 s^{-1} should induce shear thinning as is shown by the rheometric results for the simple shear viscosity (η) in figure 6.30(a) where the viscosity of the

PIB2000 fluid is shown to decrease by approximately 50 %. The rise in normal stress difference values are also shown in figure 6.30(b) at this shear strain rate. Conversely, the rheometric result for the PIB100 solution does not show any such drop in simple shear viscosity (10 % by comparison, see figure 6.29(a)) at the maximum shear strain rate of 700 s^{-1} observed in the mixing vessel at $Re = 240$ (see figure 6.42(c)). So one would not expect to observe large changes in flow behaviour. The more non-linear behaviour of the PIB2000 solution is more obvious from what is observed here and in the velocity vector plots already described and shown in figure 6.33; at $Re = 13$, larger velocity vectors were observed in regions adjacent to the top and bottom sides of the blade as opposed to at the middle of the tip and high levels of shear thinning in these regions is thought to be causing this. To have an understanding of the magnitude of these shear strain rates, the PIB2000 solution at $Re = 13$ is compared to a Newtonian fluid at a similar Re, namely Si1000, at $Re = 10$ and an increase of nearly one order of magnitude is shown. The Si100 solution, at $Re = 50$ is also compared to the PIB100 solution, at $Re = 40$ when, $De < 1$ and there is only a small difference between them signifying that the mixing flow behaviour for both fluids, in this regime, is that of a Newtonian one.

From the shear strain rate distribution data presented, the following can be concluded: The ensemble-averaged shear strain rates for the PIB100 fluid are well below the range at which significant non-linear behaviour becomes apparent in the rheometric data. Consequently, shear-thinning behaviour is not expected to be in evidence. Conversely, for the PIB2000 fluid the ensemble-average shear strain rates have reached values corresponding to that at which the viscosity is approximately 50 % of the zero-shear value and non-Newtonian effects should be present. A comparison was also made to that of a Newtonian fluid at approximately the same Re which showed shear strain rates for the non-Newtonian fluid that were nearly one order of magnitude greater.

Although the above shear strain rate values have been estimated from ensemble-averaged data, very useful for overall indications of shearing in the vessel, there may be significant shear strain rate variation with blade angle. Consequently, the distribution of shear strain rate in the $\theta = 0^0$ plane with blade angle was

calculated from phase-resolved data and is discussed in the following section.

6.4.6 Phase-resolved mean velocity measurements

Only results for the PIB2000 fluid are presented as the most prominent, if not the only, viscoelastic behaviour is shown for this fluid[4]. In addition, for the same reasons as mentioned above, only results for the $\partial U_r/\partial z$ values are presented. The $\partial U_z/\partial r$ results are included in Appendix C (see figures C.3, C.4 and C.5). Figures 6.44, 6.45 and 6.46 at Re = 0.7, 7 and 13, respectively, show the shear strain rate distribution in five ϕ planes: 2^0, 27^0, 42^0, 52^0 and 55^0. The choice of ϕ is made where the most prominent non-linear flow behaviour is observed. The figures show maximum shear strain rates of 7.5, 110 and 220 s^{-1}, respectively, which, according to the rheometric graphs in figure 6.30 would induce drops in viscosity of approximately 10 %, 55 % and 65 %, respectively and the subsequent induction of first normal stress differences of increasing magnitude. At $Re = 0.7$ and 7 the maximum shear strain rates occur at $\phi = 52^0$ adjacent to the top and bottom of the impeller blade tip. At Re = 13 the maximum values appear at the top and bottom sides of the impeller or at some values of ϕ, at the impeller blade tip as well. For every Re the shear strain rate value around the impeller is continually changing with location as the blade sweeps through 60^0 implying that the magnitude and direction of the velocity vectors at these points are also changing.

From the shear strain rate distribution data presented, the following can be concluded: The phase-resolved data show, as might be expected, an even higher shear strain rate variation and must cause more severe non-linear behaviour. An important implication is that phase-resolved data is essential in highlighting regions of the flow where the shear strain rates may be sufficiently high over parts of the impeller rotation for shear-thinning and/or viscoelastic effects to become important. These effects are now considered with respect to the phase-resolved velocity vectors as well.

---

[4]Phase-resolved data was taken for PIB100 to gain a preliminary understanding of the behavioural characteristics of such fluids but not at a Re/De high enough to show non-linear activity, so for reference these results are shown in Appendix B.

Figures 6.47, 6.48 and 6.49 show velocity vectors in the same five ϕ planes (2^0, 27^0, 42^0, 52^0 and 55^0) at Re = 0.7, 7 and 13, respectively. At $\phi = 27^0$, for $Re = 0.7$ the velocities are relatively small and those adjacent to the impeller blade are radial in the direction of the vessel wall (at the centreline) or pumping in this direction with a small inclination towards the centre of the impeller stream. As the Re increases at this value of ϕ, the magnitude of the velocity vectors and the angle of flow inclination above and below the blade increases. At the highest Re there are also signs of vortices forming at $r/T = 0.2$. At $\phi = 42^0$, for $Re = 0.7$ the radial and axial velocities increase in magnitude and the fluid begins to show the behaviour observed in section 6.4.4 where the axial direction suddenly changes and the vectors at the top and bottom right of the impeller blade tip begin to be directed away from the centre of the impeller stream. This is not shown at the higher Re for the same value of ϕ where the velocity vectors are discharging radially. At $\phi = 52^0$, for $Re = 0.7$, this behaviour becomes more evident as the vectors not only at the tip but also surrounding the impeller blade are in a direction away from the centre of the impeller stream. For those of the higher Re flows, this behaviour is just developing. At $\phi = 55^0$, for $Re = 0.7$ the behaviour culminates, the vectors at the top and bottom right of the impeller blade tip become predominantly axial and the magnitude of all vectors in the vicinity has decreased, to an extent where the radial velocity at the centre of the impeller blade tip and adjacent to it, becomes almost insignificant. However, as the Re increases, the latter is not true, the vector at this point is relatively large and increasing in the positive axial direction, towards the top of the vessel. Finally, at $\phi = 2^0$, for $Re = 0.7$ the vectors closest to the tip are directed towards the impeller and more interestingly the radial discharge from the tip has changed direction and is pumping inwardly, showing similarities to that already observed for a Newtonian fluid in the low Re range. As the Re increases the velocity vectors increase in magnitude, showing no signs of inward pumping but predominantly axial flow discharge away from the centre of the impeller stream, at most of the locations close to the blade.

Before further discussion, the change in flow behaviour of the PIB2000 by comparison to a Newtonian fluid at a similar Re must be discussed. For this

reason the velocity vectors for the Si1000 solution, at $Re = 10$ at the same five values of ϕ, close to the impeller blade, are shown in figure 6.50. The vectors are shown to discharge predominantly radially from the impeller in the direction of the mixing vessel wall, at some instances only at a very small inclination either towards or away from the centre of the impeller stream, depending on the value of ϕ. Primarily, the vectors do not show; (i) predominantly axial discharge, at certain values of ϕ, at any point in the vicinity of the blade or; (ii) a change in direction of radial discharge, from a positive to a negative one (inward and outward pumping). Results of the Si1000 solution at $Re = 28$ are also shown to reiterate these effects of a Newtonian fluid at an even higher Re but for brevity, are included in Appendix C (see figure C.6).

A view from the top of the mixing vessel of the normalised radial velocities for the PIB2000 solution are shown in figures 6.51 and 6.52 at $Re = 0.7$ and 13, respectively. The measurements are at the point: $r/T = 0.186$ (the closest point of measurement to the impeller blade tip) and $z/T = 0.333$ (the centreline of the impeller blade). Both figures show the radial velocity components forming a daisy-petal like shape over 360^0 which repeats itself 6 times, once for the passage of each blade. At $Re = 0.7$ the majority of the radial velocities are in a positive direction away from the blade, but in the region directly behind the blade, on the suction side, the velocities change direction and become negative; as already discussed, at this Re the inertial forces are low and the flow pattern is dominated by the viscous and pressure forces. At $Re = 13$ all velocities are in a direction away from the blade. The velocities reach a maximum at about 50^0, infront of the blade on the pressure side, and then suddenly drop to their smallest value at $\phi = 0^0$, before increasing again. Figure 6.53 combines the previous two and incorporates additional measurement data at $Re = 7$ and shows the change in radial discharge at this point with increasing Re. For reference, the relevant PIB data for $Re = 7$ are shown in figure C.7 in Appendix C.

Although a radial impellers (such as the Rushton) role in mixing may be thought of as to generate high velocity gradients primarily in the radial ($\partial U_r/\partial z$) and tangential ($\partial U_\theta/\partial \theta$) directions, in the impeller vicinity, such accelerations may be resisted by a viscoelastic fluid through the development of a non-linear

behaviour. As already been shown in chapters 3 to 5, the non-linear behaviour of such fluids is a complex one and stems from the understanding that they have shear strain rate dependent shear and elongational viscosity ($\eta(\dot{\gamma})$ and $\eta_\epsilon(\dot{\epsilon})$, respectively) and exhibit large values of normal stress difference, $N_1(\dot{\gamma})$. For a full understanding of these fluid characteristics, see chapter 3, but in essence, the drops in shear viscosity, the rise and then subsequent decrease in elongational viscosity (see chapter 3) and the increase in the N_1 values are certainly changing the fluid mixing patterns and perhaps even resisting this mechanism.

On a molecular level, this process has been hypothesised by Baid and Metzner (1977) as a stiffening tendency caused by the rapid orientation and extension of the polymer molecules: With high radial ($\partial U_r/\partial z$) and tangential ($\partial U_\theta/\partial\theta$) gradients and lower axial ($\partial U_z/\partial z$) gradients present in the flow around a Rushton turbine, the flow is more elongational in the two former directions and comparatively non-elongational in the axial one. The resulting elongation of fluid elements in the radial and tangential directions is thus resisted by the elongational viscosities produced and the flow in the axial direction is therefore less, if at all, inhibited by viscoelastic response. As a result, a change from radial to axial flow pattern may be plausible. In other words, the centrifugal forces are resisted by viscoelastic effects and the discharge direction is varied accordingly. This is what has already been presented and discussed above: At certain values of ϕ the fluid discharges axially from the impeller tip and as Re increases the magnitude of even the largest radial velocities increase in the axial direction.

Greene et al. (1982) studied the mixing of viscoelastic fluids stirred by an axial flow impeller (a 6-blade pitched blade turbine) at $Re = 330$ to 34408[5] (and possibly from at a lower Re value as not all viscosities are given). They observed that the most striking change was the increase of the impeller discharge angle as more Separan (a viscoelastic additive) was added to the fluid: The angle of less than 30^0 observed with water increased to 90^0 at the highest Separan concentration considered. They stipulated that the change in flow pattern could be expected to result in substantial changes in mixing time. Three reasons cited for such changes

[5]A Re of this magnitude is reached due to the low zero-shear viscosity values of the fluids used.

were: The fluid's apparent and zero-shear viscosity which increased with Separan addition; the fluid becoming increasingly pseudoplastic as Separan was added; and Separan addition causing large increases in the viscoelastic character of the fluid. The first two reasons were thought to be of minor importance in comparison to the third as experiments with a viscous Newtonian fluid ($\eta = 0.104\ Pa.s$) showed only a minor increase in the fluid discharge angle. This is supported by their analysis which showed that the apparent viscosity of one Separan solution, calculated using the average shear strain rate, was only 0.018 $Pa.s$, much less than that of the Newtonian viscous solution, although the discharge angle of the latter was much less than the non-Newtonian and far more viscous fluid. Their results point clearly to strong correlation between flow pattern and level of fluid viscoelasticity, and a similar correlation was drawn using the first normal stress difference as an indicator of viscoelastic response level.

Quraishi et al. (1977) examined the increase in mixing time for turbine agitators associated with the circulation of viscoelastic substances, and proposed three reasons for this behaviour; (i) an increase in elongational viscosity; (ii) suppression of trailing vortices and; (iii) suppression of the microscale turbulence. The first has already been shown and discussed but the latter two are of great interest and warrant discussion for the non-Newtonian working fluids in this chapter: From the phase-resolved measurement data obtained for PIB2000, figures 6.54, 6.55 and 6.56, for $Re = 0.7$, 7 and 13, respectively, show $< U_r > /V_{tip}$ and $< U_z > /V_{tip}$ varying with ϕ over 60^0 (from the leading to the following blade), at $z/T = 0.373$ (which corresponds to the point closest to the top right edge of the impeller blade tip), at two radial distances from the blade: $r/T = 0.186$ and 0.224. Where; (i) the radial velocities show flow discharging away from the impeller blade at all Re, except at $Re = 0.7$ where inward pumping is shown as well; (ii) peaks in radial velocity on the pressure side of the blade at approximately $\phi = 50^0$ are shown, which is very similar to that of Si1000; (iii) axial velocities peak in the positive direction towards the top of the mixing vessel but have smaller negative values at other values of ϕ. The drop in radial and axial velocities as r/T increases is noticeably larger by comparison to that of a Newtonian fluid: Both the radial and axial velocities, for PIB2000, are shown to peak between $0.1V_{tip}$ and $0.25V_{tip}$

(depending on Re) as the blade rotates and subsequently these values decrease by approximately 15 % at certain values of ϕ by moving a small distance further from the blade. This is compared to a maximum decrease of approximately 5 % for the Newtonian solution (see figure 6.25) by the same distance. One can postulate that the PIB2000 solution is thickening and resisting propagation of the flow behaviour observed closer to the blade and thus suppressing the formation of vortices further from the blade, and possibly microscale turbulence too. This is even more evident in figure 6.57 where the same plots are made for PIB2000, at $Re = 13$, at the centreline of the impeller blade ($z/T = 0.333$), where; a drop of 25 and 15 % is observed for the radial and axial velocities, respectively, as r/T is increased. For reference, these plots, at a lower Re are shown in Appendix C (see figures C.8 and C.9).

To help quantify the difference in the magnitude of velocity at the impeller tip, between the Newtonian and non-Newtonian fluids, one should observe the behaviour of the radial and axial velocities in figures 6.58(a) and 6.58(b), respectively. In both figures the velocity measurements are taken at the top right corner of the blade (as before). The normalised radial velocity is qualitatively and almost quantitatively identical for the PIB2000, PIB100 and Si1000 solutions. The axial velocity values show the largest difference by comparison of each fluid: The values for the PIB2000 solution are approximately 50 % larger than that of the Newtonian fluids in the region in front of and behind the blade, at $50^0 \leq \phi \leq 60^0$ and $0^0 \leq \phi \leq 10^0$, respectively. This is coherent with what has already been shown of the axial velocities in the vector plots for PIB2000. It is also clear from both figures that at $Re = 8$ the PIB100 solution shows the same profiles as the Si1000 solution enforcing the assumption that the former is behaving as a Newtonian fluid due to the lack of non-linear activity over this range of Re.

6.4.7 Time-resolved velocity measurements

Another important consequence of non-Newtonian fluid mixing is the likelihood of triggering of chaotic motion that was already mentioned in the introduction to this Thesis. As shown in the figures previously presented, the distribution of shear strain rates in a stirred vessel can span a very wide range (0 to 700 s^{-1}).

Consequently, a correspondingly wide range of local viscosity conditions will be encountered across the vessel volume which makes the physical interpretation of the flow patterns rather challenging. Obviously, the shear strain rates at different localities in the vessel depend on the local velocity fields and gradients and, where viscoelastic fluids are concerned, as in the present case, history effects due to the viscoelastic behaviour increasing substantially the complexity of the phenomena to be studied due to the non-linearity introduced by such behaviour. In turn, non-linearity may amplify small asymmetries of the system such as those stemming from imperfect rotation of the shaft or manufacture of the vessel internals, possibly resulting in chaotic structures such as those that have been observed through flow visualisation by Alvarez et al. (2002). It is interesting to note that Alvarez et al. (2002) observed such chaotic behaviour even with weakly viscoelastic carbo-methyl-cellulose (CMC) non-Newtonian fluids, but found a complete absence of chaotic effects when Newtonian fluids were used under otherwise identical conditions. Essentially, the chaotic behaviour observed by Alvarez et al. (2002) showed a mixing structure that oscillates periodically at the same frequency as that of the rotational speed of the impeller shaft.

With the aim to quantify such chaotic behaviour for the PIB2000 solution, time-resolved velocity measurements of the radial and axial components were made in the region, $0.0745 \leq r/T \leq 0.149$ and $0.447 \leq z/T \leq 0.596$. This region being chosen on the assumption that chaos could be found in approximately the same vicinity above the impeller, as in the work of Alvarez et al. (2002). Measurements were recorded at discrete points in this region and for one point in particular ($r/T = 0.112$, $z/T = 0.522$) the results are shown in figures 6.59(a) and 6.59(b). The rotational speed of the Rushton impeller shaft, at $Re = 13$, is 2304 rpm (38.4 Hz), and for both the radial and axial velocities, in these figures, periodic fluctuations of approximately 38 Hz are discernible. However, the best way to assess the influence of periodicity to the flow is by quantifying the changes of the strength of the frequency components along the impeller stream, therefore a spectral analysis of the velocity recordings shown in figures 6.59(a) and 6.59(b) was performed to calculate the energy spectrum, E(f).

The energy spectrum, E(f) is computed from the discrete Fourier transform

of the fluctuating velocity, u, defined as:

$$u = U - < U > \tag{6.7}$$

where U is the instantaneous velocity and $< U >$ is the mean.

Since the velocity realisations with LDA are obtained at random intervals complications are introduced in the calculation of $E(f)$. However, it is possible to obtain 'pseudo-equi-time spaced' data by conditionally resampling the velocity recording. A suitable resampling interval was chosen such that:

$$u'^2_{raw} \approx u'^2_{resampled} \approx \int_0^\infty E(f)df \tag{6.8}$$

where:

$$u' = \sqrt{< U^2 >} \tag{6.9}$$

And, u'^2_{raw} and $u'^2_{resampled}$ are associated to the raw and resampled data respectively. The difference between the three terms in equation 6.8 is reduced to less than 1 % for both the radial and axial velocities and the resampled values for u are calculated by nearest neighbour interpolation.

Figures 6.60(a) and 6.60(b) show the energy spectrum, E(f) versus frequency, f, for the radial and axial components of the velocity and both show a sharp peak at a frequency of 38.592 and 38.594 Hz, respectively. These frequencies are almost identical and clearly indicate a periodic motion in the flow with a frequency equal to that of the impeller shaft, subsequently showing a chaotic motion comparable to that of Alvarez et al. (2002). In addition, figure 6.60(b) shows another smaller but distinctive peak at a frequency of 77.621 Hz, which is approximately twice that of the largest peak, a harmonic of the impeller rotational frequency.

Although all other points over the region studied showed discernible periodic fluctuations in velocity, the data acquisition rate was not high enough in both the radial and axial components to satisfy the Nyquist criterion. This typically occurred at locations furthest away from the impeller blade, at the center of a vortex and adjacent to the blade where either one of the velocity components prevailed.

6.4.8 Discussion and conclusions

In this chapter, detailed LDA velocity measurement data obtained for a stirred vessel have been presented for five different fluids. Three are Newtonian and of varying viscosity: water, Si100 and Si1000. The remaining two are non-Newtonian, viscoelastic fluids: PIB100 and PIB2000. Ensemble-averaged and phase-resolved velocity measurement data were used to gain an understanding of fluid flow behaviour which, traverse the turbulent to laminar regimes and for the non-Newtonian, exhibits non-linear, complex flow behaviour.

Initially, water was studied in a turbulent flow regime, at $Re = 4253$. This provided a good starting point as excellent comparisons were made with the measurement data of Micheletti (2004) and Lee (1995) which was not only an indicator of high fidelity, giving confidence to the accuracy of the results, but provided a good link for comparison to laminar flow behaviour which is the primary focus of this treatise. Ensemble-averaged mean velocity measurements were taken at $Re = 4253$, 486, 61 and 49 and as the Re decreased from its highest value to $Re = 61$, two interesting features emerged; (i) the mixing flow pattern changed from one similar to those encountered in turbulent flow to a sigmoid pattern and; (ii) the r.m.s. levels diminished to zero. Both an indication of laminar flow.

To study the Newtonian flow behaviour in the region $Re \leq 50$, with the same mixing vessel configuration, the viscosity of the fluid was increased. The Si100 and Si1000 solutions, with a viscosity 100 and 1000 times that of water, respectively, were used and initially ensemble-averaged mean velocity measurement data were taken for each. The former at $Re = 50$, 1 and 0.5 and the latter at $Re = 28$, 10 and 1. For both fluids, a further change in flow pattern was revealed as Re decreased from its highest value to 1: The mean velocity vectors changed from being predominately radial at the impeller blade tip at higher Re (50, 28 and 10) to discharging in a direction towards the bottom of the vessel at low Re (1 and 0.5). The sigmoid flow pattern observed for water was not observed for either fluid and thus the flow behaviour did not scale well with Re and/or N, however, there is evidence of a similar pattern but the extent of this is greater and the velocities, smaller in magnitude. However, the decrease in radial and axial velocities accompanying the reduction in Re, was not subsequently accompanied

by a further reduction in r.m.s. levels to near zero values as already observed for water. Contrarily, an increase was shown. This was due to the changing in flow discharge direction, both radially and axially as observed from the phase-resolved data for Si1000. These data also revealed the mixing mechanism as the impeller blade rotated; maximum positive velocities close to the pressure side of the blade and minimum (negative for low Re) velocities on the suction side. Additionally, the location and size of the re-circulation regions were also investigated and shown to move further from the impeller blade tip and increase, respectively, with an increase in Re.

The last two fluids studied were PIB100 and PIB2000, both non-Newtonian, viscoelastic solutions. Ensemble-averaged measurement data were taken in the range $1 \leq Re \leq 240$ and $0.7 \leq Re \leq 13$, respectively. Both fluids exhibited a flow behaviour that predominantly discharged radially from the impeller blade tip over the range of Re and did not change to one that discharged at an angle towards the base of the mixing vessel at a low Re, as the Newtonian fluids showed. This alone warranted a comprehensive study of the flow discharge from the impeller blade, for all the fluids. To do this, a number of different approaches were taken; (i) at one point, close to the bottom right corner of the impeller blade, radial and axial velocities and the angle of discharge, ζ were individually studied; (ii) the flow numbers (Fl) and circulation flow numbers (Fl_c) were calculated; (iii) the radial mean velocities and r.m.s. values along the impeller centreline were assessed and finally; (iv) the mixing Deborah number (De) was calculated and plotted against the angle of discharge. For each, the respective conclusions have been drawn; (i) at $10 \leq Re \leq 100$, water showed noticeable differences in discharge by comparison to that of the other fluids, which themselves showed only small differences within the margins of experimental error. This was due to the axial velocities of water that differed greatly in magnitude and direction at this point, by comparison to the other fluids. Again, due to the noticeably different flow discharge behaviour of the water flow, the flow behaviour for all the fluids is shown not to scale with Re and/or N. However, this exercise did not reveal any viscoelastic behaviour for the PIB100 and PIB2000 solutions; (ii) the Fl accounted for the discharge from the whole impeller blade tip and revealed a much lower value for water by comparison

to the other fluids (which themselves again only showed small differences) in the region, $60 \leq Re \leq 240$. This was explained by the formation of the 'S' shaped flow pattern for water, as one would expect the fluid pumping capacity, determined by Fl to decrease if it discharges at an angle from the blade. The circulation flow number (Fl_c) includes the flow entrained in to the impeller stream and for this reason was expected to be larger then Fl. However, for PIB100, Fl_c drops in value at $Re = 80$, where, $Fl_c \approx Fl$, a possible reason for this, in the absence of a change in the discharge flow direction for PIB100, is that the pumping capacity of the impeller at this value is consumed by the onset of elastic forces in the fluid, although this was not conclusive; (iii) the centreline radial mean velocities and r.m.s. values showed similar trends for both the Newtonian and non-Newtonian fluids at similar Re and both showed a decrease with increasing r/T. This was explained by the large and more dominant inertia effects at this point, and finally; (iv) the De plots provide an indication of the degree to which the elastic forces in the fluids could be affecting the flow discharge behaviour.

To gain a better understanding of the fluid behaviour of the PIB100 and PIB2000 solutions, ensemble-averaged velocity measurement data were used to calculate the distribution of shear strain rates in the vicinity of the impeller. For the highest Re, the values shown for the PIB100 solution were well below the range at which shear thinning becomes apparent in the rheometric data, consequently, a shear-thinning and/or viscoelastic behaviour in the mixing vessel, was not evident. Conversely, the ensemble-averaged shear strain rates, for the PIB2000 solution reached values corresponding to those at which the viscosity was approximately 50 % of the zero-shear value in the rheometric data. However, phase-resolved shear strain rates for this fluid showed an even higher variation (of the order of 65 %) and the vector and shear strain rate plots for this revealed more noticeable non-linear behaviour. In short, as the impeller blade rotated, the fluid discharged radially from the tip, however, over approximately 30^0 the shear strain rates were high enough to induce severe non-linear behaviour. The outcome of such behaviour caused the flow to discharge axially from the tip (at certain angles, almost perpendicular to the centreline of the impeller stream), subsequently resisting the propagation of fluid motion in the radial direction and

the velocity vectors adjacent to the top and bottom sides of the blade increased in magnitude. It must be remembered that the behavioural characteristics of such fluids, and their causes, are very complex (as this treatise has proven) and cannot be summarised here. A full discussion of these effects is given in the text.

The closing part of this chapter discussed the importance of chaotic mixing and quantified the existence of such behaviour through time-resolved velocity measurement data of the radial and axial components, for the PIB2000 solution. A region close to the impeller blade was studied and at certain points the data acquisition rate was high enough to calculate the energy spectrum. The results showed the fluid flow periodically fluctuating at a frequency equal to that of the impeller shaft. This behaviour provided evidence of chaotic motion in the mixing vessel and is similar to that observed by Alvarez et al. (2002), who studied a similar, viscoelastic, shear thinning fluid which gives confidence to the results obtained here.

Fluid	Kinematic viscosity, ν $[m^2/s]$	Refractive index (25^0C)	Abbreviation
Water	1 x 10^{-6}	1.33	Water
Silicon oil 1	1 x 10^{-4}	1.403	Si100
Silicon oil 2	1 x 10^{-3}	1.403	Si1000
polyisobutylene 1	1.25 x 10^{-4} (zero-shear)	1.47	PIB100
polyisobutylene 2	2.14 x 10^{-3} (zero-shear)	1.47	PIB2000

Table 6.1: The abbreviation used for each working fluid. The number in each abbreviation indicates its factor of viscosity in comparison to that of water.

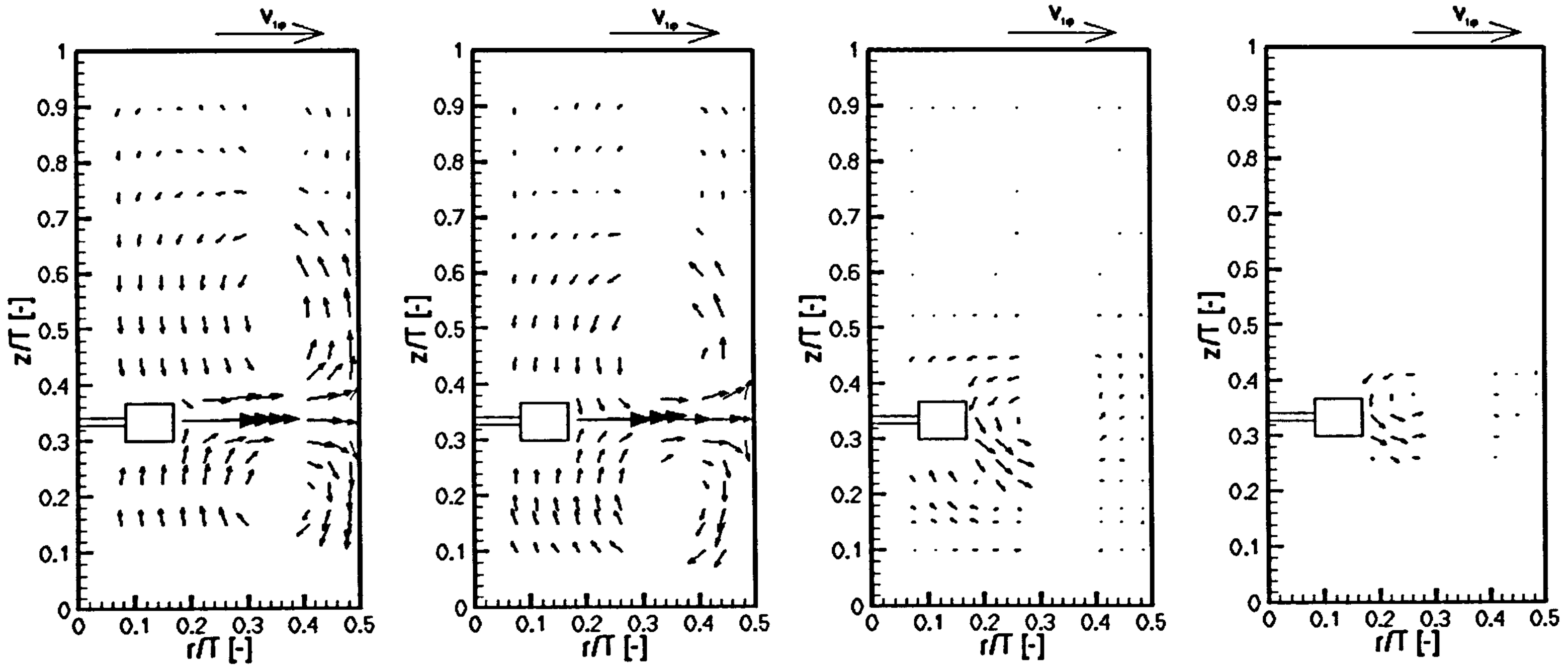

Figure 6.1: Ensemble-average velocity vectors for water, in the $\theta = 0^0$ plane. (a) $Re = 4253$; (b) $Re = 486$; (c) $Re = 61$; (d) $Re = 49$.

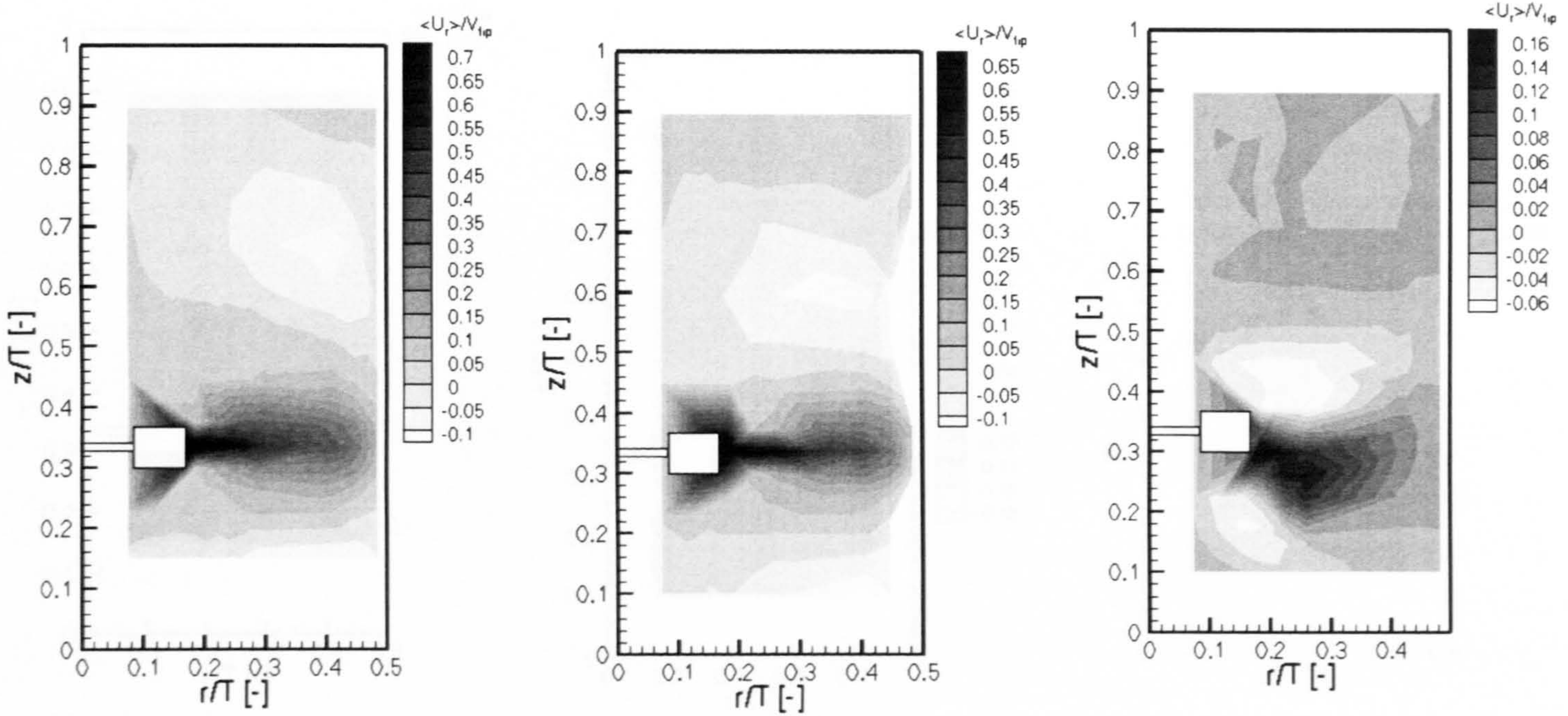

(a) (b) (c)

Figure 6.2: Ensemble-average radial velocity contours for water, in the $\theta = 0^0$ plane. (a) $Re = 4253$; (b) $Re = 486$; (c) $Re = 61$.

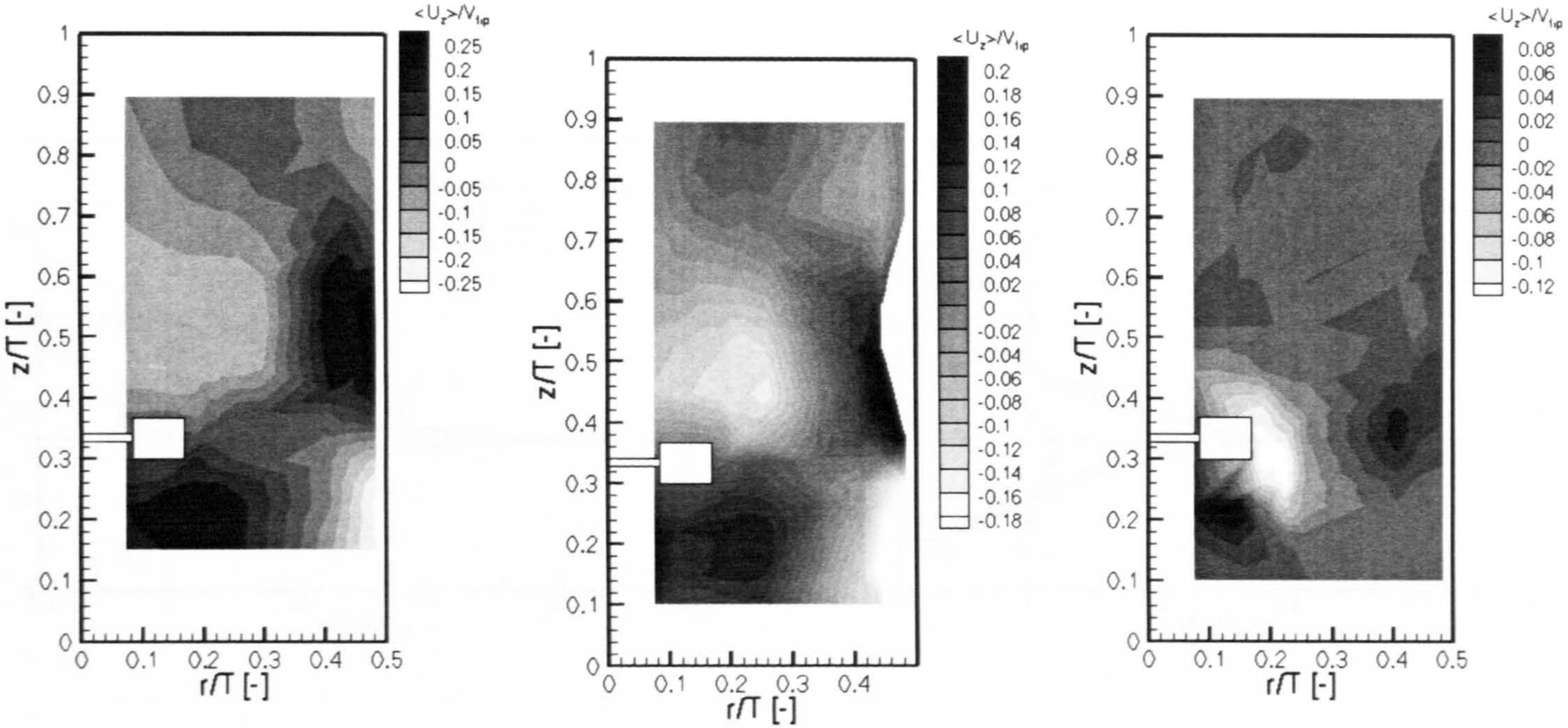

(a) (b) (c)

Figure 6.3: Ensemble-average axial velocity contours for water, in the $\theta = 0^0$ plane. (a) $Re = 4253$; (b) $Re = 486$; (c) $Re = 61$.

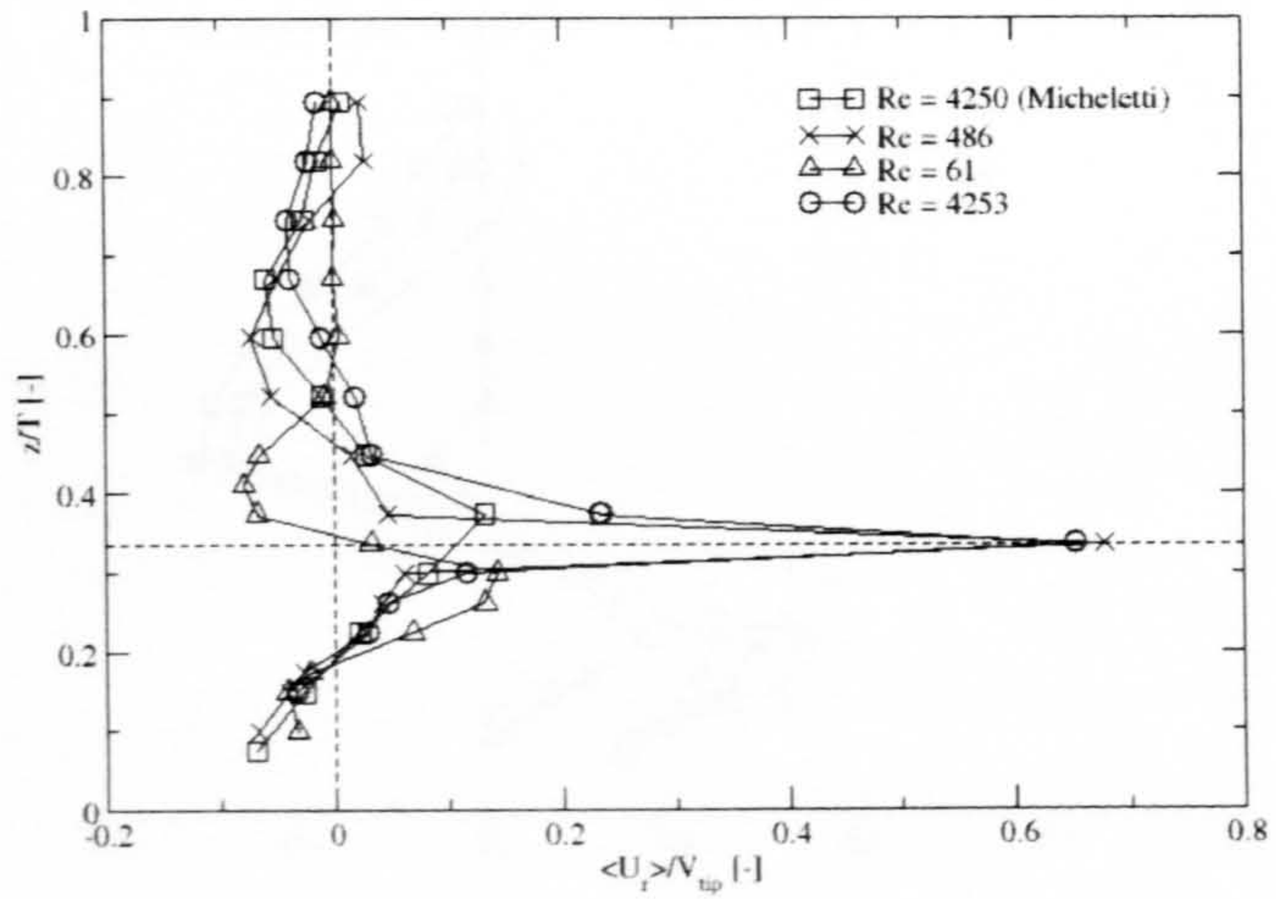

(a)

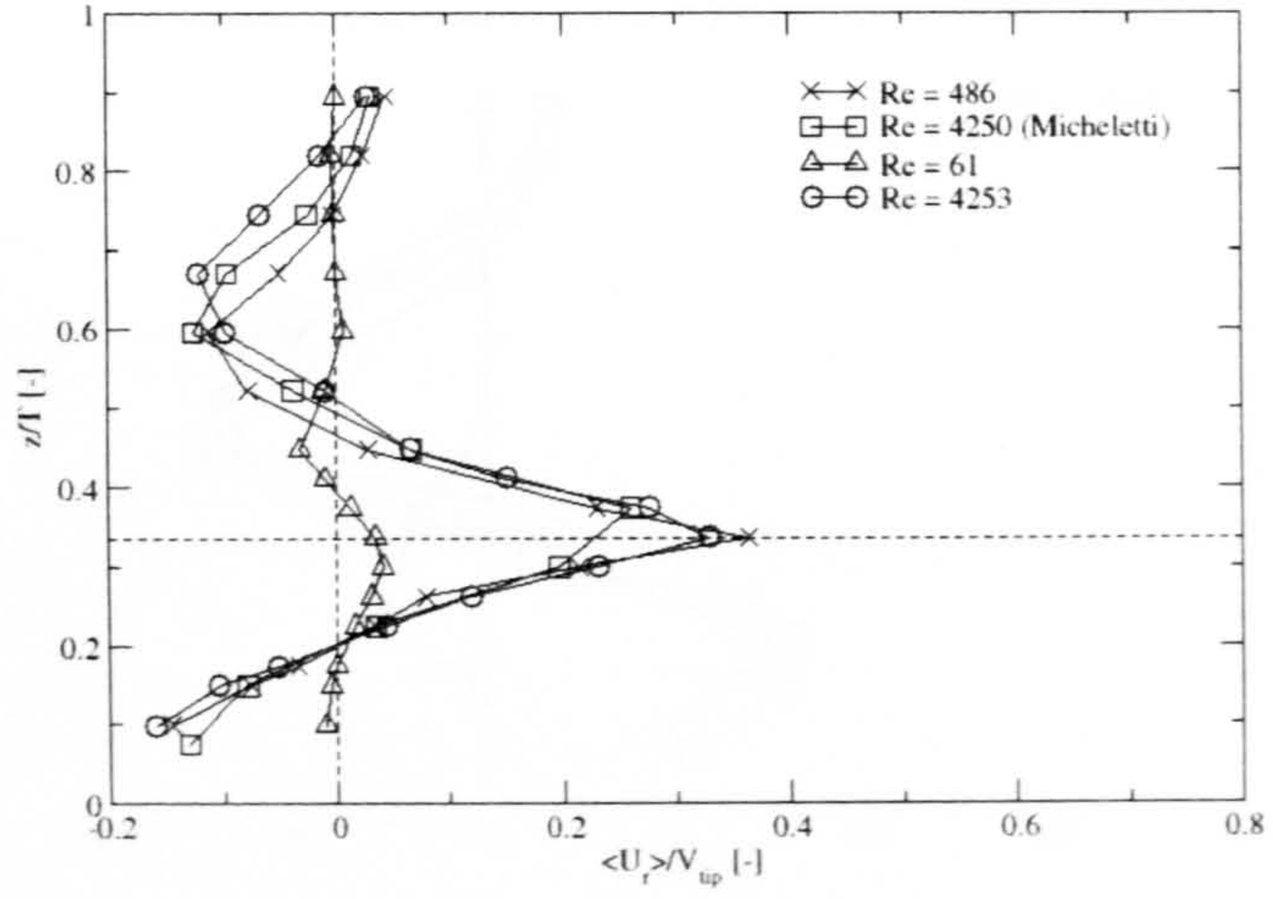

(b)

Figure 6.4: Mean radial velocity values for water at; (a) $r/T = 0.22$ and; (b) $r/T = 0.41$, in the $\theta = 0^0$ plane.

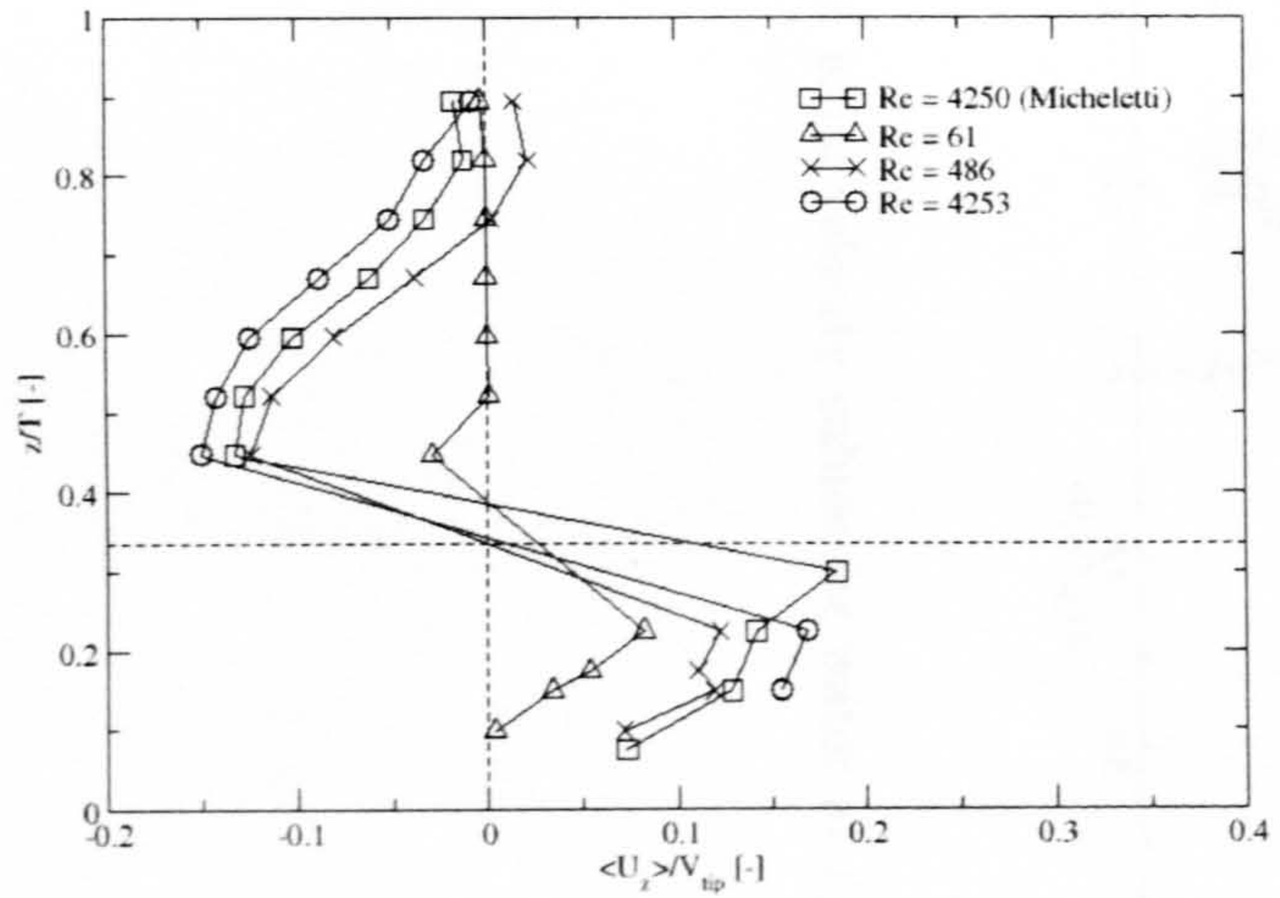

(a)

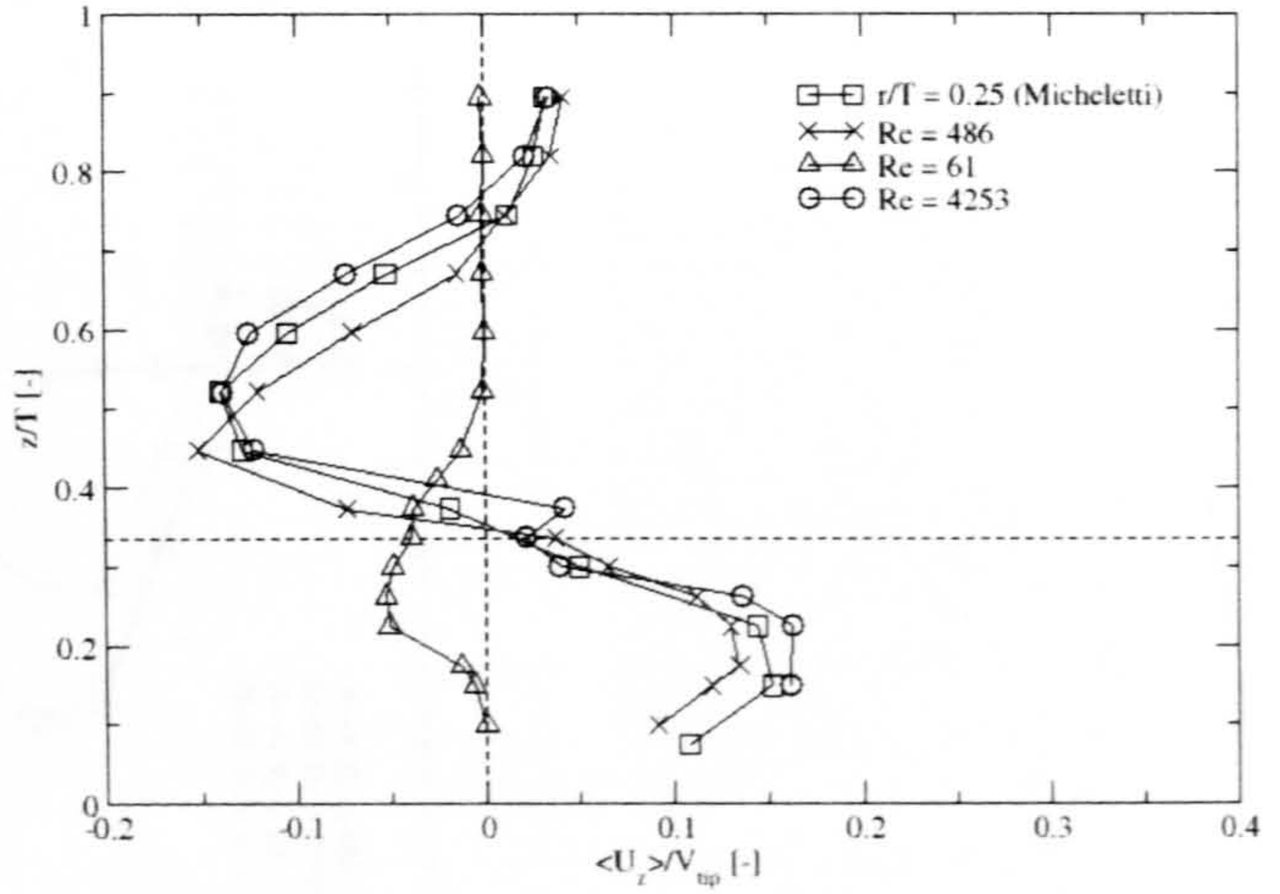

(b)

Figure 6.5: Mean axial velocity values for water at; (a) $r/T = 0.15$ and; (b) $r/T = 0.26$, in the $\theta = 0^0$ plane.

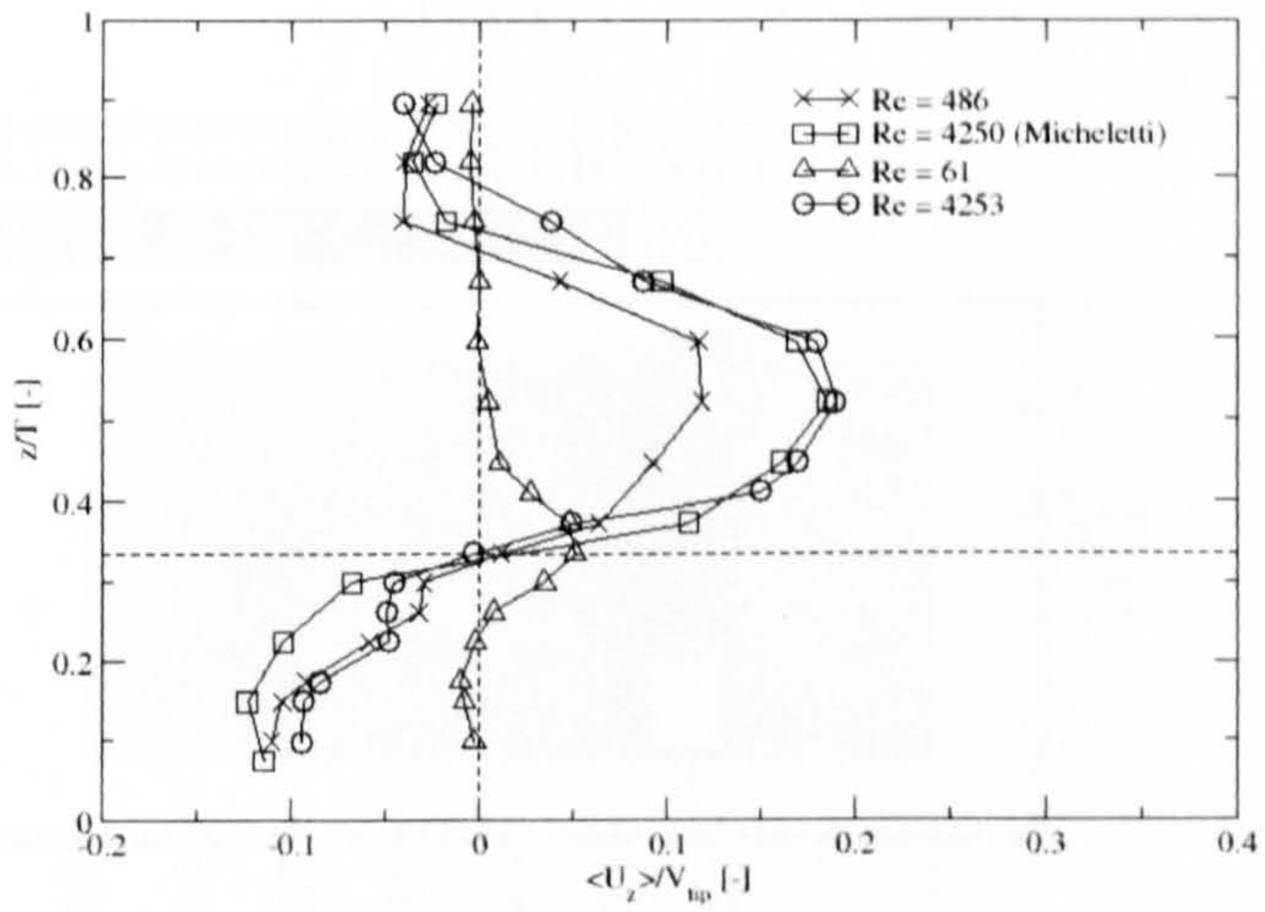

Figure 6.6: Mean axial velocity values for water at $r/T = 0.41$, in the $\theta = 0^0$ plane.

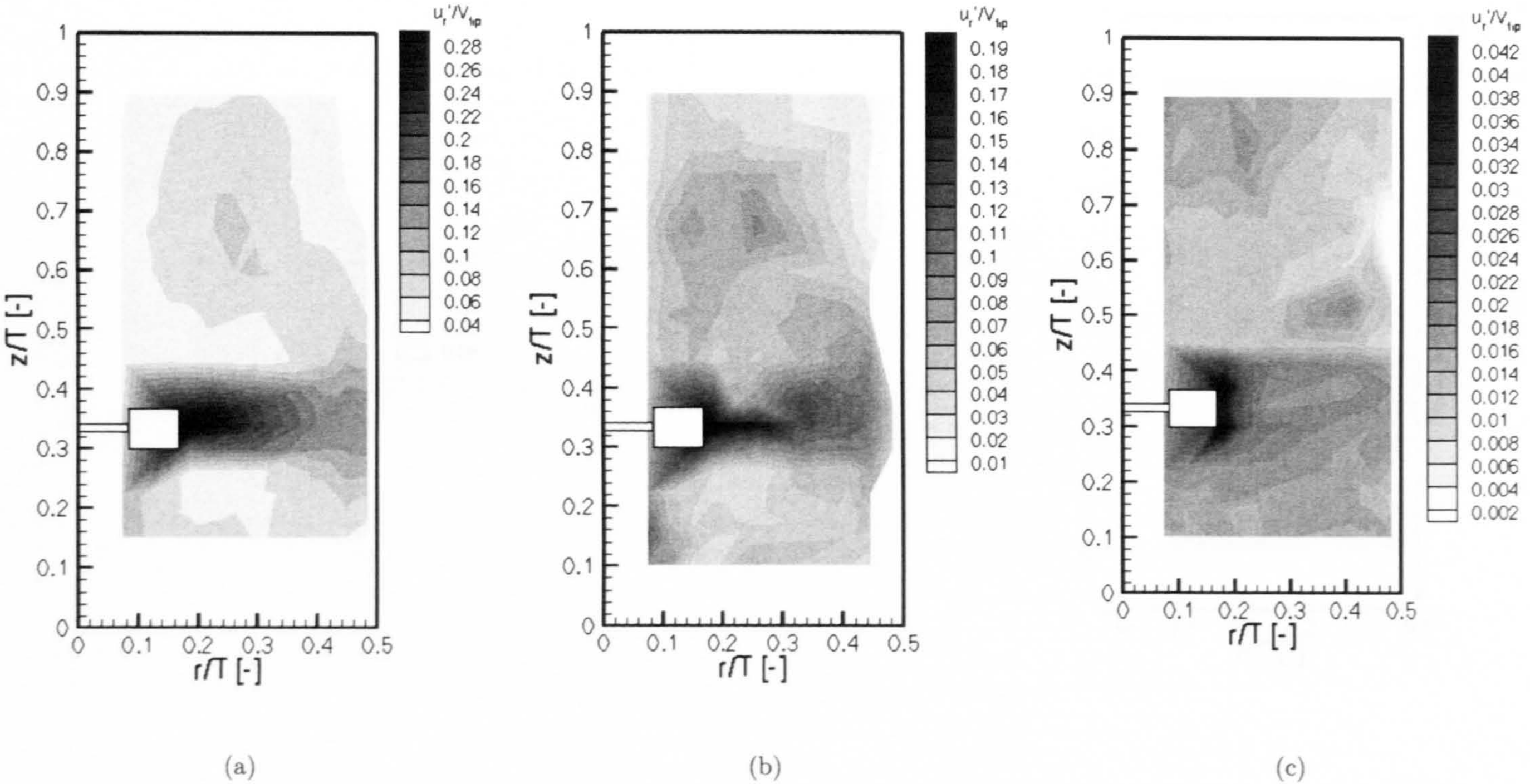

(a) (b) (c)

Figure 6.7: Ensemble-average radial r.m.s. contours for water, in the $\theta = 0^0$ plane. (a) $Re = 4253$; (b) $Re = 486$; (c) $Re = 61$.

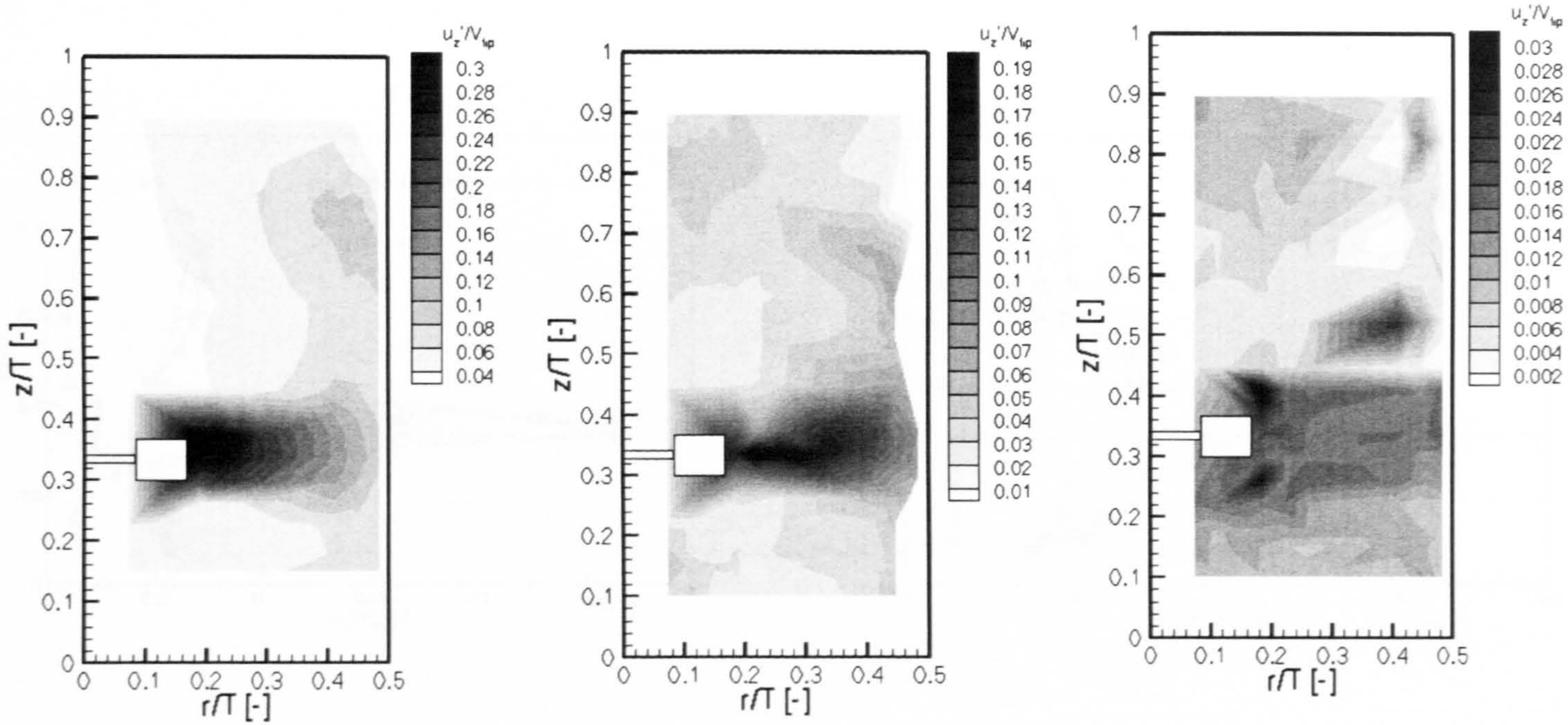

(a) (b) (c)

Figure 6.8: Ensemble-average axial r.m.s. contours for water, in the $\theta = 0^0$ plane. (a) $Re = 4253$; (b) $Re = 486$; (c) $Re = 61$.

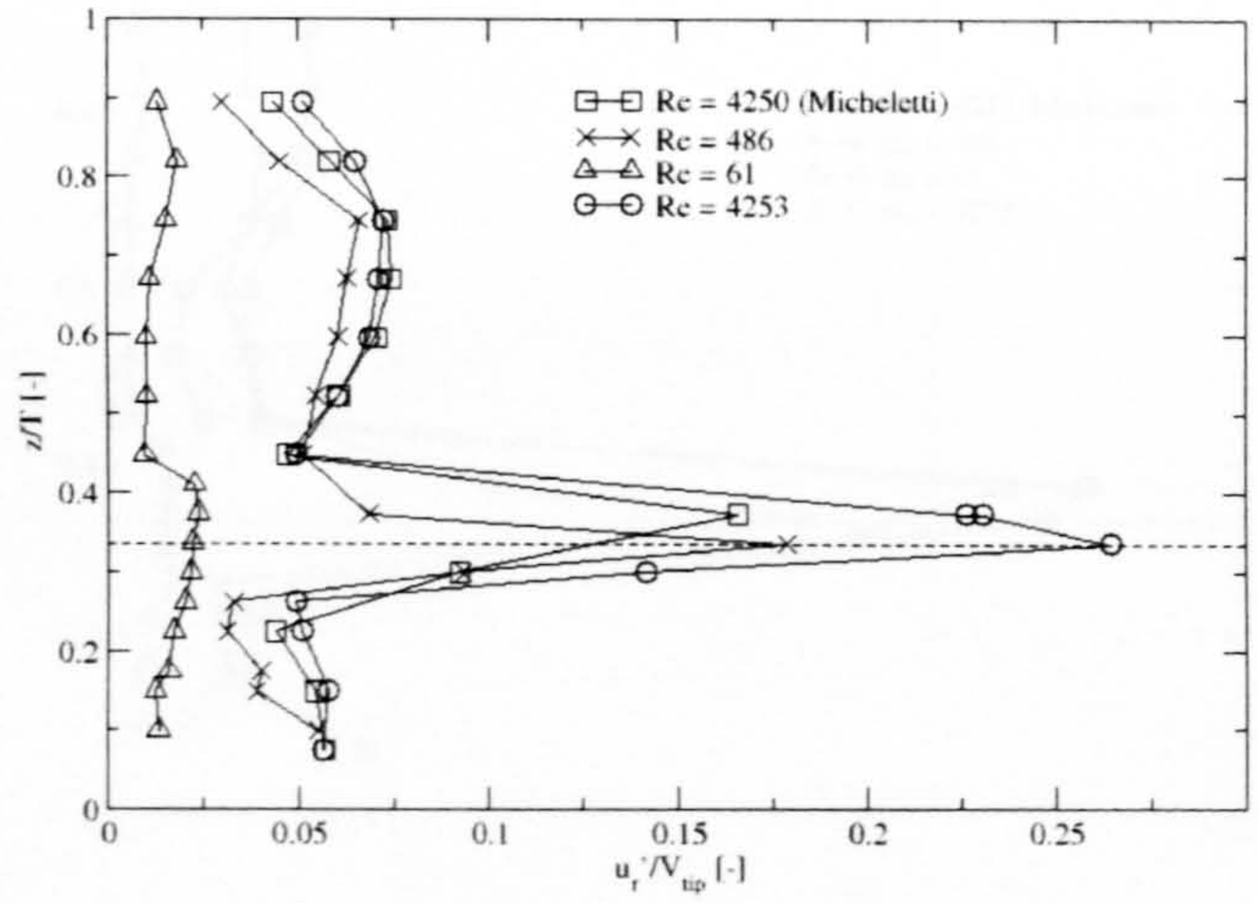

(a)

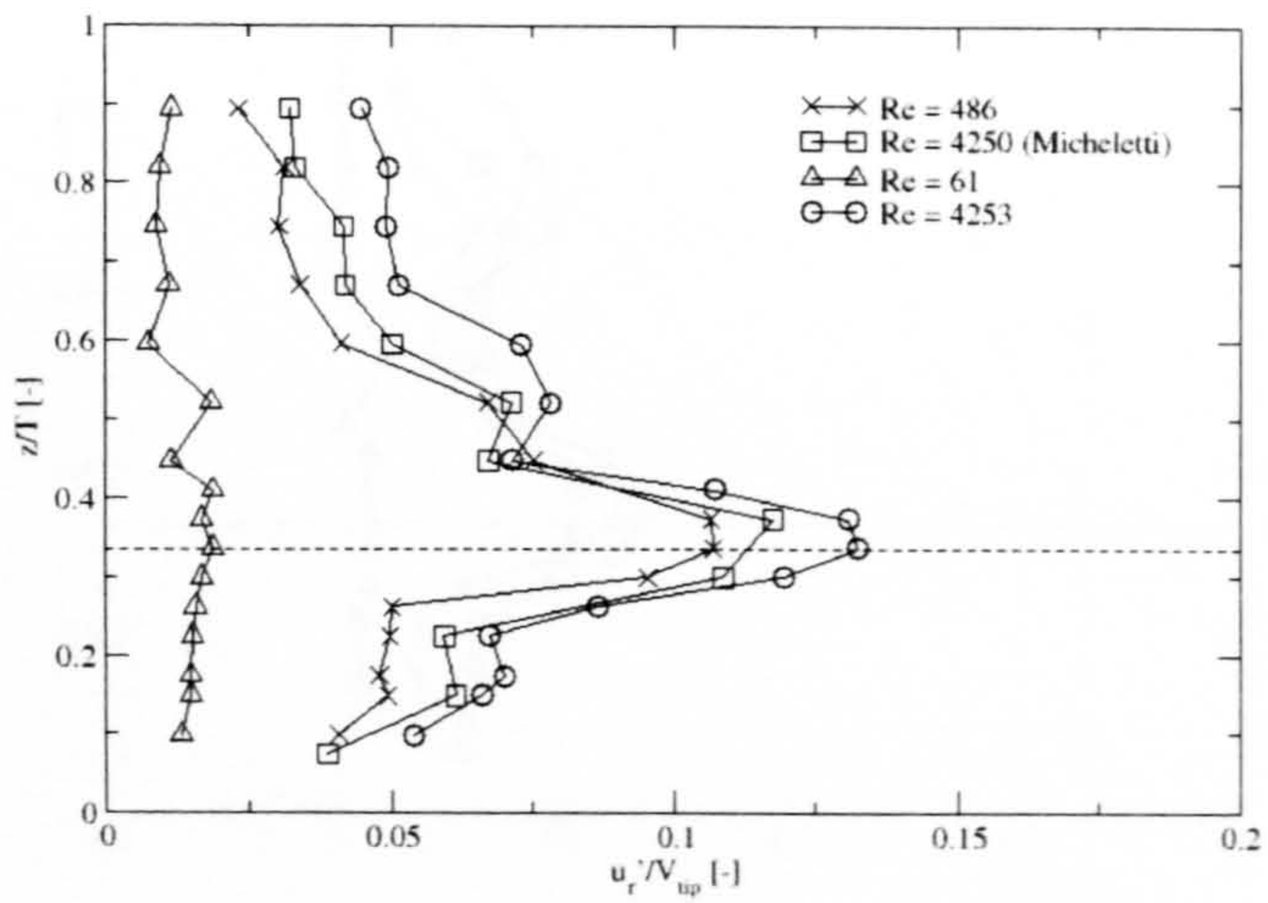

(b)

Figure 6.9: Mean radial r.m.s. values for water at; (a) $r/T = 0.22$ and; (b) $r/T = 0.41$, in the $\theta = 0^0$ plane.

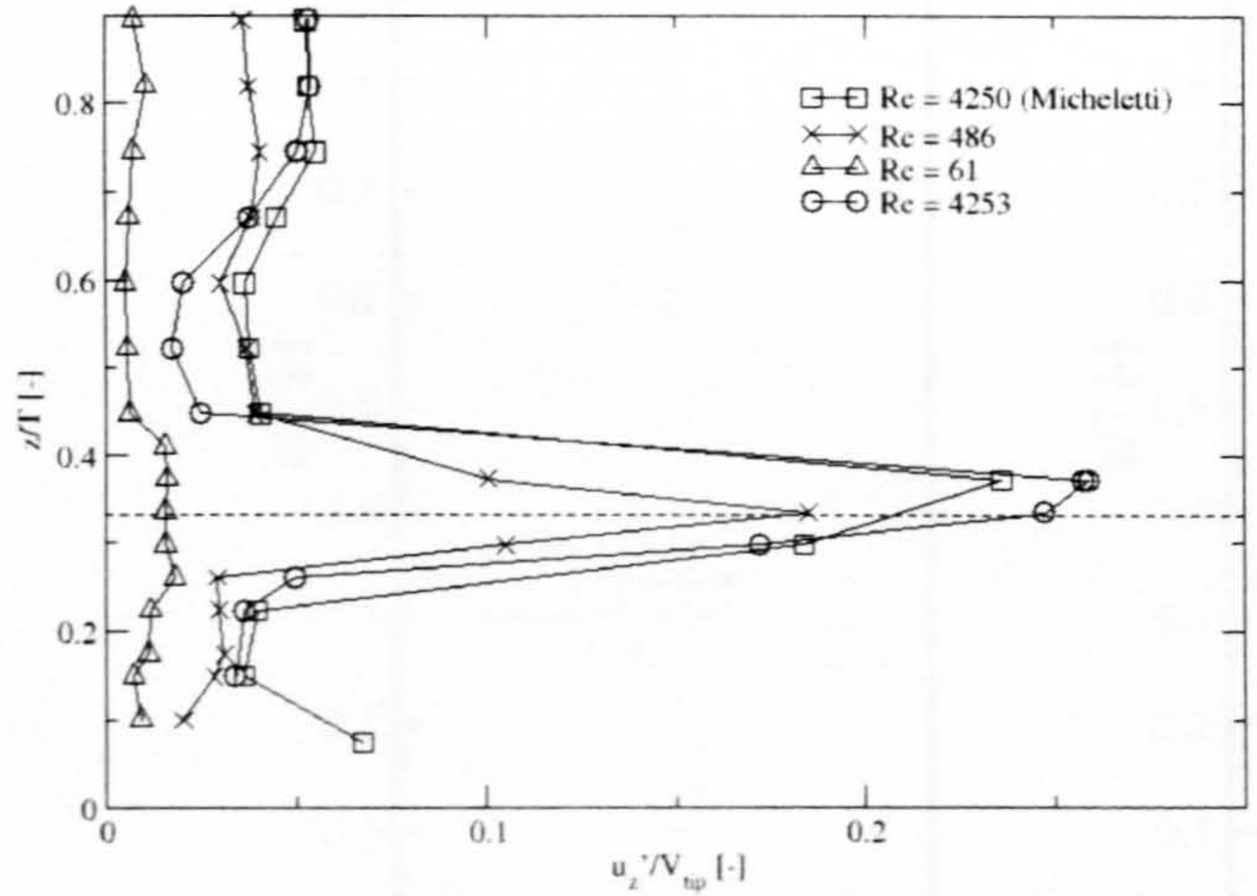

(a)

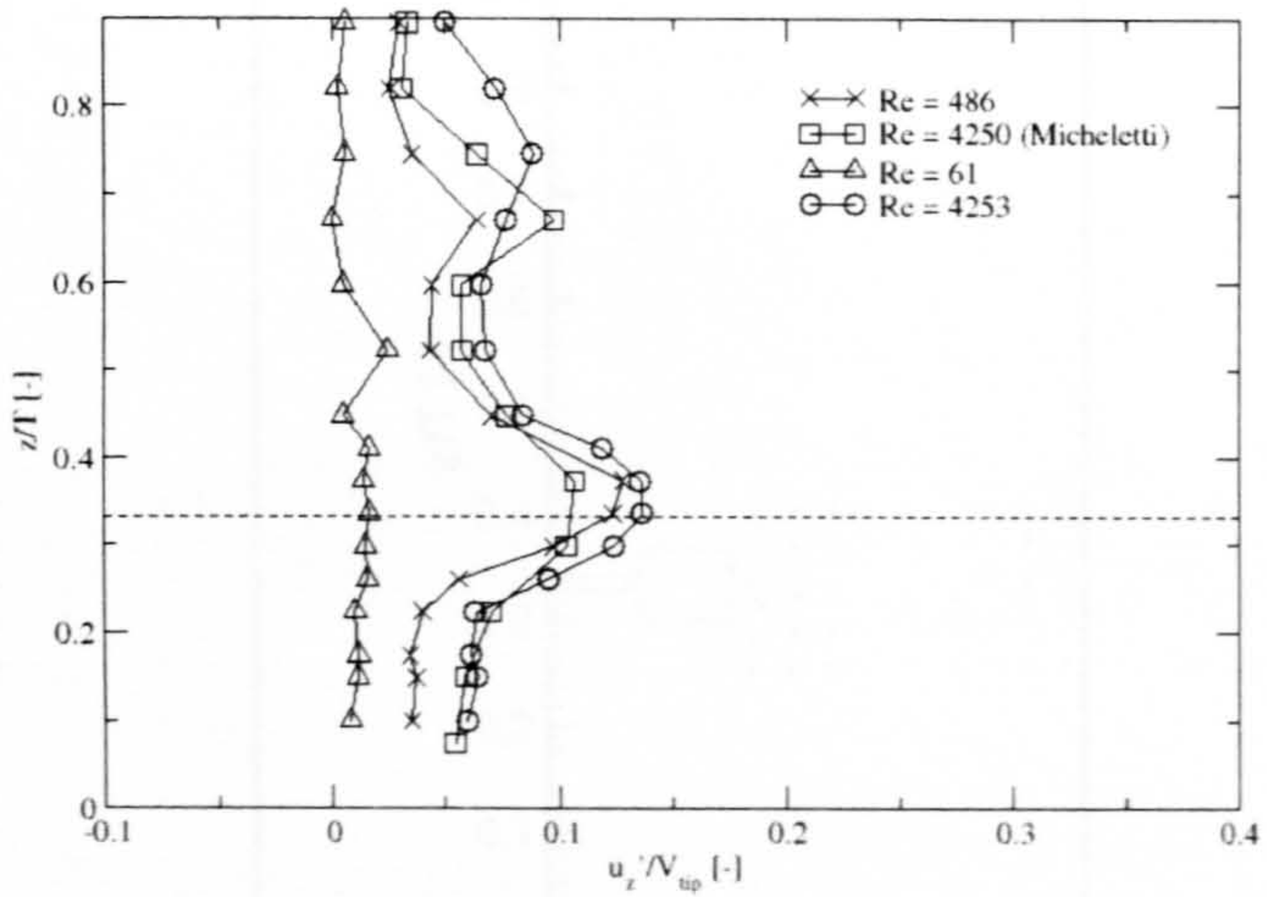

(b)

Figure 6.10: Mean axial r.m.s. values for water at; (a) $r/T = 0.26$ and; (b) $r/T = 0.41$, in the $\theta = 0^0$ plane.

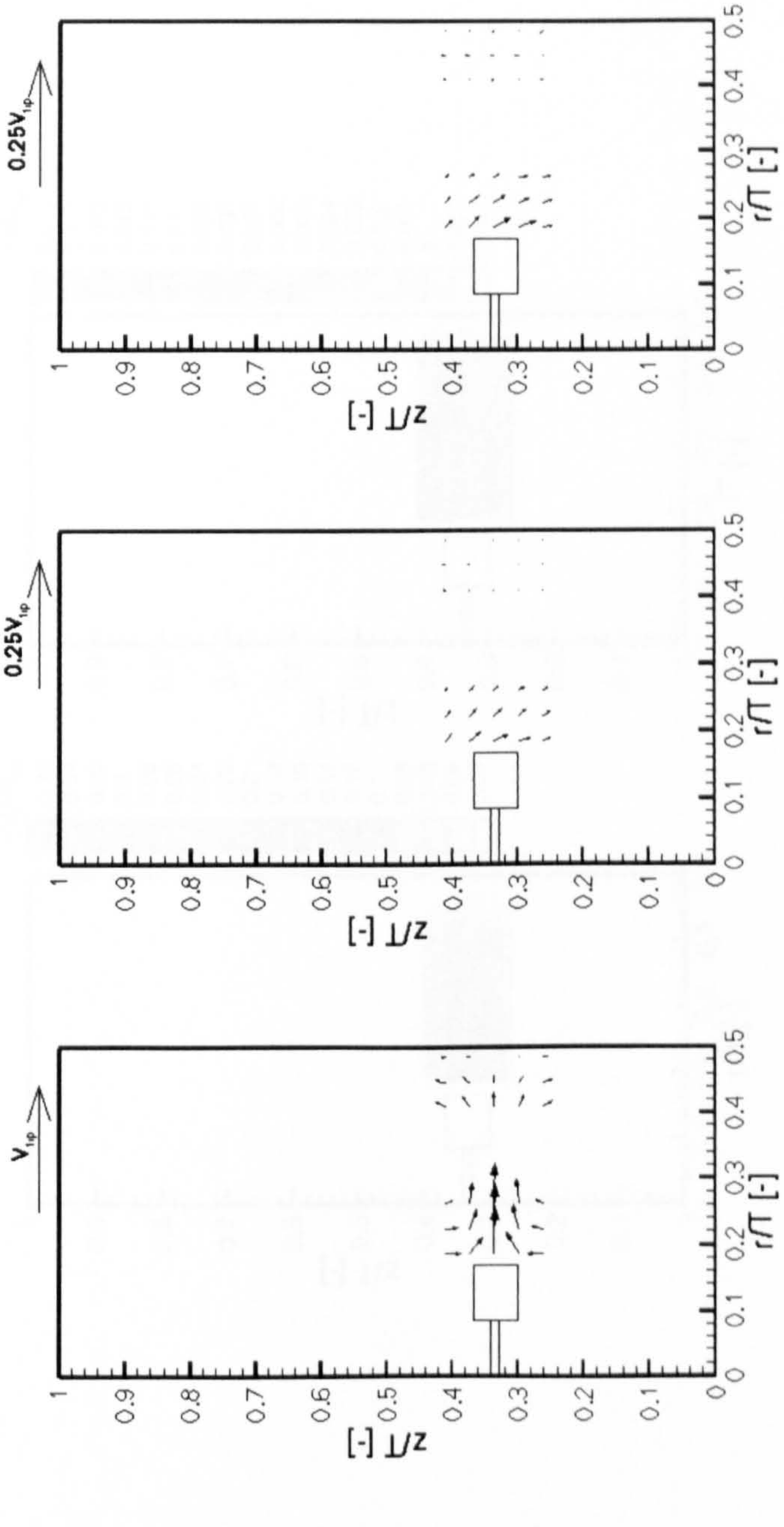

(c)

(b)

(a)

Figure 6.11: Ensemble-average velocity vectors for Si100, in the $\theta = 0^0$ plane. (a) $Re = 50$; (b) $Re = 1$; (c) $Re = 0.5$.

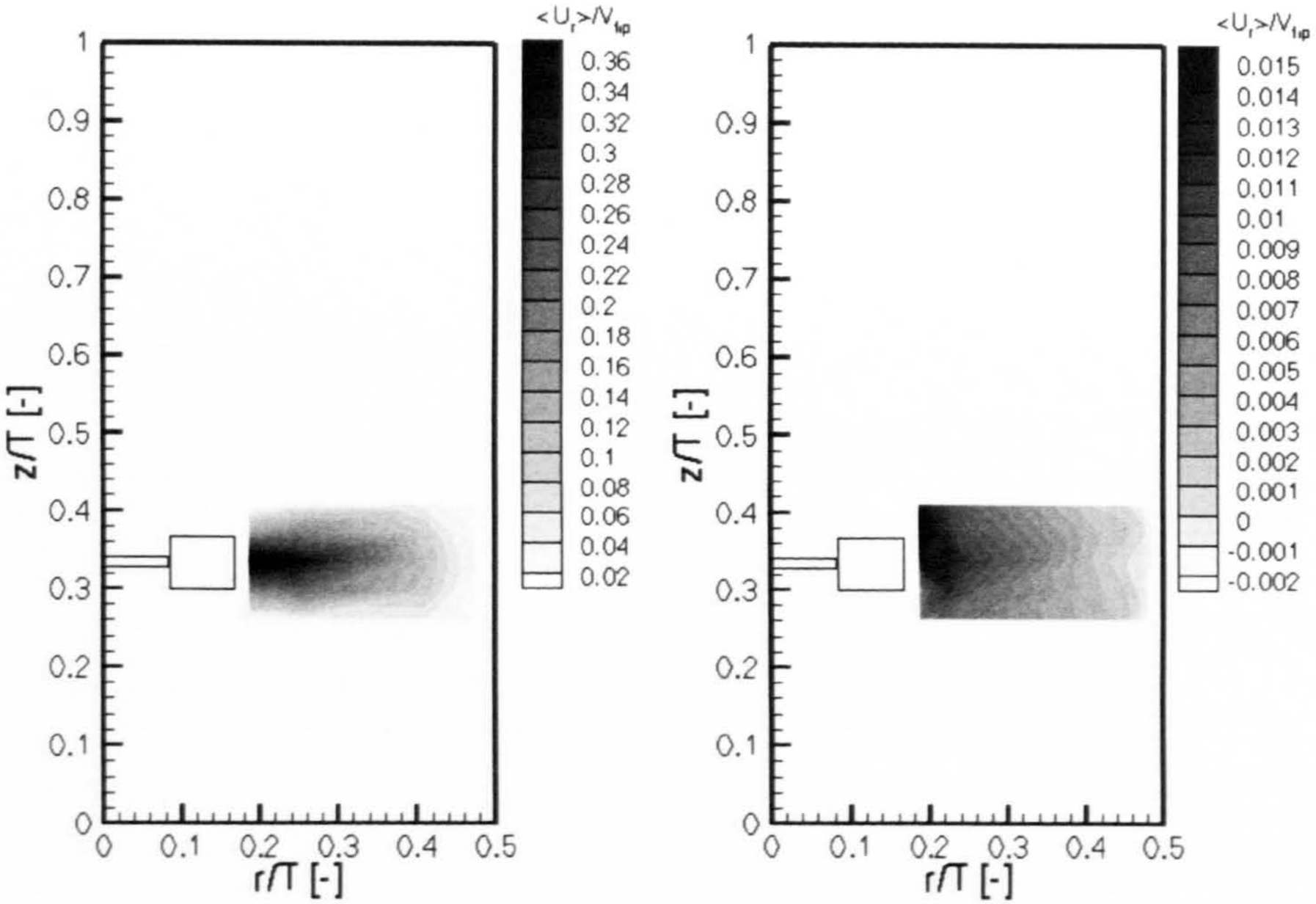

(a) (b)

Figure 6.12: Ensemble-average radial velocity contours for Si100, in the $\theta = 0^0$ plane. (a) $Re = 50$; (b) $Re = 1$.

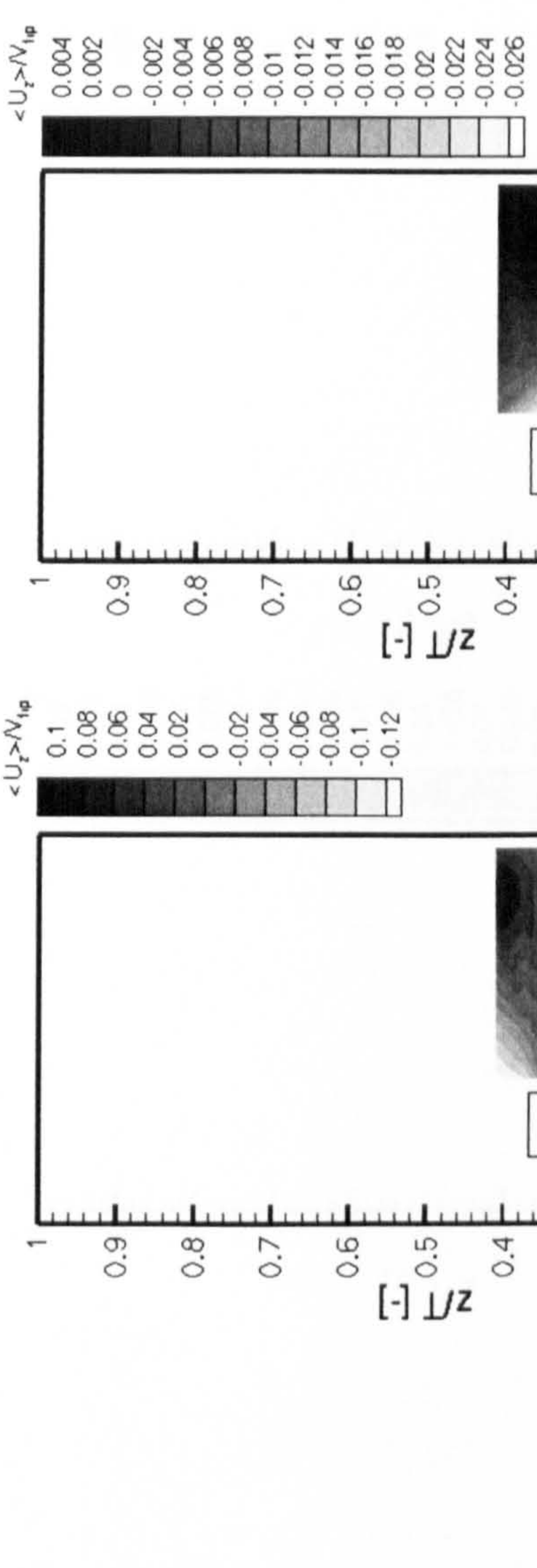

Figure 6.13: Ensemble-average axial velocity contours for Si100, in the $\theta = 0^0$ plane. (a) $Re = 50$; (b) $Re = 1$.

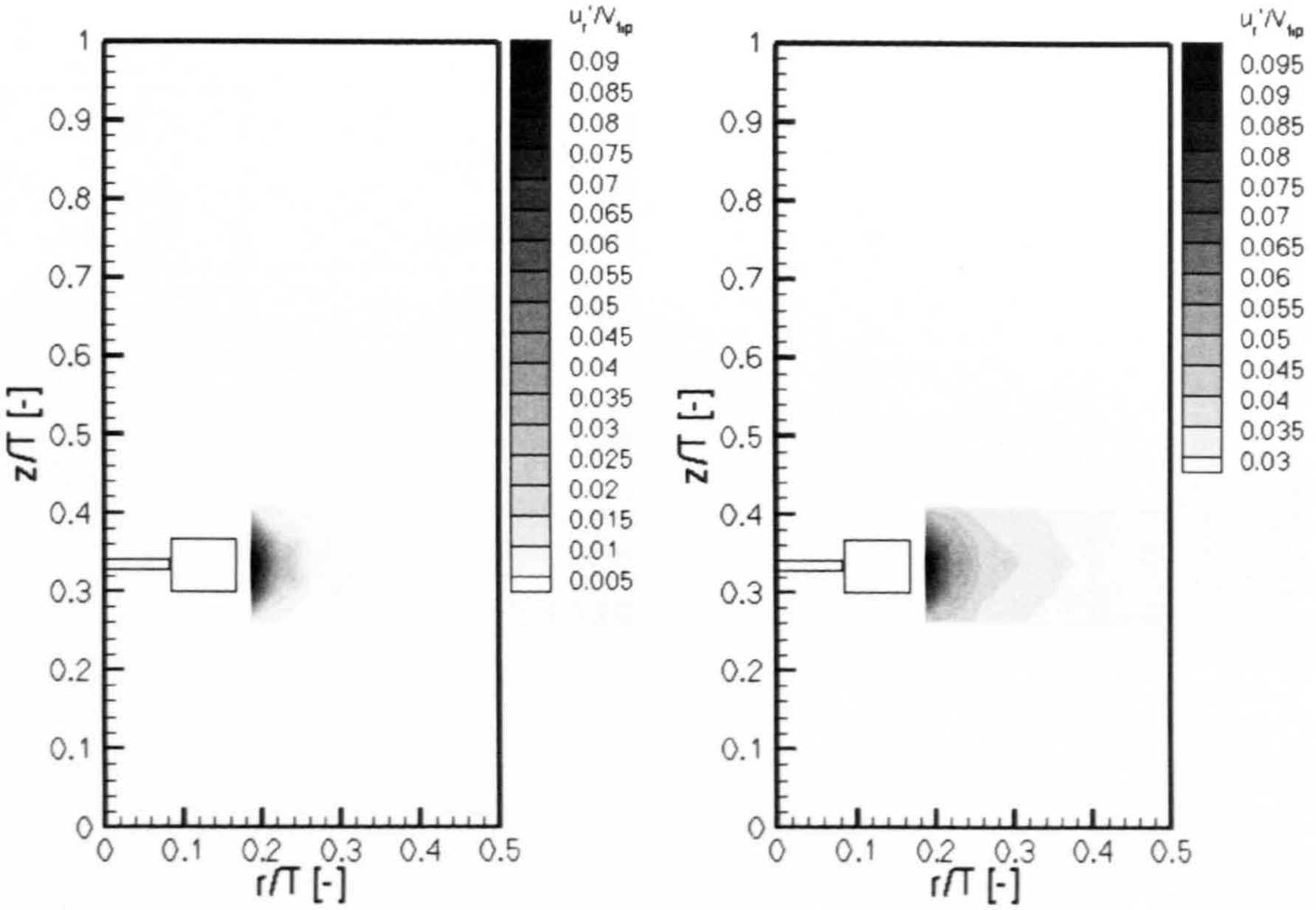

(a) (b)

Figure 6.14: Ensemble-average radial r.m.s. contours for Si100, in the $\theta = 0^0$ plane. (a) $Re = 50$; (b) $Re = 1$.

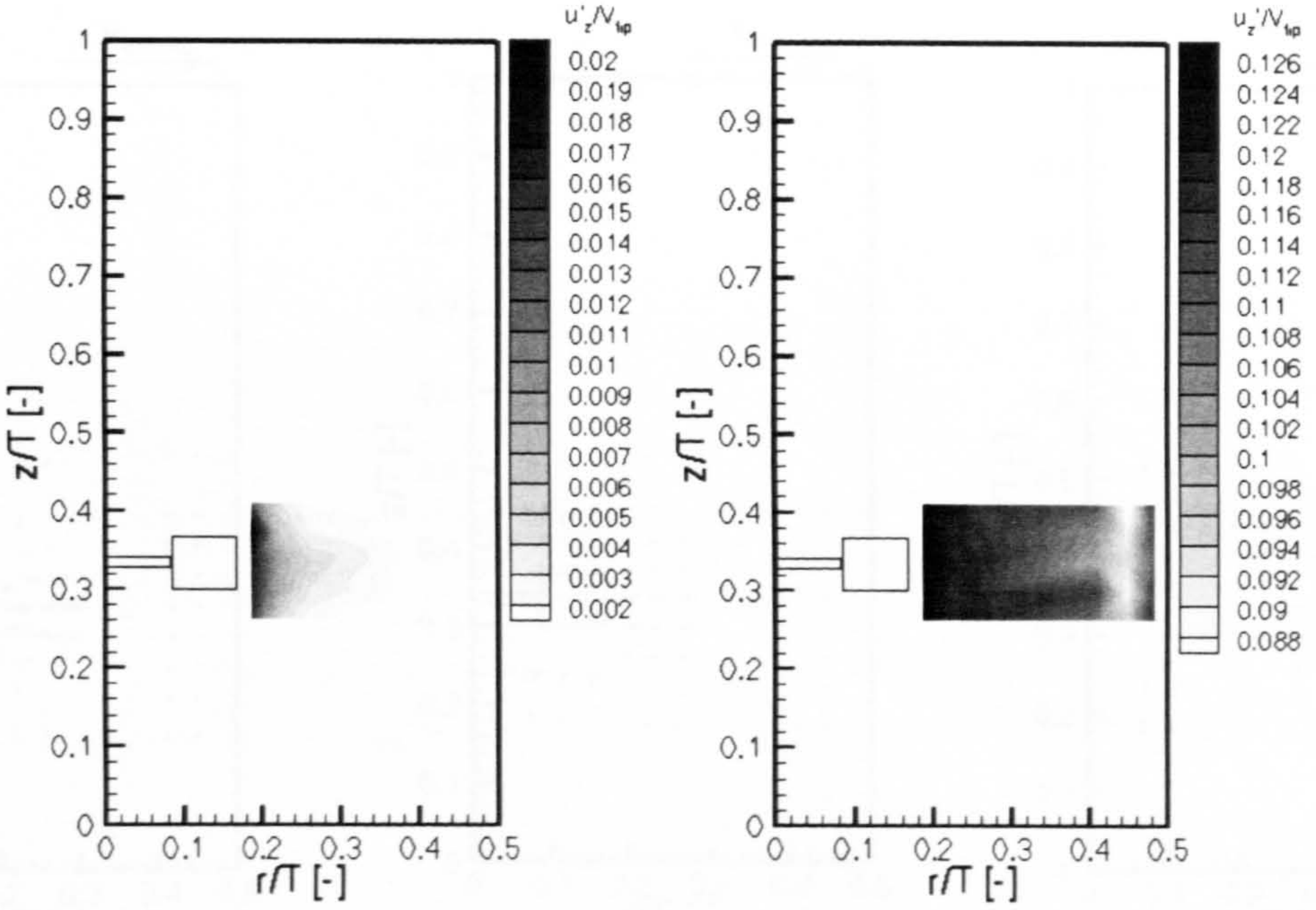

(a) (b)

Figure 6.15: Ensemble-average axial r.m.s. contours for Si100, in the $\theta = 0^0$ plane. (a) $Re = 50$; (b) $Re = 1$.

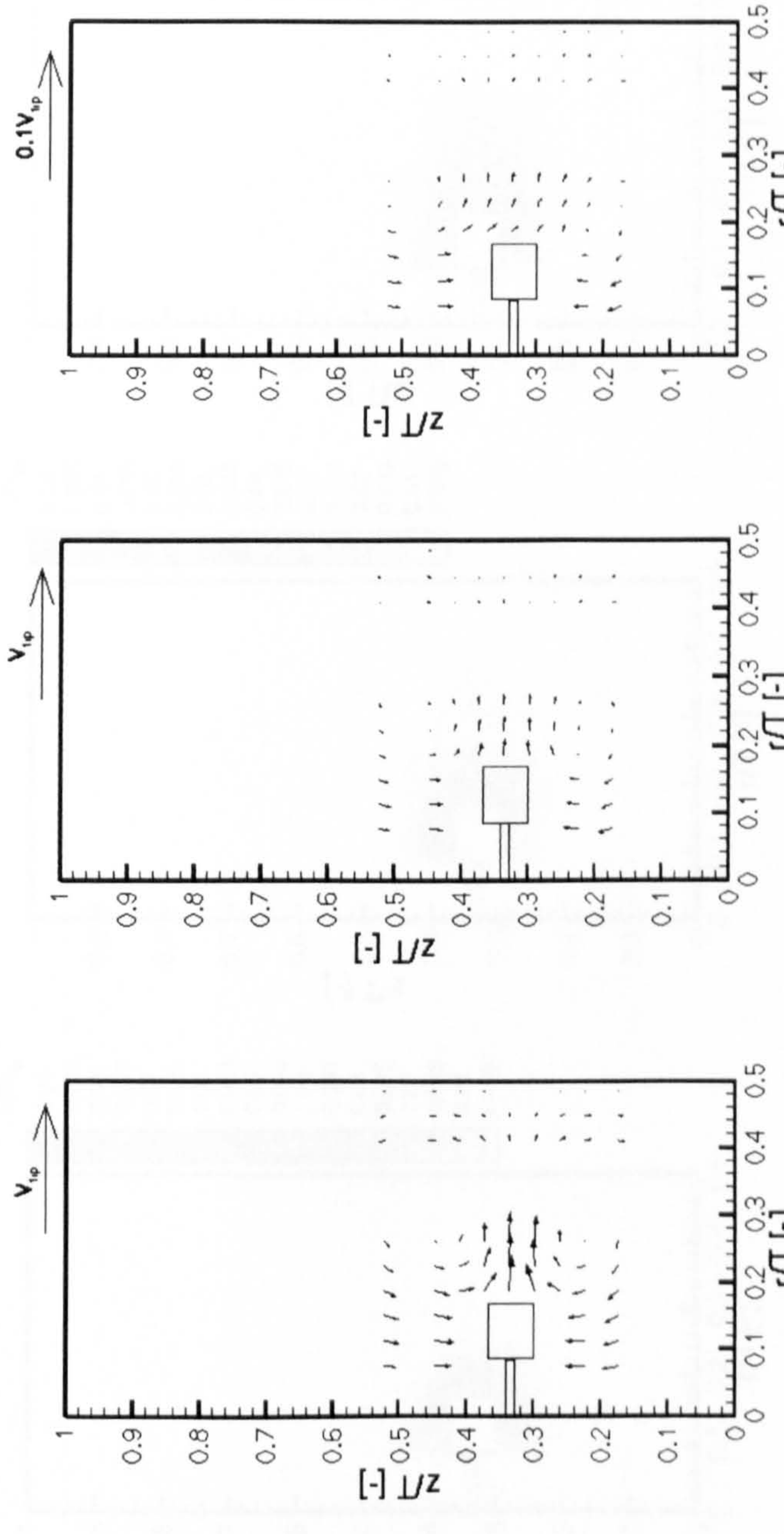

Figure 6.16: Ensemble-average velocity vectors for Si1000, in the $\theta = 0^0$ plane. (a) $Re = 28$; (b) $Re = 10$; (c) $Re = 1$.

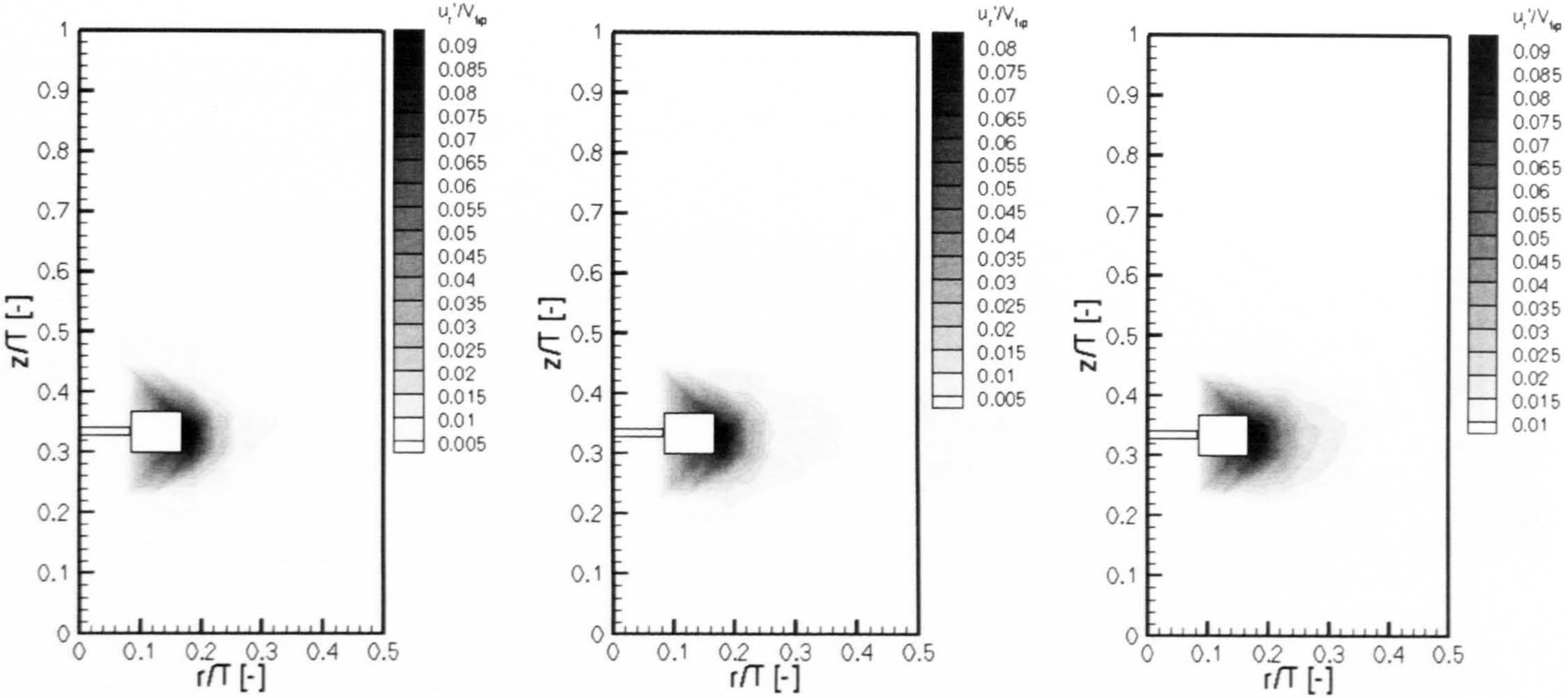

(a) (b) (c)

Figure 6.17: Ensemble-average radial r.m.s. contours for Si1000, in the $\theta = 0^0$ plane. (a) $Re = 28$; (b) $Re = 10$; (c) $Re = 1$.

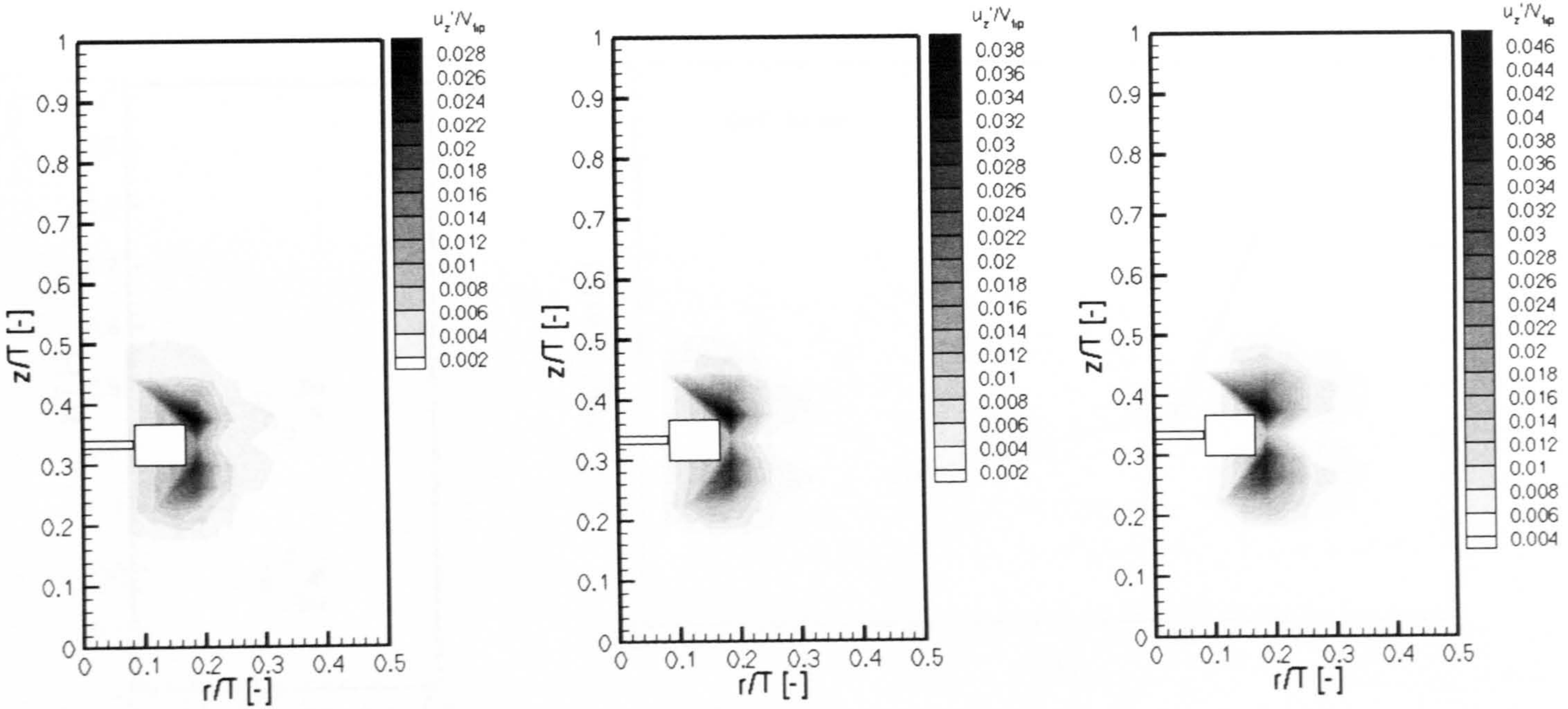

(a) (b) (c)

Figure 6.18: Ensemble-average axial r.m.s. contours for Si1000, in the $\theta = 0^0$ plane. (a) $Re = 28$; (b) $Re = 10$; (c) $Re = 1$.

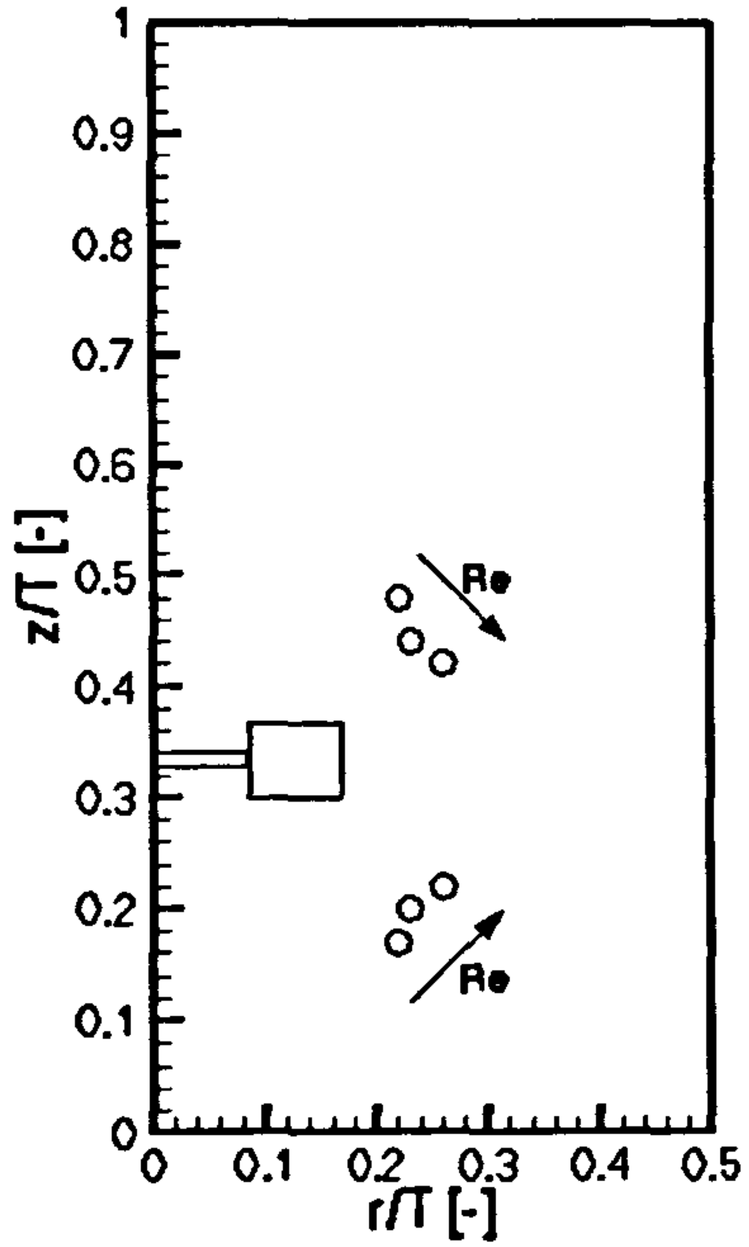

(a)

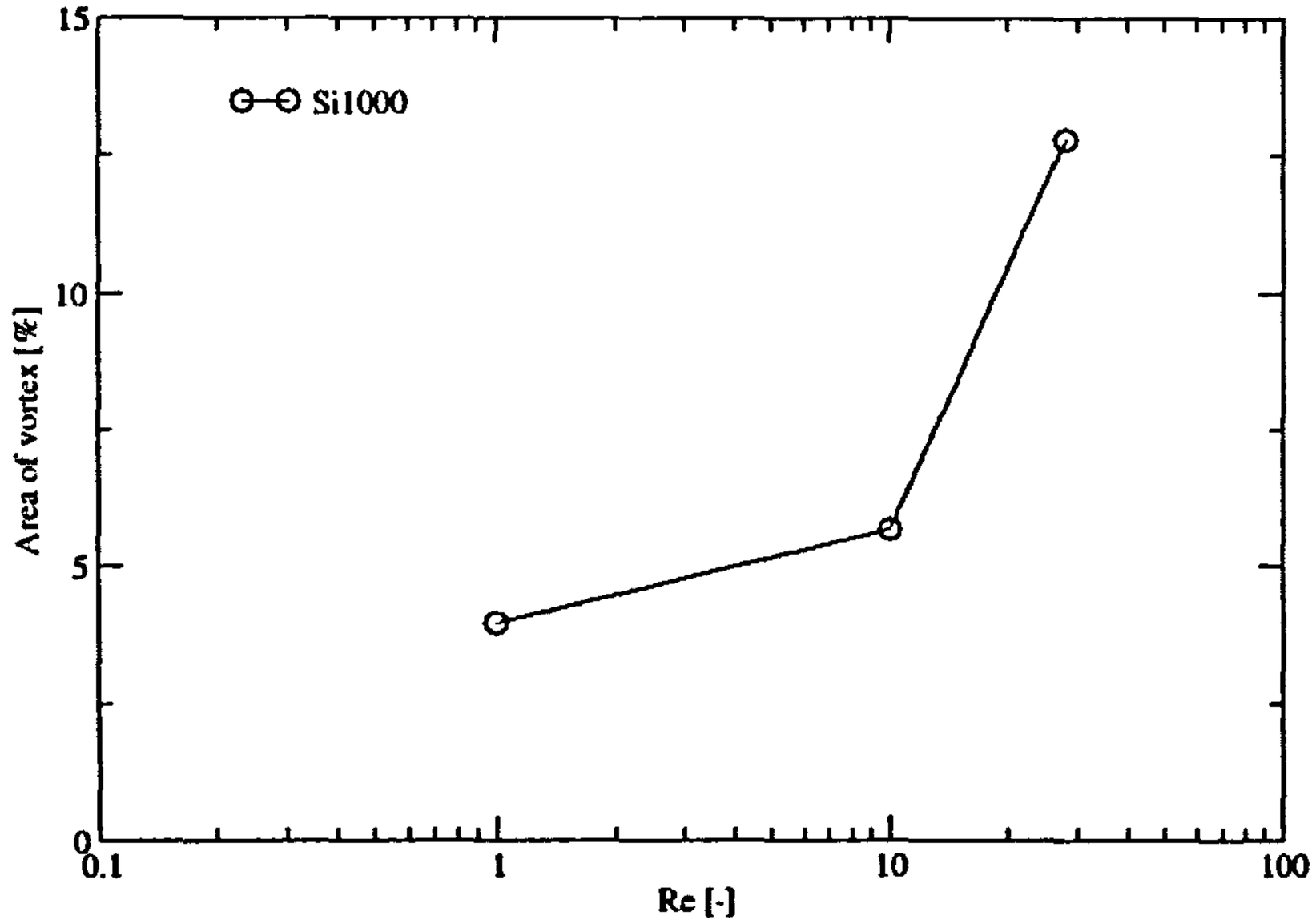

(b)

Figure 6.19: (a) Loci of vortex centres at $Re = 1$, 10 and 28 for Si1000. (b) The area of the vortex above the impeller blade as a percentage of the mixing vessel cross-section.

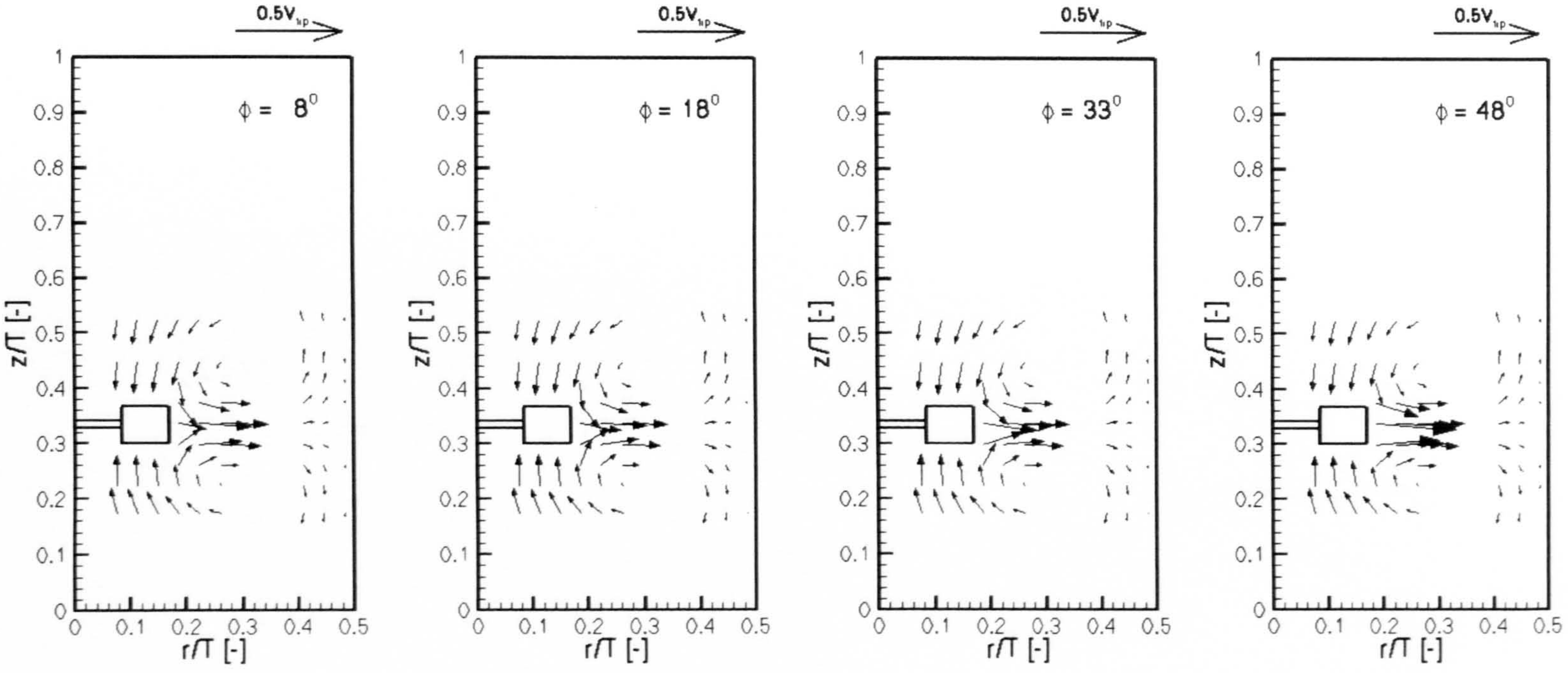

(a) (b) (c) (d)

Figure 6.20: Phase-resolved velocity vectors for Si1000 at $Re = 28$, in the $\theta = 0^0$ plane at $\phi = 8^0$, 18^0, 33^0 and 48^0.

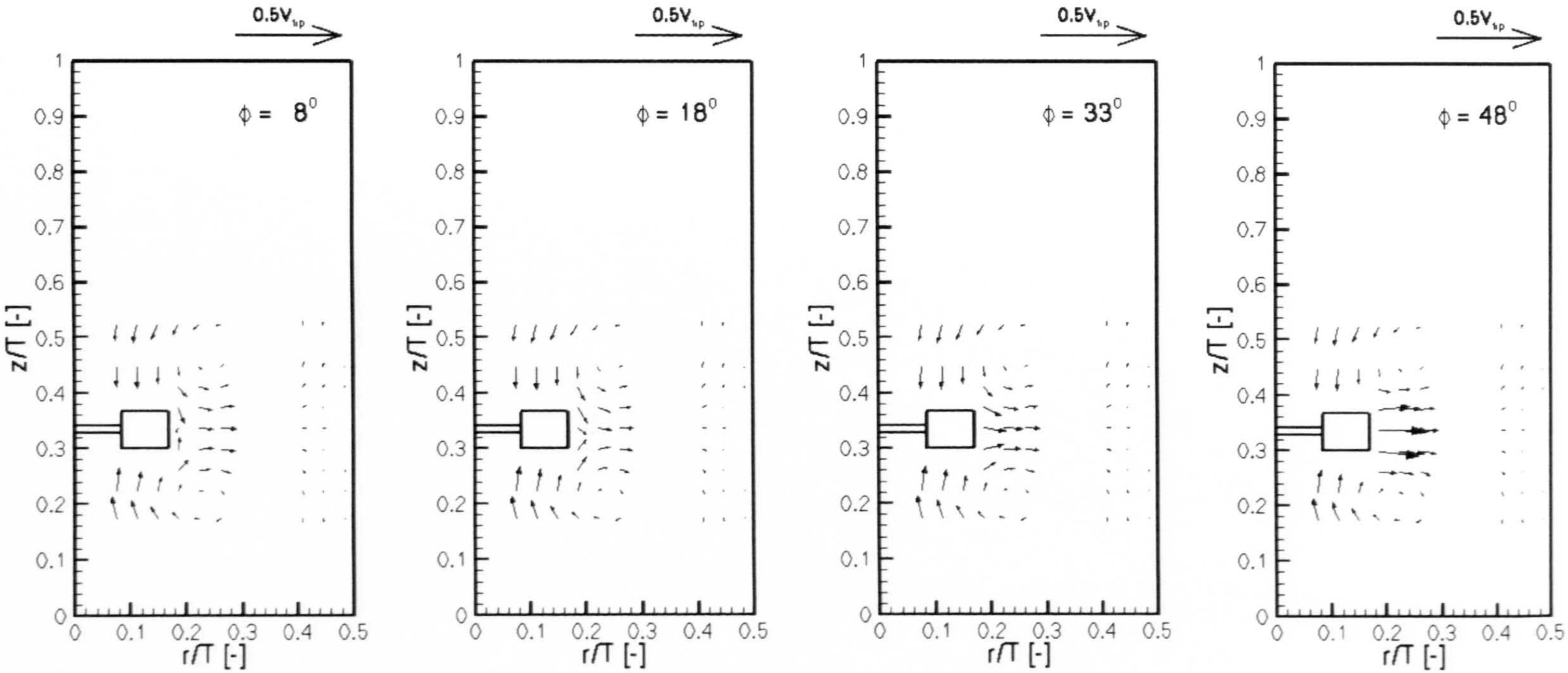

(a) (b) (c) (d)

Figure 6.21: Phase-resolved velocity vectors for Si1000 at $Re = 10$, in the $\theta = 0^0$ plane at $\phi = 8^0$, 18^0, 33^0 and 48^0.

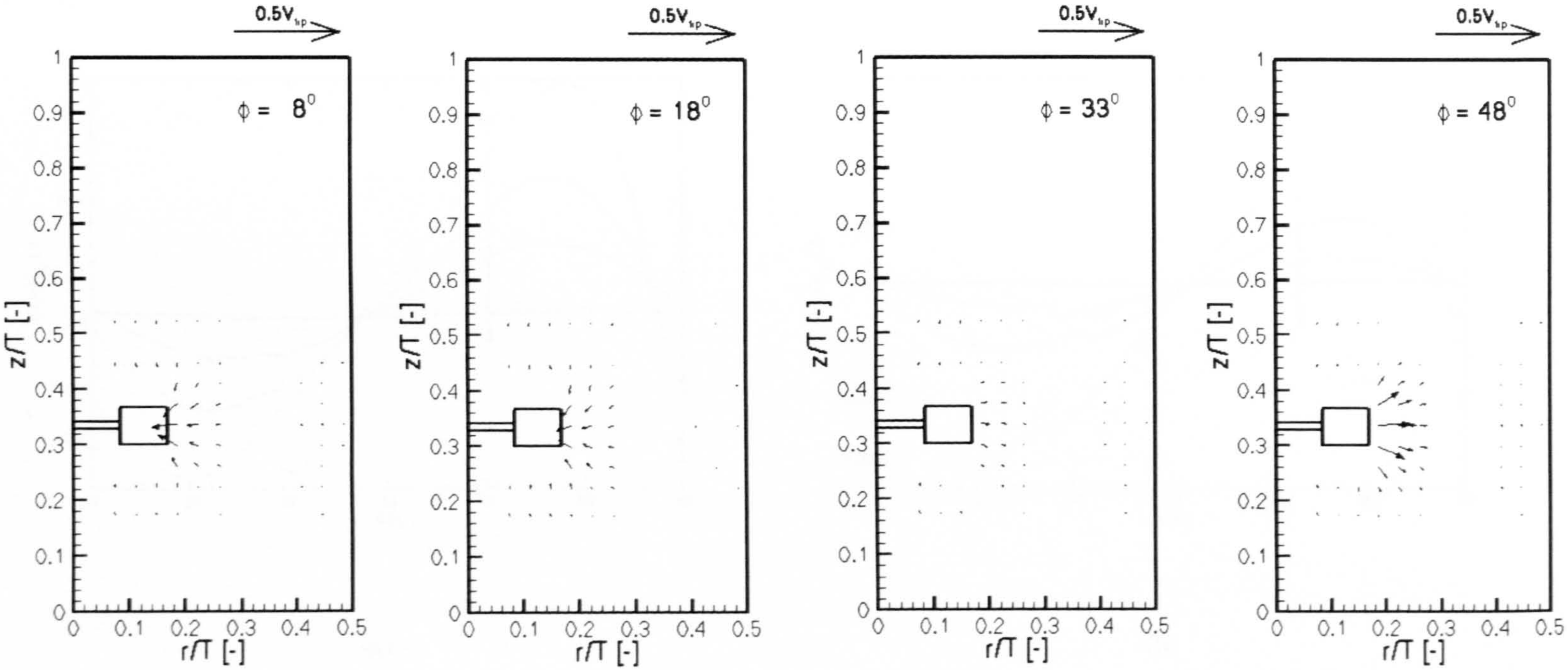

(a) (b) (c) (d)

Figure 6.22: Phase-resolved velocity vectors for Si1000 at $Re = 1$, in the $\theta = 0^0$ plane at $\phi = 8^0$, 18^0, 33^0 and 48^0.

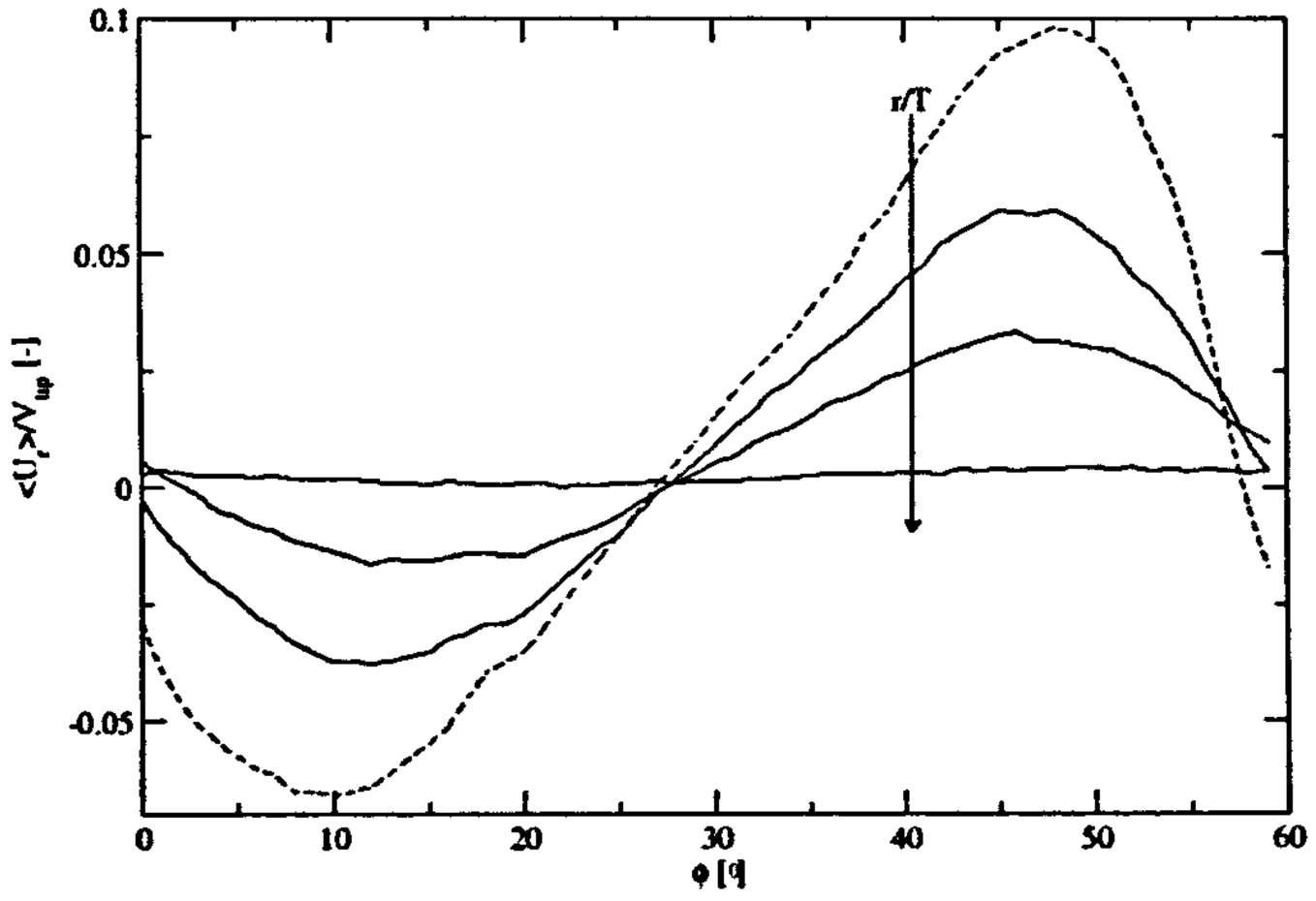

(a)

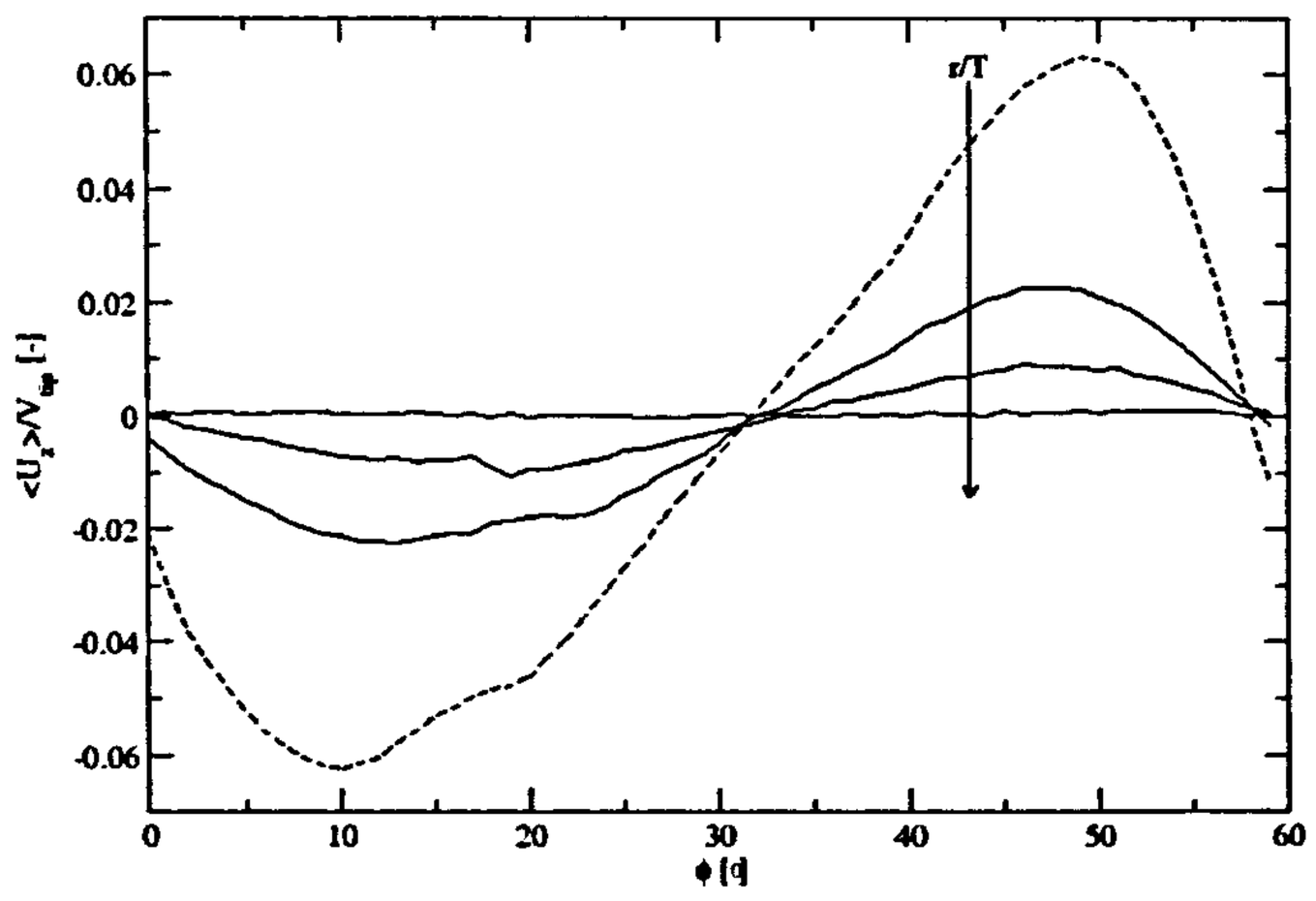

(b)

Figure 6.23: Normalised radial (a) and axial (b) velocity components versus ϕ at $Re = 1$, for Si1000. The axial positions of the curves all correspond to the point closest to the top of the impeller blade ($z/T = 0.373$) while the radial positions correspond to $r/T = 0.186$, 0.224, 0.261 and 0.411, the value of which increases in the direction of the arrow.

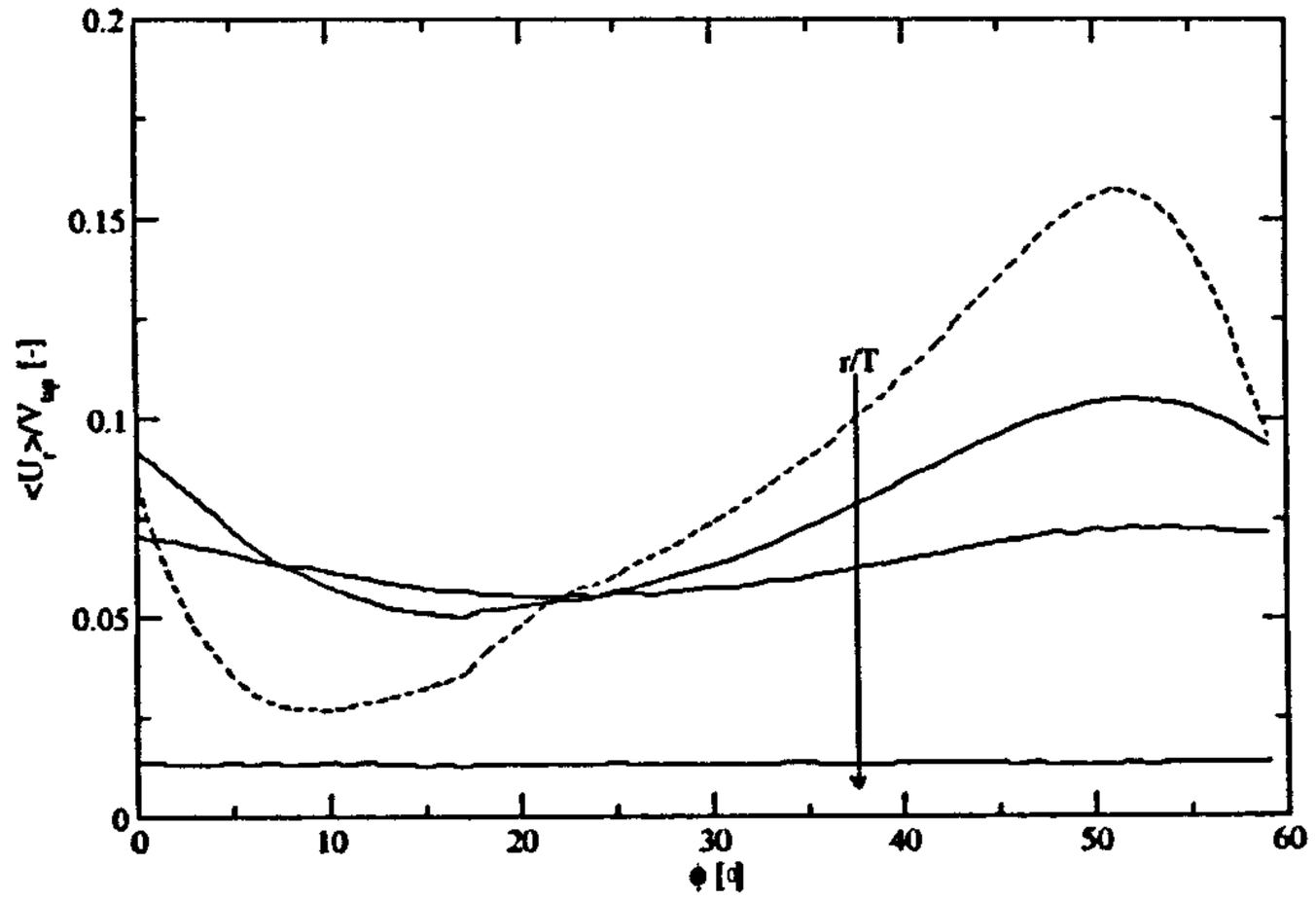

(a)

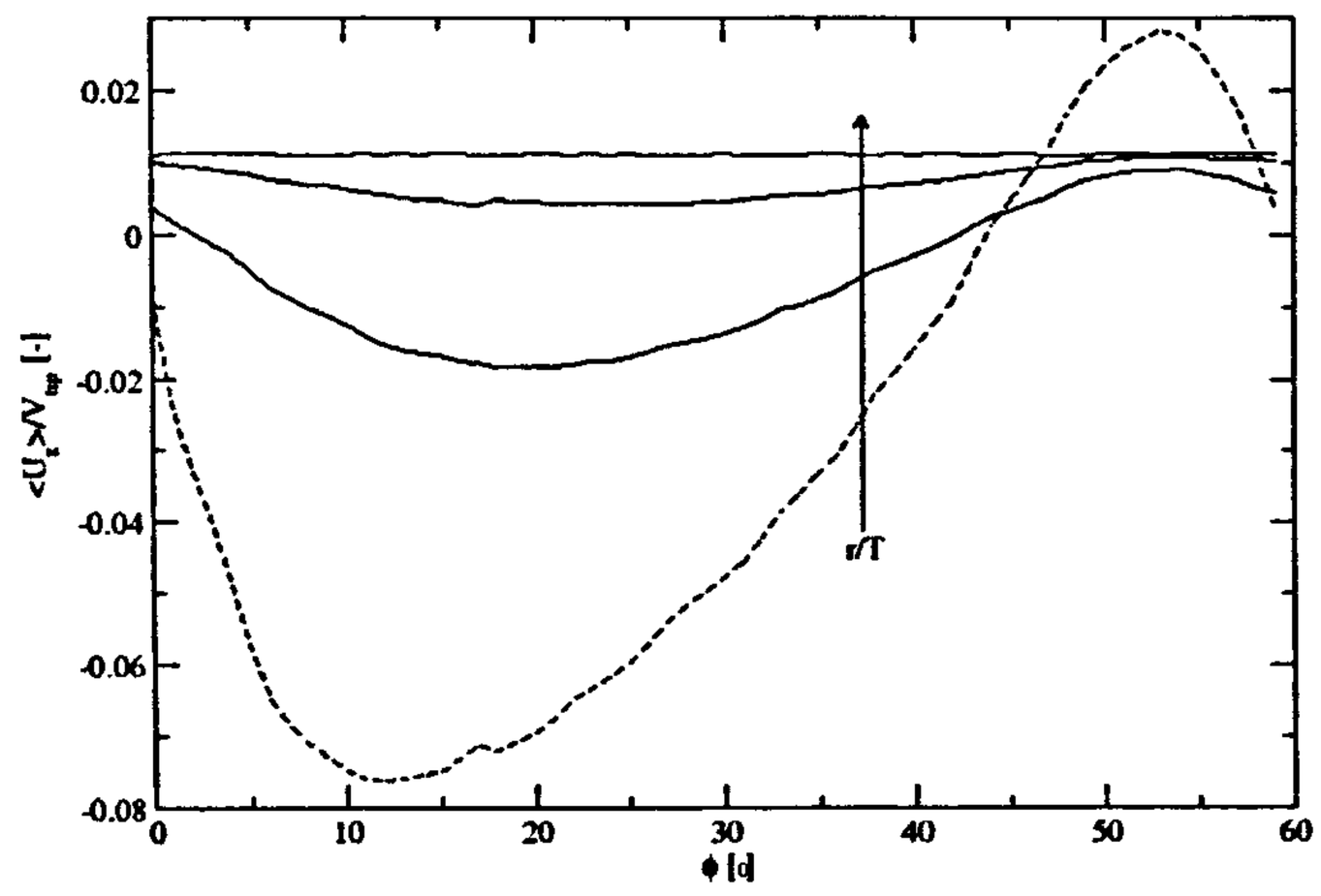

(b)

Figure 6.24: Normalised radial (a) and axial (b) velocity components versus ϕ at $Re = 10$, for Si1000. The axial positions of the curves all correspond to the point closest to the top of the impeller blade ($z/T = 0.373$) while the radial positions correspond to $r/T = 0.186$, 0.224, 0.261 and 0.411, the value of which increases in the direction of the arrow.

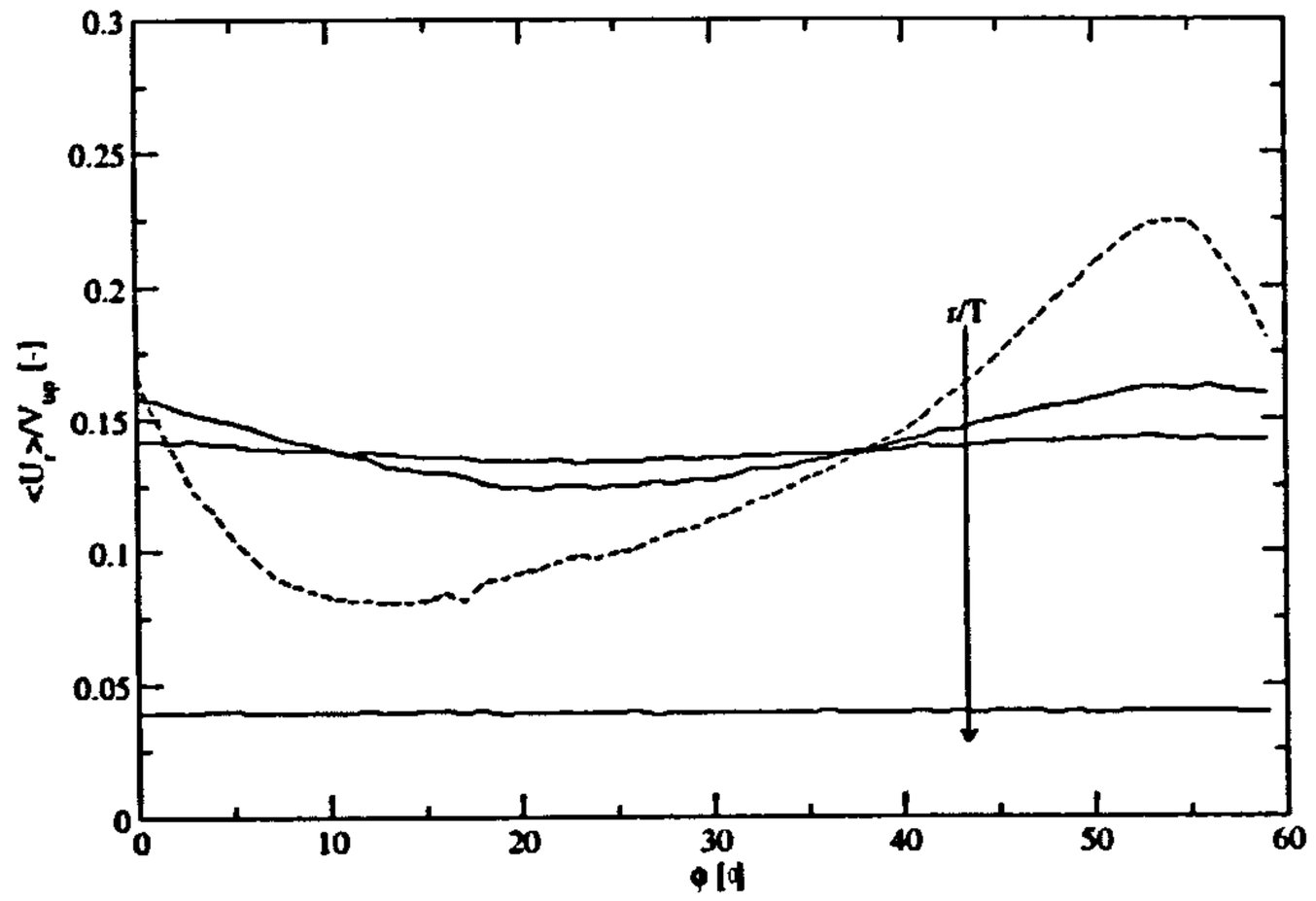

(a)

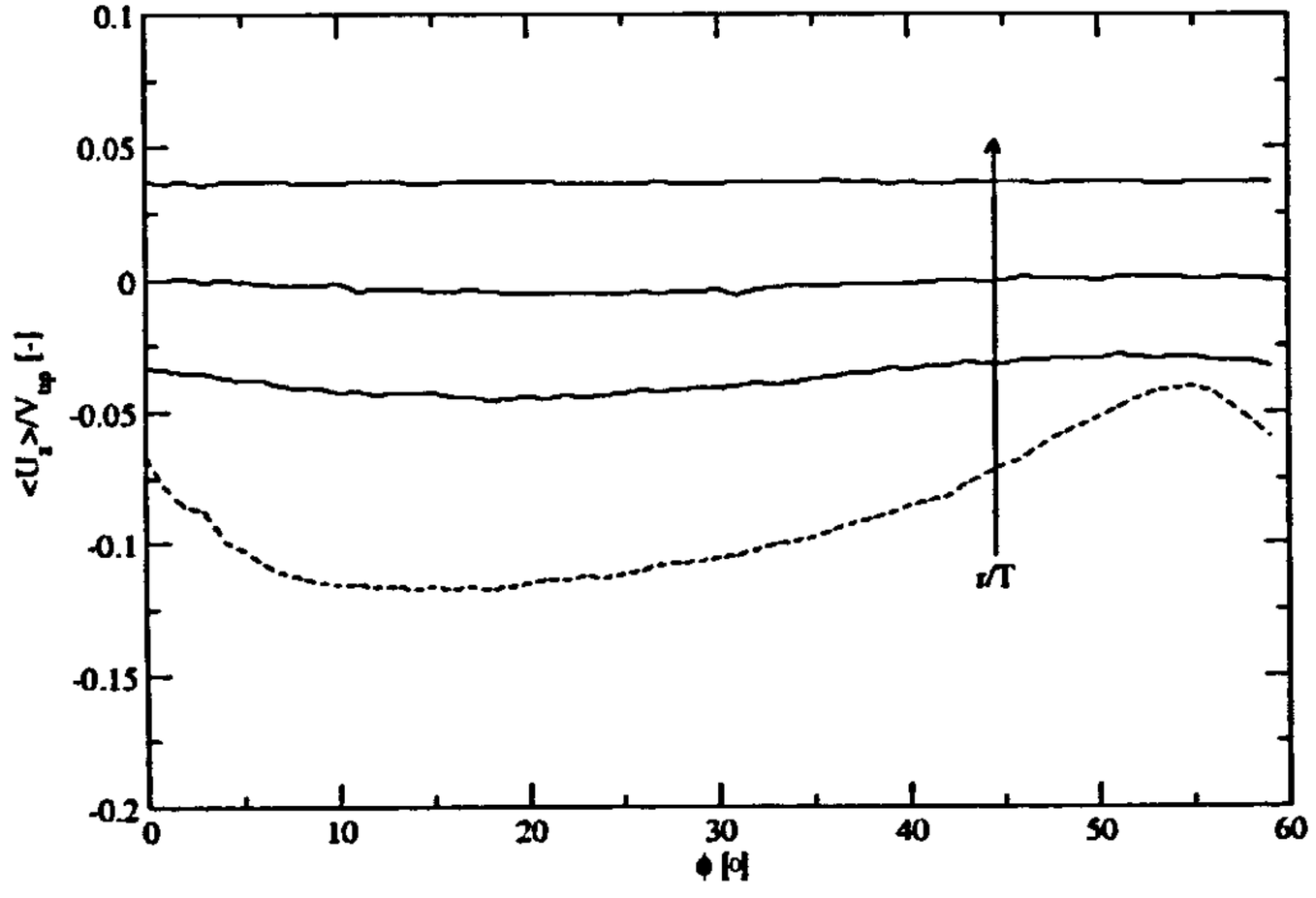

(b)

Figure 6.25: Normalised radial (a) and axial (b) velocity components versus ϕ at $Re = 28$, for Si1000. The axial positions of the curves all correspond to the point closest to the top of the impeller blade ($z/T = 0.373$) while the radial positions correspond to $r/T = 0.186$, 0.224, 0.261 and 0.411, the value of which increases in the direction of the arrow.

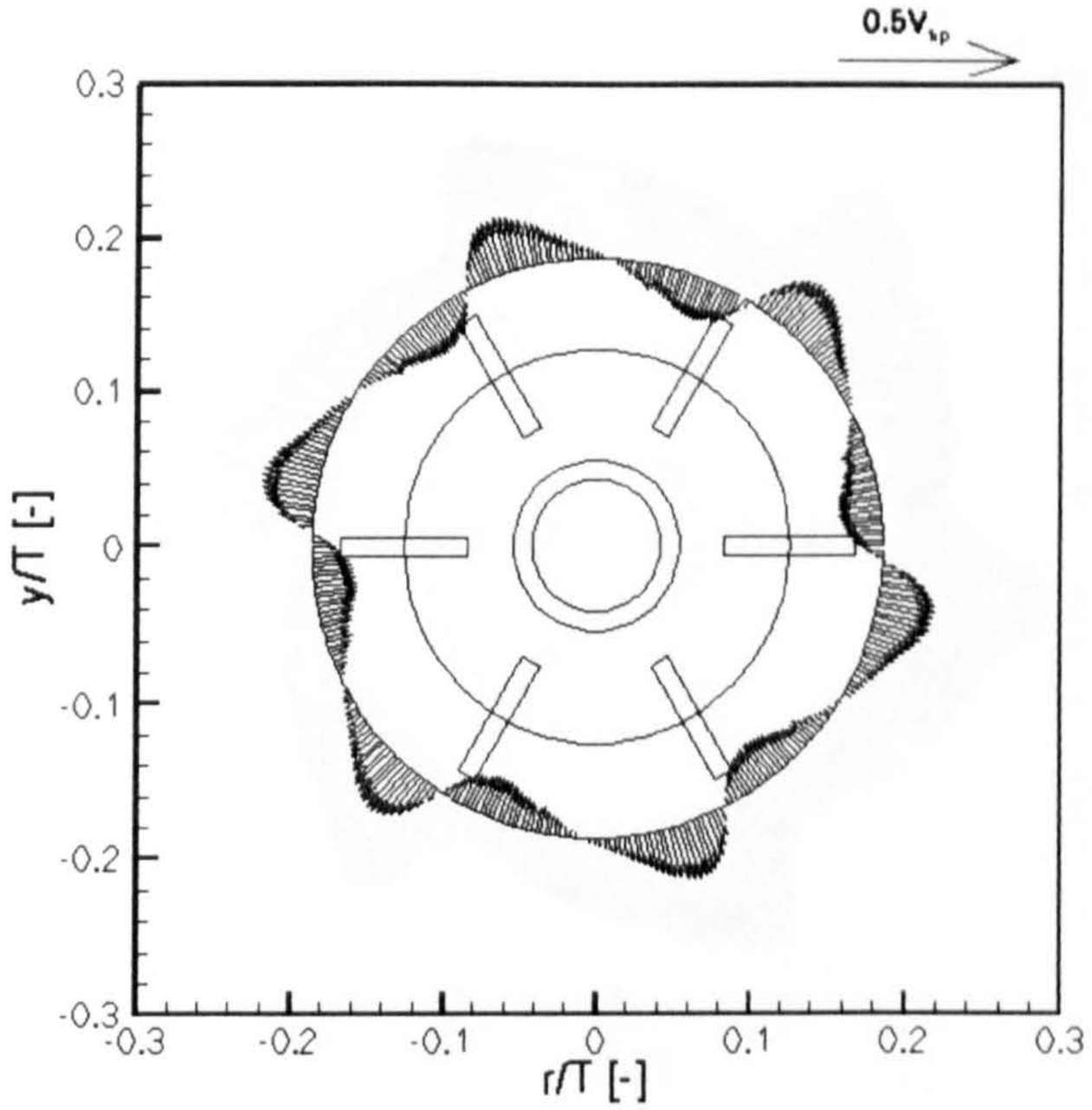

Figure 6.26: Plots of the normalised radial velocity components (U_r/V_{tip}) at $Re = 1$, for Si1000. The results are taken at an axial position equal to the height of the mid-plane of the impeller blade ($z/T = 0.333$) and at a radial position closest to the impeller blade, $r/T = 0.186$.

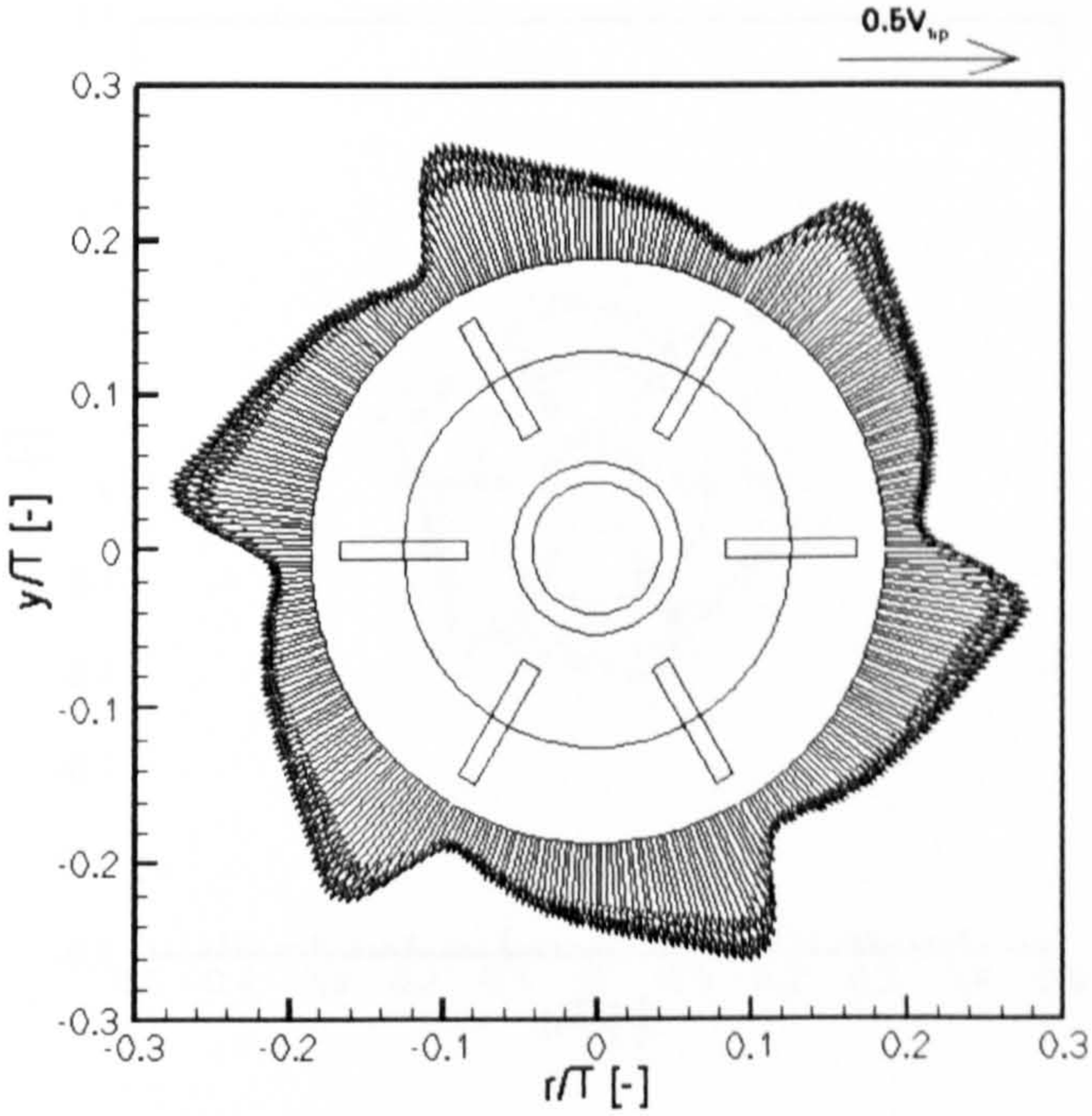

Figure 6.27: Plots of the normalised radial velocity components (U_r/V_{tip}) at $Re = 28$, for Si1000. The results are taken at an axial position equal to the height of the mid-plane of the impeller blade ($z/T = 0.333$) and at a radial position closest to the impeller blade, $r/T = 0.186$.

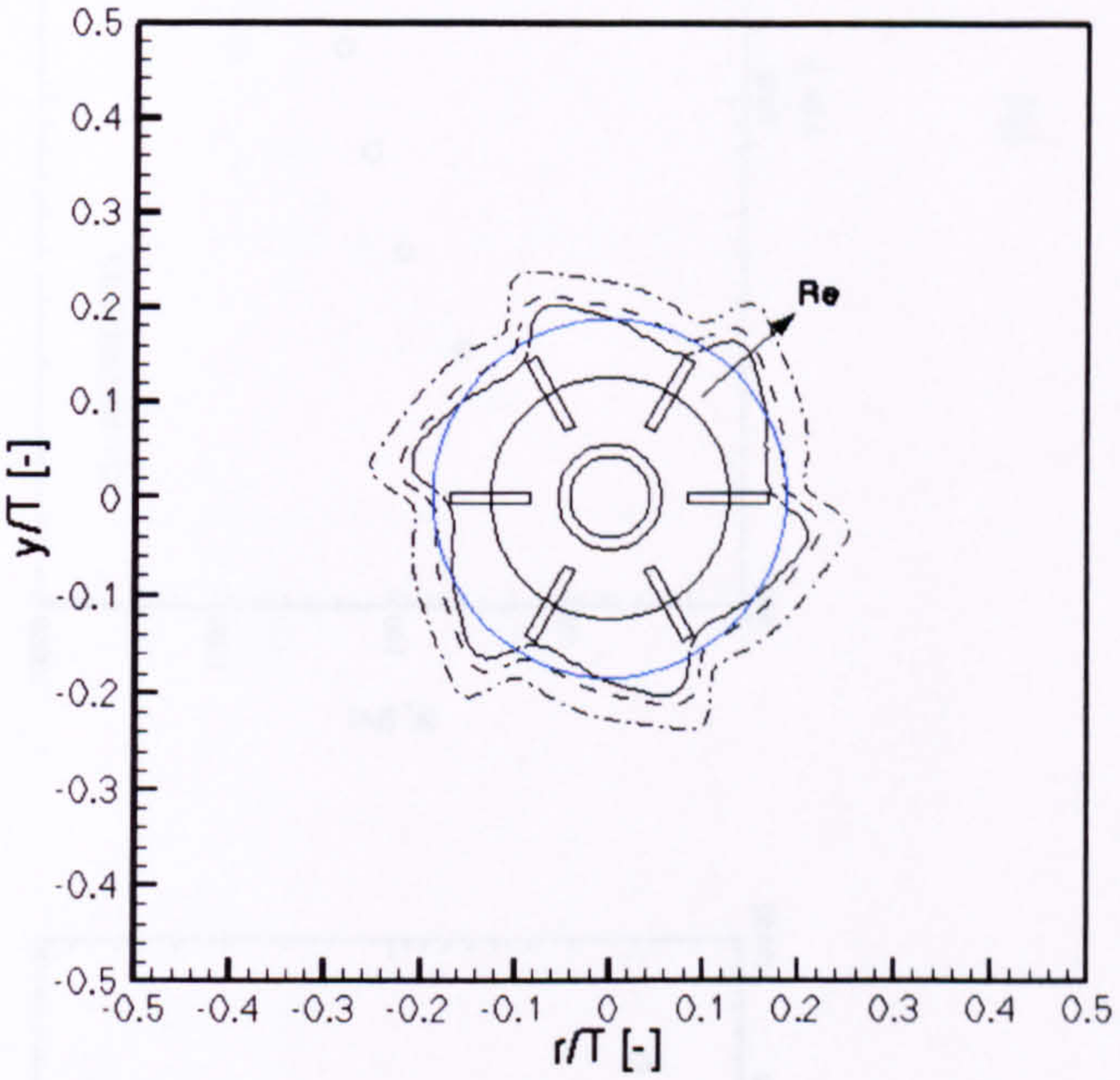

Figure 6.28: Profiles of the normalised radial velocity components (U_r/V_{tip}) at Re = 1, 10 and 28, increasing in the direction of the arrow shown above, for Si1000. The results are taken at an axial position equal to the height of the mid-plane of the impeller blade ($z/T = 0.333$) and at a radial position closest to the impeller blade, $r/T = 0.186$.

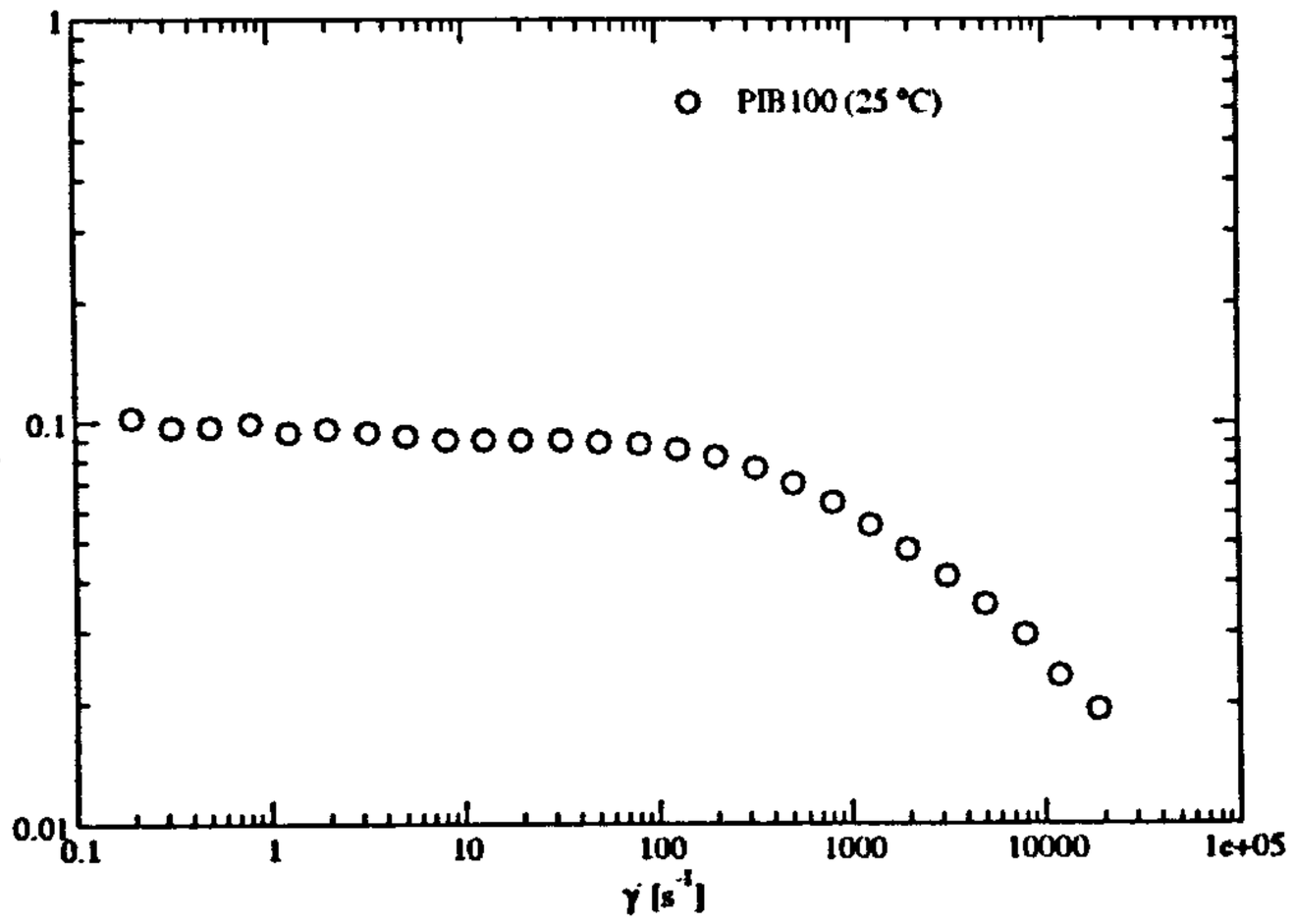

(a)

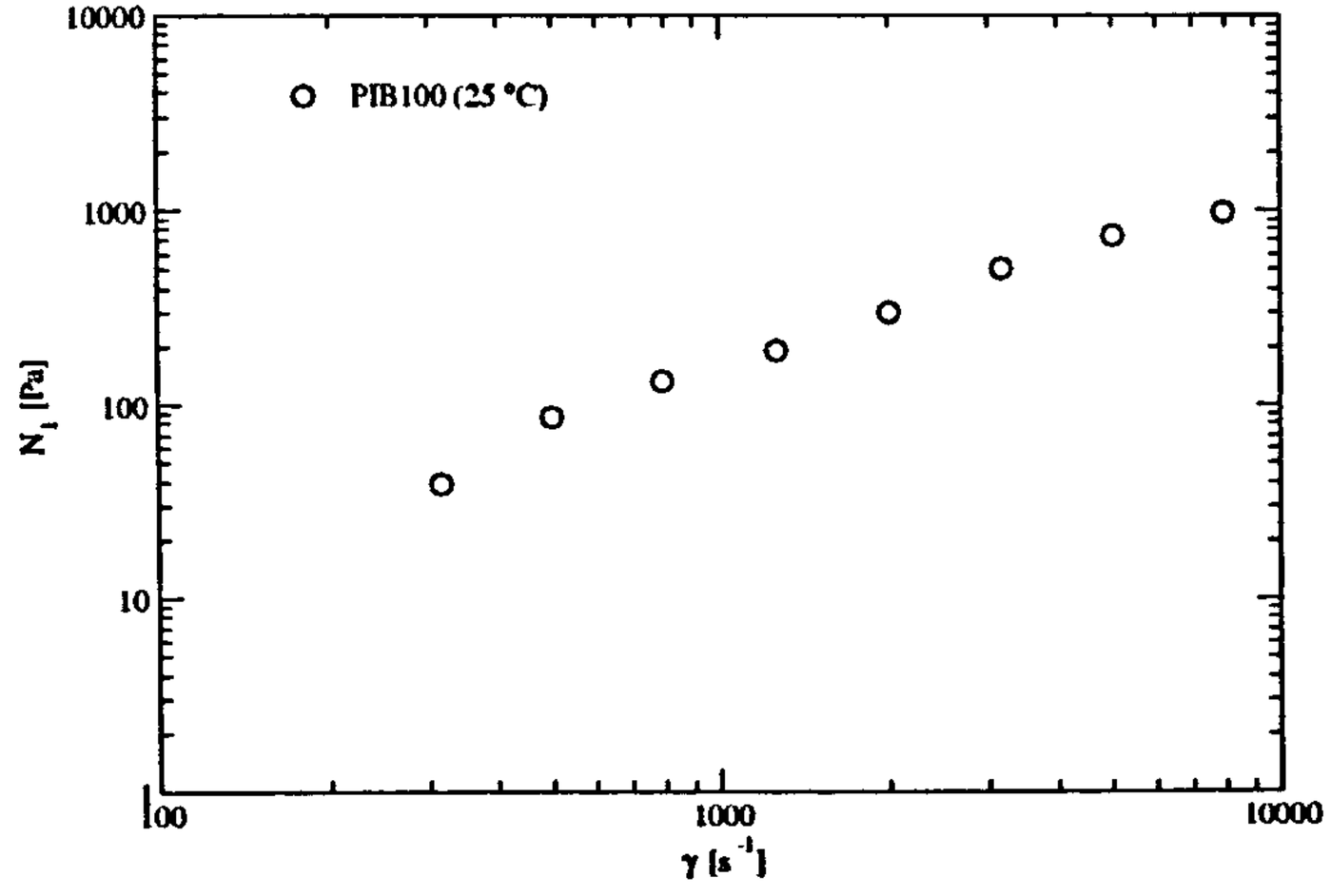

(b)

Figure 6.29: Measured values of non-linear; (a) steady state shear viscosity, $\eta(\dot{\gamma})$ and; (b) first normal stress difference (N_1), at a reference temperature of 25 ^0C, for PIB100.

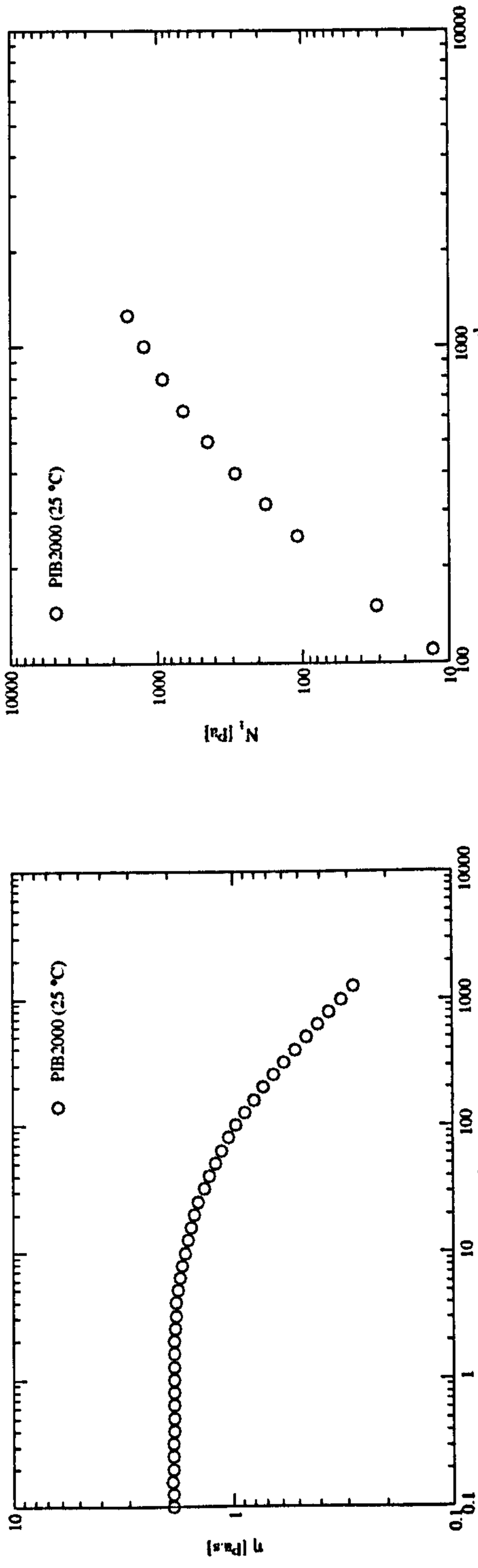

Figure 6.30: Measured values of non-linear; (a) steady state shear viscosity, $\eta(\dot{\gamma})$ and; (b) first normal stress difference (N_1), at a reference temperature of 25 ^0C, for PIB2000.

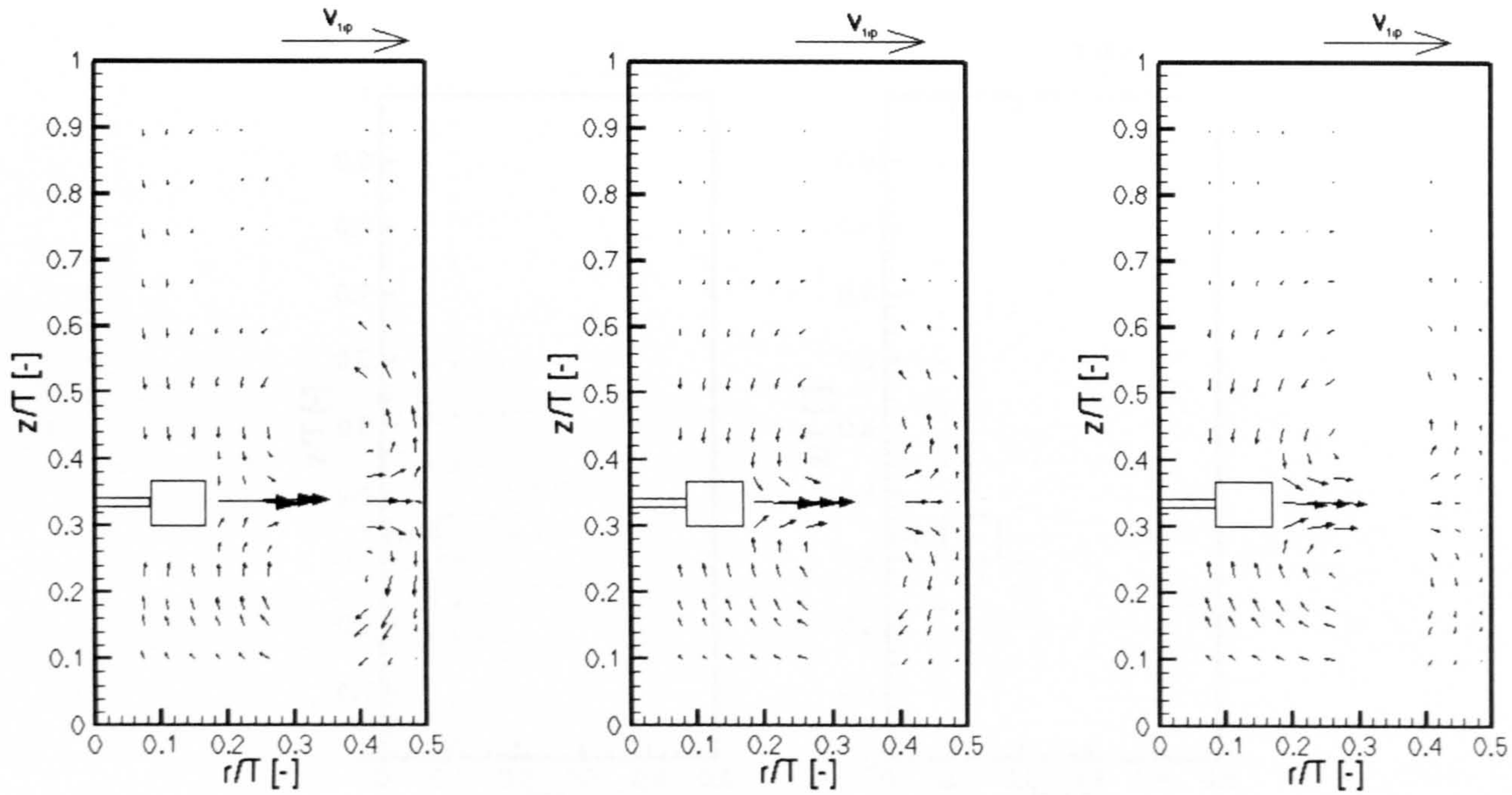

(a) (b) (c)

Figure 6.31: Ensemble-average velocity vectors for PIB100, in the $\theta = 0^0$ plane. (a) $Re = 240$ and $De = 5.84$; (b) $Re = 80$ and $De = 1.942$; (c) $Re = 40$ and $De = 0.974$.

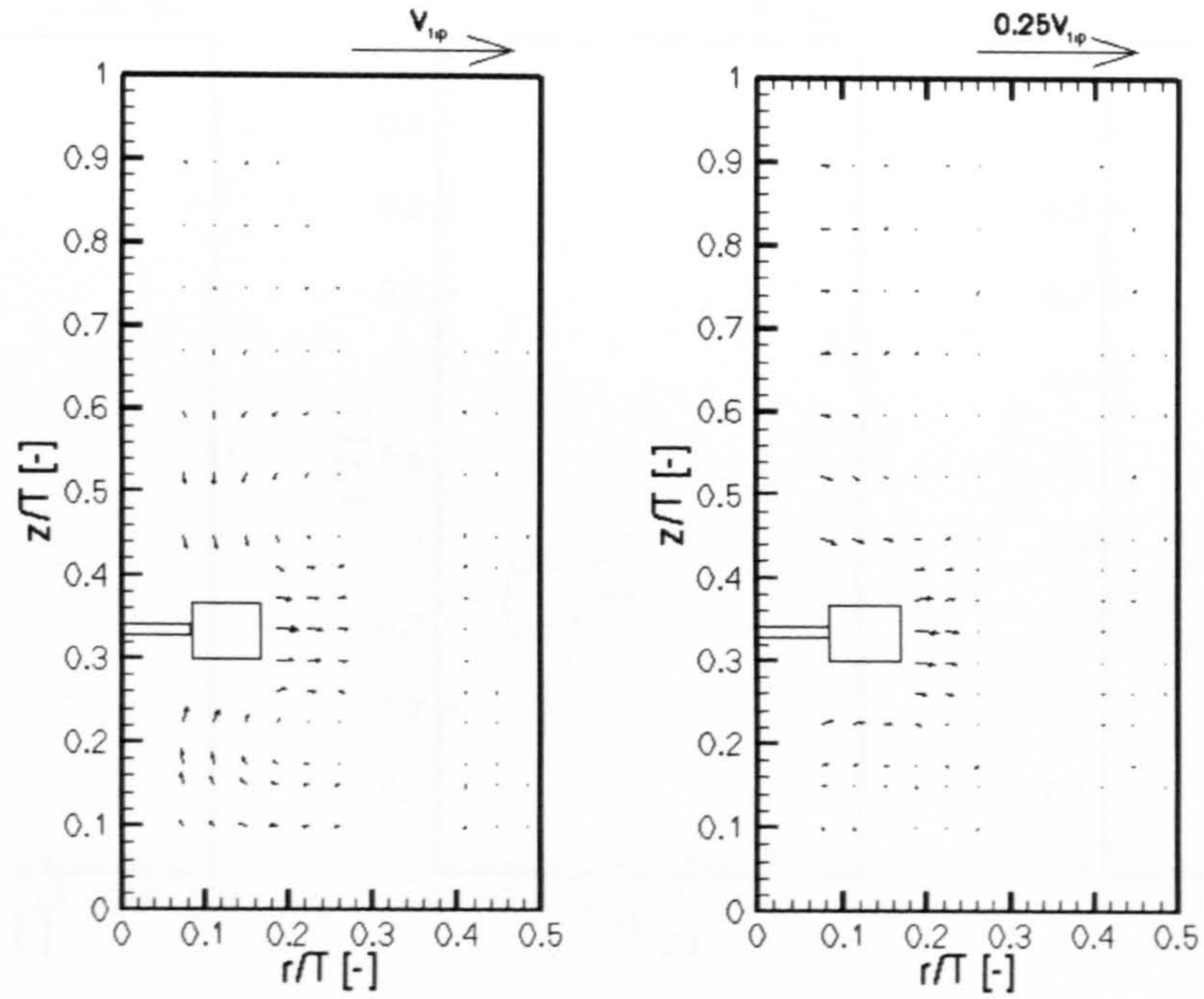

(a) (b)

Figure 6.32: Ensemble-average velocity vectors for PIB100, in the $\theta = 0^0$ plane. (a) $Re = 8$ and $De = 0.194$; (b) $Re = 1$ and $De = 0.0236$.

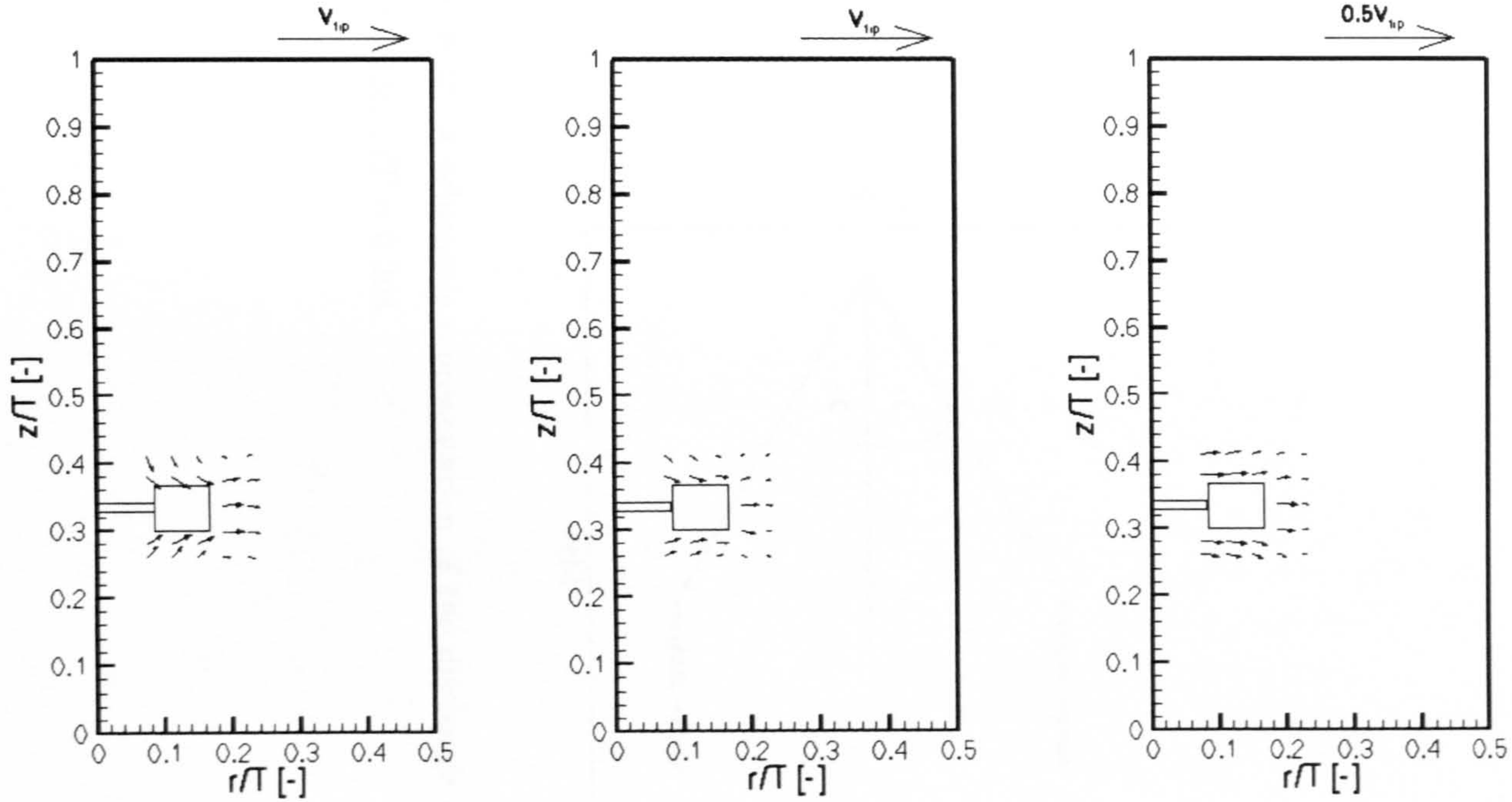

(a) (b) (c)

Figure 6.33: Ensemble-average velocity vectors for PIB2000, in the $\theta = 0^0$ plane. (a) $Re = 13$ and $De = 107.481$; (b) $Re = 7$ and $De = 57.09$; (c) $Re = 0.7$ and $De = 5.742$.

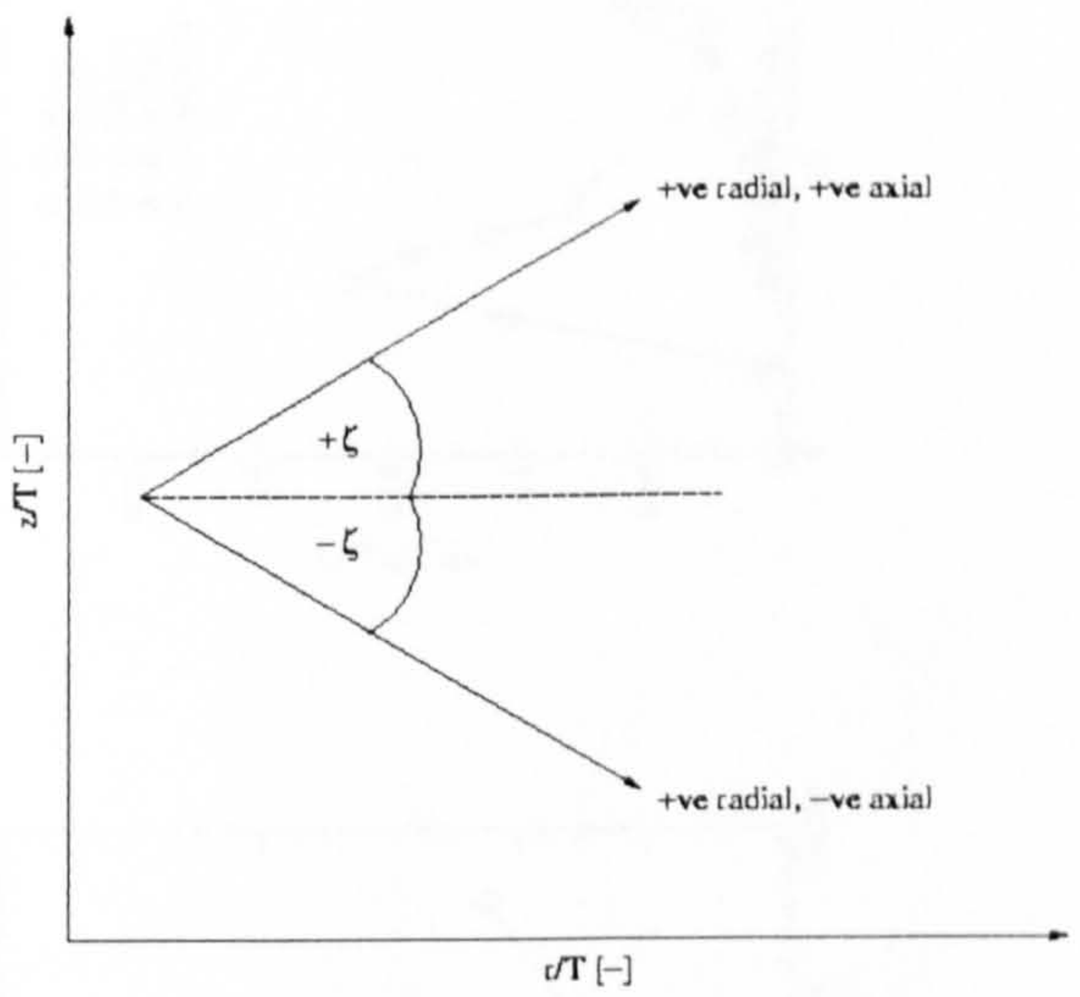

Figure 6.34: A schematic representation of the discharge angle, ζ, at the point $r/T = 0.224$, $z/T = 0.298$.

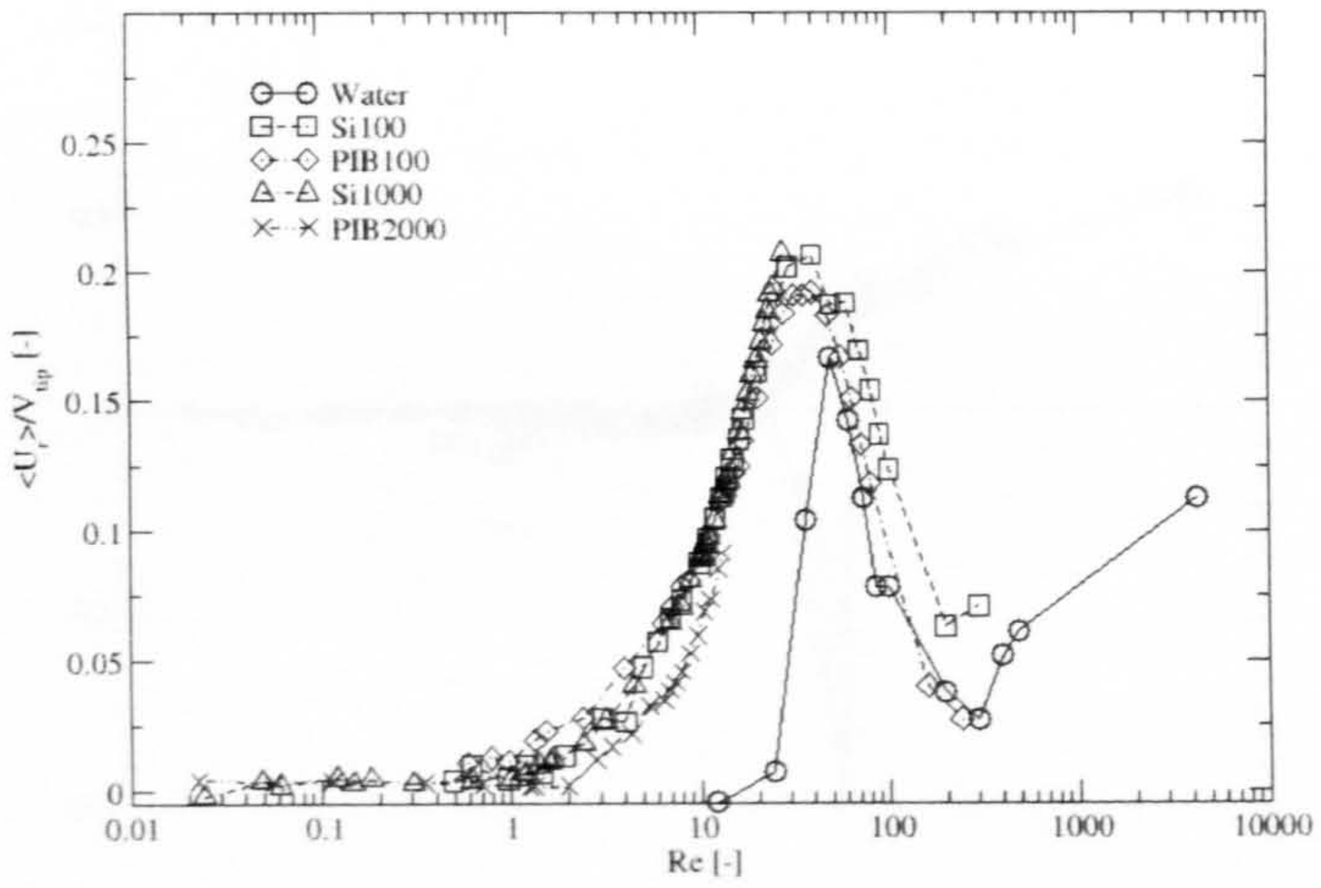

(a)

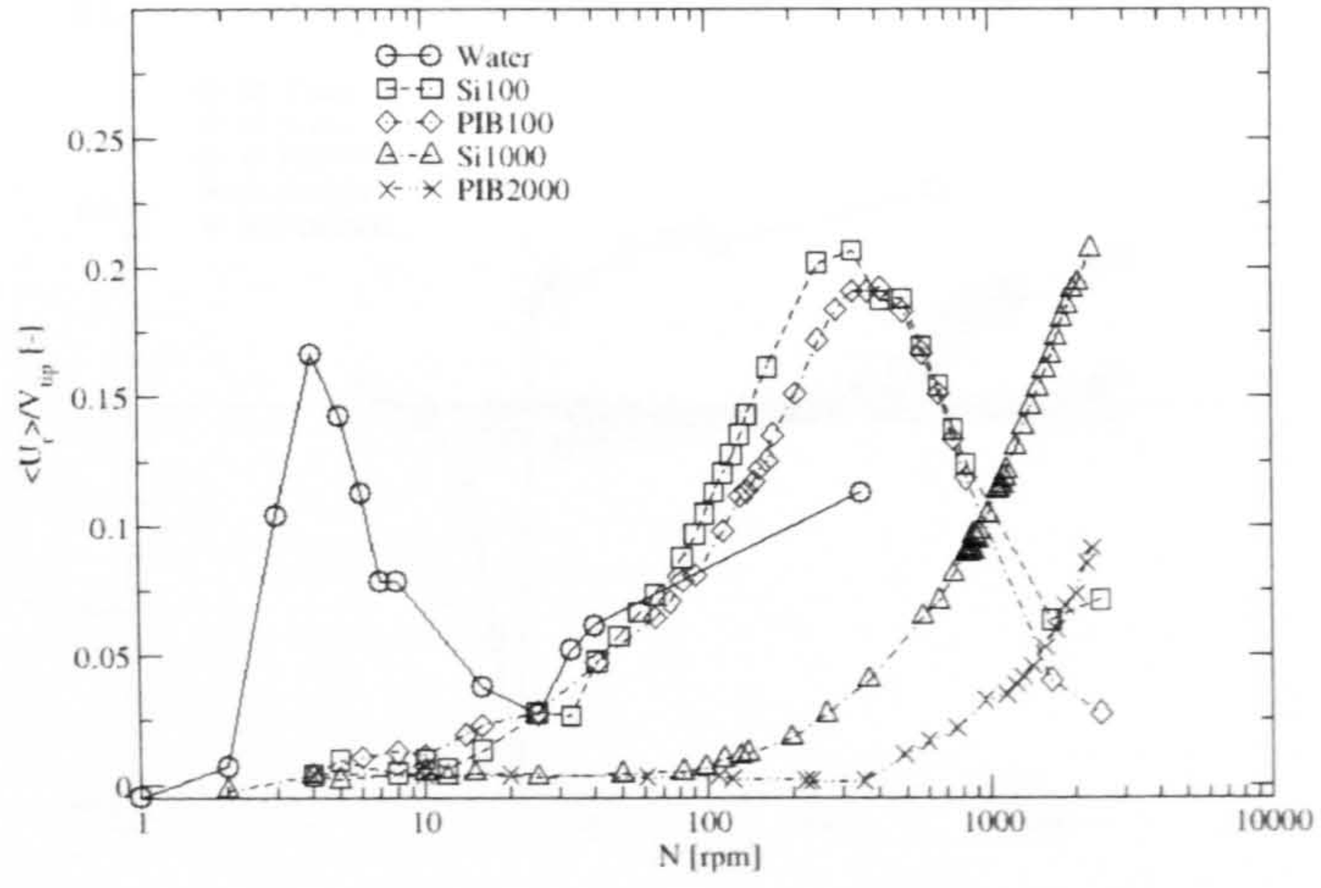

(b)

Figure 6.35: Normalised radial velocity measurements versus; (a) Re and; (b) N, at the point of discharge, $r/T = 0.224$, $z/T = 0.298$.

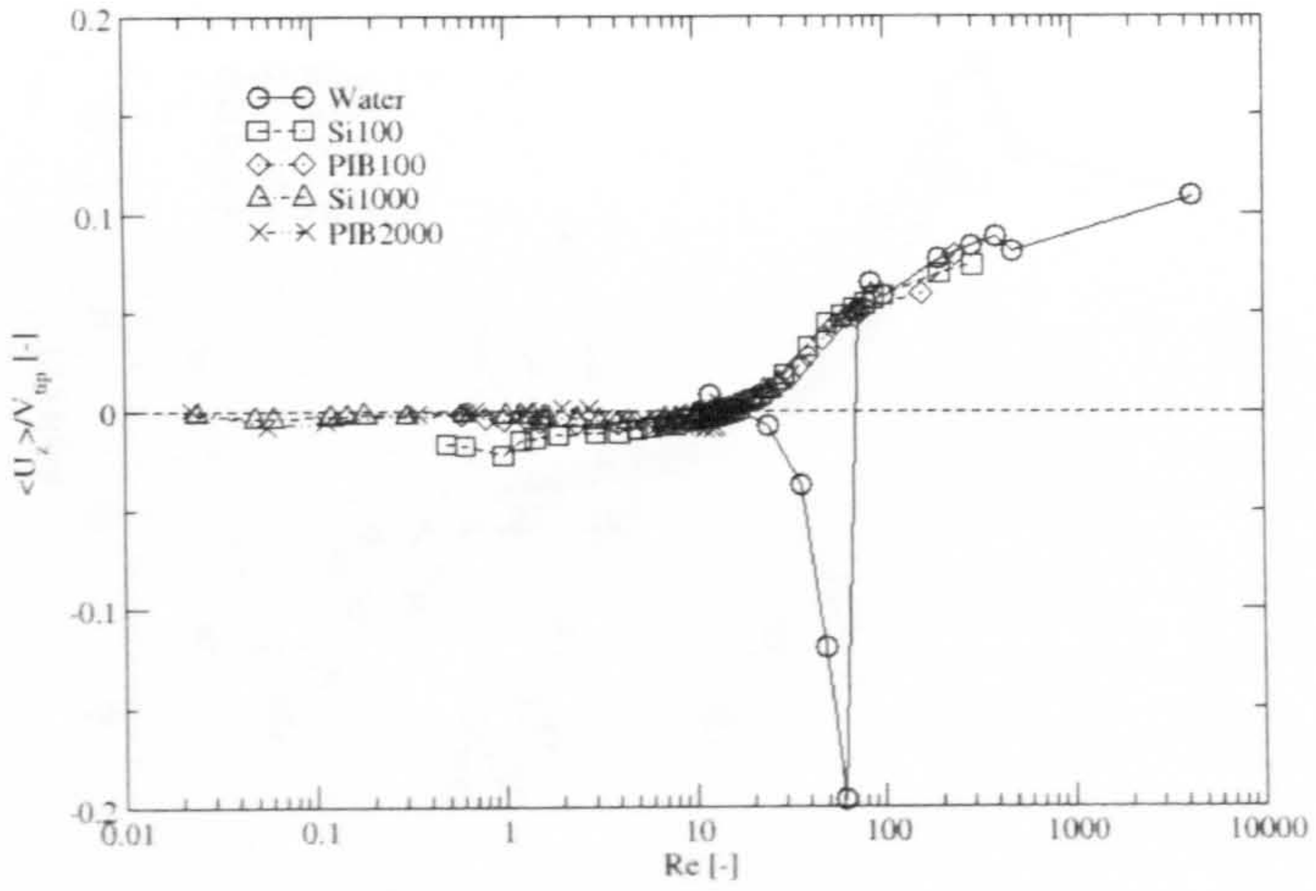

(a)

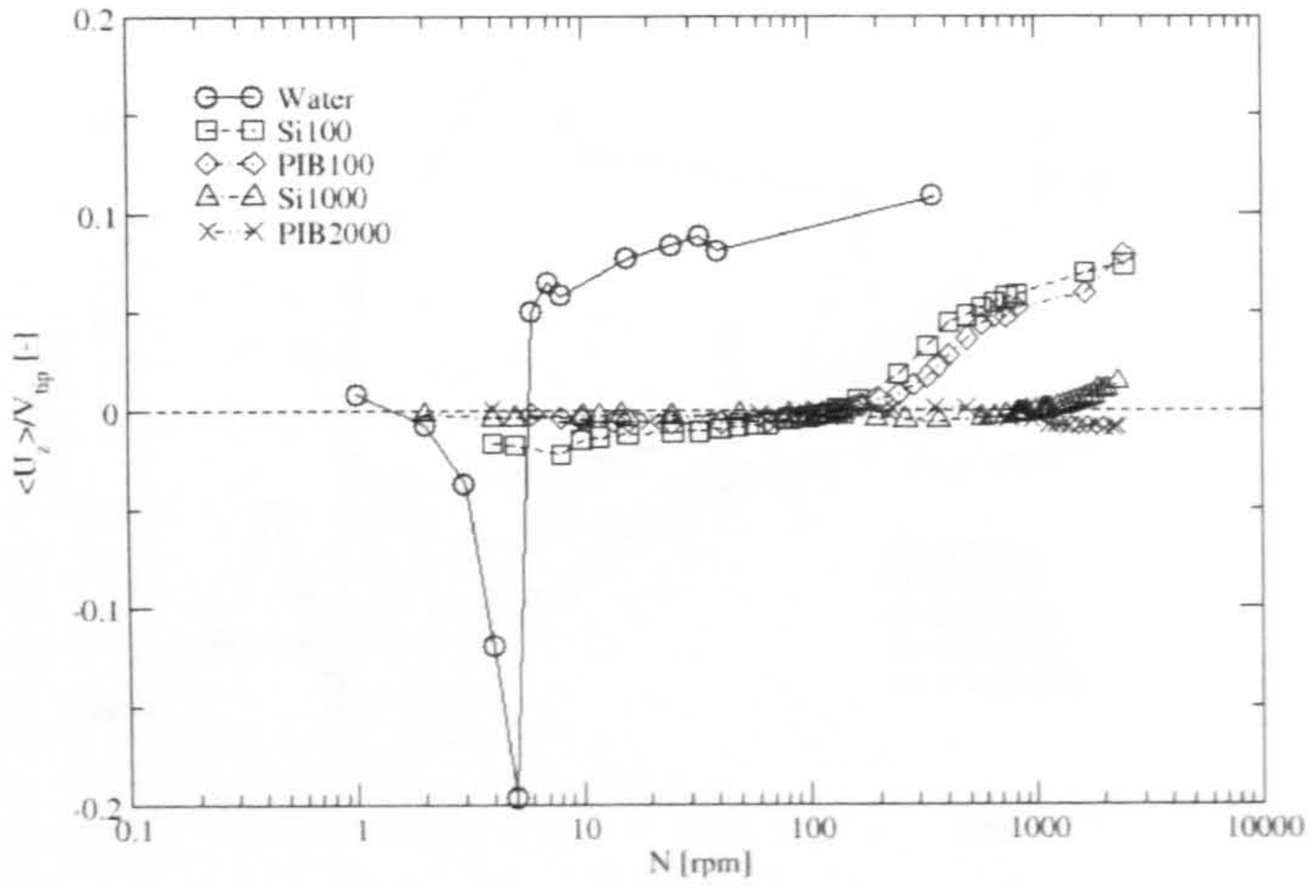

(b)

Figure 6.36: Normalised axial velocity measurements versus; (a) Re and; (b) N, at the point of discharge, $r/T = 0.224$, $z/T = 0.298$.

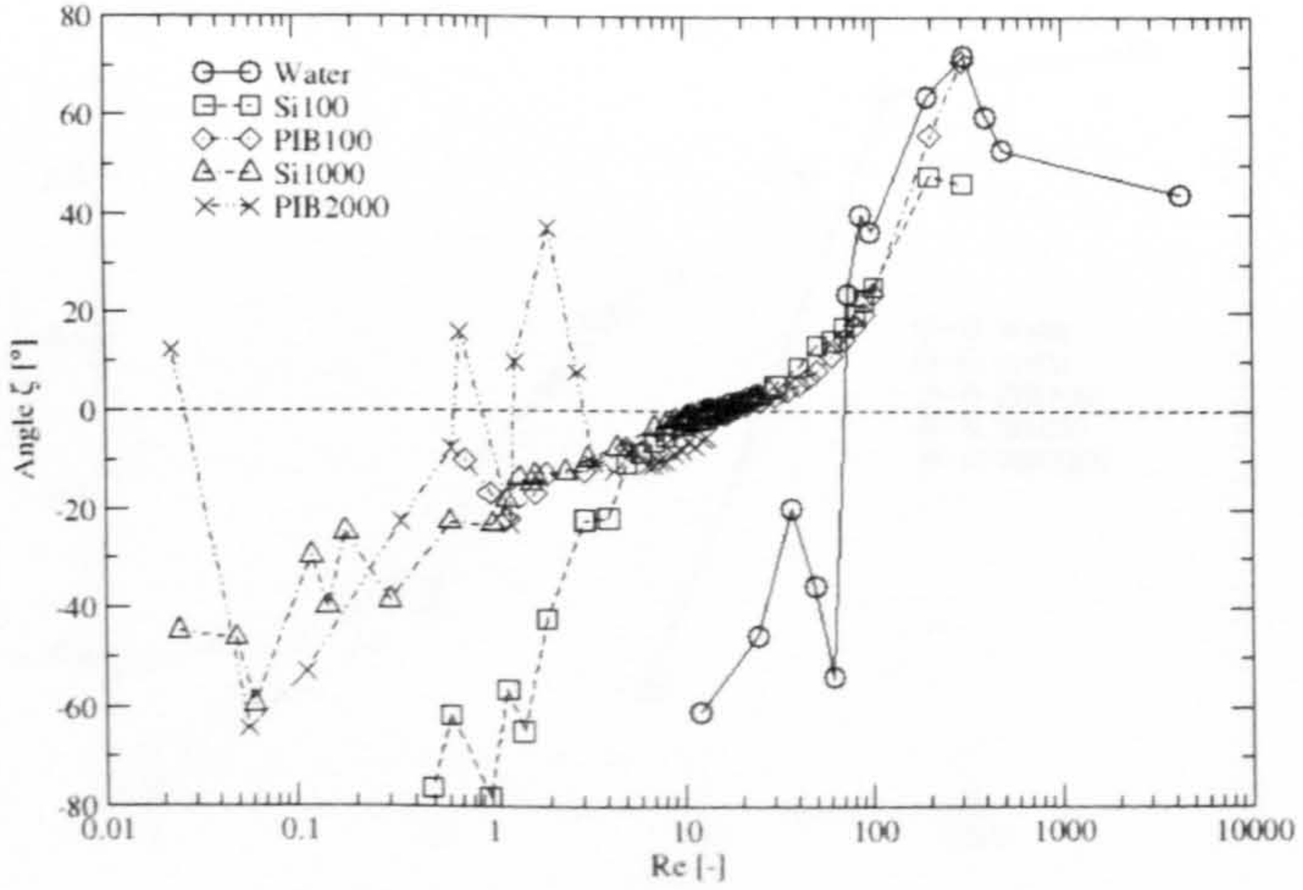

(a)

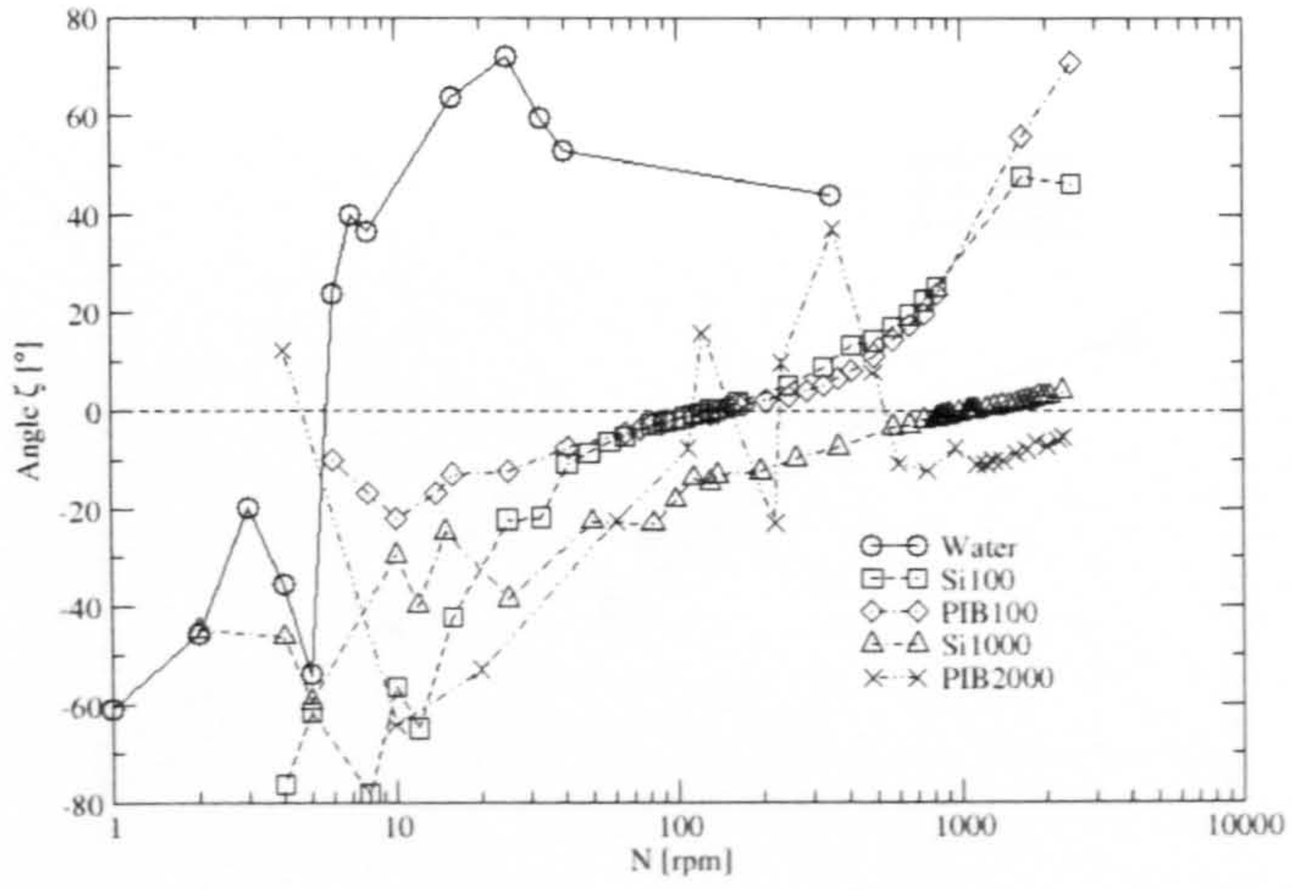

(b)

Figure 6.37: The angle of discharge, ζ, at the point, $r/T = 0.224$, $z/T = 0.298$, versus; (a) Re and; (b) N.

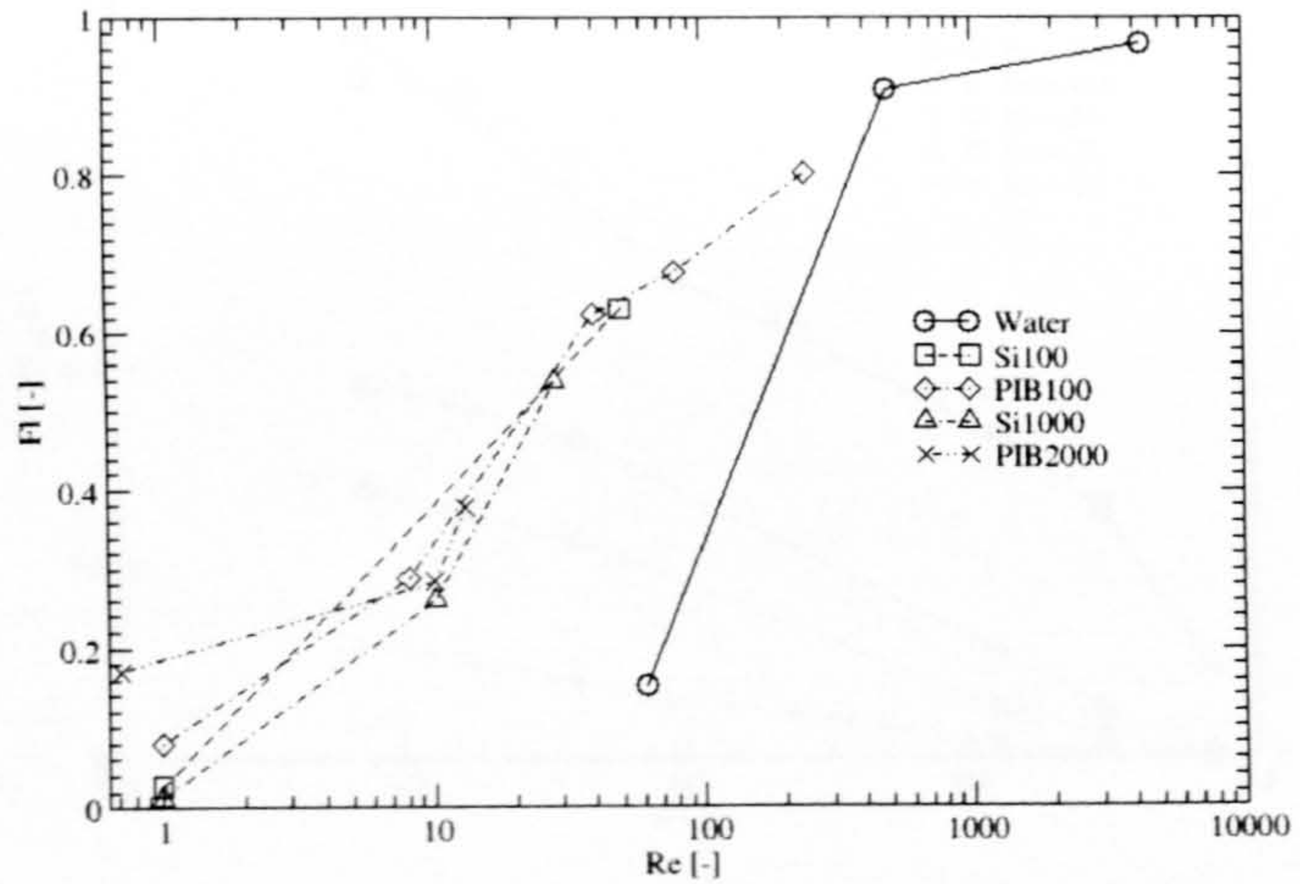

(a)

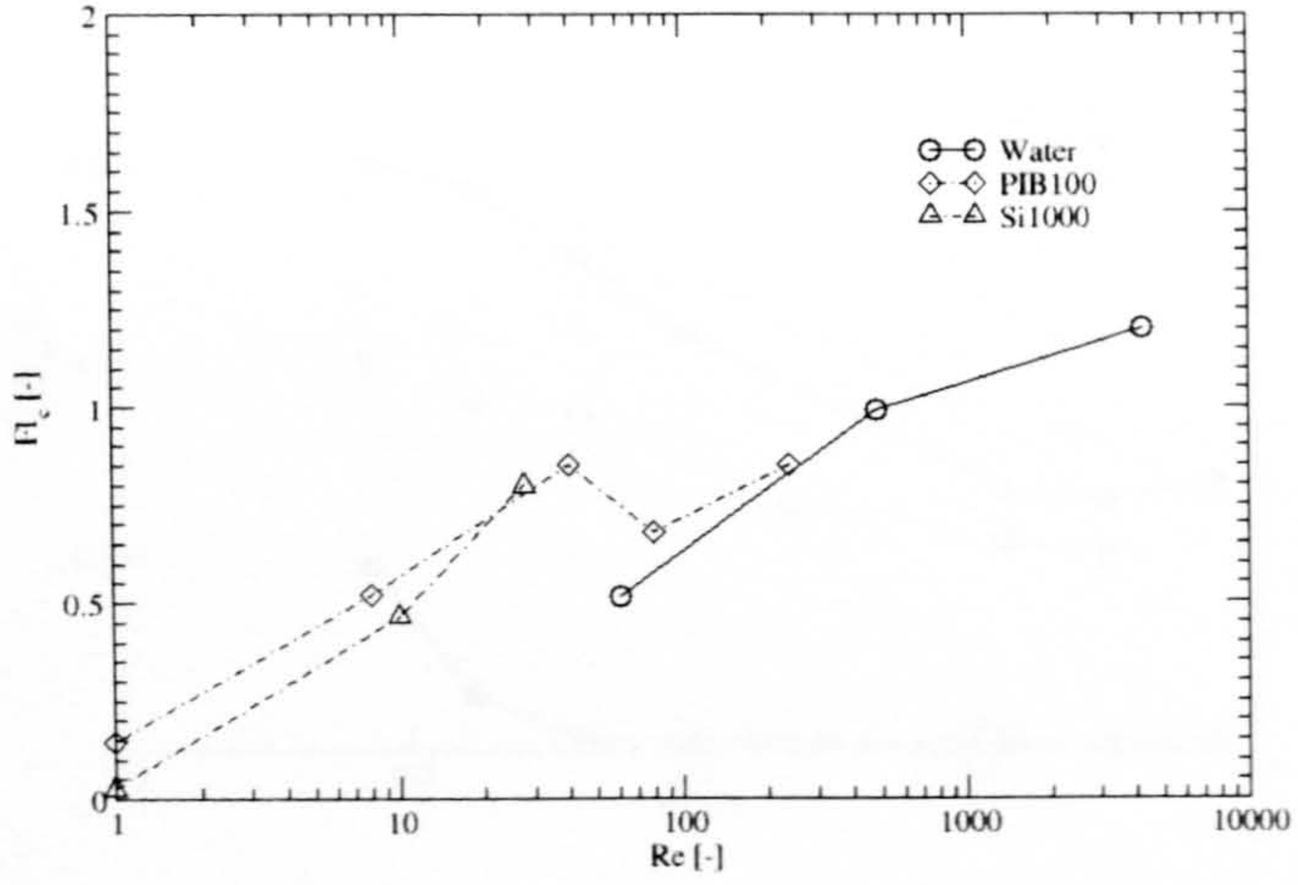

(b)

Figure 6.38: (a) Fl and; (b) Fl_c, versus Re.

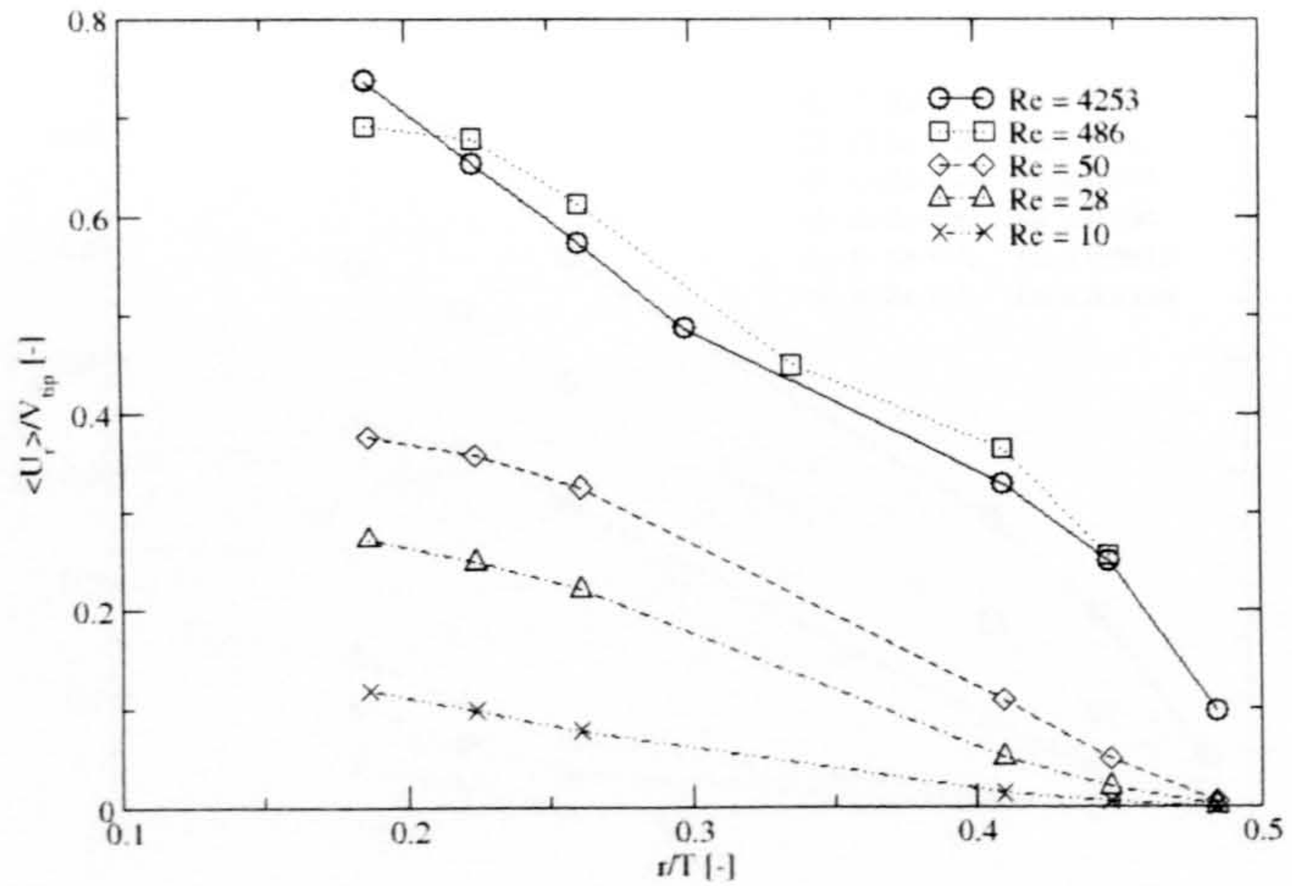

(a)

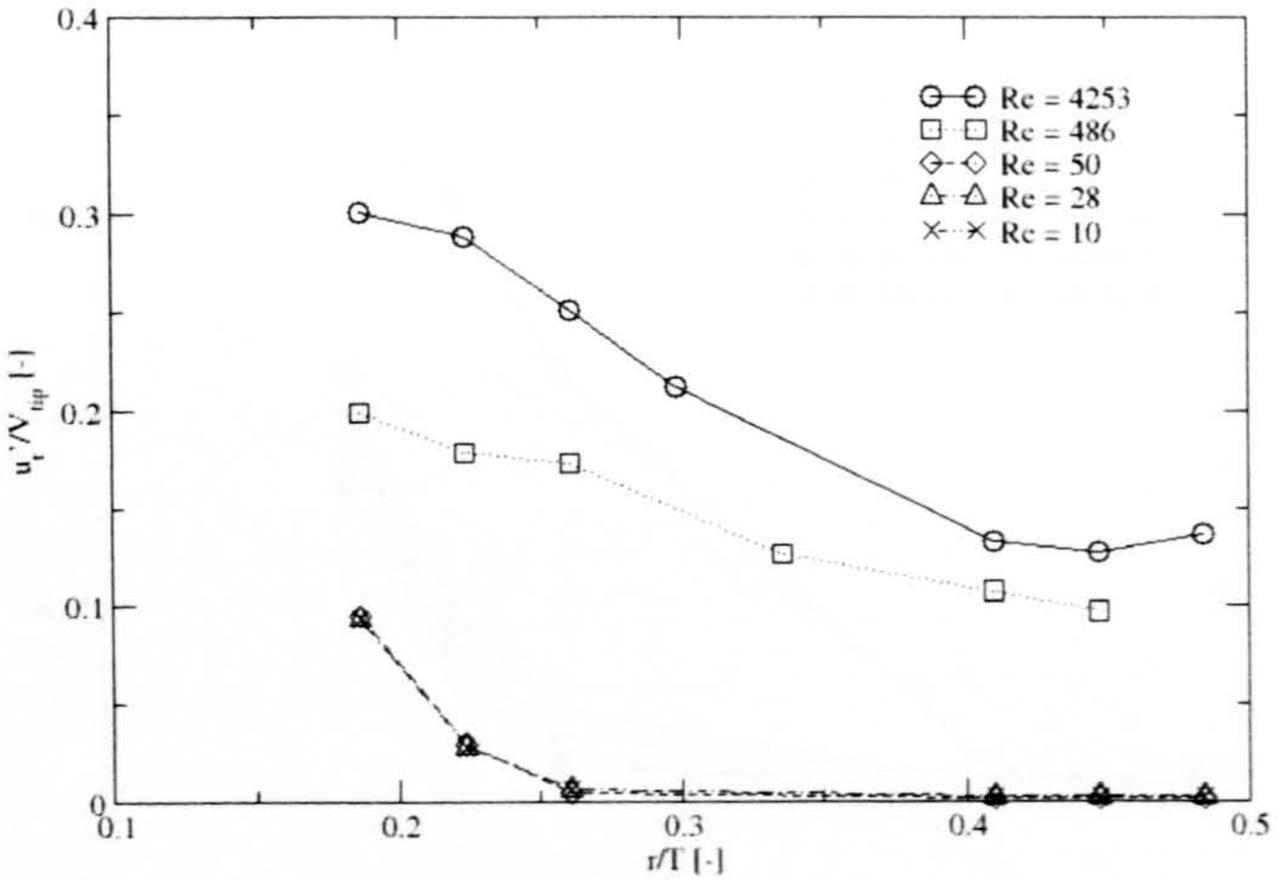

(b)

Figure 6.39: Ensemble-average; (a) radial velocity and; (b) radial r.m.s. values versus radial position (r/T), along the centre of the impeller stream $(z/T = 0.33)$, for a Newtonian fluid, in the $\theta = 0^0$ plane, at varying Re.

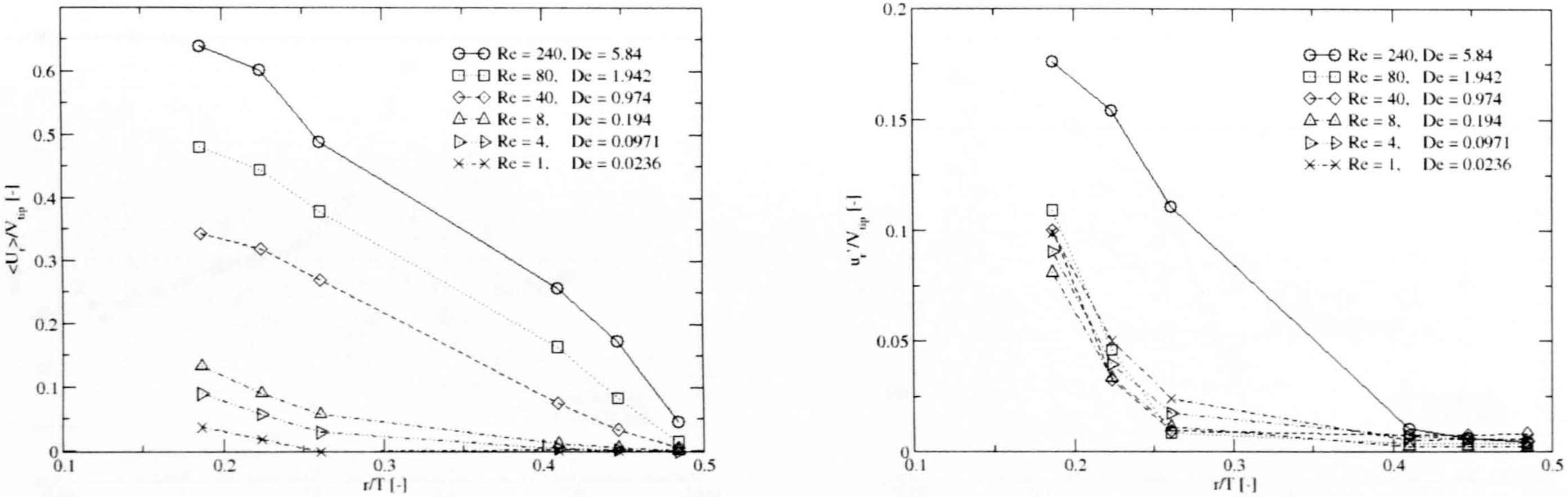

(a) (b)

Figure 6.40: Ensemble-average; (a) radial velocity and; (b) radial r.m.s. values versus radial position (r/T), along the centre of the impeller stream ($z/T = 0.33$), for PIB100, in the $\theta = 0^0$ plane, at varying Re.

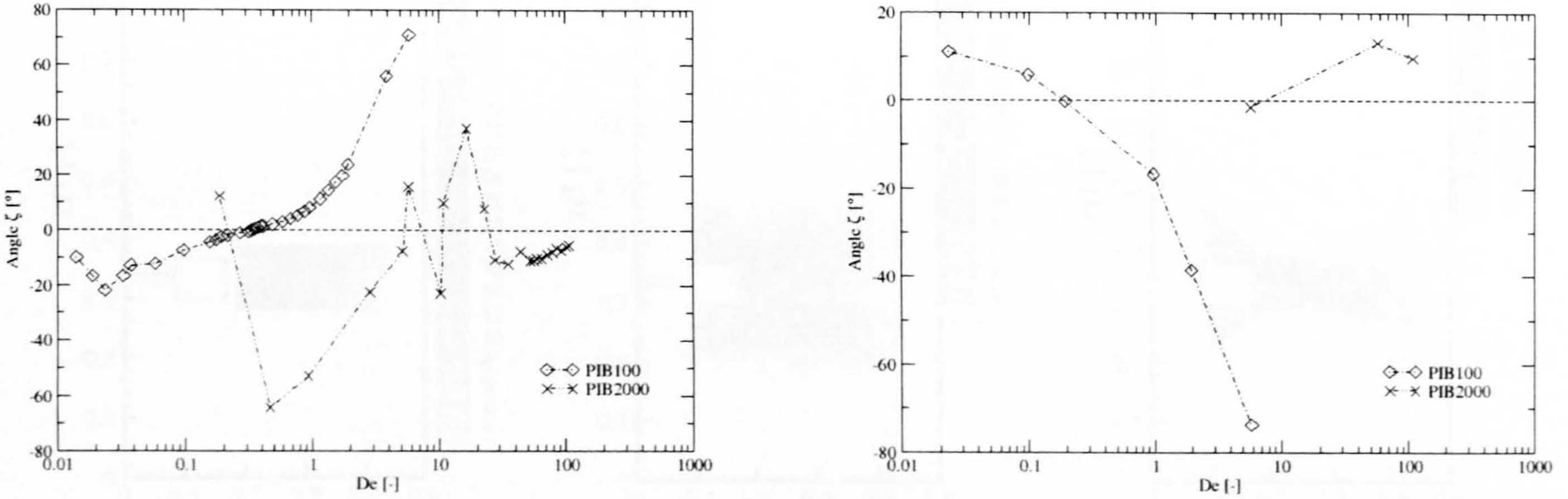

Figure 6.41: The angle of discharge, ζ versus De, at the point; (a) $r/T = 0.224$, $z/T = 0.298$ and; (b) $r/T = 0.224$, $z/T = 0.373$

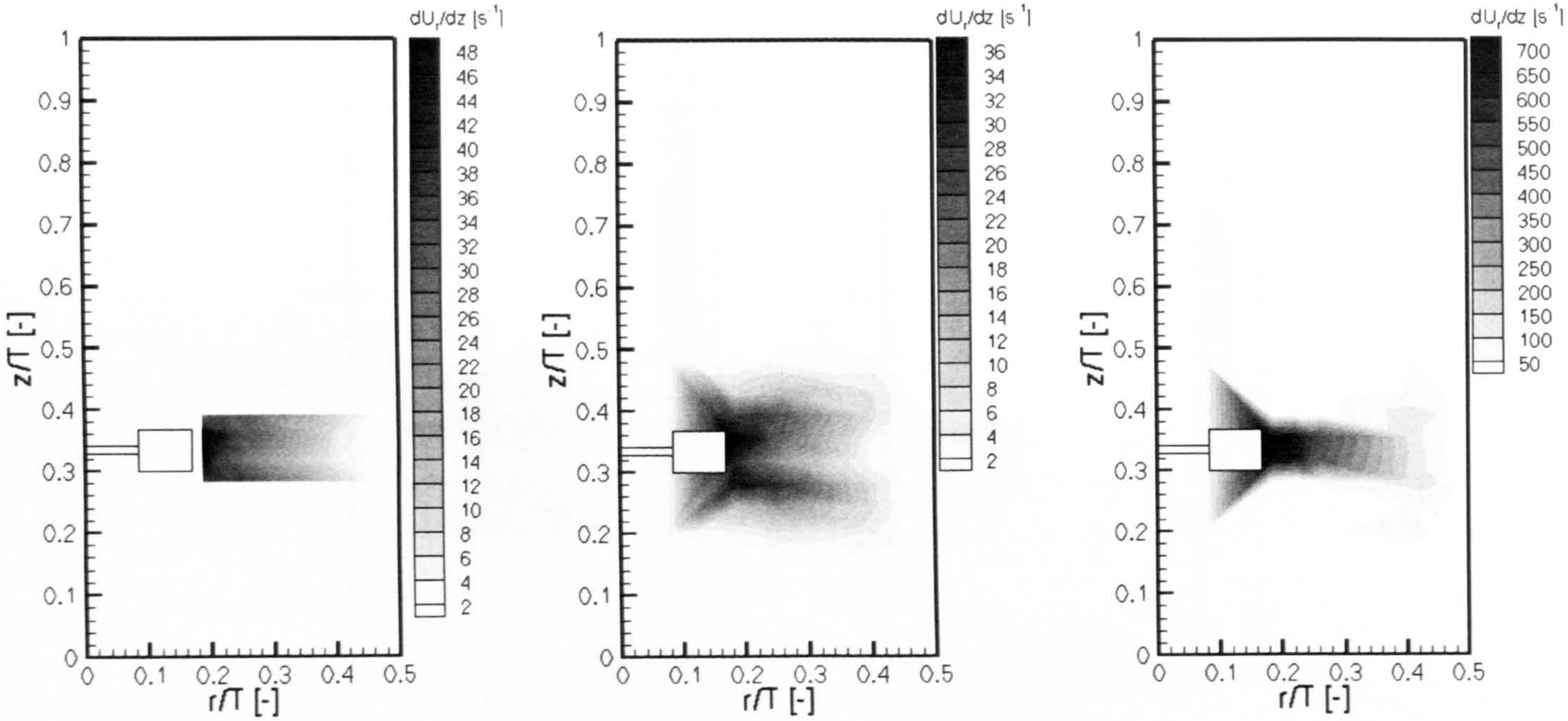

(a) (b) (c)

Figure 6.42: Ensemble-average shear strain rate ($\partial U_r/\partial z$) distributions in the $\theta = 0^0$ plane. (a) Si100 at $Re = 50$; (b) PIB100 at $Re = 40$ and $De = 0.974$; (c) PIB100 at $Re = 240$ and $De = 5.84$.

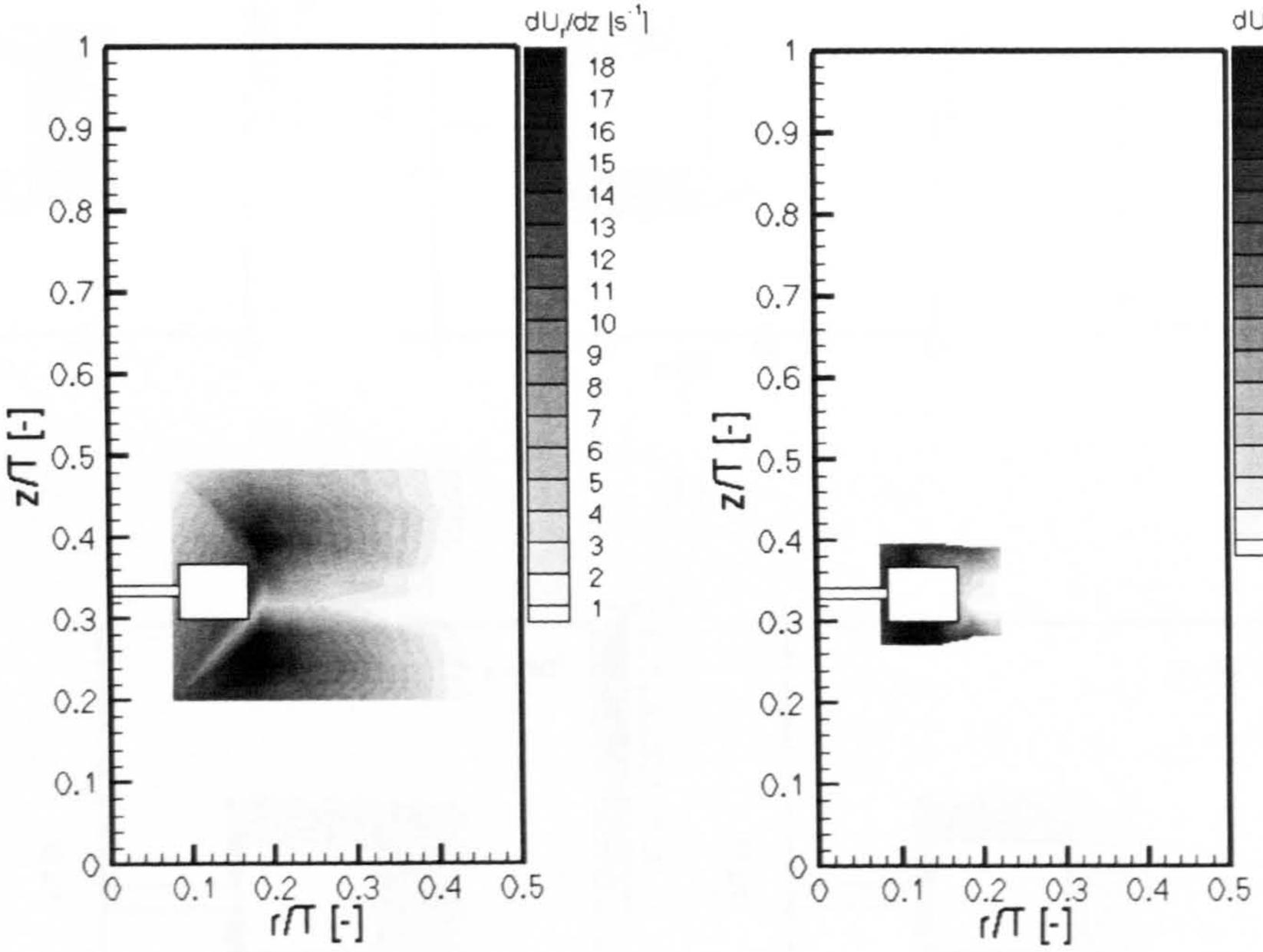

(a) (b)

Figure 6.43: Ensemble-average shear strain rate ($\partial U_r/\partial z$) distributions in the $\theta = 0^0$ plane. (a) Si1000 at $Re = 10$; (b) PIB2000 at $Re = 13$ and $De = 107.481$

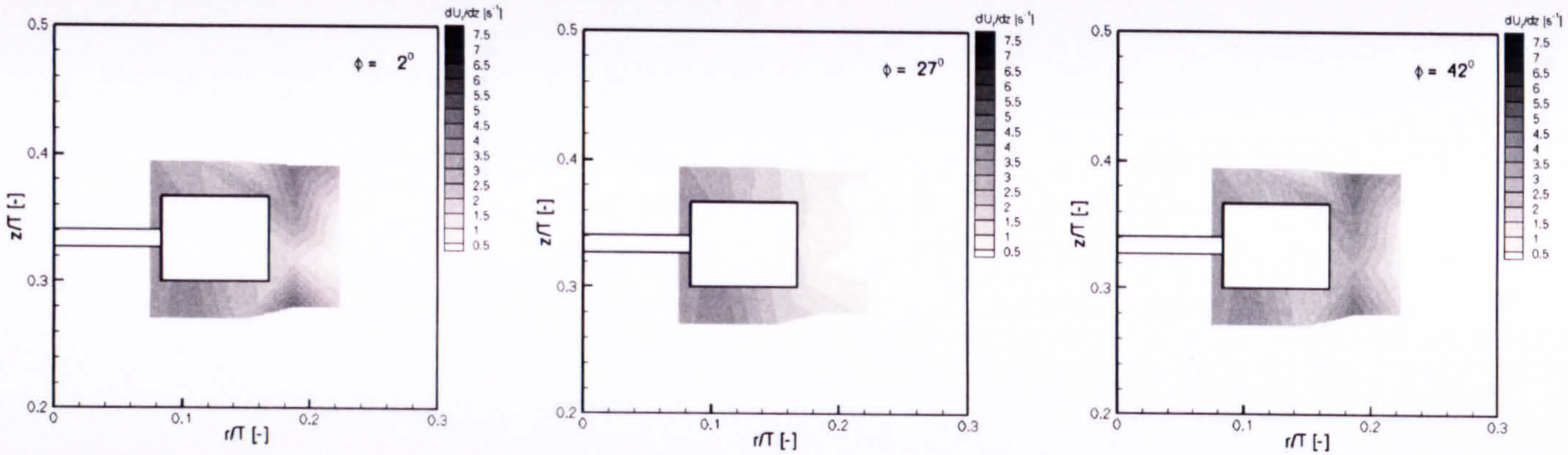

(a) (b) (c)

(d) (e)

Figure 6.44: Phase-resolved shear strain rate distribution ($\partial U_r/\partial z$) for PIB2000 at $Re = 0.7$ and $De = 5.742$, in the $\theta = 0^0$ plane at $\phi = 2^0$, 27^0, 42^0, 52^0 and 55^0.

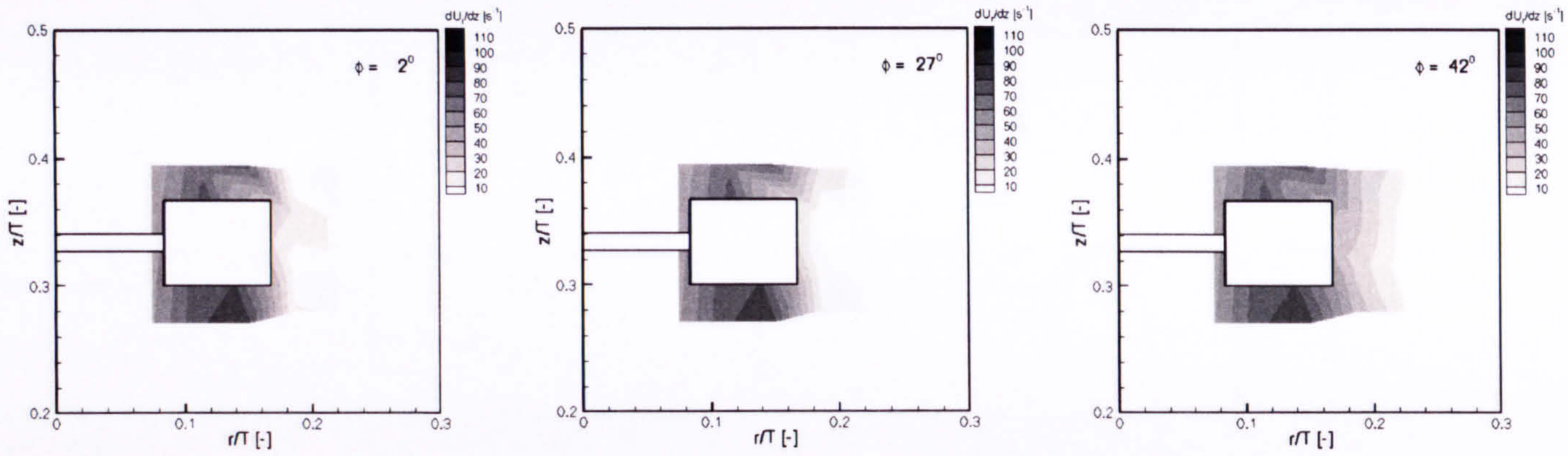

(a) (b) (c)

(d) (e)

Figure 6.45: Phase-resolved shear strain rate distribution ($\partial U_r/\partial z$) for PIB2000 at $Re = 7$ and $De = 57.09$, in the $\theta = 0^0$ plane at $\phi = 2^0$, 27^0, 42^0, 52^0 and 55^0.

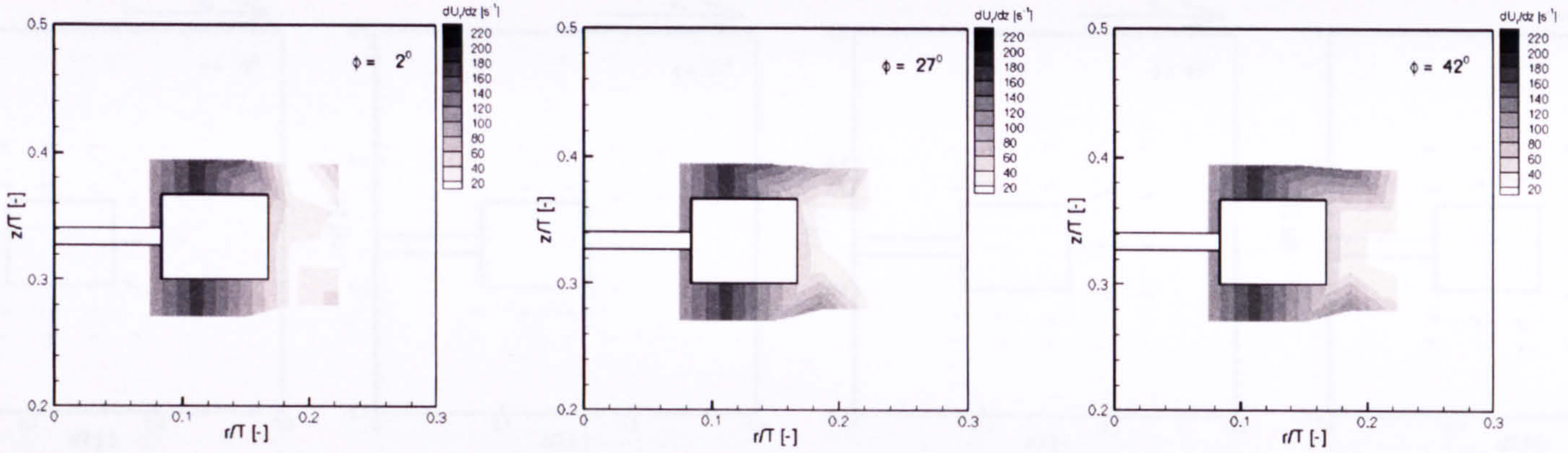

(a) (b) (c)

(d) (e)

Figure 6.46: Phase-resolved shear strain rate distribution ($\partial U_r/\partial z$) for PIB2000 at $Re = 13$ and $De = 107.481$, in the $\theta = 0^0$ plane at $\phi = 2^0$, 27^0, 42^0, 52^0 and 55^0.

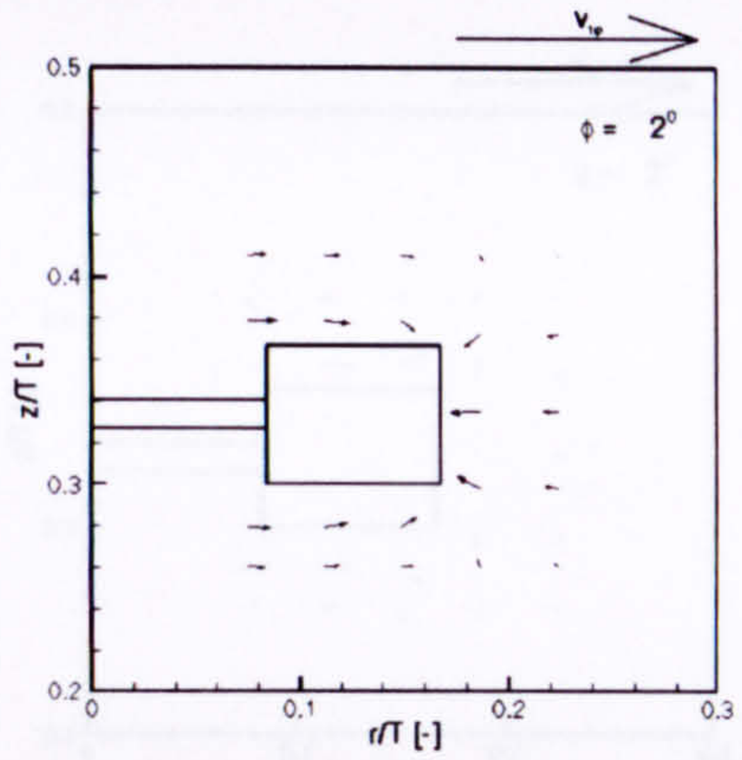

(a)

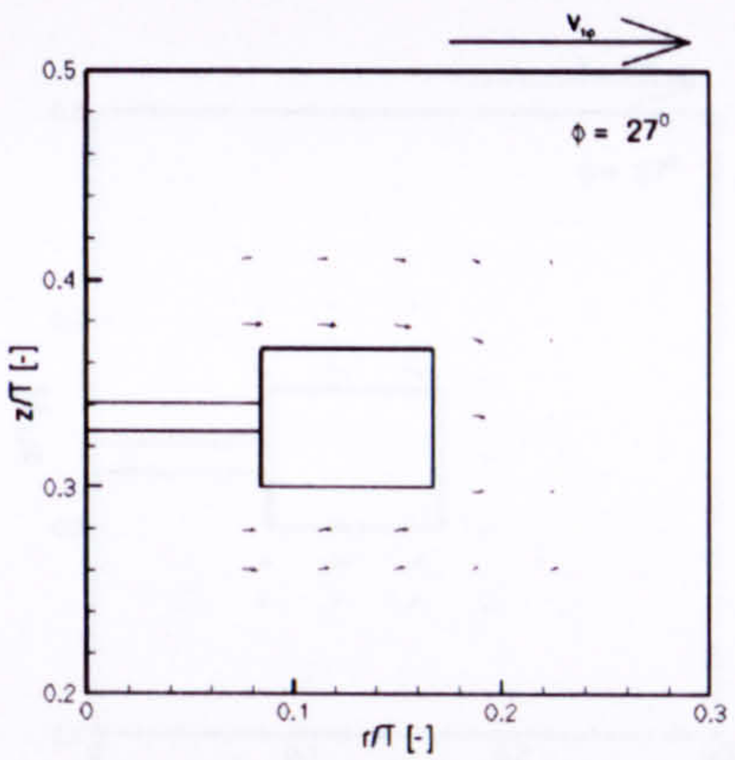

(b)

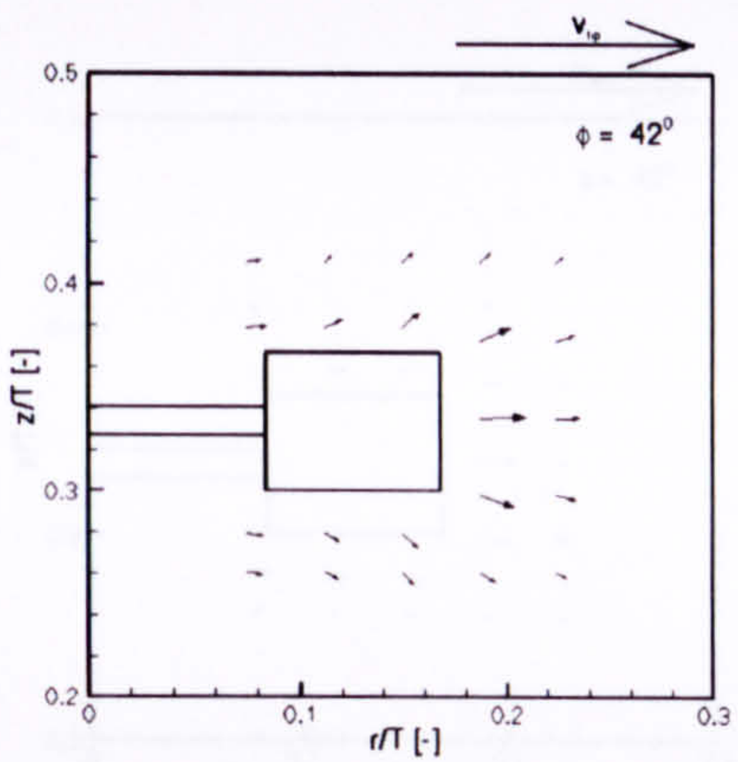

(c)

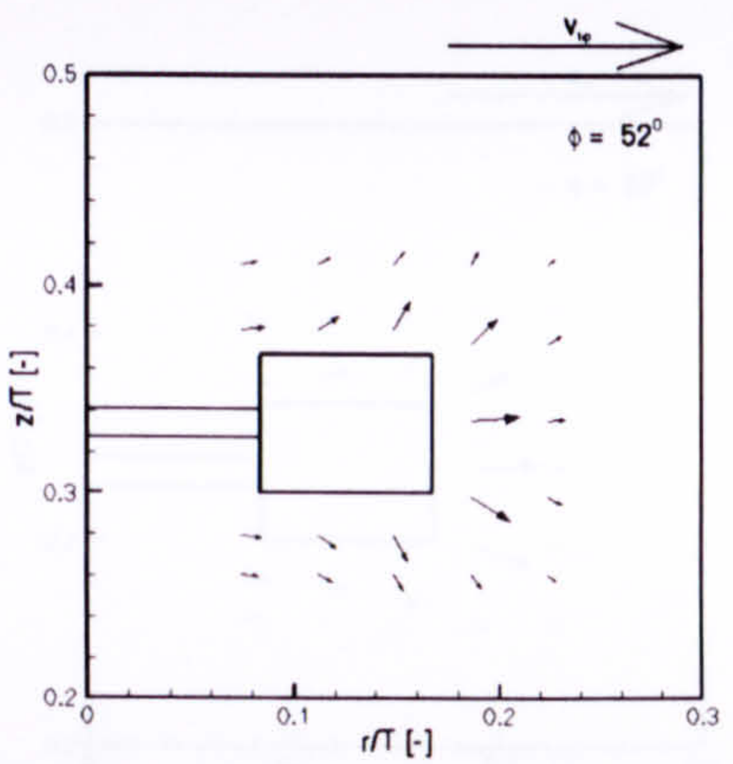

(d)

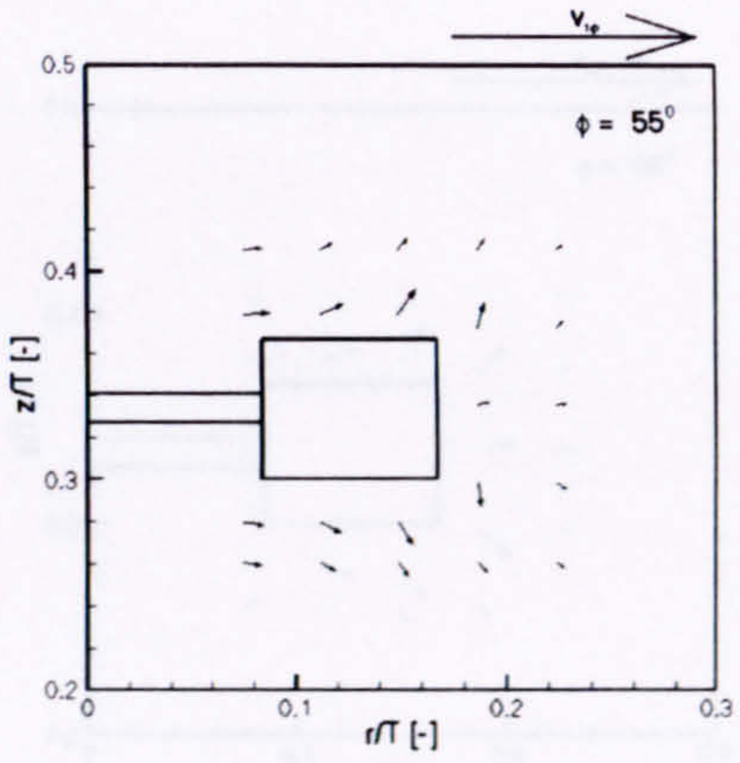

(e)

Figure 6.47: Phase-resolved velocity vectors for PIB2000 at $Re = 0.7$ and $De = 5.742$, in the $\theta = 0^0$ plane at $\phi = 2^0$, 27^0, 42^0, 52^0 and 55^0.

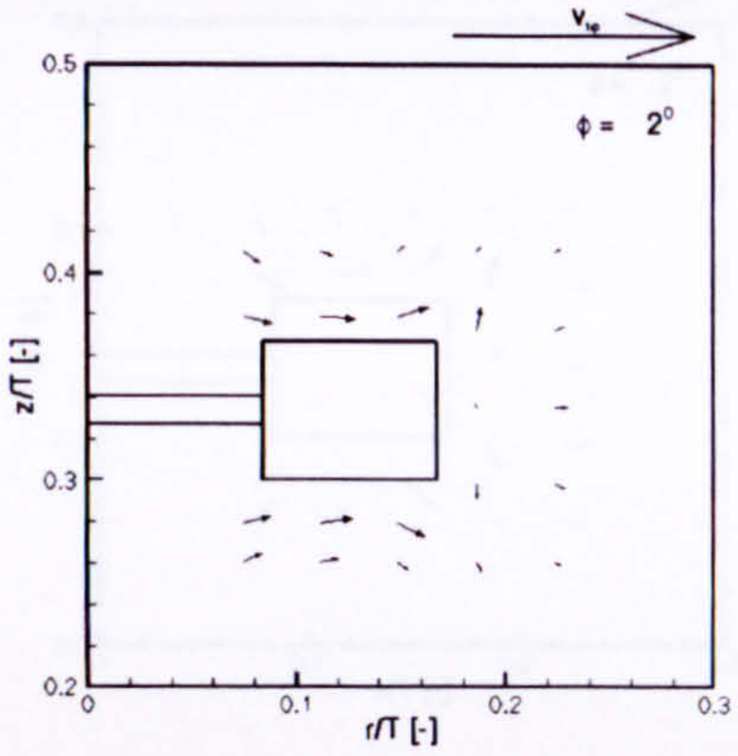

(a)

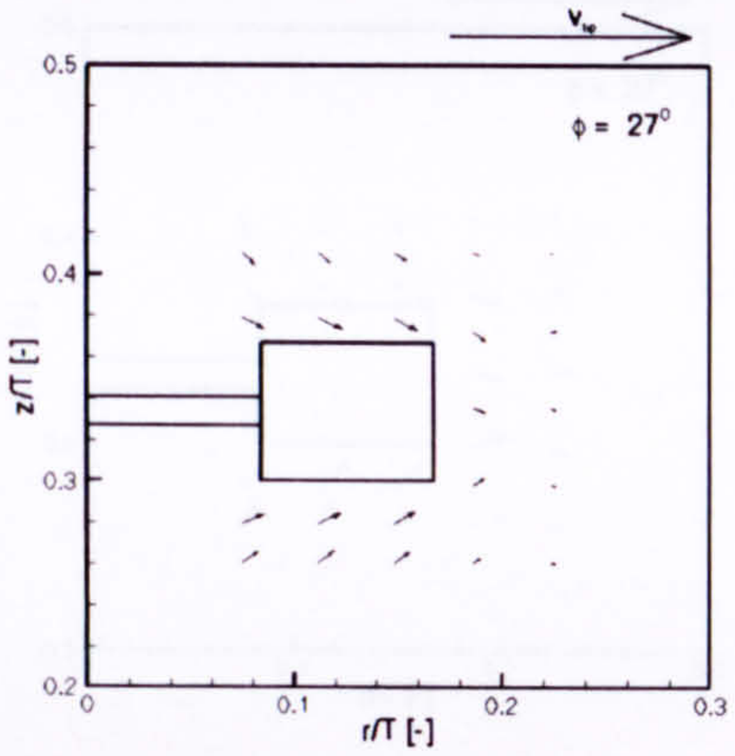

(b)

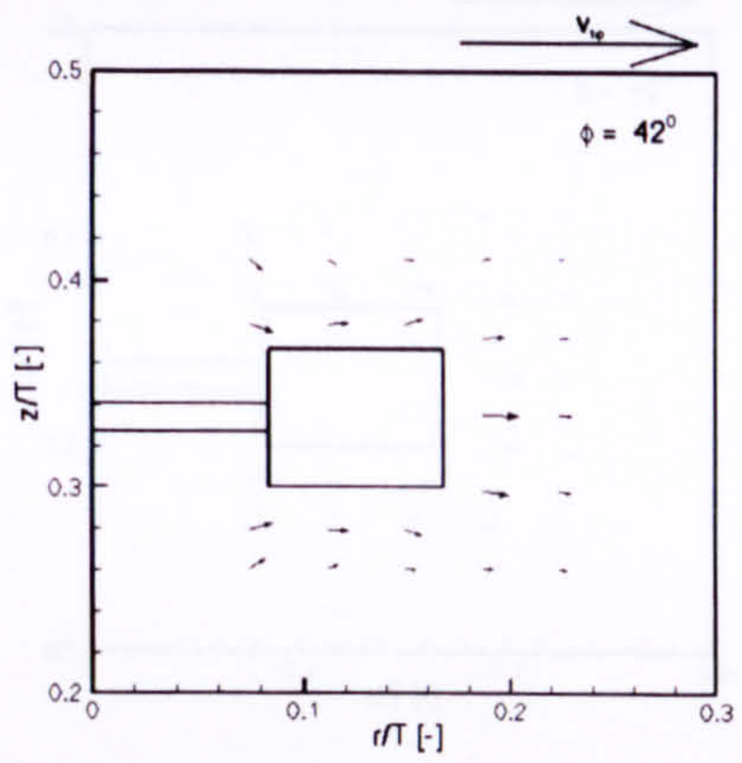

(c)

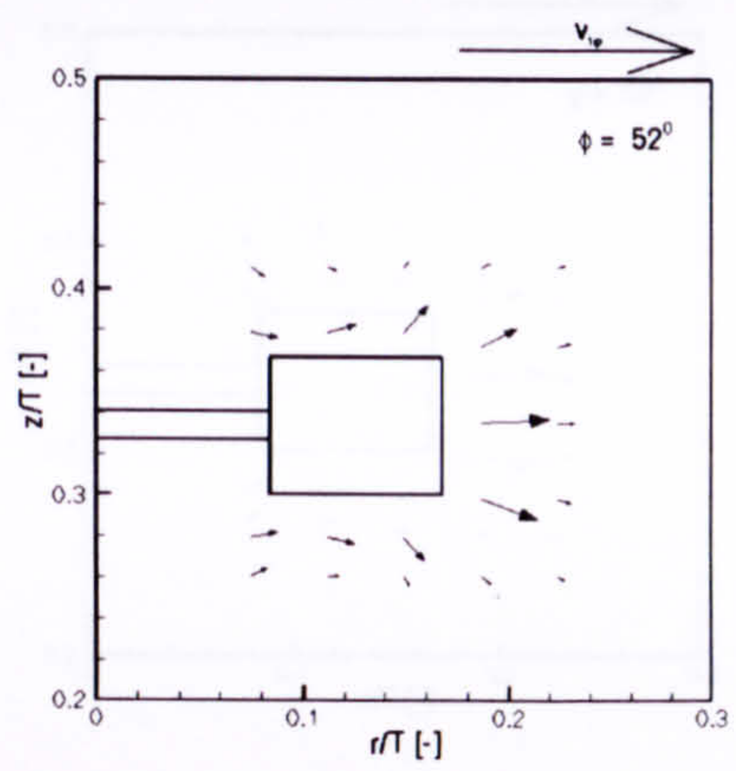

(d)

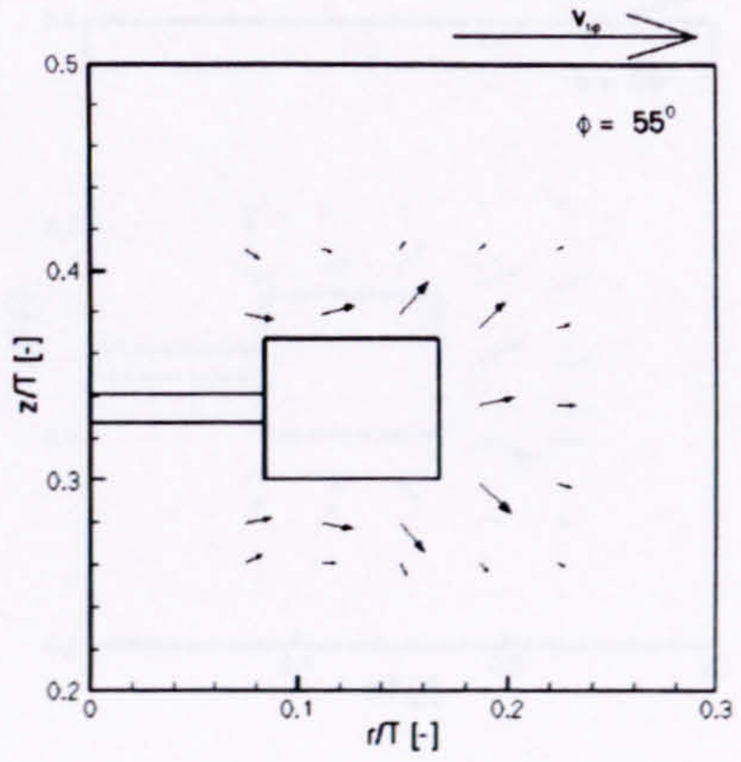

(e)

Figure 6.48: Phase-resolved velocity vectors for PIB2000 at $Re = 7$ and $De = 57.09$, in the $\theta = 0^0$ plane at $\phi = 2^0$, 27^0, 42^0, 52^0 and 55^0.

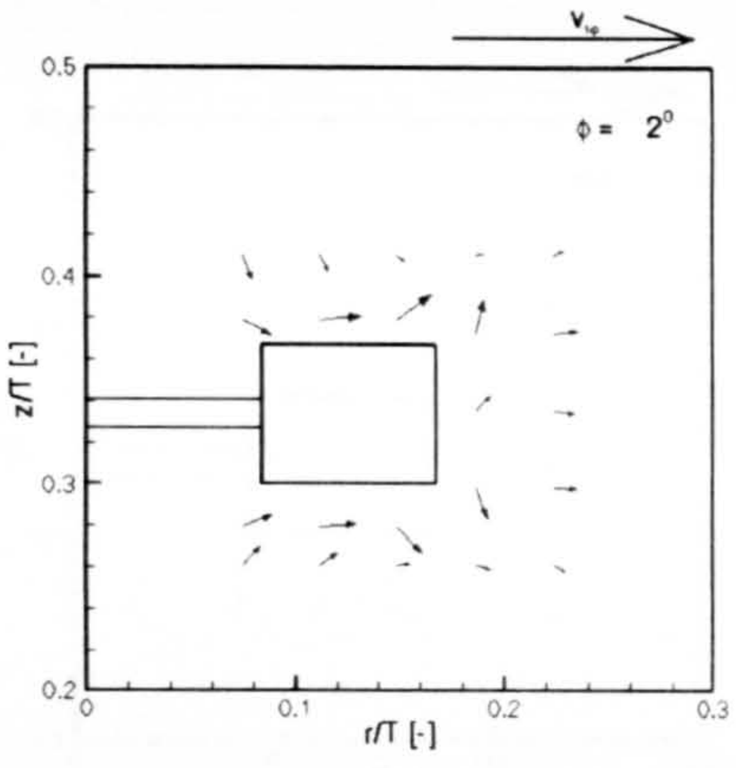

(a)

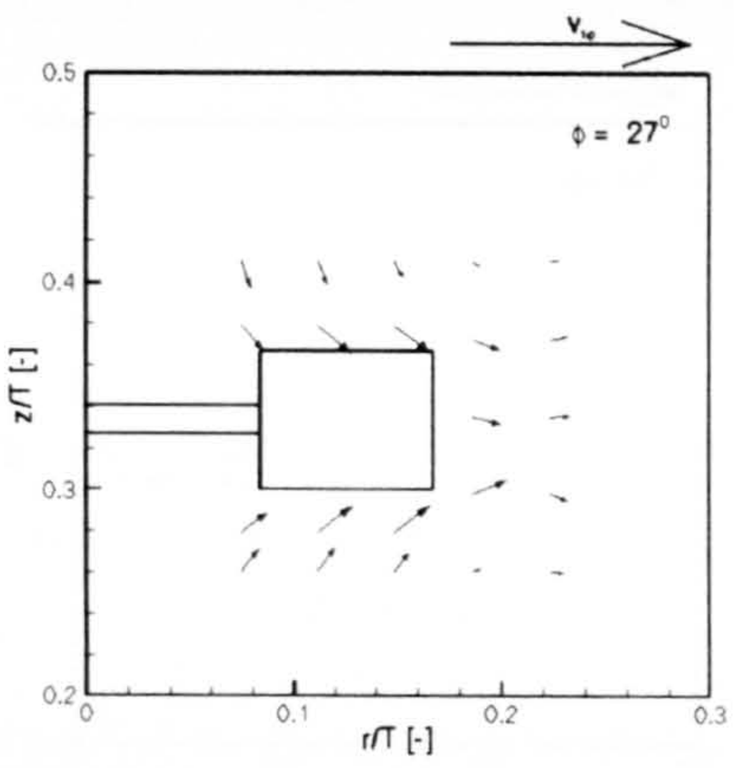

(b)

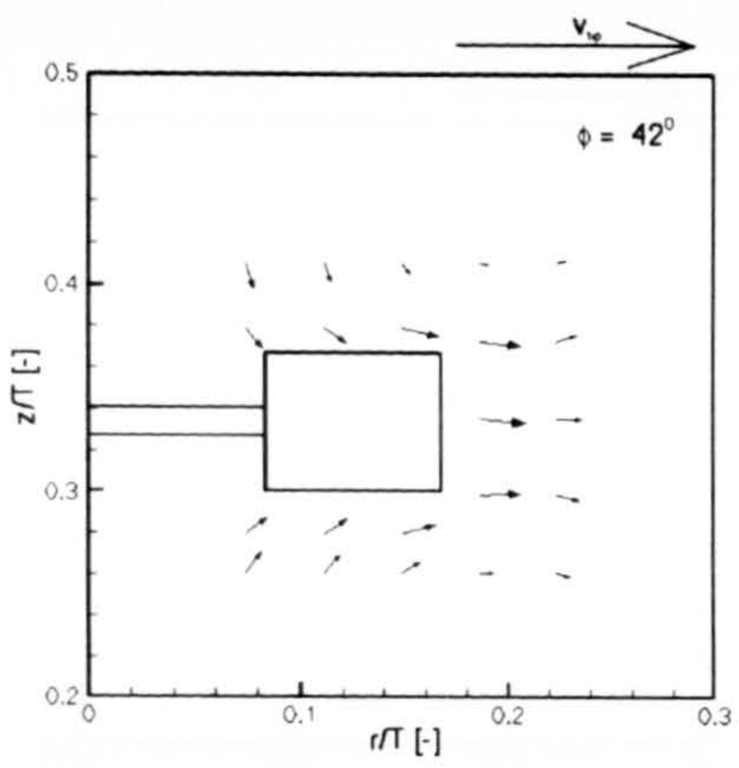

(c)

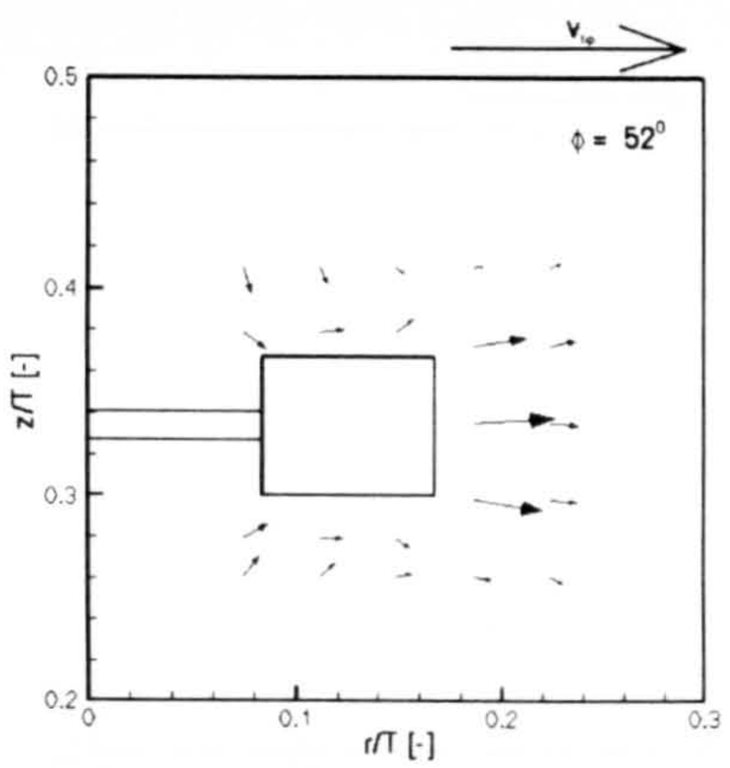

(d)

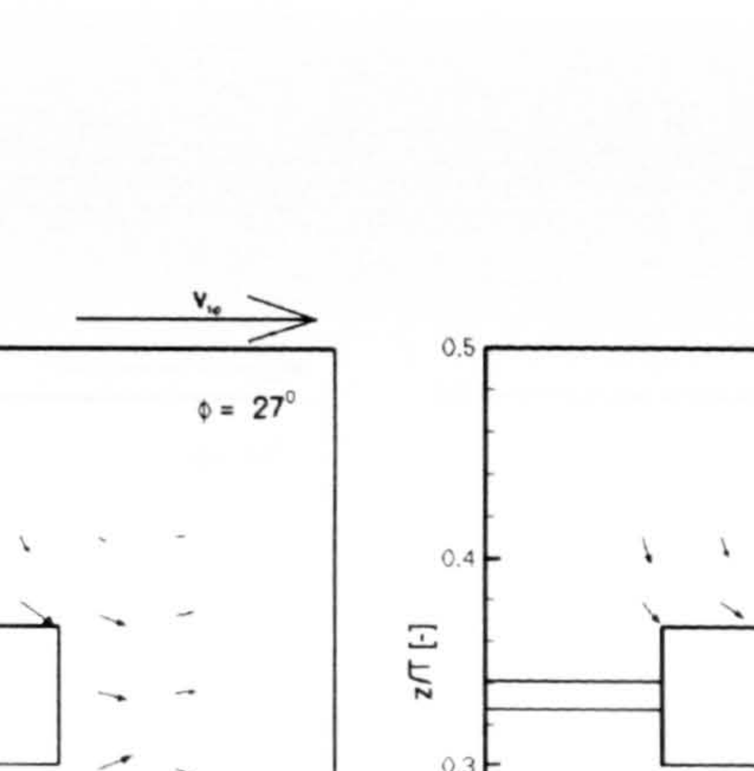

(e)

Figure 6.49: Phase-resolved velocity vectors for PIB2000 at $Re = 13$ and $De = 107.481$, in the $\theta = 0^0$ plane at $\phi = 2^0$, 27^0, 42^0, 52^0 and 55^0.

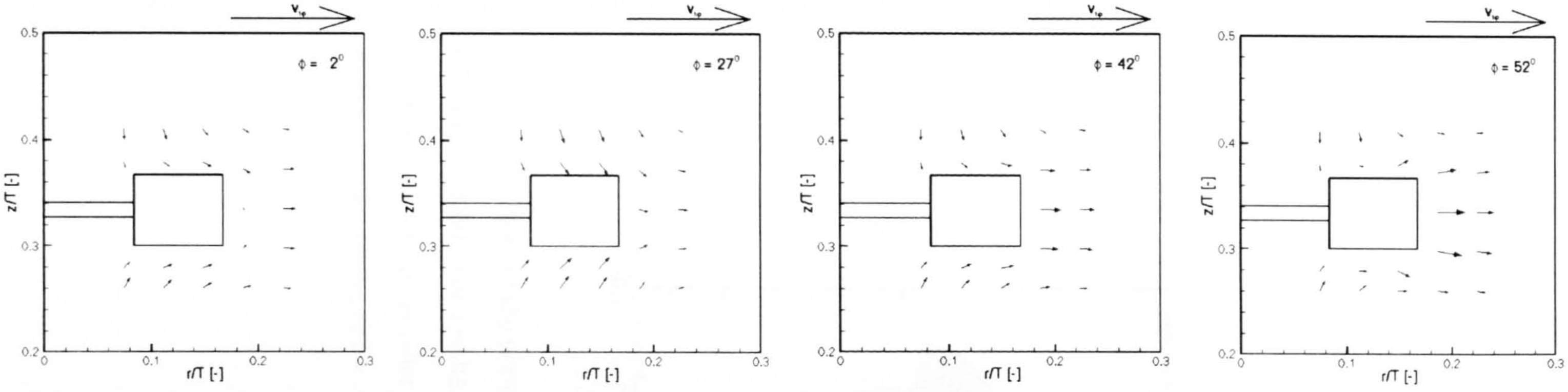

(a) (b) (c) (d)

(e)

Figure 6.50: Phase-resolved velocity vectors for Si1000 at $Re = 10$, in the $\theta = 0^0$ plane at $\phi = 2^0$, 27^0, 42^0, 52^0 and 55^0.

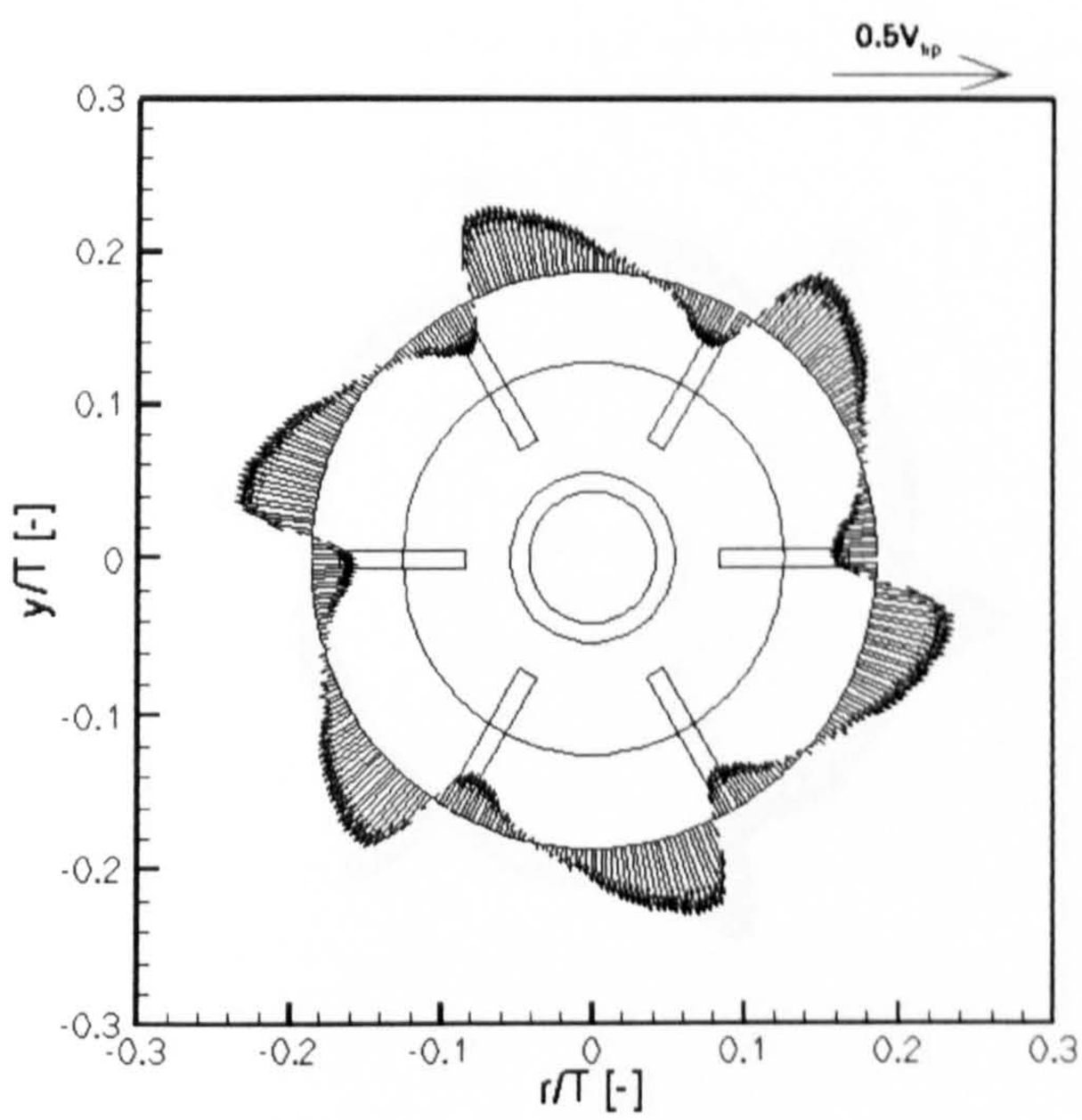

Figure 6.51: Plots of the normalised radial velocity components (U_r/V_{tip}) at $Re = 0.7$, for PIB2000. The results are taken at an axial position equal to the height of the mid-plane of the impeller blade ($z/T = 0.333$) and at a radial position closest to the impeller blade, $r/T = 0.186$.

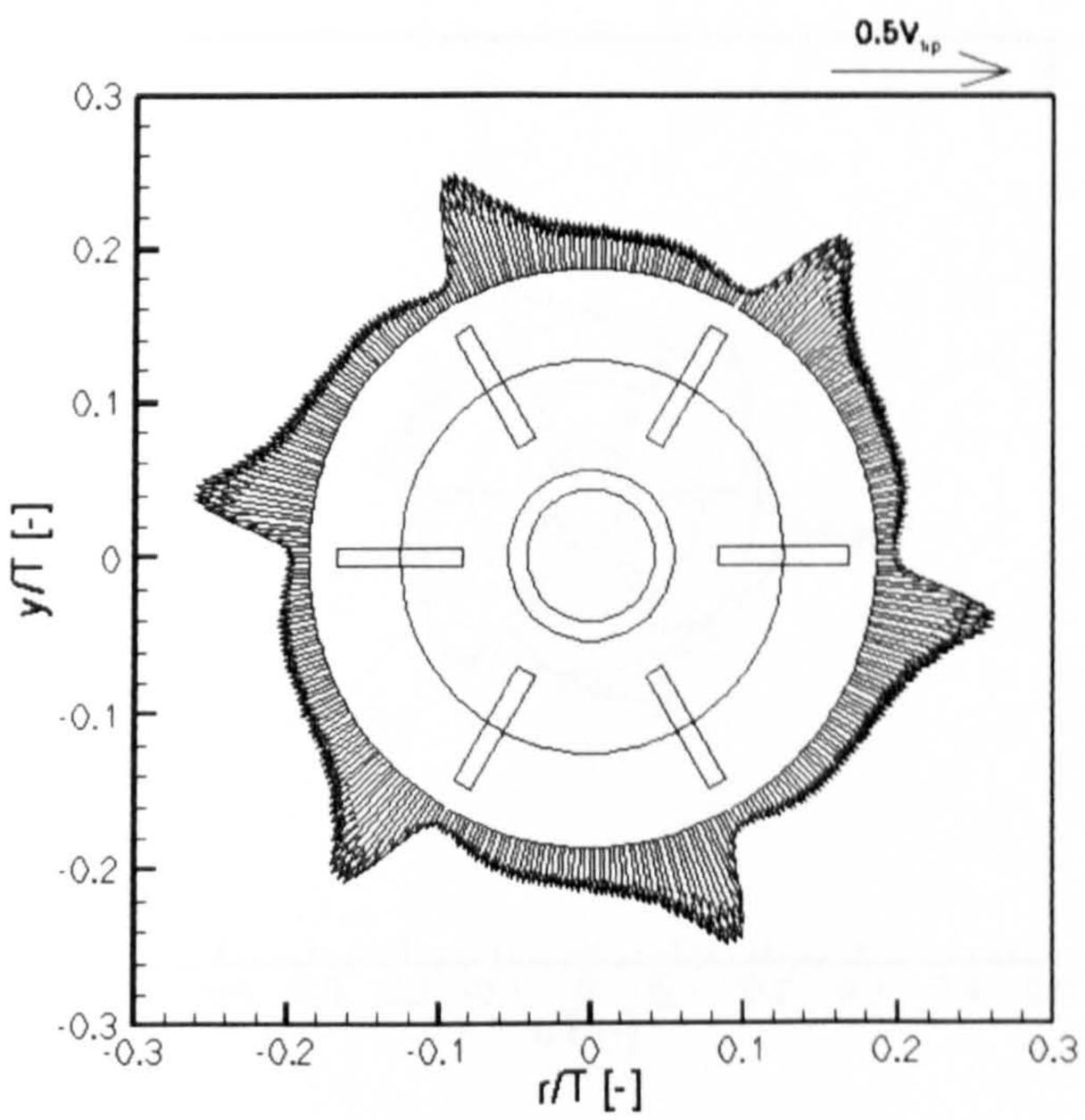

Figure 6.52: Plots of the normalised radial velocity components (U_r/V_{tip}) at $Re = 13$, for PIB2000. The results are taken at an axial position equal to the height of the mid-plane of the impeller blade ($z/T = 0.333$) and at a radial position closest to the impeller blade, $r/T = 0.186$.

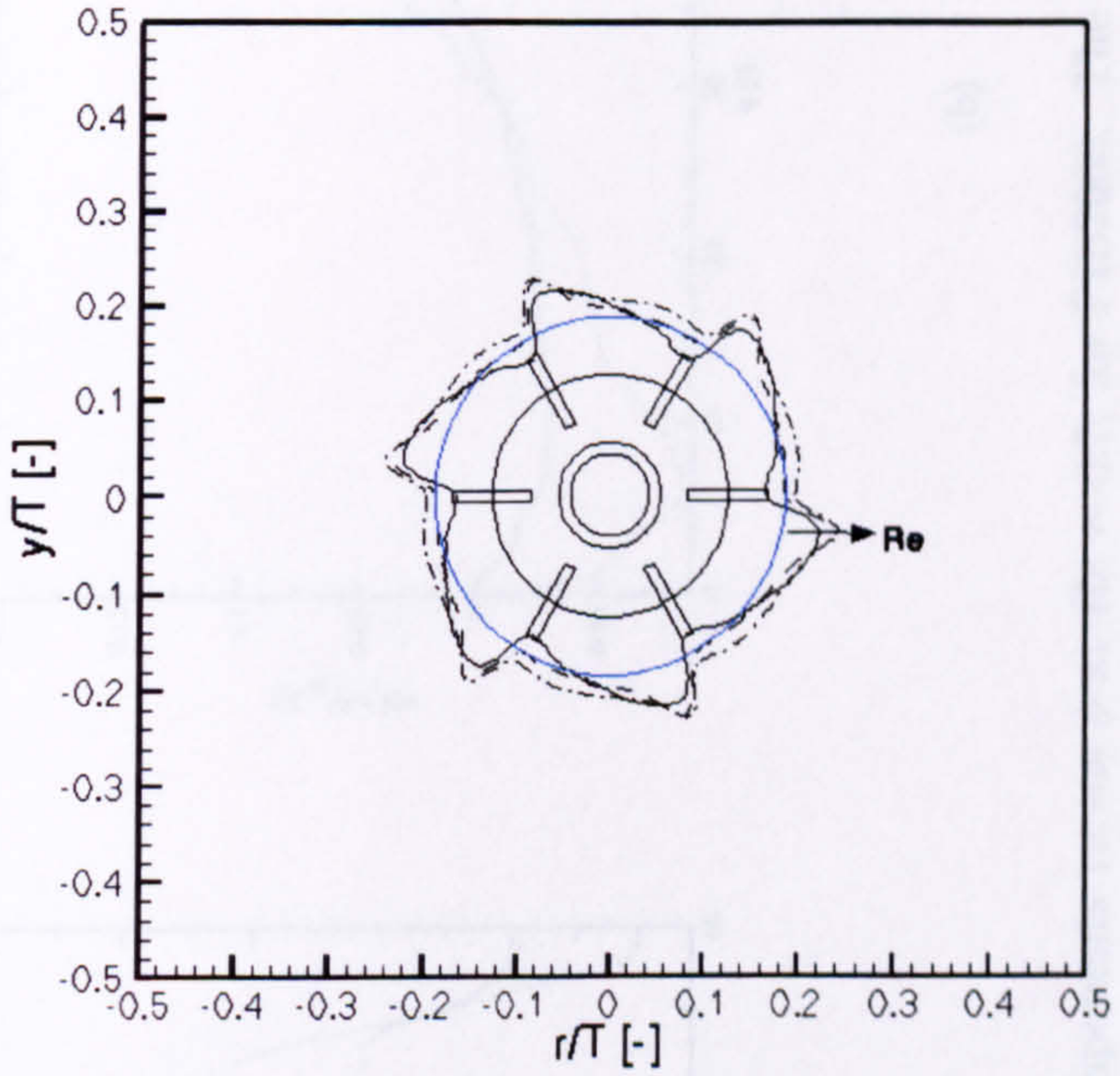

Figure 6.53: Profiles of the normalised radial velocity components (U_r/V_{tip}) at Re = 0.7, 7 and 13, increasing in the direction of the arrow shown above, for PIB2000. The results are taken at an axial position equal to the height of the mid-plane of the impeller blade ($z/T = 0.333$) and at a radial position closest to the impeller blade, $r/T = 0.186$.

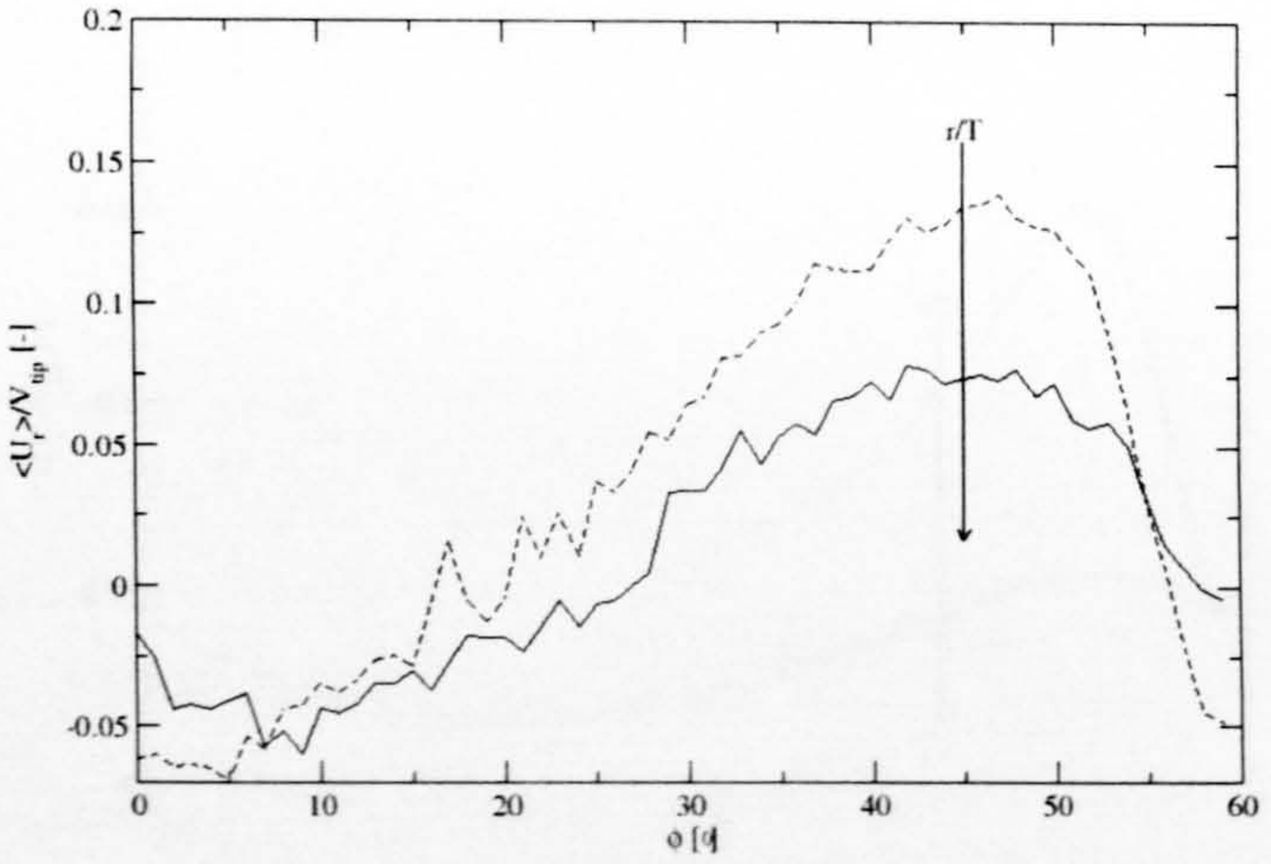

(a)

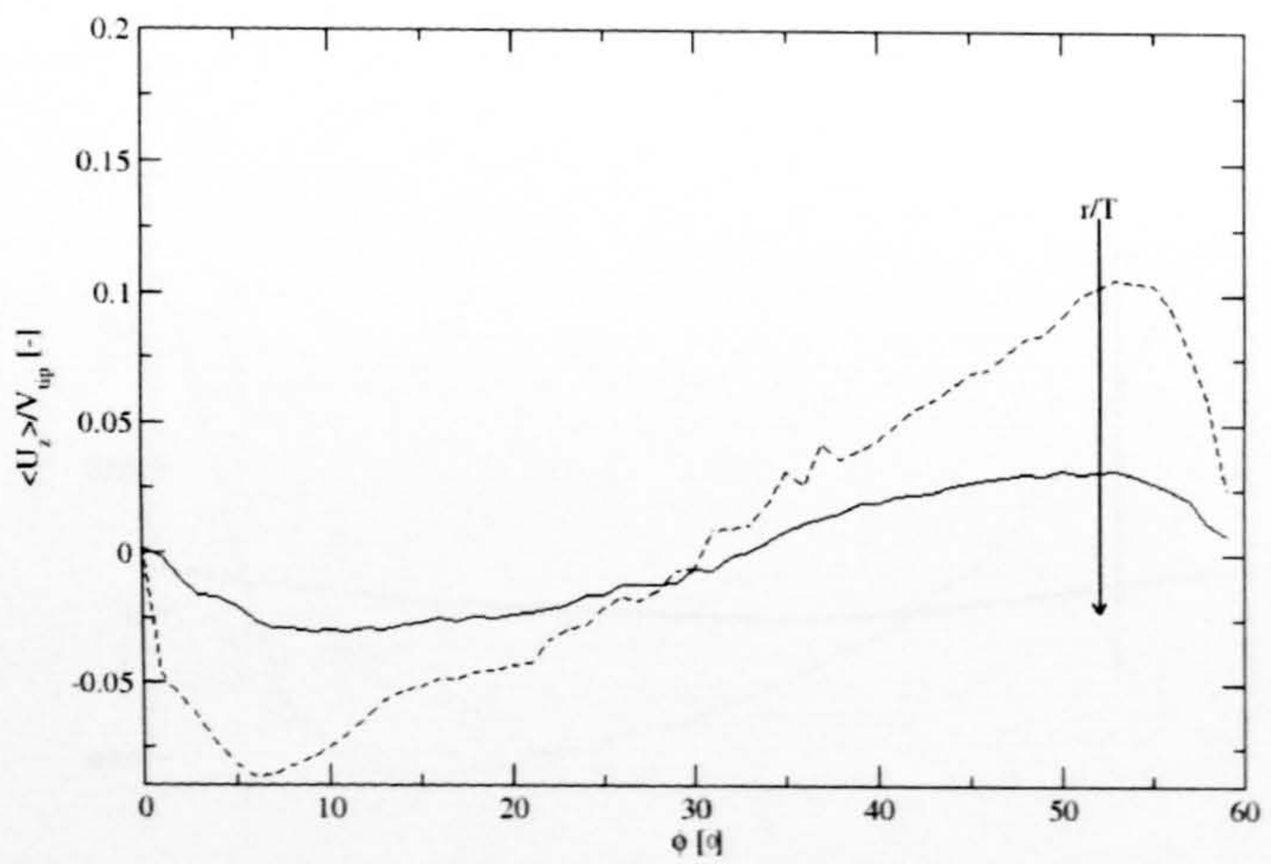

(b)

Figure 6.54: Normalised radial and axial velocity components versus ϕ at $Re = 0.7$, for PIB2000. The axial positions of the curves all correspond to the point closest to the top of the impeller blade ($z/T = 0.373$) while the radial positions correspond to $r/T = 0.186$ and 0.224, the value of which increases in the direction of the arrow.

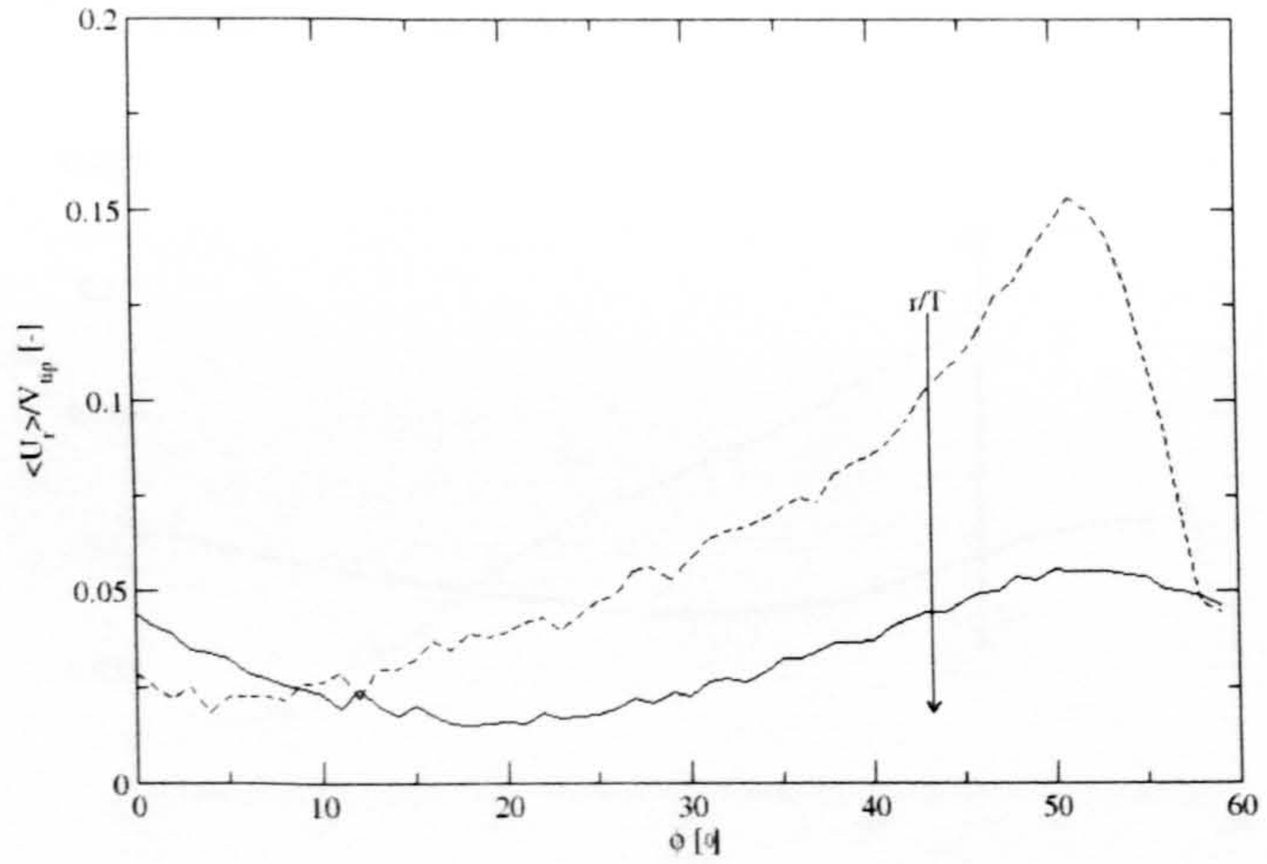

(a)

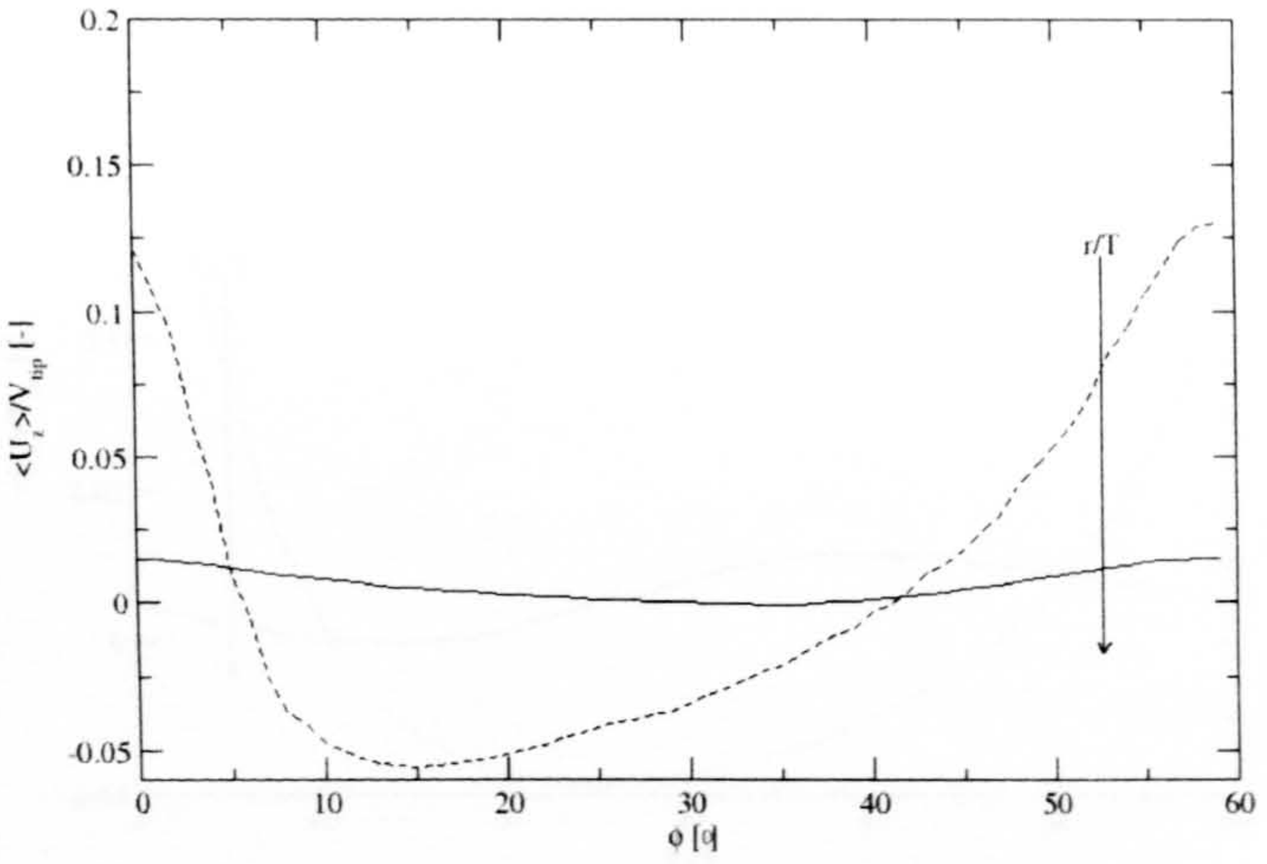

(b)

Figure 6.55: Normalised radial and axial velocity components versus ϕ at $Re = 7$, for PIB2000. The axial positions of the curves all correspond to the point closest to the top of the impeller blade ($z/T = 0.373$) while the radial positions correspond to $r/T = 0.186$ and 0.224, the value of which increases in the direction of the arrow.

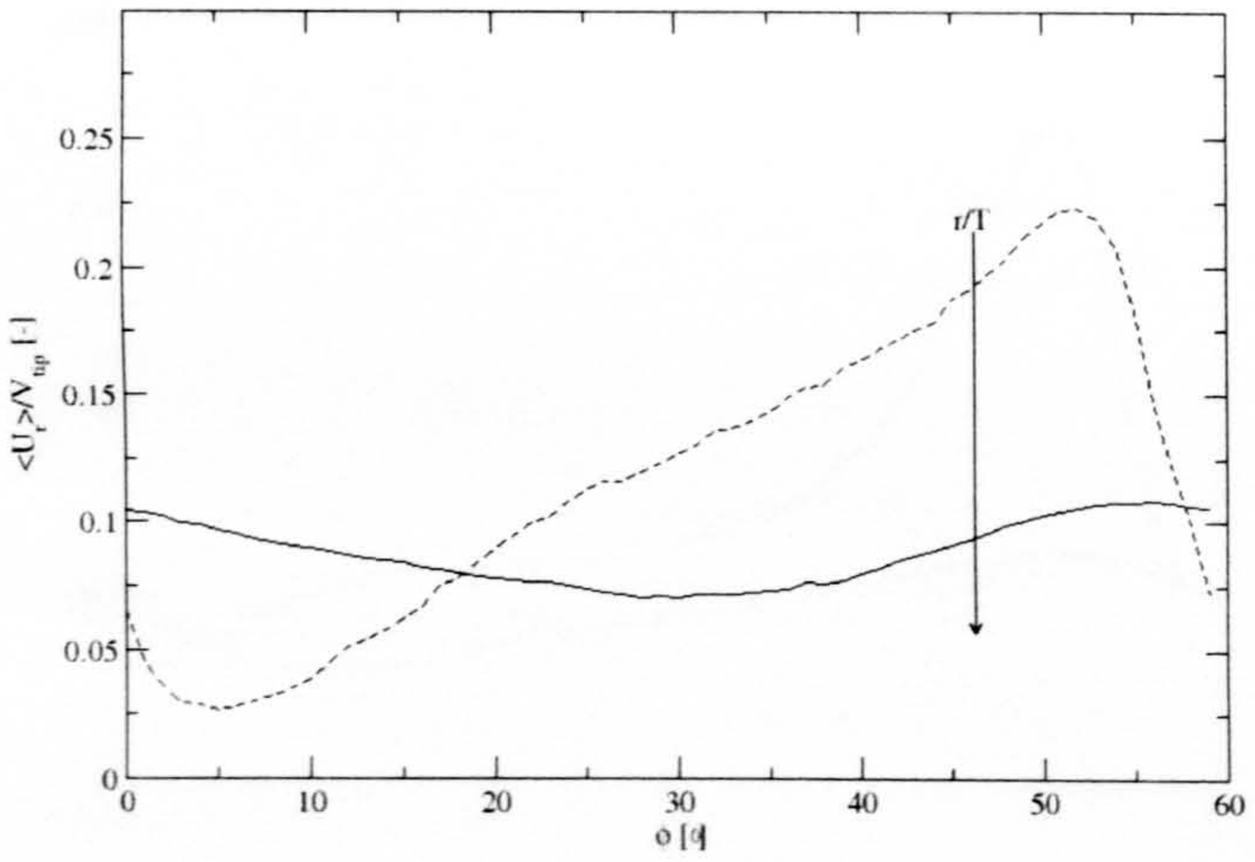

(a)

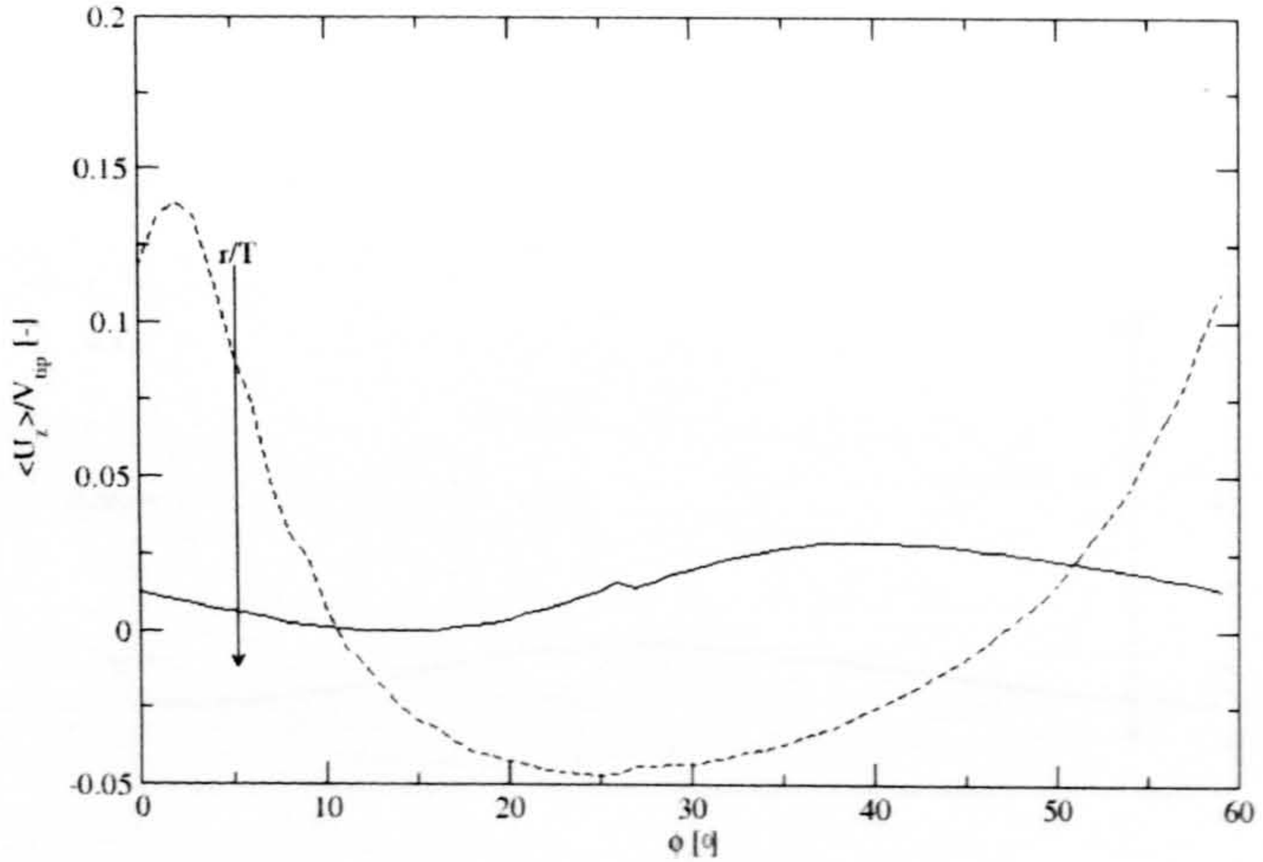

(b)

Figure 6.56: Normalised radial and axial velocity components versus ϕ at $Re = 13$, for PIB2000. The axial positions of the curves all correspond to the point closest to the top of the impeller blade ($z/T = 0.373$) while the radial positions correspond to $r/T = 0.186$ and 0.224, the value of which increases in the direction of the arrow.

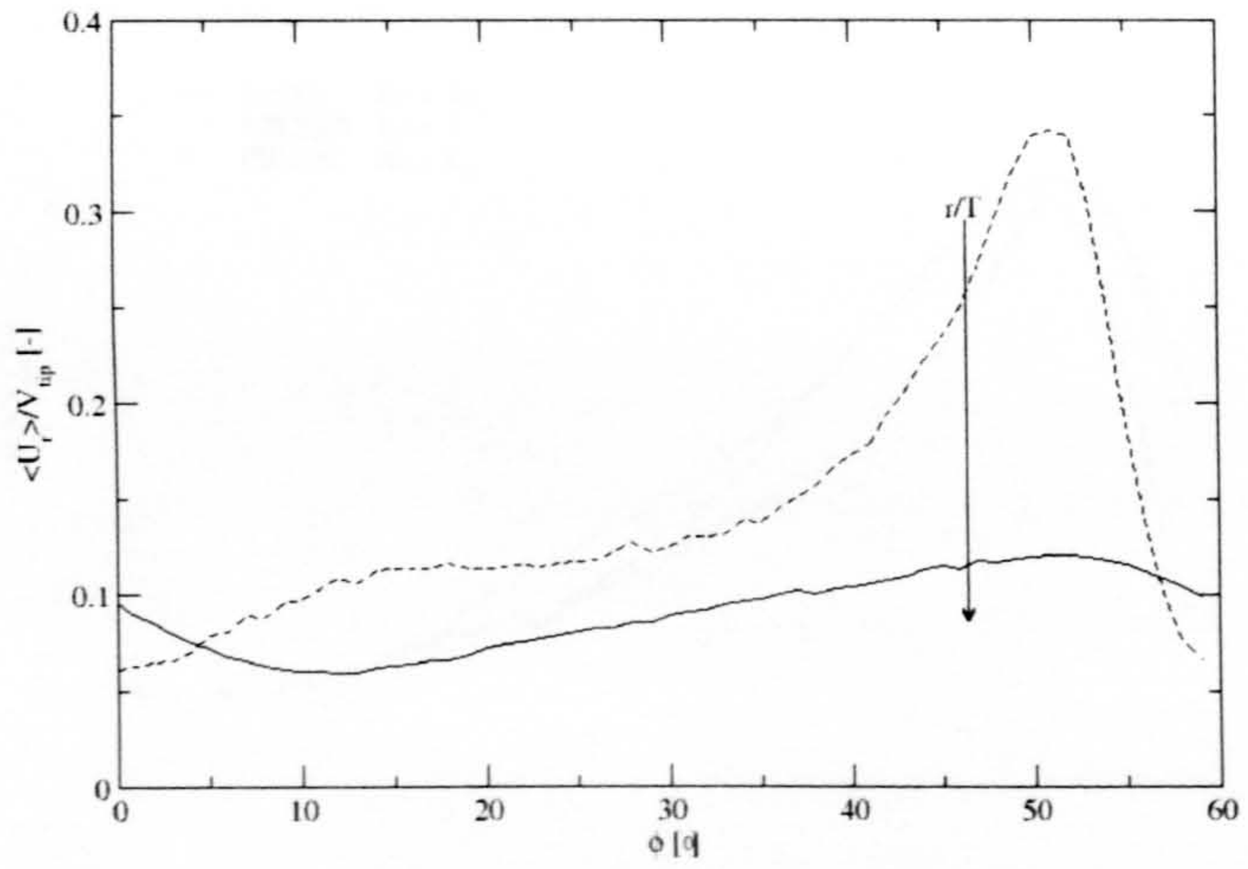

(a)

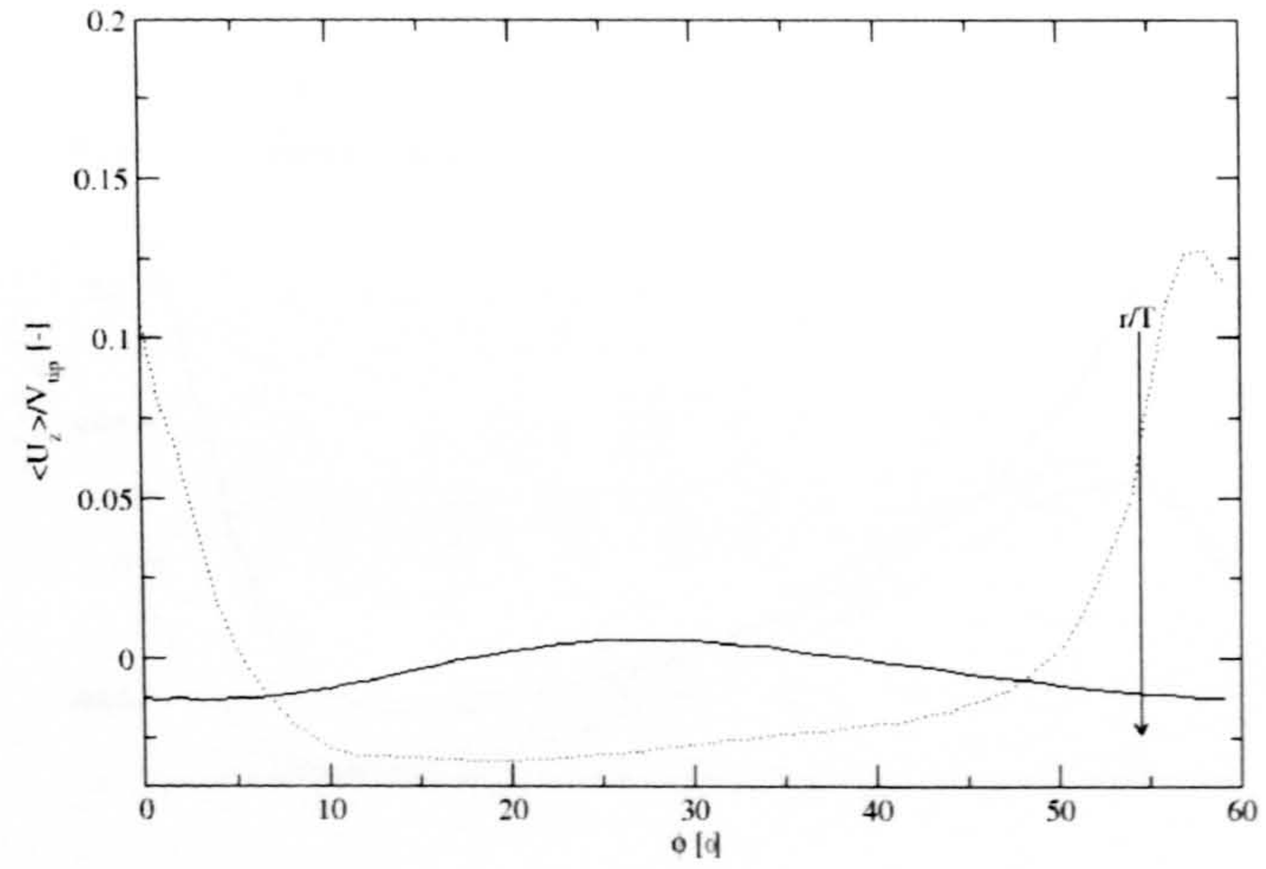

(b)

Figure 6.57: Normalised radial and axial velocity components versus ϕ at $Re = 13$, for PIB2000. The axial positions of the curves all correspond centreline of the impeller blade ($z/T = 0.333$) while the radial positions correspond to $r/T = 0.186$ and 0.224, the value of which increases in the direction of the arrow.

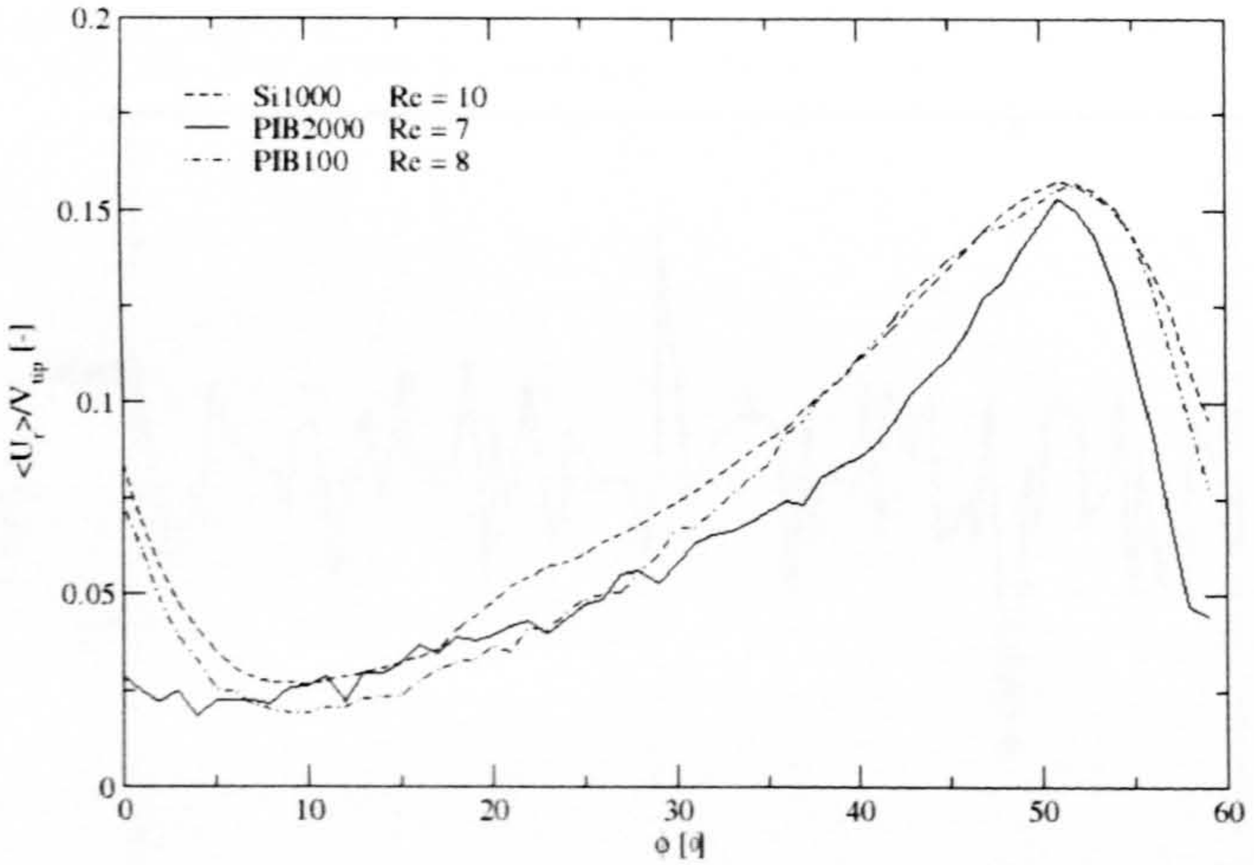

(a)

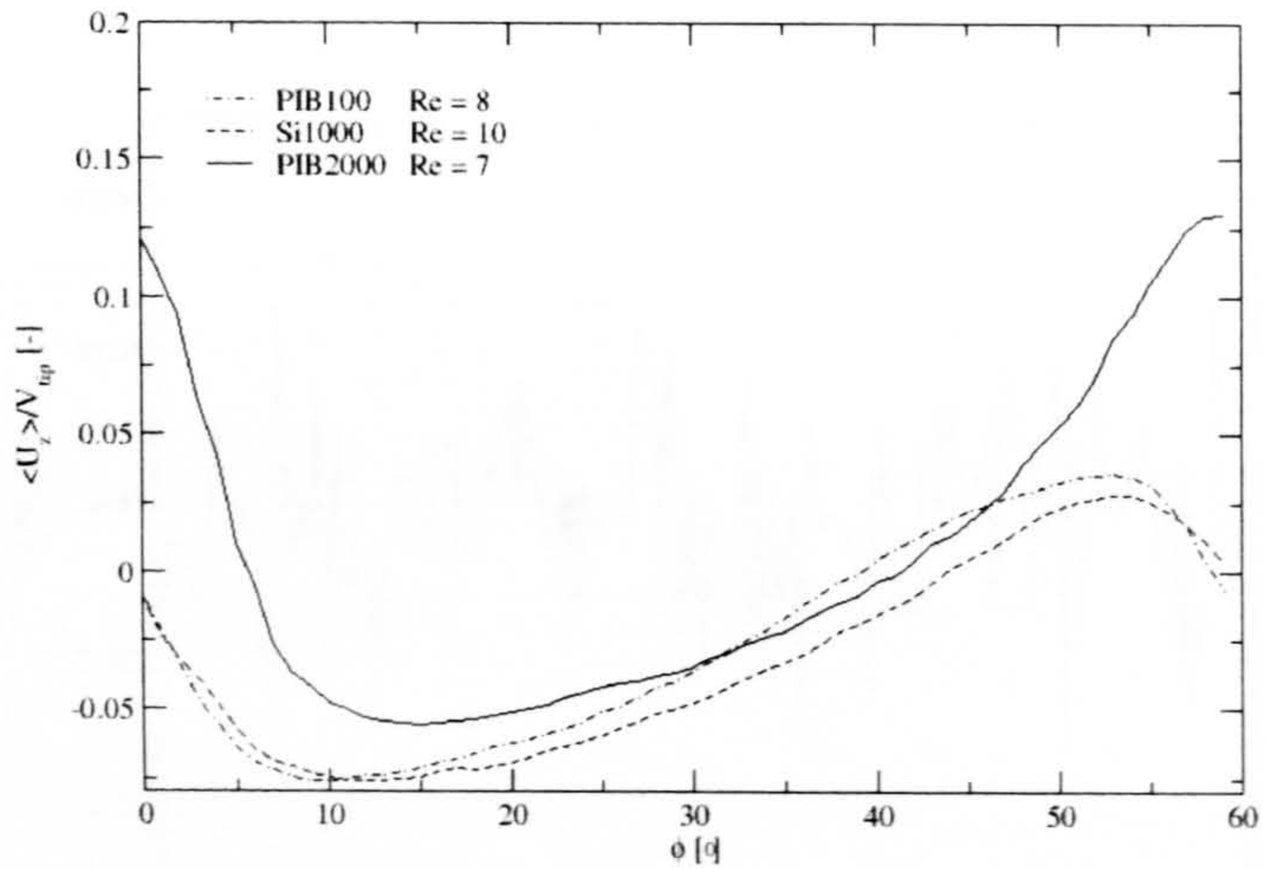

(b)

Figure 6.58: Normalised radial and axial velocity components versus ϕ for Si1000, PIB100 and PIB2000, at similar Re. The axial positions of the curves all correspond to the point closest to the top of the impeller blade ($z/T = 0.373$) while the radial position corresponds to $r/T = 0.186$.

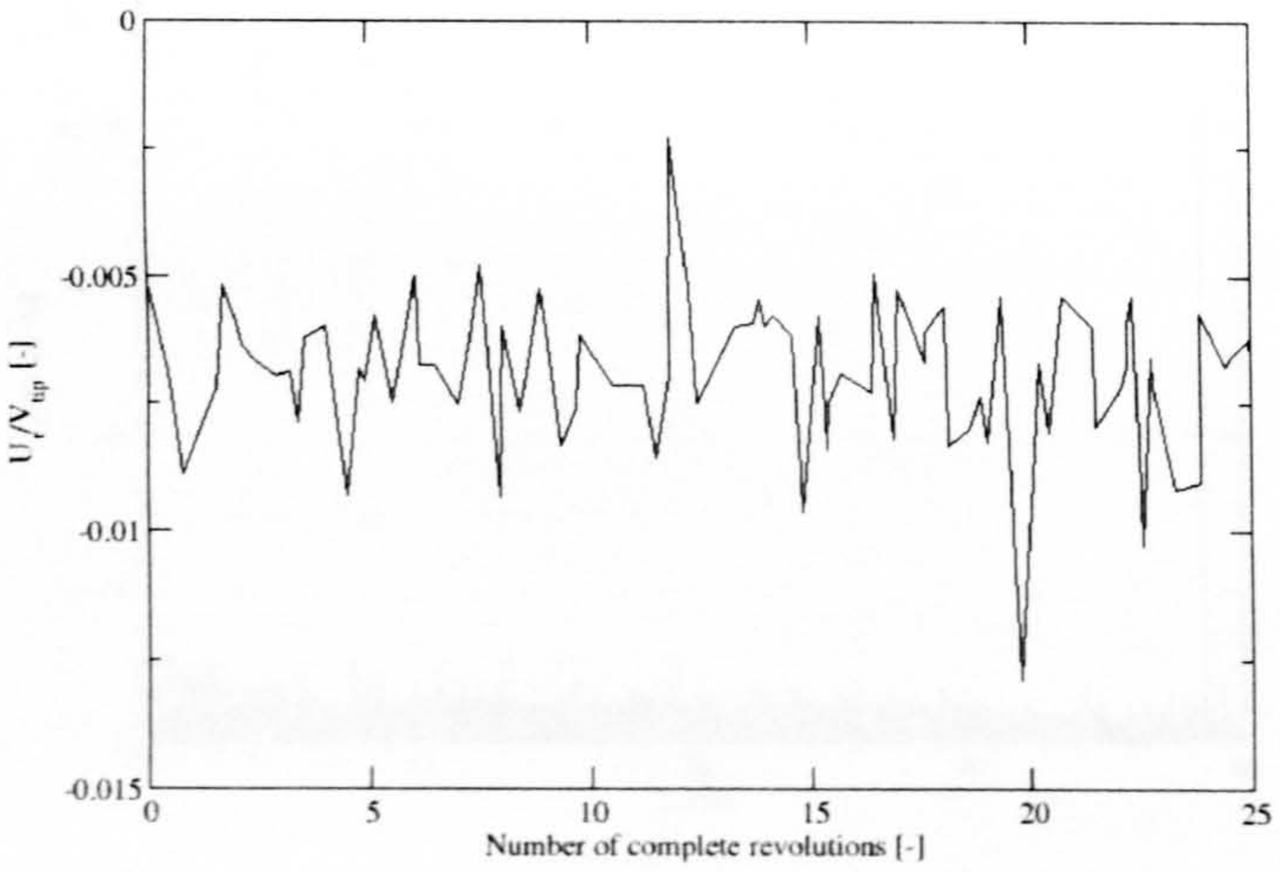

(a)

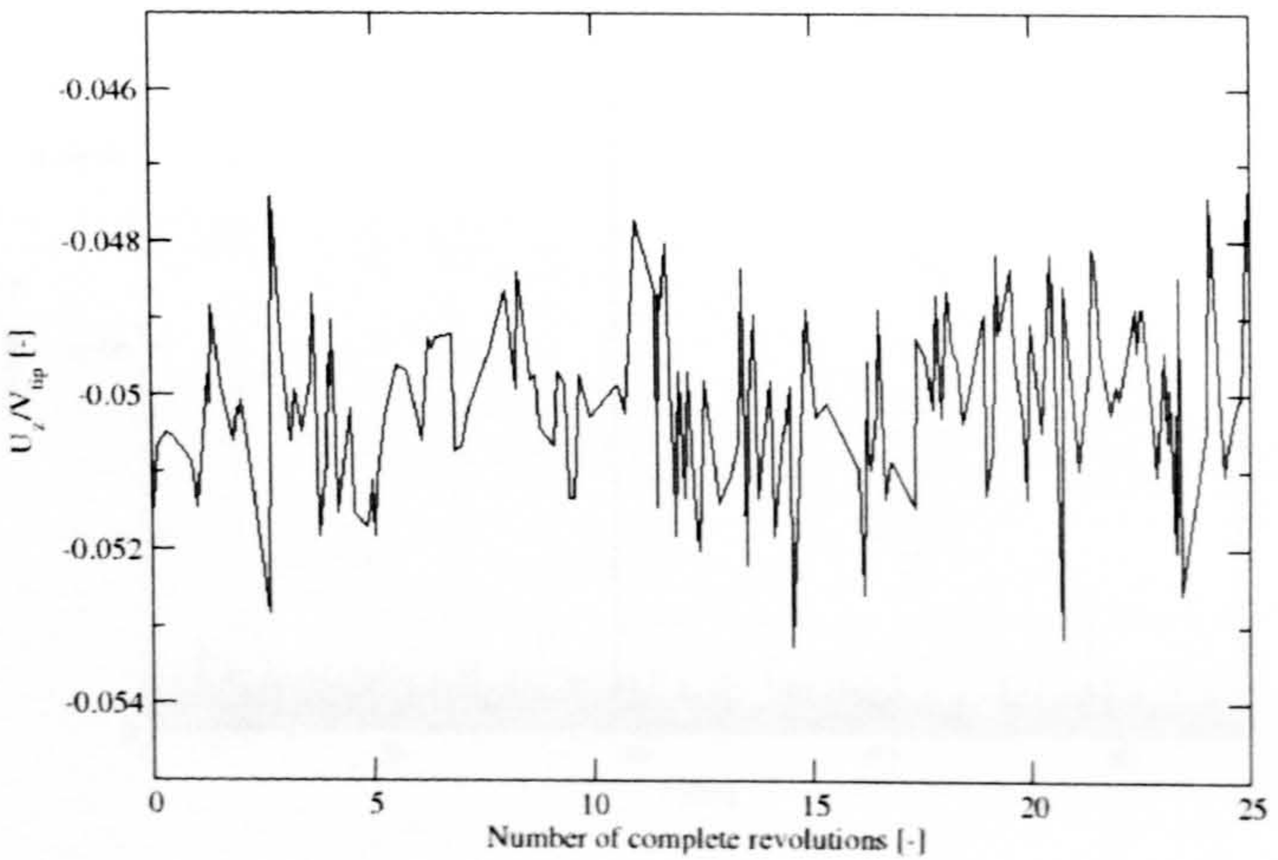

(b)

Figure 6.59: Normalised instantaneous; (a) radial velocity and; (b) axial velocity measurements, for PIB2000 at $r/T = 0.112$, $z/T = 0.522$.

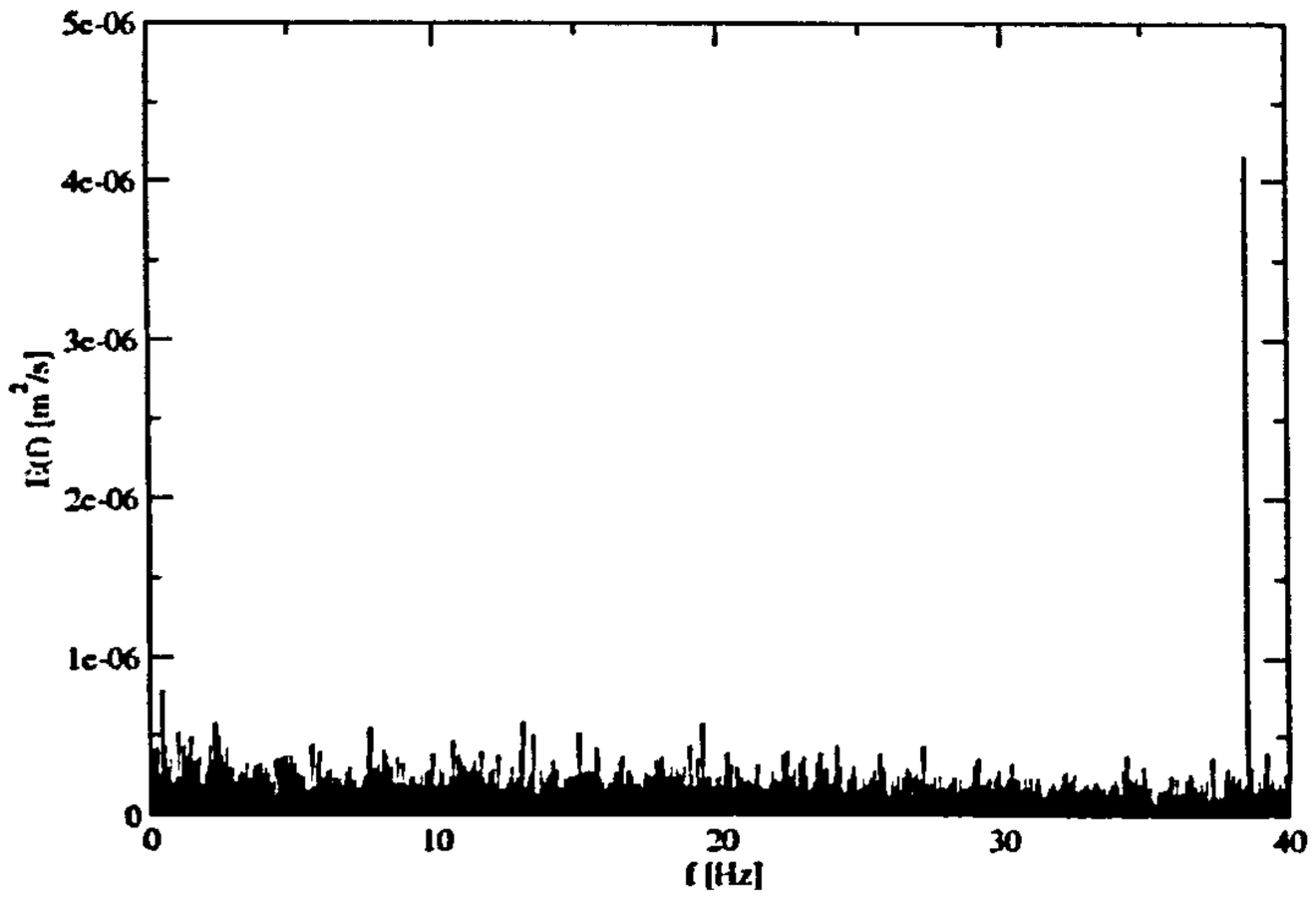

(a)

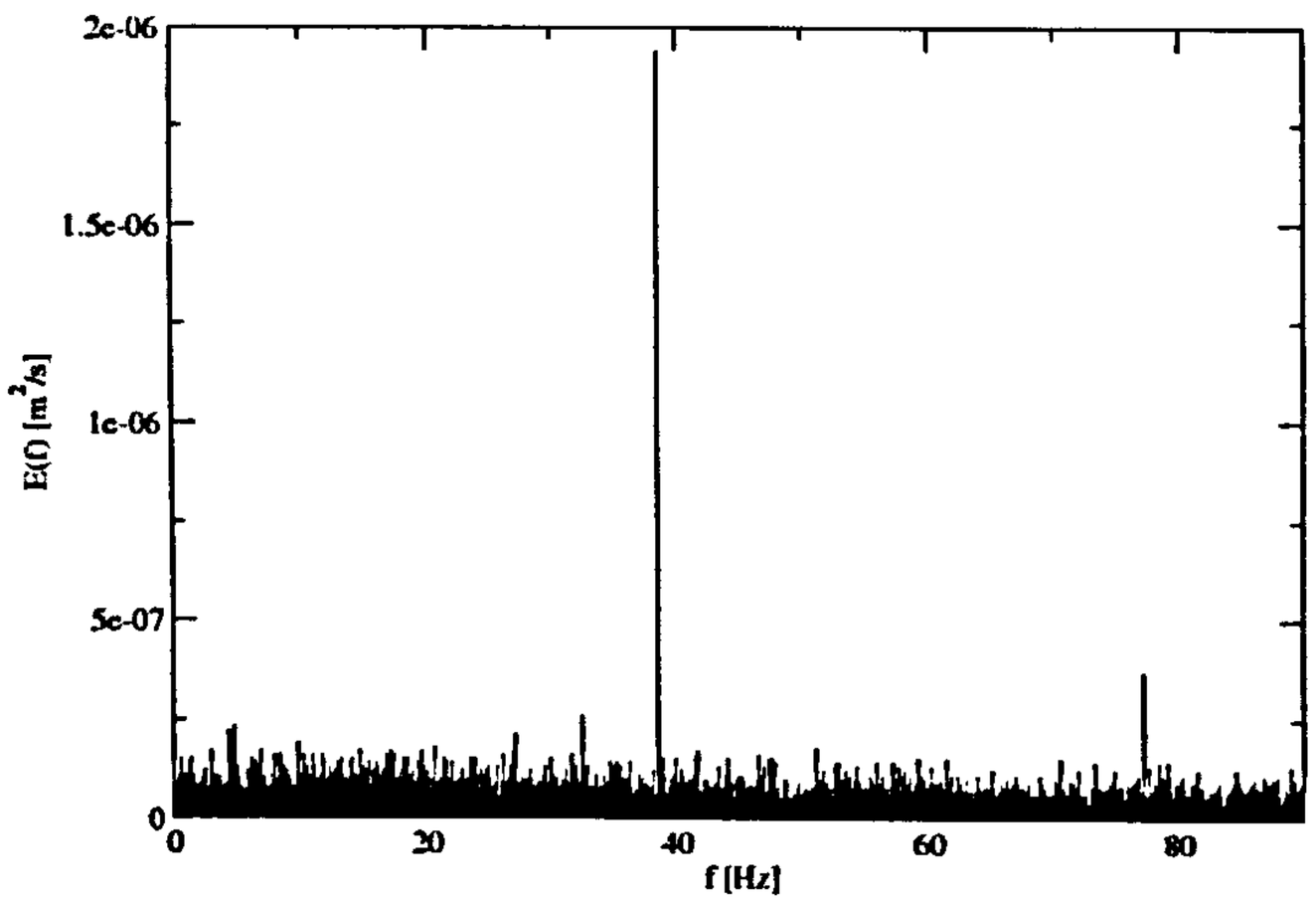

(b)

Figure 6.60: Energy spectrum of the; (a) radial velocity fluctuations and; (b) axial velocity fluctuations, for PIB2000 at $r/T = 0.112$, $z/T = 0.522$.

Chapter 7

Conclusions and recommendations for future work

This chapter is divided into three sections. In the first section, a brief account of the research carried out is given. In the second, the main findings of the thesis are outlined and in the third, areas in which further work is needed are identified.

7.1 The present contribution

The object of the research presented in this thesis was to investigate, by experimentation and simulation, the flow behaviour of Newtonian and viscoelastic fluids. Considerable effort was devoted to; (i) realising viscoelastic flow behaviour, such as shear-thinning and elastic reponse, by rheometric shear experiments, over a range of shear strain rates; (ii) obtaining the non-linear material parameters, needed by the viscoelastic constitutive models, for the CFD simulations; (iii) designing and implementing CFD simulations over a range of flow rates, and finally; (iv) obtaining measurement data by LDA experiments for a mixing vessel stirred by a Rushton turbine.

Three differential, 5 mode, non-linear constitutive viscoelastic models, namely the Giesekus and Phan-Thien and Tanner (PTT-a and PTT -b), were used to predict measurement data for $\eta(\dot{\gamma})$, $\eta^*(\omega)$, $\eta^+(t)$ and $N_1(\dot{\gamma})$ for two polyisobutylene (2.5 % and 6 % PIB) solutions, rheometrically characterised by Lee (2003) under linear oscillatory (infinitesimal strain) and steady (finite strain) shear experiments, along with values for $\eta_\epsilon(\dot{\epsilon})$ over a range of strain rates.

A considerable amount of effort was then devoted to the implementation, modification and optimisation of the viscoelastic constitutive models for the simulation of planar flows past a symmetrically confined cylinder and subscquently

for idealised blade/baffle flows, namely; (i) past an array of symmetrically confined cylinders; (ii) through a contraction flow, and; (iii) past a blade/baffle obstruction.

Laser-Doppler anemometry was chosen as the measurement technique to determine the velocity characteristics: Ensemble-averaged, phase-resolved (ensemble-averages over 1^0 of impeller shaft revolution) and time-resolved measurements of the velocity variations were obtained by LDA in a vessel of 80.5 mm diameter stirred by a Rushton impeller. From the time-resolved measurements, the energy spectra was obtained. From the ensemble-average and phase-resolved data the radial and axial mean velocity and r.m.s. velocity values were obtained.

7.2 Main findings of the investigation

From rheometric shear data, the 2.5 % and 6 % PIB solutions showed qualitative similarities by comparison: With increasing shear strain rate they both exhibited; (i) shear thinning and; (ii) an increase in first normal stress difference. For both fluids, predictions for elongational viscosity, which could not be validated due to the absence of available measurement data, showed a thinning behaviour, except in the case where the PTT -b model predicted a thickening behaviour for the 2.5 % PIB solution. Where comparisons to measurement data could be made, predictions for both PIB solutions showed excellent quantitative agreement.

Firstly, the flow behaviour of both fluids was studied for a steady planar flow past a symmetrically confined cylinder where the constitutive viscoelastic models were extensively tested. Predictions for both fluids were compared to LDA and FIB measurement data of Baaijens (1994b) and Baaijens et al. (1995) for similar fluids over a range of De. For the 2.5 % PIB solution, predictions for velocity and stresses were obtained in the range, $De \leq 5.75$. Good quantitative agreement was made with LDA and FIB measurement data in the range, $0 < Re \leq 2.315$ where slightly larger differences were observed for the predictions of shear stress and normal stress differences by comparison to the velocity values which have been accounted for by the possible causes of error given in chapter 4. The differences between predictions and measurement data for N_1, at $De = 2.9$, in a region

upstream of the cylinder have posed a small doubt in the model's capability to fully capture the larger values of N_1, as the fluid begins to show elastic responses at higher flow rates.

For the 6 % PIB solution, predictions for velocity and stress were obtained in the range, $5.61 \leq De \leq 6.53$. The predictions were compared to measurement data at the lower De and excellent qualitative agreement was shown. More specifically, predictions for velocity showed good quantitative agreement with differences within approximately 15 % of the data and as before the shear stress and normal stress difference values showed slightly larger differences, which again posed a small doubt in the model's capability to fully capture the flow behaviour. Neither of the two fluids studied here showed negative velocities or vortex regions at any point in the flow domain.

From these simulations, the numerical instabilities reported and discussed in chapter 1 became apparent and the limit in the size of De for which the predictions could be obtained was realised. Moreover, those predictions that were successfully validated gave confidence to the implementation and study of other geometries. To improve the understanding of viscoelastic flow behaviour in laminar mixing operations in stirred vessels, idealised blade/baffle geometries were subsequently studied. These being, an array of symmetrically confined cylinders, a contraction geometry and a blade/baffle obstruction. These each exhibit at least one geometric feature of a 3-dimensional mixing vessel, stirred by a Rushton impeller.

The array of cylinders represented a recurring geometry exhibiting a flow periodicity similar to that of a rotating impeller, so the inter-cylinder distance in the array was similar in size to the distance between the adjacent blades of the Rushton turbine: It was concluded that the presence of additional cylinders did not alter the flow behaviour or cause instabilities to the flow. However, instabilities were found by Verhelst and Nieuwstadt (2004) for a similar geometry and fluid, but under different flow conditions, and it was therefore concluded that the absence of flow instabilities and changes in flow pattern, in this study, be explained by; (i) the inter-cylinder spacing being larger than the critical one, and; (ii) the flow rate being smaller than that which is required to cause them,

and not, therefore, by the models failure to do so.

Subsequently, the contraction flow geometry provided a different geometric configuration by comparison to the cylinder flows, i.e. the geometry did not exhibit curved surfaces but instead the flow was obstructed by a vertical wall, a sharp corner and abruptly contracted in a narrow channel. Predictions for velocity and normal stress difference values were obtained for both fluids along the centreline of the geometry and those of the 2.5 % PIB solution, at $De = 1.39$, were successfully validated against measurement data of Quinzani et al. (1995). The predictions for both fluids were qualitatively similar but for a decrease of approximately 50 % in values for N_1, shown by 6 % PIB as the De decreased. This was not shown by the 2.5 % PIB solution. This was not proven to be incorrect as comparisons could not be made with data. However, the anomaly suggested that the models failed to fully capture the fluid behaviour at $De = 4.27$. Despite this, the predictions revealed interesting flow behaviour: At the entrance to the contraction channel steep changes in velocity values were accompanied, almost simultaneously, by a rise in normal stress difference values and this was suspected to be caused by the stretching of the polymer chains. Subsequently, on cessation of fluid acceleration (namely, in either channel where a constant velocity is observed), the polymer chains relaxed and the normal stress difference values decreased to zero.

In the third part of the numerical work, the blade/baffle geometry was used to model a single blade of a Rushton impeller. Predictions for both PIB fluids were obtained within the range of De previously studied and validated. This therefore gave confidence to the results presented here. Quantitative and qualitative similarities are shown by comparison of both fluids: Maximum values for stress were observed in a region adjacent to the tip of the blade where values of velocity increased most rapidly from zero. Maximum values for velocity were observed in a region approximately half way between the tip of the blade and the wall of the flow domain, in a direction perpendicular to the tip. At the highest De ($De = 2.34$) locally high, absolute, values of stress were observed in the vicinity of the blade, that stem from the tip. It was also interesting to observe the decrease in predictions for stress as De increased, in the region adjacent to the tip of the

blade and this is explained in chapter 5.

All the CFD predictions obtained in this thesis are unique in that; (i) to the best knowlege of the author no predictions have been published for fluids identical to the ones studied herein; (ii) for the 2.5 % and 6 % PIB solutions or for any similar fluids, no published work has reported a *De* as high as those of this thesis, using the finite volume method with a structured grid and, finally; (iii) it has rigorously exposed the limitations of these viscoelastic models in characterising the flow behaviour of such fluids at high deformation rates, enabling a more realistic progression towards other complex geometries and finally towards their use in an industrial application such as mixing. Additionally, a Newtonian fluid with a viscosity 1000 times that of water and equal to the zero-shear viscosity of the 2.5 % PIB solution showed a region of recirculation developing and growing in size behind the blade/baffle in the range, $0 \leq Re < 56$.

Finally, experimental work was carried out whereby detailed LDA measurements were obtained to provide an extensive quantification of the flow fields around the Rushton impeller, for five different fluids. Three fluids were Newtonian, each with different viscosity: water, Si100 and Si1000, and the remaining two were non-Newtonian, viscoelastic fluids: PIB100 and PIB2000, each of a different zero-shear viscosity but both showing the same rheometric properties, namely; (i) shear thinning and; (ii) a rise in normal stress differences. By investigation, a number very interesting flow features emerged for each fluid. For water, as the *Re* decreased in the range, $4253 \geq Re \geq 61$ the mixing flow pattern changed from one similar to those encountered in turbulent flow to a sigmoid pattern and the r.m.s. levels decreased. In the range $Re \leq 50$ (using the Si100 and Si1000 Newtonian solutions), a change in flow pattern was revealed as *Re* tended to zero: The mean velocity vectors changed from being predominately radial at the impeller blade tip to discharging in a direction towards the bottom of the vessel. There was evidence of a similar sigmoid flow pattern but the extent of this was greater and the velocities, smaller in magnitude, which indicated that the flow patterns were not scaling directly with *Re* and/or *N*. Furthermore, the decrease in *Re* was not accompanied by a reduction in r.m.s. levels as observed for water. Conversely, an increase was shown, which was explained by the chang-

ing in flow discharge direction, both radially and axially as observed from the phase-resolved data for the Si1000 solution. Additionally, the location and size of the re-circulation regions were also investigated and they were shown to move further from the impeller blade tip and increase in size, with an increase in Re.

For the PIB100 and PIB2000 solutions, measurement data was acquired in the range, $1 \leq Re \leq 240$ and $0.7 \leq Re \leq 13$, respectively. The ensemble-averaged measurement data for both fluids showed a flow behaviour that predominantly discharged radially from the impeller tip over both ranges and did not show a discharge towards the base of the vessel at an angle as great as that observed for water, at $Re \approx 50$. However, the flow discharge pattern for these fluids is comparable to that of the Si100 and Si1000 solutions and, with the aim to uncover viscoelastic characteristics of the PIB solutions, a comprehensive study of the flow discharge behaviour was conducted. This involved studying the mean radial and axial velocities, both ensemble-average and phase-resolved, in the vicinity of the blade, along with the r.m.s. levels, flow numbers, circulation flow numbers and Deborah numbers. The following observations were made: The circulation flow number (Fl_c) includes the flow entrained in to the impeller stream and for this reason it is expected to be larger than Fl. However, for PIB100, Fl_c drops in value at $Re = 80$, where, $Fl_c \approx Fl$. A possible reason for this, in the absence of a change in the discharge flow direction for PIB100, is that the pumping capacity of the impeller at this value is consumed by the onset of elastic forces in the fluid, although this was not conclusive; (iii) the centreline radial mean velocities and r.m.s. values showed similar trends for both the Newtonian and non-Newtonian fluids at similar Re and both showed a decrease with increasing r/T, and finally; (iv) the De plots provide an indication of the degree to which the elastic forces in the fluids could be affecting the flow discharge behaviour.

To investigate further, ensemble-averaged velocity measurement data was used to calculate the distribution of shear strain rates in the vicinity of the impeller. For the highest Re, the values shown for the PIB100 solution were well below the range at which shear thinning becomes apparent in the rheometric data, consequently, a shear-thinning and/or viscoelastic behaviour in the mixing vessel, was not evident. Conversely, the ensemble-averaged shear strain rates, for

the PIB2000 solution reached values corresponding to those at which the viscosity was approximately 50 % of the zero-shear value in the rheometric data. Moreover, phase-resolved shear strain rates for this fluid showed an even higher variation of the order of 65 %. Vector and shear strain rate plots for these data revealed noticeable viscoelastic behaviour: As the impeller blade rotated, the fluid discharged radially from the tip, however, in the regions directly in front of and behind the blade, on the pressure and suction side, respectively, the shear strain rates became high enough to induce severe non-linear behaviour. The outcome of such behaviour caused the flow to discharge axially from the tip (perpendicular to the centreline of the impeller stream) which subsequently resisted the propagation of fluid motion in the radial direction. Also, the velocity vectors increased in magnitude in this direction. It must be remembered that the behavioural characteristics of such fluids, and their causes, are very complex (as this thesis has proven) and for this reason are not summarised here but were given in chapter 6.

Finally, the importance of chaotic mixing is discussed and quantified by the use of the time-resolved velocity measurement data for the radial and axial components. Chaotic behaviour was only observed for the PIB2000 solution where at certain points in the vicinity of the impeller blade the data acquisition rate was high enough to calculate the energy spectrum. The results showed the fluid flow periodically fluctuating at a frequency equal to that of the impeller shaft. This behaviour was not only evidence of chaotic motion in the mixing vessel but this exact behaviour, with an almost identical frequency, was found by Alvarez et al. (2002), who studied a similar, viscoelastic, shear thinning fluid.

7.3 Recommendations for future work

The numerical work presented in this thesis has shown that the accurate prediction of non-Newtonian flows even for relatively simple flow configurations involves computational time and storage requirements that place modelling of the full stirred tank geometry with such methods beyond the computational power currently available. The advent of parallel super-computers and the exponential increase in computational power achieved in recent years should however make

such calculations possible in the near future and such studies should be attempted.

A more important drawback of the modelling effort, however, is the instability of the numerical methodology which limits modelling at present, even with the state-of-the-art methodology employed here, to modest Deborah numbers. Developments in numerical methodology are therefore urgently needed if the empiricism involved in the present CFD models, most of which treat the non-Newtonian aspects of the fluids in a relatively crude and often phenomenological manner, is to be removed and replaced by a rigorous approach such as the present one.

The present work helped highlight some of the complexities of laminar non-Newtonian flow behaviour in stirred vessels, but clearly the topic is immense in breadth as well as in complexity in view of the non-linear behaviour of such fluids and further study is needed to provide more comprehensive insight into the related flow processes. The range of properties exhibited by such fluids necessitates that other fluids are also investigated in a similar manner: for example, thixotropic or rheopectic fluids, or those that exhibit shear strain rate dependent thickening behaviour.

Similarly, the selection of the Rushton impeller for study in this work was made solely in view of the extensive prior knowledge of its performance in turbulent flow conditions. In practice, however, Intermig, anchor and other impellers designed for viscous fluid mixing are employed and it would be instructive to conduct similar studies with such impellers and compare the results with those already obtained by, for example, Alvarez et al. (2002) for CMC solutions. Use of PIV systems for such purposes would facilitate measurements to be made simultaneously across a plane in the flow and would therefore make data acquisition less laborious than with LDA.

It would also be instructive to investigate, in more detail, the chaotic fluid motion that has already been detected for the PIB2000 solution in the present study. For example, it would be useful to examine fluids with increased viscoelasticity and employ flow visualisation and dye insertion techniques to establish under what flow conditions and for which fluid parameters chaos is triggered in laminar mixing of non-Newtonian fluids. It would also be insightful to use an impeller blade motor that is capable of running at higher levels of torque as it would then

be possible to generate the higher shear strain rate values for the fluids of higher viscosity/viscoelasticity.

Appendix A

Photos of experimental configurations

A.1 Introduction

This appendix shows 3 photos, in .jpg format, of the apparatus used for the experimental research of this thesis. The photos are on the CD at the back of this thesis. They show; (1) a view of the vessel, the motor (mounted on top) and laser beams; (2) a side view of the vessel, motor, work bench, 3D-traverse and laser probe, and; (3) a close-up view of the vessel with the impeller in motion.

Appendix B

Stirred vessel movies

B.1 Introduction

This appendix shows 8 movies of the fluids in a mixing vessel, stirred by a Rushton turbine impeller. All are in '.avi' file format and on the CD attached to the back of the thesis. Each movie shows phase-resolved LDA velocity measurement data taken in the $\theta = 0^0$ plane, over 360^0 of impeller revolution, where the data are arranged in 1^0 averages. The mixing flow pattern has been shown to reproduce itself after every 60^0 of impeller revolution and it is for this reason that each movie is a concatenation of images at 1^0 from $\phi = 0^0$ to 59^0. The fluids presented here are: (i) Si1000; (ii) PIB100 and; (iii) PIB2000, each at a *Re* of: (i) 1, 10 and 28; (ii) 1 and 8 and; (iii) 0.7, 7 and 13, respectively. At certain *Re* movies show a close-up view of the impeller blade, instead of the whole vessel, which allows the viewer to observe more clearly areas of high deformation. All movies are referenced from chapter 6, where, a full description of the mixing vessel, the fluids and the measurement technique can be found, along with a full discussion of results and conclusions. Each '.avi' file is labelled with the fluid name and *Re*.

Appendix C

Additional stirred vessel results

C.1 Introduction

With the use of ensemble-averaged and phase-resolved LDA velocity measurement data this appendix shows shear strain rate distribution plots, vector plots and profiles for the Si100, Si1000, PIB100 and PIB2000 solutions in a mixing vessel stirred by a Rushton turbine impeller. All figures are referenced from chapter 6 and are described fully in each caption.

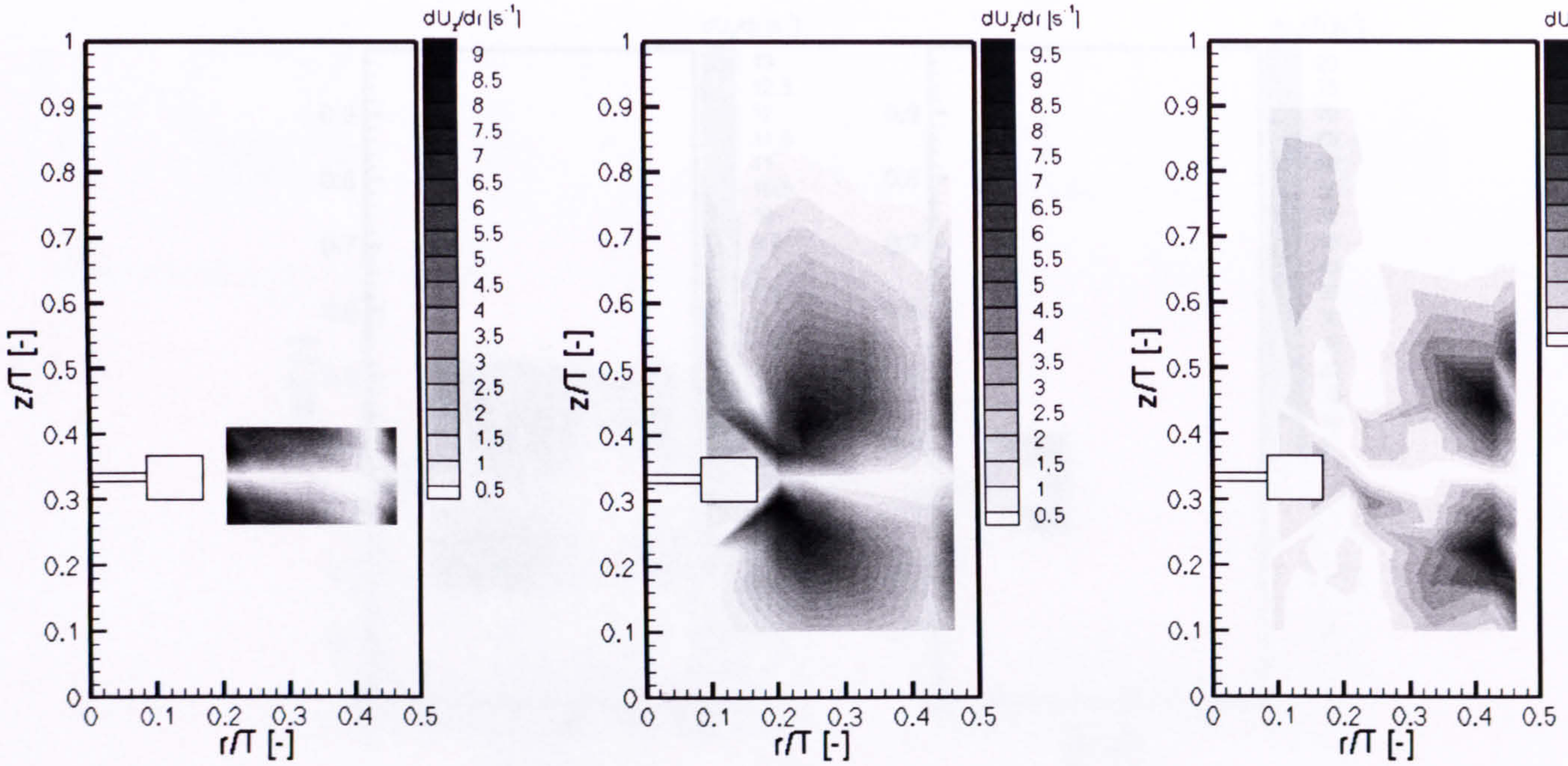

Figure C.1: Ensemble-average shear strain rate ($\partial U_z/\partial r$) distributions in the $\theta = 0^0$ plane. (a) Si100 at $Re = 50$; (b) PIB100 at $Re = 40$ and $De = 0.974$; (c) PIB100 at $Re = 240$ and $De = 5.84$.

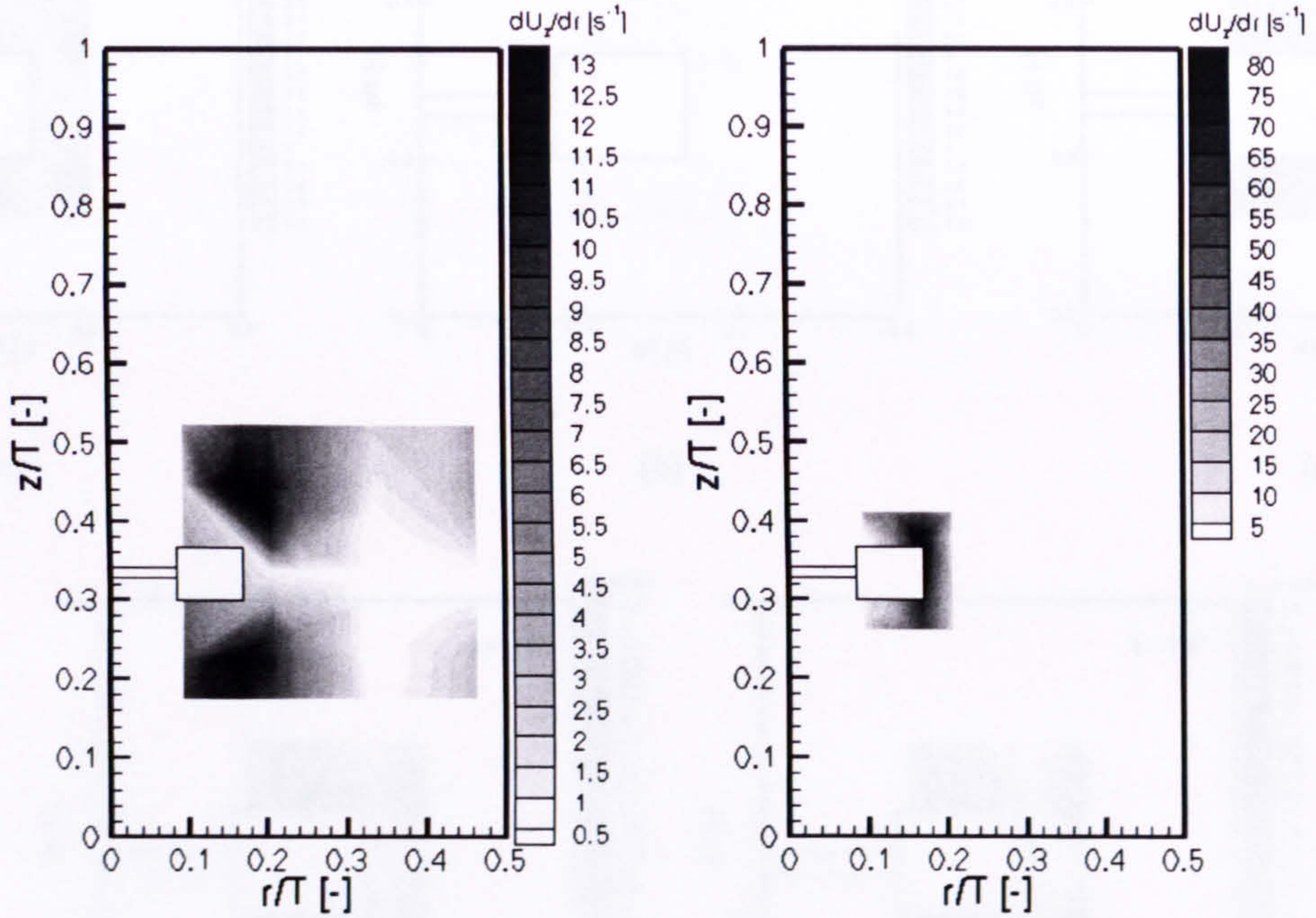

(a) (b)

Figure C.2: Ensemble-average shear strain rate ($\partial U_z/\partial r$) distributions in the $\theta = 0^0$ plane. (a) Si1000 at $Re = 10$; (b) PIB2000 at $Re = 13$ and $De = 107.481$.

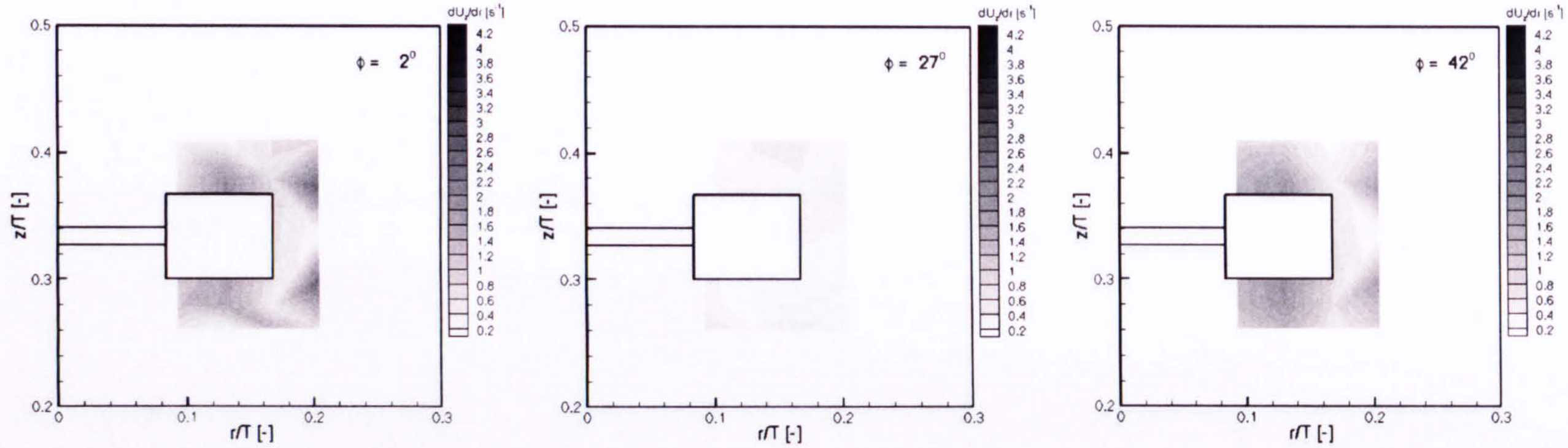

(a) (b) (c)

(d) (e)

Figure C.3: Phase-resolved shear strain rate distribution ($\partial U_z/\partial r$) for PIB2000 at $Re = 0.7$ and $De = 5.742$, in the $\theta = 0^0$ plane at $\phi = 2^0$, 27^0, 42^0, 52^0 and 55^0.

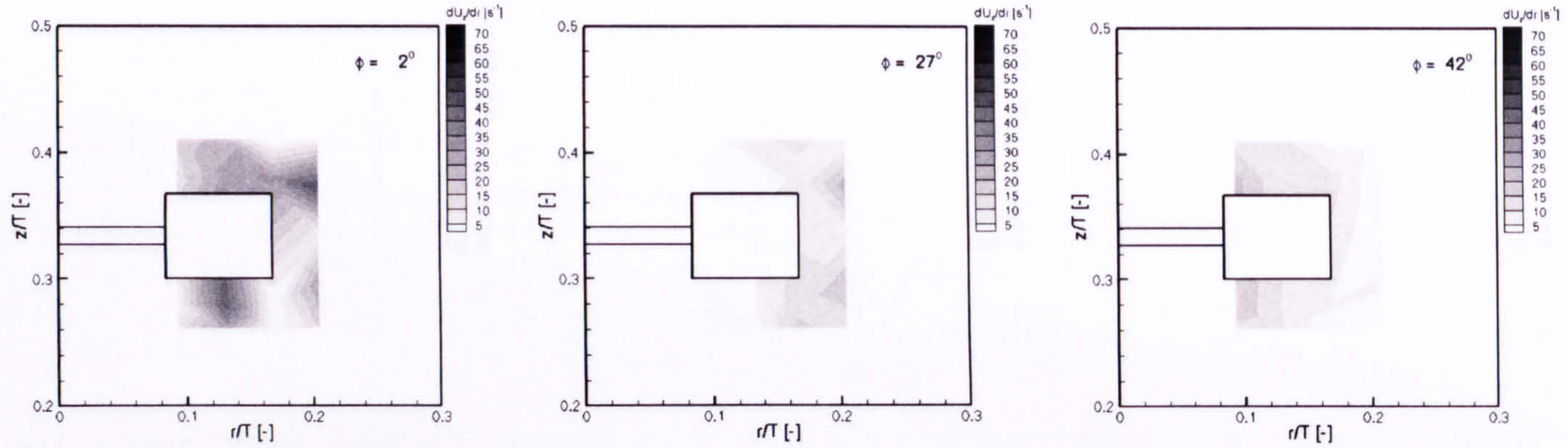

(a) (b) (c)

(d) (e)

Figure C.4: Phase-resolved shear strain rate distribution ($\partial U_z/\partial r$) for PIB2000 at $Re = 7$ and $De = 57.09$, in the $\theta = 0^0$ plane at $\phi = 2^0$, 27^0, 42^0, 52^0 and 55^0.

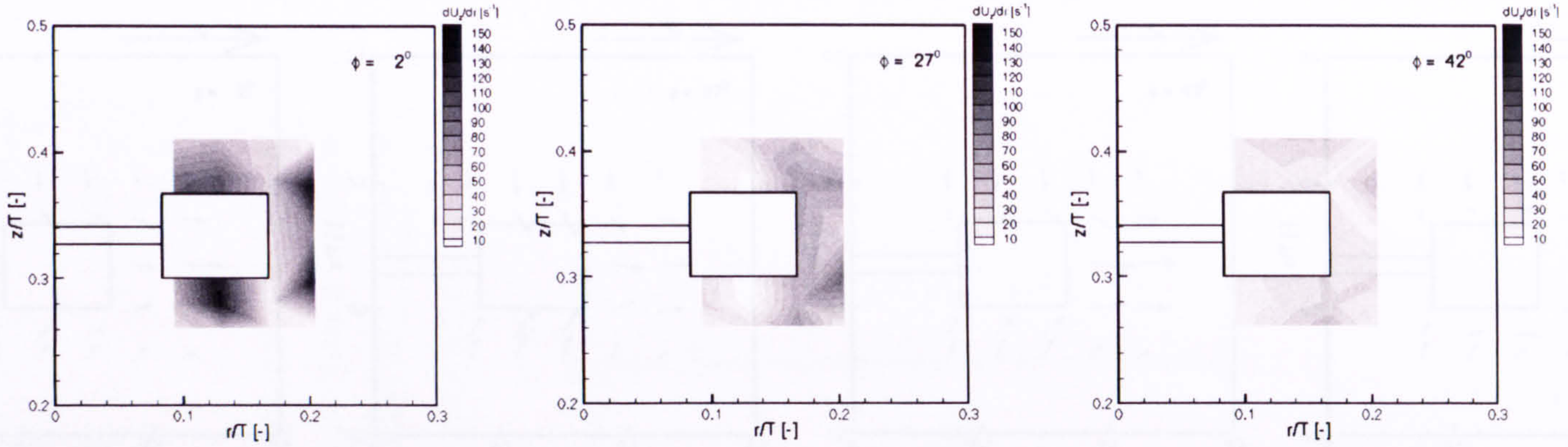

(a) (b) (c)

(d) (e)

Figure C.5: Phase-resolved shear strain rate distribution ($\partial U_z/\partial r$) for PIB2000 at $Re = 13$ and $De = 107.481$, in the $\theta = 0^0$ plane at $\phi = 2^0$, 27^0, 42^0, 52^0 and 55^0.

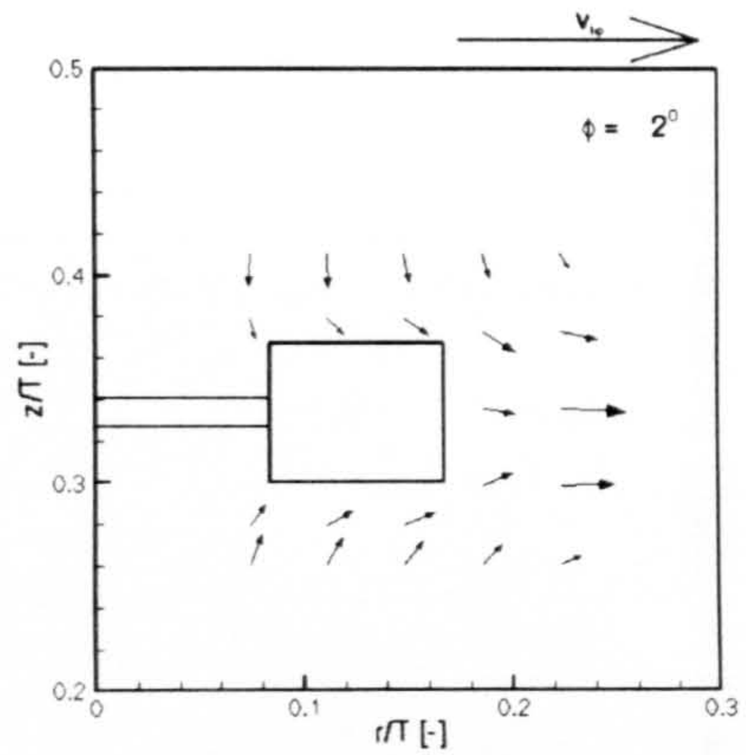

(a)

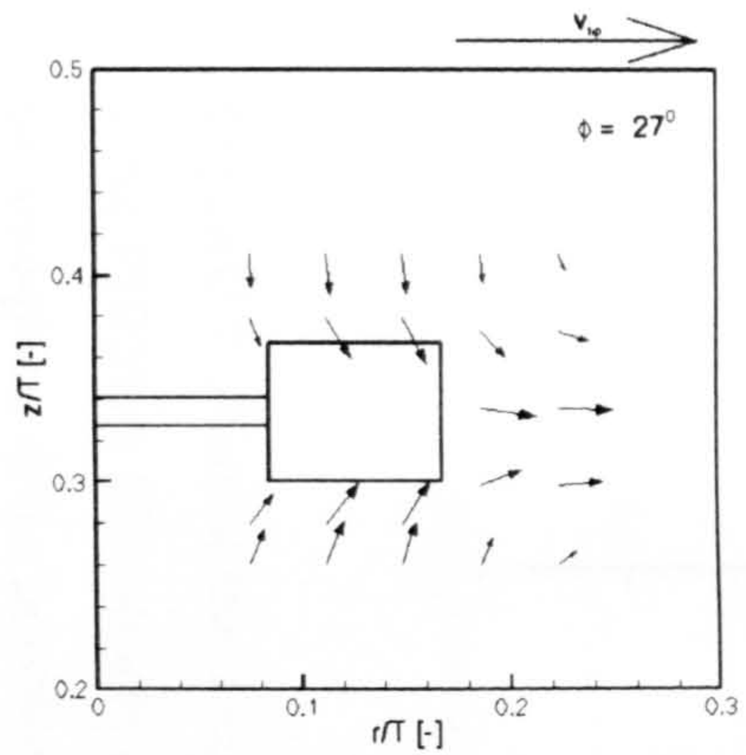

(b)

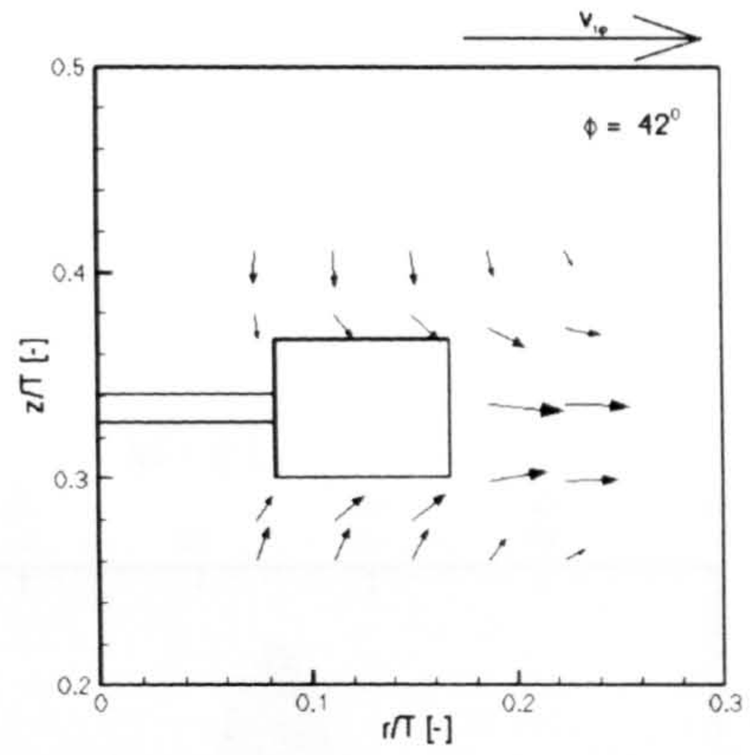

(c)

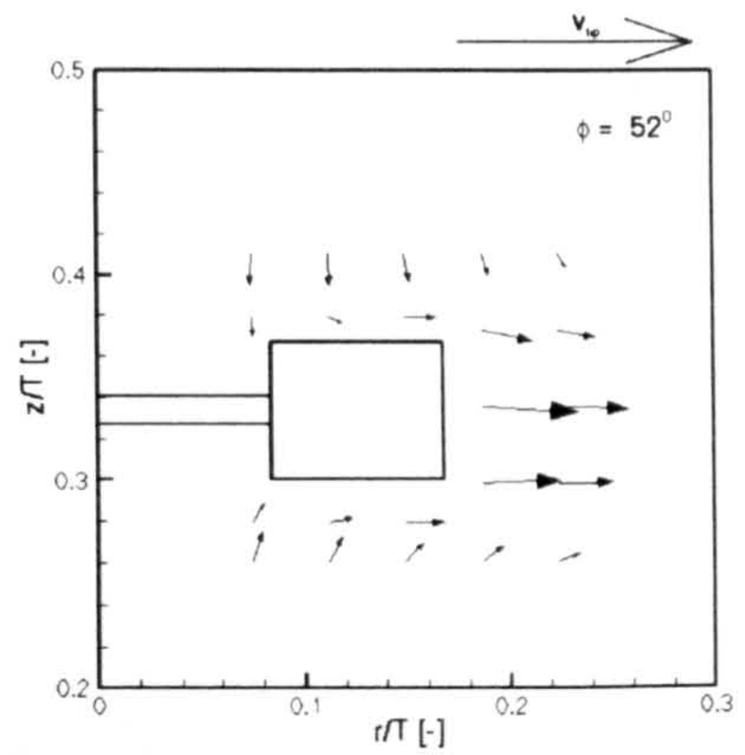

(d)

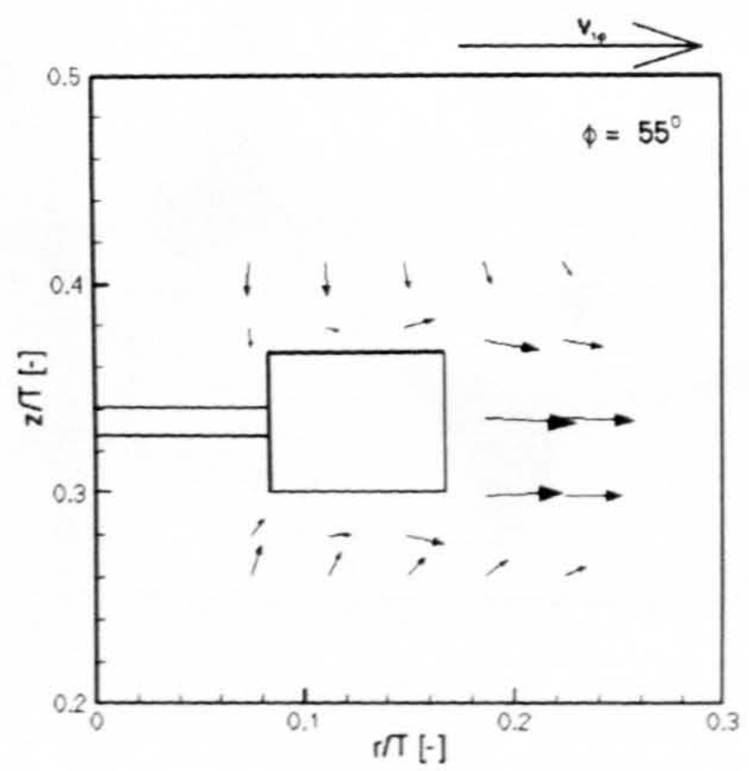

(e)

Figure C.6: Phase-resolved velocity vectors for Si1000 at $Re = 28$, in the $\theta = 0^0$ plane at $\phi = 2^0$, 27^0, 42^0, 52^0 and 55^0.

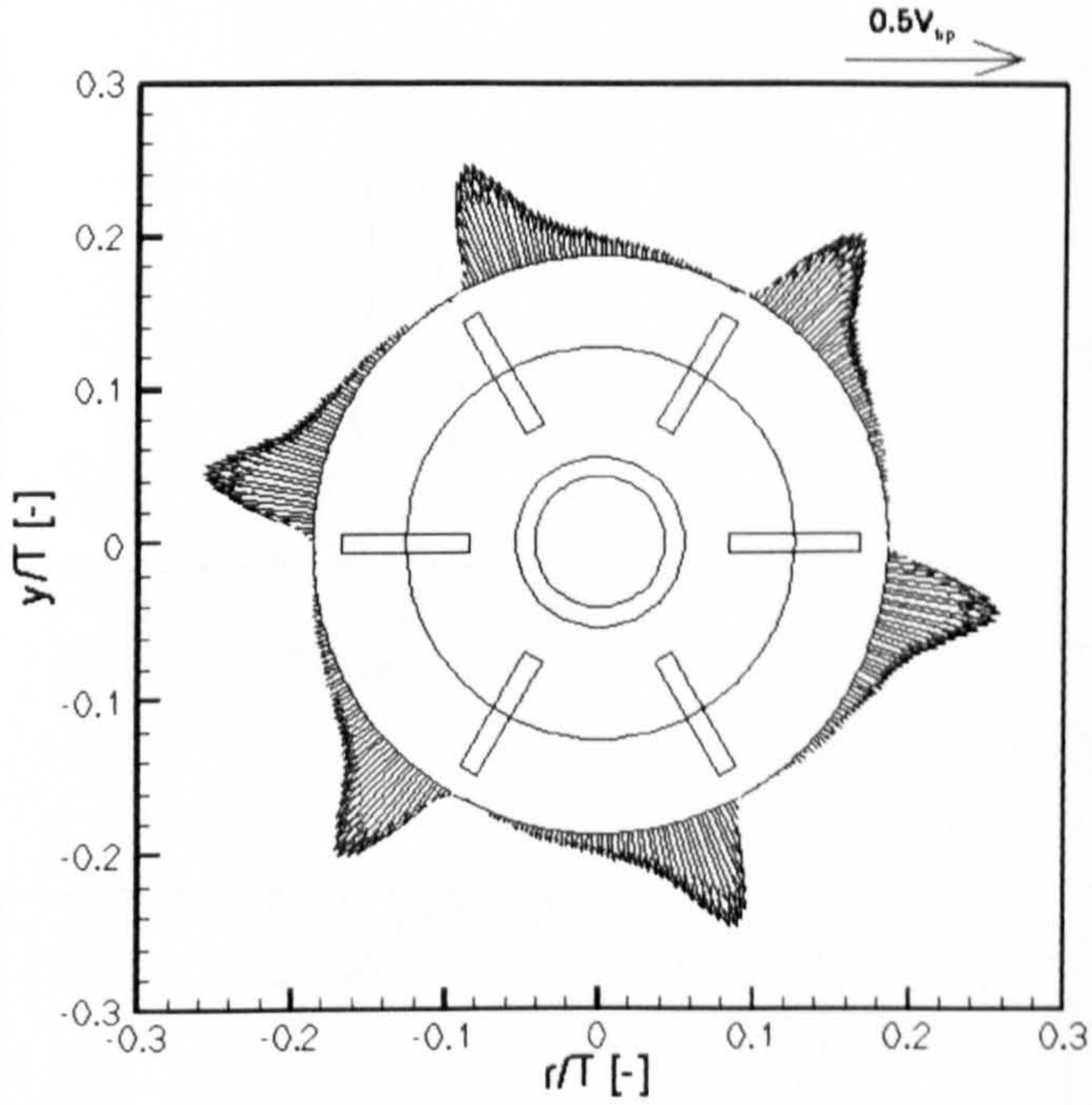

Figure C.7: Plots of the normalised radial velocity components (U_r/V_{tip}) at $Re = 7$, for PIB2000. The results are taken at an axial position equal to the height of the mid-plane of the impeller blade ($z/T = 0.333$) and at a radial position closest to the impeller blade, $r/T = 0.186$.

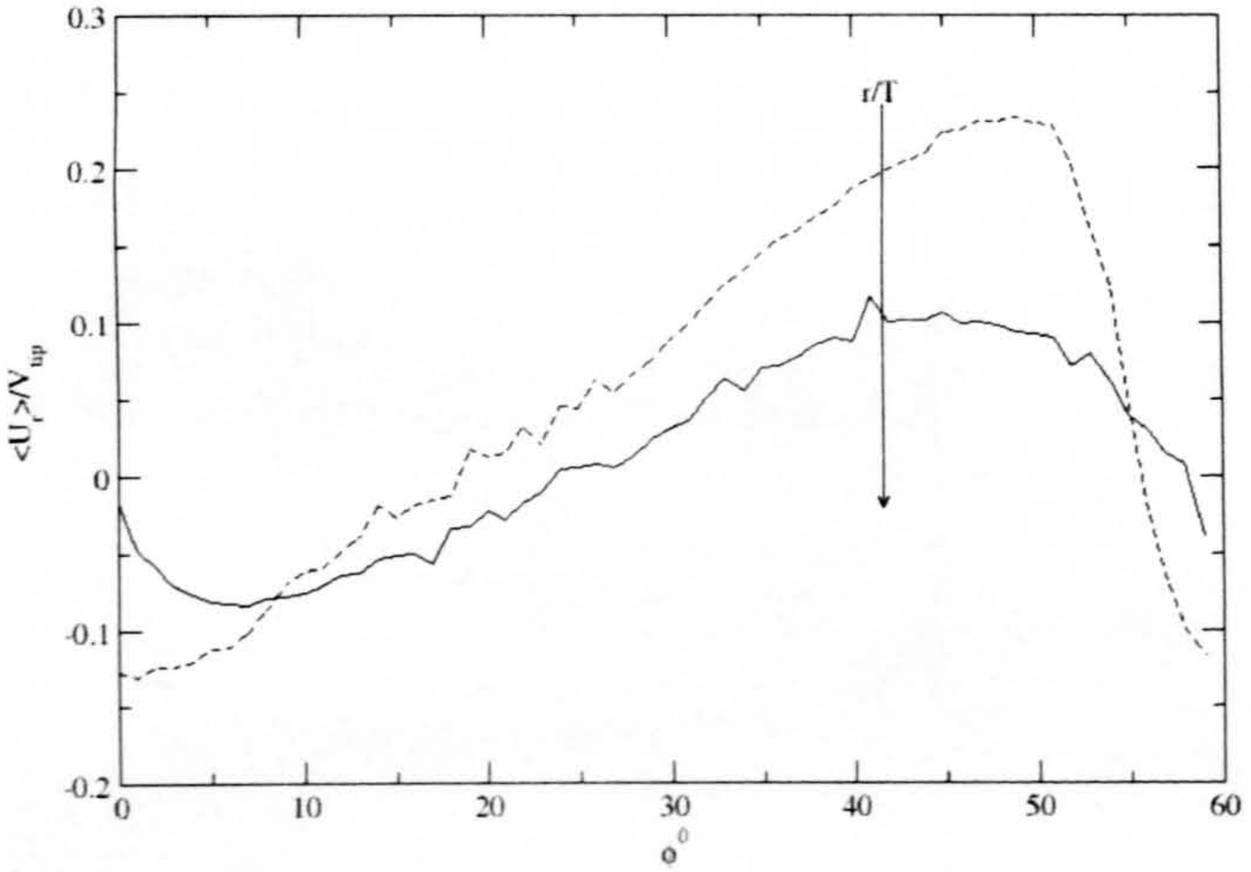

(a)

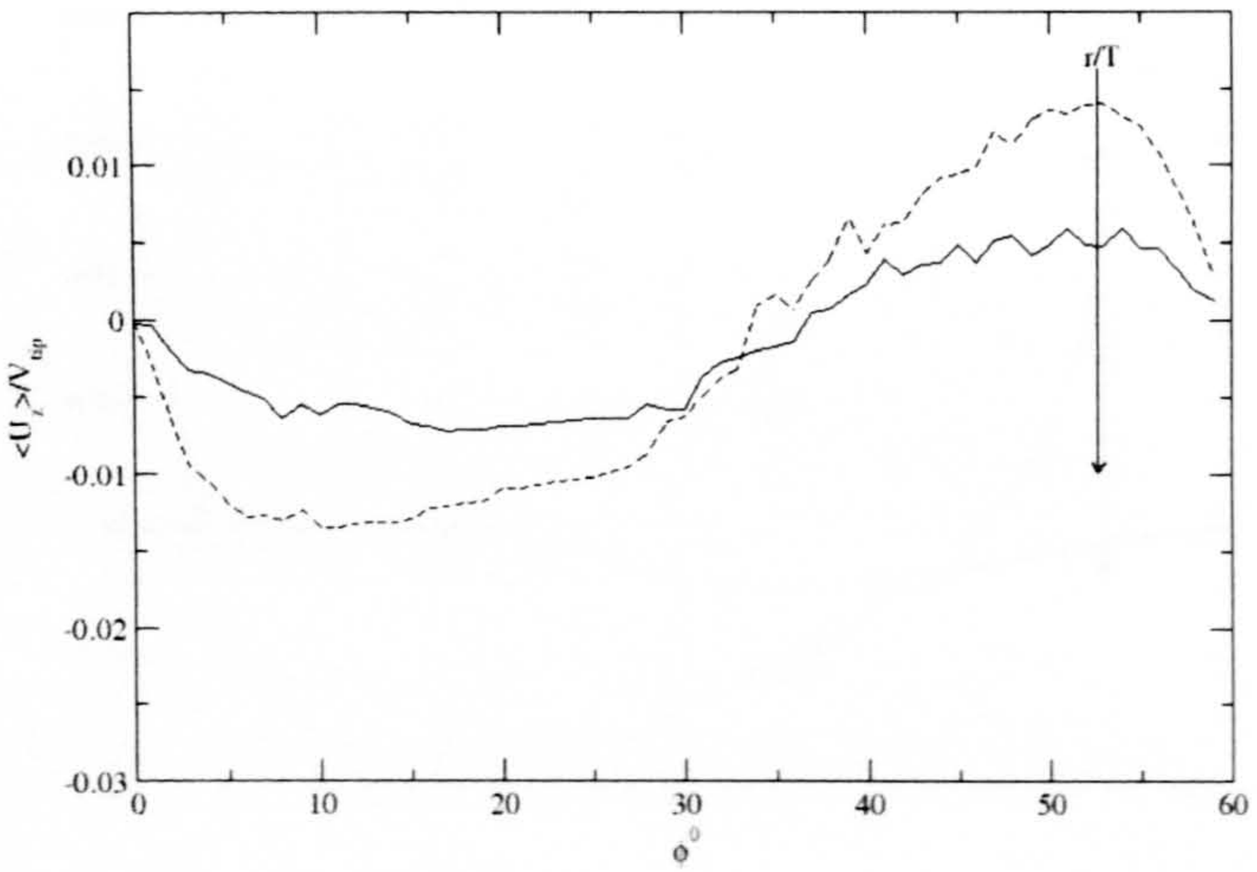

(b)

Figure C.8: Normalised radial and axial velocity components versus ϕ at $Re = 0.7$, for PIB2000. The axial positions of the curves all correspond to the centreline of the impeller blade ($z/T = 0.333$) while the radial positions correspond to $r/T = 0.186$ and 0.224, the value of which increases in the direction of the arrow.

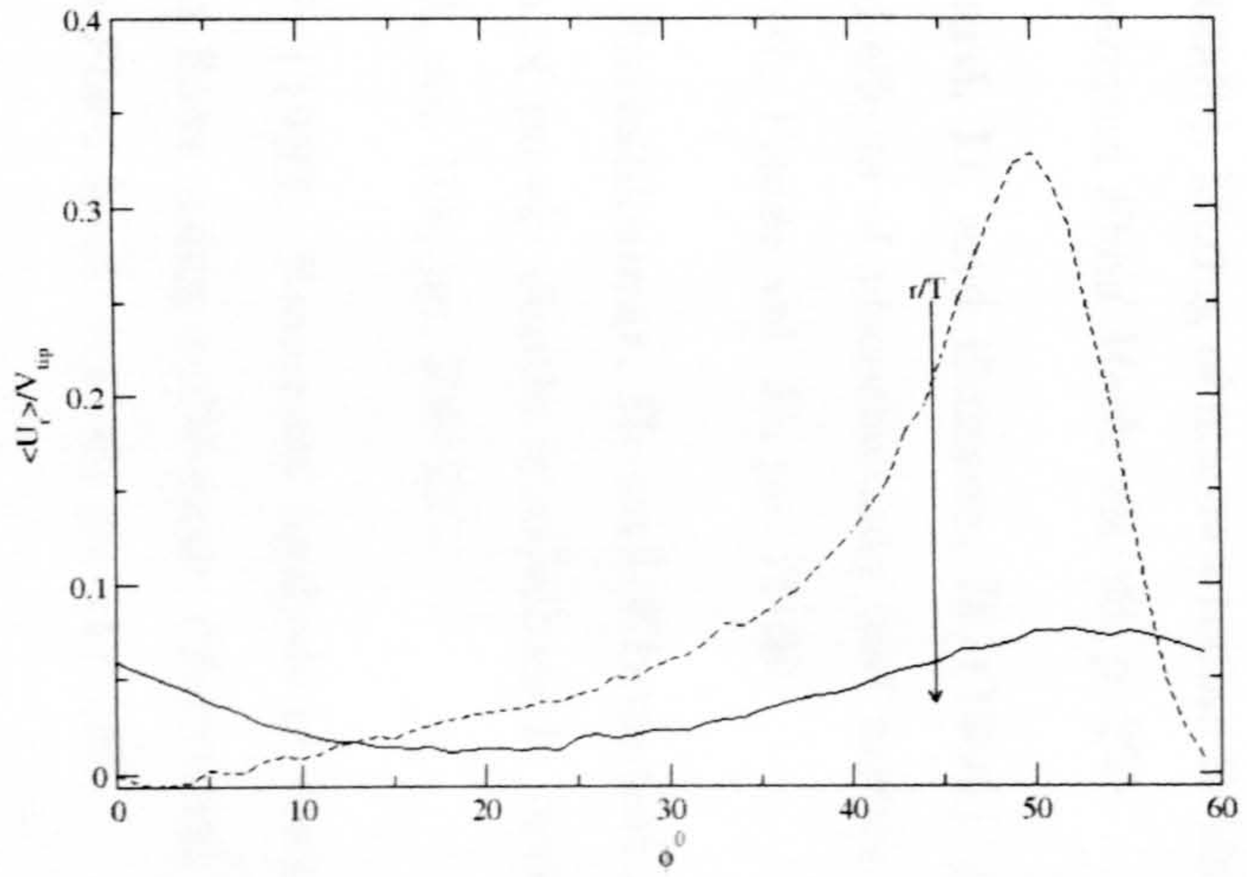

(a)

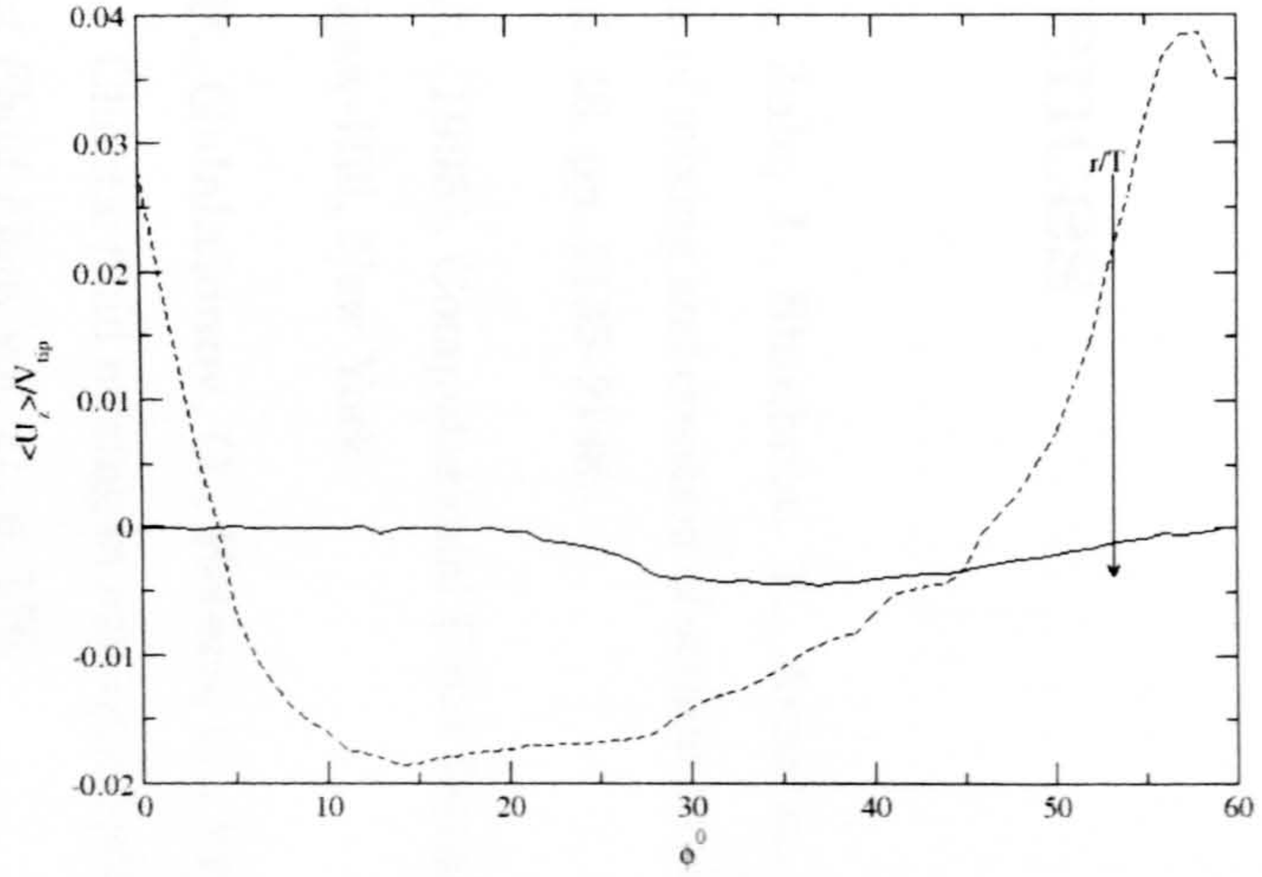

(b)

Figure C.9: Normalised radial and axial velocity components versus ϕ at $Re = 7$, for PIB2000. The axial positions of the curves all correspond to the centreline of the impeller blade ($z/T = 0.333$) while the radial positions correspond to $r/T = 0.186$ and 0.224, the value of which increases in the direction of the arrow.

References

Alvarez, M., Zalc, J., Shinbrot, T., Arratia, P. and Muzzio, F. (2002). Mechanisms of mixing and creation of structure in laminar stirred tanks. *AIChE Journal*, vol. 48, pp. 2135–2148.

Anderson, J. (1995). Computational Fluid Dynamics, the basics with applications. McGraw-Hill, New York.

Anderson, P., Galaktionov, O., Peters, G., van de Vosse, F. and Meijer, H. (2000a). Chaotic fluid mixing in non-quasi-static time-periodic cavity flows. *Int. J. Heat Fluid Flow*, vol. 21, p. 176.

Anderson, P., Galaktionov, O., Peters, G., van de Vosse, F. and Meijer, H. (2000b). Mixing of non-newtonian fluids in time-periodic cavity flows. *J.Non-Newtonian Fluid Mech*, vol. 93, p. 265.

Anne-Archard, D. and Boisson, H. (1995). A finite element simulation of the crossed-effects of viscoelasticity and inertia in an agitated vessel. *Int. J. Numer. Meth. Fluids*, vol. 21, pp. 75–90.

Arora, K., Sureshkumar, R. and Khomami, B. (2002). Experimental investigation of purely elastic instabilities in periodic flows. *J.Non-Newtonian Fluid Mech*, vol. 108, pp. 209–226.

Baaijens, F. (1993). Numerical analysis of start-up planar and axisymmetric contraction flows using multi-mode differential constitutive models. *J. Non-Newtonian Fluid Mech*, vol. 48, pp. 147–180.

Baaijens, F. (1994a). Non-isothermal viscoelastic flow past a cylinder. In Pro-

ceedings IUTAM symposium on numerical simulation of non-isothermal flows of viscoelastic liquids, the Netherlands, to be published.

Baaijens, F., Baaijens, H., Peters, G. and Meijer, H. (1994). An experimental and numerical investigation of a viscoelastic flow around a cylinder. *J. Rheology*, vol. 38, no. 2, pp. 351–376.

Baaijens, F., Selen, S., Baaijens, H., Peters, G. and Meijer, H. (1997). Viscoelastic flow past a confined cylinder of a low density polyethylene melt. *J. Non-Newtonian Fluid Mech*, vol. 68, pp. 173–203.

Baaijens, H., Peters, G., Baaijens, F. and Meijer, H. (1995). Viscoelastic flow past a confined cylinder of a polyisobutylene solution. *J. Rheology*, vol. 39, no. 6, pp. 1243–1277.

Baaijens, J. (1994b). Evaluation of constitutive equations for polymer melts and solutions in complex flows. Ph.D. thesis, Eindhoven University of Technology (EUT).

Baid, K. and Metzner, A. (1977). Rheological properties of dilute polymer solutions determined in extensional and shearing experiments. *Trans. Soc. Rheol*, vol. 21, pp. 237–260.

Baloch, A., Ding, D., Townsend, P. and Webster, M. (1992). Some transient studies of non-newtonian non-isothermal flows in two and three dimensions. In Proc. XI Int. Cong. Rheology, Theoretical and applied rheology, Brussels, pp. 250–252.

Barakos, G. and Mitsoulis, E. (1995). Numerical simulation of viscoelastic flow around a cylinder using an integral constitutive equation. *J. Rheology*, vol. 39, no. 6, pp. 1279–1292.

Bartels, P. (1988). An experimental study on turbulent mixing of viscoelastic fluids. Ph.D. thesis, Technische Universiteit Delft.

Benedict, L. and Gould, R. (1998). Concerning time and length scale estimates from burst-mode lda autocorrelation measurements. *Experiments in Fluids*, vol. 24, pp. 246–253.

Bertrand, F., Tanguy, P., Brito de la Fuente, E. and Carreau, P. (1999). Numerical modelling of the mixing flow of second-order fluids with helical ribbon impellers. *Computer methods in applied mechanics and engineering*, vol. 180, pp. 267–280.

Bird, R. B., Armstrong, R. C. and Hassager, O. (1987). Dynamics of polymeric liquids. Wiley-Interscience, New York.

Cambridge (2002). Rheometric data for PIB solutions, personal communication, Cambridge University.

Connelly, R. and Kokini, J. (2004). The effect of shear thinning and differential viscoelasticity on mixing in a model 2d mixer as determined using FEM with particle tracking. *J.Non-Newtonian Fluid Mech*, vol. 123, pp. 1–17.

Distlehoff, M., Laker, J., Marquis, A. and Nouri, J. (1995). The application of a strain gauge technique to measurement of the power characteristics of five impellers. *Exp. fluids*, vol. 20, pp. 56–58.

Dong, L., Johansen, S. and Engh, T. (1994). Flow induced by an impeller in an unbaffled tank. *Chem Eng Sci*, vol. 49, pp. 549–560.

Dou, H. and Phan-Thien, N. (1998). Parallelisation of an unstructured finite volume code with PVM: Viscoelastic flow around a cylinder. *J. Non-Newtonian Fluid Mech*, vol. 77, pp. 21–51.

Drain, L. (1980). The laser Doppler technique. John Wiley and Sons, Chichester.

Ducci, A. (2004). Direct measurement of the vicous dissipation rate of turbulent kinetic energy in a stirred vessel with two-point LDA. Ph.D. thesis, King's College London.

Durao, D., Laker, J. and Whitelaw, J. (1980). Bias effects in laser doppler anemometry. *J. Phys E: Sci Instrum*, vol. 13, p. 442.

Durrani, T. and Greated, C. (1977). Laser systems in flow measurement. Plenum Press, New York.

Durst, F., Melling, A. and Whitelaw, J. (1976). Principles and practice of laser Doppler anemometry. Academic Press.

Dyster, D., (graduate), E. K., Jaworski, Z. and (fellow), A. N. (1993). A LDA study of the radial discharge velocities generated by a Rushton turbine. *IChemE*, vol. 71, pp. 11–23.

Fan, Y., Tanner, R. and Phan-Thien, N. (2000). A numerical study of viscoelastic effects in chaotic mixing between eccentric cylinders. *J. Fluid Mech*, vol. 412, p. 197.

Fieser, L. (1962). Advanced organic chemistry. Chapman and Hall, London.

Galletti, C., Lee, K., Paglianti, A. and Yianneskis, M. (2004a). Reynolds number and impeller diameter effects on instabilities in stirred vessels. *AIChE*, vol. In Press.

Galletti, C., Paglianti, A. and Yianneskis, M. (2004b). Observations on the significance of instabilities, turbulence and intermittent motions on fluid mixing processes in stirred reactors. In Proc. ISMIP-5 conference, Seville, June 2004.

George, W. and Lumley, J. (1973). The laser-doppler velocimetry and its application to the measurement of turbulence. *J. Fluid Mech*, vol. 60, pp. 321–362.

Giesekus, H. (1982). A simple constitutive equation for polymer fluids based on the concept of deformation-dependent tensorial mobility. *J.Non-Newtonian Fluid Mech*, vol. 11, pp. 69–109.

Greene, H., Carpenter, C. and Casto, L. (1982). Mixing characteristics of an axial impeller with Newtonian and non-Newtonian fluids. In Fourth European Conference on Mixing, pp. 109–126.

Hartt, W. and Baird, D. (1996). The confined flow of polyethylene melts past a cylinder in a planar channel. *J.Non-Newtonian Fluid Mech*, vol. 65, pp. 247–268.

Harvey, A., West, D. and Tufillaro, N. (2000). Evaluation of laminar mixing in stirred tanks using a discrete-time particle-mapping procedure. *Chem Eng Sci*, vol. 55, p. 667.

Hockey, R. and Nouri, J. (1996). Turbulent flow in a baffled vessel stirred by a 60^0 pitched blade impeller. *Chem Eng Sci*, vol. 51, pp. 4405–4421.

Hockey, R., Nouri, J. and Pinho, F. (1989). Flow visualisation of Newtonian and non-Newtonian fluids in a stirred reactor. In Int. Symp. flow Visualisation, pp. 976–987.

Hoesel, W. and Rodi, W. (1977). New biasing elimination method for laser-doppler velocimeter counter processing. *Rev Sci Instrum*, vol. 48, p. 7.

Hulsen, M., Peters, E. and Van den Brule, B. (2000). Instationary eulerian viscoelastic flow simulations using time separable rivlin-sawyers constitutive equations. *J. Non-Newtonian Fluid Mech*, vol. 89, pp. 209–228.

Issa, R. (1986). Solution of the implicitly discretised fluid flow equations by operator-splitting. *Journal of computational physics*, vol. 62, pp. 40–65.

Jana, S., Tjahjadi, M. and Ottino, J. (1994). Chaotic mixing of viscous fluids by periodic changes in geometry: baffled cavity flow. *AIChE Journal*, vol. 40, p. 1769.

Kamiwano, M., Saito, F. and Kaminoyama, M. (1990). Velocity distribution and apparent viscosity of a pseudoplastic liquid in a stirred vessel. *International Chemical Engineering*, vol. 30, pp. 274–281.

Koutsakos, E., Nienow, A. and Dyster, K. (1990). Laser anemometry study of shear thinning fluids agitated by a Rushton turbine. In fluid mixing V, Bradford, UK, IChemE, symposium series No. 121, pp. 51–73.

Kumar, S. and Homsy, G. (1996). Chaotic advection in creeping flow of viscoelastic fluids between slowly modulated eccentric cylinders. *Phys. Fluids*, vol. 8, p. 1774.

Kuncewicz, C. (1992). Three-dimensional model of laminar liquid flow for paddle impellers and flat-blade turbines. *Chem Eng Sci*, vol. 47, pp. 3959–3967.

Lamberto, D. (1997). Enhancing laminar mixing in stirred tank reactors using dynamic flow perturbations. Ph.D. thesis, Rutgers University.

Lamberto, D., Alvarez, M. and Muzzio, F. (1999). Experimental and computational investigation of the laminar flow structure in a stirred tank. *Chem Eng Sci*, vol. 54, pp. 919–942.

Lamberto, D., Muzzio, F., Swanson, P. and Tonkovic, A. (1996). Using time-dependent RPM to enhance mixing in stirred vessels. *Chem Eng Sci*, vol. 51, p. 733.

Larson, R. (1988). Constitutive equations for polymer melts and solutions. Butterworths., Boston.

Larson, R. G. (1999). The structure and rheology of complex fluids. Oxford University Press, Inc., University of Michigan, Ann Arbor.

Lee, J. (2003). Rheometric measurements of PIB solutions, personal communication, King's College London.

Lee, K. (1995). An experimental investigation of the trailing vortex structure and mixing characteristics of stirred vessels. Ph.D. thesis, King's College London.

Leong, C. and Ottino, J. (1989). Experiments on mixing due to chaotic advection in a cavity. *J. Fluid Mech*, vol. 209, p. 463.

Leong, C. and Ottino, J. (1990). Increase in regularity by polymer addition during chaotic mixing in two-dimensional flows. *Phys. Rev. Lett*, vol. 64, p. 874.

Liu, A. (1997). Viscoelastic flow of polymer solutions around arrays of cylinders: Comparison of experiment and theory. Ph.D. thesis, Massachusetts Institute of Technology.

Liu, A., Bornside, D., Armstrong, R. and Brown, R. (1998). Viscoelastic flow of polymer solutions around a periodic, linear array of cylinders: comparisons of predictions for microstructure and flow fields. *J.Non-Newtonian Fluid Mech*, vol. 77, pp. 153–190.

Luo, X. (1996). A control volume approach for integral viscoelastic models and its application to contraction flow of polymer melts. *J.Non-Newtonian Fluid Mech*, vol. 64, pp. 173–189.

Manica, R. and De Bortoli, A. (2004). Simulation of sudden expansion flows for power-law fluids. *J.Non-Newtonian Fluid Mech*, vol. 121, pp. 35–40.

McLaughlin, D. and Tiederman, W. (1973). Biasing correction for individual realisation of laser anemometry measurements in turbulent flows. *Physics of Fluids*, vol. 6, p. 2082.

Melling, A. (1975). Investigation of flows in non-circular ducts and other configurations by laser doppler anemometry. Ph.D. thesis, Imperial College London, University of London.

Metzner, A. and Taylor, J. (1960). Flow patterns in agitated vessels. *AIChE*, vol. 6, pp. 109–115.

Metzner, A. and Whitlock, M. (1958). Flow behaviour of concentrated (dilatant) suspensions. *Trans. Soc Rheol*, vol. 2, pp. 239–254.

Micheletti, M. (2004). Study of fluid velocity and mixing characteristics in stirred solid-liquid suspensions. Ph.D. thesis, King's College London.

Mistubishi, N. and Hirai, N. (1969). Power requirements in the agitation of non-Newtonian fluids. *Journal of Chemical Engineering of Japan*, vol. 2, pp. 217–224.

Mitchell, A. and Griffiths, D. (1980). The finite difference method in partial differential equations. Wiley, Chichester.

Mitsoulis, E. (2004). On creeping drag flow of a viscoplastic fluid past a circular cylinder: wall effects. *Chem Eng Sci*, vol. 59, pp. 789–800.

Mompean, G. and Deville, M. (1997). Unsteady finite volume simulation of oldroyd-b fluid through a three-dimensional planar contraction. *J.Non-Newtonian Fluid Mech*, vol. 72, pp. 253–279.

Moore, I. and Cossor, G. (1995). Velocity distributions in a stirred tank containing a yield stress fluid. *Chem Eng Sci*, vol. 50, pp. 2467–2481.

Niederkorn, T. and Ottino, J. (1993). Mixing of a viscoelastic fluid in a time-periodic flow. *J. Fluid Mech*, vol. 256, p. 243.

Niederkorn, T. and Ottino, J. (1994). Chaotic mixing of shear-thinning fluids. *AIChE Journal*, vol. 40, p. 1782.

Nienow, A. (1997). On impeller circulation and mixing effectiveness in the turbulent flow regime. *Chem Eng Sci*, vol. 52, pp. 2557–2565.

Nienow, A., Wisdom, D., Solomon, J., Machon, V. and Vlcek, J. (1983). The effect of rheological complexities on power consumption in an aerated, agitated vessel. *Chem Eng Commun.*, vol. 19, pp. 273–293.

Nikiforaki, L., Montante, G., Lee, K. and Yianneskis, M. (2003). On the origin, frequency and magnitude of macro-instabilities of the flows in stirred vessels. *Chemical Engineering Science*, vol. 58, pp. 2937–2949.

Nouri, J. and Whitelaw, J. (1990a). Effect of size and confinement on the flow characteristics in stirred reactors. In fifth Int. symp. appls. laser techniques fluid mechanics, Lisbon, 9-12 July, p. 23.2.

Nouri, J. and Whitelaw, J. (1990b). Flow characteristics of stirred reactors with Newtonian and non-Newtonian fluids. *AIChE*, vol. 36, pp. 627–629.

Oliveira, P. and Pinho, F. (1999). Plane contraction flows of upper convected maxwell and phan-thien-tanner fluids as predicted by a finite-volume method. *J.Non-Newtonian Fluid Mech*, vol. 88, pp. 63–88.

Olsson, T. (1994). A solver for time dependent viscoelastic fluid flows. *J. Non-Newtonian Fluid Mech*, vol. 51, pp. 309–340.

OpenCFD (2004). OpenFOAM: Simulation software and consultancy. London.

Paul, E., Atiemo-Obeng, V. and Kresta, S. (2004). Handbook of industrial mixing. Wiley, New York.

Phan-Thien, N. and Dou, H.-S. (1999). Viscoelastic flow past a cylinder: drag coefficient. *Comput. Methods Appl. Mech. Engrg*, vol. 180, pp. 243–266.

Quinzani, L., Armstrong, R. and Brown, R. (1995). Use of coupled birefringence and LDV studies of flow through a planar contraction to test constitutive equations for concentrated polymer solutions. *J. Rheology*, vol. 39, no. 6, pp. 1201–1228.

Quraishi, A., Mashelkar, R. and Ulbrecht, J. (1977). Influence of drag reducing additives on mixing and dispersing in agitated vessels. *AIChE*, vol. 23, pp. 487–492.

Reed, X., Princz, M. and Hartland, S. (1977). Laser doppler measurements of turbulence in a standard stirred tank. In proc 2nd Eur conf on mixing, pp. B1.1–B1.26.

Rice, M., Hall, J., Papadakis, G. and Yianneskis, M. (2005). Investigation of laminar flow in a stirred vessel at low reynolds numbers. *Submitted to Chemical Engineering Science.*

Sasmal, G. (1995). A finite volume approach for calculation of viscoelastic flow through an abrupt axisymmetric contraction. *J.Non-Newtonian Fluid Mech*, vol. 56, pp. 15–47.

Skartsis, L., Khomami, B. and Kardos, J. (1992). Polymeric flow through fibrous media. *J. Rheology*, vol. 36, p. 589.

Smith, J. and Smit, L. (1988). Bhra fluid engineering, cranfield, england. In Proc. 6th Eur. Conf. on Mixing, Pavia, Italy, p. 297.

Smith, M., Joo, Y., Armstrong, R. and Brown, R. (2003). Linear stability analysis of flow of an oldroyd-b fluid through a linear array of cylinders. *J.Non-Newtonian Fluid Mech*, vol. 109, pp. 13–50.

Stasa, F. (1985). Applied finite element analysis for engineers. Holt, Rinehart and Winston, London.

Swanson, P. and Ottino, J. (1990). A comparative computational and experimental study of chaotic mixing of viscous fluids. *J. Fluid Mech*, vol. 213, p. 227.

Szady, M., Salamon, T., Liu, A., Bornside, D., Armstrong, R. and Brown, R. (1995). A new mixed finite element method for viscoelastic flows governed by differential constitutive equations. *J.Non-Newtonian Fluid Mech*, vol. 59, pp. 215–243.

Szalai, E., Arratia, P., Johnson, K. and Muzzio, F. (2004). Mixing analysis in a tank stirred with Ekato intermig® impellers. *Chem Eng Sci*, vol. 59, pp. 3793–3805.

Talwar, K. and Khomami, B. (1995). Flow of viscoelastic fluids past periodic square arrays of cylinders: inertial and shear thinning viscosity and elasticity effects. *J.Non-Newtonian Fluid Mech*, vol. 57, pp. 177–202.

Tatterson, G. (1991). Fluid mixing and gas dispersion in agitated tanks. McGraw-Hill, New York.

Tennekes, H. and Lumley, J. (1972). A first course in turbulence. MIT Press, Cambridge, Massachusetts.

Thakur, R., Vial, C., Djelveh, G. and Labbafi, M. (2003). Mixing of complex fluids with flat-bladed impellers: effect of impeller geometry and highly shear-thinning behaviour. *Chemical Engineering and Processing*, vol. In Press.

Thien, N. P. and Tanner, R. (1977). A new constitutive equation derived from network theory. *J.Non-Newtonian Fluid Mech*, vol. 2, pp. 353–365.

Ulbrecht, J. and Carreau, P. (1985). Mixing of viscous non-Newtonian liquids. In J.J. Ulbrecht and G.K. Patterson (Eds.), Mixing of liquids by mechanical agitation. Gordon and Breach Science Publishers, New York.

Van der Molen, K. and Van Maanen, H. (1978). Laser-Doppler measurements of the turbulent flow in stirred vessels to establish scaling rules. *Chem Eng Sci*, vol. 33, p. 1161.

Venneker, B. (1999). Turbulent flow and gas dispersion in stirred vessels with pseudoplastic fluids. Ph.D. thesis, University of Delft.

Verbeeten, W., Peters, G. and Baaijens, F. (2002). Viscoelastic analysis of complex polymer melt flows using the extended Pom-Pom model. *J.Non-Newtonian Fluid Mech*, vol. 108, pp. 301–326.

Verhelst, J. and Nieuwstadt, F. (2004). Viscoelastic flow past circular cylinders mounted in a channel: experimental measurements of velocity and drag. *J.Non-Newtonian Fluid Mech*, vol. 116, pp. 301–328.

Versteeg, H. K. and Malalasekera, W. (1995). Computational fluid dynamics. Prentice Hall, London.

Wapperom, P. and Renardy, M. (2005). Numerical prediction of the boundary layers in the flow around a cylinder using a fixed velocity field. *J.Non-Newtonian Fluid Mech*, vol. 125, pp. 35–48.

Yanta, W. (1973). Turbulence measurements with a laser-Doppler velocimeter. White Oak, Silver Spring, Report NOLTR 73-94.

Yianneskis, M., Popiolek, Z. and Whitelaw, J. (1987). An experimental study of the steady and unsteady flow characteristics of stirred reactors. *J. Fluid Mech*, vol. 175, p. 555.

Youcefi, A., Anne-Archard, D., Boisson, H. and Sengelin, M. (1997). On the influence of liquid elasticity on mixing in a vessel agitated by a two-bladed impeller. *J. Fluids Eng. (Trans. ASME)*, vol. 119, pp. 616–622.

Zalc, J., Szalai, E., Alvarez, M. and Muzzio, F. (2002). Using CFD to understand chaotic mixing in laminar stirred tanks. *AIChE*, vol. 48, pp. 2124–2134.